Luminescent and Paramagnetic Lanthanide Based Complexes as Biological Probes and Diagnostic Imaging Agents

Brian K. McMahon, B. Sc. (UCC)

March 2011

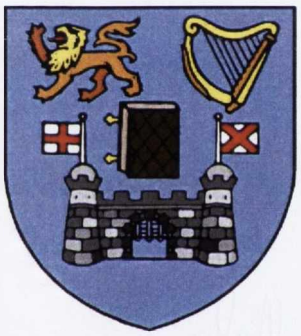

University of Dublin
Trinity College

Based on research carried out under the direction of
Prof. Thorfinnur Gunnlaugsson

A thesis submitted to the School of Chemistry, University of Dublin, Trinity College for the degree of Doctor of Philosophy

Declaration

This thesis is submitted for the degree of Doctor of Philosophy to the University of Dublin, Trinity College and has not been submitted before for any degree or examination to this or any other university. Other than where acknowledged, all work described herein is original and carried out by the author alone. Permission is granted so that the Library may lend or copy this thesis upon request. This permission covers only single copies made for study purposes, subject to normal conditions of acknowledgment.

I would like to dedicate this thesis to

Thank you for your endless patience and support

Acknowledgements

Firstly, I would like to thank my supervisor Prof. Thorri Gunnlaugsson for welcoming me into his research team and providing me with endless support and guidance throughout my PhD. From day one, his amazing enthusiasm and fascination with chemistry was evident, making my time within the TG group an extremely educational and above all enjoyable experience.

I would also like to thank our collaborators Prof. Clive Lee (RCSI), Dr. Colin McCoy (QUB), Dr. Dermot Brougham (DCU), Dr. Christian Kerskens (TCD) and Dr. Rustam Rakhmatullin (TCD) for all their help and advice over the years. Many of the achievements within this thesis would not have been possible without the generous use of their equipment.

I wish to thank all the staff members in the School of Chemistry, especially Dr. John O'Brien, Dr. Manuel Reuther and Dr. Martin Feeney for their assistance with characterisation. They were always happy to see yet another lanthanide cyclen complex!!!

To my new German friend Peter Mauer, I am very grateful for all your help. You managed to make the gruelling hours of cutting and grinding sheep bones enjoyable with the many stories about your wacky neighbours. I wish you the very best of luck on finishing your PhD and in your future years ahead.

To all past and present group members of the TG group; Gary, Niamh, Danny, Rebecca, Doireann, Jen, Christophe, Aline, Cidália, Emma, Sam, Swagata and Jon. Thanks for making the country boy's transition to the big smoke a whole lot easier. Ye were a great bunch of people to work with.

A massive thanks to everyone that helped in the proof reading of this thesis, especially Celia (The Bonnet) and Oxana. Even though ye were not in Ireland at the time, ye were never more then an email away. I am very grateful for all yer help.

To Rob (Boring Bob), Laura (Girthy), Elaine (Worf), Dawn (Donald) and Dave (Cranky Caffrey). What can I say? Thanks a million for everything guys. The daily banter made those tough days easier. Here is to many more eventful nights out. Bring them on!!!

To Steve, besides the millions of spectroscopic questions I have irritated you with over the years, thanks for the endless supply of chocolate. You have truly turned me into the MILKA man!!!

A big thanks to my buddy and housemate Aidan. You have definitely kept me sane over the last few years, reminding me that it will all be worth it in the end. No more THESIS talk in the apartment, that's a promise. Looking forward to the "submission party" now, whatever it may bring. Thanks to Lorraine, another great friend. I always looked forward to your trips to Dublin, even if it was like an episode of Questions and Answers!! (I'm not able ;-)). To the rest of the Dublin gang, keep those funny nights coming.

Finally, the biggest thank you has to go to my amazing family. From the beginning of my college years, I have had your constant support and encouragement, something I am truly grateful for. In appreciation, I would like to dedicate this thesis to you.

Abstract

This thesis entitled "Luminescent and Paramagnetic Lanthanide Based Complexes as Biological Probes and Diagnostic Imaging Agents" is divided into seven chapters. Chapter 1, the introduction, is divided into two sections. The first half begins with an introduction to luminescent sensing, detailing the advantages which the unique photophysical and magnetic properties of the lanthanide metal ions have to offer. In order to highlight the variety of potential applications of these metal ions, a review of some of the more recent lanthanide probes developed to date is presented. The remainder of Chapter 1 gives a brief introduction into the anatomy and physiology of bone structure, specifying the principle cause for microdamage formation. A review of the most recent histological stains developed for detection of damaged bone structure is also discussed, followed by a brief description of potential *in vivo* based microdamage detection methods.

Chapter 2 presents in detail the design, synthesis and photophysical evaluation of novel cyclen based Tb(III) and Eu(III) bone imaging agents. All systems allow for the incorporation of the microcrack specific iminodiacetate functionality within their overall structures and bear an antenna to allow for indirect excitation of the lanthanide metal. The effect of pH on the luminescent properties of these lanthanide complexes is investigated, with particular emphasis being placed on their response within the physiological pH window. A series of metal ion studies demonstrate that diamagnetic ions such as Ca^{2+}, Mg^{2+}, Cd^{2+} and Zn^{2+} have little effect on the emission properties of these complexes. However, for paramagnetic metal ions like Cu^{2+}, Hg^{2+}, Co^{2+} and Fe^{2+}, a quenching effect of the lanthanides luminescence is observed. The selectivity of these compounds for regions of damaged bone structure is highlighted using solid state bone studies, with a more intense emission response being observed at the damaged bone sites then that seen at the smooth healthy bone surfaces. An increase in selectivity for those complexes which bear a greater number of iminodiacetate chelating units within their ligand structure is also shown.

Chapter 3 begins by discussing the ability of the Eu(III) and Tb(III) imaging agents synthesised in Chapter 2 to allow for the selective detection of *in vitro* microscratches induced on the external surface of bovine bone material using epifluorescence and laser scanning confocal microscopy imaging techniques. Analysis of the images obtained confirm the solid state bone studies, with more efficient contrast gained with those complexes incorporating three iminodiacetate functionalities. The essential requirement of the iminodiacetate unit for microdamage detection was demonstrated by analysing a series of control lanthanide complexes which have their iminodiacetate groups protected as their

diethyl ester forms. Factors such as scratch depth and sample thickness were shown to have a significant effect on the contrasting abilities of these agents and must therefore be kept constant if limits of detection are to be determined. Using a bulk bone staining procedure, these agents were also successful in penetrating the bone matrix and selectively labelling regions of internal microdamage.

Chapter 4 begins by a brief introduction into the theory of Magnetic Resonance Imaging (MRI) concentrating on the use of Gd(III) based contrast agents for biomedical imaging. Complexation of the cyclen ligands synthesised in Chapter 2 with the paramagnetic Gd(III) metal along with the formation of two more Gd(III) complexes which do not incorporate an antenna functionality is described. All complexes demonstrate pH independence within the physiological pH window, with any significant changes in the relaxivity occurring in the acidic and basic regions of the pH scale. All MRI agents display very little modulation in their relaxivity in the presence of a range of metal ions, with the anion screening studies only displaying significant effect for the Gd(III) complex with a hydration state of two. A 7T animal MRI scanner is used in order to demonstrate the ability of these agents to selectively label and therefore provide a contrast of damaged bone structure.

Chapter 5 discusses the synthesis, characterisation and photophysical evaluation of a Tb(III) luminescent sensor, designed for the detection of biologically important thiols such as cysteine, homocysteine and glutathione in aqueous solution. The detection method used involves 1,4-Michael addition of the nucleophilic SH functionality to a maleimide unit incorporated within the complexes ligand structure. Saturation of the alkene double bond results in more efficient population of the Tb(III) excited state and a subsequent enhancement in its emission intensity. The ability of the Tb(III) complex to monitor the enzymatic conversion of oxidised glutathione to its reduced form using the nicotinamide adenine dinucleotide phosphate dependant enzyme glutathione reductase is also presented.

Chapter 6 presents a Tb(III) luminescent probe, which incorporates a phenyl iminodiacetate unit within its framework and subsequently allows for the detection of low levels of Cu^{2+} and Hg^{2+} ions. This complex signals the presence of both ions by means of a quenching effect of the Tb(III) luminescence. Although a similar quenching response is observed in the presence of Co^{2+}, Ni^{2+} and Fe^{2+}, this occurs at a slightly higher concentration then that observed for Cu^{2+} and Hg^{2+}, suggesting more efficient chelation of these ions within the iminodiacetate receptor unit.

Finally, Chapter 7 outlines the experimental parameters used, and presents the synthesis and characterisation of the compounds discussed within this thesis.

Abbreviations

a.u.	Arbitrary Units
AcOH	Acetic Acid
ADP	Adenosine Diphosphate
AFM	Atomic Force Microscopy
Ala	Alanine
AMP	Adenosine Monophosphate
Arg	Arginine
Asn	Asparagine
Asp	Aspartic Acid
ATP	Adenosine Triphosphate
AuNP	Gold Nanoparticles
b	Broad
BAPTA	1-2-bis(*o*-aminophenoxy)ethane-*N,N,N′,N′*-tetraacetic acid
BMMB	4,4'-bis(mercaptomethyl)benzophenone
BODIPY	Boron-dipyrromethene
BRU	Bone Remodelling Unit
CCD	Colour Video Camera
CN	Co-ordination Number
CPM	*N*-(4'-(7-diethylamino-4-methylcoumarin-3-yl)phenylmaleimide
cyclen	1,4,7,10-tetraazacyclododecane
Cys	Cysteine
d	Doublet
DCM	Dichloromethane
DMF	Dimethyl Formamide
DMSO	Dimethyl Sulfoxide
DNS	Dinitrobenzenesulfonyl
DOTA	1,4,7,10-tetraazacyclododecane-1,4,7,10-tetraacetic acid
DTPA	Diethylene Triamine Pentaacetic acid
DTT	1,4-Dithiothreitol
DXA	Dual-Energy X-ray Absorptiometry
EDTA	Ethylenediaminetetraacetic Acid
EDX	Energy Dispersive X-ray
Et_3N	Triethylamine

Equiv.	Equivalents
ES	Electrospray
ESMS	Electrospray Mass Spectrometry
ET	Energy Transfer
EtOAc	Ethyl Acetate
EtOH	Ethanol
FAD	Flavin Adenine Dinucleotide
Glu	Glutamic Acid
Gly	Glycine
GR	Glutathione Reductase
GSH	Glutathione (Reduced)
GSSG	Glutathione (Oxidised)
h	Hours
HA	Hydroxyapatite
Hcy	Homocysteine
HEPES	(4-(2-hydroxyethyl)-1-piperazineethanesulfonic Acid
Hex	Hexane
His	Histidine
HPLC	High Performance Liquid Chromatography
HRMS	High Resolution Mass Spectrometry
HSA	Human Serum Albumin
ICT	Internal Charge Transfer
IE	Intensity Enhancement
IR	Infrared
ISC	Intersystem Crossing
Leu	Leucine
Ile	Isoleucine
LMWTs	Low Molecular Weight Thiols
Ln	Lanthanides
Ln*	Lanthanide Excited State
LOD	Limits of Detection
Lys	Lysine
m	Multiplet
MALDI-TOF	Matrix Assisted Laser Absorption Ionisation - Time of Flight
MeCN	Acetonitrile

MeOH	Methanol
Met	Methionine
min	Minute
MLCT	Metal to Ligand Charge Transfer
MND	Motor Neurone Disease
M.P	Melting Point
MRI	Magnetic Resonance Imaging
NAC	*N*-Acetyl cysteine
NADPH	Nicotinamide Adenine Dinucleotide Phosphate
NIR	Near Infrared
NMR	Nuclear Magnetic Resonance
NMRD	Nuclear Magnetic Relaxation Dispersion
PBR	Peripheral Benzodiazepine Receptor
PeT	Positron Emission Tomography
PET	Photoinduced Electron Transfer
Phe	Phenylalanine
ppm	Parts Per Million
Pro	Proline
qt	Quaternary
q	Quartet
RBF	Round Bottom Flask
RF	Radio Frequency
room temp.	Room Temperature
ROS	Reactive Oxygen Species
s	Singlet
Sar	Sarcosine
SD	Standard Deviation
SEM	Scanning Electron Microscopy
Ser	Serine
S_NAr	Nucleophilic Aromatic Substitution
t	Triplet
TEAP	Tetraethyl Ammonium Hydroxide
Thr	Threonine
TLC	Thin Layer Chromatography
TLM	Transmitted Light Microscopy

TMS	Tetramethylsilane
TRIS	Tris(hydroxymethyl)aminomethane
Trp	Tryptophan
Tyr	Tyrosine
μCT	Micro-Computed Tomography
UV-vis	Ultra Violet-Visible
Val	Valine
WHO	World Health Organisation

Table of Contents

Chapter 4: *MRI Active Gd(III) Contrast Agents for Detection of Damaged Bone Structure*

Chapter 5: *Lanthanide Luminescent Thiol Sensor*

Publications

Selective Imaging of Damaged Bone Structure (Microcracks) Using a Targeting Supramolecular Eu(III) Complex As a Lanthanide Luminescent Contrast Agent

J. Am. Chem. Soc., **2009**, *131*, 17542-17543

Lanthanide luminescence sensing of copper and mercury ions using an iminodiacetate based Tb(III)-cyclen chemosensor
Tetrahedron Lett., **2010**, *51*, 5406-5410

Luminescent terbium contrast agent for bone microdamage detection
Aust. J. Chem , **2011**, *64*, 600-604

Chapter 1

Introduction

1.1 Introduction

Supramolecular chemistry is a rapidly growing area of science, with its foundations based on three key concepts: fixation, co-ordination and recognition. With roots extending not only into chemistry but also biological and physical sciences, this interdisciplinary field of science involves the formation of highly complex molecular systems through the association of two or more chemical species.[1, 2] Held together by intermolecular interactions such as electrostatic, hydrogen bonding, metal coordination, π-π stacking and van der Waals forces, these supramolecular systems have claimed their place in both material and biological sciences, with functionalities ranging from optical electronic devices[3, 4] and switches[5, 6] to the control and monitoring of complex cellular biological processes.[7]

The formal arrival of this new area of research began with Charles Pedersen, Donald Cram and Jean-Marie Lehn being awarded the 1987 Nobel Prize in chemistry for their involvement in the development and study of the cation binding abilities of crown ethers,[8] cavitands[9] and cryptands,[10, 11] respectively. Such recognition paved the way for the rapid development of many other types of macrocyclic and macropolycyclic ligands such as spherands, calixarenes,[12] cyclophanes[13] and cryptophanes,[14] all bearing the same principle; formation of host-guest complexes with little or no direct attachment *i.e.* no covalent linkage. Recent literature seems to concentrate on what is believed to be the most important concept of this growing field, molecular recognition.[15-17] Through a greater understanding of the host-guest relationship, the design of highly selective host species can be achieved, increasing the variety of applications of these supramolecular systems.

With this in mind, the main objective of this thesis is to expand on the knowledge of this relatively young field of chemistry, detailing the design, synthesis and evaluation of novel luminescent and magnetic supramolecular architectures with applications varying from metal ion recognition to diagnostic biological imaging of bone structure. In recent years, Gunnlaugsson and co-workers, as well as the groups of Parker, Pope, Bünzli, Faulkner *etc.* have focused a lot of their research efforts on bridging the fundamentals of supramolecular chemistry with the unique electronic properties of the lanthanide (Ln) metal ions resulting in the development of highly efficient luminescent signalling systems.[15-19] To allow the reader to gain a full appreciation of the material described within this thesis, it is necessary to briefly touch on all aspects detailed throughout, beginning with an introduction to luminescent sensing, explaining the advantages which the unique photophysical and magnetic properties of the Ln metal ions have to offer. In order to highlight the variation in the applications of these metal ions, a review of some of the more recent Ln probes developed to date will be given.

Another objective of this chapter is to illustrate the main diagnostic application of this PhD project by introducing the reader to the well-known bone related disease; osteoporosis. A general description of bone anatomy and the principle cause of this condition, microcrack formation, will be discussed. The final section will detail previous methods of microcrack visualisation, highlighting the progression which is occurring from the classical *in vitro* based histological staining to more advanced *in vivo* detection techniques.

1.2 Molecular sensors

Over the last few years, one of the main areas within the field of supramolecular chemistry has been the development of molecular sensors for the selective complexation of suitable guest species. In both chemical and biological systems, ions and molecules occur in abundance and as many of these play an important role in biological and chemical processes, the detection of such *in vitro* and *in vivo* is essential.[20] Although the majority of research has focused on the development of highly selective sensors for cations and neutral molecules, more recently a large emphasis has also been placed on anion detection.[21-23]

Sensors are divided broadly into two classes: biosensors and chemosensors. Devices incorporating biological receptors such as antibodies, aptamers or large biopolymers fall into the category of biosensors, whereas chemosensors utilise an abiotic or synthetic receptor for analyte recognition and thus transform chemical information into analytically useful signals.[24-26] Through careful design of artificial receptors, chemosensors can be tailored to overcome drawbacks such as sensitivity to pH and oxidising agents and their photophysical properties adjusted to meet specific requirements.[27-30]

The overall design of fluorescence chemosensors, depicted by the illustration in Figure 1.1, incorporates a recognition site and a signalling moiety with a communication mechanism between both. Fluorescent chemosensors were first designed with the receptor moiety being an integral part of the signalling unit. In these systems, referred to as *intrinsic* chemosensors (Figure 1.1a), direct interaction of the guest analyte with the fluorophore moiety resulted in subsequent modification of its emission properties. A more recent approach involves the separation of the host receptor unit from the signalling moiety *via* a covalently linked spacer group. Referred to as *conjugated* chemosensors (Figure 1.1b), this design has the advantage of independent optimisation of both the receptor and signalling unit, which when incorporated together can result in much more efficient and selective chemosensor development.

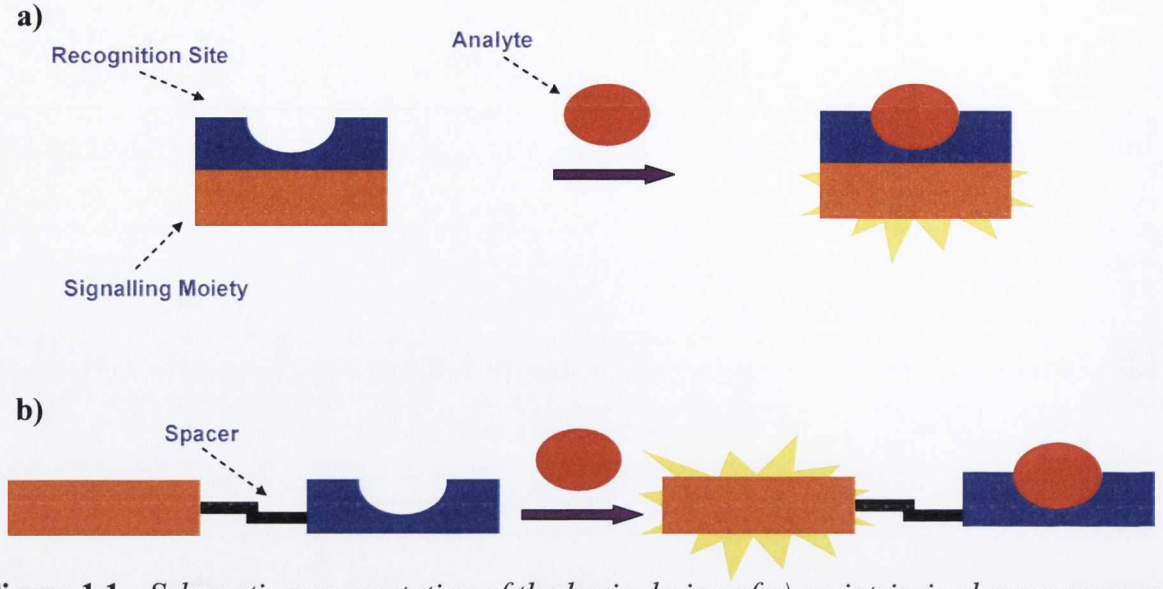

Figure 1.1: *Schematic representation of the basic design of a) an intrinsic chemosensor and b) a conjugated chemosensor.*

The role of the receptor moiety is to selectively and efficiently bind a guest/analyte, which can be dependent on factors such as ligand properties (ionic radius, co-ordination number and hardness, *etc.*) and the nature of the solvent (pH, ionic strength, polarity).[31] Once a guest/analyte is bound, the signalling component acts as a signal transducer, converting the recognition/binding event into an easily readable optical or magnetic response. In the case of fluorescent signalling responses, the two types of chemosensors which have gained a great deal of attention are photoinduced electron transfer (PET) and internal charge transfer (ICT) based chemosensors.[28, 32, 33] Recently the need for more advanced luminescent systems, which can be employed for more efficient online detection *in vivo,* sparked the development of sensors which bear long lived emission lifetimes. Such delayed emission has the advantage of overcoming the poor signal-to-noise ratio caused by short lived background emission (autofluoresence) and light scattering from the surrounding biological environment.[27] With their unique photophysical and magnetic properties, the Ln have been exploited to maximise their use as luminescent chemosensors and also as responsive contrast agents for magnetic resonance imaging (MRI).[34-36] As this thesis focuses exclusively on the use of these metal ions, the following sections will give a brief summary of their chemical and electronic properties, concentrating mainly on the magnetic and luminescent advantages they have to offer.

1.3 Lanthanide metal ions

The 15 elements from lanthanum (La) to lutetium (Lu), located in the *f* series of the periodic table are commonly known as *lanthanoids* (Ln). Characterised by the gradual filling

of their 4*f* orbitals which are well shielded by the outer core 5*s* and 5*p* subshells, these "rare earth elements" display similar chemical resemblance but differ greatly in their physical properties. Similarities in the chemical properties of the Ln metals result from the small and regular decrease in their ionic radii across the series, known as the Ln contraction.[37] Existing essentially in their trivalent state, Ln^{III}, and bearing a [Xe]4f^n electronic configuration, these 'hard' metal ions possess high charge densities and their bonding is electrostatic in nature. Ln ions display large and variable co-ordination numbers (CN = 6-12) with 8 and 9 often being the most common. As 'hard' acids, Ln ions show preferential binding to 'hard' bases such as oxygen, nitrogen or fluorine based ligands, rather than 'soft' bases such as phosphorous, sulphur, or iodine. In recent years, these unique features have led to an increased interest in the use of Ln complexes for a variety of different applications. For example luminescent Ln ions such as terbium (Tb(III)), europium (Eu(III)), samarium (Sm(III)) (visible emission) and more recently neodymium (Nd(III)), ytterbium (Yb(III)) and holmium (Ho(III)) (near-infrared (NIR) emission), have been used as diagnostic tools in biomedical analysis, shift reagents for NMR spectroscopy[38] and as luminescent labels for fluoroimmunoassays.[28] With the introduction of more advanced NMR imaging techniques, the development of metal based contrast agents, in particular gadolinium (Gd(III)) complexes, for medical MRI has occurred.[39] As Chapter 4 will give a more detailed description of the MRI theory, the following section will only briefly summarise the magnetic properties of the Ln ions, focusing more on the unique luminescent properties they have to offer.

1.3.1 Magnetic and luminescent properties of the lanthanides

All Ln ions are paramagnetic with the exception of La(III) and Lu(III). Amongst them Gd(III) bears a high electronic spin (S = 7/2) and due to its symmetric S-state, has a long electronic relaxation time T_{1e}. As a result, Gd(III) complexes are presently the most widely used MRI contrast agents in clinical practice.[39] In the absence of any contrast agent, the signal intensity observed within the body depends on factors such as the proton spin density and the water proton relaxation rates in the presence of a strong magnetic field. However, by the introduction of a Gd(III) based contrast agent within the body, an increase of both the spin-lattice ($1/T_1$) and spin-spin ($1/T_2$) relaxation rates of the water protons can occur, resulting in a signal enhancement in regions of the body in which the Gd(III) contrast agent has localised.[36] This relaxation rate enhancement occurs as a result of dipole-dipole interactions between the fluctuating local magnetic field caused by the 7 unpaired electrons of the Gd(III) ion and the nuclear spin of the water protons in close proximity. The ability of a contrast agent to alter $1/T_1$ or $1/T_2$ is represented quantitatively as relaxivity, r_1 or r_2,

respectively. As shown by Equation 1.1, proton relaxivity ($mM^{-1}s^{-1}$) is the change in relaxation rate after the introduction of the contrast agent ($\Delta(1/T_{1,2})$), normalised to the concentration of the contrast agent or metal ion [M].

$$r_{1,2} = \frac{\Delta(1/T_{1,2})}{[M]} \qquad \textbf{Equation 1.1}$$

Water molecules, which are directly bound to the Gd(III) ion and are therefore located within the first co-ordination sphere, feel the paramagnetic effect from the Gd(III) ion the strongest. These inner sphere water molecules can then exchange with bulk solvent molecules and result in a propagation of the paramagnetic effect to the bulk.[36] Depending on the rate of water/proton exchange, k_{ex}, the number of co-ordinated water molecules (q) and the metal to water proton distance (Gd-H), this inner sphere contribution can have a significant effect on a complex's overall relaxivity. There also exists an outer sphere contribution, which is due to random translational diffusion of the bulk solvent molecules, and results in the outer most water molecules moving in closer proximity to the paramagnetic centre.

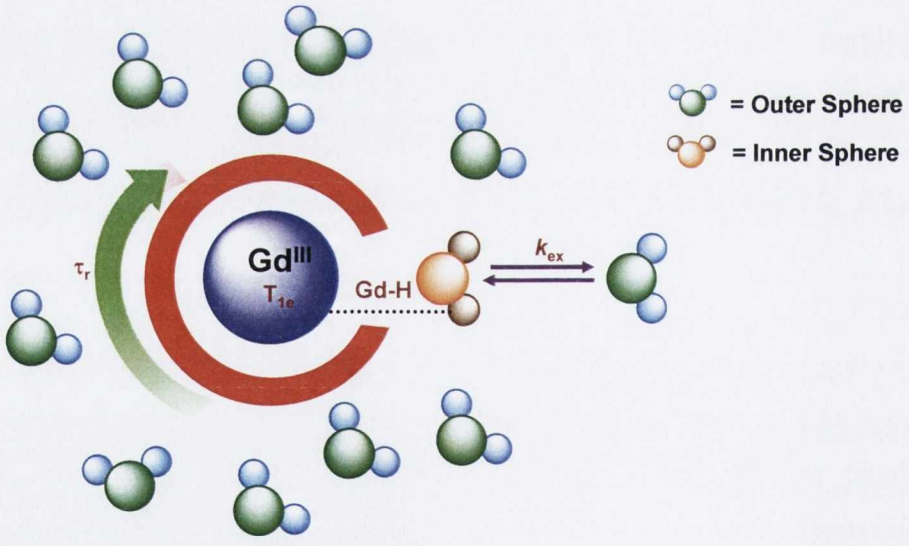

Figure 1.2: *Schematic representation of a Gd(III) complex highlighting all the major factors which affect its relaxivity value. (Redrawn)*[36]

The rotation of the complex in solution, which is characterised by the term rotation correlation time, τ_r, also plays a significant role in the MRI efficiency of the Gd(III) complex. Due to the relatively fast rotation of small molecular Gd(III) chelates, τ_r can often behave as the limiting factor for the complex's relaxivity (Figure 1.2). This observation has led to the development of larger molecular complexes such as dendrimer and polymer based conjugates

which have an enhanced relaxivity value due to a slower rotation in solution.[35] In summary, factors which have to be considered in the design of efficient Gd(III) based MRI imaging agents are the external field, the electronic properties of the Gd(III) ion, water exchange, molecular rotation, inner and outer sphere contribution and the metal to water proton distance.[36-38]

Along with the Ln magnetic properties, the unique photophysical properties that Ln ions possess, such as long wavelength emissions, sharp line-like emission bands and relatively long lived excited states (microseconds for Yb(III) and Nd(III) to milliseconds for Eu(III) and Tb(III)), makes them attractive for application in time-gating procedures (Figure 1.3a).[32] As previously mentioned in Section 1.2, this enables Ln luminescence to be clearly distinguished from the much shorter lived (sub-microseconds) autofluorescence of biological material giving a much improved signal-to-noise ratio. As a result, Ln emission is often referred to as 'delayed luminescence'.

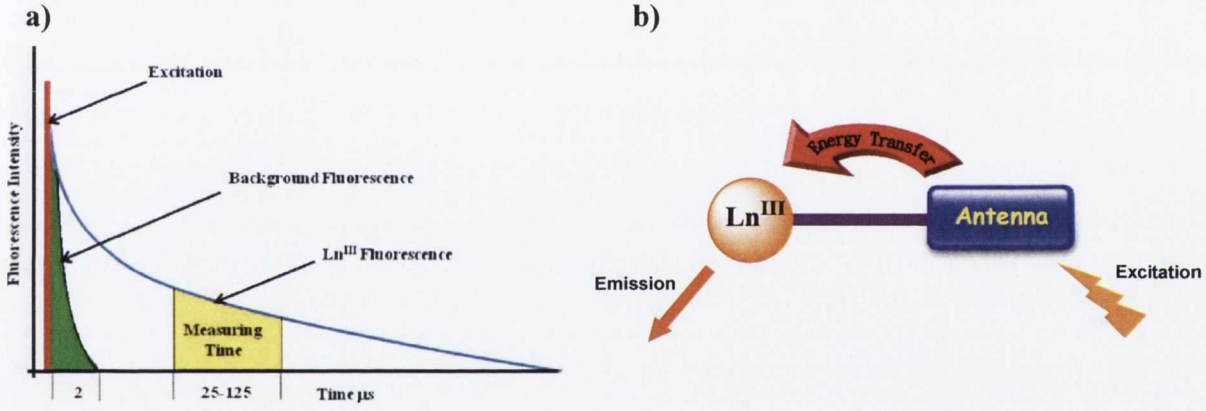

Figure 1.3: *Graphical representation of a) the time-gating procedure displaying the long lived emission of the Ln ions and b) the indirect excitation process of the Ln metal ion centre.*[40]

Nevertheless, in order to maximise the capability of Ln luminescence *in vivo*, their drawbacks must be recognised and the subsequent re-design of potential co-ordinating ligands carried out to help overcome these obstacles. For example, the Laporte-forbidden nature of their *f-f* transitions, results in weak absorption, with extinction coefficients of less than 4 $M^{-1}cm^{-1}$.[34, 40, 41] As a result, unless a laser excitation source or a high ion concentration is used, direct excitation of these photophysically "silent" ions rarely yield highly luminescent sensors. One method used to overcome this problem is the indirect excitation of the Ln ion *via* the "antenna effect".

As illustrated in Figure 1.3b, this involves an intramolecular energy transfer process from a sensitising chromophore, or antenna to the Ln metal ion centre.[41-43] Through careful incorporation of an antenna moiety into a suitable coordinating ligand, successful population

of the Ln excited state can be achieved. The antenna moieties used for the sensitisation of the Ln ion usually consist of well-known aromatic systems, however, more recently an interest in the use of transition metals as the excitation source has developed.[44, 45] Such systems, like the mixed Ln – Ru(II) based self assemblies developed by the Gunnlaugsson group, allow for efficient indirect excitation of visible and NIR emitting Ln, using the metal to ligand charge transfer (^{3}MLCT) band of the Ru(II) metal. These types of bimetallic systems help exploit a region of the electromagnetic spectrum which is of great current interest, especially in the field of biomedical diagnostics.[46, 47]

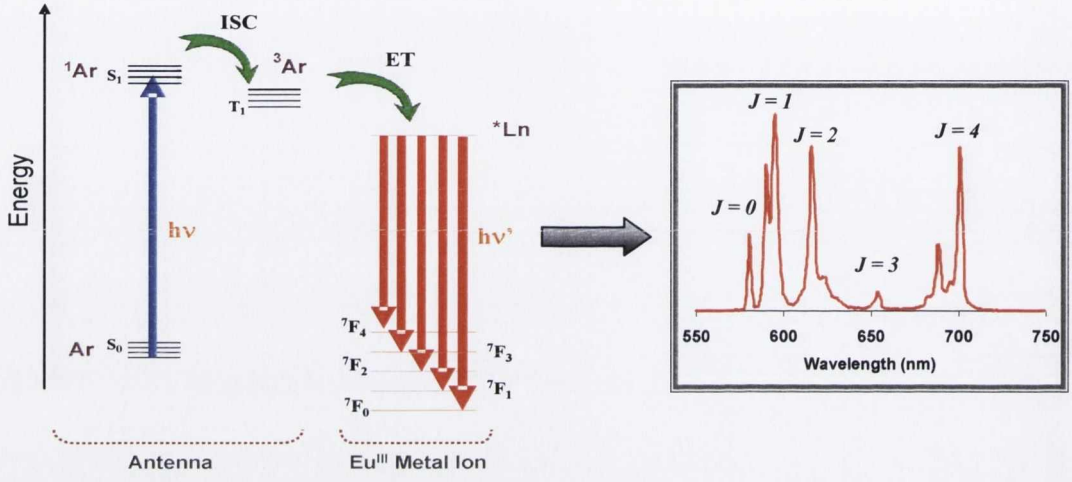

Figure 1.4: *a) Jablonski diagram illustrating sensitisation of a Ln ion by an antenna and b) the characteristic Eu(III) emission spectra which can occur as a result.*[15]

The process by which the photophysical emission from a Ln ion is produced using a simple aromatic antenna (phenyl or naphthyl chromophore), can be summarised in a Jablonski diagram (Figure 1.4). The ground state sensitising aromatic antenna (Ar) is excited to its singlet excited state (^{1}Ar) when absorption of a photon ($h\nu$) of a suitable wavelength occurs. This energy can be transferred into the antenna's triplet state (^{3}Ar) *via* a spin forbidden process known as intersystem crossing (ISC). Due to the presence of the Ln ion, a heavy atom, significant amounts of spin-orbit coupling occur which make this spin forbidden process possible. Provided that the energy of the triplet state lies at least 1700 cm^{-1} above the accepting Ln energy level, subsequent population of the Ln excited state (*Ln) will occur *via* an intramolecular energy transfer (ET) process. This requirement prevents any unwanted thermally activated back-energy transfer to the ^{3}Ar state which would occur if the energy gap was too small. However, a compromise must be met, as if the energy distance between both levels is too large, successful population of the *Ln state would be hindered. Upon efficient *Ln excitation, the energy can then be lost from the Ln metal through emission of light ($h\nu'$), resulting in the characteristic Ln emission spectra, as shown for the Eu(III) ion in Figure 1.4. Eu(III) and Tb(III), the two most rigorously studied emissive Ln metal ions have their *Ln

states ($^5D_0$ and $^5D_4$) lying at 17200 cm^{-1} and 20500 cm^{-1}, respectively. Therefore, chromophores which have their excited state 1700 cm^{-1} above these values, such as bipyridines, terpyridines, substituted phenyls, and naphthyl groups are favoured.[34, 41]

The spectrum shown in Figure 1.4 consists of five intense emission bands, arising from transitions from the $^5D_0$ excited state to the ^7F_J (J = 0, 1, 2, 3, 4) ground levels of the Eu(III) ion. For the case of the Tb(III) metal ion, transitions from the $^5D_4$ emissive state to the ^7F_J (J = 6, 5, 4, 3) ground levels result in four main emission bands. Depending on the Ln complex under study, some fine structure can occur in their emission bands, which is due to the loss of degeneracy of the J levels. The extent to which the degeneracy is removed depends on the symmetry of the metal environment, where complete loss, giving $2J+1$ non-degenerate bands, only occurs when the symmetry of the complex is extremely low. [42]

Two accepted mechanisms exist to describe the energy transfer process which occurs from the ^{3}Ar excited state of the antenna to the Ln excited state. Firstly, the Dexter (or exchange) mechanism is a non-radiative energy transfer process involving a double electron exchange between the excited state of the sensitising antenna and the Ln metal ion. This is a short range process as it requires efficient orbital overlap between the donor (antenna) and acceptor (Ln) species. This through bond interaction displays an e^{-r} dependency, where r is the distance between the sensitising antenna and the Ln metal ion.[37, 48] An alternative approach, known as the Förster (or dipole-dipole) mechanism involves the coupling of the dipole moment associated with the ^{3}Ar excited state of the antenna and the dipole moment of the 4*f* orbitals of the Ln ion. This energy transfer process occurs through space and has a r^{-6} distance dependence.[49] The efficiency of both mechanisms can be enhanced by decreasing the distance between the sensitising antenna moiety and the Ln metal centre.

It must be understood that there exists a number of other non-radiative and radiative pathways, not shown in the Jablonski diagram in Figure 1.4a, which are in constant competition with the successful population of the Ln excited state.[34, 41, 50] Such pathways involve:

- Radiative deactivation of the ^{1}Ar singlet excited state to the Ar ground state resulting in molecular fluorescence.
- Radiative deactivation of the ^{3}Ar triplet excited state to the Ar ground state by the spin forbidden transition $^3Ar \rightarrow Ar$ resulting in molecular phosphorescence.
- Non-radiative decay of the ^{1}Ar singlet excited state through collisions and vibrational interactions with surrounding molecules.
- Quenching of the ^{3}Ar triplet excited state by interactions with molecular oxygen.

- Non-radiative decay of the Ln excited state through vibrational interactions with other molecules, such as water.

In order to maximise the population of the Ln excited state and thus obtain highly emitting Ln based sensors, these competitive pathways must be controlled through careful ligand design allowing efficient ISC and ET processes to occur. This will ensure that the lifetimes of the ^{1}Ar and ^{3}Ar excited states are short, therefore minimising the effects of any other deactivation mechanism. As previously mentioned, the presence of the heavy Ln metal ion in these systems will promote spin-orbit coupling and enhance the efficiency of the ISC process, whereas, reduction in the distance between the antenna and the Ln metal centre, r, will ensure that the lifetime of the ^{3}Ar excited state is short due to effective ET to the *Ln state. The long lifetime of the Ln excited state and its vulnerability to vibrational quenching, mainly by O-H but also other high frequency oscillators (N-H and C-H), is also of major concern and will therefore be discussed in more detail in the following section.

1.3.2 Lanthanide luminescent quenching

One of the main deactivation pathways associated with Ln luminescence is the vibrational quenching by metal bound H_2O molecules. This occurs as a result of energy transfer from the Ln excited state into energy matched O-H stretching vibrations. Horrocks *et al.*[51, 52] were the first to propose an empirical method to calculate the number of O-H oscillators directly bound to the metal ion (q value) for a variety of Eu(III) complexes. This method was based on the assumption that, in deuterated water, the O-D oscillators contribute little to the deactivation process of the excited state and that all other deactivation pathways are the same as in H_2O.[53] Therefore, by recording the luminescent lifetimes (τ) of the Ln excited state both in H_2O and D_2O, the difference can be used as a determination of the q value. Studies carried out by Parker and co-workers[54] led to a refinement of Horrock's equations by taking into account not only the deactivation by O-H, but also deactivation by N-H oscillators. Equation 1.2 and 1.3 are now commonly used for Eu(III) and Tb(III) complexes respectively.

$$q(Eu(III)) = A[(1/\tau_{H2O}-1/\tau_{D2O})-0.25-0.075x] \pm 0.5 \qquad \textbf{Equation 1.2}$$

$$q(Tb(III)) = A[(1/\tau_{H2O}-1/\tau_{D2O})-0.06] \pm 0.5 \qquad \textbf{Equation 1.3}$$

In these equations, **A** is referred to as the proportionality constant and is specific for a given Ln ion. It is a measure of the degree of quenching from the metal bound H_2O

molecules for a particular Ln metal. For Eu(III) and Tb(III), **A** is 1.2 ms and 5.0 ms, respectively. The correction terms of -0.025 and -0.06 represent quenching by second sphere H_2O molecules, whereas -0.075x represents the quenching effect due to N-H oscillators (**x** is the number of these N-H oscillators directly bound to the metal). More recently, Supkowki *et al.*[55] carried out further refinement on Equation 1.2, which resulted in a smaller error of ± 0.3 being obtained, however, this was found only to be suitable for complexes with a large number of metal bound water molecules, *e.g.* ≥ 5.

As the rate of luminescence quenching was found to be proportional to the *q* value, focus has been directed to the synthesis of a variety of thermodynamically and kinetically stable polydentate co-ordinating ligands for the development of Ln complexes where the high co-ordination requirement of the Ln ion is fulfilled.[39, 50, 56, 57] The next section will detail some examples of these types of ligands, focusing on macrocyclic systems based on the 1,4,7,10-tetraazacyclododecane (cyclen) framework.

1.4 Lanthanide macrocyclic complexes

In order for the Ln metal to form stable complexes in aqueous solution, the co-ordinating ligand must consist of several donor atoms which satisfy the hard, polarising nature of these metal ions. The principle idea behind the initial design of macrocyclic ligands was to use pre-organised cavities (*e.g.* crown ethers and cryptands), which bear several donor atoms capable of metal interaction and contain a cavity diameter that is well adapted to the size of the metal ion. Such organisation ensures a minimal amount of re-organisation energy is required upon complexation, as both the free and bound ligand conformation are similar.[37, 56] However, the requirement for more flexible based frameworks, which in turn would lead to more stable metal complexation resulted in the development of a new generation of chelating macrocycles. These systems (*e.g.* cyclen, calixarene and cyclodextrin derivatives), referred to as 'predisposed' type ligands, are based on an induced fit principle as they bear functionalised pendant arms which form an enclosed cavity by wrapping around the metal centre. Although more re-organisation energy is required upon complexation with the metal ion, the enthalpy gain associated with the strong metal-ligand interaction compensates for this.[56]

Ligands such as **1**–**3**, which are based on the cyclen framework, are ideal candidates for Ln complexation because of their ability to form kinetically inert and thermodynamically stable metal complexes.[39] Besides stability, these ligands also fulfil the high Ln co-ordination number requirement, by providing 8 potential co-ordinating sites, four from the macrocyclic nitrogen atoms and four from the flexible pendant arms. Demonstrated by the examples

shown below, a variety of groups can be used for functionalisation of the macrocycle ring, with carboxylates (1), amides (2) and phosphinates (3) being the most common.

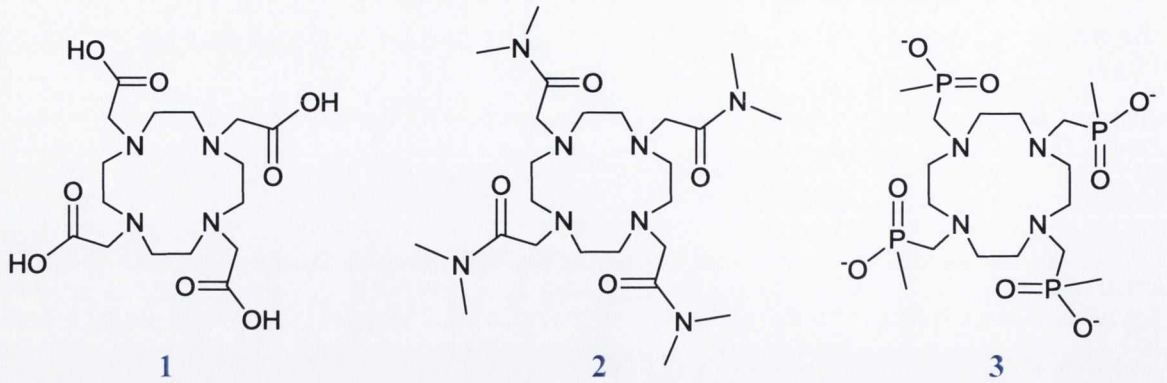

1 2 3

Metal complexation studies of 1,4,7,10–tetraazacyclododecane-1,4,7,10-tetraacetic acid (DOTA), 1, date back as far as the early 1980s, with the first crystal structure for the Eu(III) analogue being solved in 1984.[58] The most renowned metal complex of DOTA is the MRI contrast agent $[Gd(DOTA)H_2O]^-$ which is now known commercially as "Dotarem". The thermodynamic stability constant K_{GdL} of this metal complex is $10^{25.6}$, a value which ensures that dissociation of the Gd(III) metal ion from the chelating ligand does not occur *in vivo*.[39] The possibility of dissociation in solution is undesirable as free Gd(III) metal as well as unchelated ligand can cause disruption to biological systems within the body. Because of the similarities in ionic size of the Ln ion to Ca^{2+}, replacement of Ca^{2+} in proteins can inevitably occur upon exposure to high Ln metal concentration.[59] On the other hand, unchelated ligand can also potentially bind to biologically relevant metal ions due to the presence of the empty macrocyclic binding pocket.

This potential binding of metal ions to such tetra substituted cyclen based ligands was investigated in work carried out by Parker *et al.*,[60, 61] where initial studies utilising ligand 2 demonstrated its selective ability to bind Ca^{2+} and Na^+ metal ions in the presence of other alkali and alkaline earth metals in solution. ^{13}C NMR and IR spectroscopy studies were used to determine the formation of a 1:1 metal ligand complex, where shifts in the carbon resonances of the ligand and IR shifts in the amide carbonyl moieties were monitored. This neutral octadentate ligand along with other tetra amide derivatives were also capable of forming stable cationic complexes with Ln metals ions and their ability to behave as Gd(III) based contrast agents was investigated.[62] As well as cation mediated dissociation, for example, replacement of the Ln ion by metal ions in solution, the stability of Ln complexes with respect to acid-catalysed dissociation is also of major concern. This dissociation pathway can depend on the overall charge on the complex but also the nature of the pendant arms. Therefore, the use of more acidic anionic donor arms like the phosphinate groups used

in ligand **3**, which show great resistance to protonation, can increase the stability of the complex in acidic media.[42]

Overall, the principle studies carried out on ligands with similar structures to those of **1–3** involved structural determination upon complexation with a variety of Ln metal ions and their ability to behave as thermodynamically stable Gd(III) based MRI contrast agents. The absence of a sensitising chromophore to allow for indirect excitation of the Ln centre limits the luminescence studies which can be carried out for such ligands. However, due to the ease of incorporation of an antenna moiety to one or more of the amine sites of the cyclen macrocycle, a large variety of responsive Ln luminescent complexes have been developed to date, each bearing a different aromatic system capable of sensitisation.[34] The next section will therefore focus on examples of these luminescent based systems, as well as some magnetic based probes, highlighting the wide variety of applications they have to offer.

1.5 Various applications of cyclen based lanthanide complexes

1.5.1 pH responsive lanthanide based probes

Determination of the pH environment of biochemical events has commonly relied on the use of chromogenic pH indicators which often only take advantage of the lower wavelengths of the electromagnetic spectrum. However, recently the requirement for longer wavelength probes which display higher pH sensitivity has resulted in the development of a large variety of Ln based luminescent systems. These have the potential to be used in the monitoring of various pathological and physiological processes by accurate analysis of the pH environment.[63-69] *In vivo* cellular imaging is also another principle application of these Ln probes, where they can selectively distinguish the more acidic intracellular vesicles within the cell such as endosomes, phagosomes and lysosomes.

In the design of luminescent Ln based pH sensors, there are two approaches commonly used to obtain an intense signal response at various pH values. Firstly, protonation or deprotonation of the antenna moiety can effect the energy associated with its singlet excited state resulting in a signal change due to an enhancement or hindrance of the energy transfer process to the Ln excited state. Another method involves the use of Ln complexes which vary their co-ordination environment (q value) at different pH values. This usually occurs for systems were one or more of the chelating pendant arms can no longer bind to the Ln metal as a result of protonation at low pH values. Such a response can result in the co-ordination of an extra H_2O molecule to the Ln metal centre with subsequent quenching of the Ln emission being observed. The following examples will highlight how both approaches have been applied in the development of novel Ln based pH sensors.

Woods and Sherry reported a series of tetra amide based complexes, **4–6**, which incorporated a phenol or pyridine based antenna to allow for sufficient excitation of the corresponding Eu(III) metal centre.[64] The ability of these Ln systems to behave as potential pH probes was analysed using spectroscopic, NMR and voltammetric techniques. Luminescence studies confirmed that the intensity ratio between the $J = 1$ (594 nm) and $J = 2$ (613 nm) emission bands of **4** depends greatly on the pH of the solution being analysed. In an acidic environment, the emission at 594 nm is much more intense than that at 613 nm, however, upon basification to higher pH, the intensity ratio of the bands begins to change with emission at 613 nm reaching a maximum. The authors suggest that this sudden change in the intensity ratio is a result of the hypersensitivity of the $J = 2$ band to its co-ordination environment.

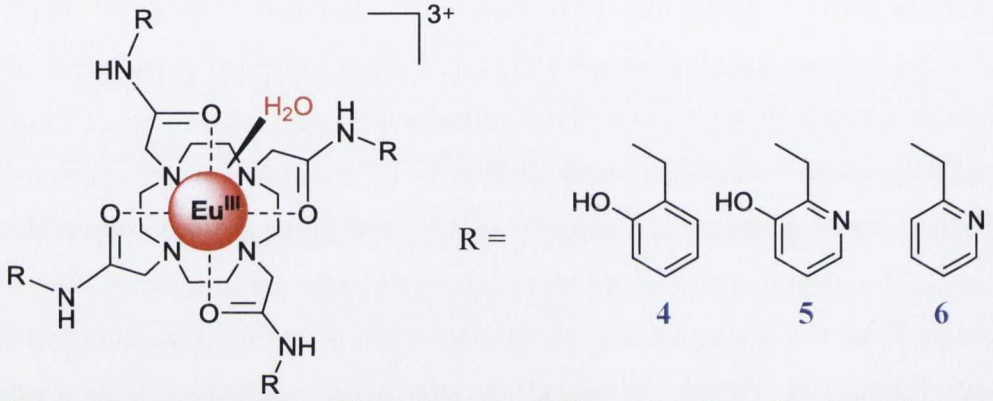

This unique response offers the possibility of using the intensity ratio as a determination of the solution pH, making the measurement independent of the Eu(III) complex concentration. The authors also demonstrated that depending on the complex used, the most significant changes in the intensity ratio could be fine tuned to a particular region of the pH spectrum, where for example **5** was most responsive between pH 7 and 9. ^{1}H NMR studies were carried out to confirm that the observed changes at high pH for these complexes were due to deprotonation of the amide functionalities which resulted in an increase in electron donation to the metal centre and a subsequent change in the emission properties.

As Woods and Sherry reported, by varying the antenna moiety used, a large variety of different Ln complexes displaying very different pH responses can be developed. This response variation can be seen, for example, in the quinoline based Eu(III) complex, **7**, developed by Gunnlaugsson and co-workers.[67] Unlike the pH sensors **4** – **6**, complex **7**, which only allows for the incorporation of a single antenna moiety, displayed a reversible "on-off" response of its emission as a function of the solution's pH. The behaviour of this sensor in acidic and basic environments was very different, with the emission being completely quenched at pH values above 9. The opposite effect was seen in acidic media, where efficient population of the Eu(III) excited state was possible and subsequent strong

Eu(III) emission was observed. With a pK_a value of 5.93, determined by potentiometric titrations, the deprotonation of the quinoline nitrogen was suggested as a possible cause of the sudden decrease in Eu(III) emission observed beyond pH 4.5. This coupled with possible deprotonation of the quinoline carboxylic amide and the metal bound H_2O molecule, could evidently cause the complete quenching of the metal's emission. Successful non covalent incorporation of **7** into water permeable hydrogels comprised of poly[methyl methacrylate-co-2-hydroxyethyl methacrylate] was also achieved, with the sensor retaining its response properties within. One advantage of efficient incorporation of these types of sensors into soft matter such as hydrogels, is the possibility of their use as material based real-time sensors in medical and pharmaceutical monitoring.

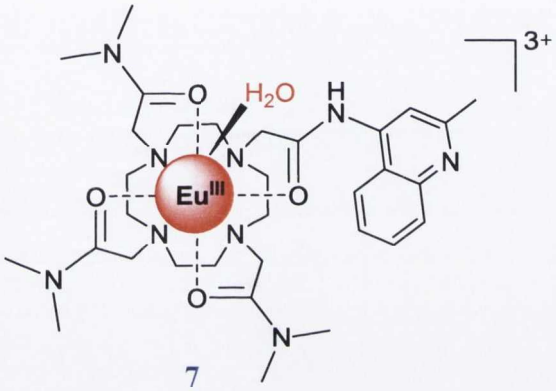

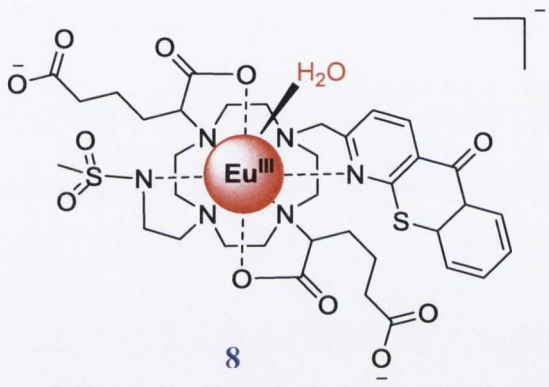

Parker and co-workers[63] used an alternative approach in the design of their pH probe, **8**, where instead of using a simple protonation and deprotonation process of the azathioxanthone sensitiser to render a pH response, the chelating ligand was functionalised with a pH dependant alkylsulfonamide moiety. The co-ordination potential of the ligand varied from 8 in basic media to 7 at lower pH due to subsequent protonation of the chelating nitrogen of the sulfonamide moiety. Modulation of the emission band intensities as a result of this protonation process were monitored with substantial and reversible changes being observed in the splitting of the $\Delta J = 1$, $\Delta J = 2$ and $\Delta J = 4$ transitions. The authors highlighted the appearance of two new emission bands at 627 nm and 680 nm upon basification of the pH from 5 to 8 with a subsequent 80% change in the intensity ratios of the 680 nm ($\Delta J = 4$) and 587 nm ($\Delta J = 1$) emission bands within this pH range. Mouse embryonic fibroblast (NIH 3T3) cells in conjugation with epifluorescence and confocal fluorescence imaging were used to determine the cellular uptake potential of **8**. Image analysis suggests the potential localisation of the complex within protein-rich regions of the nucleolus as well as ribosomal and perinuclear uptake. A series of emission intensity ratio *vs.* pH plots were used to

determine the intracellular pH of the protein-rich regions of the NIH 3T3 cells demonstrating the ability of **8** to behave as a ratiometric intracellular pH probe for living cells.

A series of Gd(III) based MRI complexes which upon variation of their pH environment displayed significant changes in their relaxivity values has also been developed.[63, 70, 72-74] The majority of these systems display the observed pH response as a result of changes in one or more of the key factors which determines a complexes overall relaxivity *e.g.* q, (number of bound water molecules), τ_R (rotational correlation time), and τ_M (the residence lifetime of these inner sphere water molecules). Hovland *et al.*[70] designed the Gd(III)DO3A derivative **9**, which displayed a 142% enhancement in its relaxivity value between the pH range 6 to 8. It was suggested that this observed increase was as a result of the formation of colloidal aggregates in solution, caused by the higher lipophilicity of the deprotonated neutral complex compared to the protonated positively charged species. This resulted in an increased τ_R for **9** and thus explains the large enhancement observed in the complexes relaxivity. At lower pH, no significant change was observed, however above pH 10, the relaxivity of the complex decreased dramatically from 19.1 $mM^{-1}s^{-1}$ to *ca.* 12.5 $mM^{-1}s^{-1}$. In such a basic medium, it was presumed that this was due to competition of the hydroxide ions in solution with the water for occupancy of the single co-ordination site on the Gd(III) ion. It is well known that a reduction in the q value of a Gd(III) complex and thus elimination of any inner sphere contribution would bear a dramatic effect on the complexes overall relaxivity value.

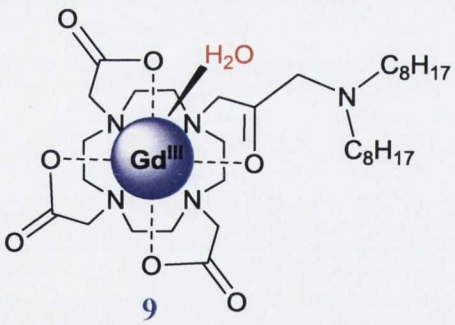

9

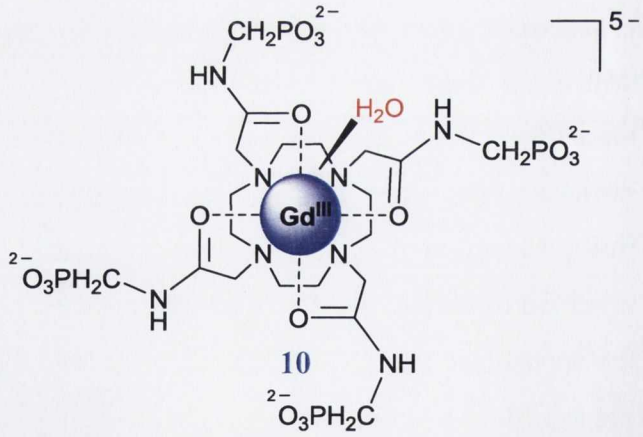

10

The most well-known MRI pH sensor which has gained a great deal of attention over the last ten years and is the only Gd(III) complex which has been applied for *in vivo* monitoring of pH is Gd(III)DOTA-4AmP^{-5} **10**.[69, 71] Developed by Sherry and co-workers in 1999, **10** responds to pH as a result of changes in its proton exchange between the bound water molecule and the remaining bulk water. Unlike other tetra amide based ligands which only show pH dependence in the presence of extremely acidic and basic media, **10** had an unusual pH response, with an increase in relaxivity being observed between pH 4 and 6,

reaching a maximum at pH 6, gradually decreasing to a minimum at pH 8.5 and then at pH 10.5 displaying a dramatic increase again. Bearing four phosphonate groups with pK_a's in the pH range 6.5 to 8 and therefore being monoprotonated below a pH of 8, subsequent hydrogen bonding of these phosphonate groups to the single Gd(III) bound water molecule provides a catalytic pathway for exchange of the bound water protons with protons of the bulk water. This helps explain the observed increase in relaxivity as the pH is lowered from pH 8.5 to 6. The authors suggested that below pH 6, further protonation of the phosphonate groups interferes with the H-bonded exchange network and results in the observed decrease in relaxivity below this pH. This complex in conjugation with a pH insensitive Gd(III) complex, Gd(III)DOTP^{-5} was used successfully to map extracellular tissue pH in mouse kidney[72] and in rat brain glioma.[73] By using a "dual injection method" and comparing the difference in image intensities using the two complexes, assuming both have identical pharmacokinetics and tissue biodistribution, an estimation of the tissue pH could be determined. More recently, a derivative of **10** has been developed which allowed for it's incorporated into a generation five G5-PAMAM dendrimer. Overall, this allowed for the introduction of 96 molecules of **10** onto the surface of the dendrimer, with a large enhancement in relaxivity being observed due to an increase in the τ_r of the complex.[74]

The above examples are only a select few of a large variety of cyclen based Ln systems which, as already discussed, show significant change in either their photophysical (excited state lifetimes, emission intensity and metal co-ordination environment) or magnetic properties (relaxivity) upon alteration of their pH environment. Another active area of research in recent years has been the development of ion responsive supramolecular Ln systems which can show strong and selective binding to a particular cation or anion of interest. This recognition event, as shown by the examples in the following section should, like that seen for the pH probes, show some measurable change in the photophysical and magnetic properties of the Ln metal.

1.5.2 Cation and anion responsive lanthanide based probes

A number of methods exist for the design of ion responsive Ln luminescent based probes. The most common involves the incorporation of the analyte receptor unit into the chromophoric moiety, which upon ion recognition, results in a change in the physical properties of the sensitising antenna, such as its excited state energy, redox properties or even structural change.[34, 41, 75] These modifications can in turn affect the energy transfer process to the Ln metal centre and therefore alter its emission properties. It is also possible to design a system which allows for direct attachment of the analyte species to the Ln metal centre

through displacement of weakly bound ligands such as H_2O. This binding event results in a change in the co-ordination environment and a subsequent modulation of its photophysical properties. In the case of the MRI based complexes, like that seen for the pH probes, changes in key factors associated with relaxivity coupled with a specific binding functionality can also be beneficial for selective ion detection. The following examples will highlight how both luminescent and magnetic techniques have been applied to develop extremely sensitive and above all highly selective Ln ion sensors.

With the recent discovery of its link to neuronal injury, the degenerative condition Alzheimer's disease[76] and its ability to suppress or induce apoptosis, the selective detection of Zn^{2+} *in vivo* has become a topical area of research within the field of Ln sensing.[77-81] Sensors **11** and **12**, both incorporating the chromophoric bis-picolyl Zn^{2+} binding unit within the cyclen framework, were recently reported by Pope *et al.*,[77] and Esqueda *et al.*,[78] respectively. Luminescence measurements of the Eu(III) complex **11**, which were carried out in a simulated physiological environment (140 mM NaCl, 4 mM KCl, 1.16 mM $MgCl_2$, and 2.3 mM $CaCl_2$), showed that at pH 7.4 a quenching effect of the Eu(III) emission occurred upon addition of $ZnCl_2$. The authors explain that upon binding of the cation to the receptor unit, the overall conformation of the ligand changes so that the nitrogen atom of the bridging 2,6-pyridyl moiety, which was initially chelated to the Eu(III), detaches itself and becomes involved in the encapsulation of the Zn^{2+} ion. This binding event causes an increase in the degree of solvation around the Eu(III) centre and therefore accounts for the observed decrease in emission. This assumption was confirmed by carrying out a series of lifetime measurements in the absence and presence of the Zn^{2+} ion and, as expected, an increase in the q value was observed.

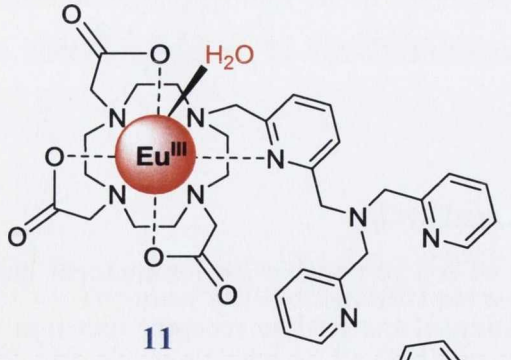

11

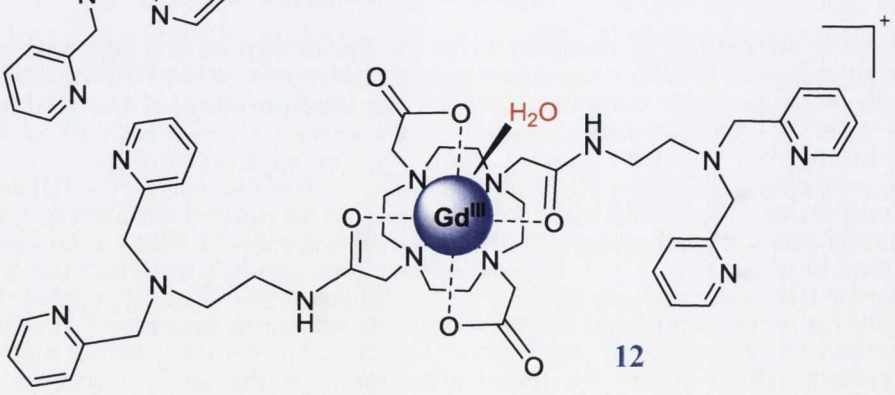

12

The Zn^{2+} binding ability of the Gd(III) complex **12** was determined by carrying out a series of relaxivity measurements in a magnetic field of 23 MHz (37 °C, pH 7.6, 0.1 M TRIS buffer). In the absence of the metal ion, the relaxivity of the complex was found to be 5.0 ± 0.1 $mM^{-1}s^{-1}$, however, this value gradually increased to 6.0 ± 0.1 $mM^{-1}s^{-1}$ upon addition of 2 equivalents of Zn^{2+}, with no change being observed on further additions of Zn^{2+}. As expected, based on the structure of **12** which contains two bis-picolyl units, the relaxivity measurements suggested the formation of a 1:2 (Gd:Zn) complex with a detection limit of 30 μM Zn^{2+} being calculated. Although **12** showed great selectivity over metals ions like Ca^{2+} and Mg^{2+}, a 2:1 complex was also formed in the presence of Cu^{2+} with a relaxivity value of 6.3 ± 0.1 $mM^{-1}s^{-1}$ being recorded. The observed increase in the relaxivity values upon addition of both Zn^{2+} and Cu^{2+} were attributed to an increase in the water or proton exchange rate (k_{ex}), which is known to be quite slow for such Gd-DOTA-bis amide type complexes. The most interesting result observed was its interaction with human serum albumin (HSA), a protein which shows high abundance in both blood and cerebal spinal fluid. In the absence of Zn^{2+} ions, the complex showed very poor binding abilities with little enhancement in its relaxivity value. However when 2 equivalents of Zn^{2+} were added to **12** prior to the addition of HSA, a very different response was observed. The relaxivity of the Zn^{2+} bound Gd(III) complex increased by *ca.* 165 % with a value of 17.4 ± 0.5 $mM^{-1}s^{-1}$ being measured upon protein binding. This significant relaxivity enhancement is explained by an overall increase in the Gd(III) complex size upon protein interaction and thus a subsequent slower rotational correlation time.

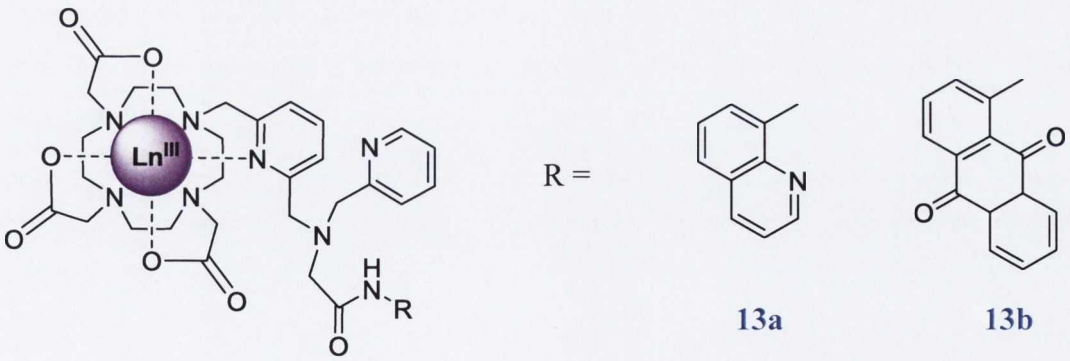

13a **13b**

More recently, Pope and co-workers reported the dual emissive lanthanide probes **13a** and **13b**, which allowed for the incorporation of the long-wavelength absorbing chromophores 8-aminoquinoline and 1-amino-9,10-anthraquinone, respectively.[82] The Nd(III) and Yb(III) analogues demonstrated dual emission upon excitation at 355 nm with visible, ligand-centred fluorescence as well as NIR lanthanide emission being observed. Successful sensitisation of the Eu(III) complexes was also demonstrated upon excitation of

these chromophores, however, a more intense response was displayed when the complexes were excited through the pyridyl antenna (λ_{ex} = 280 nm). A series of d-block metal ion studies were carried out on the Eu(III) complexes, with Cu^{2+} displaying the most significant quenching effect on the pyridyl, anthraquinone, quinoline and Eu(III) emission bands. In the presence of Hg^{2+}, the pyridine fluorescence was quenched, however, the anthraquinone and quinoline emission displayed a slight enhancement. The overall intensity and relative ratio of the Eu(III) $^5D_0 \rightarrow {}^7F_J$ transitions were also modulated suggesting a change in the coordination environment of the Eu(III) metal. For the case of the Cd^{2+} and Zn^{2+} ions, enhancement of the pyridine fluorescence was observed, with little change in the Eu(III) emission intensities. The authors also investigated the NIR response of the Yb(III) and Nd(III) analogues in the presence of Hg^{2+}, with the Yb(III) complex of **13a** displaying a four fold enhancement upon the addition of the metal ion. Increased rigidity of the ligand framework and more efficient shielding of the Yb(III) ion from the outer sphere solvent molecules upon binding were suggested as possible causes of the observed emission increase. A contrasting response was displayed for the Nd(III) analogues, with a reduction in the overall NIR emission intensities being observed, due to an increase in the complexes inner sphere hydration states upon Hg^{2+} interaction.

The incorporation of the macrocyclic crown ether moiety to the cyclen framework has proven successful for the selective detection and monitoring of alkali metals such as Na^+ and K^+.[16, 83-85] Closely associated with hypertension, stroke and cardiovascular disease, the ability to detect such ions is becoming of great importance. Gunnlaugsson *et al.*[16, 83] previously reported sensors **14a** and **14b**, where the functionalisation of one of the cyclen sites with a diaza-15-crown-5 ether moiety (**14a**) or a diaza-18-crown-6 ether moiety (**14b**), gives high selectively for either Na^+ of K^+ ions. pH studies on both Tb(III) complexes showed that as a result of protonation of the aniline moiety adjacent to the cyclen framework and deprotonation of the receptor amide, the Tb(III) emission was almost completely 'switched off' between the pH range 4 to 9. However, at physiological pH, upon addition of Na^+ or K^+ ions (0.1 – 1 M), the Tb(III) emission is 'switched on' with up to a 40 fold enhancement in intensity being observed. Owing to the size effects of the aza crown ether rings used, **14a** was most effectively switched on in the presence of the smaller Na^+ ions, whereas **14b** showed more selectivity for the larger K^+ ions. The authors suggest that the metal ion binding process results in a structural change in the receptor, where the ring becomes almost deconjugated from the aromatic moieties, resulting in an increased oxidation potential of the receptor. This in turn leads to a more efficient energy transfer process to the Tb(III) excited state and thus explains the observed increase in emission intensity.

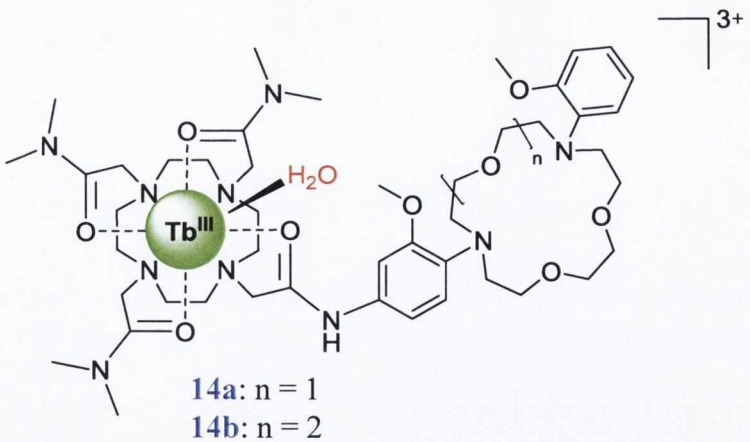

14a: n = 1
14b: n = 2

In order to achieve higher selectivity for K^+ ions over Na^+, Pierre and co-workers developed the Tb(III) sensor **15**, which incorporated an azaxanthone antenna linked to a diaza-18-crown-6 receptor unit *via* a phenyl moiety.[75, 86] Based on work previously carried out by Gokel and co-workers[87], it was anticipated that selectivity for K^+ could be achieved by cation-π interaction of the metal ion with the arene unit. Although Na^+ would also exhibit complexation within the crown ether, due to its smaller size, formation of this cation-π interaction would be hindered. In the absence of K^+, due to the large separation of the Tb(III) ion and the sensitising antenna, **15** displayed relatively weak emission upon excitation at 332 nm. However, upon K^+ addition (10 mM), due to the conformational change associated with the complex, the sensitising antenna is brought in closer proximity to the metal centre resulting in a 22-fold enhancement in the Tb(III) emission intensity with a binding affinity of 0.33 mM^{-1} being determined. A 93-, 260-, 105- and 61-fold selectivity for K^+ over Na^+, Li^+, Mg^{2+} and Ca^{2+} ions was also demonstrated for **15**.

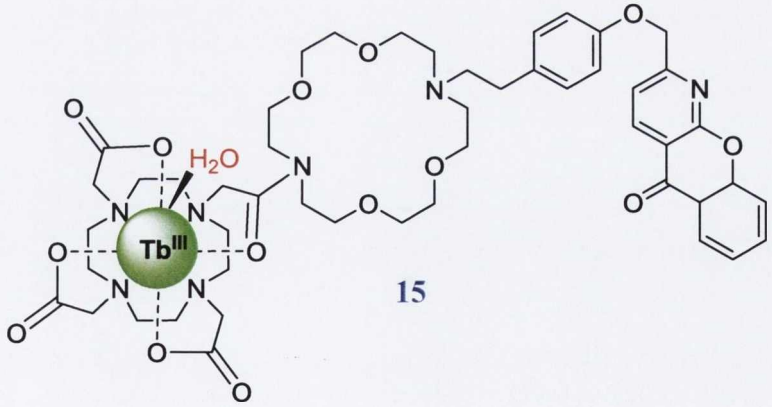

15

More recently, Pierre and co-workers developed the ratiometric Eu(III) complex **16**, where through incorporation of a diaza-18-crown-6 receptor moiety and a phenanthridine antenna, high sensitivity and selectivity in the mM range for K^+ was achieved.[54] Upon titration of this alkali cation in water at physiological pH, an almost two fold enhancement in the Eu(III) emission intensity was observed. With the added advantage of co-ordination of the phenanthridine antenna to the K^+ ion encapsulated within the crown ether, a much higher

binding affinity than expected of 26 ± 0.8 μM^{-1} was determined. This enabled detection within the concentration range 0 – 10 mM, making this probe ideal for monitoring extracellular K^+, where its concentration typically ranges from 3.5 – 5.3 mM. The authors also successfully highlighted the ratiometric potential of **16**, by demonstrating that if the complex was excited at 256 nm, the observed Eu(III) emission was highly dependent on the concentration of K^+. However, when excited at 400 nm, the Eu(III) luminescence observed displayed independence in the presence of the metal ion. This provides the potential for more accurate determination of K^+ concentration within biological media. The selectivity of **16** for K^+, over other physiologically important cations such as Ca^{2+}, Mg^{2+} and Li^{2+} was also demonstrated, with negligible responses being observed in the presence of these metals. Only a 35% increase in emission intensity was observed upon the addition of 137 mM Na^+, compared to the 83% enhancement displayed in the presence of 10 mM K^+.

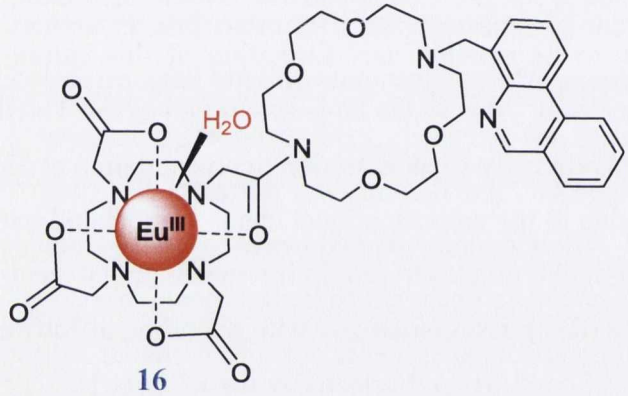

16

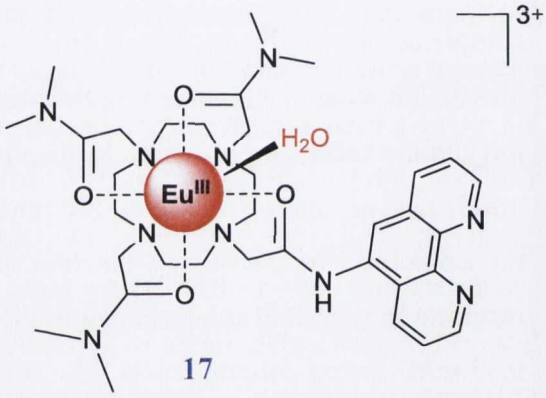

17

Gunnlaugsson *et al.*[88] reported the cationic Eu(III) complex **17**, which in the presence of Cu^{2+} ions results in the formation of a polynuclear hetero metallic Cu^{2+}-Eu(III) macrocyclic complex. It was believed that co-ordination of two or three Eu(III) complexes to one Cu^{2+} ion, through metal interaction of the phenanthroline moiety, resulted in the 'switching off' of the Eu(III) emission. The reversibility of this emission quenching was confirmed by the addition of EDTA, which removed the Cu^{2+} ion from the receptor moiety and resulted in the Eu(III) emission of **17** being switched back on. This unique on-off sensor for Cu^{2+} ions showed no emission response in the presence of Zn^{2+} or group I/group II metal ions. However, in the presence of other transition metals such as Co^{2+}, Fe^{2+} and Fe^{3+}, modulation of Eu(III) emission was observed. More in depth studies confirmed that preferentially either two or three equivalents of **17** complexed to each of the transition metal ions including Cu^{2+} giving rise to either a linear *f-d-f* or branched (tris) f_3-*d* hetero nuclear complex.[89]

Que *et al.*[90] demonstrated high Cu^{2+} selectivity using the Gd(III) complex **18**, which allowed for the incorporation of a pendant iminodiacetate site to the cyclen framework. In the

absence of Cu^{2+} ions, the hard anionic carboxylate groups showed co-ordination to the Gd(III) metal centre, resulting in a q value of *ca.* 0 being attained. Such removal of any inner sphere contribution resulted in a low relaxivity value of 3.76 $mM^{-1}s^{-1}$ at 400 MHz. Recognition and subsequent binding to Cu^{2+} ions increased the inner sphere contribution as the iminodiacetate arms showed preferential binding to the Cu^{2+} ions over the Gd(III) centre. With an increase in the q value to 1, a subsequent relaxivity enhancement of 41% was observed upon formation of the 1:1 Cu^{2+}: Gd(III) metal complex. The Gd(III) complex showed high selectivity for the Cu^{2+} ions over other abundant cellular alkali and alkaline earth cations such as Mg^{2+}, Ca^{2+}, Na^{+} and K^{+}, with no relaxivity enhancement being observed in the presence of these cations. It was also shown that Zn^{2+} and Fe^{2+} ions triggered a much lower relaxivity response; with no effect on the ability of **18** to sense Cu^{2+} being observed.

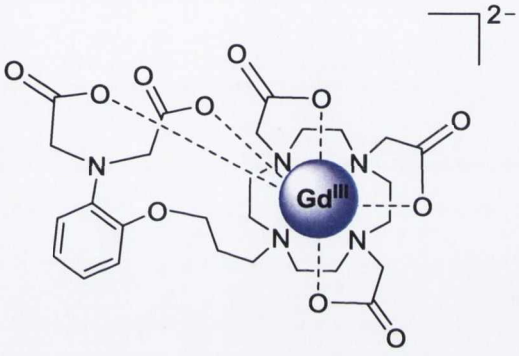

18

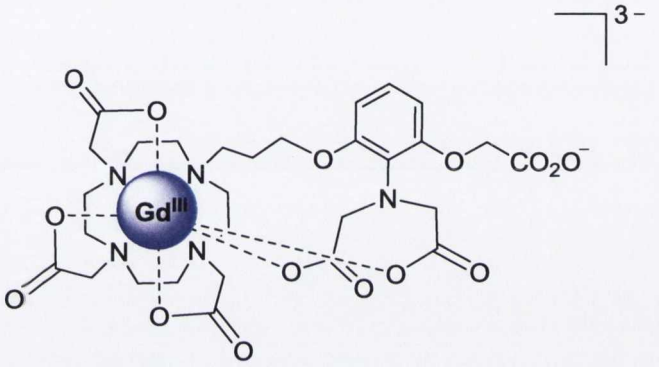

19

The iminodiacetate receptor unit, which was previously described to show Cu^{2+} binding, has upon structural modification gained a great deal of attention in the sensing of other metal ions in solution such as Ca^{2+}, Mg^{2+} and Zn^{2+}.[79, 80, 91-94] For example, Angelovski and co-workers designed the Gd(III) complex **19**, which exploited the Ca^{2+} chelating abilities of the APTRA (*o*-amino-phenol-*N,N,O*-triacetate) binding unit.[92] The authors selected this low affinity Ca^{2+} recognition moiety (K_d = 20 - 25 μM)[95] over a high affinity chelator (K_d = 0.1 - 0.4 μM), such as BAPTA, as such strong receptors have often displayed saturation of their binding sites above a 1 μM concentration of Ca^{2+} ions. This saturation effect results in minimal sensory response occurring at higher Ca^{2+} concentration.[91] The relaxivity measurements of **19** were carried out at 400 MHz in KMOPS buffer at pH 7.4. These measurements showed an increase in the relaxivity of the Gd(III) complex from 3.5 $mM^{-1}s^{-1}$ to 6.9 $mM^{-1}s^{-1}$ upon addition of one equivalent of Ca^{2+}. This 97% relaxivity enhancement showed no significant change upon addition of other competing metal ions such as Zn^{2+} and Mg^{2+} and the reversibility of the Ca^{2+} binding event was demonstrated using EDTA. Similar to previous examples, the authors explain that the observed increase in the relaxivity value was due to an increase in the hydration number of the Gd(III) complex.

Parker and co-workers reported the structurally similar Gd(III) complexes **20a** and **20b**, which upon interaction with Ca^{2+} and Zn^{2+} ions respectively, displayed an increase in their overall proton relaxivities.[94] The eight coordinate pyro-EGTA based complex **20a**, showed a 67% enhancement in r_{1p} at 1.4 T in the presence of 1 mM $CaCl_2$, with the six co-ordinate complex **20b** showing more preferential binding to Zn^{2+}, with a 73% increase in r_{1p} being observed. Addition of EDTA to both Gd(III) solutions resulted in restoration of the relaxivity values, verifying the reversibility of the metal binding event for both complexes. Confirmation that the observed enhancement in relaxivities was due to an increase in the hydration state of the Gd(III) metal ion was gained by carrying out a series *q* value measurements on the Eu(III) analogues of these complexes. No significant changes (< 25%) were observed in the relaxivities for **20a** and **20b** in the presence of K^+, Na^+, Mg^{2+} and Cu^{2+} ions. The authors suggest that the poor response displayed for Cu^{2+} could be as a result of the ion displaying preferential binding with the more remote amino-diacetate moieties, which would in turn have little effect in the co-ordination environment of the Gd(III) centre. The effect of $NaHCO_3$ on the relaxivities of these complexes in the presence and absence of the Ca^{2+} and Zn^{2+} ions was also discussed, with a 25% and 30% reduction in r_{1p} for **20a** and **20b** respectively, being observed upon the addition of 50 mM of $NaHCO_3$ to the metal bound complexes. No modulation in relaxivities was displayed in the absence of these ions.

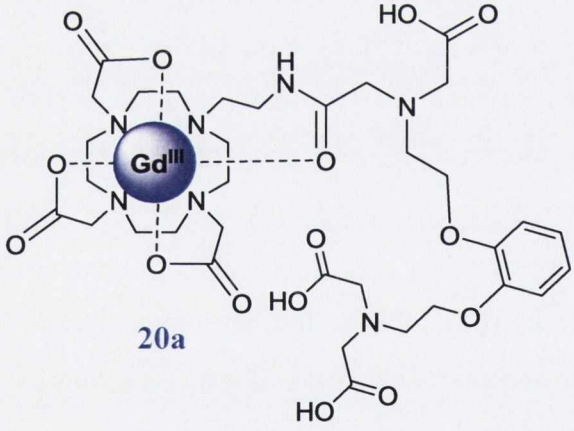

20a

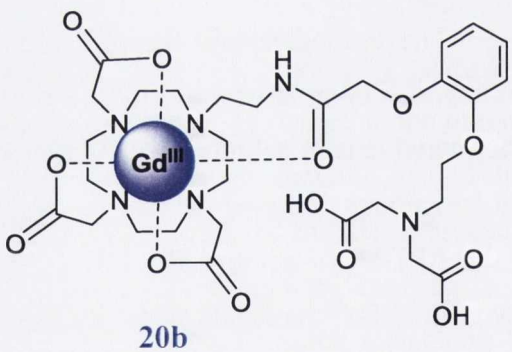

20b

More recently, Que *et al.*[96] reported the Gd(III) complex **21**, a highly selective Cu^+ MRI contrast agent using a thioether-rich unit as the recognition moiety. Based on a similar principle, the pendant receptor arms hindered any inner-sphere water access in the absence of the metal ions, resulting in a relaxivity value of 2.6 $mM^{-1}s^{-1}$ at 60 MHz being recorded. However, upon Cu^+ recognition, the observed increase in the complexes *q* value resulted in a relaxivity enhancement of 340% (Scheme 1.1). The authors also explained that a major advantage of using the bulkier pendant arms is a reduction in the sensitivity to common biologically abundant anions. The sterically crowed Gd(III) core prevents any potentially co-

ordinating anions such as lactate, citrate and phosphate causing a marked decrease in the relaxivity value through chelation to the metal centre.

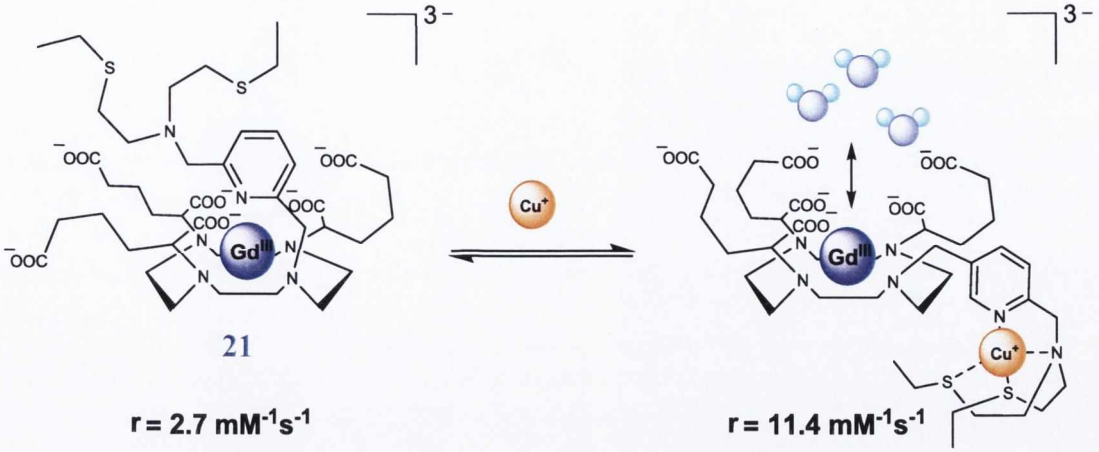

Scheme 1.1: Encapsulation of a Cu^{+} ion *via* the thio-rich pendant unit of **21**.[96]

A very different Ln luminescent method for metal ion sensing, as shown in Scheme 1.2, was reported by Viguier *et al.*,[97] where a catalysis approach to selectively detect Cu^{+} ions was applied. The authors explain that one of the major challenges with the detection of these metal ions *in vivo* is that they are usually not in their free form, but preferentially co-ordinated to a copper binding protein (*e.g.* metallothioneine) or biothiol (*e.g.* glutathione). This drawback initiated their approach of using the Cu^{+} catalysed "click" reaction to couple the alkynyl Eu(III) complex **22** and the dansyl azide chromophoric moiety **23** together to form the new highly luminescent Eu(III) complex **24**. The Cu^{+}-glutathione complex was used as the experimental catalyst due to its high abundance within the human body. By monitoring the luminescence of **24**, which upon successful formation should show efficient excitation by **23**, the ability of this technique to detect complexed Cu^{+} ions was achieved.

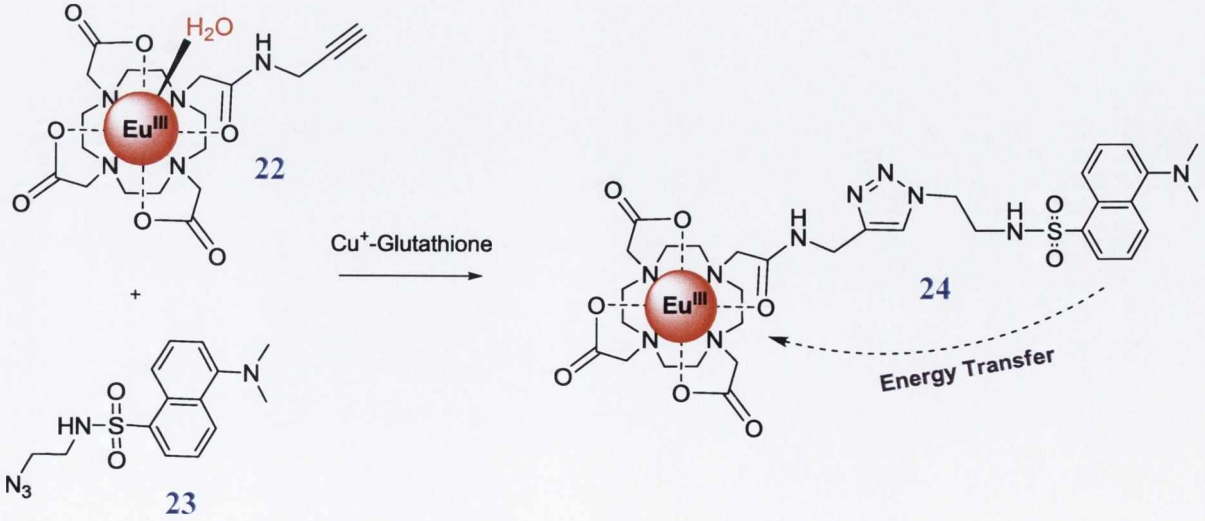

Scheme 1.2: *Synthesis of the Eu(III) complex* **24** *using a* Cu^{+}*-glutathione catalysed click reaction.*[97]

As previously discussed, another approach commonly used for metal ion sensing involves the design of co-ordinatively unsaturated Ln based systems which upon direct analyte binding to the Ln centre, show a subsequent change in the co-ordination environment of the complex resulting in a modulation of the emission response of the metal. An example of this type of method can be seen for the heptadenate complexes **25a** and **25b**, previously reported by Parker and co-workers, which in aqueous solution, displayed very weak Ln emission properties due to the presence of the two metal bound H_2O molecules.[98, 99] However, these types of unsaturated systems offer the advantage that in the presence of various halides and oxyanions, displacement of one or more of the co-ordinated H_2O molecules results in a significant increase in the Ln luminescence. Anions such as I^-, Br^-, Cl^- and NO_3^- displayed no observable change in the emission or lifetime properties of complexes **25a** and **25b**, however, F^-, $CH_3CO_2^-$, SO_4^{2-}, CO_3^{2-}, HCO_3^- and $H_2PO_4^-$ ions all competed with H_2O for a co-ordination site on the metal complex. Lifetime measurements were used to confirm that the observed effect was in fact a result of a decrease in the q values of the Ln complexes.

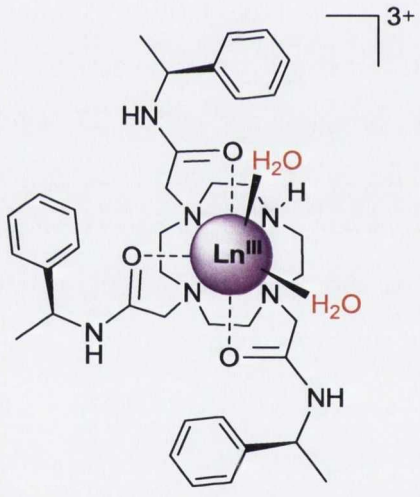

25a: Ln = Eu(III)
25b: Ln = Tb(III)

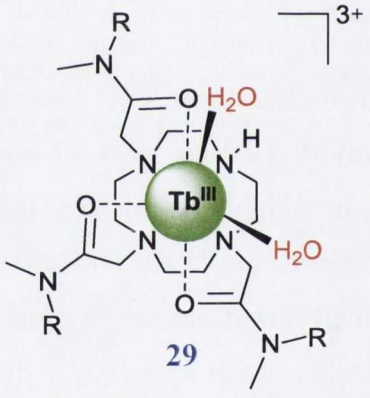

29

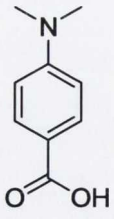

26

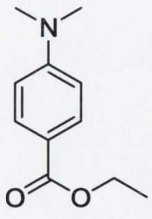

27

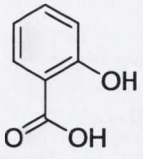

28

Gunnlaugsson *et al.*,[100] also applied a similar anion sensing approach for the detection of a series of aromatic moieties, **26–28**, using the cationic heptadentate Tb(III) complex **29**. A larger emission enhancement (up to *ca.* 700-fold) for these systems was observed upon successful anion binding. H_2O displacement was not the only factor that caused an emission increase but also the incorporation of the benzylic sensitising antenna to the system, which gives the added advantage of more efficient population of the Tb(III) excited stated *via*

indirect excitation. Lifetime measurements concluded that upon addition of **26** to the Tb(III) complex, the *q* value decreased to zero, suggesting chelation of the carboxylate to the Ln centre *via* the formation of a four-member bidentate ring chelate. Confirmation of this binding event was achieved by analysis of the ester analogue **27**, which caused no H_2O displacement and thus no modulation in the Tb(III) emission or lifetimes of the complexes. Faulkner and co-workers showed that upon successful co-ordination of the visible chromophore **30**, it was possible through formation of a ternary complex with **31**, to achieve efficient energy transfer to the NIR emitting Yb(III) metal.[101] In methanolic solutions, the carboxylate functionality of the tetrathiafulvalene antenna initiated displacement of the bound H_2O molecules, promoting the energy transfer process to the NIR emitting Ln.

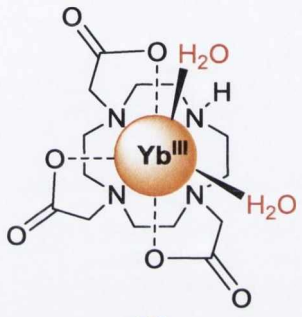

31

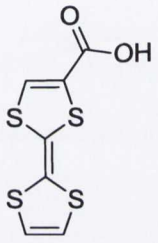

30

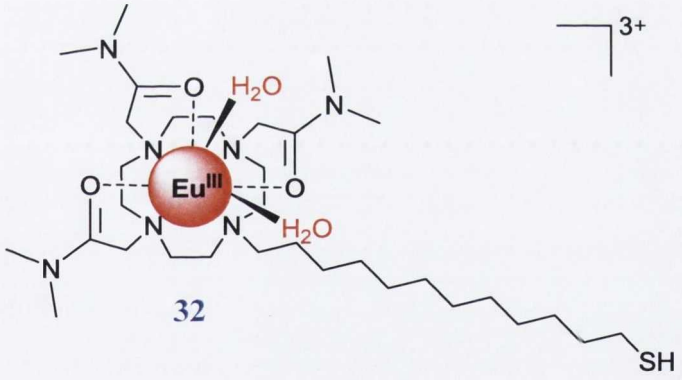

32

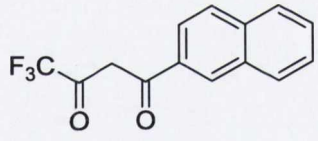

33

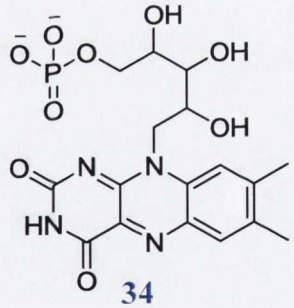

34

In 2009, the Gunnlaugsson research group took this anion displacement technique a step further by the development of the heptadentate Eu(III) complex **32**, which through the possession of a long alkyl thiol chain showed successful adsorption onto the surface of gold nanoparticles (AuNP) with an average diameter of 5 nm.[102] Successful indirect excitation of **32** both on and off the AuNP was achieved through displacement of the metal bound H_2O molecules with the β-diketone antennae **33**. Luminescence studies estimated that *ca.* 230 Eu(III) complexes were attached to each AuNP and that phosphate containing molecules

such as ADP, AMP, ATP and NADP displayed a 20–50% quenching effect of the Eu(III)-**33** ternary complex attached to the AuNP. The most significant response was seen for the biologically relevant phosphate, flavin mononucleotide **34**, where an almost complete quenching of the Eu(III) emission was observed. Such a response suggests efficient displacement of the sensitising antenna **33** resulting in the Eu(III) complex forming a new ternary complex with **34**. The inability of **34** to successfully excite the Eu(III) metal *via* energy transfer thus explains the dramatic decrease in emission intensity.

From the wide variety of luminescent and MRI based Ln probes described above, it is clear that a huge emphasis is placed on optimising their sensitivity and selectivity as cation and anion sensors in aqueous solution. However, their ability to be used as responsive probes for cellular imaging has also earned a great deal of attention in recent years. It is anticipated that with the development of more selective, non invasive imaging probes which show rapid rates of uptake, egress and intracellular compartmentalisation, a greater understanding of the overall structure and function of certain key cellular process such as cell division (mitosis) can be gained. It is also possible that these systems could potentially be used as diagnostic and therapeutic agents in biomedical imaging. The following section will therefore briefly highlight various examples from the vast array of such Ln probes which have shown efficient cellular uptake and the cellular information or diagnostic/therapeutic potential gained from such studies.

1.5.3 Lanthanide based cellular imaging probes

Parker and co-workers have concentrated significant amounts of their research efforts on the design and evaluation of over sixty emissive Eu(III) and Tb(III) cellular probes, all designed using the macrocyclic cyclen framework as their common core. Extensive cellular uptake studies demonstrated that the rate of cell penetration and the specific localisation of these systems depended greatly on the overall structure of the probe. Upon further investigation it was discovered that it was the nature and mode of linkage of the sensitising moiety (antenna) that primarily determined such factors, with the complexes charge, lipophilicity and any other donor structures (chelating arms) playing no significant role. A large variety of sensitisers have been investigated, including tetraazatriphenylenes, acridones, azaxanthones, azathiaxanthones and pyrazoyl-azaxanthones, each enabling excitation within the spectral range 337–410 nm. For example, the tetraazatriphenylene and thioxanthone based complexes **35** and **36**, respectively, displayed efficient cellular permeation with relatively strong Ln emission being observed within NIH/3T3 cells (mouse skin fibroblasts).[103, 104] After 4 h incubation with 0.3 mM **35**, fluorescence microscopy confirmed

complete distribution of the complex throughout the cytoplasm. However, after longer periods of time, **35** began to preferentially localise within the nuclear membrane. Selective staining of the nucleolus of NIH/3T3, HeLa (human endothelial carcinoma) and HDF (human dermal fibroblasts) cells was achieved using complex **36**. Colocalistaion studies, using the commercially available nucleolar stain SYTO RNA-Select, were carried out to confirm that the bright spots observed within the nucleus were in fact due to excitation of **36** localised specifically within the nucleolus organelle. Cell viability experiments were also carried out and showed that upon loading of the cells with 100 μM **36**, over 90 % of the cells remained in a healthy state after a 24 h incubation period.

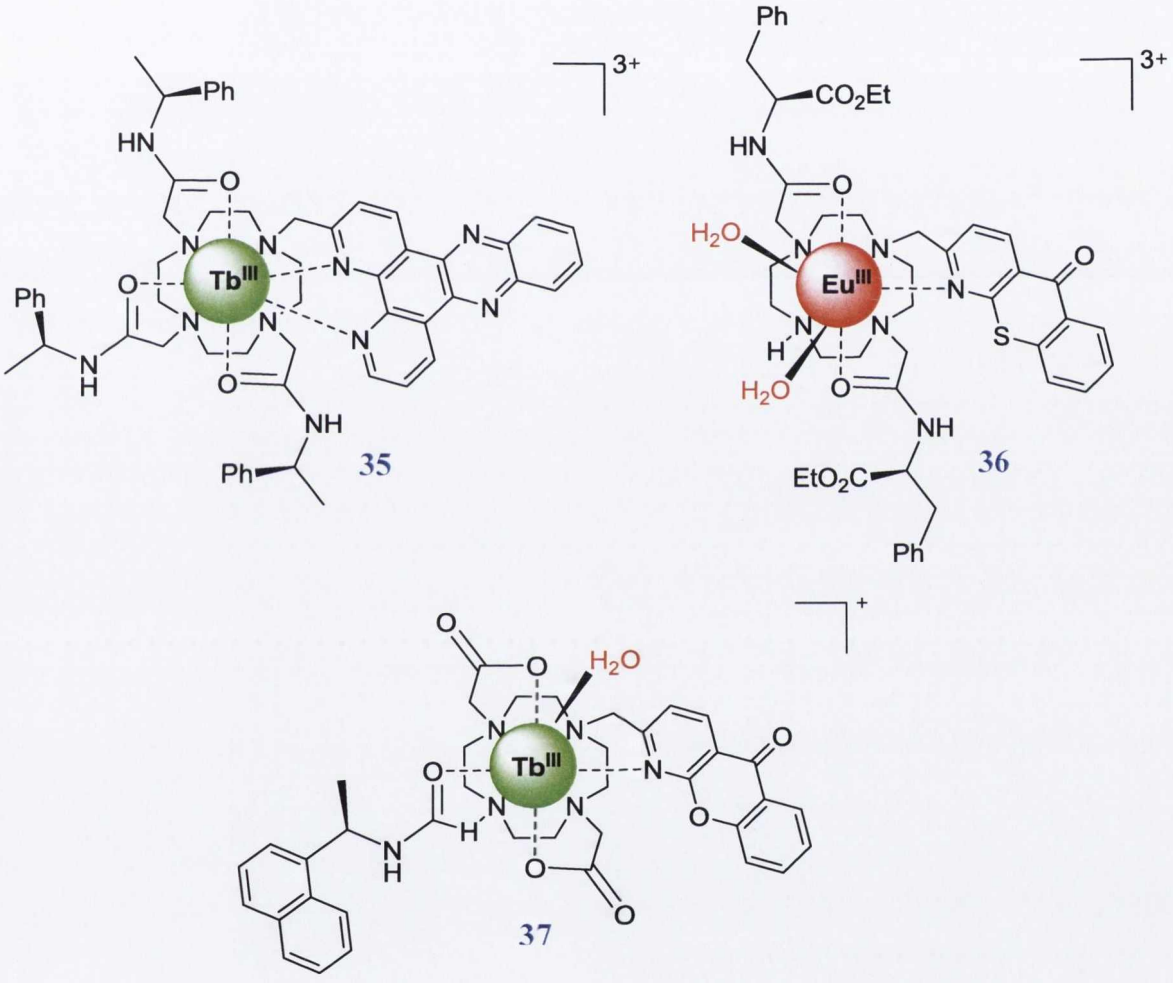

More recently, Parker and co-workers have concentrated on the design of the Tb(III) complex **37**, which allowed for the incorporation of both a naphthyl moiety and a sensitising azaxanthone group to the ligand structure.[105] The presence of the relatively long lived excited state of the naphthyl functionality allowed for successful singlet oxygen ($^1O_2$) formation due to the quenching of its excited state by atmospheric oxygen. In order to visualise the cellular uptake of **37**, it was necessary to directly excite the Tb(III) centre using a 488 nm laser as excitation through the sensitising azaxanthone group (355 nm) resulted in poor emission

within the cells. However, cell viability experiments using bright field analysis showed that upon excitation at 355 nm, almost 70% of the cells displayed some type of deformity 30 minutes after irradiation. The authors suggest that successful energy transfer from the azaxanthone antenna to the triplet excited state of the naphthyl group promotes singlet oxygen formation and thus explains the observed cell damage. This Tb(III) complex therefore not only has the ability to penetrate the cell membrane but also has the advantage of selective damage upon successful irradiation.

The ability to monitor one of the most important cellular process, mitosis, was recently demonstrated using the Tb(III) complex **38**, which allowed for the incorporation of two azaxanthone chromophores, positioned *trans* to each other. Microscopy analysis confirmed that when low concentrations of these probes (<1 μM) were used, selective staining of cells undergoing mitosis was achieved, with cells at each stage of the mitotic cycle being observed due to sufficient chromosomal staining. It was attempted to monitor a single mitotic cell over time, using **38** to allow for visualisation of all the various stages, however, the study was ceased after an hour due to the phototoxicity associated with the intensity of the laser used for imaging.

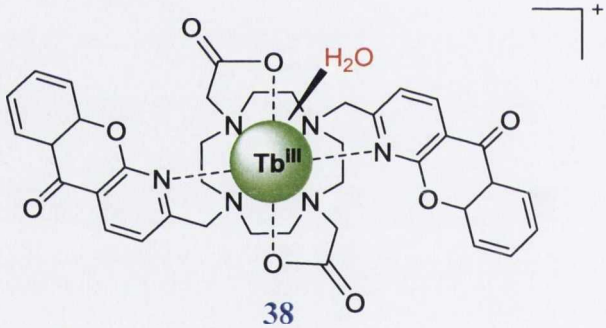

38

Bornhop and co-workers applied a more diagnostic approach to their Ln based complexes **39** and **40**, which were designed with the objective to behave as multimodal (MRI and luminescent) contrast agents for the detection of peripheral benzodiazepine receptor (PBR) in C6 glioblastoma (brain cancer) cells.[106] With overexpression of PBR bearing links to a variety of diseases such as breast cancer, glioblastoma, Alzheimer's disease, Huntington's disease and multiple sclerosis, its efficient detection in cell physiology has earned great attention.[107, 108] The selectivity for PBR was gained by the incorporation of the high affinity PBR receptor, PK11195, to a tri functional Ln chelate with a suitable antenna for sensitisation. Upon cellular uptake of **39**, using C6 glioma cells, quinoline-sensitised emission from the Eu(III) metal centre was clearly observed. Using the mitochondrial dye JC-1, it was confirmed that the Eu(III) complex showed selective localisation in the outer mitochondrial membrane, a region were PBR is known to express. Cellular studies using a "cocktail" mixture of both **39** and **40** displayed the ligands bimodal capabilities, with

successful detection of overexpressed PBR from the same population of C6 cells using both fluorescence and MRI imaging techniques.

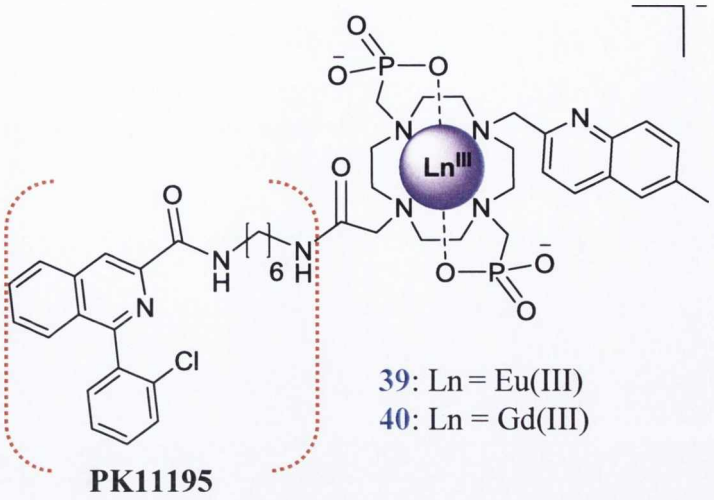

PK11195

39: Ln = Eu(III)
40: Ln = Gd(III)

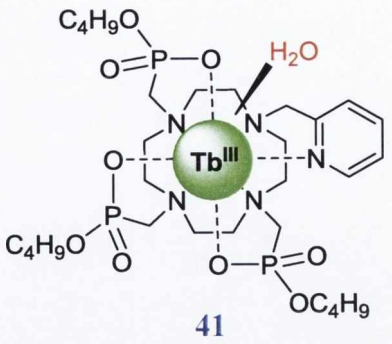

41

The early detection of squamous cell carcinoma (oral cancer lesions), a condition which accounts for almost 95% of all malignant oral lesions in the world, was also investigated by Bornhop and co-workers, with the development of the Tb(III) complex **41**.[109] Upon excitation of the pyridine antenna, successful detection of squamous cell carcinoma using a Syrian hamster cheek pouch model was achieved. Although the exact mechanism for uptake has not been elucidated, **41** had the advantage of selectively detecting these dysplastic lesions over simply traumatised damaged tissue.

The use of water soluble biocompatible drug-polymer conjugates as an efficient drug delivery mechanism has become an important area of research due to the diagnostic and therapeutic advantages they have to offer. A greater understanding of the pharmacokinetics, biodistribution and drug delivery efficiency can be achieved by linking a polymeric drug carrier to a suitable imaging functionality. Non invasive visualisation of this *in vivo* drug delivery process was achieved by Ye *et al.*[110] using the Gd(III) based MRI contrast agent **42**. By conjugating the well known biodegradable drug carrier, poly(L-glutamic acid) with the tri-carboxylate Gd(III) chelate, real time *in vivo* evaluation for drug delivery in mice bearing MDA-MB-231 human breast cancer xenografts was achieved. Gd(III)-polymer conjugates with various molecular weights (87, 50 and 28 kDa) were prepared and the size effect on the blood circulation and distribution in major organs and tumour tissues as a function of time was investigated. The authors concluded that the low molecular weight conjugate (28 kDa) displayed relatively low tumour accumulation due to its rapid excretion by renal filtration. However, studies suggest that although they display a longer blood circulation time, the high

molecular weight conjugates show more efficient tumour accumulation and therefore are a more successful candidate for drug delivery.

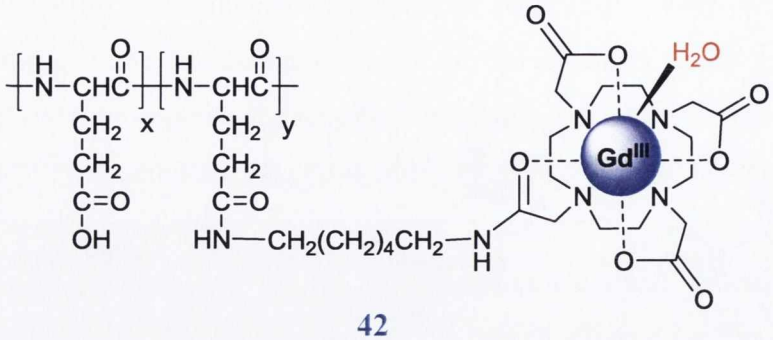

42

It is clear from the examples described above that the unique photophysical and magnetic properties of the Ln metals have resulted in a variety of applications ranging from pH responsive sensing to metal ion detection and more recently as diagnostic and therapeutic contrast agents in biomedical imaging. As a fundamental aspect of this PhD thesis involves the development of novel Ln based contrast agents (structurally similar to those previously described), for selective detection and subsequent quantification of microdamage in bone structure, the remaining sections will highlight the key features required to understand this common bone disorder.

1.6 Anatomy and physiology of bone

The skeletal system, a network of many individual bones held together by connective tissue, is one of the most important and complex organ systems found within the human body. In addition to providing the entire biomechanical framework from which the body is built, it also has many important biochemical and metabolic functions.[111] A typical adult skeleton has *ca.* 206 major bones, which can be divided into six main categories depending on their individual size and shape. Throughout its lifespan, bone is continuously undergoing moulding, reshaping and above all repair to help adapt to any external mechanical force or stress which may occur and to also provide a mechanism to replace older damaged bone with healthier stronger bone material. The main functions associated with bone are as follows:[112]

- **Mechanical** - Provides protection of softer tissue and organs within the cranial, thoracic and pelvic cavities and facilitates muscle lever action required for movement.
- **Metabolic** - Provides maintenance of mineral homeostasis, acid-base balance and promotes haematopoiesis (blood formation).[113]
- **Self repairing** - Has the ability to adjust its mass, shape, and overall properties in response to mechanical stimuli or other voluntary physical activity.[111]

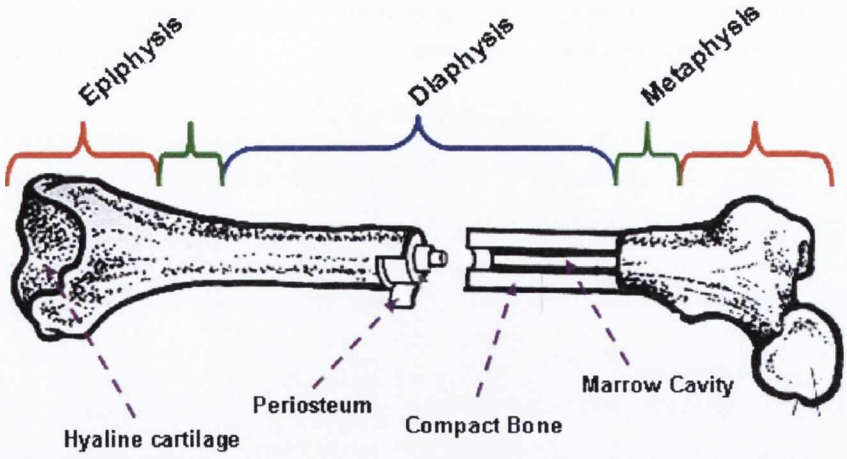

Figure 1.5: *Illustration of an adult femur highlighting the main structural components associated with bone.*[114]

The overall structure of adult bone, such as the femur illustrated in Figure 1.5, consists of a long tubular shaft called the diaphysis capped at either ended with an extended area known as the epiphysis. The conical region where these two sections meet is referred to as the metaphysis. The epiphysis region is covered with a thin layer of hyaline cartilage while a relatively strong periosteom membrane covers the remainder of the bone surface. The main function of this outer most membrane is to provide a route for circulatory and nervous supply to the bone structure. Within the periosteom, the walls of the diaphysis consist of compact bone (dense bone) which provides a protective layer around the internal marrow cavity. It is within this cavity that yellow bone marrow is found, a type of adipose tissue which is responsible for energy storage.[115]

The porosity of cortical bone is due to the presence of a large amount of haversian canals, volkmann's canals and resorption cavities which function as suitable passageways for the bone's nervous tissue and blood vessels. The haversian canals run parallel along the bone axis, while volkmann's canals provide an almost 3D network by extending roughly perpendicular to the surface (Figure 1.6). The inner regions of the metaphysis and epiphysis are made from a different type of bone material known as cancellous bone (trabecular or spongy bone) which consist of a honeycomb-like arrangement of trabecular plates and rods within the marrow compartments. Red bone marrow production occurs mainly within this bone type with blood cell formation being its main function. Cancellous bone is usually located in regions which are not heavily stressed or where stress occurs from many different directions, whereas, the opposite is seen for the heavy more durable compact bone material. Therefore, depending on the bone type and its location within the body, the ratio of compact to cancellous bone will differ. However, overall compact bone accounts for *ca.* 80% of the entire adult skeletal mass.[116]

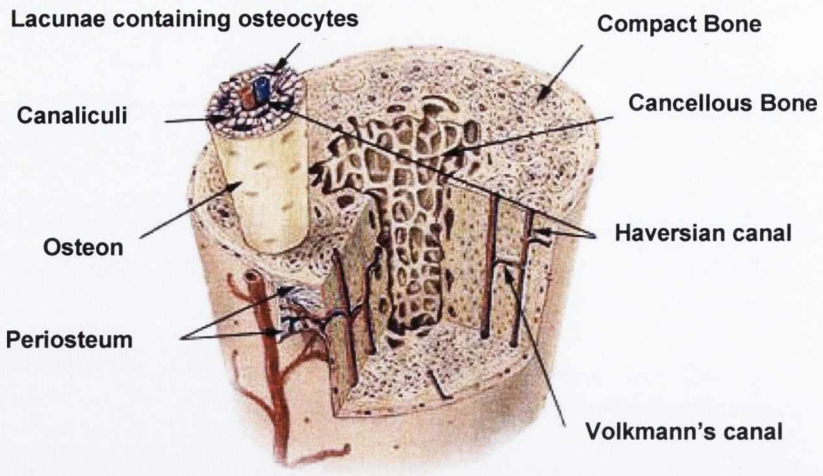

Figure 1.6: *Schematic diagram of the internal structure of bone.*[117]

1.7 Bone matrix and cellular composition

The main components of bone structure are the organic matrix (20 – 40%), inorganic matter (50 – 70%), bone cells (5 – 10%) and water. Accounting for almost two-thirds of the overall dry weight, the mineral component of bone consists mainly of calcium phosphate ($Ca_3(PO_4)_2$) and calcium hydroxide ($Ca(OH)_2$), which combine to form crystals of hydroxyapatite ($Ca_{10}(PO_4)_6(OH)_2$).[118, 119] The hydroxyapatite matrix contains many ions such as carbonate, citrate, phosphate, magnesium, fluoride, sodium and strontium which are incorporated directly into the crystal lattice or adsorbed on the crystal surface. This structure is extremely hard, but relatively inflexible and brittle. Therefore, although it can withstand strong compressions, if exposed to twisting or bending forces, the material would easily shatter. This limitation explains the requirement of the bone's organic component which consists of 90% collagen proteins. Comprised of predominantly type I collagen and a small quantity of type III, V and X, these collagen proteins are bundled together to form a series of collagen fibres. Unlike the hydroxyapatite material, these fibres are relatively strong when subjected to tension, bending and twisting forces, however, show little resistance to compression. Therefore, by the incorporation of the hard hydroxyapatite crystalline material within the relatively flexible collagen organic framework, bone has become an extremely strong, slightly flexible material which shows high resistance to shattering.[120, 121]

The dynamic nature associated with bone structure is as a result of its complex cellular composition. Bone consists of four main types of cells, osteocytes, osteoblasts, osteoprogenitor cells and osteoclasts, which together play an important role in the initiation and control of many of the principle bone processes such as growth, remodelling, repair and

mineral homeostasis. The characteristic structure and functions associated with each cell is as follows:[111, 112, 116, 121, 122]

1) Osteocytes:

This cell type is the most abundant in bone tissue accounting for almost 95% of the entire cellular composition. Each osteocyte is embedded within the bone matrix, occupying small chambers known as lacunae. The lacunae and thus the osteocyte cells are linked to each other *via* narrow canals called canaliculi which penetrate through the bone matrix, transporting essential nutrients and oxygen between the major blood vessels and the osteocyte cells (Figure 1.6). This complex 3D network promotes their function in maintaining the protein and mineral content of the surrounding matrix. The osteocyte cells also play a vital role in the repair of damaged bone tissue. Due to their ideal location and distribution throughout the bone matrix, they have the ability to behave as mechanosensors, by converting any mechanical strain on the bone into a biochemical signal and thus promoting the initiation of the repair and remodelling processes within the damaged region.[123]

2) Osteoblasts:

The osteoblasts are mononucleate cuboidal-shaped cells which are *ca.* 15 to 30 microns in size. They are commonly referred to as bone forming cells because of their ability to produce new bone matrix in a process called osteogenesis. This process involves the initial synthesis and secretion of collagenous protein to form the unmineralised organic matrix, referred to as the osteoid layer, followed by subsequent deposition of calcium salts into the organic framework, converting the osteoid matrix to bone material. Once the osteoblasts become completely surrounded by bone matrix, they begin to function as osteocyte cells.

3) Osteoprogenitor cells:

These mesenchymal (unspecialised cells) type cells are mainly located within the inner cellular layer of the periosteom or in the lining of the passageways and canals which contain the blood vessels. Their main function is to promote the production of the osteoblast cells and thus play a role in the control of the repair mechanisms of damaged bone structure.

4) Osteoclasts:

The osteoclasts are multinucleate giant cells with diameter lengths ranging from 20 to 100 microns in size. These bone resorbing cells are responsible for the removal and recycling

of the bone matrix by the erosion process known as osteolysis. This process involves the secretion of acids and proteolytic enzymes such as cathephsins K and matrix metalloproteinase 1 from the osteclasts cells to initiate the dissolution of the bone material and the subsequent release of the stored minerals. The lifetime of these cells is quite short, with the nucleus bearing a maximum life span of 10 days. Once the osteoclasts have undertaken their resorption function, these cells migrate into the marrow space, where they undergo apoptosis (programmed cell death).

1.8 Bone growth, modelling and remodelling

Due to its complex cellular composition, bone is continuously undergoing longitudinal and radial growth, modelling and remodelling during its lifetime. For example, bone growth begins at *ca.* six weeks after fertilisation and is a continuous process throughout our adolescence. The growth process can occur by two fundamental mechanisms, endochondral and intramembraneous ossification. Endochondral ossification uses a cartilage scaffold to initiate the formation of new bone material whereas the latter technique does not.[111] A common trend, however, between both methods is that regulation of the growth process is maintained through an efficient interplay between all major bone cells. Another feature of bone growth is the process of modelling. As a consequence of certain physiological changes and mechanical forces, modelling can result in an overall adjustment of the skeletal system to alleviate pressure and strain from the applied force.[123] This results in new bone formation occurring at a different location to where bone resorption initially took place. Modelling is therefore the main process by which the overall shape, size, volume and mass of the bone structure can be altered.[124, 125]

In contrast to the modelling process, bone remodelling ensures that bone resorption and formation are coupled in time and location, so that no overall change in the shape, mass or size of the bone occurs. The principle application of this bone renewal process is to maintain the strength and homeostatic balance of the bone structure. Remodelling is believed to be carried out by a structural unit called a bone remodelling unit (BRU), which consists of a tightly coupled group of osteoclasts and osteoblasts that sequentially result in the resorption of older bone material and formation of new stronger bone matrix. [115, 126] The overall bone remodelling cycle is summarised by the illustration shown below in Figure 1.7. The process involves four key stages, osteoclastic bone resorption, reversal, osteoblastic bone formation and calcification.

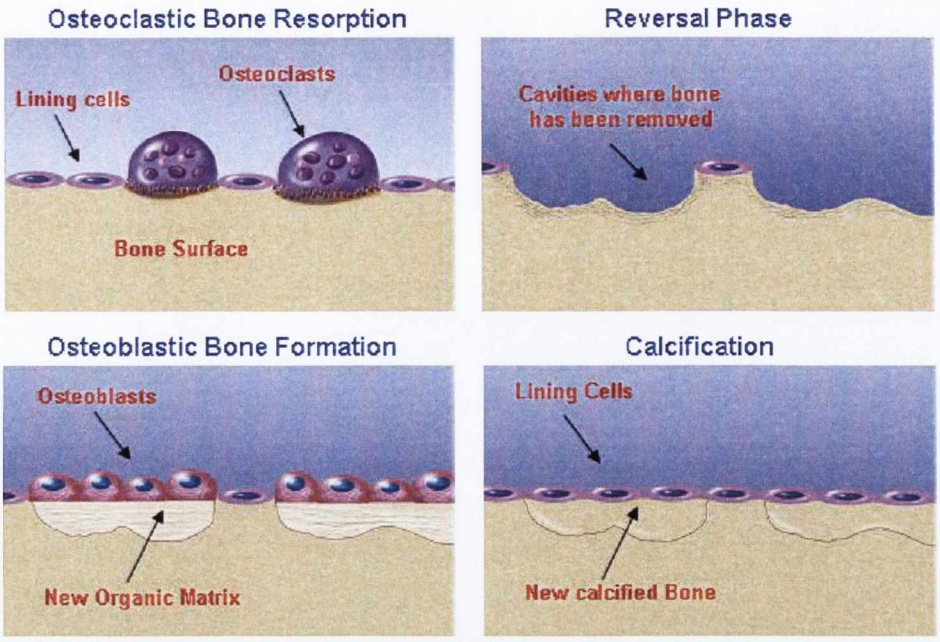

Figure 1.7: *Illustration of the major steps involved in the bone remodelling process.*[127]

The rate at which remodelling occurs is *ca.* 10% of the skeletal mass per year. The activation approach can often be random or occur at a targeted site due to the presence of damaged bone tissue. The initial step involves recruitment of the osteoclast cells to the region of interest with subsequent dissolution of the bone matrix using acidic and proteolytic enzyme secretions. For every remodelling cycle, the process can take up to 3–4 weeks. The 1–2 week reversal period simply involves the transition from bone resorption to bone formation. However, the exact signalling mechanisms which cause the initiation of this phase are unknown. The last two steps of the remodelling process involve secretion of new collagenous proteins by the osteoblast cells followed by calcification of the new bone matrix. New bone formation can take *ca.* 4 to 6 months to complete.[113, 128]

In order for the overall mass of the bone structure to remain constant during the remodelling process, the osteoblastic and osteoclastic activity must co-operate in unison. When an imbalance in this synchronistic process occurs, the formation of voids, known as microdamage or microcracks can occur in the bone structure resulting in an overall decrease in bone mass and strength. The following sections will introduce this bone condition, highlighting its principle cause and the role it plays in the development of the common skeletal disease known as osteoporosis.

1.9 Microdamage in bones

As previously discussed, bone is a rigid but dynamic organ which undergoes continuous repair, moulding and shaping throughout its lifetime. However, as a result of constant stress due to repetitive loading during normal day-to-day activities, the generation of

structural voids known as microcracks or microdamage can occur.[129-131] Studies have shown that microcracks are elliptical in shape, with transverse and longitudinal lengths of *ca.* 100 μM and 450 μM, respectively.[132, 133] It was in 1960 that Frost first made the link between microdamage formation and bone remodelling.[134] Subsequent theoretical arguments and experimental data over the years have supported this relationship and confirmed that microdamage formation is in fact a stimulus for the remodelling process.[125, 135-137] The mechanical stress that microcrack accumulation enforces on the bone matrix is thought to stimulate the osteocytes into action.[138] This will in turn increase the osteoclastic activity and therefore initiate the remodelling cycle.

These fatigue-related microcracks are particularly relevant to the aging population but are also common among athletes and those participating in strenuous activities.[139] Such structural damage gives an overall decrease in bone quality, which along with a decrease in bone mass can result in the formation of a stress or fragility fracture of the bone. A stress fracture is a partial or complete rupture in normal bone caused by repetitive stresses, rather than a single traumatic incident. They are often caused by the ability of the muscles to adapt more rapidly than the relatively weaker bone to a new activity.[140] Runners are prone to stress fractures of the metatarsals (long bones in the foot), whereas golfers are more likely to suffer fractures of their hamate (bones of the wrist). On the other hand, fragility fractures occur as a result of a single minor trauma in an area of the skeletal system which has been weakened due to microcrack generation. Provided that the bone structure is not placed under repetitive stress and its cellular activity remains efficient, bone should remain healthy, with little microdamage accumulation. However, there exist two common situations in which the amount of microcrack formation in bone structure can show a rapid increase:

1) Higher rate of damage generation than that of the remodelling/repair mechanism leading to excess damage.

2) A normal rate of damage generation which accumulates due to a defective repair or remodelling mechanism, resulting in deficient repair.

Early detection of accumulating microdamage is essential as it often leads to the development of the well known skeletal disease, osteoporosis. This condition characterised by decreased bone mass results in increased fragility of bone structure and its subsequent high susceptibility to fracture. The World Health Organisation (WHO) defines osteoporosis as bone mass 2.5 standard deviations (SD) below the mean for bone mineral density in young adults.[141] Early diagnosis of this disease is often difficult as it presents few symptoms until

the initiation of the first bone fracture. Affecting *ca.* 20 million people in the US alone, osteoporosis not only reduces one's quality of life but it can also be a huge financial burden, with various medical expenses and loss of work associated with the condition. The risk factors related to the disease are diverse with gender, race, family history, nutrition, exercise and skeletal size being the most common. Females over fifty are a major target, as the conditions seems to accelerate post-menopause, due to the rapid decrease in their estrogens levels.[119, 142] This hormonal imbalance, which affects the cellular activity and thus the bone repair mechanisms is less common in men as they continue to produce androgens until relatively late in life. As shown in Figure 1.8, osteoporotic bone appears porous in nature with little compression required to cause a rupture.

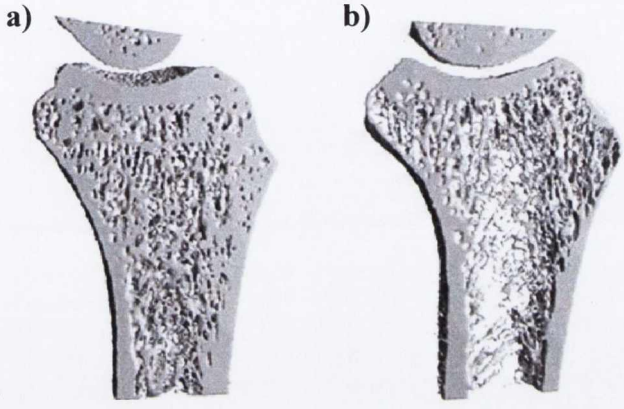

Figure 1.8: *Illustration highlighting the dense nature of healthy bone (a) in comparison to the more porous osteoporotic bone material (b).*[143]

The two most common techniques used today for the diagnosis of osteoporosis are routine X-ray imaging and dual-energy X-ray absorptiometry (DXA).[144] Although osteoporotic bone appears lighter and thinner than normal healthy bone in X-ray film, a major limitation of this method is that only diagnosis of late stage osteoporosis can be achieved. Therefore DXA, which gives a bone mineral density reading in different areas of the skeletal system and compares it to previous statistical data is the more routine method used. However, this quantitative technique gives no understanding of the quality of the different regions of the bone structure or the exact location of the accumulating microdamage. This significant drawback has driven research in a more qualitative direction, by concentrating on the development and evaluation of new contrast agents for microdamage visualisation. Therefore, the remainder of this chapter will focus on some of the most important contrast agents reported and show how microdamage detection is progressing from the original *in vitro* histological staining to more significant *in vivo* based methods.

1.10 Histological detection of microdamage

Due to the complex nature of bone structure, distinguishing microcrack regions from the remaining healthy bone matrix can often prove difficult. This has led to the investigation of a wide variety of dyes which in conjugation with a suitable microscopy technique provide an efficient contrast of the damaged areas. Frost was the first to successfully detect microcracks produced *in vivo* using the ethanol soluble dye "basic fuchsin" coupled with transmitted light microscopy.[134] As shown in Figure 1.9, this dye consists of varying mixtures of four triamino-triphenylmethane homologues, with increasing degrees of methylation; pararosaniline (**43**), rosaniline (**44**), megenta II (**45**) and new fuchsin (**46**).

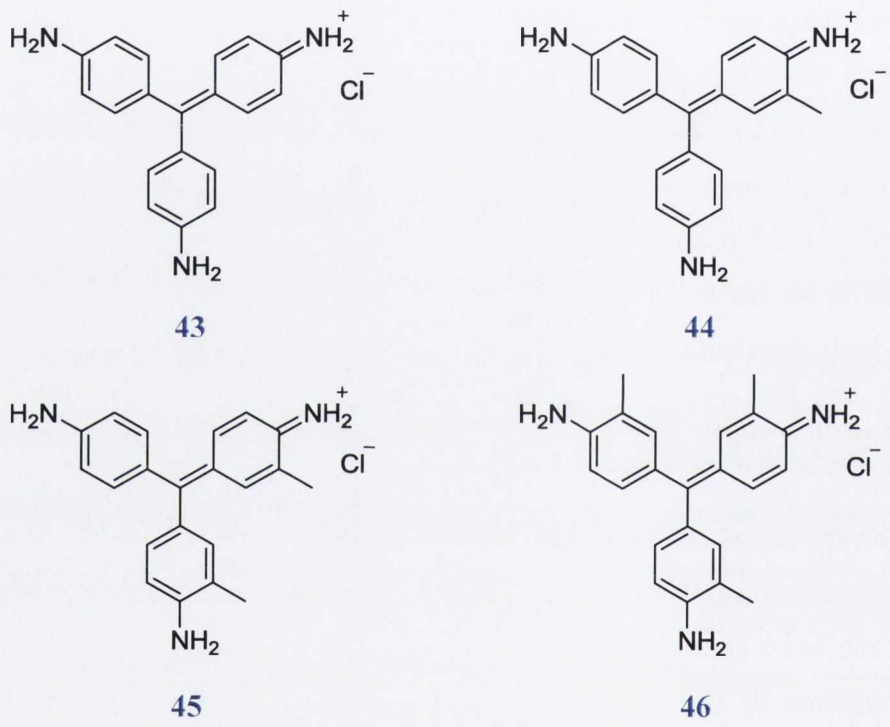

Figure 1.9: *Chemical composition of basic fuchsin*

After the bulk staining procedure, all bone preparation such as cutting, grinding and polishing was carried out in aqueous medium. As basic fuschin displays very poor water solubility, this ensured that no leaching of the dye from microcracks produced *in vivo* into artefactual damage created during the machining procedures occurred. The possibility that alcohol dehydration during the bulk staining procedure could result in shrinking, and thus create artefactual cracking, was eliminated by investigations carried out by Burr and Stafford.[145]

Detection of fuchsin stained microcracks using transmitted light microscopy can be quite laborious as variations in light intensity, magnification and depth of focus are required to successfully distinguish labelled cracks from the healthy bone matrix. This resulted in Lee

et al.,[146] exploiting the diachromic nature of basic fuchsin by examining *in vivo* microcracks in human ribs using epifluorescence microscopy. Upon green excitation (545 nm) of the fuschin stained bone samples, an intense orange emission could be seen within the microcrack regions, while the undamaged bone matrix and any artefactual cracks present remained much darker. A similar contrast was observed under UV epifluorescence (365 nm), where only labelled *in vivo* microcracks displayed a strong purple emission.

The successes associated with epifluorescence led to the investigation of various other targeting based fluorochromic based dyes for microdamage detection. It is well known that upon generation of microcracks within the hydroxyapatite matrix of the bone, cleavage of the phosphate bonds results in the exposure of charged ions, 55% of which are Ca^{2+}, on to the surface of the microcrack region.[130, 140] Therefore, the use of Ca^{2+} chelating agents should give the benefit of more efficient site selectivity and thus provide a larger contrast from the healthy bone matrix. A series of five chelating fluorochromes belonging to the tetracycline family, calcein **47**, xylenol orange **48**, alizarin complexone **49**, calcein blue **50** and oxytetracycline **51** were studied by Lee *et al.*,[147] for their potential use as microcrack labels. All five dyes were as effective at labelling as basic fuchsin, however, unlike fuchsin, which only lodges in the structural voids or may show some binding to collagen, the selectivity associated with **47–51** was due to their ability to sequester a metallic ion such as Ca^{2+} using the carboxylate and hydroxyl functionalities of their structures. As a result of the different emission wavelengths of these five dyes, sequential labelling could be used to differentiate pre-existing and test-induced microdamage as well as providing a useful technique to monitor crack growth.[148]

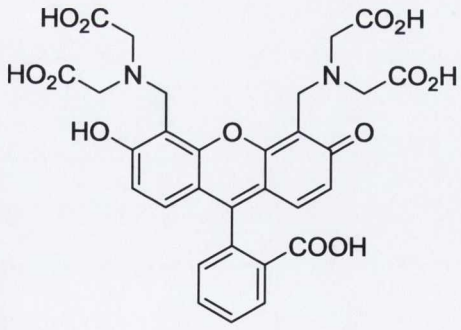

47

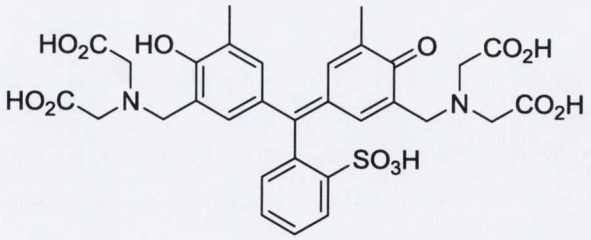

48

49

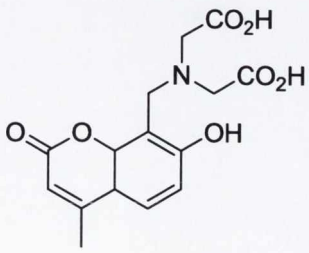

50

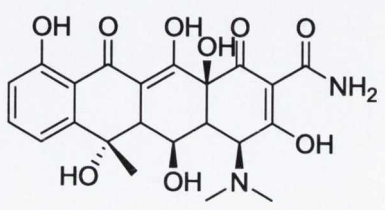

51

However, disadvantages such as limited water solubility (solubility of alizarin complexone and calcein in water are 0.1% and 0.4% respectively (*w/v*)), high pK_a (pH dependent within the physiological pH range) and the highly fluorescent nature of these dyes before any labelling sparked the requirement and study of different chelating agents which could be used to overcome these drawbacks. Gunnlaugsson and co-workers[129] reported the application of a set of commercially available PET based Ca^{2+} sensors such as calcium crimson (**52**) and calcium orange (**53**), for the selective detection of microcracks created on the surface of bone structure using an *in vitro* scratching technique previously reported by O'Brien *et al.*[133]

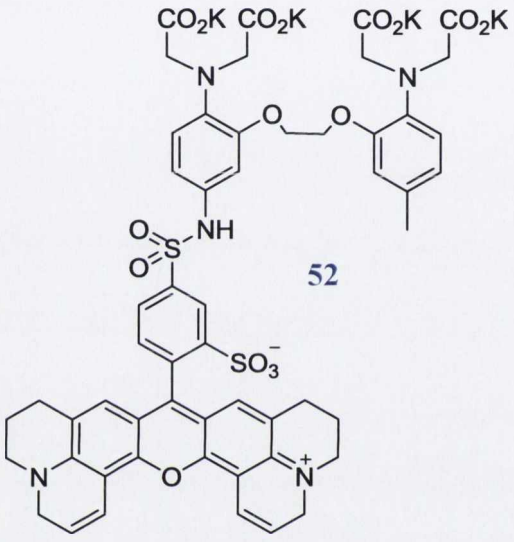

52

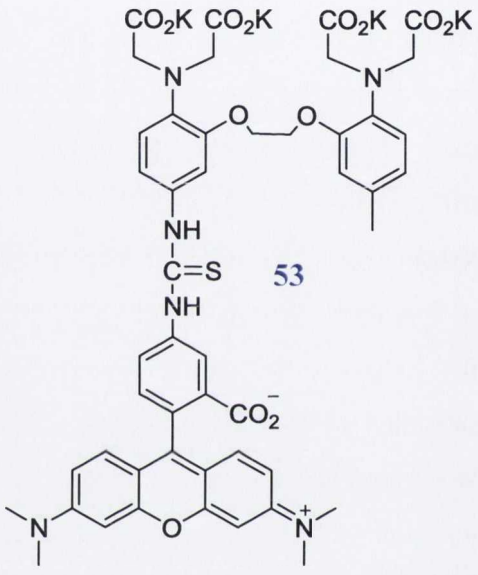

53

With previous applications in Ca^{2+} intracellular imaging, [149-151] these sensors display high water solubility, pH independence within the physiological range and due to the PET process are non-fluorescent in the absence of Ca^{2+} ions. Therefore, it was shown using epifluorescence imaging, upon binding of these dyes to the exposed Ca^{2+} sites within the scratched region, the PET quenching of the fluorophore was inhibited, with subsequent high emission intensity being observed within the scratched area. Outside the scratched region, minimal emission from the dyes was observed, verifying the much poorer binding ability of these contrast agents to the healthy undamaged bone matrix. This selectivity for the scratched regions was also confirmed using Raman and energy dispersive X-ray (EDX) spectroscopy, where a very different spectrum was recorded within the labelled scratch area from the unlabelled bone matrix.

With great success observed for those dyes incorporating the Ca^{2+} chelating iminodiacetate functionality, Parkesh *et al.*,[152] reported the PET based sensors **54a** and **54b**, using a 4-amino-1,8-naphthalimide moiety as the chromophoric platform. Epifluorescence analysis of scratched bone samples, labelled with each dye, showed upon UV excitation (365

nm) an intense green emission within the scratched regions, due to the selective binding of **54a** and **54b** to the Ca^{2+} ions exposed upon scratch generation. Similar to previously reported dyes, the poor binding ability to the remaining healthy bone surface provides the contrast required for selective detection of the bone scratches. As was the case for **52** and **53**, the authors explained that the binding of the iminodiacetate unit of **54a** and **54b** to the Ca^{2+} ions within the scratch, inhibited the PET process and thus resulted in the observed naphthalimide green emission. To further understand the mechanisms of scratch labelling, Gunnlaugsson and co-workers investigated the binding ability of the commercially available dye Rose Bengal, **55**, which only allows ionic interactions with its carboxylate group.[129] During scratch testing, the bright pink colour of the dye was clearly visible within the scratched region, reinforcing the fact that the binding process at the microcrack site is ionic in nature.

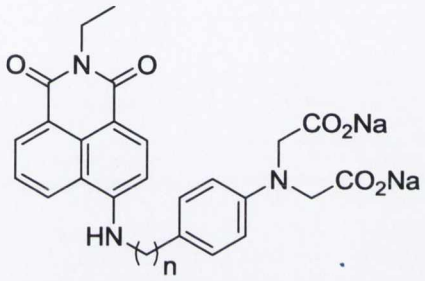

54a: n = 1
54b: n = 2

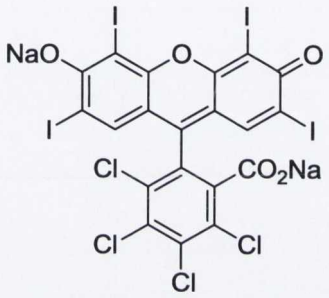

55

In summary, for all the studies discussed above, the labelling technique involves *in vitro* methods, with immersion of a bone sample in a solution of the contrast agent followed by some microscopy technique for microcrack detection. However, there exist reports of microdamage labelling using a fluorescent dye *in vivo,* where the contrast agent is intravenously administrated into a live animal, followed by microscopy analysis of the bone samples after the animal has been sacrificed. In 1993, Stover *et al.*,[153] were the first to report the ability of the fluorescent dye **47** to selectively label microdamage upon administration to a race horse. Using a dose of 15 mg/Kg of the dye, epifluorescence analysis confirmed the ability of **47** to circulate the blood system of the animal and selectively label the microcracks which were present within its bone structure. Bulk staining of the bone specimen with basic fuchsin was used as a control to ensure it was in fact microcrack labelling which was being observed. O'Brien *et al.*,[138] also reported the detection of microcracks *in vivo* using two of the other tetracycline based dyes previously discussed, **50** and **51**. The study involved administration of the fluorochromes into the circulatory system of rats, followed by formation of bone microdamage using an established rat hindlimb suspension model. After sacrifice and preparation of bone specimens from the humeri and femora of the rats,

epifluorescence microscopy showed successful labelling of microcracks with both dyes. Both of these studies successfully highlight the efficiency of those contrast agents bearing the iminodiacetate functionality to selectively bind to the exposed Ca^{2+} sites within microdamaged areas and also their ability to circulate through the blood circulatory system of the animals and localise within the bone structure.

Although histology is by far the most commonly used method for the detection of microdamage in bone structure, one major problem with this technique is that it involves invasive sampling using bone biopsies. Therefore, recent studies have begun to concentrate on the development of more efficient methods for non destructive, 3D detection and imaging of microdamage in bone structure. The following section will give a brief summary of some of these newer techniques, highlighting the advantages they could potentially possess over histological staining.

1.11 Potential non-invasive microdamage detection

The requirement for more real-time *in vivo* monitoring of microdamage in bone structure has resulted in the investigation of various contrast agents, which when coupled to techniques such as positron emission tomography (PeT), micro-computed tomography (μCT), NMR, Raman spectroscopy and high speed photography have shown great imaging potential for damaged bone structure.[154-157] Li *et al.*,[158] were the first to investigate the use of PeT scanning to detect and subsequently quantify microdamage *in vivo* using a high-resolution PeT scanner and the radioactive [^{18}F]NaF tracer. Due to the ability of the PeT scanner to detect regional concentrations of radioactivity and the specificity of the [^{18}F]NaF tracer for areas of abnormal osteogenesis (bone growth), this technique allowed for successful detection of *in vivo* microdamage in live rats. Incorporation of the [^{18}F] fluoride ion into the bone surface occurs through ion exchange with the hydroxyl group of the hydroxyapatite matrix, with a preference for regions of high bone turnover and remodelling. Basic fuchsin histological staining was used to ensure the "dark spots" which appeared in the PeT images were in fact areas of microdamage accumulation.

Another imaging technique which has gained a great deal of attention for microdamage detection is μCT. Tang *et al.*,[159] and Wang *et al.*,[160] reported the use of the radio opaque contrast agents lead-uranyl acetate and barium sulphate, respectively, for detection of microdamage in trabecular bone. Both studies involved microdamage creation by applying stress of varying force to bone specimens followed by successful 2D and 3D visualisation of damaged regions using μCT. The authors explain that the observed contrast was caused by precipitation of the contrast agents within the microdamaged region, which

results in an enhancement of the voxel intensity for that particular area due to the higher X-ray attenuation. At present, all μCT analysis has been *in vitro* imaging with image resolution and contrast agent dosage limiting the *in vivo* detection using clinical CT scanners. However, it is unknown whether the synthesis of more efficient and targeting contrast agents coupled with the development of higher resolution CT scanners will in time overcome these limitations and promote the capability of *in vivo* microdamage imaging.

One major problem with the opaque contrast agents previously discussed is that they were non-specific and therefore localised in any structural voids including the vascular canals and free spaces of the bone structure. In 2006, Gunnlaugsson and co-workers worked to improve the targeting ability through the synthesis of a series of iodinated contrast agents which incorporated the Ca^{2+} chelating iminodiacetate functionality.[161]

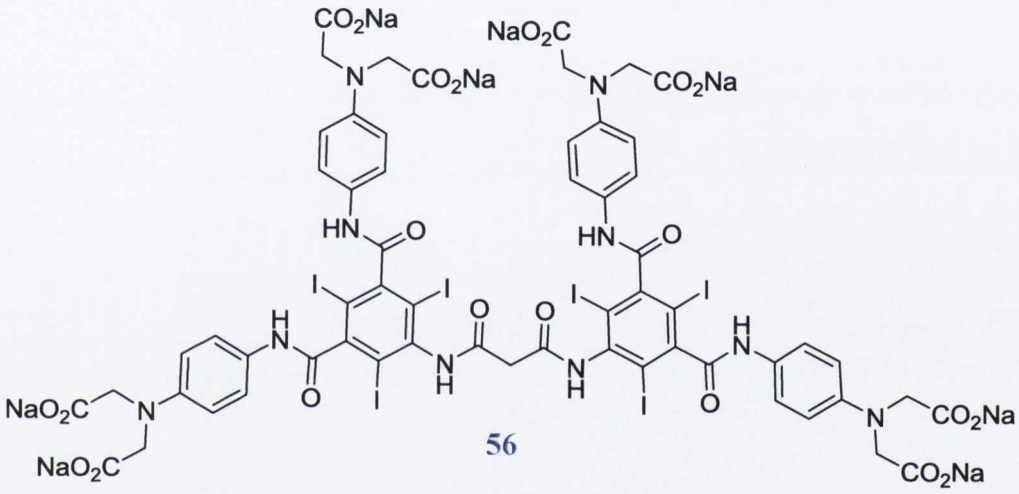

56

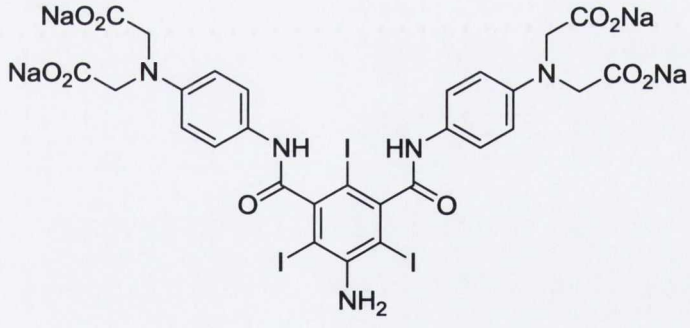

57

As seen from the structures of ligands **56** and **57**, the design of these contrast agents was based on a 1,3,5 triiodobenzene platform. It was anticipated that successful chelation of the iminodiacetate binding pockets of these ligands to the exposed free Ca^{2+} ions would increase concentration of iodine within the damaged sites and allow X-ray imaging, such as μCT, to distinguish such sites from the surrounding healthy bone surface. When applied to an unscratched bone sample in the powdered form, a significant contrast could be seen in the areas were the dye seemed to have bound or lodged within the surface. However, when the

dyes were used in solution studies of scratched bone specimens, no major contrast of the scratched regions could be seen from the healthy bone matrix. The authors suggest that the most likely reason for this is due to the beam hardening effect which masks any contrast which could be seen from the contrast agents.

In 2010, due to their ease of functionalisation, relative biocompatibility, colloidal stability and above all high X-ray attenuation, Roeder and co-workers investigated the use of AuNP as potential X-ray imaging agents for microdamage detection.[162] As shown in Scheme 1.3, successful functionalisation of the AuNP with the natural amino acid glutamic acid was achieved. Such attachment to the gold surface *via* the primary amine left the carboxylate groups free for potential chelation to the Ca^{2+} ions exposed upon microdamage generation. After immersion of the scratched bone samples in an aqueous solution of the AuNP for two days, transmitted light microscopy showed selective labelling of the damaged regions through visualisation of the characteristic red colour of the AuNP. Other techniques such as scanning electron microscopy (SEM) and atomic force microscopy (AFM) were used to confirm that the observed contrast was caused by more efficient binding of the AuNP to the damaged regions over the remaining healthy bone matrix. The observed selectivity for these functionalised AuNP makes them promising candidates as potential *in vivo* targeting X-ray contrast agents for damaged bone tissue, however, as of yet, no X-ray imaging using these systems has been reported by Roeder and co-workers.

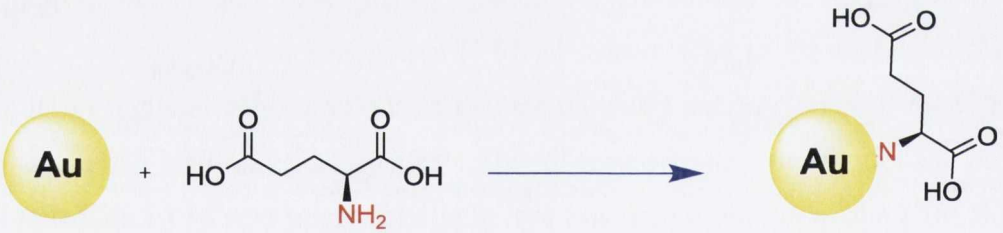

Scheme 1.3: *Illustration showing the functionalisation of a AuNP surface with glutamic acid via the amino acids primary amine.*

It is clear from the examples given above, that research is beginning to concentrate on the investigation of more *in vivo* based methods for the visualisation of microcracks in bone structure. However, the more classical histological staining techniques are not being forgotten, with more selective and targeting contrast agents still being developed. The work presented within this thesis will tackle both areas, developing contrast agents which can be used for histological staining but also offer the potential to be used for in vivo imaging.

1.12 Conclusion

The design and development of luminescent signalling probes has in recent years become an active area of research in supramolecular chemistry, with applications varying from simple metal ion detection to more diagnostic and therapeutic advantages in the area of biomedical research. The need for more online *in vivo* detection has resulted in a larger emphasis being placed on the development of molecular systems which bear long lived excited states, allowing them to overcome the poor signal-to-noise ratio caused by the short lived background emission (autofluorescence) and light scattering from biological material. Concomitantly, with the introduction of more advanced NMR imaging techniques, the development of metal based contrast agents for MRI imaging has also attracted a great deal of attention, especially in the field of diagnostic clinical medicine.[35, 36]

This chapter therefore began by introducing the reader to the Ln ions, highlighting the key photophysical and magnetic properties they have to offer. A large emphasis was placed on their emission properties, with the concept of indirect excitation *via* the "antenna effect" being discussed in great detail. With their potential toxicity to the body and vulnerability to luminescence vibrational quenching by metal bound water molecules, the necessity for thermodynamically and kinetically stable polydentate chelating ligands which fulfil their high co-ordination requirements was discussed. This led to the introduction of a variety of cyclen based Ln probes which have been exploited for applications varying from pH detection to cation and anion sensing. All systems were based on the same macrocyclic framework but through variation of the pendant arms on the cyclen cavity and by incorporation of an appropriate Ln metal ion, very different magnetic and luminescent probes were developed. The ability of these "rare earth metals" to be used in cellular uptake studies and in diagnostic and therapeutic imaging was also highlighted.

The remainder of this chapter concentrated on the biological aspect of this thesis, introducing the reader to bone structure and how the formation of structural voids called microcracks can lead to the development of the well-known skeletal disease, osteoporosis. A brief summary of the key anatomical and physiological aspects of bone were required to gain an understanding of how microdamage accumulation can occur and the major consequences of this destructive phenomenon. Some of the most important histological contrast agents which have demonstrated high selectivity for microcrack regions over the remaining healthy bone surface were presented. The final section of this chapter concentrated on potential non-destructive imaging techniques which when coupled with a suitable contrast agent allowed for visualisation of damaged bone structure.

1.13 Work described within this thesis

Overall the aim of this thesis is to build on the work previously carried out within the Gunnlaugsson group, developing novel luminescent and magnetic Ln based probes with applications varying from metal ion detection and microdamage imaging to monitoring of certain biological processes. All systems will be based on the macrocyclic cyclen framework, with variations in the pendant arms determining the particular application which is required.

In *Chapter 2*, the design, synthesis and photophysical evaluation of novel Ln luminescent systems which bear the potential for selective microdamage detection are described. All systems allow for the incorporation of the microcrack specific iminodiacetate functionality within their overall structures and bear an antenna to allow for indirect excitation of the Ln metal. A detailed study of the effect of pH on the photophysical properties of these systems will be discussed, with a greater emphasis being placed on any luminescence modulation. The response of these Ln probes in the presence of various physiologically important metal ions will also be described.

In *Chapter 3*, the ability of these Ln luminescent imaging agents to show selective binding to microscratched regions on the external surface of bone using both epifluorescence microscopy and laser-scanning confocal microscopy imaging techniques will be discussed. It was anticipated that the Ln complex with the greatest number of iminodiacetate binding units would show more efficient binding to the exposed Ca^{2+} sites and therefore provide the most significant contrast from the remaining healthy bone surface. The ability of these Ln complexes to penetrate bulk bone material and pass through the vascular canals allowing detection of internal microdamage will also be described.

In *Chapter 4*, the more non-invasive MRI imaging technique for detection of microdamage in bone structure will be discussed. Complexation of the ligands used in the previous chapters with the paramagnetic Gd(III) metal along with the synthesis of two more Gd(III) complexes which do not incorporate an antenna functionality will be described. Their potential as MRI contrast agents will be investigated, focusing on changes in their relaxivity values as a function of pH and in the presence of biologically important cations and anions. Finally, preliminary MRI imaging of microscratched regions both on the surface of bone and internally using a 7T animal scanner will be detailed.

In *Chapter 5*, the design, synthesis and photophysical evaluation of a novel Tb(III) thiol sensor, which incorporates the maleimide ring within its structure, will be discussed. Based on the 1,4-Michael addition of the sulfhydryl residue of the thiol molecules to the alkene bond of the maleimide functionality, any modulation in the luminescence properties of the Ln probe will be detailed. A larger emphasis will be placed on the detection of

glutathione, with a method for determining the ratio of reduced to oxidised glutathione also being described. An introduction to thiol sensing and glutathione as well as a brief literature review of some of the most significant thiol sensors reported to date will also be given.

In *Chapter 6*, the ability of a Tb(III) complex previously synthesised and evaluated for microdamage detection to display sensing of both copper and mercury in aqueous solution will be described.

Finally, in *Chapter 7*, general experimental procedures are provided and the characterisation of all the compounds described is given.

Chapter 2

Synthesis and Photophysical Evaluation of Lanthanide Luminescent Bone Imaging Agents

2.1 Introduction

As previously discussed in Chapter 1, bone is a rigid but dynamic structure, which undergoes continuous repair, moulding and shaping throughout an individual's life.[129, 130, 163] However, as a result of continuous stress due to repetitive loading during normal day-to-day activities, the generation of structural voids known as microcracks or microdamage can occur.[132, 137] These fatigue-related microcracks are particularly relevant to the ageing population but are also common amongst athletes and those participating in extreme physical sports. Such structural damage gives an overall decrease in bone quality, which along with a reduction in its mass results in weaker, more rigid bone structure.[164-166] Early detection of accumulating microdamage is essential as it can often lead to the development of the well known skeletal disease, osteoporosis.[119, 141] However, due to the complex organic matrix and crystalline hydroxyapatite composition of bone, it can be difficult to distinguish such structural damage from the remaining healthy bone surface. Hence, the development of novel contrast agents which have the ability to penetrate the bone matrix can enable a greater understanding of this complex morphology.

Building on previous work reported by Gunnlaugsson and co-workers[129, 130, 152, 161, 164, 165], the principle aim of this project was to design and develop luminescent Ln bone-targeting imaging agents which have the potential for selective detection of damaged bone structure under physiological pH conditions. The design of these cyclen based Ln complexes, incorporating the microcrack specific iminodiacetate binding moiety, envisaged a more targeting approach to microdamage bone diagnostics. A number of factors such as stability of the Ln metal ion, incorporation of an appropriate sensitising antenna and the pH independence of the agent within the physiological pH window required careful consideration when designing these complexes, with the principle aim of maximising their ability as luminescent contrast agents. The following section will begin by detailing the initial design stages of these complexes, with a description of their synthesis and characterisation also given.

2.2 Designing luminescent lanthanide bone imaging agents

One of the key advantages of using the Ln ions as potential imaging agents for microdamage detection (over all other fluorescent probes described in Chapter 1) is their longer lived excited states, which occur mainly in the μs to ms time range. This provides the possibility of time-resolved detection, which allows the desired luminescent signal to be easily distinguished from the much shorter lived background fluorescence of biological material.[37, 42] This method involves the application of a time delay between the initial

excitation of the Ln and the measurement of the resulting Ln luminescence, ensuring that any biological fluorescence has diminished to negligible levels.[34] With the benefit of providing a good signal-to-noise ratio, the advantage of using these metal ions for *in vivo* imaging is evident. However, the potential toxicity of the Ln to the human body must be considered. Due to the marked similarities in the hard acid characteristics of Ln and Ca^{2+} ions, such as ionic size, donor atom preference and coordination geometry, high exposure of free Ln ions can result in replacement of Ca^{2+} sites in proteins, bearing a significant effect on various essential biological and enzymatic processes.[39, 167] Therefore, in order to use these ions *in vivo*, the design of ligands which allow for the formation of thermodynamically stable and kinetically inert complexes is required. As extensively discussed in Chapter 1, a large variety of ligands which are based on the macrocyclic cyclen framework have been developed, where through alkylation of the amine sites with various donor pendant arms, high stability upon complexation with a Ln ion was achieved. These ligands also help fulfil the high co-ordination requirements of these metals, ensuring that the Ln are shielded from protic solvents such as H_2O, which are known to quench Ln luminescence by non-radiative vibrational deactivations through the O-H oscillators.[34, 53]

Another factor which requires consideration is the incorporation of a suitable antenna to enable indirect excitation of the Ln ion. As previously discussed, due to the "Laporte-forbidden" nature of their *f-f* transitions and therefore their low absorption coefficients, direct excitation of the Ln ion can prove difficult. To overcome this drawback, the excited state of the Ln can be populated by sufficient energy transfer from the triplet excited state of an organic chromophore, resulting in sensitised Ln luminescence. For this to occur, it is necessary that the triplet excited state of the sensitising antenna is at least 1700 cm^{-1} above the excited state of the Ln ion, as a smaller energy gap normally results in a thermally activated back-energy transfer process, making population of the Ln excited state much more difficult.[34, 168] Besides achieving successful energy transfer, it is also essential to select a chromophore which shows little dependence on pH and thus has no protonation or deprotonation sites with pK_a values within the physiological pH range.

In order to gain selectivity for the microdamaged regions of bone structure, the ligand must also bear a binding unit which displays significant preference for damaged bone structure over the remaining healthy smooth bone surfaces. With significant success being previously shown for fluorophores which incorporated the iminodiacetate functionality within their overall structures, the use of such a binding motif for this project was explored.[130, 152, 164] It was anticipated that the chelation of Ca^{2+} ions exposed upon microdamage formation *via* the iminodiacetate moiety would result in selective binding of

the complex to the damaged bone structure, which upon indirect excitation of the Ln ion, would provide a significant contrast from the undamaged healthy bone surface.

Ln.58: Ln = Tb(III), Eu(III)

Based upon those factors mentioned above, ligand **58** and the corresponding Tb(III) and Eu(III) complexes, **Tb.58** and **Eu.58**, were initially designed. On analysis of the cyclen cavity, **58** provides eight potential coordination sites for the Ln ions; four from the macrocyclic nitrogen atoms and four from the oxygen atoms of the flexible acetamide pendant arms. With a common coordination number of nine for these Ln ions, the final site is most likely to be filled by a H_2O molecule. It is important to note that the iminodiacetate chelating unit in **58** is protected as its ethyl ester form, ensuring that complexation occurs solely within the cyclen cavity. Another possible advantage in the synthesis of these ester protected Ln complexes is their potential to be used as experimental controls. It is anticipated that these complexes should display much poorer binding abilities to the damaged bone regions, and therefore may be beneficial in highlighting the essential requirement of the iminodiacetate functionality for sufficient microdamage detection.

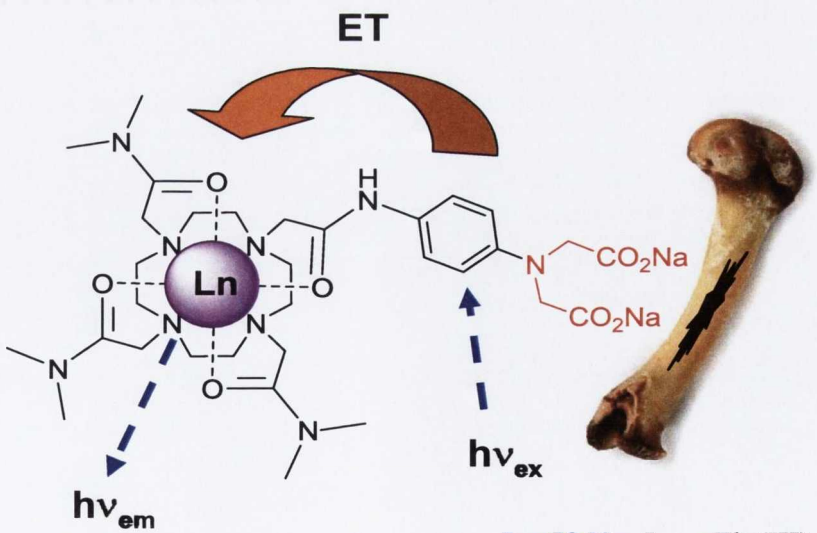

Ln.58.Na: Ln = Tb (III), Eu (III)

Figure 2.1: *Illustration showing the indirect excitation process of* ***Ln.58.Na*** *(Ln = Eu(III), Tb(III)) via the covalently attached phenyl chromophore and the iminodiacetate chelating unit required for selective microdamage detection.*

Successful base hydrolysis of the ethyl ester functionalities will allow for the exposure of the chelating iminodiacetate unit to give the more selective Ln bone imaging agents, **Tb.58.Na** and **Eu.58.Na**, shown above in Figure 2.1. The overall ligand structure allows for the incorporation of a single phenyl antenna, which upon excitation at its λ_{max} should enable sufficient population of the excited states of the Ln ions by means of an intramolecular energy transfer (ET) process, previously discussed in Chapter 1. It was not evident at this stage whether the binding event which occurs at the damaged bone region would bear significant effect on this ET process. The successful chelation of the Ca^{2+} sites could perturb the excitation process and in turn result in a decrease in the Ln luminescence response. A key reason for selecting this initial ligand design was that, based on previously reported ligand structures which have a similar phenyl iminodiacetate functionality within their framework, these Ln complexes should show very little dependence on pH within the physiological pH range.[79, 165]

The following section will give a detailed description of the synthesis and characterisation of ligand **58** and the corresponding Tb(III) and Eu(III) complexes, **Tb.58** and **Eu.58**, followed by a photophysical evaluation of these systems.

2.3 Synthesis and characterisation of ligand 58

The initial steps in the synthesis of **58** involved the formation of the pendant arm 4-(β-chloroethanamido)-1-[*N,N*-bis(ethoxycarbonylmethyl)-amino]-benzene **59**. As shown in Scheme 2.1, this involved the initial di-alkylation of aniline **60**, with ethyl bromoacetate **61**, using Na_2HPO_4 and KI in refluxing CH_3CN for 24 h. Analysis of the resulting crude mixture verified the presence of both the mono and the di-alkylated aniline products, which on purification using flash silica column chromatography (using a gradient elution of 100 → 70:30 Hexane:EtOAc), resulted in the isolation of **62**, in 56% yield. Selective nitration at the *para* position of **62** was achieved by stirring in acetic acid, at 0 °C, followed by the addition of 70% nitric acid. Recrystallisation of the crude product from EtOH gave **63**, in 93% yield. The next step involved the reduction of the nitro group to the corresponding amine, which was attained in 90% yield by catalytic hydrogenation using 10% Pd/C, in DMF. To allow for the incorporation of an amide spacer between the cyclen moiety and the phenyl chromophore in the final ligand, **64** was reacted with excess chloroacetyl chloride **65**, along with Et_3N, at -10 °C (acetone/ice bath), in CH_2Cl_2. Any unreacted **65** along with the NEt_3 salt were removed by extraction with H_2O, 0.1 M HCl and brine, to give **59**, in 86% yield.

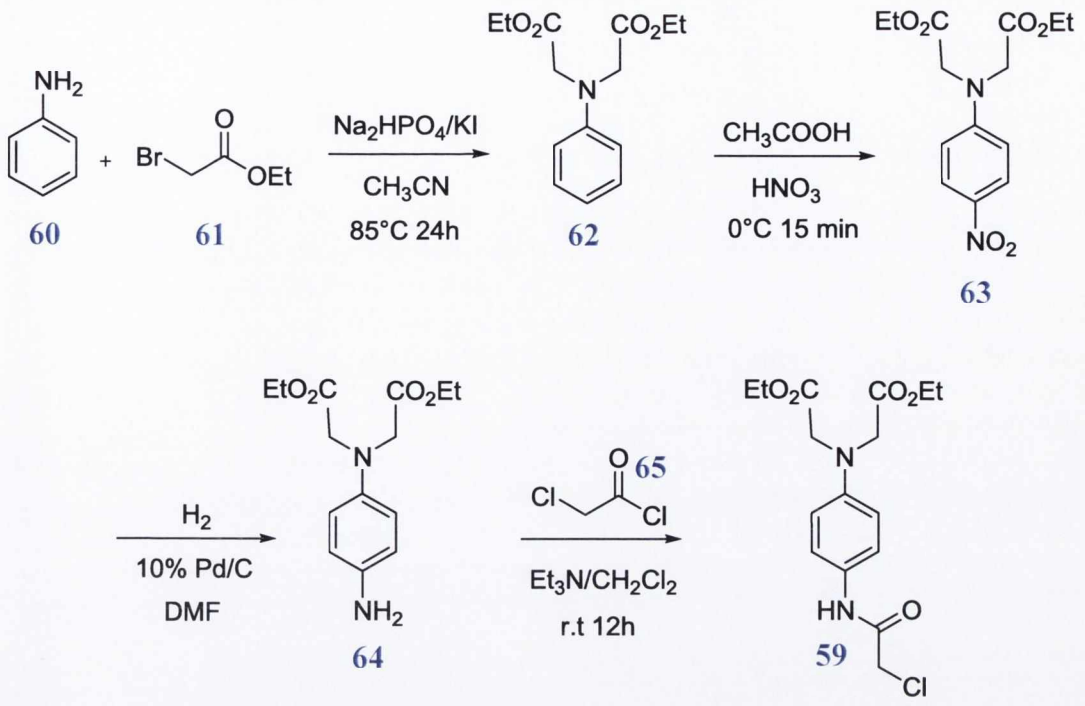

Scheme 2.1: *Synthetic pathway for* **59**.

^{1}H and ^{13}C NMR along with other conventional methods such as infrared (IR) spectroscopy and high resolution mass spectrometry (HRMS) were employed for complete characterisation of all the above compounds. In the case of **62**, **63** and **64**, the spectral data for these products was in good agreement with published characterisation.[161] The ^{1}H NMR spectrum ($CDCl_3$, 400 MHz) of **59** showed the expected two aromatic resonances at 7.36 and 6.58 ppm, with the appearance of the NH resonance at 8.24 ppm indicating successful alkylation of the amine site with **65** (Figure A1.1). Another clear indication of successful product formation was the appearance of a singlet at 4.11 ppm, corresponding to the α-chloro CH_2 protons. The CH_3 protons of the diethyl iminodiacetate moiety appeared as a triplet at 1.27 ppm, with the adjacent CH_2 groups resonating as a quartet at 4.20 ppm. The remaining CH_2 protons of **59** appeared as a singlet at 4.14 ppm. ^{13}C NMR was also employed to characterise and verify the purity of ligand **59**, whereas electrospray mass spectrometry (ESMS) analysis showed the presence of a peak at m/z = 379.10 which corresponds to the $[\mathbf{59}+Na]^+$ species in solution.

With **59** successfully synthesised in a high yield, the next step involved the introduction of this phenyl diethyl iminodiacetate pendant arm to the cyclen framework using the mono alkylation procedure recently published by Gunnlaugsson and co-workers.[169] The reaction conditions involved refluxing overnight, four equivalents of **66** with one equivalent of **59**, in dry $CHCl_3$, in the presence of Et_3N (Scheme 2.2). Isolation of **67**, in 84% yield, was achieved after successful removal of any unreacted **66** by extraction using 1 M NaOH

(Figure A1.2). The final step in the synthetic pathway to ligand **58** involved refluxing **67** with three equivalents of **68**, using K_2CO_3 and KI, in freshly distilled CH_3CN. After refluxing under argon for 5 days, formation of **58** was observed by mass spectrometry. Purification of the crude mixture by alumina column chromatography (elution gradient 100 to 90:10 CH_2Cl_2:MeOH) was required to give the desired ligand **58**, in 63% yield.

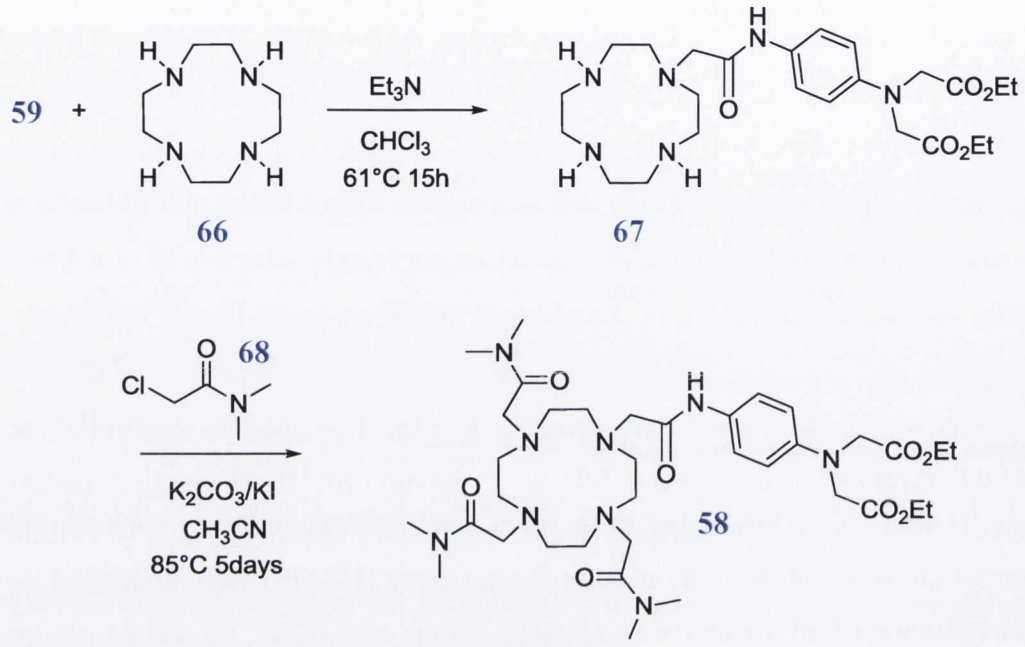

Scheme 2.2: *Synthetic pathway for ligand 58.*

The ^{1}H NMR spectrum ($CDCl_3$, 400 MHz) of **58** is shown in Figure 2.2, with the expected aromatic resonances, each of which appear as a doublet at 7.64 ppm and 6.47 ppm, respectively. The ester CH_3 protons of the diethyl iminodiacetate moiety appear as a triplet at 1.26 ppm with an overall integration of six, whereas the adjacent CH_2 protons resonate as a quartet at 4.18 ppm. The remaining methylene protons of the ester moieties appear as a singlet at 4.07 ppm. The cyclen CH_2 (16H) protons along with the CH_2 (8H) and CH_3 (18H) protons of the acetamide arms appear as a multiplet of broad overlapping peaks which resonate in the spectral range 2.0 – 3.4 ppm, with a total integration of forty two.^{13}C NMR was also employed to characterise ligand **58**, whereas ESMS analysis showed the presence of a peak at *m/z* = 770.45 which corresponds to the [**58** + Na]$^+$ species in solution. Full characterisation of ligand **58** and all precursor compounds can be found in the experimental section of Chapter 7.

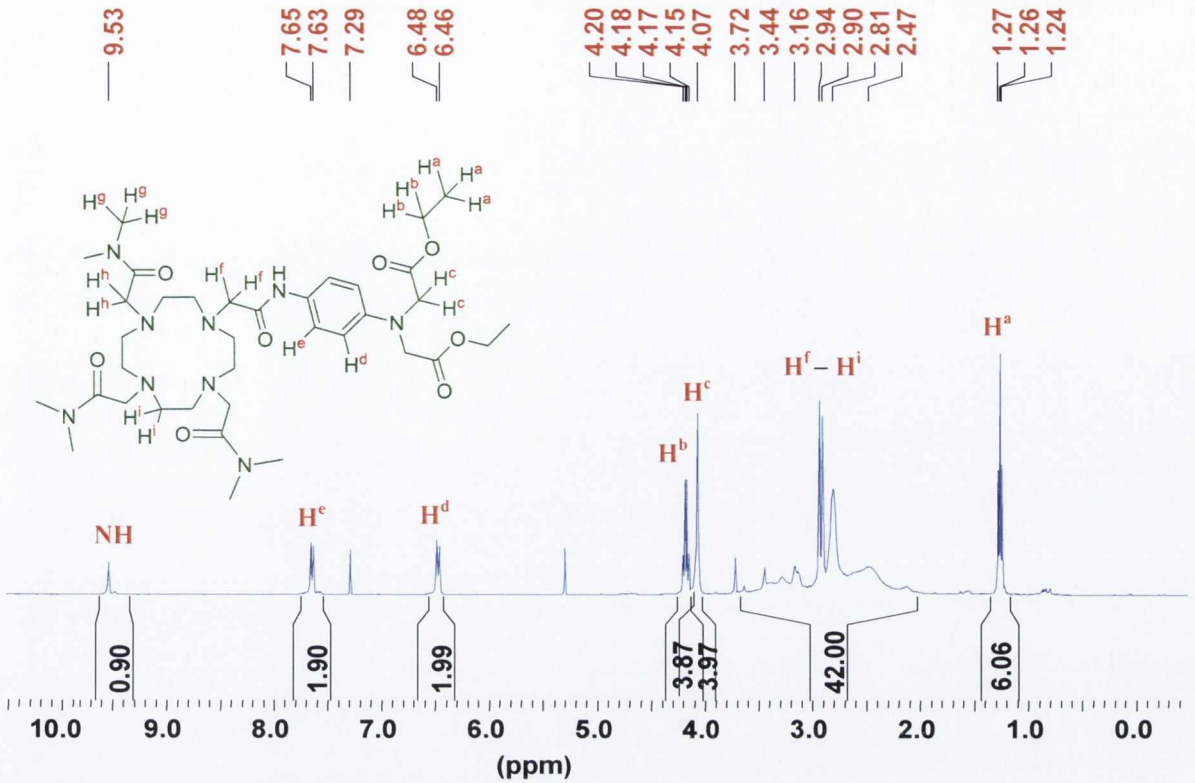

Figure 2.2: *The ^{1}H NMR spectrum (400 MHz, $CDCl_3$) of 58.*

2.4 Synthesis and characterisation of the Eu(III) and Tb(III) complexes of ligand 58

The syntheses of the Eu(III) and Tb(III) complexes of **58** were achieved by refluxing overnight **58** with an equivalent amount of either Eu(III) triflate ($Eu(CF_3SO_3)_3$) or Tb(III) triflate ($Tb(CF_3SO_3)_3$) in freshly distilled CH_3CN, under an inert environment, Scheme 2.3. Upon reaction completion, the solvent was removed under reduced pressure and the resulting residue re-dissolved in MeOH and dropped slowly into a large volume of dry diethyl ether, resulting in the precipitation of a pale orange solid. This gave **Eu.58** and **Tb.58** in 80% and 92% yield, respectively. As was the case for **58**, ^{1}H NMR, HRMS and elemental analysis were used to verify the successful formation of each of these complexes.

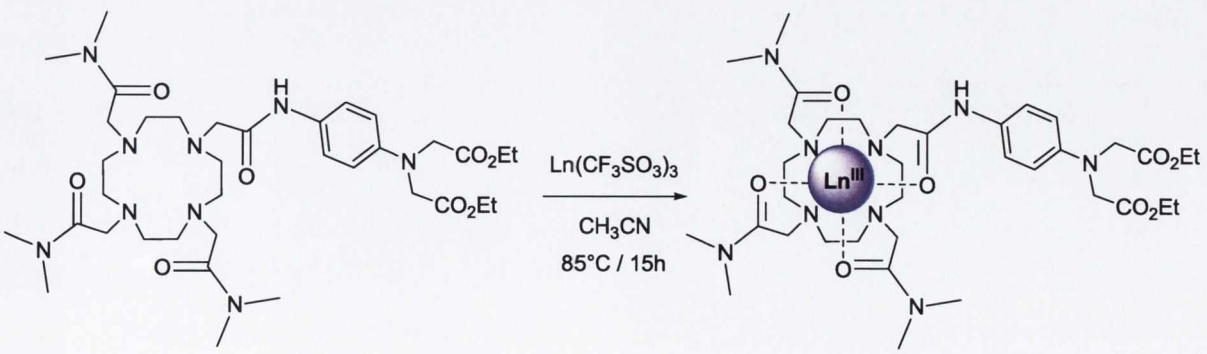

Scheme 2.3: *Synthesis of Eu.58 and Tb.58 by complexation of the appropriate Ln triflate salt with equivalent amounts of ligand 58.*

It is well known that protons in close proximity to the paramagnetic Ln ion are influenced by the presence of unpaired *f* electrons, leading to more efficient relaxation of their nuclear spins and thus results in broadening of their resonances as well as chemical shifts in the ^{1}H NMR frequency.[170] As a result, the ^{1}H NMR spectra (400 MHz, CD_3OD) of **Eu.58** and **Tb.58** displayed this characteristic broadening and shifting of signals over a large ppm range, verifying successful complexation of the Ln ions within the cyclen macrocyclic cavity (Figure A1.3). In the case of the ^{1}H NMR spectrum of **Tb.58**, shown in Figure 2.3, all the proton resonances including the equatorial and axial protons of the cyclen ring are shifted over a total spectral range of *ca.* 220 ppm.

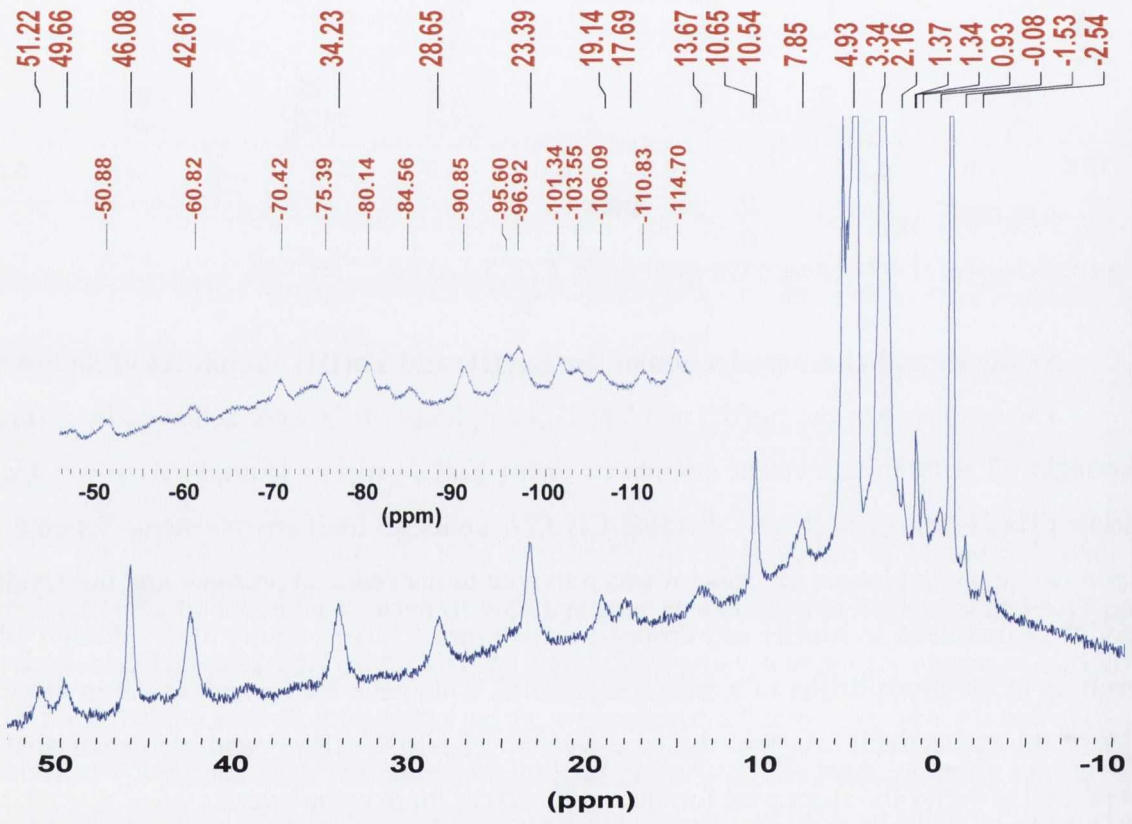

Figure 2.3: *The ^{1}H NMR spectrum (400 MHz, CD_3OD) of complex **Tb.58**.*

ESMS analysis also helped verify the formation of **Eu.58** and **Tb.58** where both spectra showed a variety of peaks, representing the *m/z* of the complexes with a varying number of triflate ions. The expected isotopic distribution pattern associated with Ln complexes was also observed. Figure 2.4 shows the mass spectra of both **Eu.58** and **Tb.58** displaying the *m/z* peak [**Ln.58** + $2(CF_3SO_3)]^+$ at 1198.29 and 1204.29, respectively.

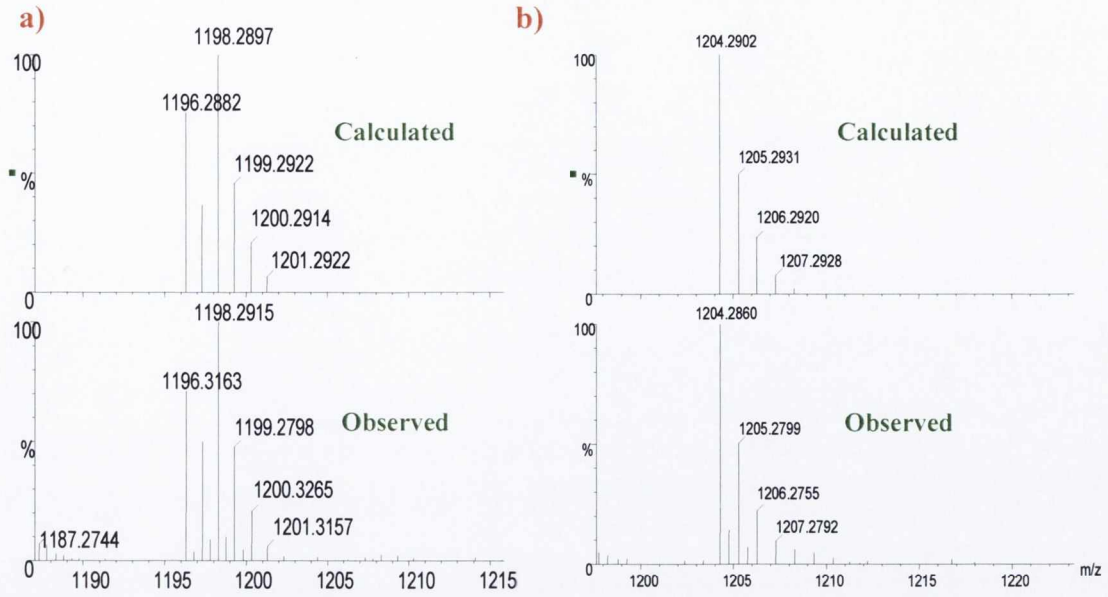

Figure 2.4: *The ESMS of (a) **Eu.58** and (b) **Tb.58** displaying the expected $^{151}Eu(III)$ and $^{159}Tb(III)$ isotopic distribution patterns for the [**Ln.58**+2(CF_3SO_3)]$^+$ species.*

Another useful method employed to support successful complexation of the Ln ion within the cyclen cavity is IR spectroscopy. Coordination of the four acetamide arms *via* the amide carbonyl bonds has been shown to cause a shift in electron density with a subsequent change in the IR stretching frequency of the carbonyl bands being observed.[171] In the case of **58**, upon complexation with the Ln ions, the IR stretching frequency of the carbonyl band shifted from 1646 cm^{-1} to 1615 cm^{-1} and 1618 cm^{-1} for **Eu.58** and **Tb.58**, respectively. In the design of ligand **58**, it was anticipated that Ln complexation would occur solely within the cyclen macrocycle and no weak interactions with the diethyl iminodiacetate moieties would take place. This assumption was verified using IR, where the stretching frequency of the ester carbonyl bands of the chelating unit displayed no major shift from 1740 cm^{-1} upon complex formation with both the Eu(III) and Tb(III) triflate salts. A summary of the frequency changes of both the amide and ester carbonyl bands for **Eu.58** and **Tb.58** are shown below in Table 2.1.

Table 2.1: *IR stretching frequency of the carbonyl bands in **58**, **Eu.58** and **Tb.58**.*

IR Frequency (cm^{-1})	*Ligand 58*	*Eu.58*	*Tb.58*
Amide C=O	**1646**	**1615**	**1618**
Ester C=O	**1740**	**1737**	**1735**

Having successfully synthesised and characterised **Eu.58** and **Tb.58**, we next evaluated the photophysical properties of these complexes. The next section will therefore present the UV-vis and fluorescence spectra obtained for these Ln systems, followed by a description of the phosphorescence spectra displayed upon excitation of the phenyl antenna.

2.5 Photophysical properties of Eu.58 and Tb.58

The UV-vis absorption spectra of **Eu.58** and **Tb.58** in a mixed MeOH/H_2O (1:99 *v/v*) solution at pH 7.4 (20 mM HEPES) and in the presence of 135 mM KCl (to maintain a constant ionic strength), showed one broad π–π^* absorption band centred at 283 nm. Excitation at 225 nm gave rise to a fluorescence emission spectrum with a λ_{max} of 350 nm with a slight shoulder at 300 nm, Figure 2.5.

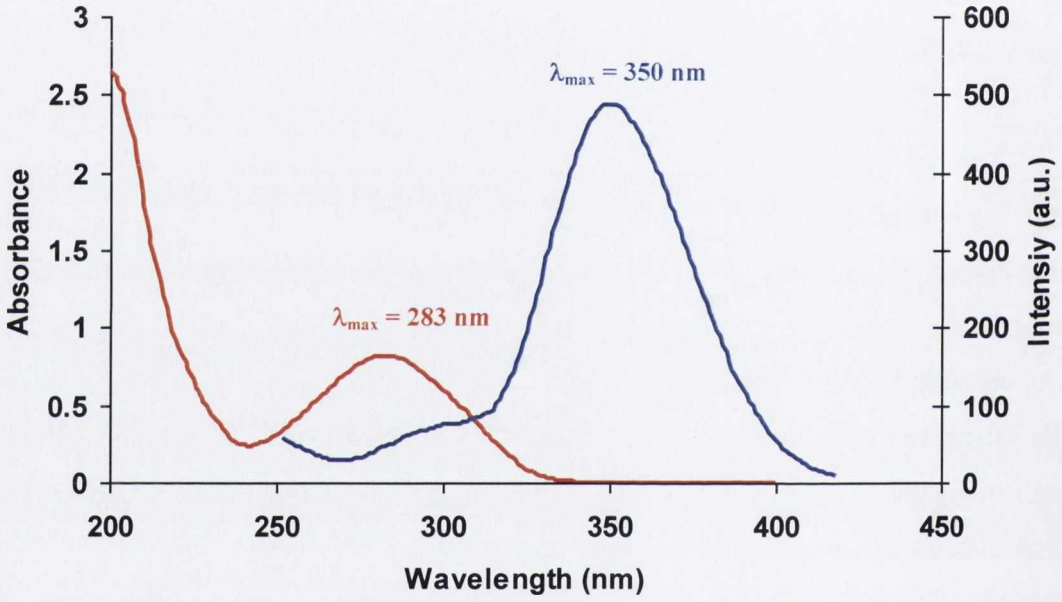

Figure 2.5: *The UV-vis absorption (–) and the fluorescence emission spectra (–) of Tb.58 and Eu.58 in mixed MeOH:H_2O (1:99 v/v) solution.*

The design of **Eu.58** and **Tb.58**, envisaged indirect excitation of both the Eu(III) and Tb(III) ions by the covalently attached phenyl antenna. It was expected that successful energy transfer *via* the antenna's triplet excited state, to the excited states of Tb(III) and Eu(III), $^5D_4$ and $^5D_0$ respectively, would occur. The phosphorescence emission spectra of **Eu.58** and **Tb.58** were recorded in a mixed MeOH:H_2O (1:99 *v/v*) solution by exciting at 283 nm (λ_{max}). The resulting characteristic emission bands shown in Figure 2.6 involves transitions from the excited $^5D_0$ state to the ^7F_J (J = 0, 1, 2, 3,4) ground state for **Eu.58** and from the $^5D_4$ state to the ^7F_J (J = 6, 5, 4, 3) state for **Tb.58**, verifying that successful energy transfer from the antenna had occurred.

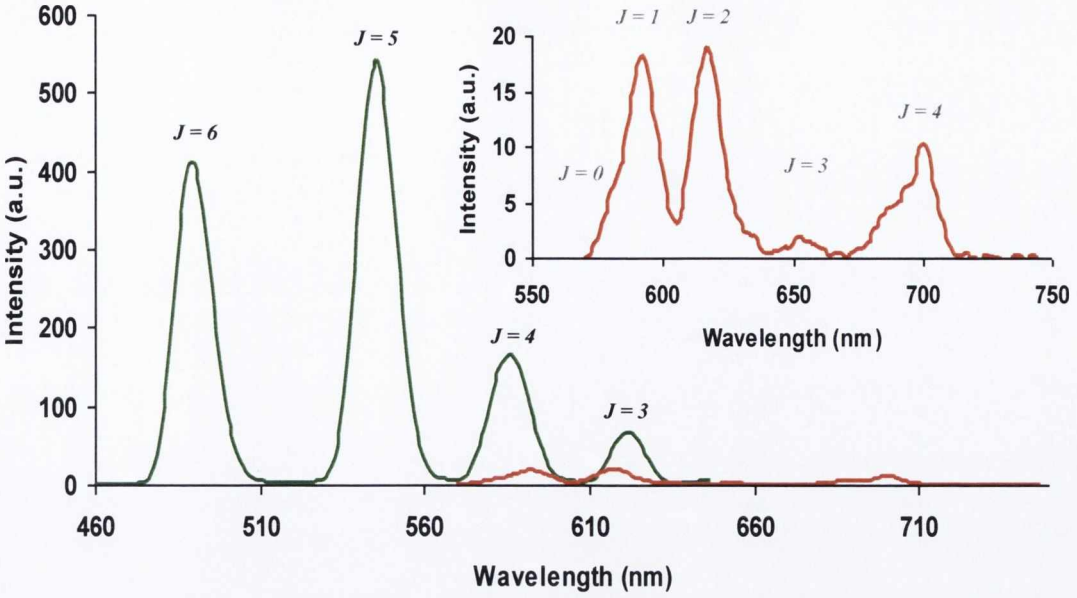

Figure 2.6: *Lanthanide luminescence spectra of* **Tb.58** *(–) and* **Eu.58** *(–) recorded in a mixed MeOH:H_2O (1:99 v/v) solution using an excitation wavelength of 283 nm. Inset: Magnified view of Eu(III) emission from* **Eu.58**.

However, as shown in Figure 2.6, the emission intensity from **Eu.58** was much weaker then that of **Tb.58** suggesting poorer population of the $^5D_0$ excited state of the Eu(III) ion *via* the phenyl antenna. As the luminescence quantum yields depends greatly on the energy distance between the antenna's triplet excited state and the excited state of the Ln ion, it is plausible that the weak Eu(III) emission is as a result of the much larger energy gap present in **Eu.58**. The $^5D_0$ Eu(III) excited state lies at 17250 cm^{-1}, which is of much lower energy then the $^5D_4$ Tb(III) excited state with an energy of 20450 cm^{-1}. Systems bearing such a large energy gap between their donor and acceptor states are more susceptible to non-radiative deactivation processes, like high energy vibrations such as O-H oscillators.[34, 53] As the indirect sensitisation process for the Eu(III) complex, **Eu.58**, by the phenyl chromophore was not as efficient as for the Tb(III) analogue, it was decided that no further measurements would be carried out on **Eu.58**. All remaining studies which will be discussed in the following sections of this chapter and in Chapter 3 were performed solely on the Tb(III) complex **Tb.58**.

2.6 Determination of metal bound water molecules for Tb.58

From the structure of ligand **58**, it was anticipated that when complexed to a Ln ion, the tetra substituted cyclen ligand would provide eight possible co-ordination sites. With Tb(III) usually possessing a co-ordination number of nine, this leaves the ninth site being occupied by a solvent molecule.[34] The technique employed to determine the hydration number (q) was to measure the excited state lifetimes ($^5D_4$) of **Tb.58** in H_2O ($\tau_{O\text{-}H}$) and D_2O

($\tau_{O\text{-}D}$), by indirect excitation of the Tb(III) ion at 283 nm. As discussed in Chapter 1 (Section 1.3.2), equation 1.3 could then be used to calculate the number of metal bound water molecules within the Tb(III) co-ordination environment. This principle is based upon the fact that the deactivation pathway caused by energy transfer to the vibrational states of the O-H oscillators is quenched upon replacement of O-H by O-D oscillators, thus it is expected to obtain longer excited state lifetimes in D_2O.[172]

Lifetimes of **Tb.58** were obtained by recording the exponential decay of the Tb(III) luminescence with respect to time. Due to the problem of complete solubility in pure water, these measurements were recorded in mixed MeOH:H_2O (1:99 *v/v*) and CD_3OD:D_2O (1:99 *v/v*) solutions. Fitting the luminescence decay to mono exponential, as shown in Figure 2.7, gave lifetime values, of $\tau_{O\text{-}H}$ = 1.32 ± 0.01 ms and $\tau_{O\text{-}D}$ = 2.03 ± 0.01 ms, resulting in a *q* value of 1.0 ± 0.25 being calculated. This indicates as expected the presence of one metal bound water molecule for **Tb.58**, giving the system a total coordination number of nine.

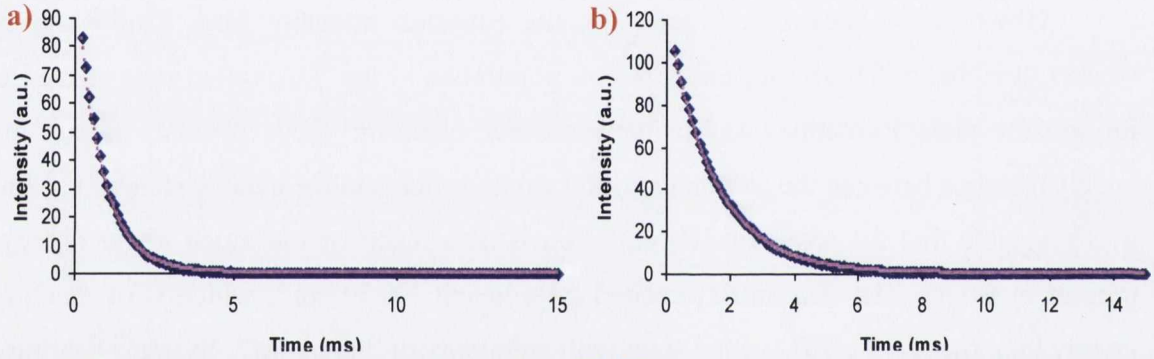

Figure 2.7: *Luminescence decay of complex **Tb.58** in a a) mixed MeOH:H_2O (1:99 v/v) solution and b) mixed CD_3OD:D_2O (1:99 v/v) solution.*

To satisfy the requirement for a beneficial contrast agent, pH independent behaviour at physiological pH is essential. Therefore the following sections will focus on a more detailed look at the photophysical properties of **Tb.58**, concentrating on pH effects.

2.7 pH investigation of Tb.58 in aqueous solution

It was clear from analysing the structure of **Tb.58** that possible protonation of the tertiary amine as well as potential deprotonation of the secondary amide could perturb the photophysical properties of the Tb(III) complex resulting in major changes in its UV-vis absorption, fluorescence and phosphorescence emission spectra. In order to investigate the sensitivity of **Tb.58** towards pH, a pH titration was carried out in a mixed MeOH:H_2O (1:99 *v/v*) solution in the presence of 0.1 M NEt_4ClO_4 (TEAP) in order to maintain a constant ionic strength. The acid and base used for these titrations were perchloric acid ($HClO_4$) and tetraethyl ammonium hydroxide (NEt_4OH), respectively. The results of these measurements will be discussed in the following sections.

2.7.1 pH dependence of the ground state properties of Tb.58

Firstly, the effect of pH on the ground state properties of **Tb.58** was investigated. At pH 12, (basification with dilute NEt_4OH), one broad absorption band centred at 278 nm was recorded. Upon titration with acid to a neutral pH, the absorption spectra of **Tb.58** displayed a slight bathochromic shift with the λ_{max} being shifted to 283 nm. This red shift was also accompanied by the formation of an isosbestic point (283 nm). Upon further acidification to a lower pH, as shown in Figure 2.8, the spectra no longer passed through this isosbestic point, displaying a minimal hypsochromic shift to 281 nm. The subsequent shift from the isosbestic point suggests the presence of a number of species in equilibrium as a function of pH. Furthermore, in acidic media, a decrease in the absorbance by *ca.* 20% compared to that observed at neutral pH was also observed. In order to obtain a clearer understanding of the overall modulation in the absorption spectra of **Tb.58** and to determine the pK_a's for these changes, the absorbance at 310 nm over the entire pH range was plotted. As shown as an inset in Figure 2.8, all major changes in the absorbance occurred outside the physiological range with the largest decrease in absorbance being observed between pH 9.7–12 and pH 4.0–1.4.

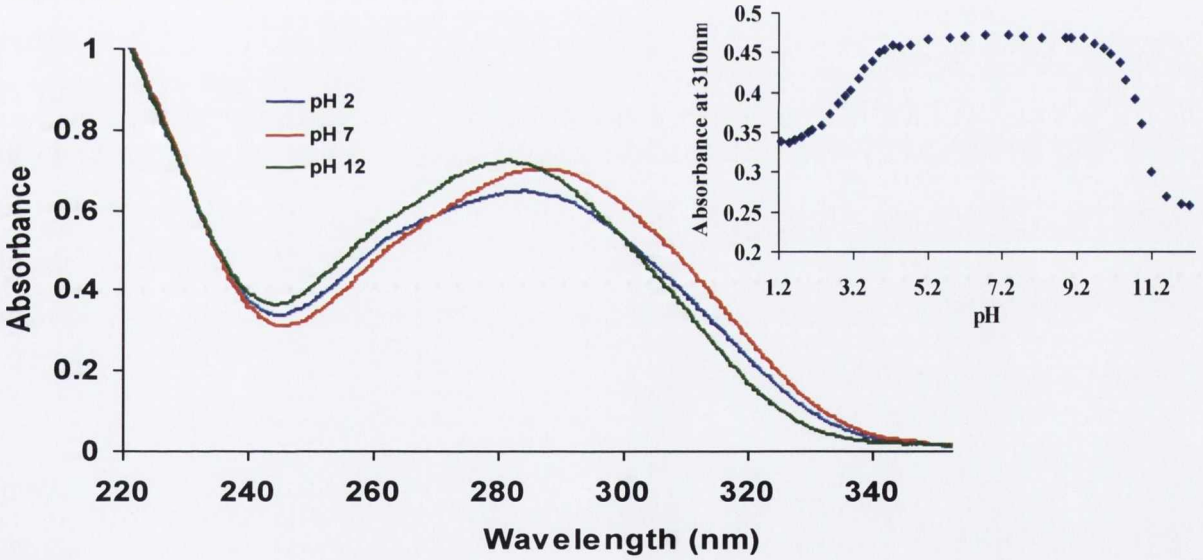

Figure 2.8: *The UV-vis absorption spectra of **Tb.58** at various pHs, recorded in a mixed MeOH:H_2O (1:99 v/v) solution [I = 0.1M NEt_4ClO_4 (TEAP)]. Inset: Changes in the UV-vis absorption spectra at 310 nm as a function of pH.*

The relevant pK_a values for **Tb.58** were obtained by fitting the changes in the UV-vis absorption measurements using Equation 2.1,

$$pK_a\,(S_0) = pH - \mathrm{Log}\,\frac{(Abs_{AH} - Abs_A)}{(Abs_A - Abs_{A^-})} \qquad \textbf{Equation 2.1}$$

where, Abs_{AH}, Abs_A and Abs_{A^-} are the absorbance of the protonated species, the absorbance of the solution at each pH value, and the absorbance of the fully deprotonated species, respectively.[173] For the case of the spectral changes observed between pH 9.7–12, a pK_a value of 10.5 ± 0.1 was calculated. We can assume with a previously reported pK_a value of *ca* 11,[16] the observed changes at this pH range are related to the deprotonation of the secondary amide moiety in **Tb.58**. Within a more acidic environment, the resulting decrease in absorbance gave a pK_a of 2.6 ± 0.1, which was assigned to protonation of the tertiary amine of the diethyl iminodiacetate functionality. With a clear understanding of the pH effects on the ground state properties of **Tb.58**, the study required further investigation, concentrating on the singlet excited state of the phenyl chromophore and more importantly the Tb(III) excited state of **Tb.58**.

2.7.2 pH dependence of singlet excited state properties of Tb.58

The fluorescence emission pH titration of **Tb.58** was performed in parallel with the UV-vis absorption measurements. Figure 2.9 shows the fluorescence spectra of **Tb.58** (in a mixed MeOH/H_2O (1:99 *v/v*) solution), as a function of pH. At pH 12, the fluorescence emission spectrum appeared as a broad emission band centred at 350 nm with a slight shoulder at *ca.* 300 nm. Upon acidification to pH 2, the emission intensity increased by *ca.* 70% overall, with no major shift being observed for λ_{max}. A plot of the changes in the intensity at 350 nm and 370 nm as a function of pH is shown in Figure 2.10, confirming that the major changes in the emission intensity occurred in the acidic and basic regions of the pH scale Again the measurements verified the presence of the large physiological pH window, where the emission was pH independent.

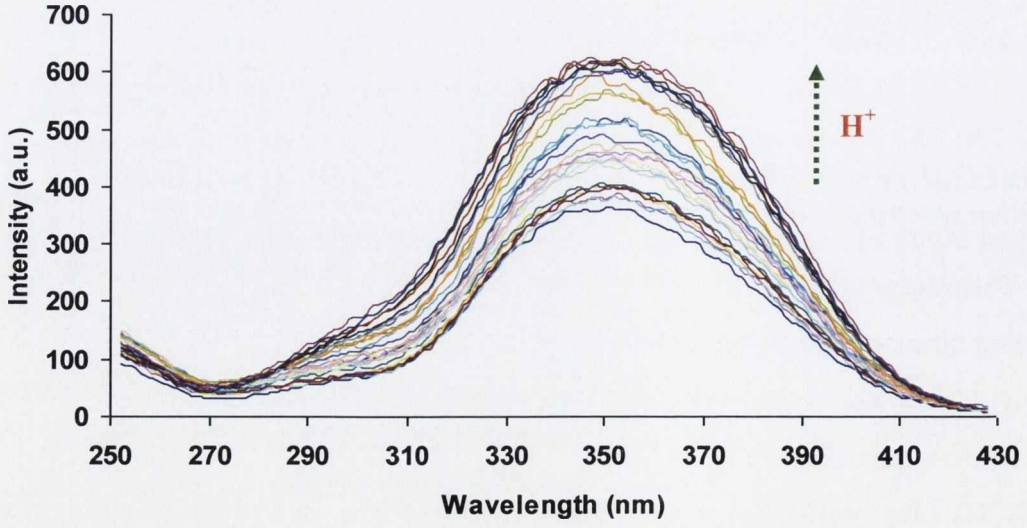

Figure 2.9: *The changes in the fluorescence emission spectra of* ***Tb.58*** *as a function of pH in a mixed MeOH:H_2O (1:99 v/v) solution [I = 0.1M NEt_4ClO_4 (TEAP)].*

It was clear from Figure 2.10, the most significant changes in the fluorescence intensity occurred within pH 3–5.5, where protonation of the tertiary amine of the diethyl iminodiacetate functionality is most likely to occur. Fitting the data in this pH range to a modified version of Equation 2.1, where the fluorescence intensities of the protonated and deprotonated species were used, a pK_a of 4.5 ± 0.1 was obtained. This value suggests that the acidity of the tertiary amine moiety is decreased upon excitation to the singlet excited state, as a lower pK_a of 2.6 ± 0.1 was obtained for the ground state studies. As was the case for the UV-vis absorption measurements, within the pH range 9.5–12, an increase in the emission intensity of **Tb.58** was observed, however, such changes were not significant enough to obtain an accurate pK_a value.

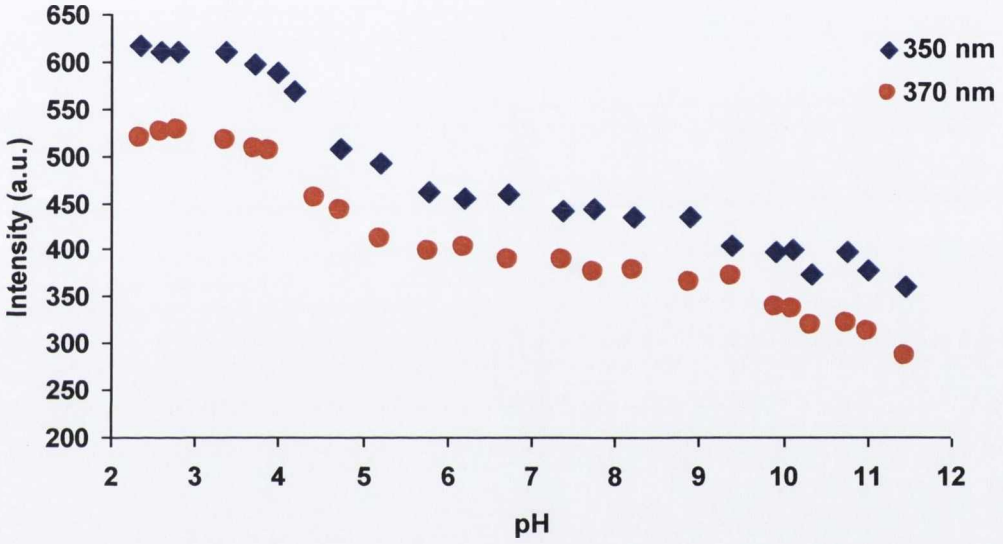

Figure 2.10: *The changes in the fluorescence emission intensity of* ***Tb.58*** *at 350 nm and 370 nm as a function of pH in a mixed MeOH:H_2O (1:99 v/v) solution [I = 0.1M NEt_4ClO_4 (TEAP)].*

In summary, the pH studies for both the UV-vis absorption and fluorescence properties of **Tb.58** displayed comparable trends. Both sets of measurements confirmed that no overall perturbation of the ground or singlet excited states was experienced within the physiological pH window and that it was essentially protonation and deprotonation of the tertiary amine and the secondary amide that were responsible for any major changes during the course of the titration. In conjugation with these studies, an investigation into the luminescence behaviour of **Tb.58** as a function of pH was also required. From the previous results obtained, it was anticipated that at pH 7.4 the Tb(III) emission from **Tb.58** would be "switched on" with any major changes in the luminescence properties occurring in a very acidic or basic environment.

2.7.3 pH dependence of the Tb(III) excited state of Tb.58

As in the case for the absorbance and fluorescence measurements, the Tb(III) luminescence response of **Tb.58** (using time-gated techniques) towards pH was recorded in a mixed MeOH/H_2O (1:99 *v/v*) solution using 0.1 M NEt_4ClO_4 (TEAP) in order to maintain constant ionic strength. The Tb(III) emission corresponding to the $^5D_4 \rightarrow {}^7F_J$ (J = 6, 5, 4, 3) transitions occurring at 490, 546, 586 and 622 nm, respectively, showed significant change with respect to its pH environment, Figure 2.11.

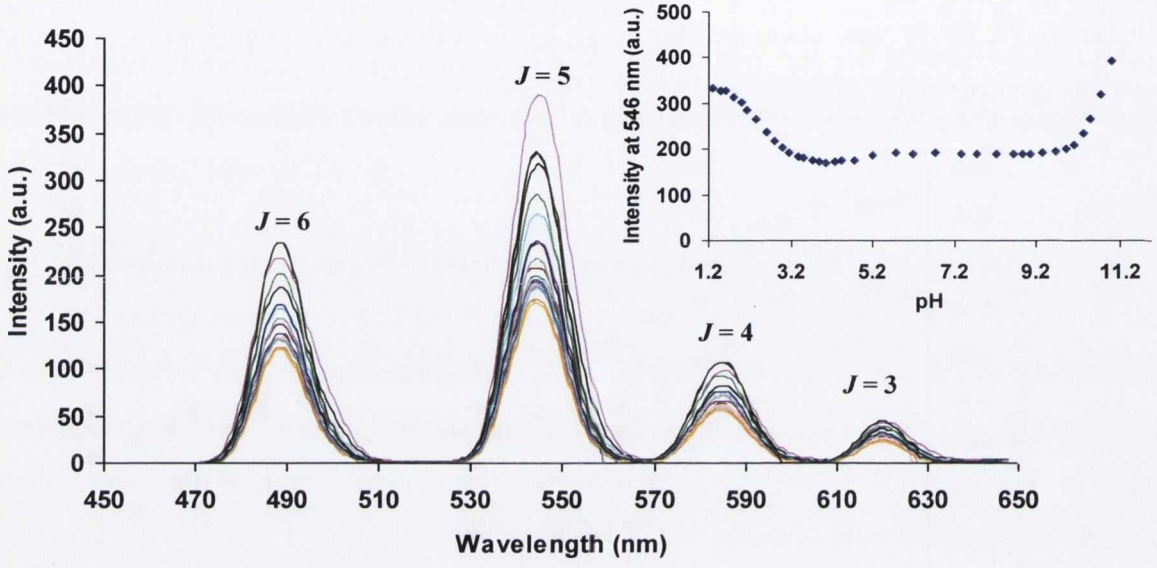

Figure 2.11: *The Tb(III) luminescence response of **Tb.58** as a function of pH in a mixed MeOH:H_2O (1:99 v/v) solution [I = 0.1M NEt_4ClO_4 (TEAP)]. Inset: Changes in the Tb(III) emission intensity at 546 nm as a function of pH.*

The changes in the Tb(III) emission at 546 nm (J = 5) as a function of pH were plotted over the entire pH range. As shown as an inset in Figure 2.11, the titration profile clearly supports the results observed for the pH dependence of the ground and singlet excited state of **Tb.58**. At pH 12, the Tb(III) emission showed an intense response, whereas at pH 10, the phosphorescence intensity decreased by *ca.* 51%. This suggests that re-protonation of the secondary amide moiety in **Tb.58** has a major effect on the energy transfer from the antenna to the Tb(III) metal ion located within the cyclen macrocyclic cavity. Again within the physiological pH range, the Tb(III) emission is "switched on" with no changes observed in emission intensity between pH 4–10. As expected, below pH 4, subsequent protonation of the tertiary amine resulted in modulation in the phosphorescence of **Tb.58**. These changes suggest that protonation of this amine site results in more efficient population of the $^5D_4$ excited state of the Tb(III) complex. A emission intensity of 302 was recorded at pH 2, compared to 170 at pH 4, corresponding to an increase of *ca.* 78% within this pH range.

The trends observed for the excited state measurements of **Tb.58** are similar to those previously reported for the crown ether based Tb(III) complexes **14a** and **14b** discussed in Section 1.5.2. As shown in Scheme 2.4, deprotonation of the secondary amide or protonation of the tertiary amine moieties can result in the lone pair of the aniline nitrogen no longer being in conjugation with the rest of the system. This deconjugation can consequently lead to suppression of the PET process, to or from the intermediate aryl singlet excited state of the phenyl antenna, leading to the observed Tb(III) emission enhancement in very acidic and basic environments.

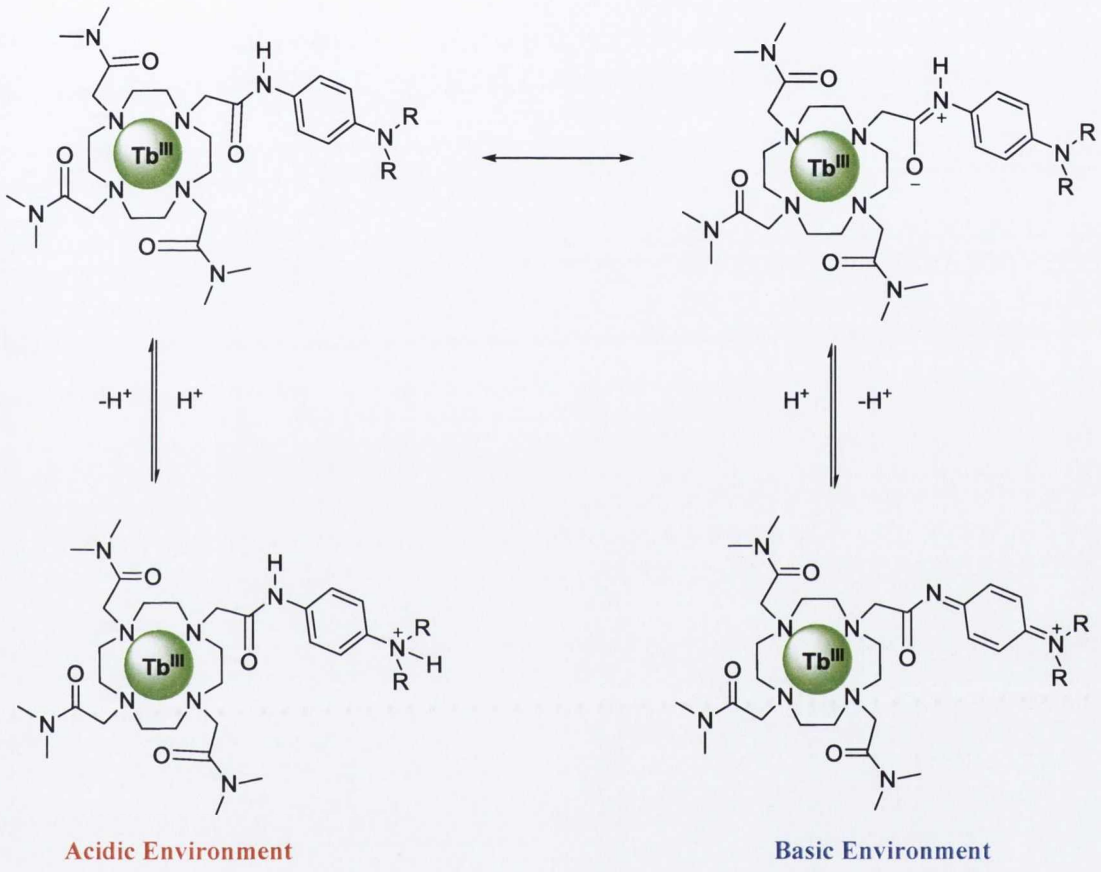

Scheme 2.4: *Illustration of the possible deconjugation of the aniline nitrogen lone pair of Tb.58, by protonation of the tertiary amine (Acidic Environment) or deprotonation of the secondary amide (Basic Environment). (R = ethyl ester)*[174]

Overall, the UV-vis absorption, fluorescence and Ln luminescence properties of **Tb.58** were modulated only at very high and low pH values, with no overall changes occurring within the physiological pH range. With a complete understanding of the principle photophysical properties of the control complex **Tb.58**, the next step involved the synthetic conversion of the diethyl iminodiacetate groups to the microcrack specific iminodiacetate functionality, followed by a complete photophysical evaluation of the product.

2.8 Base hydrolysis of the diethyl ester groups of Tb.58

As discussed in the previous section, it was necessary to hydrolyse the diethyl ester moiety of **Tb.58** to expose the microdamage specific iminodiacetate functionality. This was achieved, as shown in Scheme 2.5, by simple alkaline hydrolysis using NaOH in a mixed MeOH:H_2O (10:1 *v/v*) solution. Upon reaction completion (monitored by TLC), the solvent was removed under reduced pressure and the resulting residue re-dissolved in a minimal amount of cold MeOH. Removal of the excess NaOH from the solution was achieved by filtration using a micro syringe. To ensure complete removal of any remaining base, the MeOH solvent was evaporated to dryness and the resulting residue dissolved in a minimal amount of water, followed by dropwise addition to swirling EtOH, resulting in the precipitation of **Tb.58.Na** in 81% yield.

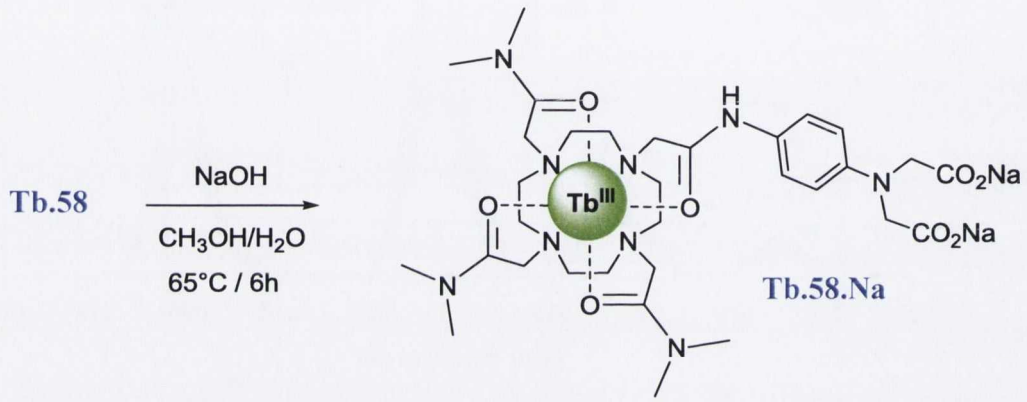

Scheme 2.5: *Synthetic step for alkaline hydrolysis of Tb.58.*

Due to the paramagnetic nature of the Ln ions, ^{1}H NMR proved insufficient in verifying whether complete hydrolysis of the ethyl ester groups in **Tb.58** had occurred (Figure A1.4). However, IR spectroscopy became a key technique in providing evidence that successful hydrolysis had resulted. For the case of **Tb.58.Na**, the disappearance of the sharp ester carbonyl signal at 1735 cm^{-1} and the subsequent appearance of a broad carboxylate carbonyl signal at 1603 cm^{-1} confirmed successful base hydrolysis of **Tb.58**. ESMS also verified formation of the carboxylate groups with a *m/z* peak [**Tb.58.Na**+2(CF_3SO_3)-2Na+2H]$^+$ appearing at 1148.24, with the calculated isotopic distribution pattern of the complex matching the observed. (Figure A1.5)

Hydrolysis of the diethyl iminodiacetate moiety altered the excited state energy levels of the phenyl chromophore and in turn led to more efficient population of the Tb(III) excited state. As can be seen in Figure 2.12, this was verified by measuring the phosphorescence spectra of **Tb.58** and **Tb.58.Na** using the same spectroscopic parameters and complex concentrations. To ensure a direct comparison could be made between both Tb(III) complexes, **Tb.58.Na** was also made up in a mixed MeOH:H_2O (1:99 *v/v*) solution.

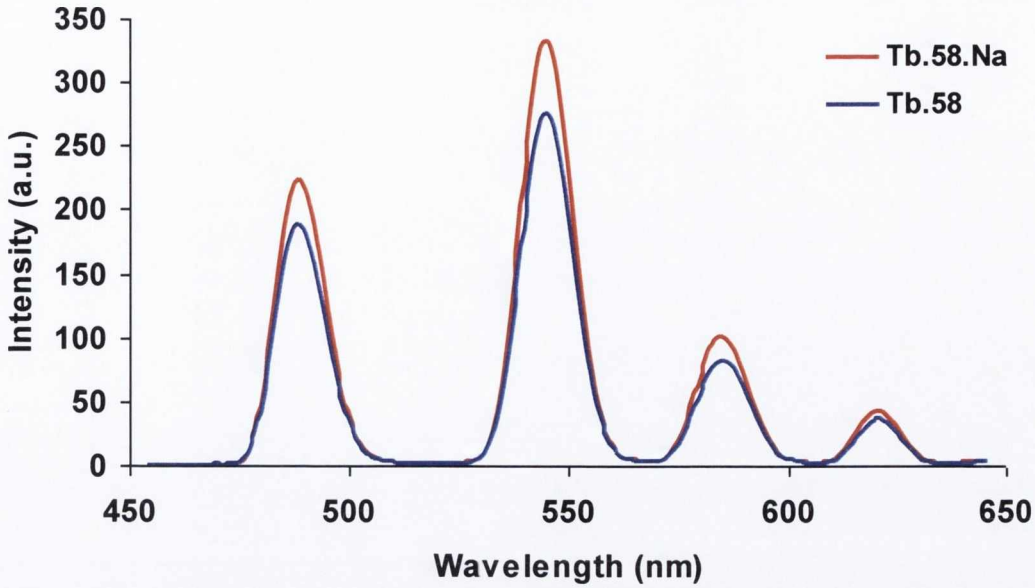

Figure 2.12: *The Tb(III) luminescence spectra of a 10 μM solution of* **Tb.58** *and* **Tb.58.Na** *in mixed MeOH:H_2O (1:99 v/v) at pH = 7.4 (20 mM HEPES, 135 mM KCl), using excitation wavelength of 283 nm.*

Conversion of the diethyl iminodiacetate unit of **Tb.58** to the microcrack specific disodium iminodiacetate moiety of **Tb.58.Na** resulted in a 20% increase in its emission intensity. Therefore, to ensure a direct comparison between both Tb(III) complexes could be made in future studies, it was necessary to investigate the effect of this functionality conversion on the pH studies previously discussed for **Tb.58**. The introduction of the new carboxylate moieties could alter the basicity and acidity of the relevant sites and in turn jeopardize **Tb.58.Na** independence within the physiological pH range. The following sections will discuss the results obtained from these investigations.

2.9 pH investigation of Tb.58.Na in aqueous solution

As was the case for **Tb.58**, the effect of pH on the ground and the singlet excited state, as well as the Tb(III) excited state properties of **Tb.58.Na** was investigated. With the most significant changes occurring for the Tb(III) excited state measurements, and taking into account **Tb.58.Na** application as a potential imaging agent, the effect of the functionality conversion on the luminescence behaviour of **Tb.58.Na** within the physiological pH range rendered more attention and will therefore be discussed in more detail in the following section. The UV-vis absorption and fluorescence spectra recorded during these measurements are shown in Figure A1.6.

2.9.1 The pH dependence of the Tb(III) excited state of Tb.58.Na

Investigation of the spectroscopic properties of the Tb(III) excited state as a function of pH was carried out in 100% H_2O with a constant ionic strength being maintained by the presence of 0.1 M TEAP. The acid and base used for this study were $HClO_4$ and Et_4NH_4OH, respectively. As expected, the Tb(III) emission at 490, 546, 586 and 622 nm displayed significant change as a function of pH, Figure 2.13.

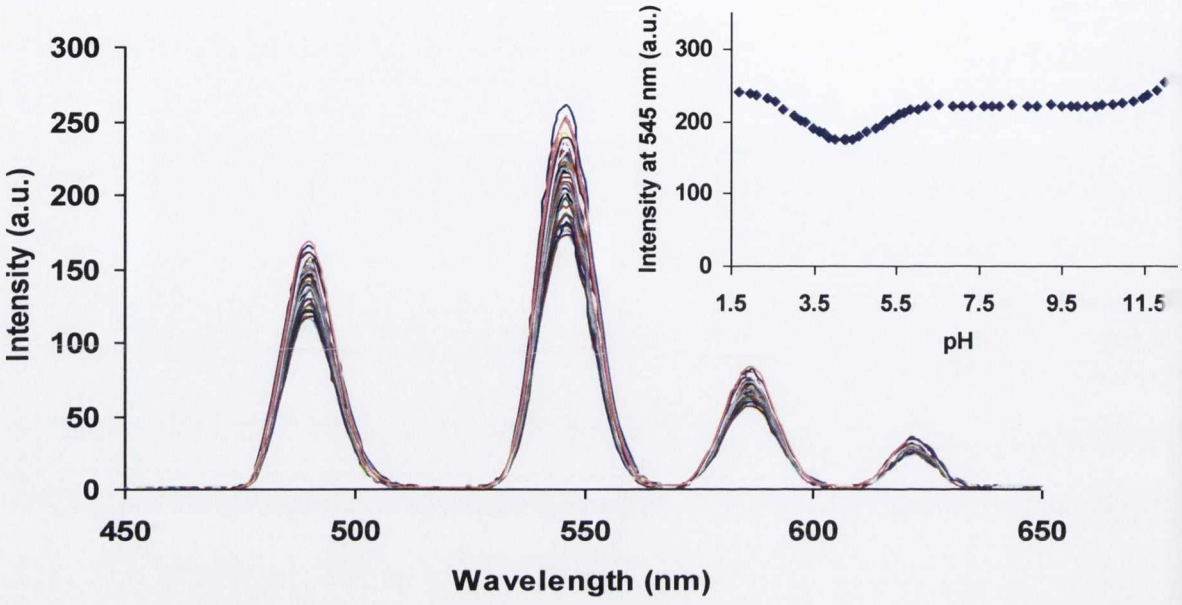

Figure 2.13: *The Tb*(III) *luminescence response of Tb.58.Na as a function of pH in H_2O [I= 0.1M NEt_4ClO_4 (TEAP)]. Inset: Changes in the Tb(III) emission intensity of Tb.58.Na at 546 nm as a function of pH.*

To determine the overall phosphorescence dependence of **Tb.58.Na** with respect to pH and to enable a direct comparison with the control complex **Tb.58**, a graph of the variation in the Tb(III) emission intensity at 546 nm over the entire pH range was plotted (Inset, Figure 2.13). On acidification from pH 12.5, the luminescence decrease due to re-protonation of the secondary amide moiety is not as significant as that observed for **Tb.58**. Another clear observation is that the basicity of the amide moiety is decreased to some extent, suggesting the pK_a of this site in **Tb.58.Na** is shifted to a slightly higher pH value. However, the most significant change in the pH response of **Tb.58.Na** was the decrease in the Tb(III) emission intensity by *ca.* 23% between the pH range 6.5-4.5. With a reported pK_a value of 4.5 for the carboxylate ion of an iminodiacetate functionality, it is plausible that within this pH range that protonation of such sites in **Tb.58.Na** resulted in a subsequent decrease in its Tb(III) luminescence.[79] As was the case for **Tb.58**, lowering the pH below 4 resulted in an increase in the Tb(III) emission which as previously discussed in Section 2.7.3 is the result of protonation of the tertiary amine of the iminodiacetate moiety.

With the pH dependence of **Tb.58.Na** over the entire pH range determined, the next stage to further investigate the efficiency of **Tb.58.Na** as a potential contrast agent within physiological conditions was to determine its luminescence response towards various metal ions, some of which show high abundance within the body (Zn^{2+}, Cd^{2+}, Co^{2+}, Ni^{2+} Mg^{2+}, Cu^{2+} and Ca^{2+}). The next section will therefore briefly discuss the changes if any in the photophysical properties of **Tb.58.Na** in the presence of these biologically relevant metal ions.

2.10 Metal ion studies of Tb.58.Na

2.10.1 Titration response of Tb.58.Na with group II metal ions

The effects on the ground state, singlet excited state and Tb(III) excited state properties in the presence of Ca^{2+} and Mg^{2+} ions were first investigated. Using a 10 μM aqueous (pH 7.4, 20 mM HEPES, 135 mM KCl) solution of **Tb.58.Na**, various aliquots of a 0.2 M solution of either $CaCl_2$ or $MgCl_2$ were added. No significant changes were seen in the photophysical properties of the Tb(III) complex, even in the presence of high concentrations (7.5 mM) of these metal ions, suggesting that in solution these ions do not bind to the disodium iminodiacetate moiety of **Tb.58.Na** or any binding that may be occurring is too weak to cause any major modulation in the photophysical properties of the Tb(III) complex (Figure A1.7). The changes in the UV-vis absorption and phosphorescence spectra in the presence of Ca^{2+} are depicted in Figure 2.14.

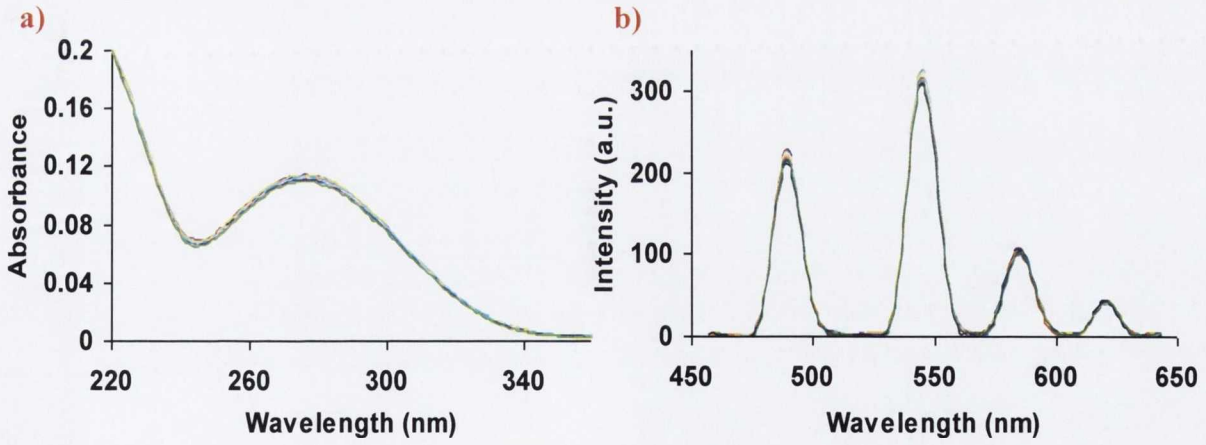

Figure 2.14: *Changes in the a) UV-vis absorption spectra and b) Tb(III) phosphorescence spectra of* ***Tb.58.Na*** *(10 μM) in the presence of $CaCl_2$ (0 – 7.5 mM) at pH = 7.4 (20 mM HEPES, 135 mM KCl).*

The response of **Tb.58.Na** towards group II metal ions is similar to that seen for the previously discussed naphthalimide based fluorescence PET sensors **54a** and **54b** reported by Parkesh *et al.*[79] Bearing the same disodium iminodiacetate receptor unit, the fluorescence and UV-vis absorption properties of these sensors displayed very little change upon addition of

Ca^{2+} or Mg^{2+} ions to the solution. Similarly, as discussed in Chapter 1 (Section 1.10), the well known microdamage chelating agents **47 – 51**, studied by Lee *et al.*[147], which also bear the same binding pocket as **Tb.58.Na** showed no significant binding to Ca^{2+} ions in solution, however, when the ability of these five chelating agents for microdamage detection was investigated, all dyes were successful in selectively labelling the scratched regions. This seems to suggest that the iminodiacetate units of these chelating agents are in fact capable of binding to the co-ordinatively unsaturated Ca^{2+} sites, which are exposed at high concentration upon microcrack generation.

2.10.2 Titration response of Tb.58.Na with transition metal ions

Similar titration studies as described in the previous section were carried out for a variety of transition metal ions such as Cd^{2+}, Zn^{2+}, Ni^{2+}, Fe^{2+}, Co^{2+}, Cu^{2+} and Hg^{2+}. It is important to note that due to interaction of the HEPES buffer with Cu^{2+} and Hg^{2+} ions and subsequent formation of a strong absorption band at 270 nm, it was necessary to carry out the Cu^{2+} and Hg^{2+} titrations in non-buffered H_2O solutions. In the case of Cd^{2+} and Zn^{2+}, the UV-vis absorption studies, as shown in Figure 2.15 clearly show the formation of an isosbestic point on the addition of high concentrations (0 – 7.5 mM) of these ions to the Tb(III) complex. These results correlate with what was previously reported by Gunnlaugsson and co-workers for the PET sensors **54a** and **54b**, which showed a strong binding affinity for Zn^{2+} and to a much lesser extent Cd^{2+}.[165] Although the interaction of these transition metal ions perturbed the ground state properties, no significant decrease or increase in the Tb(III) phosphorescence emission intensity of **Tb.58.Na** was observed, Figure 2.16.

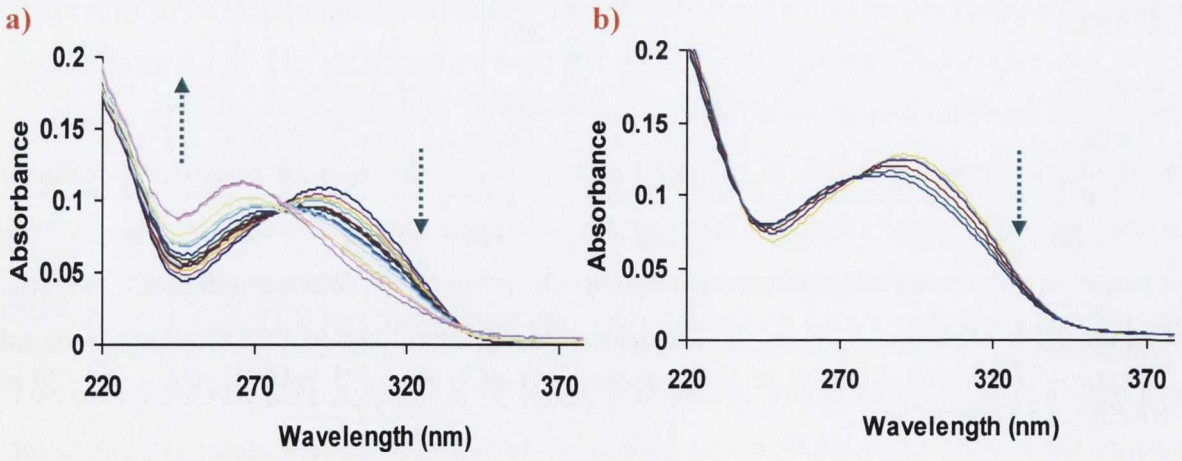

Figure 2.15: *The changes in the UV-vis absorption spectra of a)* ***Tb.58.Na*** *(11 μM) upon the addition of* $ZnCl_2$ *(0 – 7.5 mM) and b)* ***Tb.58.Na*** *(9.5 μM) upon the addition of* $CdCl_2$ *(0 – 7.5 mM) at pH = 7.4 (20 mM HEPES,* 135 mM KCl*).*

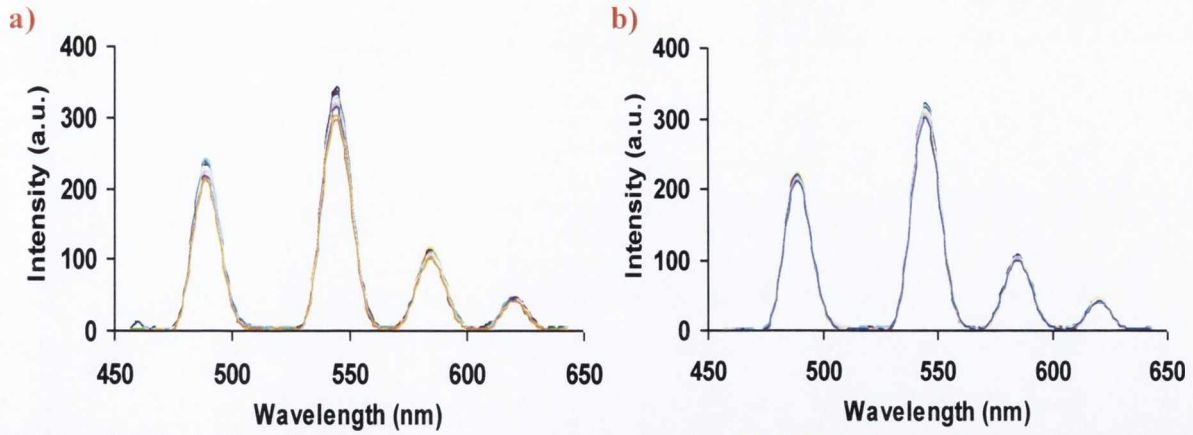

Figure 2.16: *a) The Tb(III) luminescence response of a)* ***Tb.58.Na*** *(11 μM) upon the addition of $ZnCl_2$ (0 – 7.5 mM) and b)* ***Tb.58.Na*** *(9.5 μM) upon the addition of $CdCl_2$ (0 – 7.5 mM) at pH = 7.4 (20 mM HEPES,* 135 mM KCl*).*

Unlike that previously shown for Zn^{2+} and Cd^{2+}, significant modulation in the Tb(III) emission intensity of **Tb.58.Na** was observed for the Ni^{2+}, Co^{2+}, Cu^{2+}, Hg^{2+} and Fe^{2+} ion titrations. In the presence of these metal ions, a significant quenching effect in the Tb(III) luminescence emission of **Tb.58.Na** was observed, upon binding within the iminodiacetate chelating functionality. However, upon further investigation, the observed decrease in luminescence response for some of these metal species was not solely due to interaction with the iminodiacetate binding unit but as a result of some underlying spectral issue. The only two transition metals which showed a reduction in the luminescence response of **Tb.58.Na** at low metal concentrations (20 μM) as a direct consequence of binding within the iminodiacetate chelating unit were Cu^{2+} and Hg^{2+}.

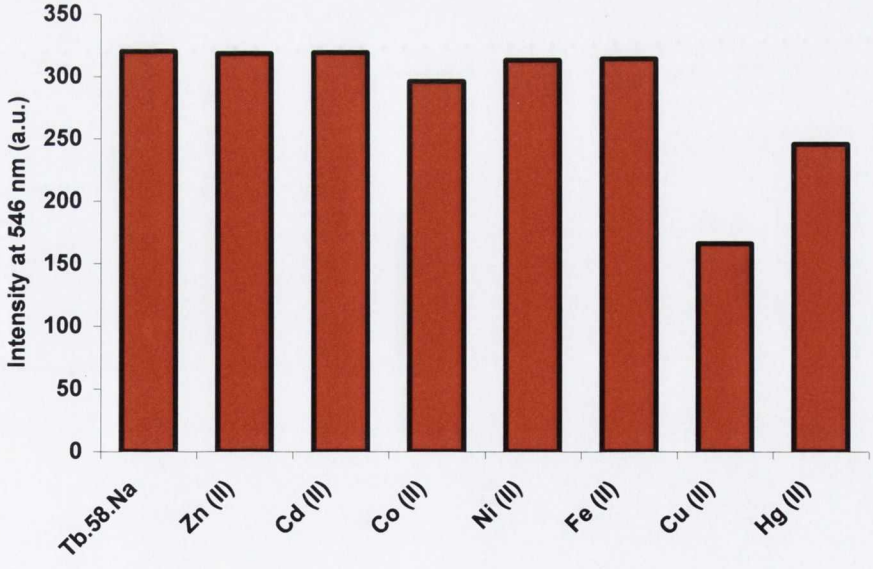

Figure 2.17: *The Tb(III) luminescence response of* ***Tb.58.Na*** *(10 μM) at 546 nm in the presence of various physiologically important transition metal ions (20 μM) in H_2O.*

Figure 2.17 summarises the modulation in the luminescence response of a 10 μM solution of **Tb.58.Na** in the presence of 20 μM of each of the transition metals ions. It can be

clearly seen that only Cu^{2+} and Hg^{2+} ions show a significant decrease in emission intensity at low concentrations, with all the other metals only causing a luminescence reduction at much higher ion concentrations. As Chapter 6 will focus exclusively on the selective binding abilities of **Tb.58.Na** to both Cu^{2+} and Hg^{2+} ions in the presence of other biologically relevant metals, no further discussion on this area will be given within this chapter.

With the aim of using **Tb.58.Na** as a luminescent contrast agent for damaged bone structure, it was necessary to investigate the behaviour of this Tb(III) complex once attached to the bone surface. As previously mentioned, it was unknown whether such chelation to the high concentration of Ca^{2+} sites exposed upon damage generation would perturb the energy transfer process to the Tb(III) metal ion sensor and in turn reduce or completely diminish the luminescence response from the metal complex. It was also crucial to investigate its selectivity for damaged bone regions over healthy smooth bone surfaces. The following section will therefore discuss a series of solid state studies which were carried out on several bovine bone samples using **Tb.58.Na** as a potential contrast agent.

2.11 Solid state studies of bovine bone samples using Tb.58.Na

In order to demonstrate the ability of **Tb.58.Na** to behave as a luminescent imaging agent for damaged bone structure, several bovine bone specimens (obtained from Prof. Clive Lee's research group in the Royal College of Surgeons Ireland (RSCI)) were sectioned and polished to give mechanically smooth bone samples (20 mm x 7 mm x 1 mm). It was essential in order to mimic the smooth bone surfaces found *in vivo* that all specimens were efficiently polished using various grades of sand paper up to P1200 grit (15 μm). It was anticipated that **Tb.58.Na** should show little affinity for these bone samples as the hydroxyapatite matrix bears little damage and therefore has few Ca^{2+} sites exposed.

Using a surgical scalpel, a series of scratches *ca.* 5 mm in length were made on the upper half of the bone specimens, leaving the remaining lower sections of the samples undamaged (Figure 2.18a). Using a 1 x 10^{-3} M aqueous solution (20 mM HEPES and 135 mM KCl, pH 7.4) of **Tb.58.Na**, the bone samples were immersed under vacuum for various periods of time up to 24 h. After each selected time frame (1 h, 2 h, 4 h and 24 h), the samples were removed from the Tb(III) complex solution and washed thoroughly using deionised water. Luminescence studies of the samples were then carried out using a Varian Cary Eclipse Fluorescence Spectrophotometer with the help of the specially modified cuvette shown in Figure 2.18b. The quartz glass slide which was attached to the lid allowed for the bone samples to be placed diagonally (45°) into the cuvette, enabling a Ln luminescence spectrum to be measured from the bone sample. Depending on the position of the sample on

the quartz glass, a spectrum from either the smooth surface or damaged bone region was attained.

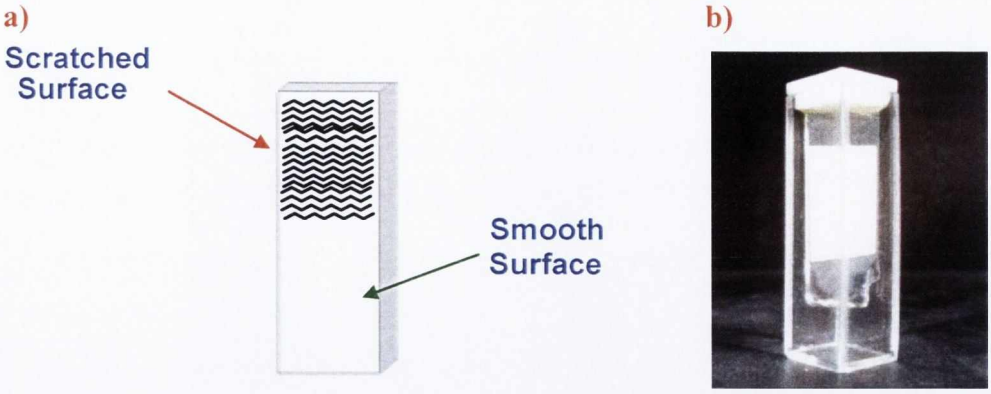

Figure 2.18: *a) Illustration of bone sample (20 mm x 7 mm x 1 mm) highlighting the scratched damaged upper bone surface in comparison to the smooth undamaged lower region of the sample. b) Photo of the specially modified cuvette with a bone sample placed inside at a 45° angle.*

The results obtained from these solid state studies clearly demonstrated upon excitation of the scratched region at 285 nm, sufficient Tb(III) emission was recorded, with the $^5D_4 \rightarrow {}^7F_J$ (J = 6, 5, 4, 3) transitions being observed. As expected, longer immersion times resulted in a subsequent increase in emission intensity from the Tb(III) complex being measured (Figure 2.19a). It is important to note, that due to the relatively small size of the scratches on the bone specimens and the difficulty in positioning the sample in the exact location each time, several spectra had to be recorded with the average spectrum for each time frame shown below in Figure 2.19.

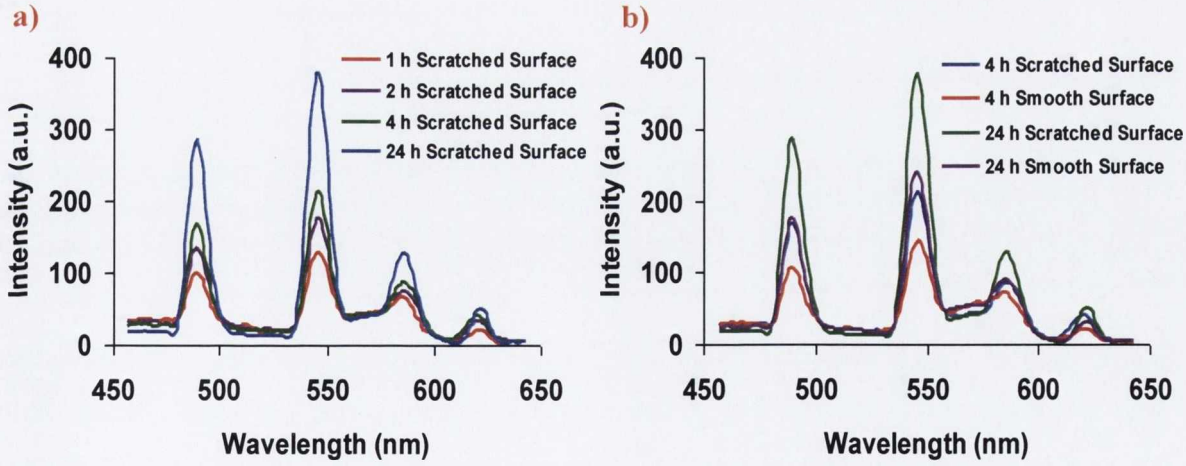

Figure 2.19: *a) The Tb(III) luminescence response of* ***Tb.58.Na*** *from the scratched region of a bone sample as a function of immersion time used. b) The Tb(III) luminescence response of* ***Tb.58.Na*** *from the scratched and smooth surface of a bone sample at 4 h and 24 h immersion times. The bone specimens were immersed under vacuum in a 1 x 10^{-3} M aqueous solution (20 mM HEPES and 135 mM KCl, pH 7.4) of* ***Tb.58.Na****.*

For all immersion times studied, **Tb.58.Na** gave a more intense emission response from the scratched regions in comparison to the undamaged smooth bone surfaces (Figure 2.19b). This suggests that **Tb.58.Na** displays some form of selectivity for the damaged hydroxyapatite surface, which could be as a result of chelation with the Ca^{2+} ions exposed upon damage formation. To help verify this, the solid state studies were repeated using the control Tb(III) complex **Tb.58**, which has its iminodiacetate functionality protected as the ethyl ester form. As shown in Figure 2.20, upon excitation of the damaged region at 283 nm, although Tb(III) emission was observed, the intensity in comparison to that seen for **Tb.58.Na** was significantly lower. For example, for the 24 h immersion time, the intensity for the $J = 5$ emission band for **Tb.58** was 107 in comparison to 378 for the **Tb.58.Na** complex. This almost 4-fold enhancement in emission intensity helps highlight the essential requirement of the chelating iminodiacetate functionality for selective damage detection.

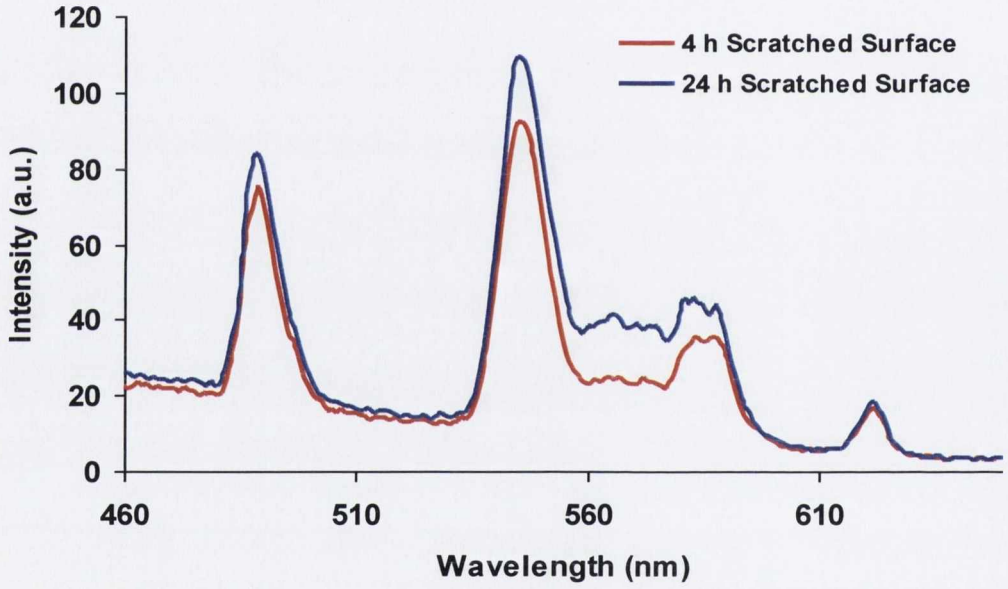

Figure 2.20: *The Tb(III) luminescence response of **Tb.58** from the scratched region of a bone sample as a function of immersion time used. The bone specimens were immersed under vacuum in a 1 x 10^{-3} M aqueous solution MeOH:H_2O (1:99 v/v) (20 mM HEPES and 135 mM KCl, pH 7.4) of **Tb.58**.*

Another interesting observation from these solid state studies is that for **Tb.58**, there was very little difference in the emission intensities between the 4 h and 24 h immersion times, with an intensity enhancement of 19% being measured. However, for **Tb.58.Na** a much larger emission enhancement of 77% was observed. This implies that when the iminodiacetate chelating unit is blocked, as in the case of **Tb.58**, the Tb(III) emission intensity observed from the scratched region is possibly as a result of the complex staining or lodging within the damaged structure of bone, with no significant Ca^{2+} interaction occurring. However, when the binding unit is in its free form, the initial staining or lodging of the

complex within the scratched region is over taken by a more efficient binding process at the damaged sites, explaining the larger enhancement observed at longer immersion times.

In summary, these results successfully demonstrated the ability of **Tb.58.Na** to show selectivity for regions of damaged bone structure. Strong Tb(III) emission was observed from the bone surface upon indirect excitation of the metal complex *via* the covalently attached phenyl antenna. The higher emission intensities observed from the scratched regions were as a result of preferential localisation of **Tb.58.Na** at these sites. Analysis of the control complex **Tb.58** verified the essential requirement of the iminodiacetate chelating unit for more efficient bone targeting, with a much lower emission intensity being observed for this complex. However, as shown in Figure 2.19b, although the Tb(III) emission was always more intense at the scratched region then at the smooth undamaged bone surface for all time frames studied, the actual difference in intensity was quite small. This could pose a problem when **Tb.58.Na** is employed to distinguish microdamage using epifluorescence and confocal laser scanning microscopy, as the emission difference from the smooth surface may not be large enough to allow for efficient damage visualisation. With this potential drawback in mind, it was decided to investigate the effect of increasing the number of iminodiacetate chelating arms on the contrasting abilities of such Ln luminescent based systems. The following section will therefore discuss the design and synthesis of similar cyclen based Ln imaging agents, with an emphasis on the advantages they could potentially have over the original **Tb.58.Na** complex design.

2.12 Structural modification of initial ligand design

With the potential for stronger chelation of the Ca^{2+} ions exposed upon microdamage formation, the three dimethyl acetamide arms which alkylated the amine sites of the cyclen framework in ligand **58** were replaced by a set of diethyl 2,2-(2-chloroacetylamino)diacetate pendant groups. By increasing the number of chelating functionalities within the new ligand design it was anticipated that more selective localisation of these Ln complexes within the damaged bone structure would occur, resulting in a more efficient contrast from the remaining smooth bone surfaces. As the phenyl antenna had proved unsuccessful in the sensitisation of both Tb(III) and Eu(III) ions, it was decided to incorporate the naphthalene chromophore into the ligand structure, which as a result of its slightly lower triplet excited state energy would allow for more sufficient population of the excited state of both these Ln ions. Taking these modifications into consideration, ligand **69** and its corresponding Eu(III) and Tb(III) complexes, **Eu.69** and **Tb.69** were designed. As was the case for **Tb.58**, these complexes have their iminodiacetate pendant groups protected as their ethyl ester forms and

should therefore show very little Ca^{2+} chelation at the damaged bone regions. Successful base hydrolysis of these control complexes should result in the formation of the more microdamage selective Ln complexes, **Eu.69.Na** and **Tb.69.Na**.

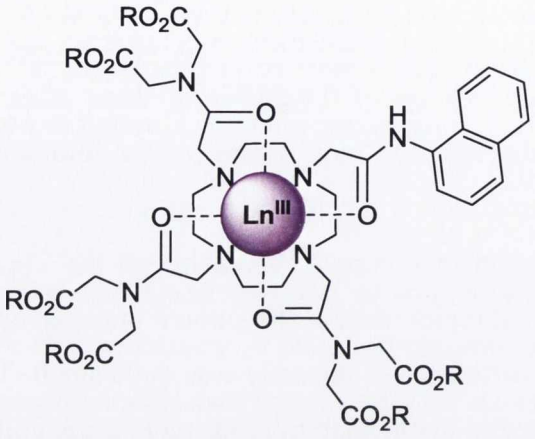

Eu.69: Ln^{III} = Eu(III), R = Et
Eu.69.Na: Ln^{III} = Eu(III), R = Na
Tb.69: Ln^{III} = Tb(III), R = Et
Tb.69.Na: Ln^{III} = Tb(III), R = Na

2.13 Synthesis and characterisation of ligand 69 and the corresponding Eu(III) and Tb(III) complexes, Eu.69 and Tb.69

The first step in the synthesis of **69** involved the formation of 2-chloro-*N*-(naphthalene-1-yl) acetamide **70** by reacting chloroacetyl chloride **65** with 1-aminonaphthalene **71** in the presence of freshly distilled NEt_3, at low temperature (-10 °C) in dry CH_2Cl_2. Unreacted **65** along with the NEt_3 salt were removed by extraction with H_2O, 0.1 M HCl and brine, resulting in the isolation of the desired product in 86% yield. Subsequent mono alkylation of **66** with **70** was achieved by refluxing overnight four equivalents of **66** with one equivalent of **70**, in dry $CHCl_3$, using Et_3N as the base. Isolation of **72** in 90% yield was achieved after successful removal of excess **66** by extraction using 1 M NaOH. The final step in the synthetic pathway to **69** involved the reaction of **72** with three equivalents of diethyl 2,2-(2-chloroacetylamino)diacetate **73** at 85 °C in freshly distilled CH_3CN in the presence of Et_3N for 7 days. After reaction completion (followed by mass spectrometry), the solvent was removed under reduced pressure and the subsequent orange oil re-dissolved in CH_2Cl_2. Removal of the Et_3N was achieved by extraction with H_2O, while further purification by alumina column chromatography using a gradient elution 100 to 80:20 CH_2Cl_2:MeOH gave **69**, as a yellow viscous oil, in 54% yield, Scheme 2.6.

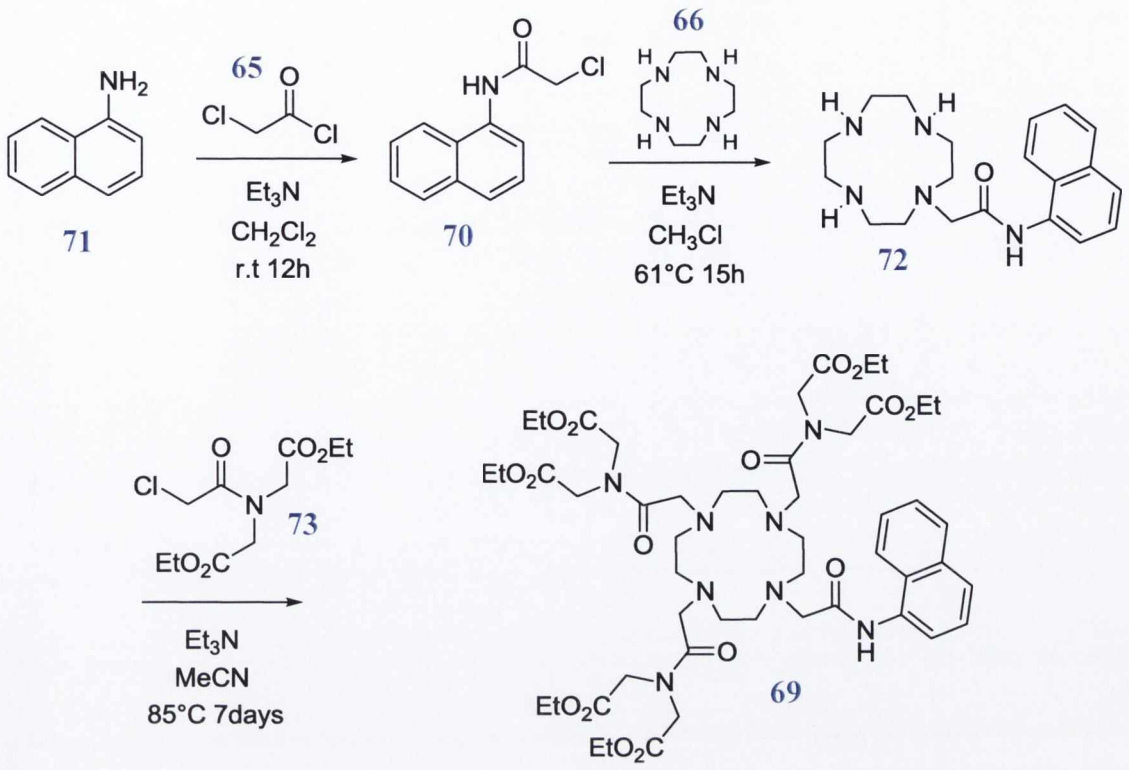

Scheme 2.6: *Synthetic pathway for ligand 69.*

The ^{1}H NMR spectrum of **69** ($CDCl_3$, 400 MHz), as shown in Figure 2.21, displayed the expected N-H signal at 10.39 ppm along with the aromatic signals of the naphthalene chromophore ranging between 7.36 – 8.35 ppm. The ester CH_3 protons of the diethyl iminodiacetate moieties appear as three sets of triplets at 1.24, 1.19 and 1.09 ppm with a total integration value of eighteen. Whereas the remaining $N(C\underline{H}_2)_2$ (12H) and the $CO_2C\underline{H}_2CH_3$ (12H) protons, as well as the $C\underline{H}_2$ (2H) of the pendant arm linking the naphthalene chromophore to the cyclen moiety appear as a series of crowded signals over the ppm range 3.72 4.31, with an overall integration of twenty six. The cyclen $C\underline{H}_2$ (16H) protons along with the $C\underline{H}_2$ (6H) protons which link the three iminodiacetate functionalities to the cyclen framework appear as a multiplet of broad overlapping peaks which resonate between the spectral range 2.6 – 3.4 ppm, with a total integration of twenty two. ^{13}C NMR analysis was also employed to characterise ligand **69** with ESMS confirming the presence of a peak at *m/z* = 1043.53 which corresponds to a $[\mathbf{69} + H]^+$ species in solution.

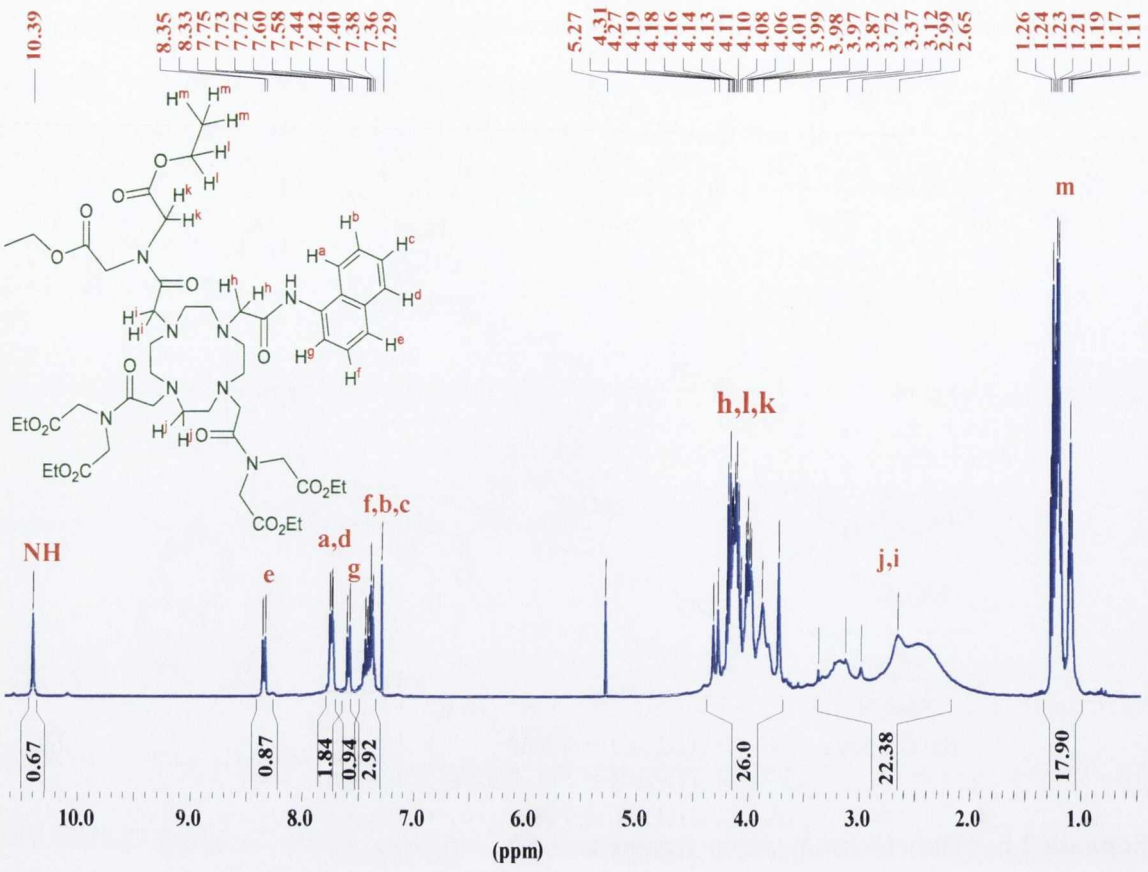

Figure 2.21: *The ^1H NMR spectrum (400 MHz, $CDCl_3$) of ligand* **69**.

The Eu(III) and Tb(III) complexes of **69** were successfully formed in 69% and 70% yield, respectively. This involved refluxing the appropriate Ln triflate salt with the cyclen based ligand in freshly distilled CH_3CN for 15 h. Subsequent precipitation from swirling dry diethyl ether resulted in the isolation of both complexes as orange solids. The ^1H NMR spectra of both **Eu.69** and **Tb.69** in $CDCl_3$ showed the characteristic broadening and shifting of all the proton resonances including the equatorial and axial protons of the cyclen ring over a large ppm range. For the case of the ^1H NMR spectrum of **Eu.69**, shown in Figure 2.22, the resonances were shifted over a 42 ppm range. The shift in the IR carbonyl signal from 1660 cm^{-1} to 1603 cm^{-1} for both **Eu.69** and **Tb.69** again proved useful in determining successful Ln complexation within the cyclen cavity. No significant shift was observed for the carbonyl signal of the diethyl iminodiacetate units (1736 cm^{-1}), confirming no weak metal interactions occurring at these sites. HRMS analysis also verified complex formation with the location of a *m/z* peak $[\mathbf{Ln.69}+2(CF_3SO_3)]^+$, displayed at 1493.3433 and 1499.3560 for **Eu.69** and **Tb.69**, respectively. The expected isotopic distribution pattern for both complexes was also observed (Figure A1.8).

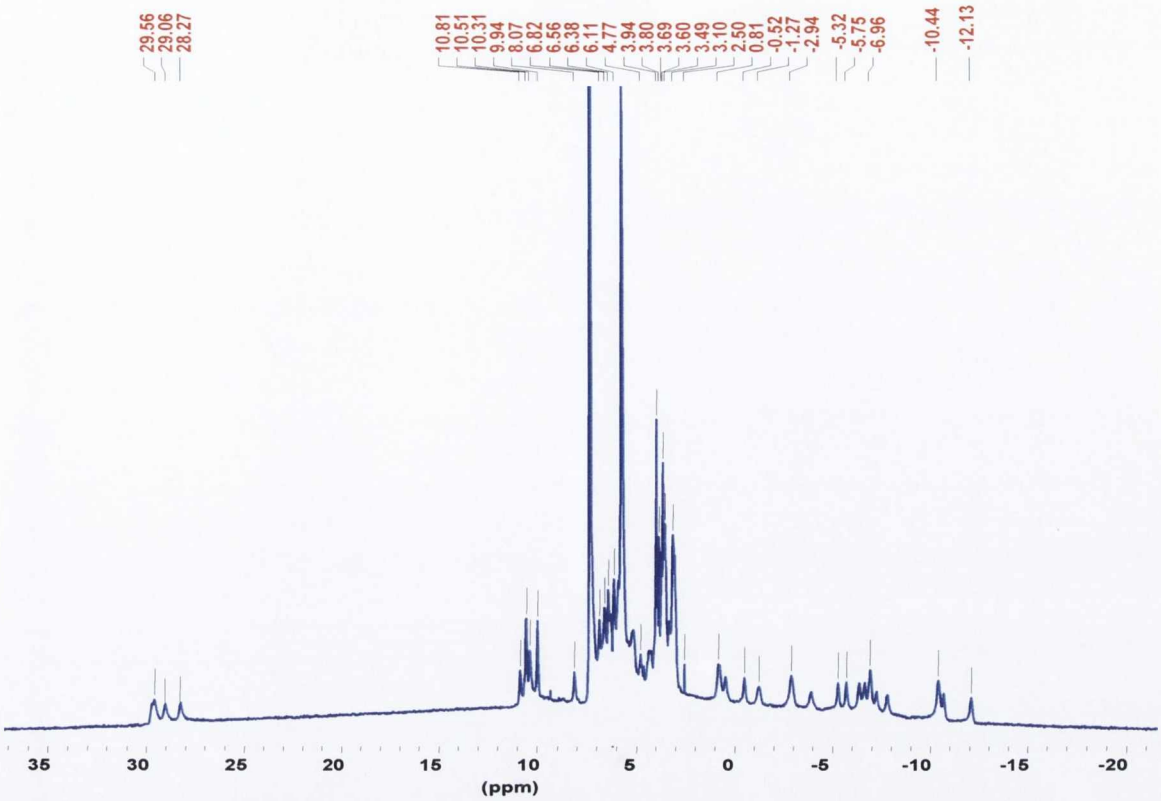

Figure 2.22: *The ^{1}H NMR spectrum (400 MHz, $CDCl_3$) of complex* ***Eu.69****.*

2.14 Photophysical properties of Eu.69 and Tb.69

The UV-vis absorption spectra of **Eu.69** and **Tb.69** in a mixed MeOH/H_2O (1:99 *v/v*) solution at pH 7.4 showed one broad $\pi-\pi^*$ absorption band centred at 282 nm. Upon excitation at 225 nm, a fluorescence emission spectrum with a λ_{max} at 265 nm and a slight shoulder appearing at 300 nm was recorded (Figure 2.23).

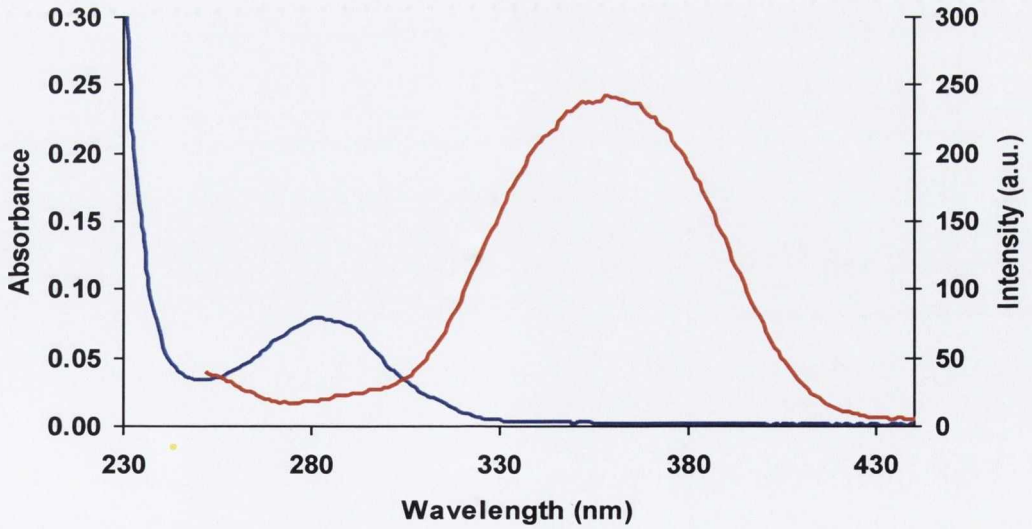

Figure 2.23: *UV-vis absorption (−) and fluorescence spectra (−) of* ***Tb.69*** *and* ***Eu.69*** *in MeOH:H_2O (1:99 v/v).*

Both Ln complexes were excited at 282 nm with the anticipation that sufficient population of the Ln excited states would result. As shown in Figure 2.24, strong metal

centred emission was observed at 580, 595, 616, 655 and 701 nm and at 490, 546, 586 and 622 nm for **Eu.69** and **Tb.69**, respectively. With the naphthalene triplet excited state lying at 21300 cm^{-1},[175] and therefore the energy distance to the Eu(III) excited state minimised, any previous problem of non-radiative deactivation and thus poor emission intensity was eliminated.

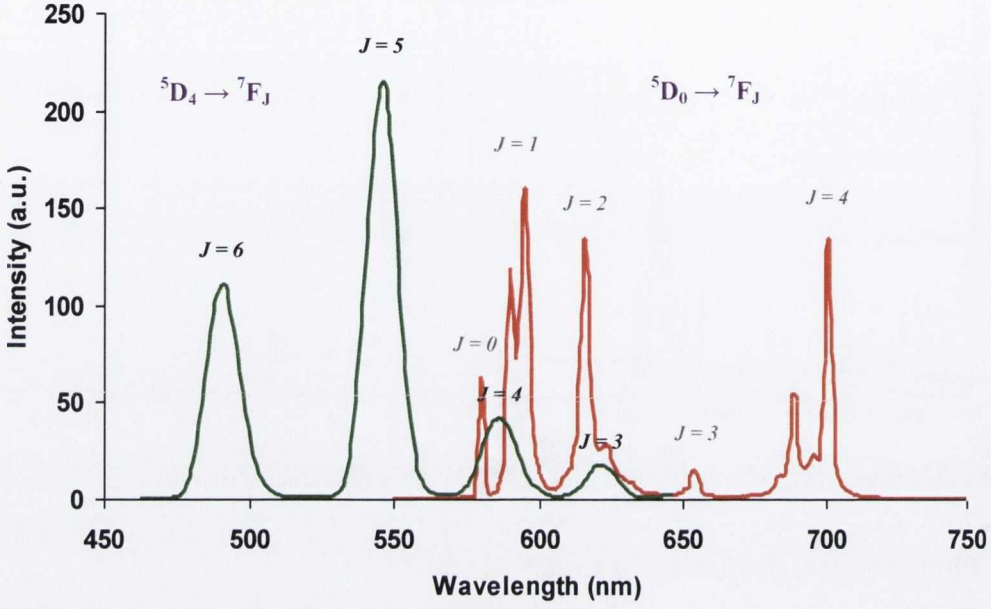

Figure 2.24: *Lanthanide luminescence spectra of **Tb.69** (–) and **Eu.69** (–) recorded in a mixed MeOH:H_2O (1:99 v/v) solution using excitation wavelength of 282 nm*

Similar to **58**, the cyclen naphthalene based ligand **69** can provide up to eight potential co-ordination sites for Ln ion complexation (four from the nitrogens of the cyclen structure and four from the oxygens of the carboxylic amides), with the final site mostly likely occupied by a solvent molecule. This was confirmed by recording the excited sate lifetimes of both **Eu.69** and **Tb.69** in H_2O and D_2O. Fitting the luminescence decay data to mono exponential resulted in lifetime values, of $\tau_{O\text{-}H} = 0.448 \pm 0.01$ ms and $\tau_{O\text{-}D} = 0.975 \pm 0.01$ ms and $\tau_{O\text{-}H} = 1.33 \pm 0.01$ ms and $\tau_{O\text{-}D} = 2.11 \pm 0.01$ ms for **Eu.69** and **Tb.69**, respectively. Using Equation 1.2 and Equation 1.3, a q value of *ca.* 1 was obtained for both complexes, verifying the presence of a single metal bound H_2O molecule within their co-ordination environments.

With both complexes successfully synthesised, characterised and a basic understanding of their co-ordination environment gained through lifetime measurements, the next step was to investigate the effect on their photophysical properties with respect to pH. It was not known whether these Ln based complexes would exhibit pH independence within the physiological pH range. Although the possible protonation and deprotonation sites are similar to those studied for **Tb.58**, it is possible that due to the structural changes associated

with these groups that their pK_a values could have shifted into the important physiological pH region. The following section will therefore briefly summarise the changes in the ground and singlet excited state of the naphthalene chromophore as a function of pH, followed by a more detailed discussion of the luminescence response for both complexes.

2.15 pH investigation of Eu.69 and Tb.69 in aqueous solution

A similar titration method as previously discussed for **Tb.58** was used, where both complexes were dissolved in a mixed MeOH:H_2O (1:99 *v/v*) solution using 0.1 M NEt_4ClO_4 (TEAP) in order to maintain a constant ionic strength. The pH environments of the complexes were altered by adding various aliquots of $HClO_4$ and NEt_4OH to the solution mixtures.

2.15.1 pH dependence of the ground and singlet excited state properties

In Section 2.7, due to the tertiary amine group of the diethyl iminodiacetate unit of **Tb.58** being directly attached to the phenyl antenna, it was shown that subsequent protonation in acidic conditions resulted in significant changes in both the ground and singlet excited state properties of the phenyl chromophore. However, as **Eu.69** and **Tb.69** do not exhibit any diethyl iminodiacetate unit directly attached to their naphthalene antenna, it was anticipated that no major changes in the chromophores photophysical properties should occur at low pH. As expected, upon basification of the solution from pH 2, any change observed in the UV-vis absorption and fluorescence spectra were negligible (Figure A1.9). However, once the pH of the solution was increased above pH 7.6, subsequent deprotonation of the secondary amide group resulted in modulation of the chromophores properties. The fluorescence spectra displayed large increases in their emission intensities of *ca.* 80% and 62% for **Eu.69** and **Tb.69**, respectively, with the UV-Vis absorption spectra displaying a 2 nm bathochromic shift from λ_{max} at 282 nm to 290 nm. These measurements also confirmed the presence of a large pH window between pH 2 and pH 7.6 where no modulation in the ground and singlet excited state properties of the naphthalene antenna occurred.

2.15.2 pH dependence of the Eu(III) and Tb(III) excited state properties

The luminescence response of both **Eu.69** and **Tb.69** differed greatly in comparison to that of **Tb.58**, where a large decrease in the emission intensity was observed in acidic and basic pH environments. As shown in Figure 2.25, at pH 12, the Eu(III) emission from **Eu.69** was almost completely "switched off", however, upon acidification to neutral pH, a 100-fold emission enhancement was observed. This "on-off" pH behaviour with increasing basicity

suggests that deprotonation of the secondary amide functionality has a dramatic effect on the energy transfer process, making population of the Eu(III) excited state much more difficult.[176] Another interesting feature, as shown in Figure 2.25b, is that at low pH values the luminescence response begins to show another dramatic emission decrease. With the pK_a of the tertiary amide group located within this pH range, it is probable that protonation of the three diethyl iminodiacetate pendant arms could be the principle cause of this observed reduction in emission intensity. The possibility that acid catalysed dissociation of the Eu(III) ion from the cyclen cavity was occurring was eliminated by the fact that the pH titration was fully reversible. Despite these significant decreases in the Eu(III) emission as a function of pH, it is clear that within the physiological pH window, the Eu(III) emission is "switched on" with no modulation in the luminescence response occurring.

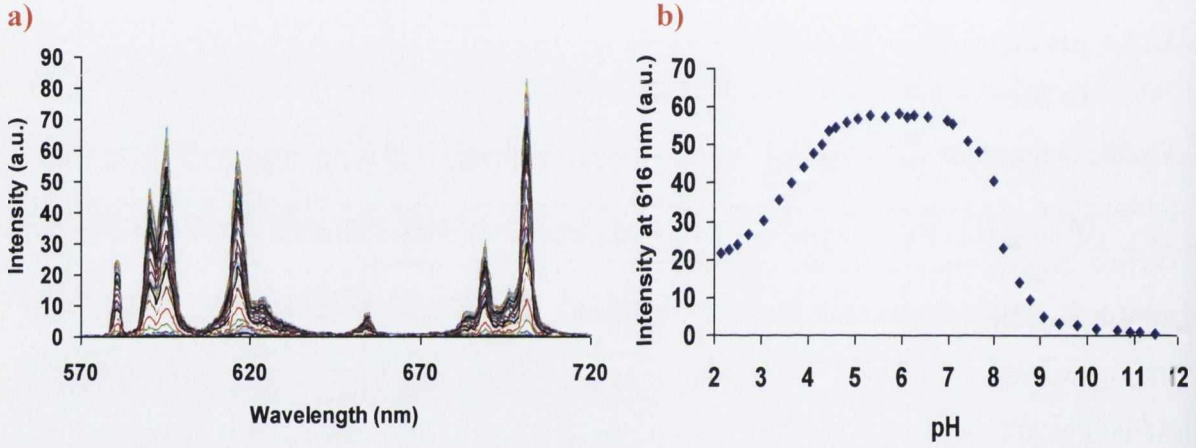

Figure 2.25: *a) The overall changes in the Eu(III) luminescence of* **Eu.69** *as a function of pH in a mixed MeOH:H_2O (1:99 v/v) solution [I = 0.1M NEt_4ClO_4 (TEAP)] b) The observed changes at 616 nm as a function of pH.*

A similar bell shaped curve was obtained when the changes at 545 nm for **Tb.69** were plotted over the entire pH scale. However, as shown in Figure 2.26b, although in basic media the luminescence response showed a similar decrease in emission intensity, the pH at which the amide functionality became deprotonated was shifted to a slightly higher pH value. A similar effect was seen at the lower region of the pH scale, where the basicity of the tertiary amide moieties was increased slightly. With the Ln ion being the only known structural difference between **Eu.69** and **Tb.69**, it is possible that this observed shift in pH response could be a direct result of this change in metal within the cyclen framework. With the protonation and deprotonation processes of **Tb.69** occurring at the very extreme ends of the pH scale, a much larger independent pH window (pH 2.5 – pH 8.4) was seen than that observed for **Eu.69**. Overall, both complexes displayed high emission intensity at physiological pH, with reductions in luminescence response only being observed in very basic and acidic media.

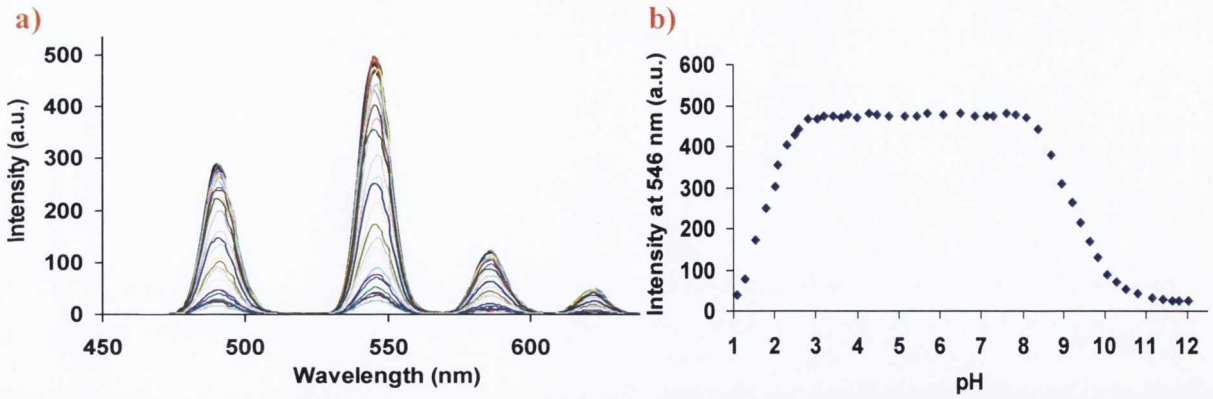

Figure 2.26: *a) The overall changes in the Tb(III) luminescence of* **Tb.69** *as a function of pH in a mixed MeOH:H_2O (1:99 v/v) solution [I = 0.1 M NEt_4ClO_4 (TEAP)] b) The observed changes at 546 nm as a function of pH.*

As was the case for **Tb.58**, the above Eu(III) and Tb(III) complexes have the microcrack specific iminodiacetate chelating units protected as their diethyl ester forms. These Ln systems will be used at a later stage as experimental controls as they should exhibit minimal chelation with the Ca^{2+} ions exposed upon microdamage formation. Therefore, the next step, which will be discussed in the following section, involves base hydrolysis of **Eu.69** and **Tb.69**, resulting in the formation of **Eu.69.Na** and **Tb.69.Na**, two potential imaging agents for damaged bone structure.

2.16 Base hydrolysis of the diethyl ester groups of Eu.69 and Tb.69

Similar to that previously described for **Tb.58**, both **Eu.69** and **Tb.69** were hydrolysed by refluxing in a mixed MeOH:H_2O (10:1 *v/v*) solution in the presence of NaOH for 5 h. Upon reaction completion (monitored by TLC), the solvent was removed under reduced pressure and the resulting orange residue re-dissolved in a minimal amount of cold MeOH. Micro-filtration was required to remove the fine NaOH precipitate which formed. To ensure complete removal of any remaining base, the MeOH solvent was evaporated to dryness and the resulting residue dissolved in a minimal amount of H_2O. Dropwise addition of this aqueous solution to swirling ethanol resulted in the precipitation of **Eu.69.Na** and **Tb.69.Na** in 90% and 76% yield, respectively. As previously discussed, with NMR spectroscopy proving insufficient in determining successful product formation (Figure A1.10), the key method of characterisation used for these complexes was IR spectroscopy. Disappearance of the sharp ester carbonyl signal and the subsequent appearance of a broad carboxylate carbonyl resonance helped confirm that base hydrolysis of **Eu.69** and **Tb.69** using the conditions described above had occurred. HRMS analysis also verified the presence of both complexes with a *m/z* peak at 1047.2191 for **Eu.69.Na**, corresponding to a

[**Eu.69.Na**-5Na+3H]$^+$ species in solution and a *m/z* peak at 1031.2394 for **Tb.69.Na**, representing a [**Tb.69.Na**-6Na+4H]$^+$ species (Figure A1.11).

As a result of the iminodiacetate chelating units in both **Eu.69.Na** and **Tb.69.Na** being directly attached to the cyclen framework, and therefore in close proximity to the Ln metal ion centre, it was unknown whether displacement of the single metal bound water molecule would occur as a result of co-ordination of one of the hard carboxylate groups to the Ln ion. To investigate this, the luminescence lifetime measurements of both complexes were carried out in 100% H_2O and D_2O, resulting in excited state lifetimes of 0.58 ± 0.01 ms and 1.74 ± 0.01 ms for **Eu.69.Na** and 1.23 ± 0.01 ms and 2.06 ± 0.01 ms for **Tb.69.Na**. Using Equation 1.2 and 1.3, a *q* value of *ca.* 1 was calculated for both Ln complexes, confirming that no displacement of the single metal bound H_2O molecule had occurred.

As already discussed in Section 2.8, hydrolysis of the diethyl iminodiacetate unit of **Tb.58** altered the excited state energy levels of the phenyl chromophore and in turn lead to more efficient population of the Tb(III) excited state. However, as **Eu.69** and **Tb.69** do not have their diethyl iminodiacetate moieties directly attached to the naphthalene antenna, it was anticipated that the base hydrolysis step would bear little significance on the energy transfer process. To verify this, it was necessary to compare the luminescence spectra of **Tb.69.Na** and **Eu.69.Na** to their previously studied ethyl ester analogues, ensuring that the spectroscopic parameters and concentrations used were identical. As shown in Figure 2.27a, an increase of *ca.* 10% was observed in the emission intensity of **Eu.69.Na**, compared to **Eu.69**. This slight increase was also reflected in the excited state lifetime measurements, with somewhat larger values being obtained for **Eu.69.Na**, It is also possible that this observed increase could be the result of some structural change around the metal centre, minimising any non-radiative deactivation process which may have been occurring.

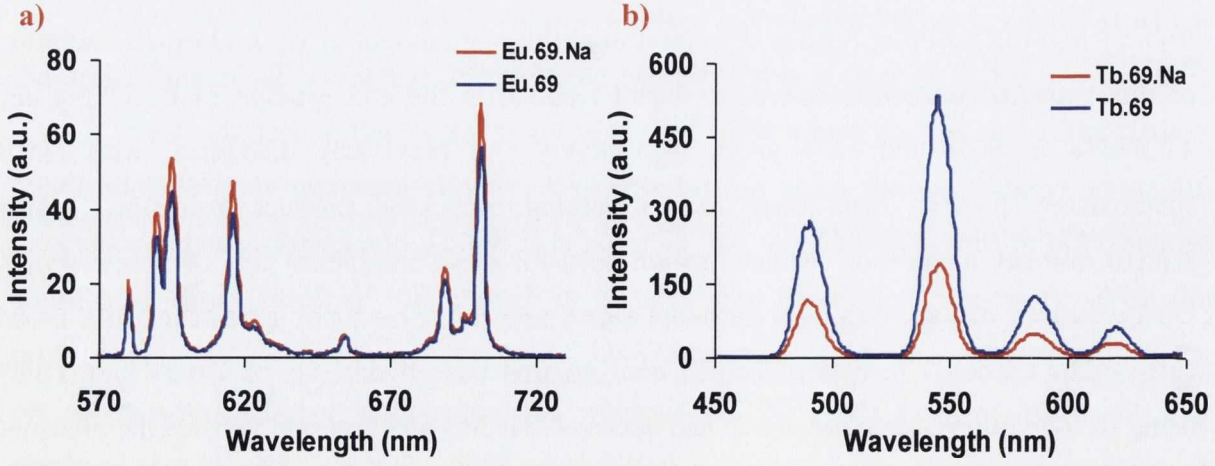

Figure 2.27: *a) The Eu(III) luminescence spectra of a 10 μM solution of **Eu.69** and **Eu.69.Na** and b) The Tb(III) luminescence spectra of a 10 μM solution of **Tb.69** and **Tb.69.Na**, in a mixed MeOH:H_2O (1:99 v/v) solution at pH = 7.4 (20 mM HEPES, 135 mM KCl), using excitation wavelength of 282 nm.*

However, on analysis of the Tb(III) complex, a very different response was observed. As shown in Figure 2.27b, the luminescence spectrum of **Tb.69.Na** is significantly reduced in comparison to its ester analogue **Tb.69**. This 65% decrease in emission intensity suggests that hydrolysis of the diethyl iminodiacetate functionalities has a considerable effect on the indirect excitation process *via* the naphthalene antenna, with subsequent population of the $^5D_4$ excited state of the Tb(III) metal ion proving much more difficult. As a result of this much poorer emission response from **Tb.69.Na**, great consideration must be taken when comparing the ability of this complex to selectively bind microdamage over its ester analogue. Although, **Tb.69.Na** may show more preferential chelation at the damaged sites then **Tb.69**, due to its much lower emission response, this may prove difficult to conclude.

With no real understanding at this stage why the emission intensity from **Tb.69.Na** is dramatically reduced, it was decided that the pH response of both the Eu(III) and Tb(III) complexes required investigation with any major differences from their ester analogues discussed. This may prove useful in determining a main cause for this much poorer response for **Tb.69.Na**. The following section will therefore highlight the results obtained from these measurements, concentrating on the luminescence response for both complexes.

2.17 pH dependence of the Eu(III) and Tb(III) excited state properties of Eu.69.Na and Tb.69.Na

As shown in Figure 2.28, no significant variation in the pH response of the Eu(III) excited state properties as a result of the hydrolysis step occurred. A similar bell shape curve as previously seen for **Eu.69** was observed when the intensity changes of the $J = 2$ (616 nm) emission band were plotted as a function of pH change. These measurements also confirmed the physiological independence of **Eu.69.Na** due to the presence of the large pH window between pH 7.5 and pH 4.5 where the luminescence response of the complex was fully "switched on", with any significant quenching in emission intensity only being observed at acidic and basic regions of the pH scale. On comparison of the pH response of **Tb.69.Na** to that of its ethyl ester form, it was clear that although the emission intensity changes at 546 nm as a function of pH displayed a similar bell shape curve to that seen in Figure 2.26, the pH range at which the complex displayed independence had shifted. As shown in Figure 2.29, as a result of the hydrolysis of the diethyl iminodiacetate functionalities of **Tb.69**, deprotonation of the secondary amide moiety now occurred at a much lower pH value. The consequence of this basicity increase for the amide group was the Tb(III) complex was no longer independent at physiological pH, with a large decrease in luminescence response now occurring above pH 6.5. This helps explain the previous observation of a 65% decrease in

emission for **Tb.69.Na**, when compared to its ethyl ester analogue **Tb.69**. Such a response suggests that upon hydrolysis of **Tb.69**, some structural change in the complex, which is not observed for the Eu(III) analogue, must be occurring, resulting in a decrease in the pK_a value for the secondary amide functionality. It is possible that this structural modification could be placing the secondary amide functionality in closer proximity to the high positive charge of the Tb(III) ion, which as a result of its electron withdrawing properties could be weakening the amide N-H bond, making its subsequent deprotonation occur at a slightly lower pH value.

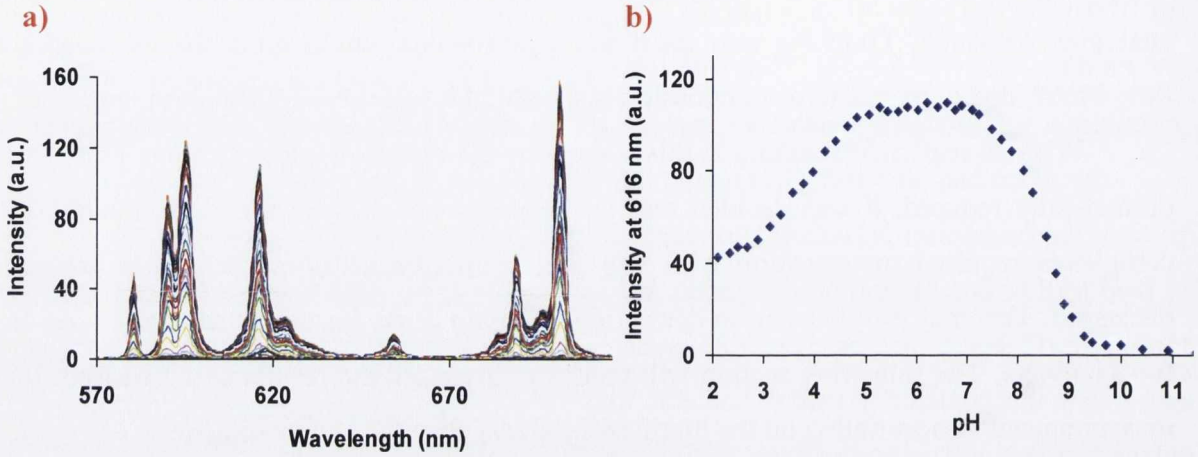

Figure 2.28: *a) The Eu(III) luminescence response of* ***Eu.69.Na*** *as a function of pH in H_2O [I = 0.1M NEt_4ClO_4 (TEAP)] b) Changes at 616 nm as a function of pH.*

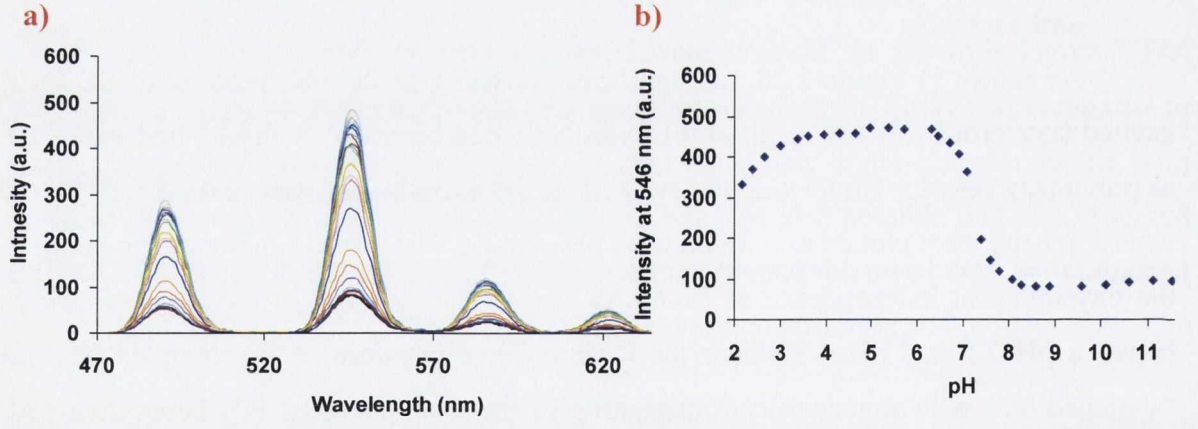

Figure 2.29: *a) The Tb(III) luminescence response of* ***Tb.69.Na*** *as a function of pH in H_2O [I = 0.1M NEt_4ClO_4 (TEAP)] b) Changes at 546 nm as a function of pH.*

Overall, **Eu.69** and **Eu.69.Na** showed similar luminescence responses as a function of pH, with both complexes displaying pH independence within the important physiological pH range. At the same concentration, the emission intensities from both complexes were similar, suggesting very little modulation in the energy transfer process as a result of the base hydrolysis step. However, on comparison of **Tb.69.Na** with its ethyl ester analogue **Tb.69**, a large deviation between their photophysical responses towards pH was observed. As a result of the shift in the pH at which the secondary amide of **Tb.69.Na** became deprotonated, its emission response at pH 7.4 was reduced by *ca.* 65% in comparison to **Tb.69**. This could

make direct comparison of both Tb(III) complexes difficult at a later stage. With a complete understanding of the pH dependence of both **Eu.69.Na** and **Tb.69.Na**, a similar metal ion study as that previously discussed for **Tb.58.Na** was the next stage in the investigation of these complexes as potential contrast agents for bone material. As the ground state, singlet excited state and Ln excited state properties of both **Eu.69.Na** and **Tb.69.Na** displayed similar responses during these metal ion investigations, the following section will only detail the photophysical modulations of **Eu.69.Na**, with the understanding that unless stated a similar response was seen for the Tb(III) analogue.

2.18 Metal ion studies for Eu.69.Na

A similar metal titration method as previously discussed for **Tb.58.Na** was used, where various aliquots of an aqueous solution of the relevant metal ion was added to a 10 μM solution (20 mM HEPES, 135 mM KCl, pH 7.4) of **Eu.69.Na**, with a UV-vis absorption, fluorescence and phosphorescence spectra recorded after each addition. With the iminodiacetate receptor units not being directly attached to the naphthalene chromophore, it was anticipated that even upon metal ion binding, very little modulation in the chromophores ground and singlet excited state properties would be observed. However, due to the close proximity of these chelating moieties to the Eu(III) metal centre, the luminescence behaviour of **Eu.69.Na** in the presence of these metal ions was unknown.

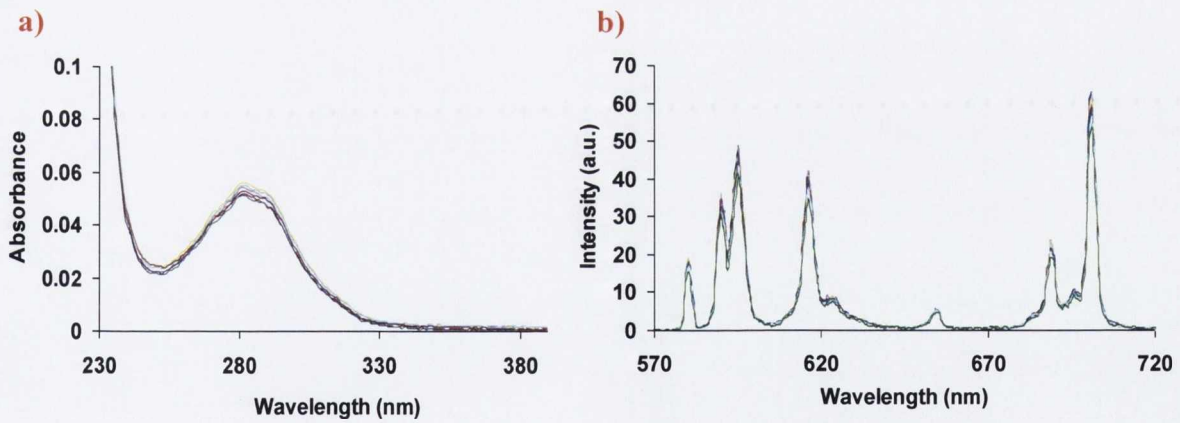

Figure 2.30: *The changes in a) the UV-vis absorption spectra and b) the phosphorescence spectra of **Eu.69.Na** (10 μM) in the presence of $CaCl_2$ (0 → 10 mM) at pH = 7.4 (20 mM HEPES, 135 mM KCl).*

As in the case of **Tb.58.Na**, upon the addition of Ca^{2+} and Mg^{2+} ions to the solution (0 – 10 mM), no significant modulations in the photophysical properties of **Eu.69.Na** were observed. Such a response suggests either little metal ion binding at the iminodiacetate units or any binding which may be occurring bears little effect on the energy transfer process to the Ln excited state. The changes in the UV-vis absorption and phosphorescence

spectra of **Eu.69.Na** in the presence of Ca^{2+} are depicted above in Figure 2.30a and Figure 2.30b, respectively. For the transition metal ions, it was previously shown by the studies carried out on **Tb.58.Na**, that although significant changes were observed in the UV-vis absorbance and fluorescence spectra in the presence of high concentrations of Cd^{2+} and Zn^{2+}, the binding of these metal ions to the chelating iminodiacetate receptor unit displayed no subsequent modulation in the Tb(III) emission properties. However, in the case of **Eu.69.Na**, where these receptor moieties are independent of the naphthalene chromophore, no significant UV-vis absorption, fluorescence or phosphorescence changes were observed. For the remaining transition metal ions studied (Cu^{2+}, Hg^{2+}, Co^{2+} and Fe^{2+}), a similar response was displayed for the ground state and singlet excited state properties of the antenna moiety. However, unlike that displayed for Zn^{2+} and Cd^{2+}, significant changes were observed in the Eu(III) emission intensity upon addition of these metal ions (Figure A1.12). As shown in Figure 2.31 and Figure 2.32, a significant quenching effect in the phosphorescence response of **Eu.69.Na** resulted in the presence of Cu^{2+} and Hg^{2+} ions, with the formation of a plateau after *ca.* 2 and 5 equivalent additions, respectively. For the case of Co^{2+} and Fe^{2+}, a larger number of equivalents were required in order for the quenching effect to occur. These results confirm those previously discussed for **Tb.58.Na**, where Cu^{2+} and Hg^{2+} ions displayed more preferential binding at the iminodiacetate receptor units, over Co^{2+} and Fe^{2+}.

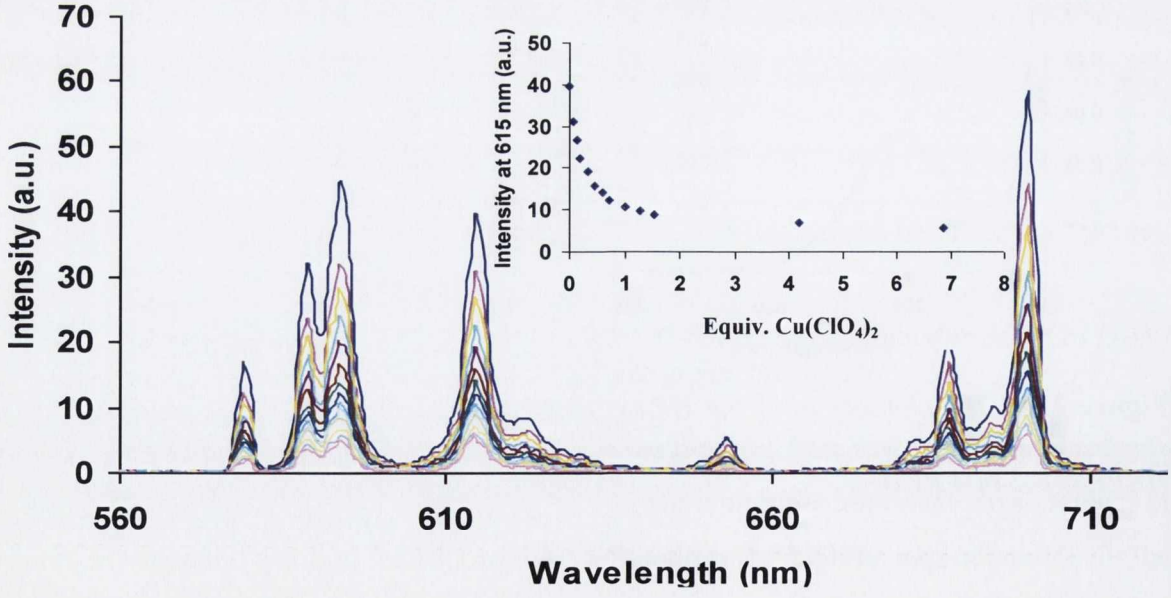

Figure 2.31: *The Eu(III) luminescence response of* ***Eu.69.Na*** *upon the addition of* $Cu(ClO_4)_2$ *in non-buffered* H_2O *solution. Inset: Changes in Eu(III) emission at 615 nm as a function of* Cu^{2+} *equivalents.*

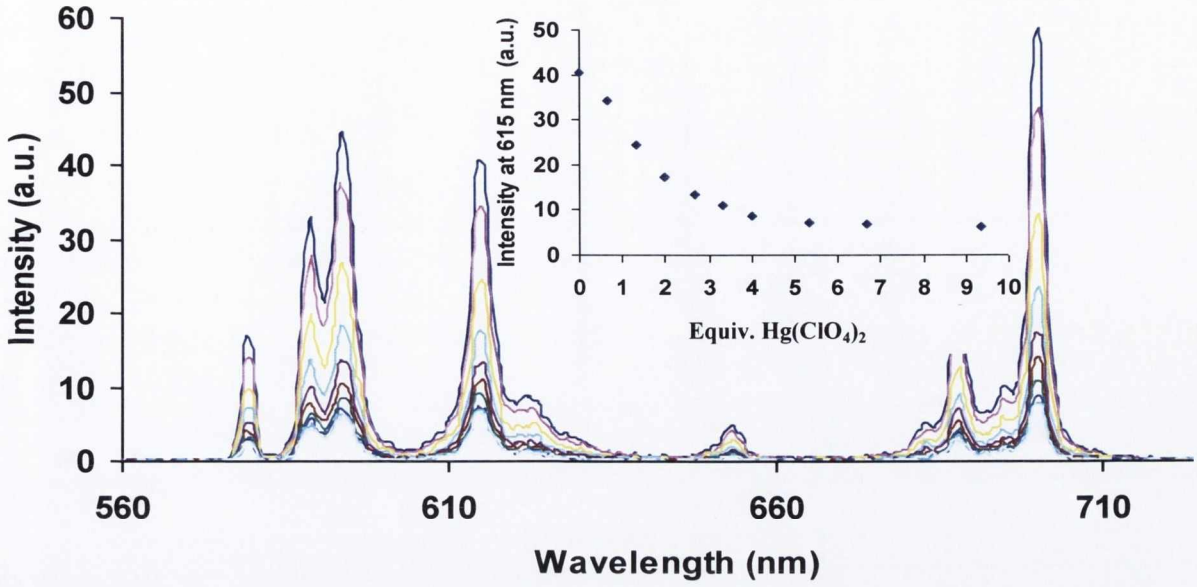

Figure 2.32: *The Eu(III) luminescence response of* ***Eu.69.Na*** *upon the addition of* $Hg(ClO_4)_2$ *in non-buffered* H_2O *solution. Inset: Changes in Eu(III) emission at 615 nm as a function of* Hg^{2+} *equivalents.*

As no quenching response was detected in the fluorescence spectra of **Eu.69.Na** upon the addition of these paramagnetic transition metal ions, the large reduction in Eu(III) emission intensity can not be the result of subsequent quenching of the antenna singlet excited state. This suggests that the energy transfer process from the triplet excited state of the chromophore to the Ln excited state is affected in some way by the binding of these metal ions. To ensure that the resulting decrease in emission intensity was not due to displacement of the Eu(III) metal from the cyclen cavity, excess cysteine was added to the solution at the end of each titration, resulting in an increase in the Eu(III) emission due to subsequent displacement of the transition metal ions from the receptor units.

In summary, it can be concluded that for Ca^{2+}, Mg^{2+}, Cd^{2+} and Zn^{2+}, any binding that may possibly be occurring within the iminodiacetate receptor units has no effect on the Eu(III) excited state properties of **Eu.69.Na**. For the remaining transition metals studied, due to their paramagnetic nature, significant quenching in the Eu(III) luminescence resulted. More preferential binding was observed for Cu^{2+} and Hg^{2+} ions, with a larger quenching response being displayed at low concentrations of these metal ions. A summary of the luminescence response of **Eu.69.Na** at 616 nm in the presence of the metal ions studied (20 μM) is displayed below in Figure 2.33.

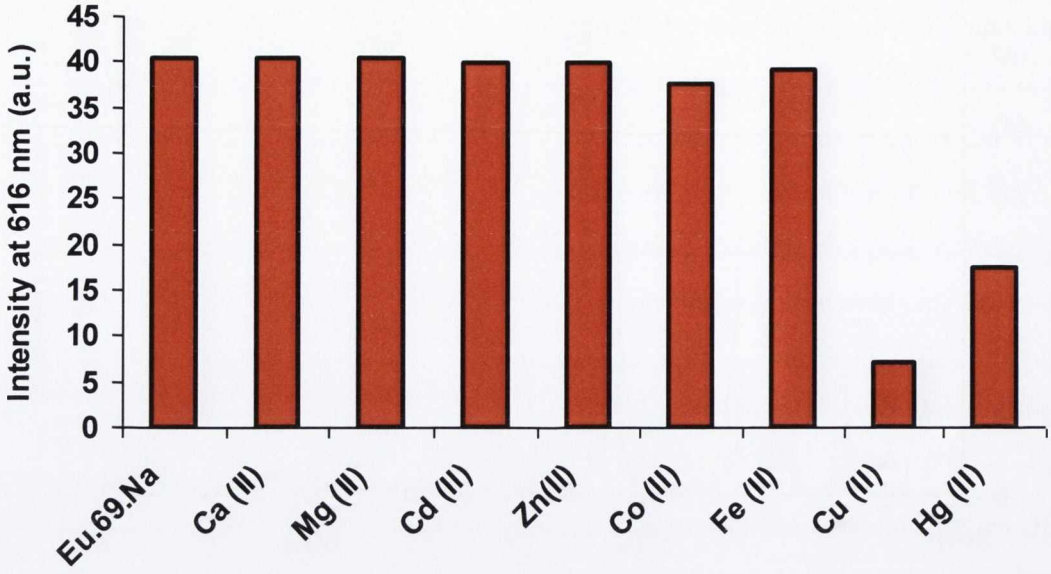

Figure 2.33: *The Eu(III) luminescence response of* ***Eu.69.Na*** *(10 μM) at 616 nm in the presence of various physiologically important metal ions (20μM) in* H_2O.

As a result of the larger number of iminodiacetate binding units within the overall structures of **Eu.69.Na** and **Tb.69.Na**, it was anticipated that these complexes would display more efficient chelation within damaged bone regions, thus providing a much stronger contrast from the remaining smooth undamaged bone surfaces. In order to investigate this, a series of solid state bone studies were carried out for **Eu.69.Na** and **Tb.69.Na**, with their ethyl ester analogues also being analysed. The following section will detail the results obtained from these bone measurements, with a direct comparison being made to **Tb.58.Na**, which only had one iminodiacetate receptor moiety incorporated within its structure.

2.19 Solid state studies of bovine bone samples using Eu.69.Na and Tb.69.Na

In order to investigate the potential of **Eu.69.Na** and **Tb.69.Na** as luminescent bone imaging agents, solid state study measurements as those previously described for **Tb.58.Na** and **Tb.58** were carried out on both complexes. The bovine bone specimens (20 mm x 7 mm x 1 mm) were prepared in a similar manner to that previously described in Section 2.11. Using a surgical scalpel, a series of scratches *ca.* 5 mm in length were made on the upper half of the bone specimens, leaving the remaining lower sections of the samples undamaged. These samples were then immersed in a 1 x 10^{-3} M aqueous solution (20 mM HEPES and 135 mM KCl, pH 7.4) of either **Eu.69.Na** or **Tb.69.Na** and stored under vacuum for various periods of time up to 24 h. After each selected time frame (1 h, 2 h, 4 h and 24 h), the samples were removed from the solutions and washed thoroughly using deionised water.

Luminescence studies of the samples were then carried out using a Varian Cary Eclipse Fluorescence Spectrophotometer with the help of the specially modified cuvette

previously shown in Figure 2.18b. In order to investigate both complexes preferential localisation within damaged bone structure, phosphorescence spectra were recorded from the scratched region and compared to those obtained from the smooth undamaged bone surface.

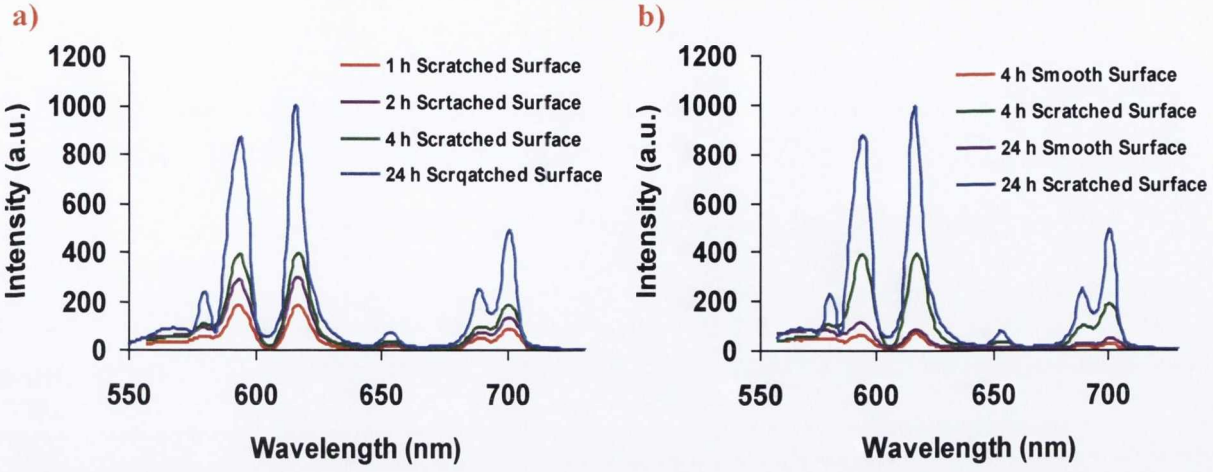

Figure 2.34: *a) The Eu(III) luminescence response of* ***Eu.69.Na*** *from the scratched region of a bone sample as a function of immersion time used. b) The Eu(III) luminescence response of* ***Eu.69.Na*** *from the scratched and smooth surface of a bone sample at 4 h and 24 h immersion times. The bone specimens were immersed under vacuum in a 1 x 10^{-3} M aqueous solution (20 mM HEPES and 135 mM KCl, pH 7.4) of* ***Eu.69.Na****.*

As displayed in Figure 2.34a, upon excitation (λ_{ex} = 282 nm) of the scratched surfaces of the bone specimens which were immersed in **Eu.69.Na**, sufficient Eu(III) emission was recorded, with the $^5D_0 \rightarrow {}^7F_J$ (J = 0, 1, 2, 3, 4) transitions being observed. As shown previously for **Tb.58.Na**, the emission intensity observed from the damaged bone surfaces increased dramatically as a function of immersion time. One observation is that in comparison to the emission intensities measured for **Tb.58.Na**, a much higher emission response was observed for **Eu.69.Na**, suggesting more efficient chelation and thus higher concentration of this Eu(III) complex at the damaged sites. Another clear indicator of more efficient chelation of the exposed Ca^{2+} ions as a result of the greater number of iminodiacetate receptor units in **Eu.69.Na** was obtained on comparison of the luminescence response at the damaged sites to those measured at the smooth healthy bone surfaces. As displayed above in Figure 2.34b, for all immersion times analysed, much greater Eu(III) emission intensities were observed from the scratched regions, where for example, a 14-fold enhancement in emission intensity was observed for the 24 h immersion time, compared to the much lower 1.6-fold enhancement observed for **Tb.58.Na** in the same time frame. This effectively highlights that increasing the number of iminodiacetate receptor units from one to three had a dramatic effect on the complexes selectivity for damaged bone structure. The essential requirement of these chelating iminodiacetate moieties was again verified by analysis of **Eu.69**.

The phosphorescence spectra shown in Figure 2.35a confirms the much poorer binding abilities of the diethyl iminodiacetate groups of **Eu.69** with the emission intensities recorded at the damaged sites being much lower then that seen previously for **Eu.69.Na**. It can also been seen that the difference between the emission response for the 4 h and 24 h immersion times is *ca.* 16 % compared to the much larger 153% enhancement observed for **Eu.69.Na**. This suggests that the luminescence response observed for **Eu.69** is most likely due to the complex staining or lodging within the damaged bone structure and not as a result of any binding process at the hydroxyapatite matrix. A final observation made from these studies was that on comparison of all the phosphorescence spectra obtained for **Eu.69.Na** and **Eu.69** at the damaged bone regions, the ratio between the $J = 1$ and $J = 2$ emission bands was significantly greater for **Eu.69** than for **Eu.69.Na**, suggesting the environment around the Eu(III) centre is different for each complex, indicating a different interaction with the bone surface.

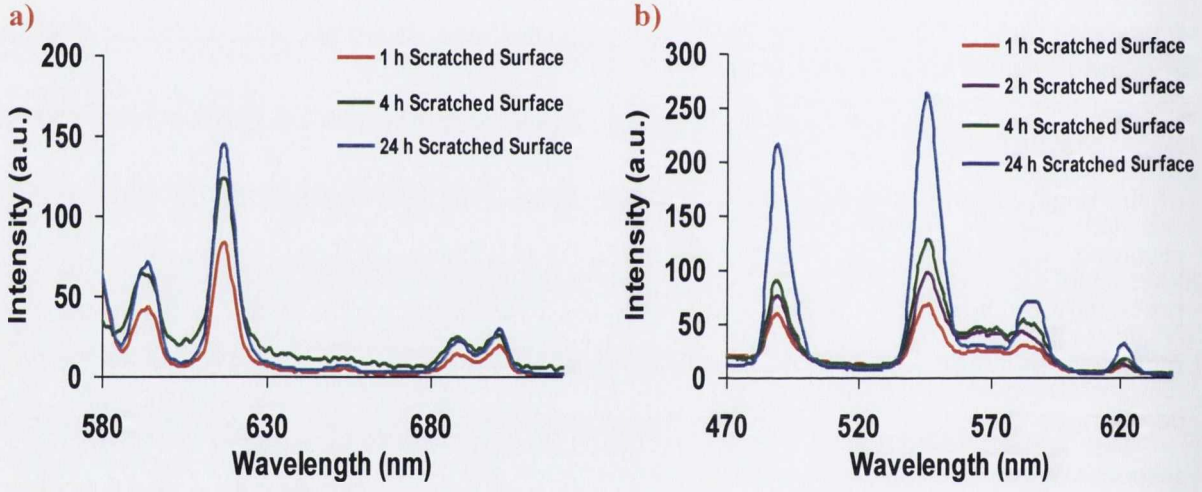

Figure 2.35: *a) The Eu(III) luminescence response of **Eu.69** from the scratched region of a bone sample as a function of immersion time used. b) The Tb(III) luminescence response of **Tb.69.Na** from the scratched region of a bone sample as a function of immersion time used. The bone specimens were immersed under vacuum in a 1 x 10^{-3} M aqueous solution (20 mM HEPES and 135 mM KCl, pH 7.4) of either **Eu.69** or **Tb.69.Na**.*

As expected, due to the pH dependence of **Tb.69.Na** within the physiological pH range and the resulting much lower emission response displayed, the Tb(III) emission intensities measured from the damaged regions of the bone samples immersed in 1 x 10^{-3} M solution of **Tb.69.Na** were significantly lower then those observed for **Eu.69.Na**. As shown in Figure 2.35b, although the general trend of emission enhancement as a function of immersion time was observed, the maximum intensity displayed after 24 h was 262 compared to 990 for the Eu(III) analogue. It is important to note that the concentration and spectroscopic parameters used were identical for **Eu.69.Na** and **Tb.69.Na**, so direct comparisons between both complexes could be made.

As anticipated, comparison of the phosphorescence spectra measured from the damaged region to those observed at the smooth undamaged surface showed much higher emission intensities for all time periods. However, as a result of the background emission from the bone sample itself which occurred between 400 nm and 600 nm, once the emission intensity decreased below 50, it was difficult to distinguish the Tb(III) emission bands of **Tb.69.Na**. This can be clearly seen in Figure 2.36a, where the $J = 5$ emission band at 546 nm, for the luminescence spectrum measured at the smooth surface after 24 h immersion, can only be slightly seen above the background noise from the bone sample. This made determination of the intensity enhancement within the scratched region much more difficult. From these spectra, a 4-fold enhancement in emission intensity was estimated, which is significantly lower then the 14-fold measured for **Eu.69.Na**. It is not known whether this difference in emission enhancement is as a direct result of the large background noise from the bone sample, making the estimated value for **Tb.69.Na** inaccurate or due its much poorer emission response at pH 7.4. A greater understanding in this emission enhancement variation observed for **Tb.69.Na** and **Eu.69.Na** will be gained through microscopy analysis using imaging techniques such as epifluorescence and confocal laser scanning microscopy (Chapter 3).

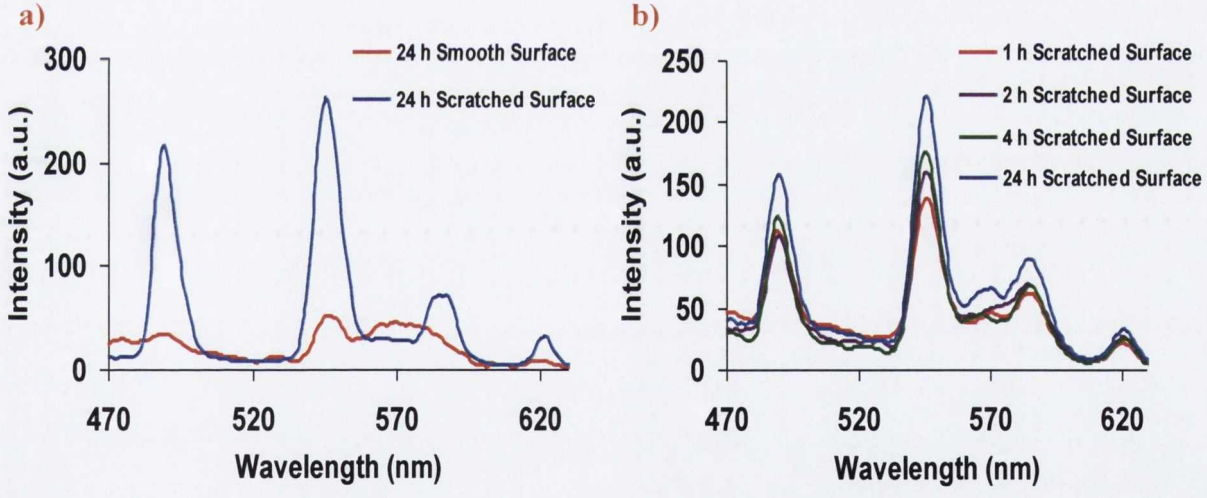

Figure 2.36: *a) The Tb(III) luminescence response of **Tb.69.Na** from the scratched and smooth surface of a bone sample after 24 h immersion. b) The Tb(III) luminescence response of **Tb.69** from the scratched region of a bone sample as a function of immersion time used.*

On analysis of **Tb.69**, initially it appeared that the emission intensities recorded were of the same magnitude to those seen using **Tb.69.Na**, suggesting that both Tb(III) complexes displayed similar selectivity for the damaged bone region. However, as previously discussed in Section 2.17, a 65% reduction in the emission response of **Tb.69.Na** at physiological pH was observed in comparison to its ester analogue. Therefore, taking this much more enhanced luminescence emission from **Tb.69** at pH 7.4 into consideration, it is possible that although

the emission intensities are comparable, more preferential chelation of **Tb.69.Na** could still be occurring. This was verified by analysis of the emission response as a function of immersion time, where **Tb.69** only displayed a small enhancement in its emission intensity over longer periods of time (Figure 2.36b). This implies that no significant chelation of the Ca^{2+} sites was occurring and the Tb(III) emission which was observed form **Tb.69** was possibly as a result of the complex lodging within the damaged structure. On further analysis of the emission enhancement between the 4 h and 24 h immersion times, **Tb.69** only displayed a 25% increase in luminescence response, compared to the 106% increase observed for **Tb.69.Na**.

In summary, it is evident from the above solid state bone measurements that increasing the number of iminodiacetate chelating units within the overall structure of these cyclen based Ln complexes had a marked effect on their preferential binding to the Ca^{2+} ions exposed upon damage generation. In comparison to **Tb.58.Na** which only displayed a 1.6-fold enhancement in emission intensity within the scratched region after 24 h, **Eu.69.Na** and **Tb.69.Na** demonstrated a 14-fold and 4-fold enhancement, respectively. As previously discussed, this much lower emission enhancement for **Tb.69.Na** compared to its Eu(III) analogue could be as a result of the Tb(III) complex displaying a much poorer response at physiological pH. It was also suggested that as a result of the extremely low emission intensity of **Tb.69.Na** from the smooth surface and therefore its overlap with the background noise from the bone sample itself, the intensity enhancement estimated could be slightly inaccurate. Analysis of **Eu.69**, the ester analogue of **Eu.69.Na**, verified the essential requirement of the iminodiacetate binding units, with much lower intensities within the scratched region being observed. It was also demonstrated that at longer periods of immersion time, the increase in the emission intensity was not as significant as that observed for **Eu.69.Na**, with only a 16% enhancement in the luminescence response between 4 h and 24 h being measured. In the case of **Tb.69**, similar emission intensities to those measured for **Tb.69.Na** were observed. However, taking the 65% reduction in the luminescence response of **Tb.69.Na** into consideration, it was concluded that although the emission intensities are comparable, the amount of **Tb.69** localised within the scratch is significantly lower. This was verified on analysis of the emission enhancement of **Tb.69** over time, were only a small increase in emission intensity at the scratched region was observed. The much poorer luminescence enhancement for both **Eu.69** and **Tb.69** at longer immersion times suggests that as a result of the iminodiacetate chelating units being protected as their ethyl ester forms, no significant interaction of the Ca^{2+} ions at the damaged sites was occurring.

2.20 Conclusion

Overall this chapter dealt with the design, synthesis and photophysical evaluation of novel cyclen based Ln complexes, where through the incorporation of the iminodiacetate chelating functionality, significant selectivity for damaged bone structure was displayed.

The first half of this chapter focused on the investigation of **Tb.58.Na**, whose ligand structure consisted of one iminodiacetate moiety directly attached to a phenyl antenna. Upon excitation at 285 nm, sufficient energy transfer from antenna's triplet excited state, to the excited states of Tb(III) ion and thus metal centred emission was observed. **Tb.58**, the ethyl ester analogue of **Tb.58.Na** was also studied. This complex was used as an experimental control with the principle aim of highlighting the essential requirements of the iminodiacetate functionality for more efficient microdamage bone detection. An extensive pH study was carried out for both complexes, where any changes in the ground state, singlet excited state and Tb(III) excited state properties as a function of pH were monitored. Overall the luminescence response of **Tb.58** and **Tb.58.Na** showed no significant modulation within the physiological pH range with any changes in emission intensity only being observed at the extreme ends of the pH scale. The Eu(III) analogue of **Tb.58.Na** was also synthesised, however, as a result of poor sensitisation *via* the phenyl chromophore, no further studies were carried out for this complex.

A series of metal ion studies were carried out for **Tb.58.Na**, where any changes in the Tb(III) emission were monitored as a function of metal ion concentration. No changes in the luminescence properties of the Tb(III) complex were displayed in the presence of the group II metal ions Ca^{2+} and Mg^{2+} and the transition metal ions Cd^{2+} and Zn^{2+}. However, due to the paramagnetic nature of Cu^{2+}, Hg^{2+}, Fe^{2+}, Co^{2+} and Ni^{2+} ions, binding of these metals within the iminodiacetate receptor unit resulted in a reduction in the Tb(III) emission intensity of **Tb.58.Na**. Hg^{2+} and Cu^{2+} displayed preferential binding, with a much stronger quenching response being observed in the presence of low concentrations of these ions.

Luminescent solid state bone studies were carried out for both complexes, where phosphorescence spectra were recorded from scratched and smooth surfaces of bovine bone specimens, which had been immersed in a 1×10^{-3} M aqueous solutions of each of the Tb(III) complexes over various periods of time. These studies confirmed the much higher selectivity of **Tb.58.Na** over the ethyl ester analogue **Tb.58** for the damaged bone regions, where a much larger enhancement in emission intensity at longer immersion times was observed for **Tb.58.Na**.

With the aim of improving selectivity for the damaged bone region, the second part of this chapter investigated the effect of increasing the number of iminodiacetate chelating units

on the binding ability of these cyclen based Ln complexes. A detailed description of the synthesis and subsequent characterisation of **Eu.69.Na** and **Tb.69.Na** as well as their ethyl ester analogues **Eu.69** and **Tb.69** was given. These complexes used a naphthalene antenna to allow for successful sensitisation of both the Eu(III) and Tb(III) metal ions and had three iminodiacetate chelating units attached to their cyclen framework. pH studies confirmed that all these complexes, except for **Tb.69.Na** displayed pH independent emission within the physiological pH window, with the Ln emission being completely "switched on". However, as a result of a shift in the pH range at which the secondary amide of **Tb.69.Na** became deprotonated, a 65% decrease in its emission intensity at pH 7.4, compared to **Tb.69** was observed.

Metal ion studies showed similar responses to those previously discussed for **Tb.58.Na**, where Ca^{2+}, Mg^{2+}, Zn^{2+} and Cd^{2+} ions caused no significant modulation in the luminescent properties of **Eu.69.Na** and **Tb.69.Na**. The remaining transition metal ions investigated displayed a significant reduction in the Ln emission intensity of both complexes, with Hg^{2+} and Cu^{2+} displaying the greatest response at low concentrations.

Using similar solid state measurements as those described for **Tb.58.Na**, a much stronger chelation effect of **Eu.69.Na** and **Tb.69.Na** for the damaged bone structure was observed. Not only were larger emission intensities within the scratched region recorded but the enhancements compared to the smooth undamaged surface were significantly higher. These studies helped verify that by increasing the number of microdamage specific iminodiacetate moieties within the complexes structure, more preferential localisation within the damaged bone regions can be attained. Analysis of **Eu.69** and **Tb.69** confirmed that no significant interaction of these complexes within the bone's structure would occur when the iminodiacetate functionalities are in their protected form.

In order to gain further insight in the potential of these cyclen based Ln complexes as luminescent imaging agents for microdamage detection and to highlight the more efficient contrast gained by incorporating more iminodiacetate moieties within the ligand structure, microscopy analysis using epifluorescence and confocal laser scanning microscopy were employed. The next chapter will discuss in detail the results and any conclusions which could be made from these imaging studies.

Chapter 3

Epifluorescence and Confocal Microscopy Analysis of Lanthanide Luminescent Bone Imaging Agents

3.1 Introduction

As previously discussed in Chapter 1, a large variety of techniques such as positron emission tomography, micro-computed tomography, nuclear magnetic resonance and high speed photography have been exploited for successful detection of microdamage accumulation in bone.[154-157] However, histology still remains one of the most popular methods for studying damaged bone structure, where microscopy analysis, in conjugation with a suitable contrast agent, can allow for the clear distinction of microcracks from the surrounding undamaged bone matrix.[129, 133, 146-148, 152]

Frost *et al.*[134] were the first to introduce the technique of bulk staining bone specimens in basic fuchsin dye, which along with transmitted light microscopy (TLM) proved successful in the detection of *in vivo* microdamage. Variations in light intensity, depth of focus and magnification were required to differentiate unstained or partially stained artifactual microdamage from those which were generated *in vivo*.[177, 178] This often difficult and time consuming technique for bone damage analysis led to Lee *et al.*[146] exploiting the diachrome nature of basic fuchsin by using both TLM and epifluorescence microscopy for *in vivo* microdamage detection. No differentiation between crack number, density or crack length was observed using both microscopy techniques, indicating comparable accuracy. However, one key advantage of epifluorescence was that upon excitation at 545 nm, a strong orange emission from those microcracks containing fuchsin was observed, with the remainder of the bone matrix appearing much darker. It was also shown that by using ultraviolet epifluorescence, only those microcracks which were fully stained displayed a strong purple emission, whereas all the partially stained microcracks failed to fluoresce and were therefore ruled out. This technique provided a rapid screening method for differentiating microcracks which were completely stained with fuchsin from partially or unstained artifactual bone damage. The success observed using epifluorescence microscopy analysis led to, as discussed in Chapter 1, the investigation of a wide variety of fluorochromic based agents, which due to the incorporation of the iminodiacetate chelating functionality, displayed high selectivity for damaged bone structure. Preferential localisation of these chelating agents at the microdamage regions was as a result of the iminodiacetate binding units displaying strong interaction with the Ca^{2+} ions exposed upon microdamage generation.[129, 130, 146, 152]

Another imaging technique which has gained a great deal of attention in recent years for more efficient microdamage detection is laser scanning confocal microscopy.[133, 179, 180] One major advantage over epifluorescence is that the laser light source can be tuned to the excitation and emission characteristics of the fluorescent dye and as a result improve the

signal-to-noise ratio by reducing the emission from the surrounding background biological tissue. Using this technique, Zioupos *et al.*[180] were able to identify microcracks labelled with fluoroscein, measuring them to an accuracy of *ca.* 10 μm and also correlate various microcrack parameters such as length and quantity with bone material properties like stiffness and strength. Another key advantage of using confocal microscopy is that the laser can be focused at a defined depth within the specimen and using its scanning mode, a thin optical section of the sample can be taken. Therefore by scanning at various depths through the entire bone section, a 3D image of the microcrack can be obtained. O'Brien *et al.*[133] performed this on fuchsin stained human rib sections and found that their elliptical microcrack 3D images were comparable to reconstructions from serial histological sections and theoretical predictions.

The aim of this chapter is to investigate the contrasting abilities of the cyclen based Ln imaging agents synthesised in Chapter 2, using epifluorescence and laser scanning confocal microscopy analysis. Although the solid state bone studies suggested that all complexes showed preferential localisation within the damaged bone regions, it was unknown whether sufficient contrast from the smooth undamaged bone surface would result. It was also necessary to investigate the effect of increasing the number of iminodiacetate binding units on the contrasting abilities of such Ln based complexes. This chapter will therefore discuss the results obtained using both microscopy techniques, highlighting the potential of these complexes as selective microdamage luminescent imaging agents. The general protocol of bone sample preparation required prior to microscopy analysis is given in Chapter 7 (Section 7.3).

3.2 Epifluorescence microscopy analysis of Tb.58.Na

The first luminescent imaging agent which was investigated for selective microdamage detection was **Tb.58.Na**. The solid state bone studies carried out for this complex confirmed its preferential localisation at sites of damaged bone structure, however, as its overall ligand design only allowed for the incorporation of one chelating iminodiacetate functionality, the emission enhancement of the microdamaged region compared to the smooth bone surface was relatively low. The first microscopy imaging technique used to investigate the ability of **Tb.58.Na** to selectively bind to the co-ordinatively unsaturated Ca^{2+} sites exposed upon scratch generation and thus provide a contrast from the remaining healthy outer bone surface was epifluorescence microscopy. A brief introduction into this useful imaging technique will be given prior to a discussion of the results obtained from the scratched bovine bone samples.

Fluorescence microscopy has become a fundamental imaging technique used in a wide spectrum of disciplines, ranging from identification of sub-microscopic cellular components in biology to diagnosis of tissue defects and disease progression in biomedical science.[181] Advances in this area of microscopy stems from a greater understanding of important cellular targets coupled with the rapid design and development of site specific targeting fluorochromes. Epifluorescence microscopy has the advantage of exciting the specimen at a desired wavelength and then through its optical composition separates the much weaker fluorescence emission from the original excitation light source.[182] The diagram shown below in Figure 3.1 illustrates the key components and overall principle behind this microscopy technique.

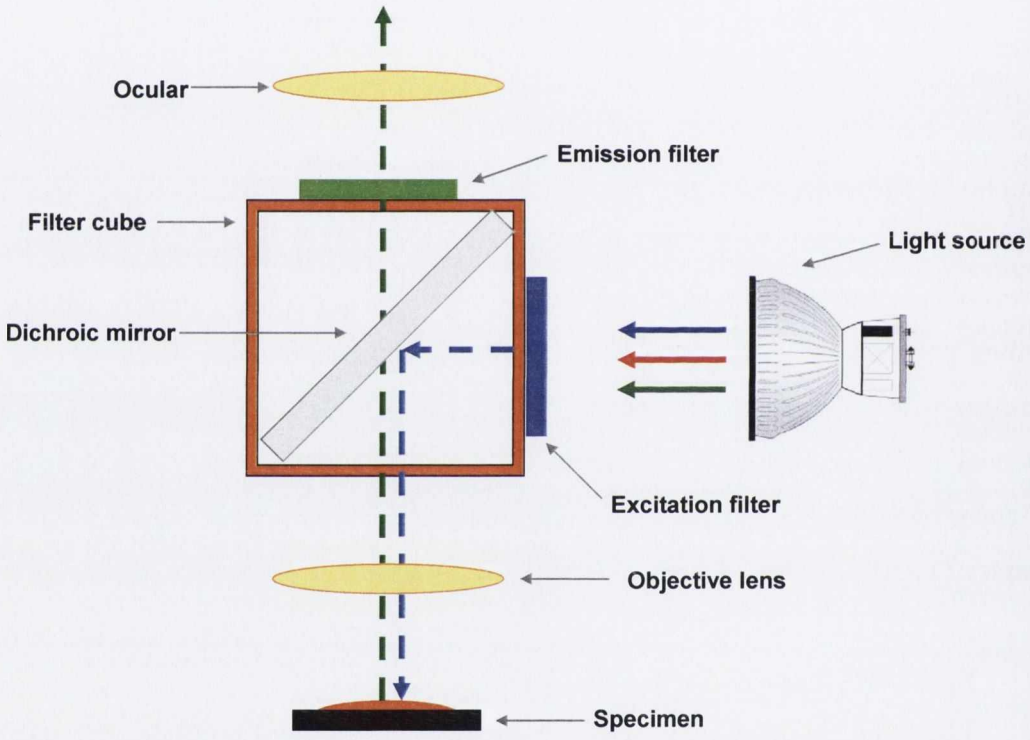

Figure 3.1: *Graphical representation of an epifluorescence microscope.*

The general theory associated with epifluorescence microscopy is that light generated by a mercury arc lamp is passed through an excitation filter allowing only light of a desired wavelength to reach and subsequently reflect off the dichroic mirror, through the objective lens to the specimen. Depending on the fluorescence ability of the specimen, any emitted light is collected and passed through an emission filter, which only allows light of a longer wavelength then the original excitation light pass through. As a result, only emitted light from the specimen will reach the detector, with any excitation light being blocked in the process. This has the advantage of providing a larger contrast between the emitting fluorescence component of the specimen and the remaining darker background. The

excitation filter, dichroic mirror and emission filter are all located within a single compartment called a fluorescence (filter) cube. Selection of an appropriate cube depends on the excitation and emission properties associated with the fluorochrome under investigation. The excitation and emission properties of the Nikon fluorescence cubes which were available for use are shown below in Figure 3.2.

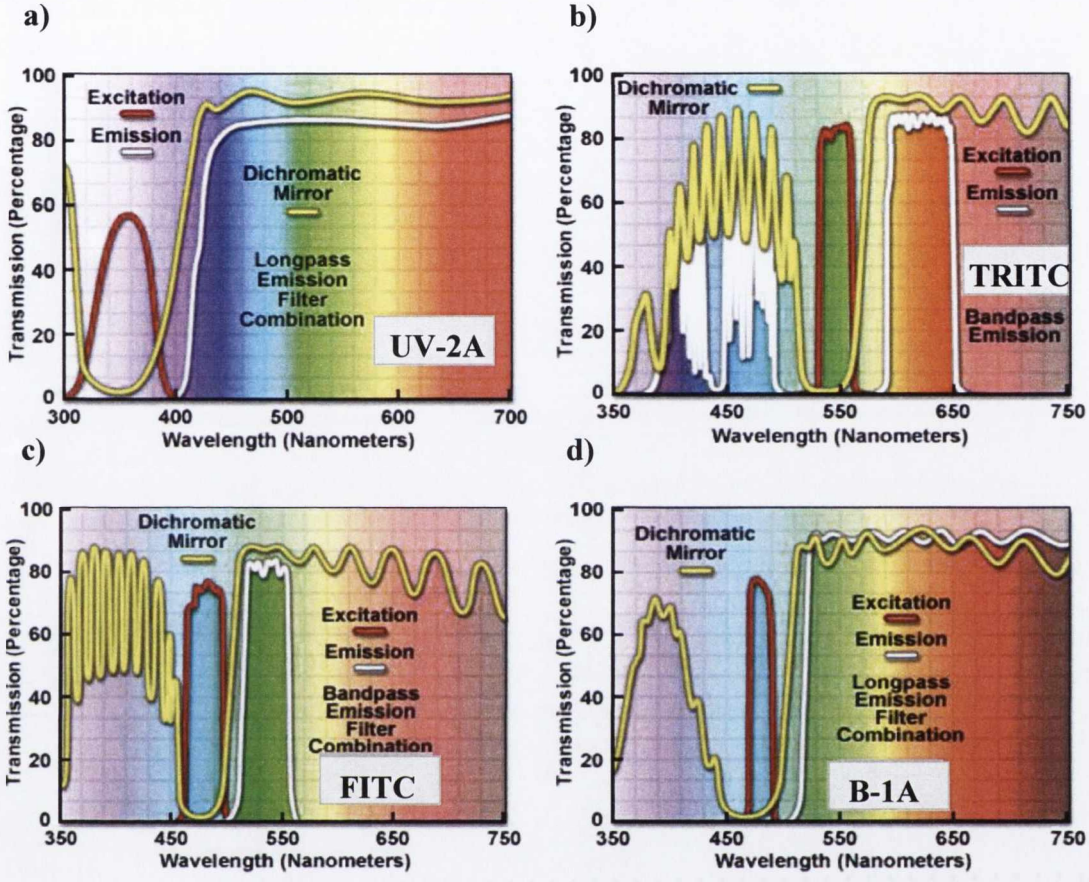

Figure 3.2: *Illustration of the excitation and emission filter combinations of the a) UV-longpass (UV-2A), b) green-bandpass (TRITC), c) blue-bandpass (FITC) and d) blue-longpass (B-1A) Nikon fluorescence cubes available for the epifluorescence microscopy analysis.*[181]

In order to use the appropriate fluorescence filter combination for the epifluorescence imaging of the scratched bone samples, it was necessary to review the photophysical properties of **Tb.58.Na**. With the broad π-π* absorption band of the ligand appearing between the spectral range 245 nm – 350 nm and the subsequent Tb(III) emission occurring between 450 nm – 650 nm, the fluorescence cube displaying the best fluorescence filter combination for **Tb.58.Na** was the UV-longpass (UV-2A). The design of this filter cube allows for UV excitation between the spectral range 330 nm – 380 nm and only collects signals at wavelengths exceeding 420 nm, enabling visualisation of red, green and blue light emission. However, as shown in Figure 3.3a, no significant contrast of the scratched bone region from the remaining undamaged bone surface could be observed even after 24 h

immersion in **Tb.58.Na**. To verify the presence of the scratch and ensure that the image was taken at the correct location, the microscope was switched to a polarised detection mode. As shown in Figure 3.3b, this technique provides an efficient method to visualise the scratched area, as depending on the direction of the bone fibres, various different colours were observed. This technique became the standard method throughout all these epifluorescence studies for accurately determining the exact location of the microscratches on the bone samples.

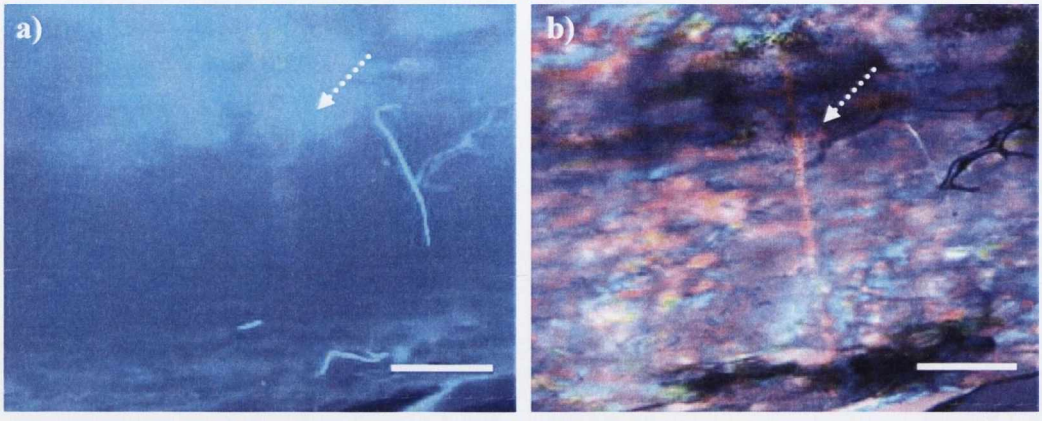

Figure 3.3: *Epifluorescence image of a) scratched bovine bone sample immersed in a 1 mM aqueous solution (20 mM HEPES, 135 mM KCl, pH 7.4) of* ***Tb.58.Na*** *for 24 h under vacuum, using the UV-longpass (UV-2A) filter cube. b) Scratched region using polarised light detection mode. (White arrows indicating scratch location) Scale bar = 500 μm.*

The above results suggest poor affinity of **Tb.58.Na** at the damaged bone regions, resulting in weak emission from the Tb(III) metal ion within the scratched areas. It is also possible due to the low excitation wavelength and large emission range of the filter cube used, that autofluorescence from the bone surface itself could be masking any emission from the Ln complex, making distinction of the scratched region extremely difficult. To investigate this, it was decided to analyse the bone samples using the green-bandpass (TRITC) and blue-bandpass (FITC) filter cubes, which only collect emission between 590 nm – 650 nm and 515 nm – 555 nm, respectively. It was anticipated that by using much shorter emission wavelength ranges, the autofluorescence from the bone surface may be minimised making the emission from the Ln complex much more distinguishable. However, the much higher excitation wavelengths of these fluorescent cubes (> 465 nm) could prove problematic. As shown in Figure 3.4a and Figure 3.4b, a very different result to that previously displayed using the UV-longpass filter cube was observed, were a slight emission increase within the scratched area could be seen for the 24 h time frame. To ensure this contrast enhancement was as a direct result of chelation of **Tb.58.Na** with the exposed Ca^{2+} ions, images of the control (0 h) scratches were taken (Figure 3.4c and Figure 3.4d). As

expected, in the absence of the contrast agent, detection of the scratched surfaces proved difficult, confirming that the emission observed from the scratched region was from localisation of **Tb.58.Na** at the damaged sites.

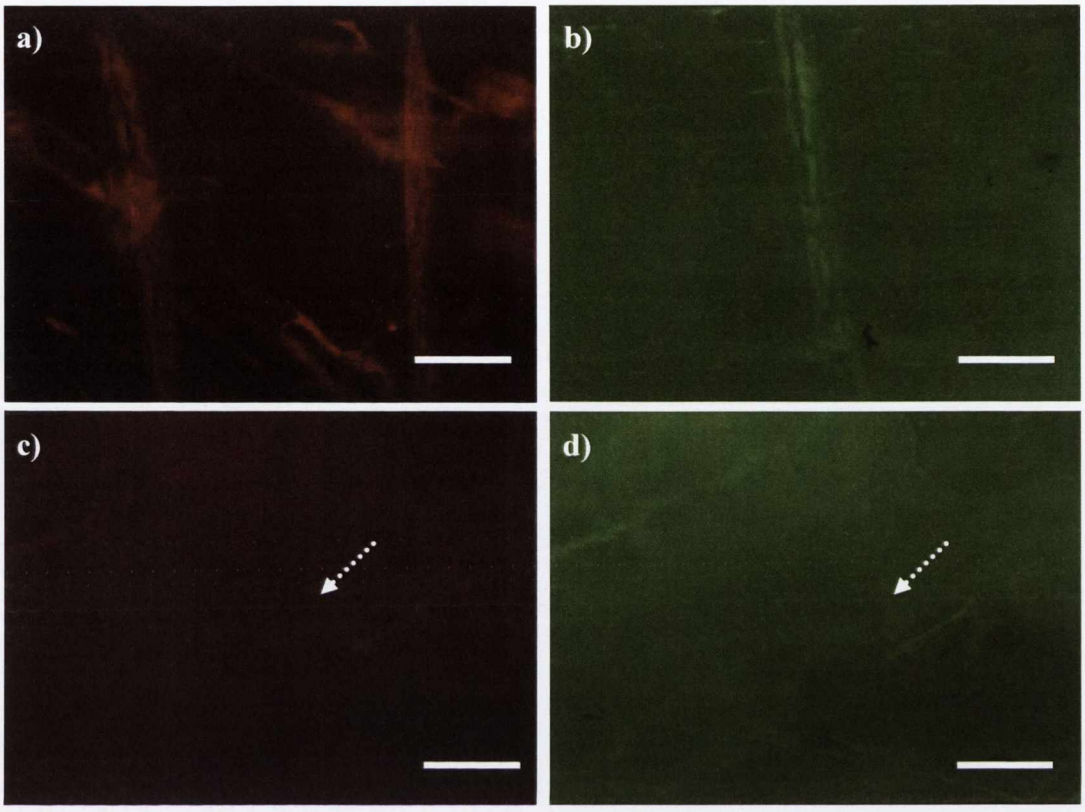

Figure 3.4: *Epifluorescence images of scratched bovine bone sample immersed in a 1 mM aqueous (20 mM HEPES, 135 mM KCl, pH 7.4) solution of* ***Tb.58.Na*** *for 24 h under vacuum, using a) the green-bandpass (TRITC), b) the blue-bandpass (FITC) filter cube. c,d) Epifluorescence images of control (0 h) scratched region. Scale bar = 500 μm.*

On comparison of the images obtained using both filter cubes, it is clear that a much poorer contrast of the scratched surface is observed for the blue-bandpass filter. As a result of its excitation parameters being at a slightly lower wavelength then the green bandpass filter and therefore within the spectral region for excitation of the collagen and other proteins within the bone structure, it is possible that the Tb(III) emission of **Tb.58.Na** is being masked slightly by autofluorescence from the bone. This was not the case for the green-bandpass fluorescence cube, as its excitation parameters are at a much longer wavelength, were interference of these bone proteins is minimised. Another interesting observation from these studies is that although **Tb.58.Na** has a UV-vis absorption band with a λ_{max} at 285 nm, when complexed to the bone at high concentration, Tb(III) emission was observed using excitation wavelengths greater than 465 nm.

In summary, epifluorescence analysis confirmed the ability of **Tb.58.Na** to display some form of preferential chelation within the scratched bone regions. UV-longpass analysis proved to no avail as the much stronger autofluorescence from the bone sample made visualisation of the Tb(III) emission extremely difficult. The higher excitation green and blue-bandpass filter cubes were therefore required to demonstrate the contrasting abilities of **Tb.58.Na**. Although Tb(III) emission from the scratched region was observed, the intensity enhancement in comparison to the smooth surface was still relatively weak after 24 h immersion, suggesting poor affinity of the contrast agent to the scratched regions. To eliminate the possibility of this weak emission response being as a result of poor excitation of the Tb(III) metal ion, confocal microscopy analysis, which uses the much more powerful laser excitation source, of the bone specimens were carried out. The following section will detail the results obtained using this imaging technique.

3.3 Laser scanning confocal microscopy analysis of Tb.58.Na

Using a similar staining method to that described in Chapter 7, Section 7.3, three scratches were made on the surface of the bovine bone specimens, each immersed in a 1 mM aqueous solution of **Tb.58.Na** for various periods of time (0 h, 4 h and 24 h). It was anticipated that if insufficient excitation was the principle cause for the poor contrasting abilities observed for the epifluorescence analysis of **Tb.58.Na**, the higher energy laser excitation source of the confocal microscope should allow for more efficient excitation of the Tb(III) complex and thus result in a much larger emission enhancement within the damaged bone structure. Also, the added advantage of being able to tune the emission wavelengths to match those observed for the Tb(III) ion would help minimise any autofluorescence from the bone sample. As shown by the reflectance image in Figure 3.5a, confocal microscopy is a much more efficient method for microdamage detection, where the microscratch can be clearly distinguished from the remaining undamaged smooth surface. Upon excitation at 458 nm, using a krypton/argon mixed gas laser, significant Tb(III) emission was observed within the scratched bone region. It is clear from the images shown in Figure 3.5c and Figure 3.5d, a more efficient contrast of the damaged bone surface occurred at longer immersion times. Similar to that carried out for the epifluorescence studies, to ensure that the observed contrast was as a direct result of Tb(III) emission, an image of the control scratch was obtained, where as shown in Figure 3.5b, no emission enhancement within the scratch resulted.

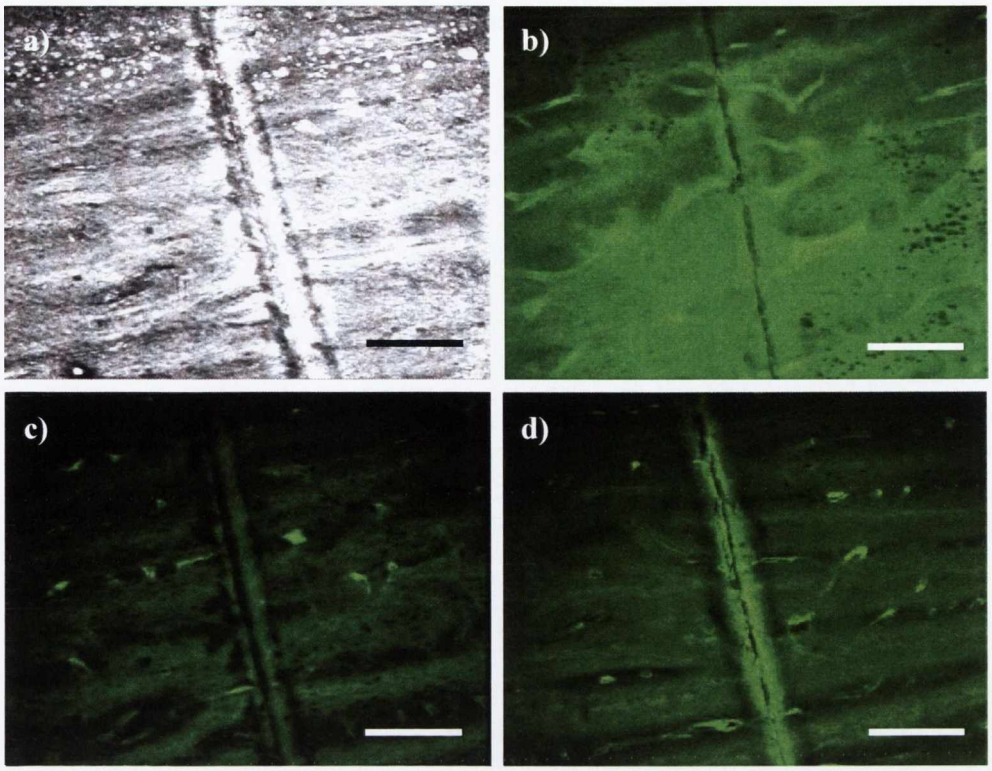

Figure 3.5: *Confocal laser scanning microscopy images of bone sample immersed in a 1 mM solution of* ***Tb.58.Na*** *(20 mM HEPES, 135 mM KCl, pH 7.4) under vacuum (λ_{ex} = 458 nm); a) Reflected light image (4 h), b) control (0 h), c) 4 h, d) 24 h. Scale bar = 300 μm.*

On comparison of the emission intensities within the scratched regions to those measured at the smooth undamaged bone surface, a 1.4-fold intensity enhancement was observed after 4 h immersion, with a slightly larger 2.8-fold enhancement occurring after 24 h. It is important to note that in order to ensure accurate intensity enhancement measurements, the intensities of several areas inside and outside the scratches were measured, with the average of these values represented by the bar charts in Figure 3.6. Although confocal microscopy analysis of the bone samples immersed in **Tb.58.Na** showed a better contrast then that observed using epifluorescence analysis, an overall intensity enhancement of 2.8 after 24 h immersion still suggests poor affinity of this Tb(III) complex at the damaged bone regions.

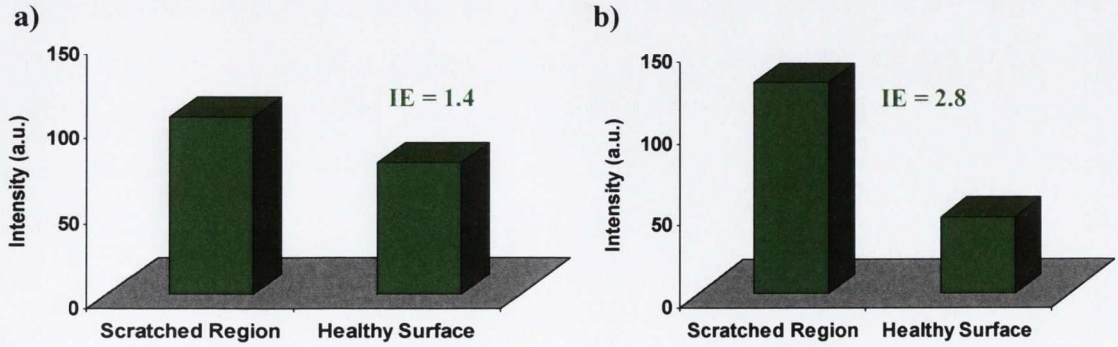

Figure 3.6: *Emission intensity enhancement between the scratched region and the outer healthy bone surface after a) 4 h b) 24 h immersion in a 1 mM aqueous solution of* ***Tb.58.Na****.*

As was the case for the solid state bone measurements, confocal microscopy analysis of **Tb.58**, the ester analogue of **Tb.58.Na**, confirmed the essential requirement of the iminodiacetate binding unit for preferential localisation within damaged bone structure. As shown by the images in Figure 3.7, almost no Tb(III) emission enhancement was observed within the scratched region after 4 h, whereas an intensity enhancement of only 1.4 was measured after 24 h immersion.

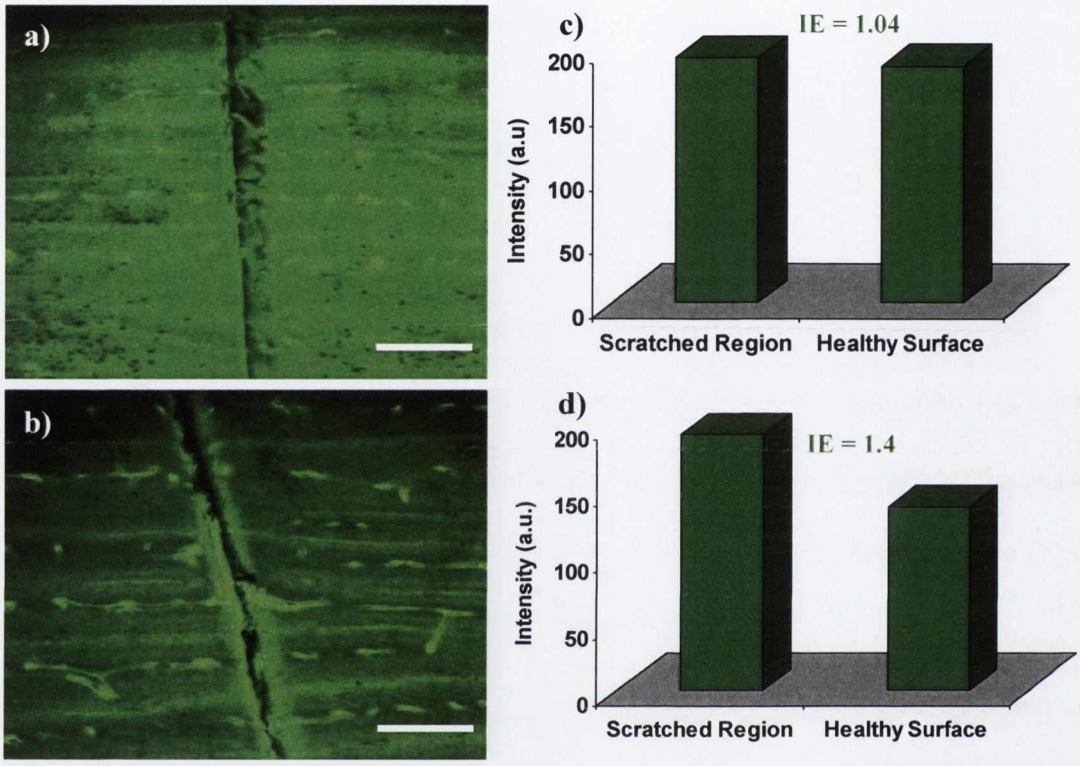

Figure 3.7: *Confocal laser scanning microscopy images of bone sample immersed in a 1 mM solution of* ***Tb.58*** *(20 mM HEPES, 135 mM KCl, pH 7.4) under vacuum (λ_{ex} = 458 nm); a) 4 h, b) 24 h. Scale bar = 300 μm. Emission intensity enhancement between the scratched region and the outer healthy bone surface after c) 4 h and d) 24 h immersion.*

This relatively low Tb(III) emission observed for **Tb.58**, confirms, as previously discussed in Chapter 2, that in the absence of the iminodiacetate binding unit, the complexes show no interaction within the damaged region and any weak emission observed was possibly as a result of the complex lodging within the damaged bone structure. However, these studies also verify the extremely poor affinity of **Tb.58.Na** for the scratched regions, as if strong binding of the Ca^{2+} ions at the damaged bone sites had occurred, a much larger enhancement compared to the control complex **Tb.58** would have been observed.

Overall, both microscopy techniques proved successful in demonstrating the poor binding affinity of **Tb.58.Na** for Ca^{2+} ions at damaged bone regions. Although larger Tb(III) emission intensities were observed from the scratched surfaces for all time frames studied,

the enhancement in comparison to the healthy undamaged bone matrix was still relatively low. As discussed in Chapter 2, in order to improve the binding abilities of these Ln based agents and thus provide a much stronger contrast of the scratched bone area, **Tb.69.Na** and **Eu.69.Na** were designed. These Ln complexes allowed for the incorporation of three iminodiacetate receptor moieties within their ligand structures and used a naphthalene antenna for sensitisation of the Ln ions. The solid state bone studies carried out for these complexes, especially for **Eu.69.Na** suggests much stronger chelation of these agents within damaged bone structure and therefore should provide an efficient contrast from the undamaged bone matrix. Similar epifluorescence studies to those described for **Tb.58.Na** were carried out using both **Eu.69.Na** and **Tb.69.Na**, the results of which are discussed in the following section.

3.4 Epifluorescence microscopy analysis of Eu.69.Na and Tb.69.Na

Similar to that previously discussed for **Tb.58.Na**, as both these complexes display a π-π^* absorption band with a λ_{max} at 282 nm, it was anticipated that by using the UV-longpass excitation filter cube, sufficient excitation of the naphthalene antenna and thus subsequent strong Ln emission should be observed. However, it was unknown whether the Ln emission from these agents would, as was the case for **Tb.58.Na**, be over shadowed by the strong autofluorescence from the bone structure.

Overall, both the 4 h and 24 h immersion scratches displayed strong emission intensities as a result of selective chelation of both **Eu.69.Na** and **Tb.69.Na** within the damaged bone structure. As shown by the images in Figure 3.8, as a result of the Ln emission from both complexes, successful identification of the microscratched region from the remaining healthy surface was achieved. It was also clear from these images, that the emission observed from the scratched area was significantly greater for **Eu.69.Na**, than **Tb.69.Na**. This verifies what was previous seen for the solid state bone studies of both these complexes, where **Eu.69.Na** displayed a much larger emission enhancement at the damaged bone surface (Chapter 2, Section 2.19). A possible reason for this poorer contrast ability is the fact that the luminescence response of **Tb.69.Na** is pH dependent and its emission intensity dramatically reduced at pH 7.4 (Chapter 2, Section 2.17). Therefore, although **Tb.69.Na** may be showing successful chelation within the scratch, the much weaker Tb(III) emission could be the result of masking by autofluorescence from the bone surface.

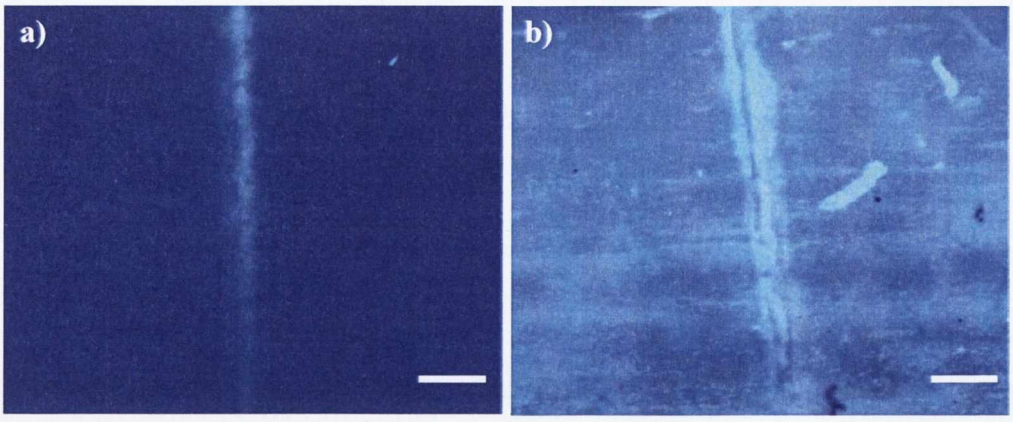

Figure 3.8: *Epifluorescence images of scratched bovine bone sample immersed in a 1 mM aqueous solution (20 mM HEPES, 135 mM KCl, pH 7.4) of a)* ***Eu.69.Na*** *and b)* ***Tb.69.Na*** *for 24 h under vacuum, using the UV-longpass (UV-2A) filter cube. Scale bar = 225 μm.*

As expected, when the green and blue-bandpass fluorescence cubes were used a much more efficient contrast of the scratched regions, than that seen for **Tb.58.Na**, was observed for both **Eu.69.Na** and **Tb.69.Na**. As demonstrated by the images shown in Figure 3.9, the strong Ln emission could now be clearly seen at the damaged sites, with the background undamaged bone matrix appearing much darker. The slightly poorer emission intensity from **Tb.69.Na** compared to that of **Eu.69.Na** was also observed in these images.

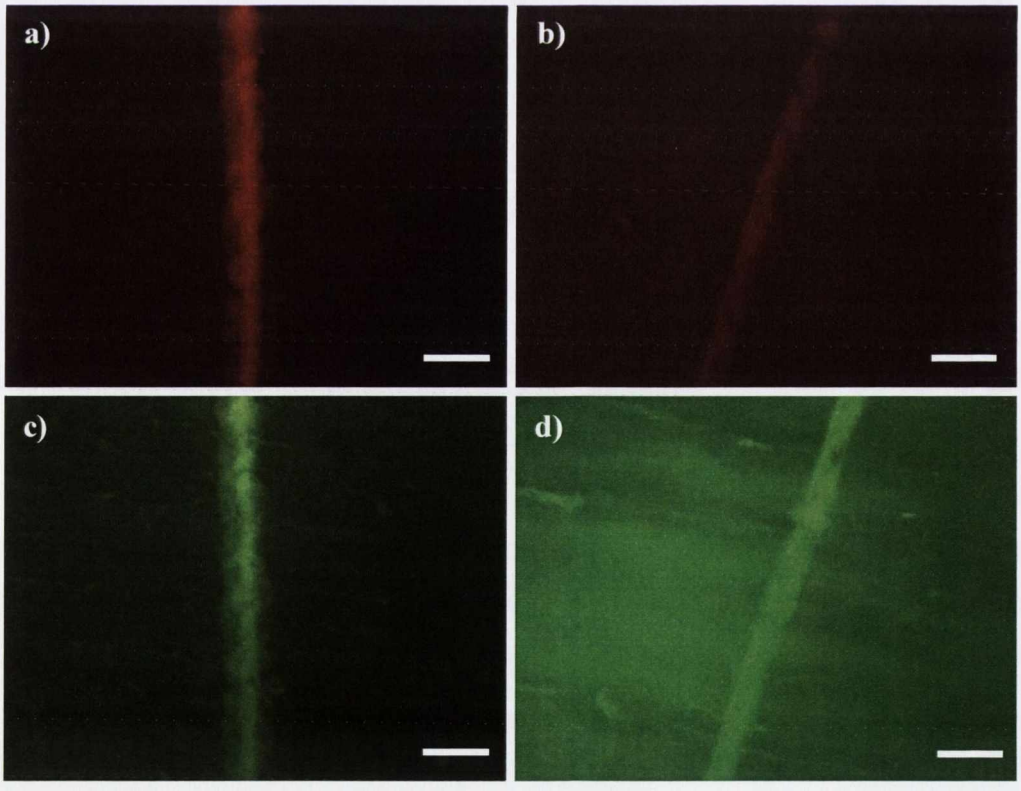

Figure 3.9: *Epifluorescence images of scratched bovine bone samples immersed in a 1 mM aqueous solution (20 mM HEPES, 135 mM KCl, pH 7.4) of a)* ***Eu.69.Na*** *and b)* ***Tb.69.Na****, using the green-bandpass (TRITC) filter cube; c)* ***Eu.69.Na*** *and d)* ***Tb.69.Na****, using the blue-bandpass (FITC) filter cube for 24 h under vacuum. Scale bar = 225 μm.*

Further evidence that increasing the number of iminodiacetate receptor units resulted in much stronger chelation at damaged bone structure was gained from the bright field images of the scratched regions immersed in **Eu.69.Na** and **Tb.69.Na** for 24 h. As shown in Figure 3.10, using bright field microscopy alone, the microscratched surfaces were easily recognisable due to the presence of a strong orange colour, with the remainder of the undamaged bone matrix appearing much darker. These results suggest that even in the absence of the filter cubes and therefore using white light alone, both **Eu.69.Na** and **Tb.69.Na** were capable of providing a significant contrast of the scratched areas, highlighting their binding affinities to the exposed Ca^{2+} ions.

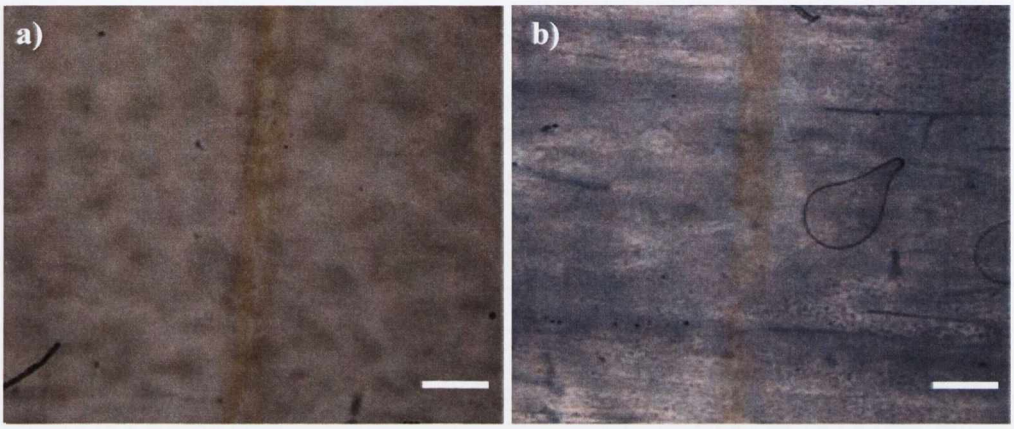

Figure 3.10: *Bright field images of scratched bovine bone samples immersed in a 1 mM aqueous solution (20 mM HEPES, 135 mM KCl, pH 7.4) of a)* ***Eu.69.Na*** *and b)* ***Tb.69.Na*** *for 24 h under vacuum. Scale bar = 225 μm.*

Similar to that seen for **Tb.58.Na**, although the UV-vis absorbance λ_{max} of **Eu.69.Na** and **Tb.69.Na** appears at 282 nm, when the blue and green-bandpass filters which employ a much higher excitation wavelength were used, strong Ln emission was observed from both complexes. This suggests that sufficient population of the Ln excited states was possible using excitation wavelengths of 465 nm and greater. To help explain this, a UV-vis absorption spectrum of the 1 mM aqueous solution of both complexes was recorded. As expected due to the extremely high concentration used, saturation of the λ_{max} occurred, however, both spectra clearly demonstrated that the tail of the absorbance band extended out as far as 550 nm. This suggests that at extremely high concentrations of these complexes, excitation at much longer wavelengths is possible. This was verified by measuring the luminescence response of the 1 mM aqueous solution of **Eu.69.Na**, using much higher excitation wavelengths. As shown in Figure 3.11, with the PMT detector at the maximum and the emission and excitation slits fully open, Eu(III) emission was clearly observed upon excitation at 450, 480, 510 and 530 nm. The spectra appear extremely noisy with the characteristic emission bands poorly defined as a result of the spectroscopic parameters used.

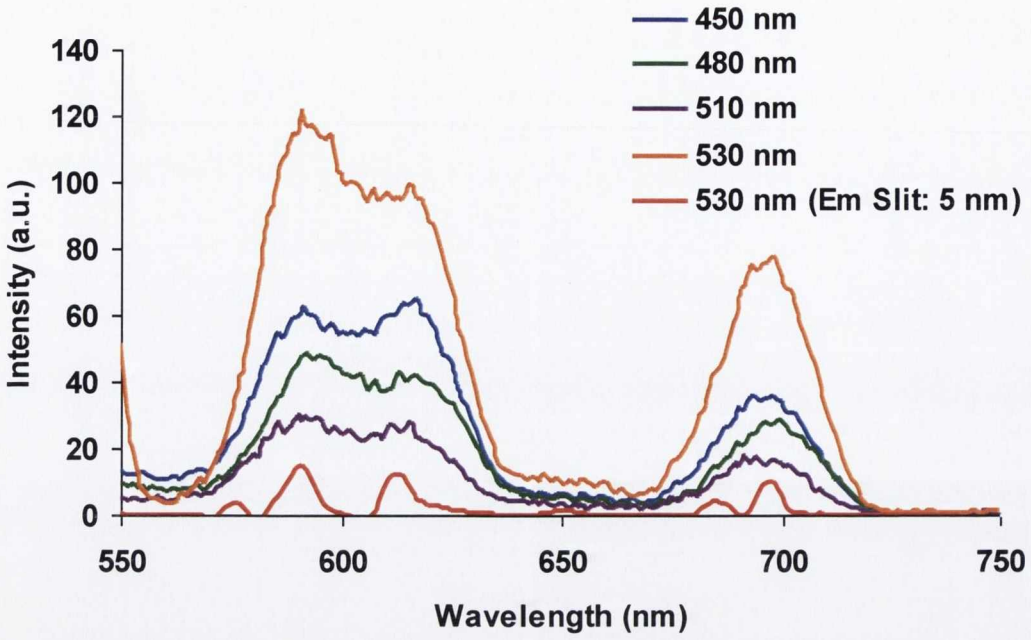

Figure 3.11: *Lanthanide luminescent spectra of a 1 mM aqueous solution (20 mM HEPES, 135 mM KCl, pH 7.4) of* ***Eu.69.Na****, using excitation wavelengths of 450, 480, 510 and 530 nm. Ex Slit: 20, Em Slit: 20, PMT: 900 V.*

Similar epifluorescence studies were carried out for **Eu.69** and **Tb.69**, the ester analogues of **Eu.69.Na** and **Tb.69.Na**. As anticipated, these complexes displayed much poorer contrasting abilities of the scratched surfaces as a result of their chelating iminodiacetate functionalities being in their protected form. As shown in Figure 3.12, using the UV-longpass filter cube, due to the poor binding affinities of these complexes and thus the weaker Ln emission observed, identification of the scratched region from the remaining undamaged bone matrix proved difficult. Comparable results were observed using the blue and green bandpass filters, where the Ln emission from both complexes was much weaker suggesting poor interaction of **Eu.69** and **Tb.69** with the Ca^{2+} ions (Figure 3.13).

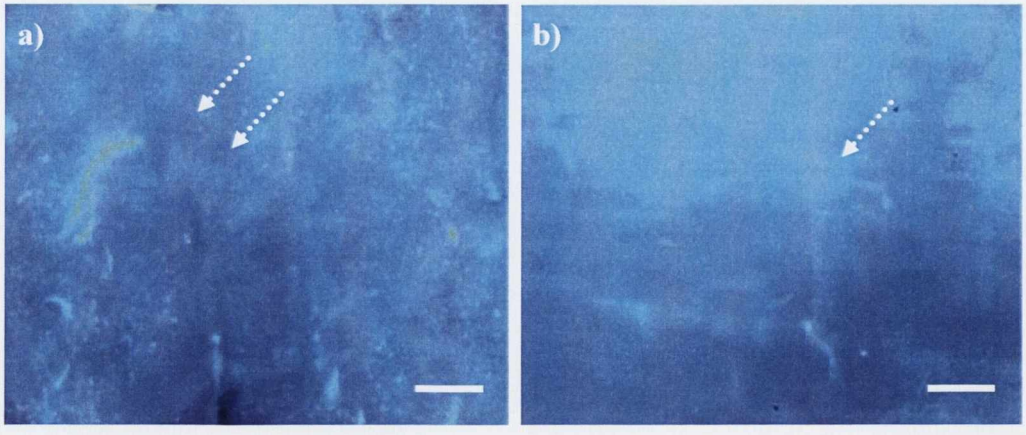

Figure 3.12: *Epifluorescence image of a scratched bovine bone sample immersed in a 1 mM aqueous solution (20 mM HEPES, 135 mM KCl, pH 7.4) of a)* ***Eu.69*** *and b)* ***Tb.69*** *for 24 h under vacuum, using the UV-long pass (UV-2A) filter cube. Scale bar = 225 μm.*

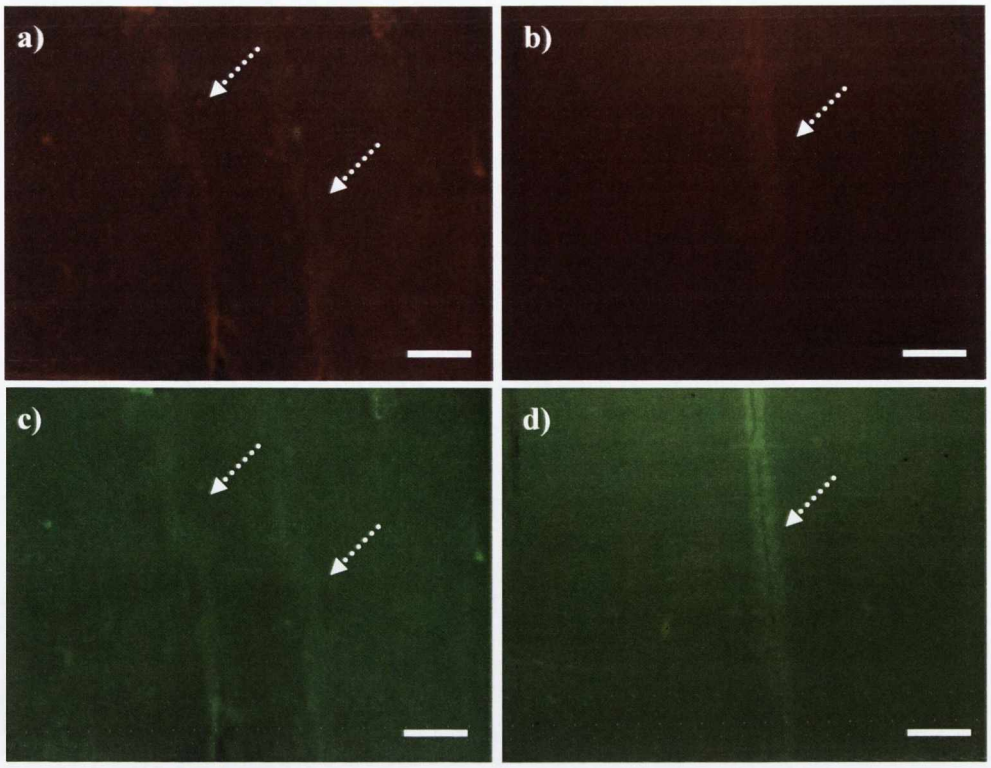

Figure 3.13: *Epifluorescence images of scratched bovine bone samples immersed in a 1 mM aqueous solution (20 mM HEPES, 135 mM KCl, pH 7.4) of a)* ***Eu.69*** *and b)* ***Tb.69****, using the green-bandpass (TRITC) filter cube and c)* ***Eu.69*** *and d)* ***Tb.69****, using the blue-bandpass (FITC) filter cube for 24 h under vacuum. Scale bar = 225 μm.*

In summary, the above epifluorescence microscopy studies of both **Eu.69.Na** and **Tb.69.Na** confirmed that both complexes displayed significant chelation at the microscratched regions and as a result provided a considerable contrast from the remaining undamaged bone matrix. The results also verified that by increasing the number of iminodiacetate receptor units within these Ln based complexes, a much stronger emission enhancement of damaged bone structure can be attained. With greater success observed for both **Eu.69.Na** and **Tb.69.Na** using epifluorescence imaging, it was anticipated that a much stronger contrast of the microscratched surfaces could be achieved using laser scanning confocal microscopy. The following section will therefore discuss the results obtained using this imaging technique.

3.5 Laser scanning confocal microscopy analysis of Eu.69.Na and Tb.69.Na

Confocal microscopy analysis of the scratched bone specimens which were immersed in a 1 mM aqueous solution of either **Eu.69.Na** or **Tb.69.Na** confirmed the epifluorescence results which were previously discussed. As displayed in Figure 3.14, strong Eu(III) emission was measured from the bone samples which were exposed to **Eu.69.Na**, with a large intensity enhancement being observed between the 4 h and 24 h immersion times. As

expected, due to preferential localisation of the Eu(III) complex within the damaged bone regions, much stronger emission responses from the microscratched areas occurred.

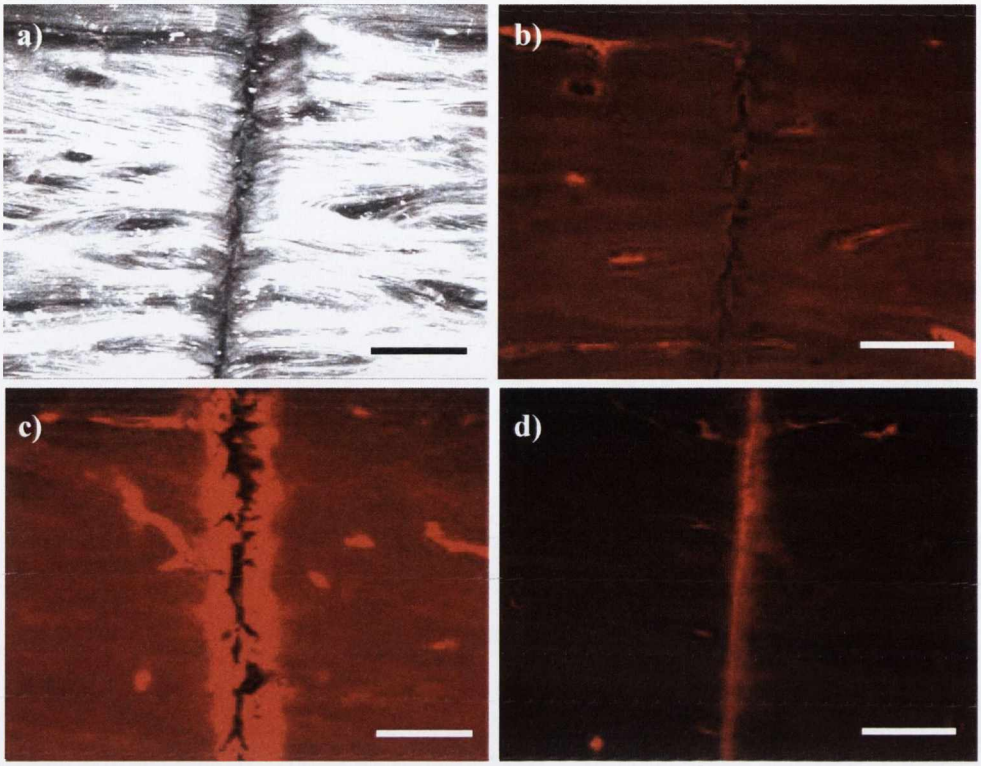

Figure 3.14: *Confocal laser scanning microscopy images of bone sample immersed in a 1 mM aqueous solution of* ***Eu.69.Na*** *(20 mM HEPES, 135 mM KCl, pH 7.4) under vacuum (λ_{ex} = 458 nm); (a) Reflected light image (0 h), (b) control (0 h), (c) 4 h, (d) 24 h. Scale bar = 150 μm.*

By measuring the emission intensities of several areas inside and outside the scratched regions, an intensity enhancement of *ca.* 2 was calculated for the 4 h immersion time. However, with **Eu.69.Na** displaying stronger Ca^{2+} chelation over longer periods of time, after 24 h a 28-fold emission enhancement within the microscratched area was observed (Figure 3.15). This significant increase in emission intensity explains the much darker bone background displayed in the 24 h confocal image.

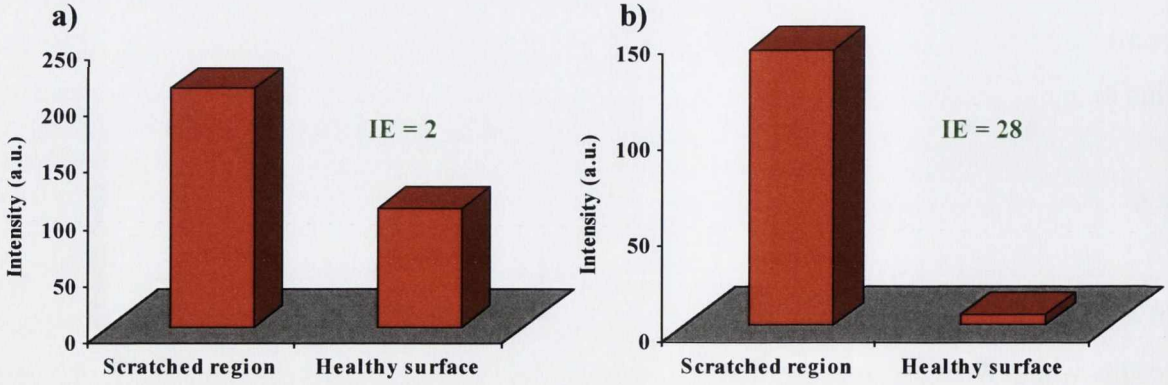

Figure 3.15: *Emission intensity enhancement between the scratched region and the outer healthy bone surface after a) 4 h and b) 24 h immersion in a 1 mM aqueous solution of* ***Eu.69.Na****.*

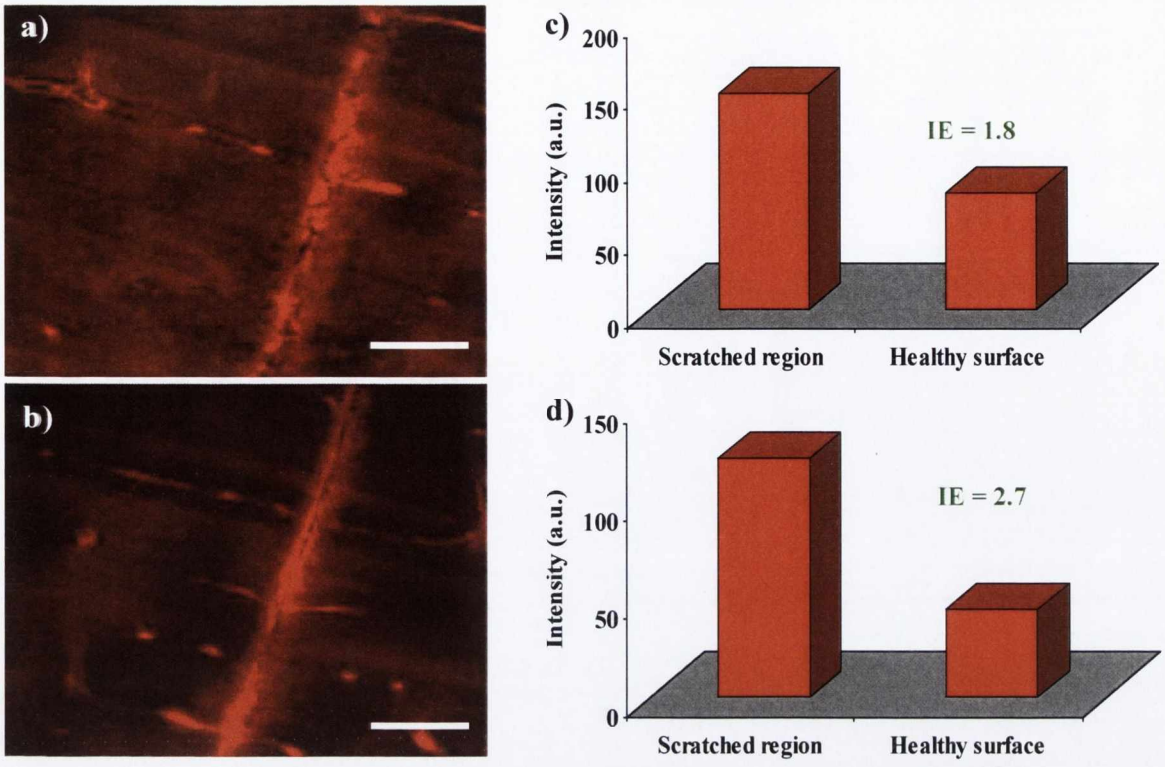

Figure 3.16: *Confocal laser scanning microscopy images of bone sample immersed in a 1 mM solution of* **Eu.69** *(20 mM HEPES, 135 mM KCl, pH 7.4) under vacuum (λ_{ex} = 458 nm); a) 4 h, b) 24 h. Scale bar = 150 μm. Emission intensity enhancement within the scratched region after c) 4 h and d) 24 h immersion.*

The ability of the ester Eu(III) complex, **Eu.69** to selectively bind within the scratched regions of the bone surface was also investigated (Figure 3.16). As expected, the confocal microscopy images confirmed that this complex had a much poorer contrasting ability, with an intensity enhancement of *ca.* 2.7 being obtained after 24 h immersion. It was also observed as shown by the bar charts in Figure 3.16 that there was very little difference in the emission intensities between the 4 h and 24 h immersion times.

As expected, due to the pH dependence of **Tb.69.Na** within the physiological pH range and the resulting much lower emission response displayed for this complex, the Tb(III) emission intensities observed within the scratched bone region were not as intense as those previously shown for the Eu(III) analogue (Figure 3.17). It was also observed that although the contrasting abilities of **Tb.69.Na** increased with longer immersion times, the overall intensity enhancement measured after 24 h was 8. This value is significantly lower then the 28-fold enhancement observed for **Eu.69.Na**. However, although the intensity enhancement for **Tb.69.Na** was much lower, the complex was still capable of providing a significant contrast, allowing clear visualisation of the microscratched regions.

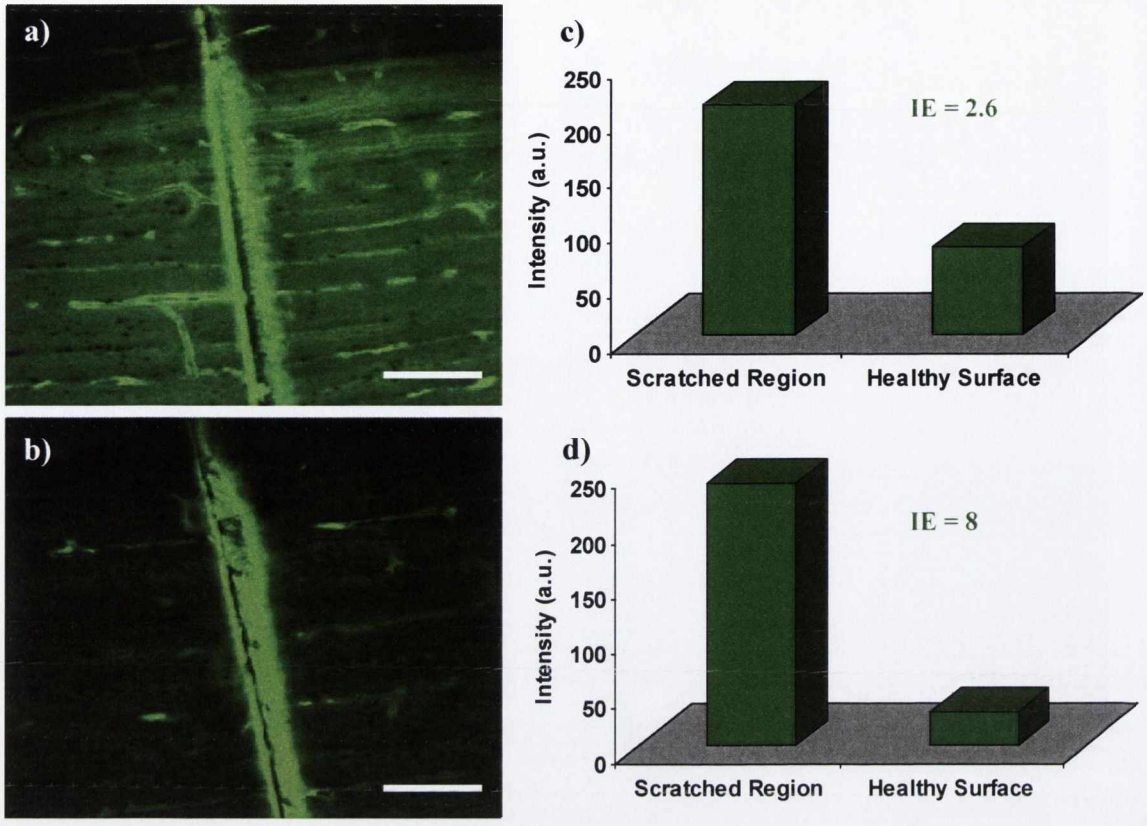

Figure 3.17: *Confocal laser scanning microscopy images of bone sample immersed in a 1 mM solution of* ***Tb.69.Na*** *(20 mM HEPES, 135 mM KCl, pH 7.4) under vacuum (λ_{ex} = 458 nm); a) 4 h, b) 24 h. Scale bar = 300 μm. Emission intensity enhancement within the scratched region after c) 4 h and d) 24 h immersion.*

As shown in Figure 3.18, on analysis of the ester analogue **Tb.69**, Tb(III) emission was clearly observed within the scratched region with an intensity enhancement of *ca.* 3 after 24 h immersion, compared to the 8-fold enhancement measured using **Tb.69.Na**. The difference between these emission enhancements is not as significant as that seen for the Eu(III) analogues, however, the results do confirm what was previously observed in the epifluorescence studies, with more efficient contrast being achieved with **Tb.69.Na**. It is also important to take into account the 65% reduction in the luminescence response of **Tb.69.Na** in comparison to its ester analogue. Therefore, although **Tb.69.Na** is possibly showing much more chelation at the damaged site then **Tb.69**, due to its reduced emission intensity, conclusion of this from the confocal images is difficult. However, with much less variation in the emission intensities between the 4 h and 24 h immersion times then that observed for **Tb.69.Na**, it is clear that very little if any chelation with the Ca^{2+} is occurring for **Tb.69**.

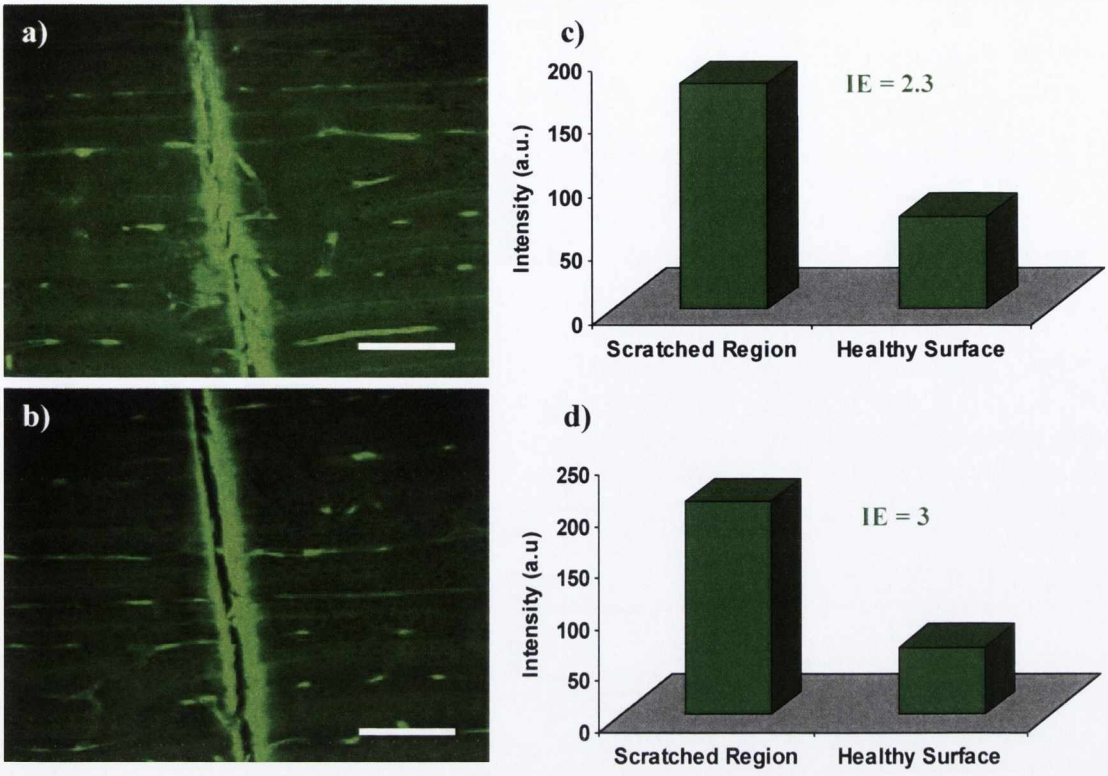

Figure 3.18: *Confocal laser-scanning microscopy images of bone sample immersed in a 1 mM solution of* **Tb.69** *(20 mM HEPES, 135 mM KCl, pH 7.4) under vacuum (λ_{ex} = 458 nm); a) 4 h, b) 24 h. Scale bar = 300 μm. Emission intensity enhancement within the scratched region after c) 4 h and d) 24 h immersion.*

In summary, the above confocal microscopy results confirmed preferential localisation of both **Eu.69.Na** and **Tb.69.Na** at the microscratched regions, which upon laser excitation, a significant contrast from the remaining undamaged bone matrix was achieved. On comparison of both these Ln agents, **Eu.69.Na** displayed a much stronger emission response within the damaged bone structure with an overall intensity enhancement of 28 after 24 h immersion. As a result of the luminescence dependence of **Tb.69.Na** at physiological pH, the emission intensity measured at the scratched surface was slightly weaker, with an 8-fold emission enhancement being calculated. Analysis of the ethyl ester analogues **Eu.69** and **Tb.69** confirmed what was previously seen for **Tb.58**, with these complexes displaying much poorer contrasting abilities of the microscratched regions. The variation in the intensity enhancements measured for the 24 h immersion times for **Tb.69** and **Tb.69.Na** was not as significant as that observed for the Eu(III) analogues. However, as **Tb.69.Na** displays a 65% reduction in its luminescence response in comparison to **Tb.69**, although it may be showing more preferential localisation within the scratch, conclusion of this from the confocal images may be difficult.

Overall, confocal microscopy analysis resulted in a more significant contrast of the scratched bone regions then that seen using epifluorescence microscopy. Possible reasons for

this include the stronger laser excitation source, minimisation of the autofluorescence by tuning the emission parameters to match those characteristic for the Ln ion under study and finally as confocal microscopy has the advantage of visualising a very thin plane of the bone specimen, higher spatial resolution of the image can be achieved as a result of suppression of the out-of-focus areas of the section.

With **Eu.69.Na** displaying the most significant contrast of the microscratched areas and therefore the greatest potential as a luminescent microdamage imaging agent, all further microscopy analysis was carried out solely on this complex. As described above, all studies so far involved using a 1 mM concentration of the chelating agent, with no time frame below 4 h being investigated. Therefore, it was critical to explore a minimal time period and concentration which could be used, where visualisation of the scratched bone surface was still possible. However, before investigation of possible limits of detection (LOD) for **Eu.69.Na**, it was necessary to optimise the scratching procedure previously employed. The effect of factors such as thickness of bone sample, depth of scratch induced and the use of vacuum or no vacuum on the contrasting abilities of **Eu.69.Na** needed to be investigated. Once a greater understanding of these possible inhibitory factors was gained, more accurate LOD for this contrast agent could be achieved.

3.6 Optimisation of scratching and staining technique

As previously mentioned, factors such as scratch depth, bone thickness and the presence of vacuum or no vacuum could play a significant role in the ability of **Eu.69.Na** to display a strong emission contrast of the microscratched regions. For all the results previously discussed, these parameters were kept constant to allow a direct comparison between all the Ln contrast agents studied. However, to gain a more in depth understanding of the contrasting abilities of **Eu.69.Na**, it was necessary to investigate any significant variations in emission response as these parameters were changed. The first factor which was investigated was the depth of the scratch. Depending on the pressure which was placed on the surgical scalpel, scratches of various depths could be induced on the bone surfaces. It was anticipated that as scratch depth is directly related to Ca^{2+} ion exposure, it was possible that upon immersion in 1 mM **Eu.69.Na** for 24 h, more preferential and stronger chelation would occur at the deeper scratches. Using the UV-longpass epifluorescence filter this assumption was verified, were as shown in Figure 3.19a, the more shallow scratches displayed weaker Eu(III) emission response and were therefore difficult to distinguish from the undamaged bone matrix. Confirmation of these results was achieved when the green-bandpass and blue-bandpass filters were employed (Figure 3.19b and Figure 3.19c).

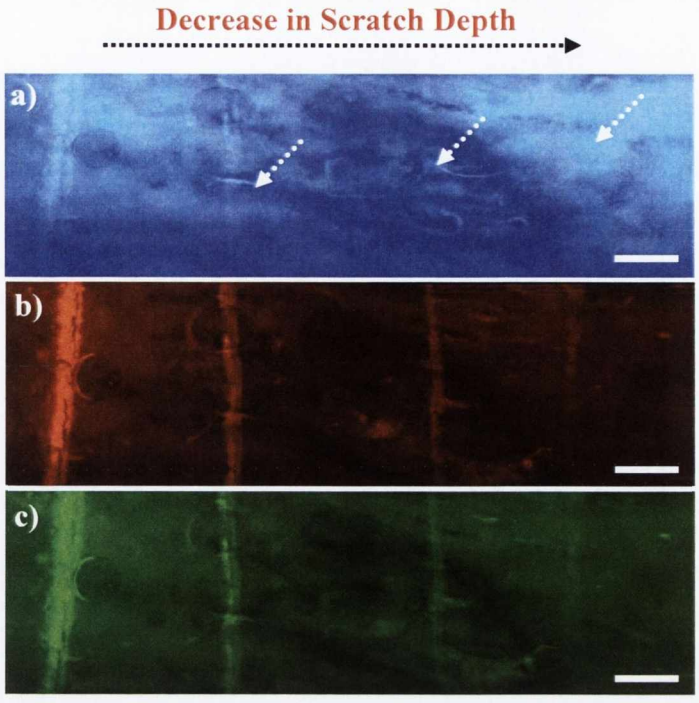

Figure 3.19: *Modulation in the emission response of* ***Eu.69.Na*** *at the scratched bone regions as a function of scratch depth using a) UV-longpass (UV-2A) b) green-bandpass (TRITC) and c) blue-bandpass (FITC) epifluorescence filter cubes. Scale bar = 250 μm.*

Based on previous literature reports, once the scratched bone specimens were immersed in an aqueous solution of the contrast agent under investigation, the sample vials were stored under vacuum.[129, 133] It had been suggested that this technique would allow for more selective chelation of the contrasts agent at the microscratched site and therefore potentially improve the emission contrast. In order to investigate this, scratched bone samples were immersed in the 1 mM aqueous solution of **Eu.69.Na** and the sample vials were stored at atmospheric pressure. Using the green and blue-bandpass filter cubes, epifluorescence images of these samples were obtained, with comparisons to those bone samples stored under vacuum made. As shown by the images in Figure 3.20, although the microscratches are clearly distinguishable from the undamaged bone matrix, the emission intensity and therefore contrast observed is slightly poorer for the samples not stored under vacuum. These results confirm that once placed under vacuum, more preferential localisation of **Eu.69.Na** within the microscratch region occurs. By measuring the intensities inside and outside the scratched areas of those samples stored at atmospheric pressure, intensities enhancements of *ca.* 1.7 and 1.3 were determined using the green and blue bandpass filters, respectively. These values are slightly lower then the 3 and 2.7 enhancement values obtained for those bone specimens stored under vacuum.

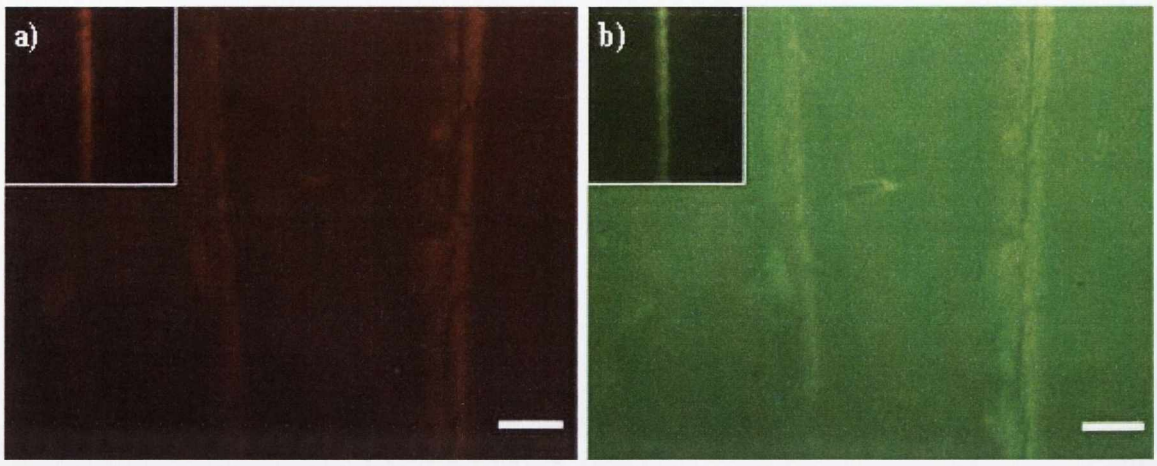

Figure 3.20: *Epifluorescence images of scratched bovine bone samples immersed at atmospheric pressure in a 1 mM aqueous solution (20 mM HEPES, 135 mM KCl, pH 7.4) of* ***Eu.69.Na*** *for 24 h, using the a) green-bandpass (TRITC) and b) blue-bandpass (FITC) filter cube. Scale bar = 250 μm Insets: Images of scratched bovine bone samples immersed in* ***Eu.69.Na*** *under vacuum for 24 h.*

The final factor which required investigation was the overall thickness of the bone samples. It was unknown whether the contrasting abilities of these Ln based complexes would show a dramatic reduction as the thickness of the bone specimens was increased. It was possible that as a result of much stronger autofluorescence from the bone structure that the Ln emission from these contrast agents would be reduced, making identification of the microscratched regions much more difficult. To investigate this, it was necessary to prepare an oblique bone specimen, whose thickness varied from 700 μm at one end to 100 μm at the other. Five scratches of similar depth were induced on the surface of this bone specimen, followed by immersion in a 1 mM aqueous solution of **Eu.69.Na** for 12 h under vacuum. Using an electronic vernier calliper, for each scratch induced, an accurate measurement of the sample thickness was determined. As shown by the images in Figure 3.21, it is clear that as the thickness of the sample was increased, the emission from the background bone surface became much stronger, masking the Eu(III) emission observed from the scratched regions and thus resulting in poorer contrast. Intensity enhancements of 2.8 and 2.6 using the green-bandpass and blue-longpass filter cubes, respectively, were determined for the scratch with a 170 μm thickness. Whereas, slightly lower enhancement values of 1.8 and 1.5 were estimated for the much thicker 680 μm scratched surface.

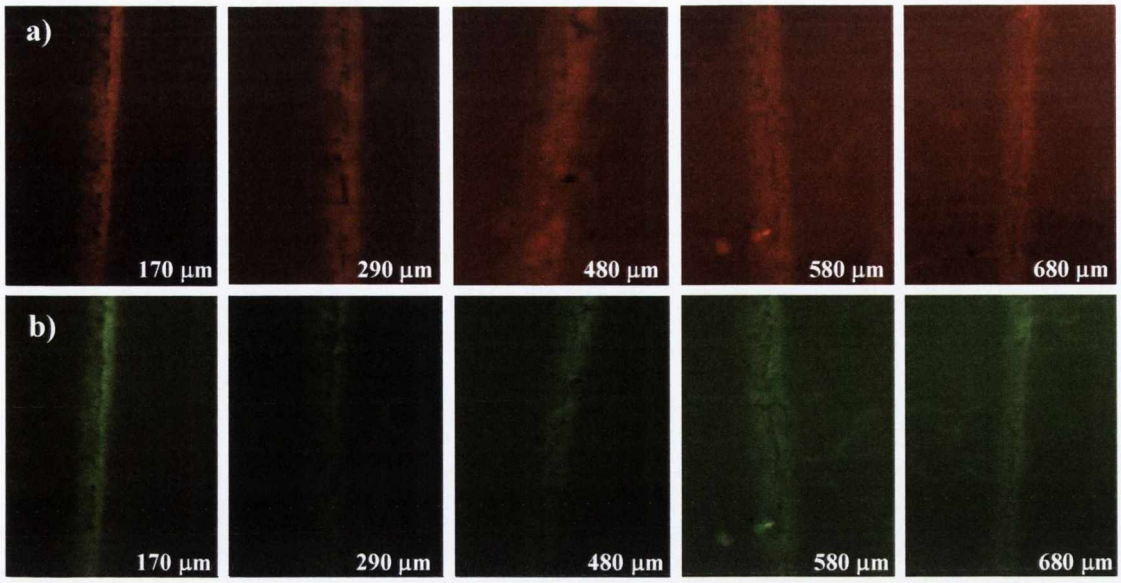

Figure 3.21: *Epifluorescence images of scratched oblique bovine bone sample immersed under vacuum in a 1 mM aqueous solution (20 mM HEPES, 135 mM KCl, pH 7.4) of* ***Eu.69.Na*** *for 12 h, using the a) green-bandpass (TRITC) and b) blue-longpass (B-1A) filter cube. (The thickness of the bone sample varied from 700 μm to 100 μm.)*

It is clear from the above measurements that in order to get an accurate indication of the contrasting abilities of **Eu.69.Na** and determine the LOD for this complex, great care and consideration is required to ensure that all the parameters during the scratching and staining procedure are constant, especially for the case of scratch depth and sample thickness, where a large variation in the intensity enhancements were observed. Therefore, in the following section, where the effect of immersion time and concentration of **Eu.69.Na** on its contrasting abilities are investigated, similar scratched depths and sample thickness throughout these measurements were used.

3.7 Investigation of potential LOD for Eu.69.Na

All previously discussed scratched bone studies were carried out using a 1 mM concentration of **Eu.69.Na**, with 4 h being the minimum staining time period investigated. However, it was necessary to monitor any modulation in the contrasting abilities of **Eu.69.Na** as the concentration of the complex and immersion times used were altered. The first study involved preparing a 0.1 mM, 1 mM, 0.5 mM and 4 mM solution of the Eu(III) chelating agent, followed by immersion of identical scratched bone specimens in each solution for 24 h under vacuum. As shown by Figure 3.22, the expected decrease in emission intensity at the scratched regions as a function of contrast agent concentration was observed using the green-bandpass and blue-longpass epifluorescence filter cubes. However, although the Eu(III) emission is extremely weak, successful identification of the microscratched region was still possible using the much lower 0.1 mM concentration.

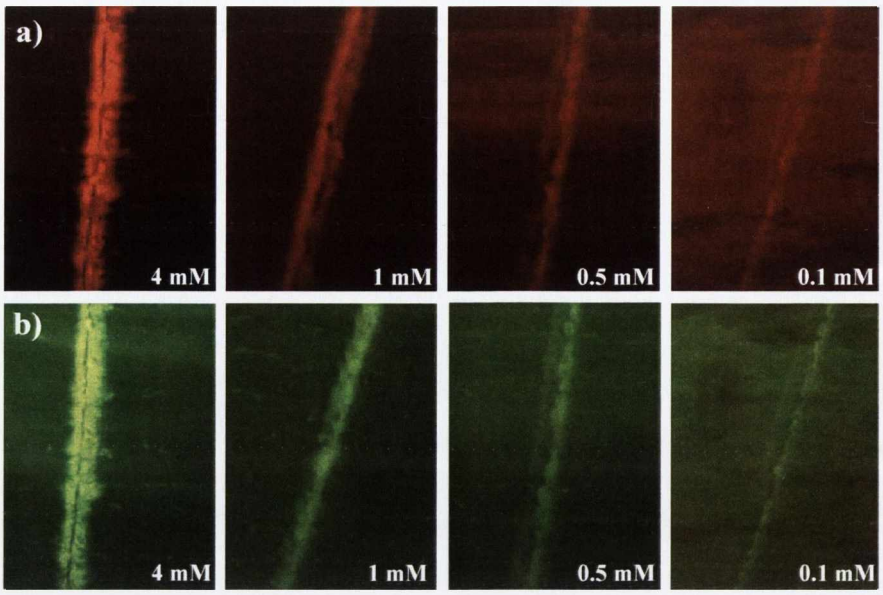

Figure 3.22: *Epifluorescence images of scratched bovine bone samples immersed under vacuum in a 4 mM, 1 mM, 0.5 mM and 0.1 mM aqueous solutions (20 mM HEPES, 135 mM KCl, pH 7.4) of* ***Eu.69.Na*** *for 24 h, using the a) green-bandpass (TRITC) and b) blue-longpass (FITC) filter cube. (Bone sample thickness ca. 250 μm)*

On comparison of the emission intensities measured inside and outside the scratched regions using the green-bandpass epifluorescence images, the intensity enhancements displayed a significant reduction upon lowering the contrast agent's concentration. For example, as represented by the bar charts in Figure 3.23, the intensity enhancement recorded using the 4 mM concentration was 5.3, in comparison to 1.3 for the much lower 0.1 mM **Eu.69.Na** solution.

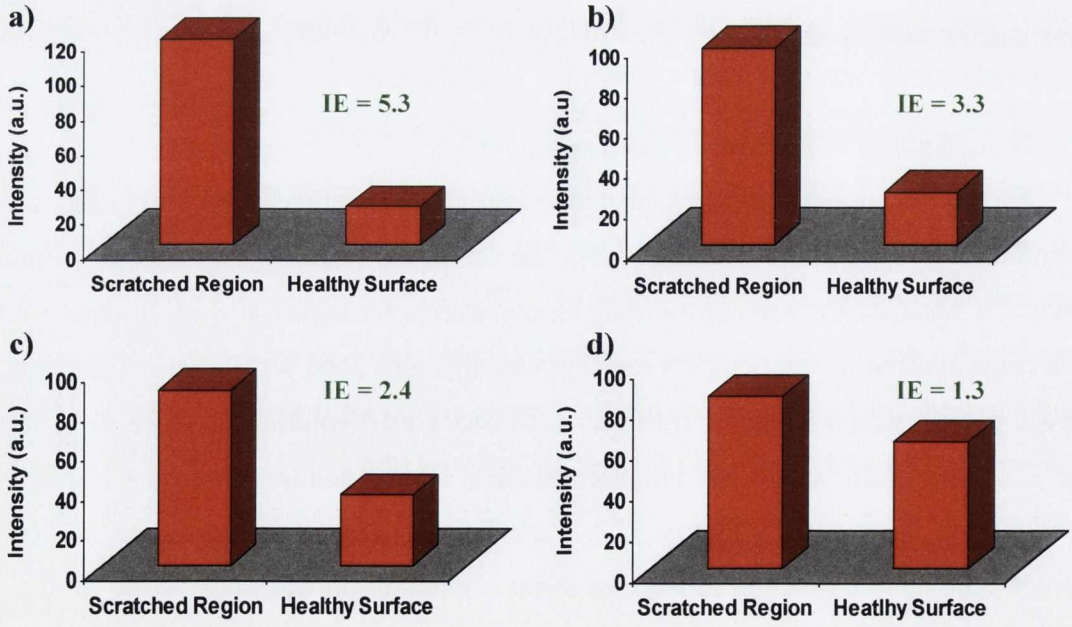

Figure 3.23: *Emission intensity enhancement (green-bandpass images) between the scratched region and the outer healthy bone surface after 24 h immersion under vacuum in a a) 4 mM, b) 1 mM, c) 0.5 mM and d) 0.1 mM aqueous solution (20 mM HEPES, 135 mM KCl, pH 7.4) of* ***Eu.69.Na****.*

Confirmation of the above results was attained on analysis of the bone specimens using the UV-longpass filter cube, where below a 1 mM concentration, distinction of the microscratched region became extremely difficult as a result of the much weaker Eu(III) emission from **Eu.69.Na** being masked by the autofluorescence from the bone structure. With a great understanding of the concentration range in which **Eu.69.Na** displays its most sufficient contrasting ability, the next step was to reduce the immersion period below 4 h, comparing the results obtained using all four concentrations previously studied. Overall, as displayed by the green-bandpass epifluorescence images shown in Figure 3.24, the luminescence response of **Eu.69.Na** from the microscratched region decreased significantly for all concentrations studied as the immersion time was reduced. Using the 0.1 mM solution, identification of the damaged bone structure became difficult below a 2 h immersion time, however, for all other concentrations, after only a 15 min staining period, clear distinction of the microscratch from the remaining undamaged bone matrix could be attained.

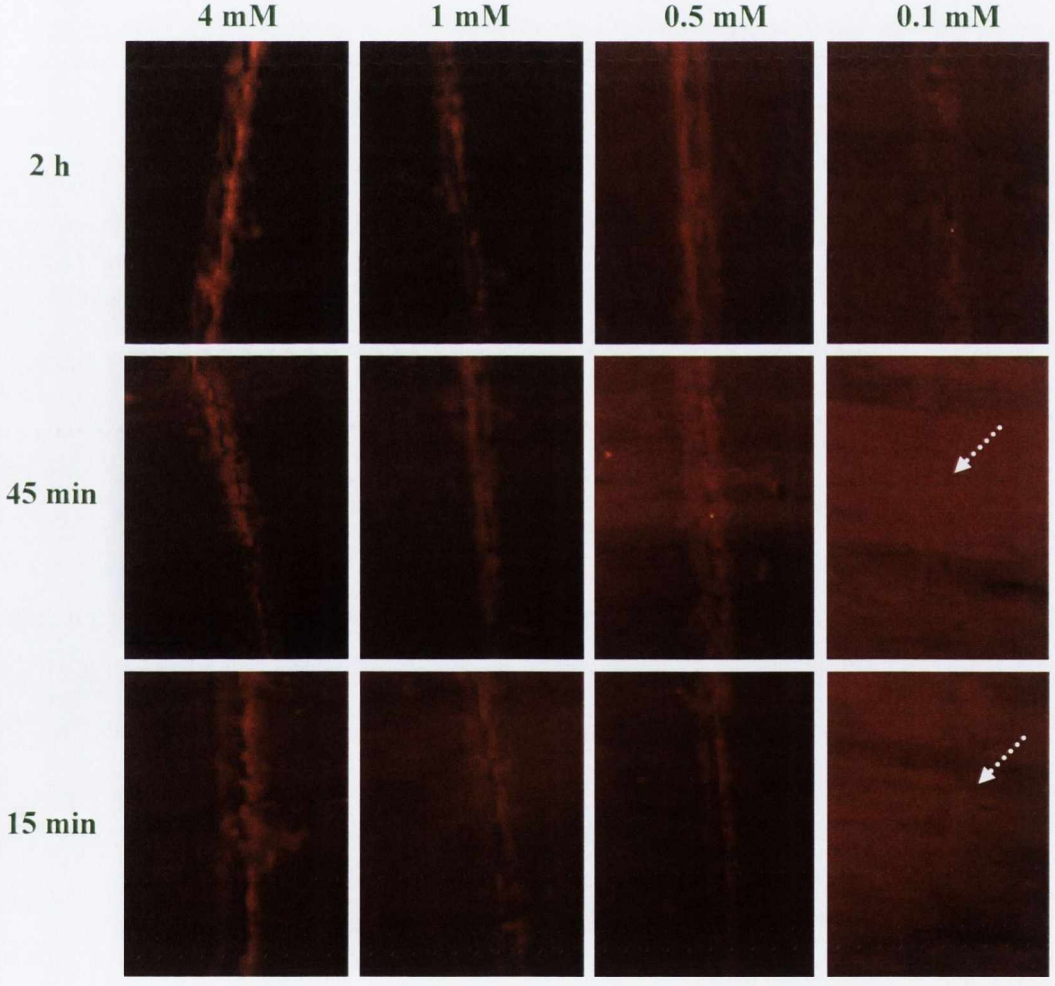

Figure 3.24: *Epifluorescence images of scratched bovine bone samples immersed under vacuum in a 4 mM, 1 mM, 0.5 mM and 0.1 mM aqueous solutions (20 mM HEPES, 135 mM KCl, pH 7.4) of* ***Eu.69.Na*** *for 2 h, 45 min and 15 min using the green bandpass (TRITC) filter cube. (Bone sample thickness ca. 250 μm)*

Measurement of the intensity enhancements after 15 min immersion for the 0.5 mM, 1 mM and 4 mM images resulted in values of 2.8, 1.8 and 1.3 being determined, respectively (Figure 3.25). These results show that provided the thickness of the bone sample was *ca.* 250 μm, **Eu.69.Na** was successful in selectively identifying scratched regions on the surface of the bone after 15 min immersion, using a 0.5 mM concentration of the contrast agent. The requirement of such a small immersion time suggests rapid chelation of the iminodiacetate binding units of **Eu.69.Na** to the Ca^{2+} ions exposed upon scratch formation.

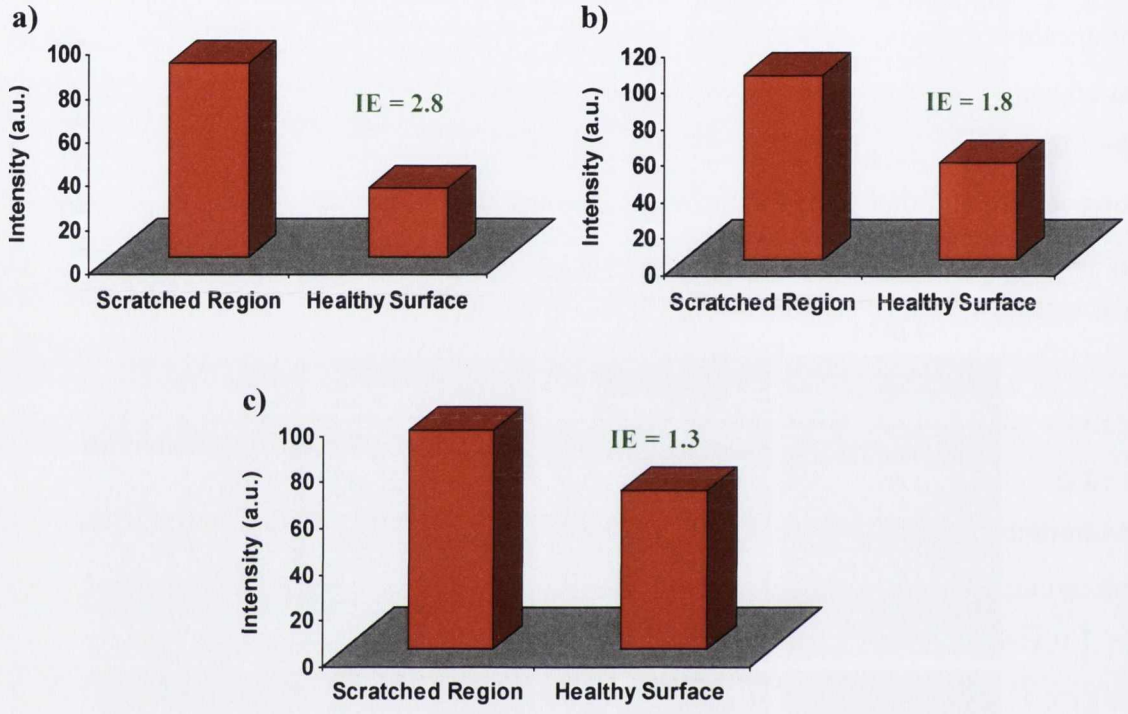

Figure 3.25: *Emission intensity enhancement (green-bandpass images) between the scratched region and the outer healthy bone surface after 15 min immersion under vacuum in an a) 4 mM, b) 1 mM and c) 0.5 mM aqueous solution (20 mM HEPES, 135 mM KCl, pH 7.4) of* ***Eu.69.Na****.*

All the above measurements were carried out with bone specimens which had an average thickness of *ca.* 250 μm, however, to delve deeper into the contrasting abilities of **Eu.69.Na**, these LOD studies were repeated using bone samples of various thickness from 250 μm to 1 mm. The 3D graph (intensity enhancement *vs.* log concentration *vs.* log immersion time) shown in Figure 3.26 summarises all the results using the green-bandpass epifluorescence filter cube, highlighting the much poorer efficiency of **Eu.69.Na** as a contrast agent for scratched bone samples with thicknesses greater then 450 μm. The plain dark blue plot represents no contrast (*i.e.* intensity enhancement of 1), with any point above this area suggesting successful visualisation of the microscratched region. It is clear from this graph, on average, with a sample thickness of 450 μm or more, the intensity enhancement never increased above 2, even using the extremely concentrated 4 mM solution and long immersion

time of 24 h. The opposite was seen for the thinner bone specimens (< 450 μm), were an average intensity enhancement of *ca.* 4 was attained using these staining conditions.

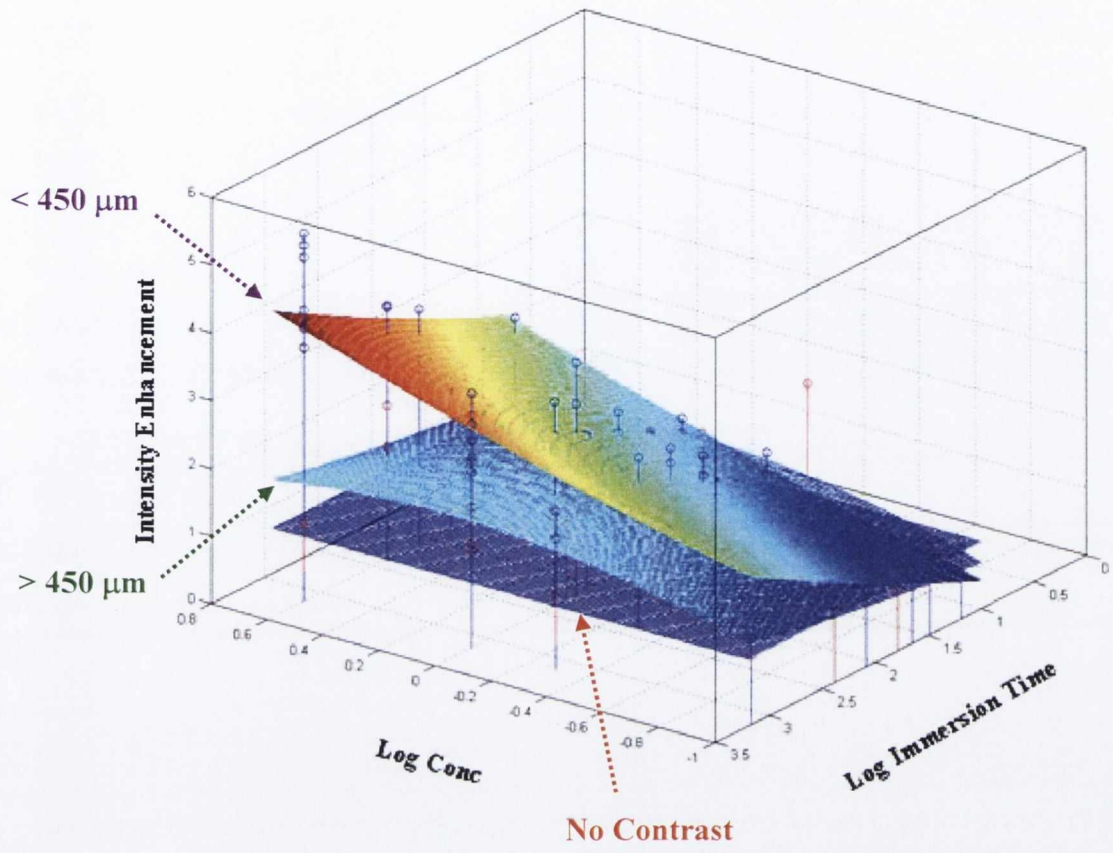

Figure 3.26: *3D graph of Intensity Enhancement vs. Log Conc vs. Log Immersion Time for scratched bone samples with thicknesses > 450 μm. The intensity enhancements were measured by comparing the emission response of* ***Eu.69.Na*** *inside and outside the microscratched region using the green-bandpass (TRITC) epifluorescence filter cube.*

In summary, these studies highlight the binding affinity of **Eu.69.Na** within damaged bone structure, with its subsequent preferential localisation resulting in a strong contrast of the microscratched regions. Using epifluorescence microscopy analysis, concentrations as low as 0.1 mM with an immersion time of 2 h allowed clear distinction of the scratch from the remaining undamaged bone matrix. However, in order to reduce this immersion time to 15 min, concentrations of 0.5 mM or greater were required. The significant effect that bone sample thickness has on the contrasting abilities of **Eu.69.Na** was also demonstrated; with thicknesses less then 450 μm being determined as optimum. With a great understanding of the potential LOD for **Eu.69.Na** and the sample preparation required to optimise the complex's efficiency as a contrast agent, the next stage involved investigating any change in emission response and therefore visualisation of the damaged bone region in the presence of biologically relevant metal ions. The following section will therefore highlight the results obtained from these measurements.

3.8 Effect on the contrasting abilities of Eu.69.Na in the presence of biologically relevant metal ions

In order to investigate the effect on the binding ability of **Eu.69.Na** to the high concentration of Ca^{2+} ions exposed upon microscratch formation in the presence of various physiologically important metal ions (Ca^{2+}, Na^{+}, Fe^{2+}, Mg^{2+}, Zn^{2+} and Cu^{2+}), a series of scratch tests were performed. The Eu(III) contrast agent solution (1 mM) was exposed to a high concentration of the chloride salt of these metals for 12 h before the staining procedure was carried out. The concentration of all the metal ions used was 10 mM, except for NaCl, where a 150 mM solution was prepared. Scratched bone specimens of equal thickness (150 μm) were immersed in each solution for 24 h under vacuum. A control **Eu.69.Na** solution, which was not exposed to any metal ion was also prepared.

As shown by the green-bandpass epifluorescence images in Figure 3.27, in the absence of any metal ion, the intensity enhancement of the scratched region was determined as 3.5, however, for those bone samples immersed in the metal ion solutions, a small decrease in the Eu(III) emission from the scratched region was observed. This suggests that in the presence of these metal ions, the chelation of **Eu.69.Na** at the damaged bone regions was slightly effected. Nevertheless, identification of the microscratch surface was still possible for all samples.

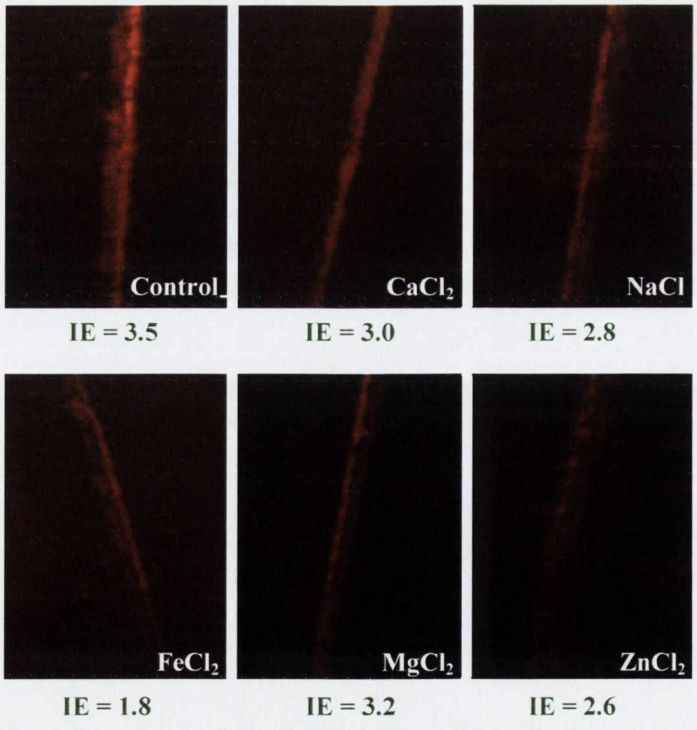

Figure 3.27: *Epifluorescence images of scratched bovine bone samples immersed under vacuum in a 1 mM aqueous solutions (20 mM HEPES, 135 mM KCl, pH 7.4) of* ***Eu.69.Na*** *for 24 h in the presence of either 10 mM $CaCl_2$, $FeCl_2$, $MgCl_2$, $ZnCl_2$ or 150 mM NaCl using the green bandpass (TRITC) filter cube. (Bone sample thickness ca. 150 μm)*

The most significant effect was seen for $FeCl_2$, where the intensity enhancement was reduced by 50% to 1.8. It is possible that strong interaction of the iminodiacetate chelating units of **Eu.69.Na** with the Fe^{2+} ions could result in much poorer binding of the complex at the scratched region and thus help explain the reduction in emission contrast. It was also no surprise that Zn^{2+} ions showed a reduction in the response from **Eu.69.Na**, as strong chelation of Zn^{2+} to the iminodiacetate functionality has previously been reported.[165] The much poorer binding to low concentrations of Ca^{2+} and Mg^{2+} ions was also verified as the effect on the contrast abilities of **Eu.69.Na** was much lower, with intensity enhancements of 3.0 and 3.2, respectively.

A very different response was observed for the Cu^{2+} ion solution, where as shown in Figure 3.28a the Eu(III) emission from **Eu.69.Na** within the scratched region was completely quenched. On further analysis using bright field microscopy (Figure 3.28b), a strong blue emission from the scratched surface was observed, suggesting chelation of the Cu^{2+} ions within the damaged bone structure and subsequently masking the Eu(III) emission from **Eu.69.Na**. To verify this, the control sample shown above in Figure 3.27 was re-immersed in a 10 mM solution of $CuCl_2$ for a further 24 h and as expected, due to Cu^{2+} localisation within the microscratched region, the strong Eu(III) emission could no longer be observed. To ensure that this Cu^{2+} chelation occurred in the absence of **Eu.69.Na**, a scratched bone sample was immersed in a $CuCl_2$ solution alone, with similar images to those shown in Figure 3.28 being attained. As discussed in Chapter 2, interaction of the iminodiacetate functionalities with Cu^{2+} resulted in reduction in the Eu(III) emission of **Eu.69.Na**, however, the strong Cu^{2+} chelation at the scratched surface made verification of this difficult.

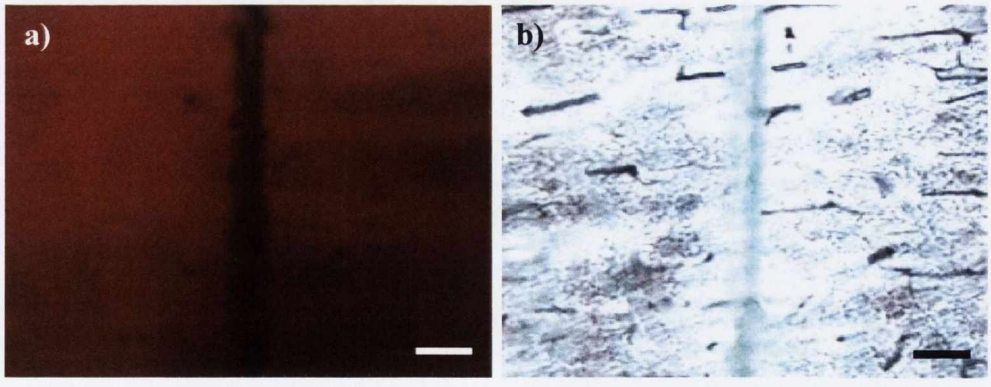

Figure 3.28: *a) Green-bandpass epifluorescence image and b) bright field image of scratched bovine bone sample immersed under vacuum in a 1 mM aqueous solution (20 mM HEPES, 135 mM KCl, pH 7.4) of* ***Eu.69.Na*** *for 24 h in the presence of 10 mM* $CuCl_2$. *Scale bar = 200 μm.*

Overall, with the exception of Cu^{2+}, all metal ions studied only displayed a small effect on the contrasting abilities of **Eu.69.Na**, with the microscratched region still being

clearly distinguishable from the remaining undamaged bone surface. It was suggested that the slight decrease in luminescence response was possibly as a result of the metal ions showing some form of interaction with the iminodiacetate moieties of **Eu.69.Na** and thus reducing its binding affinity for the damaged bone structure.

Within this chapter, all measurements discussed so far, including the LOD studies, involved inducing a microscratch on the external surface of a bone specimen followed by immersion of the sample in an aqueous solution of the contrast agent under investigation. However, it was also necessary to investigate the behaviour of these Ln based imaging agents for detecting internal microdamage of bovine bone specimens using a bulk bone staining procedure. The next section will therefore detail the process for fatigue microdamage formation followed by the bulk staining protocol employed, with the results obtained using **Eu.69.Na** as the contrast agent also highlighted.

3.9 Internal microdamage detection using Eu.69.Na as contrast agent

3.9.1 Sample preparation and internal microdamage formation

In order to produce internal microdamage within bone structure, a similar sample preparation and fatigue stressing protocol to that established by O'Brien *et al.*[138, 163] was used. Like that discussed for preparation of the scratched bone specimens, samples of cortical bone were cut from the mid-diaphysis of bovine tibiae using a low speed diamond saw. These irregular shaped bone samples were placed in a small steel box (50 x 25 x 25 mm) and dental cement (suprastone, Kerr, Italy) was poured over them, with the samples allowed to set overnight in order to fix them in position. Using a special high speed coring tool (Perkano Ltd., Dublin), which displayed a cutting rate of 10 mm/min and internal diameter 6.6 mm, with a rotation speed of 350 rpm, cylindrical sections of bone of length 35 mm and diameter 6.6 mm were obtained. As shown in Figure 3.29a, these cylindrical bone samples were waisted in the centre using a CNC lathe, which resulted in gauge diameter of 5.25 mm over a 7 mm gauge length. Waisting the centre of these bone specimens provided a weak region where internal microdamage would be dominant in comparison to the remainder of the sample. All machining procedures were carried out under wet conditions, ensuring that the bone specimens were not allowed to dry at any stage.

Internal microdamage was induced within the waisted section using an INSTRON 8501 servo-hydraulic testing machine by applying axial compressive forces at one end of the bone specimen. An illustration of the set up used is shown in Figure 3.29b. It has been previously demonstrated that provided significant stress is applied to the bone sample, the formation of microdamage within the waisted region will occur.[138] A slight modification of

O'Brien's procedure was applied, where a translucent flexible tube containing 1 mM **Eu.69.Na** was placed around the sample during the machining process. Brass end caps were attached to the bone specimen before testing to minimise any overall structural damage which may occur during compression. These end caps were then fitted with parallel aluminium plates and attached to the INSTRON testing machine. This set up ensured correct axial alignment of the bone specimen and therefore eliminated any potential bending stresses.

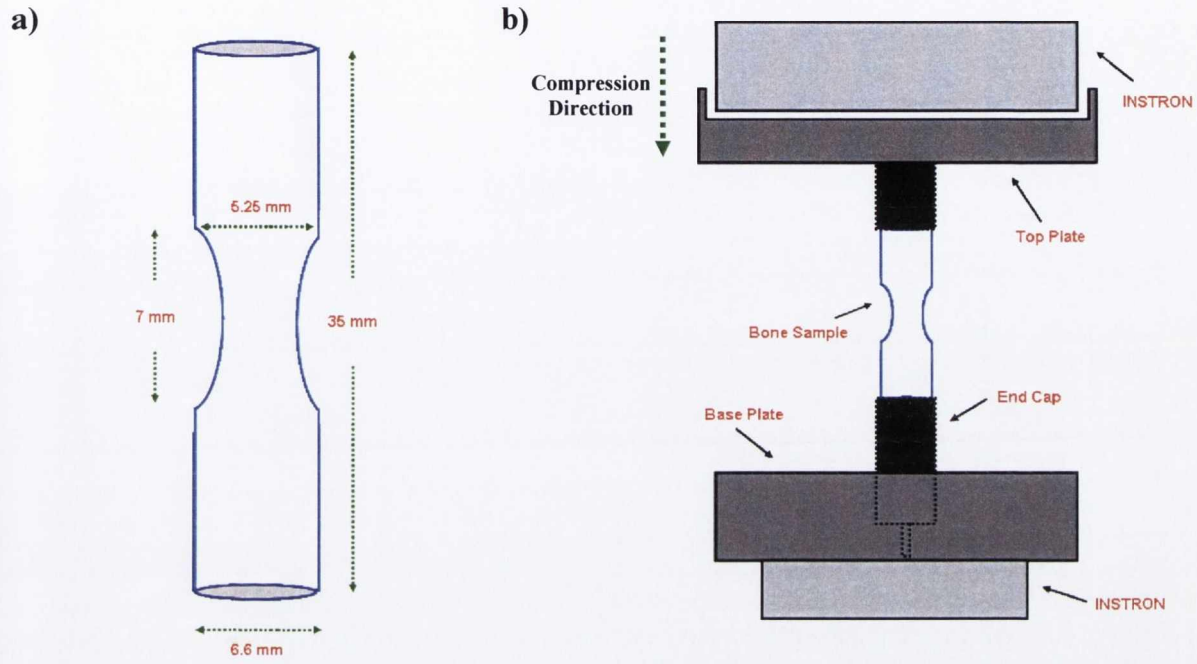

Figure 3.29: *Illustration of a) bone sample displaying waisted centre of 7 mm in length and 5.25 mm diameter and b) set up used to induce internal microdamage using axial compressive forces.*[163]

After completion of the compression forces, the bone specimens were removed from the INSTRON testing machine and re-immersed in a fresh 1 mM aqueous (20 mM HEPES, 135 mM KCl, pH 7.4) solution of **Eu.69.Na** and stored under vacuum for 24 h. It was anticipated that during this bulk bone staining period the contrast agent would penetrate the bone matrix *via* the vascular network and selectively label the internal microcracks which were created during the machining process described above. After removal from the contrast agent solution, the bone specimen's surfaces were washed thoroughly with distilled water. To ensure complete removal of any contrast agent which may still be found within the vascular canals, the samples were re-immersed in distilled water and placed under vacuum for a 5 min period. This washing procedure was repeated 5 times with the hope that any remaining uncomplexed **Eu.69.Na** would be removed. Using a band saw, the waisted region of the bone specimens were cut into sections of *ca.* 200-250 μm thick and then ground to a 150 μm thickness using sand paper (P1200 grit). After mounting the specimens on to a microscopy slide using DPX, the bone samples were analysed using epifluorescence microscopy.

3.9.2 Epifluorescence microscopy analysis of internal microdamage

If selective chelation of **Eu.69.Na** was to occur within the microdamaged regions, successful visualisation of the cracks from the remaining undamaged bone matrix would be possible using epifluorescence analysis. As shown by the image in Figure 3.30a, when the UV longpass filter cube was used, a very slight emission enhancement of the boundaries for the larger microcracks was displayed. However, on further analysis, no smaller microcracks which may be propagating from the much larger ones could be observed. A similar intensity enhancement resulted using the green-bandpass and blue-longpass fluorescence cubes (Figure 3.30b and Figure 3.30c).

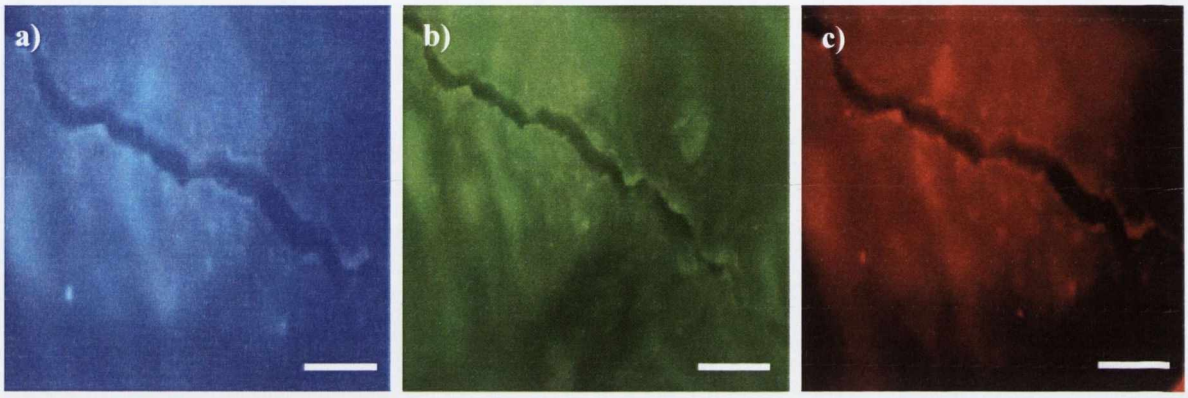

Figure 3.30: *Epifluorescence images of a 150 μm thick sample from the waisted section of the bulk bovine bone sample immersed under vacuum in a 1 mM aqueous solution (20 mM HEPES, 135 mM KCl, pH 7.4) of* ***Eu.69.Na*** *for 24 h, using the a) UV longpass (UV-2A) b) blue-longpass (FITC) and b) green-bandpass (TRITC) filter cube. (Internal microdamage was induced using axial compression forces of the bone specimen) Scale bar = 50 μm.*

These results demonstrate that although a very slight enhancement of the larger cracks from the bone surface was observed, the contrast using a 1 mM concentration of **Eu.69.Na** was still relatively poor, making visualisation of the much smaller microcracks extremely difficult. One possibility for such a poor response is that the concentration of the contrast agent may be too low. It is important to note that for these bulk bone studies, a larger surface and greater number of microcracks must be labelled in comparison to the single microscratch analysed during the scratching tests. The contrast agent must also pass through the vascular system and through the internal structure of the bone specimen before it finally can undergo interaction at the microcrack regions. Therefore, in order to try and increase the contrasting abilities of **Eu.69.Na** for internal microdamage, the above fatiguing and staining procedure was repeated using a 4 mM concentration of the Eu(III) contrast agent. Epifluorescence analysis of these bone specimens were found to be more successful, with a much stronger emission contrast of the microcracks from the undamaged bone surface being observed. As shown in Figure 3.31, using the green-bandpass filter cube, the Eu(III) emission from

Eu.69.Na could be clearly seen, suggesting preferential localisation of the contrast agent at the damaged sites.

Figure 3.31: *Epifluorescence image of a 150 μm thick sample from the waisted section of the bulk bovine bone sample immersed under vacuum in a 4 mM aqueous solution (20 mM HEPES, 135 mM KCl, pH 7.4) of* ***Eu.69.Na*** *for 24 h, using the green-bandpass (TRITC) filter cube. (Internal microdamage was induced using axial compression forces of the bone specimen) Scale bar = 50 μm.*

The most significant result observed from these studies was that, unlike that seen previously using the 1 mM **Eu.69.Na** solution, visualisation of extremely small microcracks (identified by white arrow in Figure 3.31), which would not be detected in the absence of any contrast agent, was now possible. This highlights the efficiency of **Eu.69.Na** to penetrate the bone matrix *via* the vascular canals and selectively bind at the damaged bone regions. Another interesting observation was that only microcracks which were induced by the fatigue stressing were labelled. This is demonstrated in the green-bandpass epifluorescence image shown in Figure 3.32, where artefactual microdamage *i.e.* damage formed during the cutting and sectioning process was not labelled with any contrast agent (green arrow). This suggests that no leaching of **Eu.69.Na** into the artefactual cracks occurs once the sample is removed from the immersion solution, ensuring that if **Eu.69.Na** was to be used to quantify the amount of microdamage induced, overestimation as a result of labelling of artifactual damage would not occur. During the fatigue stressing of the sample shown in Figure 3.32, as a result of excessive compression, the sample completely cracked in the centre of the waisted section. This resulted in the exposure of an extremely rough edge where a large concentration of Ca^{2+} ions would be found. Therefore when the sample was immersed in the contrast agent solution, selective labelling of this rough surface was also probable. The large emission enhancement of this edge, identified by the yellow arrow, can be seen in Figure 3.32, highlighting the selectivity of **Eu.69.Na** for areas of damaged bone structure.

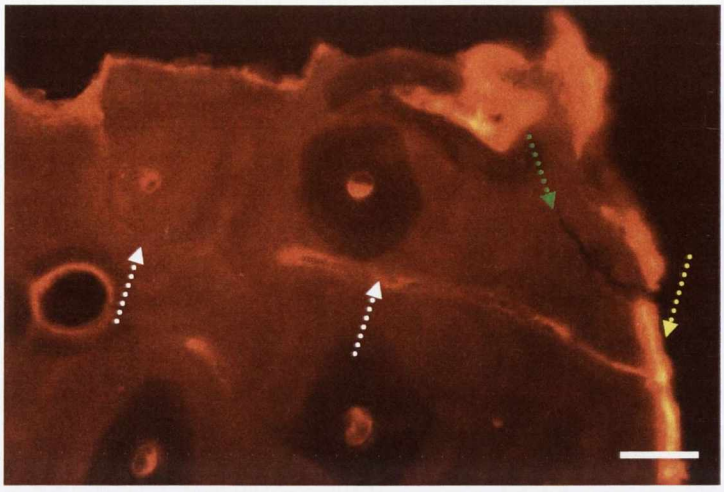

Figure 3.32: *Epifluorescence image of a 150 μm thick sample from the waisted section of the bulk bovine bone sample immersed under vacuum in a 4 mM aqueous solution (20 mM HEPES, 135 mM KCl, pH 7.4) of* ***Eu.69.Na*** *for 24 h, using the green bandpass filter cube. (White arrows indicate labelled microdamage induced by the fatigue testing whereas the green arrow highlights unlabelled artefactual damage.) Scale bar = 100 μm.*

In summary these studies demonstrated the ability of **Eu.69.Na** to label internal microdamage using a bulk bone staining method, provided a 4 mM concentration of the contrast agent was used, over an immersion period of 24 h. Selective interaction within the large microcrack regions, as well as the much smaller cracks made their identification and possible quantification a much more straightforward process. The strong binding affinity for the Ca^{2+} ions exposed upon microcrack formation was confirmed by the fact that no leaching of the dye into artefactual microdamage occurred during the cutting and sectioning processes. This ensured that if **Eu.69.Na** was used for quantification of microdamage induced, overestimation would not occur.

3.10 Conclusion

This chapter presents in detail a critical investigation into the ability of the Ln luminescent imaging agents, which were synthesised in Chapter 2, to selectively label damaged bone structure and therefore provide a contrast from the remaining undamaged bone surface. The two imaging techniques which were employed for analysis were epifluorescence and laser scanning confocal microscopy. Initially **Tb.58.Na**, which consists of one iminodiacetate binding unit within its overall framework, was investigated. Overall, using epifluorescence microscopy, poor emission contrast of the scratched bone regions was observed, suggesting weak chelation of this Tb(III) imaging agent with the Ca^{2+} ions. Although, a more efficient contrast was shown using confocal microscopy, an intensity enhancement of 2.8 after 24 h immersion is still relatively low. These imaging studies confirm the solid state results previously discussed in Chapter 2, where although Tb(III)

emission was displayed from the scratched regions, only a small difference in its intensity compared to that measured at the smooth surface was observed. Analysis of its ester analogue **Tb.58**, which should display little chelation at the damaged bone sites, resulted in an intensity enhancement of 1.4 after 24 h immersion. This helped verify the weak binding affinity of **Tb.58.Na**, whereas if strong chelation of the Ca^{2+} ions was occurring, a much larger enhancement compared to the control complex **Tb.58** would be expected.

With the potential for much stronger chelation within the scratched bone regions, **Eu.69.Na** and **Tb.69.Na**, which have three iminodiacetate receptor moieties incorporated into their overall structure, were next analysed. Greater success was achieved with these complexes when epifluorescence analysis was used. Unlike that seen for **Tb.58.Na**, the Ln emission was no longer completely masked by the autofluorescence from the bone structure, allowing clear visualisation of the microscratches using the UV longpass, green-bandpass and blue-bandpass fluorescence cubes. A general trend of slightly poorer emission contrast from **Tb.69.Na** in comparison to its Eu(III) analogue was observed. The pH dependence of **Tb.69.Na** at pH 7.4 and therefore its reduction in emission intensity was suggested as a possible reason for this response. Confocal microscopy analysis of both complexes confirmed their efficient chelation, with strong Ln emission being observed within the scratched region. After 4 h immersion, a significant contrast from the undamaged bone matrix was observed. **Eu.69.Na** displayed the greatest potential as a luminescent imaging agent, with a 28-fold intensity enhancement of the microscratched region being determined after a 24 h staining period. Again a much poorer response was observed for **Tb.69.Na**, with an intensity enhancement of only 8 after 24 h immersion being measured. As expected, on analysis of the diethyl ester analogues of both complexes, much poorer contrast of damaged bone structure resulted. However, for the Tb(III) complexes, the difference between their emission enhancements was not as significant as that seen for the Eu(III) analogues. The intensity enhancement estimated for **Tb.69** was 3, which is only slightly lower then the 8-fold enhancement measured for **Tb.69.Na**.

Using **Eu.69.Na** as the contrast agent and epifluorescence imaging analysis, the effect of factors such as scratch depth, sample thickness and the use of vacuum or no vacuum on the complexes contrasting abilities of the microscratched regions were investigated. With a greater understating of these potentially inhibiting factors gained, an extensive LOD study for **Eu.69.Na** was carried out. Concentrations ranging from 4 mM to 0.1 mM and immersion times as low as 15 min were investigated. Overall with a sample thickness of 250 μm, using the 0.1 mM concentration, a minimum immersion time of 2 h was required, however, for all other concentrations studied, identification of the scratched region was possible after only a

15 min staining period. By repeating these LOD measurements on bone samples with thicknesses ranging from 250 μm to 1 mm, the significant effect that sample thickness has on the ability to visualise the microscratches was demonstrated. A 450 μm thickness or less for the bone specimens was determined as optimum. Therefore, if **Eu.69.Na** was to be used as a histological contrast agent to determine the presence of *in vivo* induced microcracks in a bone specimen, the samples would need to be prepared with a maximum thickness of 450 μm prior to immersion.

The final section of this chapter dealt with the ability of **Eu.69.Na** to selectively detect fatigue induced internal microcracks using a bulk bone staining method.[138, 163] The results of these studies demonstrated that when a 1 mM concentration of **Eu.69.Na** was used, only a slight enhancement of the microcrack boundaries was observed, with no visualisation of any smaller microcracks achieved. Increasing the concentration to 4 mM proved more successful, with the larger cracks displaying a significant emission contrast compared to the healthy undamaged bone surface and identification of the much smaller microcracks also possible. Differentiation of microcracks induced during the fatigue stressing to artefactual damage formed during the cutting and sectioning processes was also possible, reducing the possibility of overestimation during microcrack quantification. Overall these bulk bone staining studies highlighted the ability of **Eu.69.Na** to penetrate the bone matrix *via* the vascular canals and selectively label microcracks within the internal structure of bone material.

With great success achieved for these Eu(III) and Tb(III) based imaging agents using epifluorescence and confocal microscopy analysis, the next investigations involved moving towards a more non-invasive imaging technique by replacing these luminescent Ln ions with the MRI active Gd(III) metal. The following chapter will therefore discuss the synthesis of these Gd(III) contrast agents, followed by an investigation of their potential to behave as MRI imaging agents for damaged bone structure.

Chapter 4

MRI Active Gd(III) Contrast Agents for Detection of Damaged Bone Structure

4.1 Introduction

Magnetic resonance imaging (MRI) has become one of the most powerful non-invasive diagnostic imaging techniques used in clinical medicine today. With the ability to generate anatomical 3D images, of spatial resolution as low as 10 μm, it can provide significant physiological and pathological information on various tissues and organs of the human body.[36, 183] MRI has the ability to highlight differences and therefore provide a contrast amongst various tissues by comparison of their proton densities, water proton relaxation times (T_1 and T_2) and water diffusion rates. Faced with the challenge of poor sensitivity, research has concentrated on the development of contrast agents, which in conjugation with the MRI technique has lead to significant enhancements in the image contrast between healthy and pathological tissues.[39, 184] The phenomenon of magnetic resonance was brought to the scientific front in 1946 by Felix Bloch and Edward Purcell, both of whom were awarded the Nobel Prize in 1952 for their independent contribution to this field.[185, 186] Between 1950 and 1970, NMR was developed and exploited for chemical and physical analysis of molecular species. It wasn't until 1971 that Damadian *et al.*[187] demonstrated the variation in the nuclear magnetic relaxation times between normal and cancerous tissues, which motivated scientists into investigating the use of magnetic resonance for the detection and understanding of various diseases.

This chapter will therefore briefly introduce the key physical properties of NMR required to understand the MRI technique, followed by an introduction to contrast agents, concentrating on those based around the Gd(III) metal ion. The key factors involved in the improved MRI contrast obtained in the presence of these agents will also be discussed. After this introduction to MRI, a series of Gd(III) cyclen based complexes, similar to those which were described in Chapter 2 and 3 will be presented, with their potential as MRI contrast agents for damaged bone structure studied.

4.2 Physical properties of NMR

4.2.1 Nuclear spin and magnetic moment

Atomic nuclei possess a net intrinsic angular momentum (P) referred to as spin, which is composed of the spins of the individual protons and neutrons located within the nucleus. The magnitude of this fundamental property is defined by Equation 4.1, where h is Planck constant and I is the spin quantum number. Protons, neutrons and electrons all have $I = 1/2$ and are therefore often referred to as the "spin 1/2" particles. Therefore, the overall spin quantum number of a nucleus depends on the number of unpaired protons and neutrons, where for example nuclei with an even mass number will have I values of even multiples of

1/2 (I = 0,1, *etc*), while nuclei with an odd mass number will have *I* values of odd multiples of 1/2 (I = 1/2, 3/2, *etc*). [188]

$$P = \hbar\sqrt{I(I+1)};\ \hbar = h/2\pi \qquad \text{Equation 4.1}$$

The most commonly used nuclei for NMR analysis are those which have a spin quantum number $I = 1/2$, *e.g.* ^{1}H, ^{13}C, ^{19}F, ^{31}P. In addition to spin quantum numbers, these nuclei also exhibit magnetic properties, with their spinning charged protons resulting in a dipolar magnetic moment, μ. The magnetic moment is also a vector quantity, oriented parallel to the spin angular momentum and with a magnitude defined by Equation 4.2, where γ is a proportionality constant, known as the gyromagnetic ratio, which is unique for a given nucleus.[36]

$$\mu = \gamma P \qquad \text{Equation 4.2}$$

When the nucleus is placed in an external magnetic field (B_0), the nuclear spins, which are otherwise randomly oriented, align in definite directions relative to the direction of the magnetic field. For the ^{1}H nucleus, two spin states are possible, where as shown in Figure 4.1 the nuclear spin can align (at a slight angle) in either a parallel (+ 1/2) or anti-parallel (-1/2) orientation.

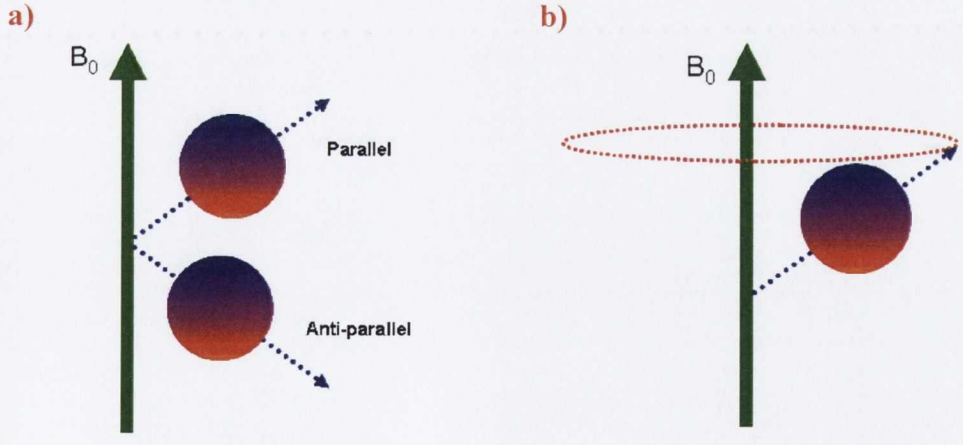

Figure 4.1: *a) The possible orientations for the nuclear spin of the ^{1}H nucleus (I = 1/2) in the presence of an external magnetic field b) precession of the nuclear spin.*[189]

Also illustrated in Figure 4.1, the nuclear spin will not only align with B_0 but also precess with a certain frequency (ω_L) defined by the Larmor Equation 4.3. It is evident from this equation that by increasing the B_0 applied, an increase in the precessional frequency of the nuclear spin will also be observed.

$$\omega_L = B_0\gamma \qquad \text{Equation 4.3}$$

The difference in energy of the two spin states is directly related to the strength of the magnetic field applied, with those nuclear spins in the parallel position being of lower energy than those anti-parallel to B_0. When many ^1H nuclei are placed in the magnetic field, some will align in the anti-parallel orientation with the majority adopting the lower energy parallel alignment. The vector sum of the magnetic moments of the excess nuclear spins in the low energy state results in a net macroscopic magnetisation, M_0, which as shown in Figure 4.2 is orientated along the magnetic field direction, which by convention is along the z axis.[188, 189]

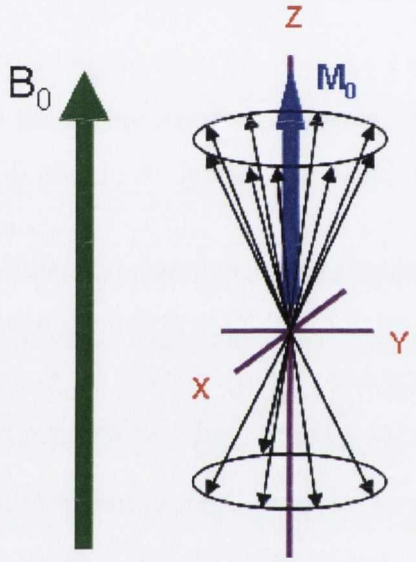

Figure 4.2: *Illustration of the orientation of nuclear spins of ^1H nuclei in the presence of a magnetic field B_0 and the resulting net magnetisation M_0.*[189]

4.2.2 Creation of magnetic resonance signal

On the application of a radiofrequency (RF) pulse, the nuclear spins which are found in the low parallel energy state absorb energy and make a transition into the higher anti-parallel energy state, with the subsequent shift in energy causing the net magnetisation (M_0) to rotate away from B_0 towards the transverse x-y plane.[36] After a certain time frame of the RF pulse being applied, a 90-degree flip of the net magnetisation will result. An illustration of this perturbation of M_0 is shown in Figure 4.3.

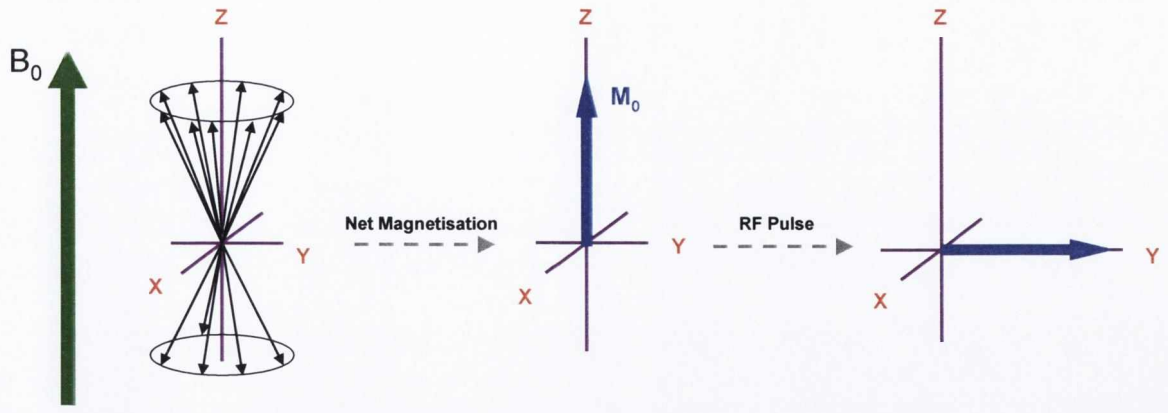

Figure 4.3: *Illustration of the 90-degree flip of the net magnetisation upon application of a radiofrequency pulse to the sample.*

Due to the thermodynamic instability of this perturbed state of magnetism, the net magnetisation will over time revert or "relax" back to its original equilibrium position along the z axis. This so-called relaxation process plays a critical role in the theory and practice of MRI. The two key mechanisms which allow the nuclei to return to their low energy state are spin-lattice (longitudinal) relaxation characterised by a time constant T_1 and spin-spin (transverse) relaxation characterised by time constant T_2. The former process, as its name suggests, involves an exchange of energy between the nuclear spins and the surrounding environment, which is referred to as the lattice regardless of the physical state of the system. This occurs as a result of interaction of the magnetic moment of the nuclei with the fluctuating magnetic field created by the random motions of the molecules in the surrounding medium. This random process allows for recovery of M_0 in an exponential manner, as described by Equation 4.4 and shown in Figure 4.4.[190, 191]

$$M_z(t) = M_0(1 - e^{-t/T}) \qquad \textbf{Equation 4.4}$$

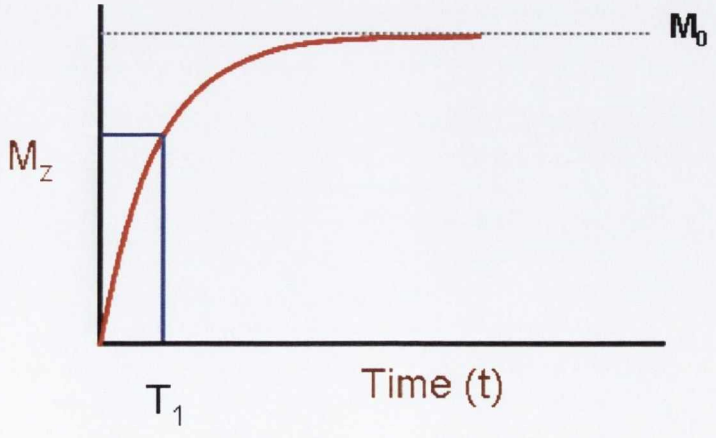

Figure 4.4: *Exponential recovery of the longitudinal magnetisation vector M_z.*

It is important to note that at $t = T_1$, the longitudinal magnetisation has recovered to 63% of its original value with almost full recovery (98%) being achieved at $t = 5 \times T_1$. In the case of spin-spin relaxation, this process involves interactions with neighbouring nuclear spins without the exchange of energy with the lattice. The magnetisation in the x-y plane, M_{xy} which is generated upon the application of the 90° RF pulse decays towards zero during this process. In the immediate time frame after RF excitation, all the nuclear spins precess in phase within the transverse x-y plane, however, as a result of the fluctuating magnetic field caused by the random molecular motion, "flip-flop" transitions will occur, where the neighbouring spins will exchange energy states. As a result of these transitions, the phase coherence begins to be lost, with a decay in the magnetisation (M_{xy}) in the x-y plane occurring.[190] This relaxation process and therefore return to an equilibrium state, as illustrated in Figure 4.5, can be defined by Equation 4.5.

$$M_{xy}(t) = M_0(e^{-t/T_2}) \qquad \textbf{Equation 4.5}$$

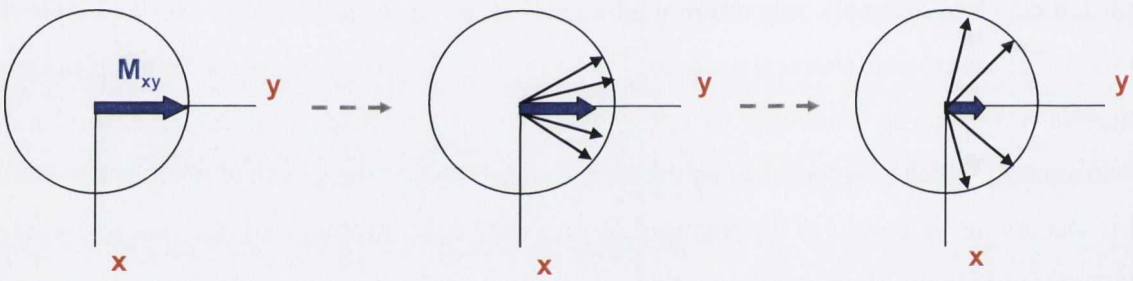

Figure 4.5: *Schematic representation of the spin-spin (transverse) relaxation process.*[191]

Both these processes, spin-lattice and spin-spin relaxation and their corresponding time constants T_1 and T_2, depend greatly on factors such as the external magnetic field (B_0) applied and the environment in which the nuclei is present. This provides the fundamental principle for the MRI technique, where the protons of the H_2O molecules in the various tissues return to equilibrium or relax at different rates, providing the contrast amongst different tissues and organs within the body.

4.3 Magnetic resonance imaging (MRI)

4.3.1 Relaxivity

Naturally when placed in the presence of a strong magnetic field (B_0), the proton nuclei from the H_2O molecules found within body tissue can become magnetised and align their nuclear spin along the B_0 field. When a 90° RF pulse is applied, the net magnetisation flips, with subsequent relaxation to the equilibrium state occurring using either the spin-

lattice or spin-spin process described in the previous section. With various tissues displaying different proton densities and relaxation rates ($1/T_1$ and $1/T_2$), a contrast and thus differentiation between these tissues can be made.[36, 183] However, as a result of the poor sensitivity of MRI, a method which would allow for a more significant contrast enhancement is often sought. This has lead to the use of MRI contrast agents which cause a dramatic variation of the H_2O proton relaxation rates, thus providing physiological information beyond that obtained in uncontrasted images.[184, 192] These agents can be paramagnetic, superparamagnetic or ferromagnetic and can shorten the relaxation times of the bulk water protons in close proximity. As illustrated in Figure 4.6, the dipolar magnetic interaction between the electronic magnetic moment of the contrast agent and the much smaller nuclear magnetic moments of the protons of the nearby H_2O molecules is the principle cause of this shorting of both T_1 and T_2. A contrast agent is characterised as either a "T_1 agent" or "T_2 agent", depending whether the reduction in the relaxation time caused by the presence of the contrast agent is greater for T_1 or T_2; T_1 agents provide a positive image contrast as the image signal intensity increases as a function of T_1 reduction, however, T_2 agents provide negative image contrast as the MRI signal decreases as a result of T_2 shortening.[193]

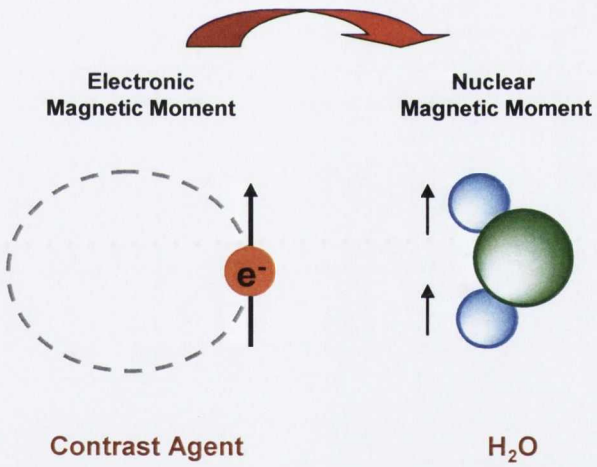

Figure 4.6: *Interaction of contrast agent with proton nuclei of H_2O molecules.*

The ability of a contrast agent to alter the relaxation rates of the proton nuclei is represented quantitatively as relaxivity ($mM^{-1}s^{-1}$), r_1 or r_2, where the subscript refers to either the longitudinal ($1/T_1$) or transverse ($1/T_2$) relaxation rate. As defined by Equation 4.6, it is the change in $1/T_1$ or $1/T_2$ normalised to the concentration of the contrast agent or metal ion [M][39]

$$r_{1,2} = \frac{\Delta(1/T_{1,2})}{[M]} \qquad \textbf{Equation 4.6}$$

Although there is a number of manganese and iron based contrast agents previously reported in the literature, the majority of contrast agents which are approved for clinical use are the T_1 Gd(III) based complexes.[35] As this chapter focuses on the development of similar Gd(III) agents, the remainder of this introduction will concentrate on various factors which bear a significant effect on the r_1 and therefore contrasting abilities of these systems.

4.3.2 Gd(III) based contrast agents

As a result of its seven unpaired electrons, Gd(III) is the most stable paramagnetic ion, which along with its symmetric S-state and therefore relatively long electronic relaxation time (T_{1e}) has the greatest potential of all Ln as a MRI contrast agent. However, as is the case with all Ln ions, the toxicity of the free Gd(III) metal must be recognised and therefore the use of thermodynamically and kinetically stable chelating ligands, which fulfil the high coordination number of these metal ions, is required. The high affinity of Gd(III) towards polyaminocarboxylic acids, either linear or cyclic, has been exploited, with highly stable Gd(III) complexes being formed (log K_{ML} > 20).[39] The first contrast agent approved for clinical use was Gd(III)-DTPA (Magnevist®), followed by Gd(III)-DOTA (Dotarem®) and Gd(III)-DTPA-BMA (Omniscan®), the structures of which are shown in Figure 4.7.[36]

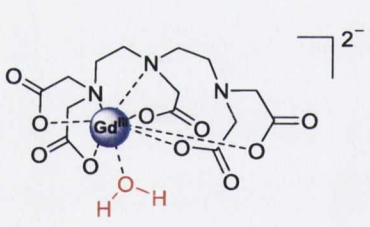

Magnevist®

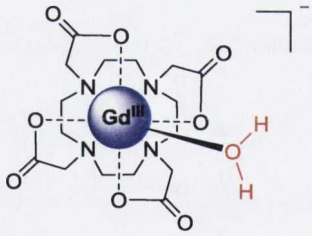

Dotarem®

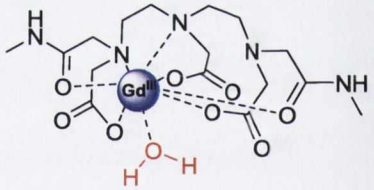

Omniscan®

Figure 4.7: *Structures of the clinically approved Gd(III) based contrast agents Magnevist®, Dotarem® and Omniscan®.*

Upon the introduction of a Gd(III) agent, the observed relaxation rate ($1/T_{i,obs}$) of the surrounding H_2O molecules is, as shown by Equation 4.7, the sum of the diamagnetic ($1/T_{i,d}$) and the paramagnetic relaxation rates ($1/T_{i,p}$), where the diamagnetic term corresponds to the relaxation rate of the solvent nuclei in the absent of the paramagnetic Gd(III) ion.

$$1/T_{i,obs} = 1/T_{i,d} + 1/T_{i,p} \quad (i = 1,2) \qquad \textbf{Equation 4.7}$$

As previously mentioned, due to the large number of unpaired electrons, the resulting strong local magnetic field around the paramagnetic Gd(III) centre provides a more efficient relaxation mechanism for the solvent nuclei. However, as this field reduces dramatically with

distance, specific chemical interactions and random translational diffusion, which bring the solvent H_2O molecules in close proximity to the metal ion, are important. Those H_2O molecules which are located in the first coordination sphere and as a result of complete H_2O or proton exchange with the surrounding bulk solvent molecules allow for the propagation of the paramagnetic effect are referred to as the inner sphere H_2O molecules. Depending on the rate of water/proton exchange, k_{ex}, the number of co-ordinated water molecules (q) and the metal to water proton distance (Gd-H), this inner sphere contribution can have a significant effect on a complex's overall relaxivity. There also exists an outer sphere contribution where the interaction with the Gd(III) ion is governed solely by translational diffusion of the bulk solvent molecules towards the paramagnetic centre. The final contribution which involves hydrogen bonded H_2O molecules is referred to the second sphere, however, due to the lack of understanding of its involvement in relaxivity, it is often not distinguished from the outer sphere contribution. Therefore, the overall relaxation rate enhancement ($1/T_{i,p}$) as a result of the paramagnetic Gd(III) ion is defined by Equation 4.8. [36, 39, 194]

$$1/T_{i,p} = (1/T_{ip})_{\text{inner sphere}} + (1/T_{ip})_{\text{outer sphere}} \qquad \textbf{Equation 4.8}$$

Another important factor which affects the overall relaxivity of these Gd(III) based contrast agents is rotational diffusion. Characterised by the correlation rotational time τ_R, this factor involves the speed of tumbling or rotation of the Gd(III) chelates in solution. For small-molecular weight Gd(III) complexes, their often fast rotation ($\tau_R \sim 0.1$ ns) can behave as the limiting factor for proton relaxivity. This has lead to the covalent or non covalent attachment of larger molecules such as dendrimers, polymers and proteins to the Gd(III) complexes which as a result of their much larger overall size and therefore larger τ_R, display an increase in their relaxivity.[35] However, it is important to note that this increase in relaxivity with slower rotation is field dependent, where at much higher magnetic fields, the relaxivity begins to decrease with increasing τ_R. This factor as well as those previously mentioned have been extensively investigated, leading to the development of more efficient Gd(III) based MRI imaging agents for *in vitro* and *in vivo* analysis.[192]

With the aim of this chapter to investigate novel Gd(III) cyclen based agents for detection of damaged bone structure, it is necessary to highlight any previously reported Gd(III) complexes, which have been used for bone structure analysis. The following section will therefore briefly summarise the most significant examples present in the literature.

4.4 Gd(III) MRI contrast agents for bone structure analysis

All the previously reported Gd(III) bone imaging agents have phosphoric acids incorporated into their ligand designs. For example the Gd(III) complexes of the acyclic phosphonate ligand EDTP (**74**) and DTPP (**75**) were the first set of examples proposed as potential bone targeting contrast agents by Bligh *et al.*[195] Initial studies involved relaxivity measurements of both complexes in the absence and presence of hydroxyapatite (HA), one of the main constituents of bone material. However, as a result of strong interaction of the phosphonate groups with HA, release of the Gd(III) metal ion from such ligand frameworks was occurring, demonstrating the extremely poor stability of these acyclic type ligands.

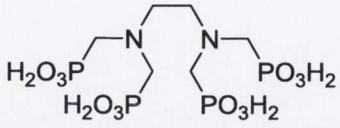

74

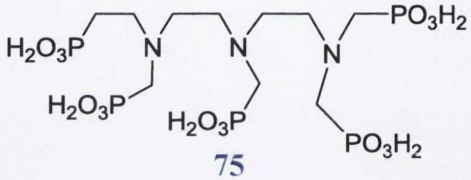

75

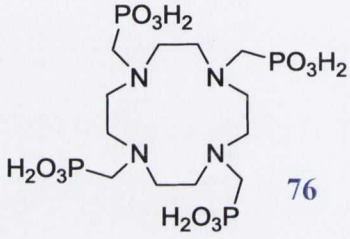

76

To overcome this problem of poor stability, Alves *et al.*[196] developed the macrocyclic DOTP ligand **76**, which once complexed to a Gd(III) metal ion, had no metal bound H_2O molecules ($q = 0$) in the inner coordination sphere, however, was still able to behave as a positive "T_1" MRI contrast agent due to the presence of the H_2O molecules in its second sphere. When the relaxivity modulation of this complex upon adsorption on to HA was investigated, another unforeseen problem occurred; where the ^1H relaxation enhancing ability was quenched due to expulsion of the second sphere H_2O molecules as a result of the strong phosphonate binding.

The greatest success was achieved by Lukes and co-workers, with their complexes incorporating the bis(phosphonic acid) moiety, which is known to seek calcified tissue with a high turnover (*i.e.* areas of natural growth and pathological changes).[197-200] This functionality has also been known to act as an antiresorptive agent in several types of bone diseases such as osteoporosis, Paget's disease and rheumatoid arthritis.[201] As shown by the ligands **77** – **79**, the introduction of an amide or phosphinic acid linkage between the bis(phosphonic acid) moiety and the cyclen framework ruled out the problem of second sphere H_2O molecule expulsion and also resulted in Gd(III) complexes with q values equal to one. All complexes displayed strong adsorption to HA, with for example the relaxivity of Gd(III) complex of **77**

being 24.0 $s^{-1}mM^{-1}$ at 20 MHz, which is 4.5 times higher then that seen for the free unadsorbed complex. One interesting observation was that when a slightly longer alkyl linker was used, as in the case of **78**, the enhancement in relaxivity upon adsorption on to HA was not as significant, with a value of *ca.* 11 $s^{-1}mM^{-1}$ at 20 MHz being measured. The authors suggests that the increased flexibility of the C_3 linker between the macrocycle and bis(phosphonic acid) moiety in ligand **78** could be the principle cause for this reduced response. The radioactive ^{177}Lu complexes of both **77** and **78** were also formed, with *in vivo* radioimaging studies in a rat confirming the potential of both complexes to target bone structure.

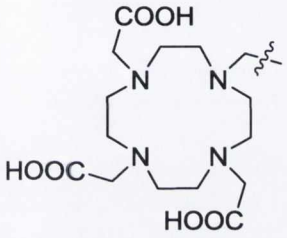

77

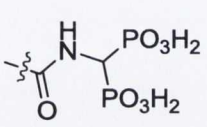

78

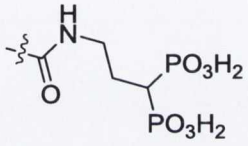

79

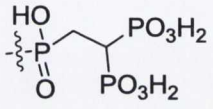

Although these complexes displayed a large enhancement in relaxivity upon adsorption to HA, no MRI imaging studies with bovine bone material has been reported to date. The ^{117}Lu complexes of **77** and **78** did confirm selective targeting of bone structure using radioimaging, however, the Gd(III) analogues have not been investigated. A potential drawback of using the extremely strong chelating bis(phosphonic acid) moiety is that the selectivity of these complexes could be limited. With such strong interaction towards bone structure, it is possible that the MRI contrast agent would attach to the majority of the bone surfaces, making distinction of damaged bone areas difficult. This potential selectivity problem welcomes a set of MRI imaging agents, where through fictionalisation with a slightly poorer chelating moiety, may prove useful for selective imaging of damaged bone structure, as the agent would show preferential localisation in the sites of damaged HA then at the undamaged healthy bone surfaces.

4.5 Objective of project

The principle aim of this project is to investigate the MRI imaging potential of several cyclen based Gd(III) contrast agents, which allow for the incorporation of the selective microdamage chelating iminodiacetate unit within their ligand frameworks. The Gd(III) complexes of ligands **58** and **69** will be formed, with the synthesis of two structurally similar ligands and their corresponding Gd(III) complexes discussed. With no requirement of a

sensitising antenna moiety for MRI imaging, the two new ligands **80** and **81**, have a similar design to **69**, however, the naphthalene pendant arm is replaced by an extra diethyl iminodiacetate group for **80** and a C_4 alkyl chain for **81**. The relaxivity of the hydrolysed Gd(III) complexes of all these ligands will be measured, with the effects of pH, Ca^{2+} ion concentration and the presence of various other biologically relevant metal ions and anions on the ^1H nuclei relaxation rates detailed. Finally, preliminary MRI imaging of damaged bone structure using these agents to provide a significant contrast from the undamaged bone matrix will be discussed.

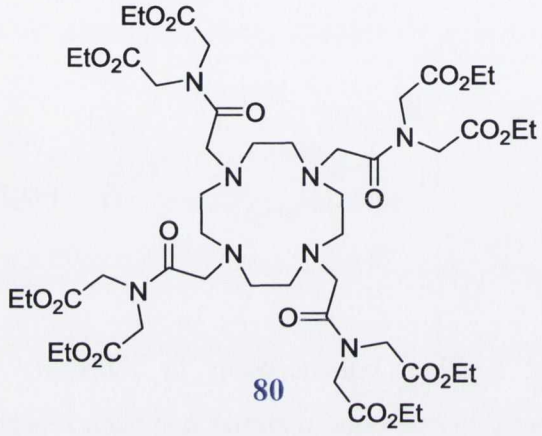

80

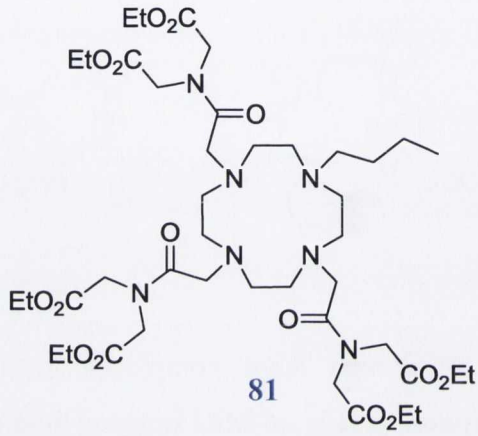

81

4.6 Synthesis and characterisation of ligands 80 and 81

With no requirement of an antenna moiety for MRI imaging and with great success previously observed for **Eu.69.Na** and **Tb.69.Na** for selective microdamage chelation, it was decided that the new ligand designs would be structurally similar to ligand **69**, however, the naphthalene moiety would be replaced by other pendant functional groups. As observed from the epifluorescence and confocal microscopy analysis in Chapter 3, an increase in the number of chelating iminodiacetate moieties had a significant effect on the contrasting abilities of these types of Ln complexes. Therefore for ligand **80**, an extra diethyl iminodiacetate moiety was used to replace the antenna functionality. It was anticipated that upon hydrolysis of this extra receptor unit, that an increase in selectivity for damaged bone structure may be gained. For ligand **81**, a simple alkyl chain was used instead of the naphthalene pendant arm. With the loss of one of the carbonyl functionalities, the Gd(III) complex of this ligand would potentially have two metal bound water molecules and therefore should display a much higher relaxivity value than the other $q = 1$ complexes.

The synthesis of **80**, as shown by Scheme 4.1, was carried out in one step, where **66** was reacted with 4.2 equivalents of **73**, using K_2CO_3 and KI in refluxing CH_3CN for 9 days. After reaction completion, the solvent was removed under reduced pressure and the resulting

orange oil re-dissolved in CH_2Cl_2. After filtration of the inorganic salts, purification of the crude product was carried out by alumina column chromatography using a gradient elution 100 to 95:5 CH_2Cl_2:CH_3OH. This purification method was repeated three times to give **80**, as a yellow viscous oil, in 40% yield.

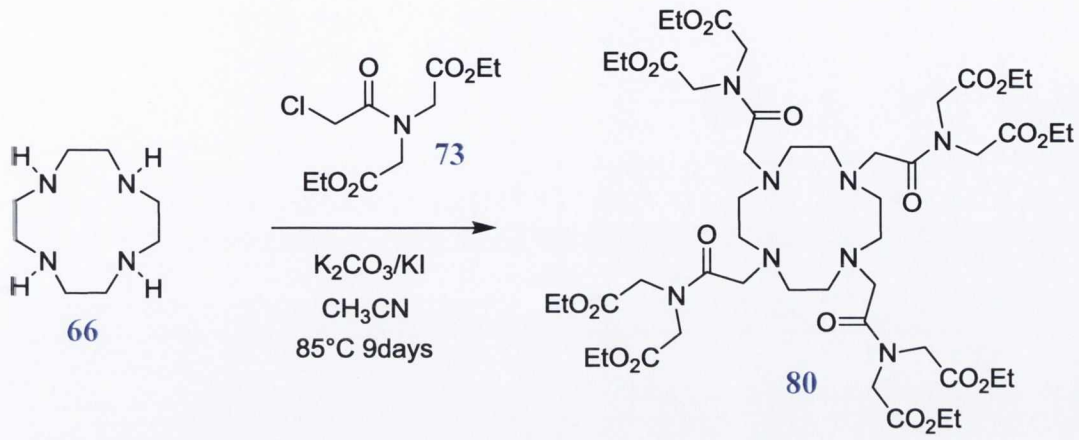

Scheme 4.1: *Synthetic pathway of ligand 80.*

As anticipated, the ^1H NMR spectrum of **80** in $CDCl_3$, as shown in Figure 4.8, displayed comparable resonances to those previously observed for the structurally similar ligand **69**. The ester CH_3 protons of the diethyl iminodiacetate moieties appeared as two sets of overlapping triplets with a total integration of twenty four, whereas the remaining $N(C\underline{H}_2)_2$ (16H) and the $CO_2C\underline{H}_2CH_3$ (16H) protons appeared as a series of crowded signals over the ppm range 4.0 – 4.2. The cyclen CH_2 (16H) protons along with the CH_2 (8H) protons which link the iminodiacetate moieties to the cyclen framework appeared as a multiplet of extremely broad overlapping peaks which resonated between the spectral range 2.0 – 3.6 ppm and with a total integration of twenty four. The appearance of the two separate triplet signals for the CH_3 units of the diethyl iminodiacetate moieties suggests loss of symmetry for these groups. This was verified using ^{13}C NMR, where two distinct carbon resonances for these CH_3 functionalities were observed at 14.14 and 14.19 ppm. Other conventional methods such as IR spectroscopy and MALDI-TOF analysis were used to characterise ligand **80** with the presence of a peak at m/z = 1111.53, corresponding to a $[\mathbf{80}+Na]^+$ species in solution.

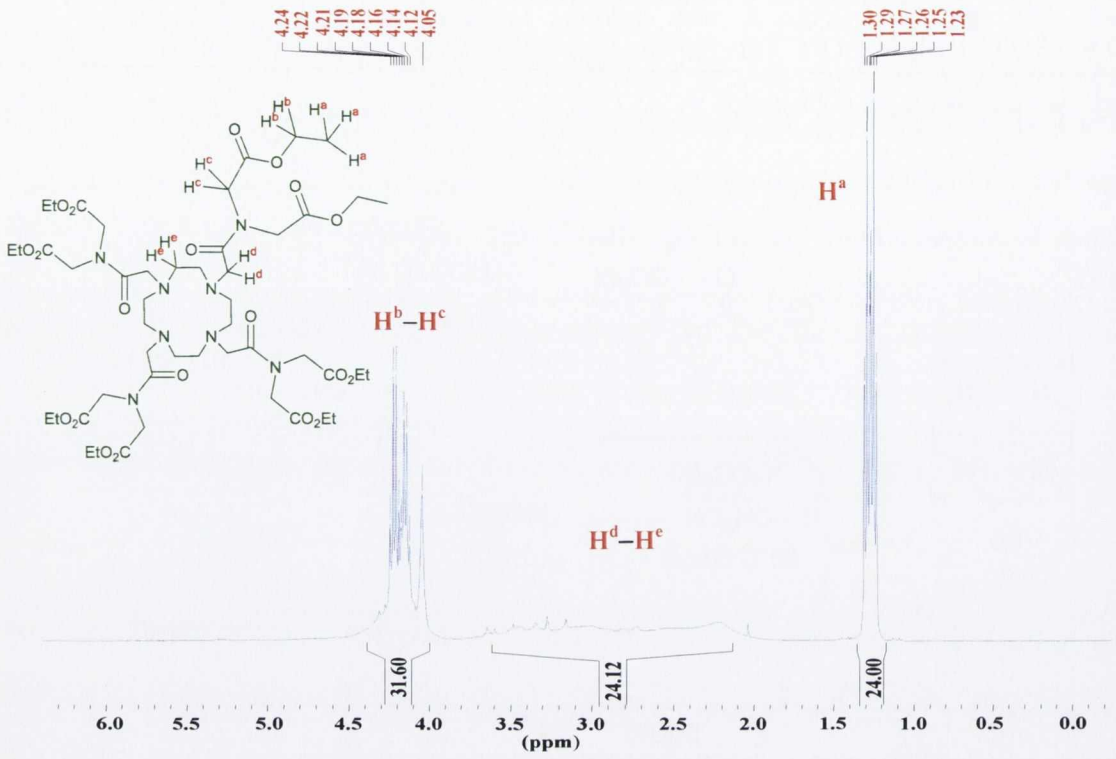

Figure 4.8: *The ^1H NMR spectrum (400 MHz, $CDCl_3$) of ligand 80.*

In the initial design stages of a suitable ligand, which when complexed to the Gd(III) ion would allow for the presence of two metal bound water molecules, it was attempted to tri functionalise the cyclen framework with the diethyl iminodiacetate pendant arms (**73**), leaving one of the cyclen amine sites unalkylated. However, significant problems were encountered during the purification stages, with separation of the tri functionalised product from the tetra substituted species proving difficult. This led to the design of ligand **81**, whose first synthetic step involved mono alkylating the cyclen framework with a short C_4 alkyl chain. This was achieved, as shown in Scheme 4.2, by refluxing overnight four equivalents of **66** with one equivalent of 1-bromobutane **82** using Et_3N in freshly distilled $CHCl_3$.[169] As previously discussed in Chapter 2 for the synthesis of ligand **58** and **69**, the Et_3N and any unreacted **66** was successfully removed by extraction with 1 M NaOH, to give the mono alkylated product **83** as a clear oil, in 79% yield (Figure A2.1). Functionalisation of the remaining cyclen amino sites was achieved by refluxing one equivalent of **83** with 3.2 equivalents of **73** using K_2CO_3 and KI in CH_3CN for 6 days. After reaction completion (followed by TLC analysis), the solvent was removed under reduced pressure, with the subsequent dark orange oil re-dissolved in CH_2Cl_2. Removal of the inorganic bases was achieved by filtration, with purification being carried out by alumina column

chromatography using an elution gradient 100 to 80:20 CH_2Cl_2:CH_3OH. The desired product **81** was obtained as a viscous yellow oil in 29% yield.

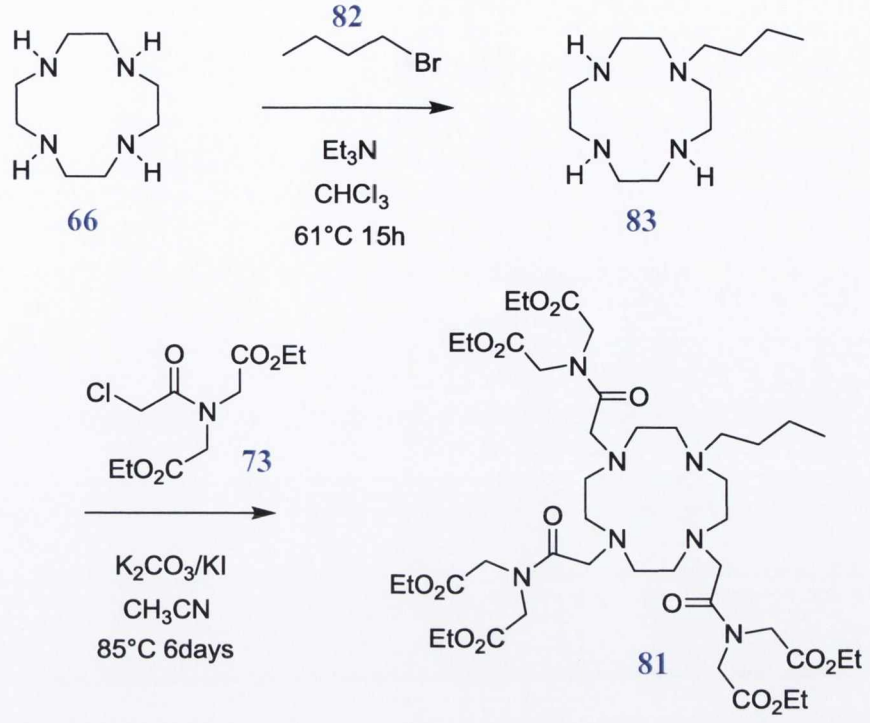

Scheme 4.2: *Synthetic pathway of ligand **81**.*

The ^{1}H NMR ($CDCl_3$, 400 MHz) spectrum of **81**, as shown in Figure 4.9, displayed the characteristic resonances for these types of diethyl iminodiacetate functionalised cyclen structures. The ester CH_3 protons (18H) of the diethyl pendant arms as well as two of the CH_2 groups (4H) from the alkyl chain appeared as a series of crowded peaks between the ppm range 1.2 – 1.4. The only signal from the C_4 alkyl group which did not overlap with other peaks from the ligand structure was the CH_3 resonance which appeared as a multiplet between 0.8 and 0.95 ppm. The sixteen cyclen protons as well as the six protons from the three CH_2 groups linking the pendant units to the cyclen framework and the two protons from the remaining CH_2 group of the alkyl chain were observed as a broad multiplet of overlapping peaks in the spectral range 2.1 – 3.4 ppm. Finally, the twenty four protons from the CH_2 groups of the three diethyl iminodiacetate functionalities resonated between 4 and 4.3 ppm. It is clear from the ^{1}H NMR spectrum of **81**, that other then the CH_3 resonance of the alkyl group, all the other CH_2 groups are difficult to see due to overlapping, however, by comparison with the ^{1}H NMR of the mono alkylated product **83**, an estimation of the ppm in which the signals for these groups appeared could be made (Figure A2.1). ^{13}C NMR was also employed to determine successful formation of **81**, with ESMS confirming the presence of a peak at m/z = 916.52 which corresponds to a $[\mathbf{81}+H]^+$ species in solution.

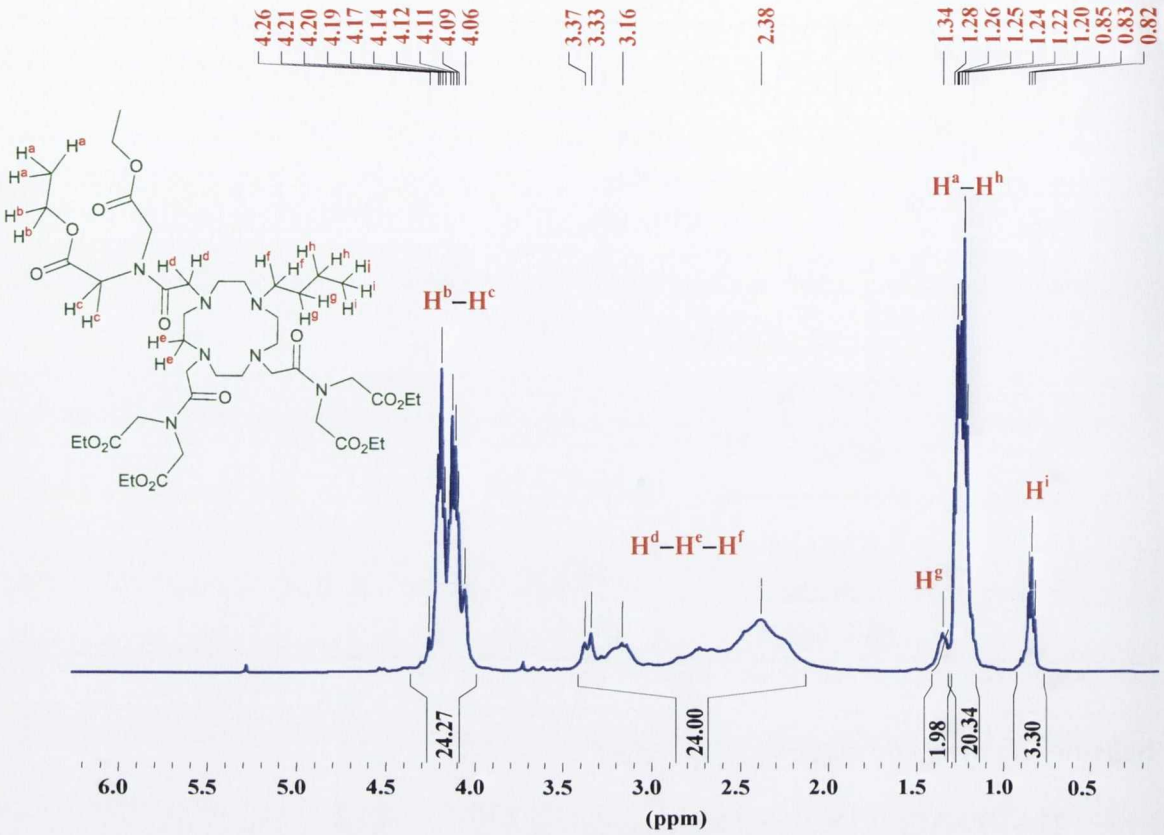

Figure 4.9: *The ^{1}H NMR spectrum (400 MHz, $CDCl_3$) of ligand 81.*

4.7 Synthesis and characterisation of Gd.58.Na, Gd.69.Na, Gd.80.Na and Gd.81.Na

A similar Ln complexation procedure to that previously described in Chapter 2 was employed to allow for successful formation of the Gd(III) complexes of ligands **58**, **69**, **80** and **81**. This involved refluxing, under an inert atmosphere, each ligand with one equivalent of $Gd(CF_3SO_3)_3$ in CH_3CN overnight to give **Gd.58**, **Gd.69**, **Gd.80** and **Gd.81** in 93%, 88% 96% and 94% yield, respectively. It is important to note that due to the presence of the Gd(III) metal ion, NMR spectra for these complexes could not be attained. Therefore, IR spectroscopy became the most significant characterisation method, where shifts in the amide carbonyl stretching frequencies were used to determine successful Gd(III) complexation. It is important to note that for all these complexes, the chelating iminodiacetate functionalities are protected as their ethyl ester forms, therefore no shifts in the ester carbonyl bands as a result of metal chelation is expected. A summary of all the relevant carbonyl shifts for these complexes and their corresponding ligands are shown below in Table 4.1.

Table 4.1: *IR stretching frequencies of the carbonyl bands in* **58**, **Gd.58**, **69**, **Gd.69**, **80**, **Gd.80**, **81** *and* **Gd.81**.

Ligand/Gd(III) Complex	Amide C=O (cm^{-1})	Ester C=O (cm^{-1})
58	**1646**	**1740**
Gd.58	1616	1737
69	**1660**	**1736**
Gd.69	1603	1737
80	**1659**	**1735**
Gd.80	1603	1737
81	**1656**	**1738**
Gd.81	1603	1739

HRMS using MALDI TOF analysis also confirmed formation of the Gd(III) complexes for each ligand, with the expected isotopic distribution pattern being observed. Figure 4.10 shows the mass spectra of both **Gd.80** and **Gd.81** displaying the *m/z* peak $[M+2(CF_3SO_3)]^+$ at 1544.38 and 1371.35, respectively. The mass spectra of **Gd.58** and **Gd.69** are shown in Figure A2.2.

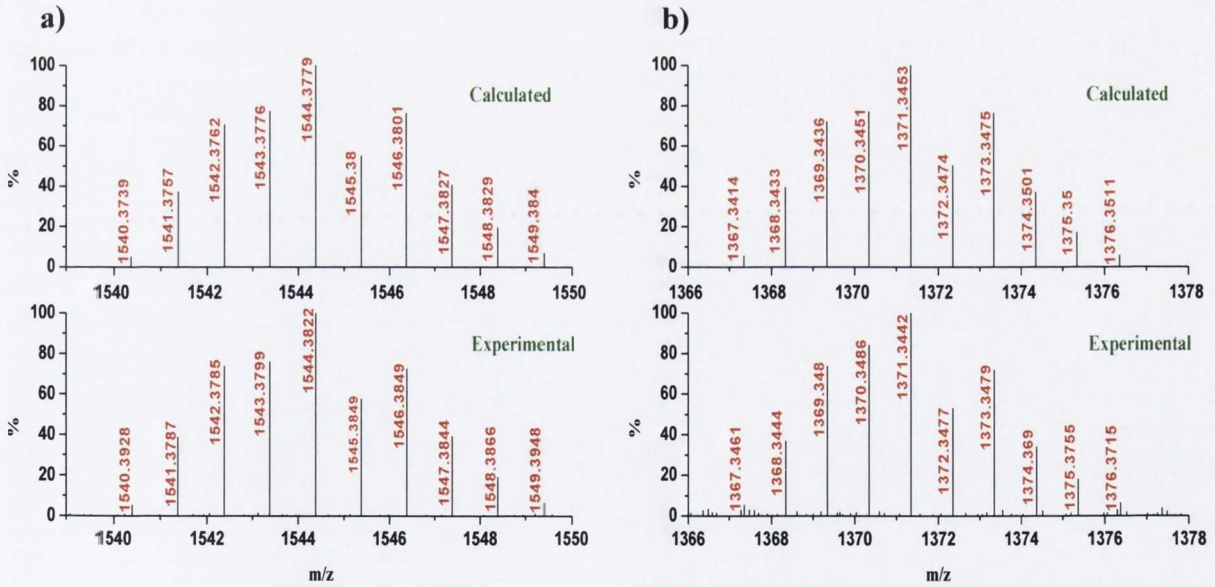

Figure 4.10: *HRMS using MALDI-TOF analysis of a)* **Gd.80** *and b)* **Gd.81** *displaying the expected* ^{157}*Gd(III) isotopic distribution pattern for the* $[M+2(CF_3SO_3)]^+$ *species.*

With all complexes successfully synthesised, the next step involved the synthetic conversion of the diethyl iminodiacetate groups to the microcrack specific disodium iminodiacetate functionalities, using the base hydrolysis procedure previously discussed in Chapter 2. This involved refluxing each ligand in the presence of NaOH in a mixed CH_3OH:H_2O (10:1 v/v) solution for 6 h. Upon reaction completion (followed by TLC), the

solvent was removed under reduced pressure and the resulting orange residues re-dissolved in a minimal amount of cold CH_3OH. After filtration of the fine precipitate through a micro syringe, the CH_3OH solvent was evaporated to dryness, and the residue dissolved in a minimal amount of H_2O and precipitated from EtOH to give **Gd.58.Na**, **Gd.69.Na**, **Gd.80.Na** and **Gd.81.Na** in 81%, 74%, 84% and 63% yield, respectively. IR spectroscopy was again the principle characterisation technique used to confirm successful hydrolysis, with the disappearance of the ester carbonyl shifts and the subsequent appearance of much broader carboxylate stretching frequencies, which often overlapped with the amide carbonyl resonances. The wavenumbers where these stretches appeared were 1603 cm^{-1}, 1592 cm^{-1}, 1590 cm^{-1} and 1591 cm^{-1} for **Gd.58.Na**, **Gd.69.Na**, **Gd.80.Na** and **Gd.81.Na**, respectively. The expected $^{157}Gd(III)$ isotopic distribution pattern for all complexes was also observed using MALDI-TOF analysis (Figure A2.3).

In order to verify that **Gd.80.Na** and **Gd.81.Na** have q values of one and two, respectively, it was necessary to synthesis the Eu(III) analogues of these complexes. Through direct excitation of the Eu(III) metal ion at 395 nm, the luminescence excited state lifetimes of **Eu.80.Na** and **Eu.81.Na** were measured both in H_2O and D_2O. With values of $\tau_{O\text{-}H} = 0.62 \pm 0.01$ ms and $\tau_{O\text{-}D} = 2.17 \pm 0.01$ ms being recorded for **Eu.80.Na** and using Equation 1.2, a q value of *ca.* 1 ± 0.25 was calculated, indicating one metal bound inner sphere water molecule. For the case of **Eu.81.Na**, a q value of 2 ± 0.25 was calculated from the $\tau_{O\text{-}H} = 0.36 \pm 0.01$ ms and $\tau_{O\text{-}D} = 1.29 \pm 0.01$ ms lifetime values measured, confirming that the Eu(III) metal ion had two inner sphere H_2O molecules. The lifetime spectra for **Eu.81.Na** in H_2O and D_2O, both fit to a mono exponential decay are shown below in Figure 4.11.

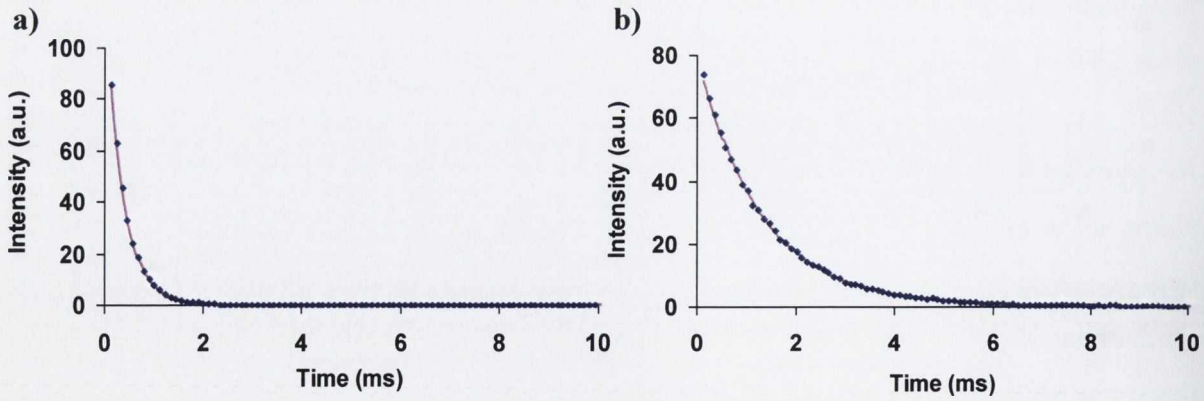

Figure 4.11: *Luminescence decay of complex **Eu.81.Na** in a) H_2O and b) D_2O fit to a mono exponential decay (–).*

With all Gd(III) complexes synthesised, characterised and an understanding of the number of metal bound H_2O molecules found within their inner coordination spheres, the next stage was to investigate the MRI activity of these complexes by measuring their spin

lattice relaxation times (T_1) at several magnetic fields (B_0). From these measurements, determination of relaxivity values (r_1) for **Gd.58.Na**, **Gd.69.Na**, **Gd.80.Na** and **Gd.81.Na** was obtained. The following section will therefore discuss the T_1 measurements carried out for all the Gd(III) chelates at high magnetic fields of 400 MHz and 600 MHz using an inversion-recovery NMR sequence.

4.8 Measurement of T_1 and r_1 for all Gd(III) complexes at 400 MHz and 600 MHz

All high field T_1 measurements were carried out in collaboration with Dr John O'Brien (NMR technician, TCD) using an inversion-recovery NMR sequence. This method is a multi-pulse experiment in which the net magnetisation (M_0) of the ^1H nuclei of the H_2O molecules aligned along the external B_0 field in the NMR tube are first inverted using a 180° pulse ("inversion"). A delay time (τ) is set to allow the ^1H nuclei to relax back ("recovery") to their more stable equilibrium state before a 90° RF reading pulse is applied to measure the extent of relaxation.[202] The experiment is repeated using various τ values, with more efficient recovery of the net magnetisation occurring at longer τ. As shown by the illustration in Figure 4.12, if short τ values are used, the M_0 will only have slightly inverted back to its equilibrium position, with a "negative" spectrum being obtained.

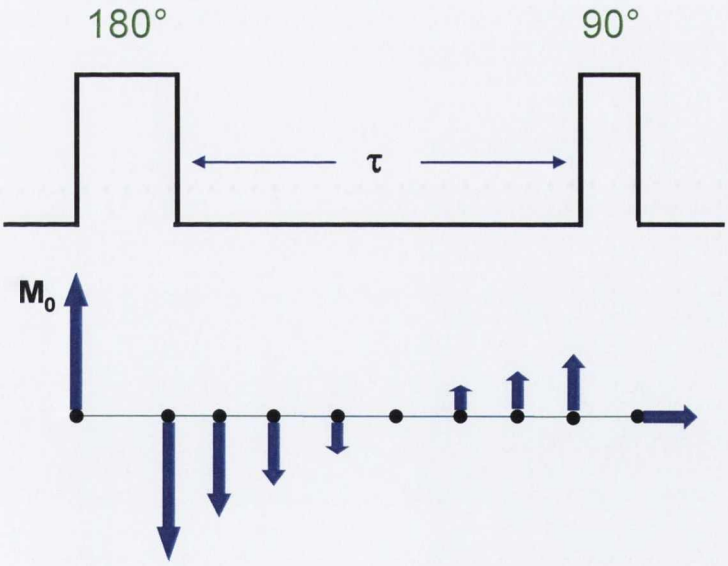

Figure 4.12: *Illustration of an inversion-recovery NMR sequence employed for the T_1 measurements at high field (400 MHz and 600 MHz).*[202]

A series of inversion-recovery NMR spectra with increasing values of τ are acquired from these experiments, where for $\tau = 0$ an upside down spectrum, with the H_2O resonance at its maximum height being observed. As the delay is increased, this inverted peak will become less intense, pass through zero and finally become positive, with a fully upright H_2O resonance with maximum height being displayed at long τ times. By plotting the integration

of the H_2O resonances as a function of time τ, and fitting the data to Equation 4.4 using the data analysis program Origin Pro 8.1, an accurate determination of T_1 can be obtained. In the absence of any Gd(III) agent, the relaxation rate ($1/T_{1d}$, d = diamagnetic) of the ^1H nuclei of the H_2O molecules is *ca.* 0.08 s^{-1} at 25 °C, a value which is dramatically enhanced when a Gd(III) chelate is introduced into the NMR tube. It is important to note, as previously described by Equation 4.7, $1/T_{1d}$ must be subtracted from the relaxation rate obtained using the inversion-recovery method ($1/T_{1obs}$) to give the paramagnetic relaxation rate ($1/T_{1P}$) for **Gd.58.Na**, **Gd.69.Na**, **Gd.80.Na** and **Gd.81.Na**. An example of a plot of the integrations of the H_2O resonance as a function of time τ for **Gd.69.Na** using an external field (B_0) of 400 MHz is shown in Figure 4.13. By fitting the data to Equation 4.4, a T_{1obs} value of 0.0851 s and a subsequent $1/T_{1obs}$ value of 11.75 s^{-1} were obtained. On subtracting the diamagnetic relaxation rate ($1/T_{1d}$) of 0.08 s^{-1} (Equation 4.7), a $1/T_{1p}$ of 11.67 s^{-1} and therefore a T_{1p} of 0.086 s for **Gd.69.Na** was measured.

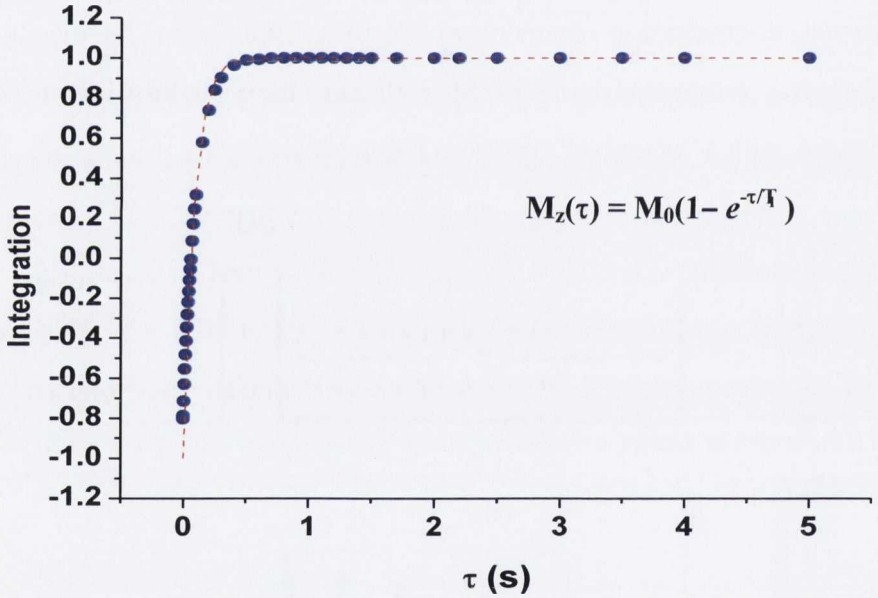

Figure 4.13: *Plot of integration of the H_2O resonances as a function of delay time τ using the inversion-recovery NMR sequence in an external magnetic field of 400 MHz at 25°C in the presence of 2.6 mM* ***Gd.69.Na*** *in D_2O. The data was fit using the equation $M_z(\tau) = M_0(1 - e^{-\tau/T_1})$.*

This inversion-recovery NMR method was applied to determine the paramagnetic relaxation times (T_{1p}) of all the Gd(III) complexes using external magnetic fields (B_0) of 400 MHz and 600 MHz (Figure A2.4). A summary of all the T_{1p} values obtained and the concentrations for the Gd(III) complexes used are shown below in Table 4.2.

Table 4.2: *T_{1p} values measured for Gd.58.Na, Gd.69.Na, Gd.80.Na and Gd.81.Na at 400 MHz and 600 MHz using an inversion-recovery NMR method at 25 °C.*

Complex	Conc (mM)	T_{1p} at 400 MHz (s)	T_{1p} at 600 MHz (s)
Gd.58.Na	3.2	0.058	0.066
Gd.69.Na	2.6	0.086	0.092
Gd.80.Na	2.8	0.088	0.095
Gd.81.Na	2.1	0.097	0.124

As the rate of relaxation of the ^1H nuclei is extremely dependant on concentration of the Gd(III) chelate present, it was necessary that before calculation of r_1 using Equation 4.6 and the T_{1p} values shown in Table 4.2, a method for accurate determination of the complex's concentration in the solution was required. The bulk magnetic susceptibility shift technique previously reported by Peters and co-workers was employed, where through exploitation of the shift characteristics of the Gd(III) metal ion, an accurate determination of the complex's concentration can be made.[203] The technique involved using two NMR tubes, one which had the non coordinating probe 1,4-dioxane in D_2O and the other which had both the Gd(III) complex of interest and the probe. By measuring the Gd(III) induced shift of the probe's ^1H NMR resonance (Δ_x) and using Equation 4.9, the concentration of the Gd(III) chelate in $molL^{-1}$ can be determined. The parameters T and μ_{eff} are the absolute temperature and effective magnetic moment for the Gd(III) metal ion (7.94), respectively.

$$\Delta_{eff} = \frac{4\pi c}{T}\left(\frac{\mu_{eff}}{2.84}\right)^2 \times 10^3 \qquad \textbf{Equation 4.9}$$

With the exact concentrations of the Gd(III) complexes known (Table 4.2), the relaxivity values (r_1) of **Gd.58.Na**, **Gd.69.Na**, **Gd.80.Na** and **Gd.81.Na** were calculated at both 400 MHz and 600 MHz using Equation 4.6. It is important to note that all the previous T_1 measurements were carried out in D_2O, therefore to determine the expected r_1 in H_2O and taking the viscosity difference between D_2O and H_2O into account, the r_1 values obtained from these D_2O measurements need to be divided by a factor of 1.24.[204] Table 4.3 summaries the expected r_1 values in H_2O for all the Gd(III) complexes.

Table 4.3: *Expected relaxivity values (r_1, $s^{-1}mM^{-1}$) in H_2O of Gd.58.Na, Gd.69.Na, Gd.80.Na and Gd.81.Na at 400 MHz and 600 MHz at 25 °C.*

Complex	r_1 at 400 MHz ($s^{-1}mM^{-1}$)	r_1 at 600 MHz ($s^{-1}mM^{-1}$)
Gd.58.Na	4.3	3.8
Gd.69.Na	3.6	3.3
Gd.80.Na	3.2	2.9
Gd.81.Na	3.9	3.1

The expected decrease in r_1 at higher magnetic fields is evident for each complex, with **Gd.58.Na** displaying the highest r_1 values overall. However, one important observation from these studies was that the r_1 measurements for **Gd.81.Na**, which has two metal bound water molecules, were much lower than expected, with values in a similar range to those measured for the q = 1 complexes. To investigate a potential cause for these low r_1 measurements for **Gd.81.Na** and to determine the T_{1p} and thus relaxivity profile of all the Gd(III) chelates at lower magnetic fields (10 KHz – 10 MHz), the fast field-cycling NMR method was employed, the results from which are described in the following section.

4.9 Measurement of r_1 for all the Gd(III) chelates at low magnetic fields

Unlike the high field NMR studies described above, fast field-cycling NMR relaxometry allows the measurements of the longitudinal relaxation times (T_1) over a wide range of low magnetic fields (B_0) by rapidly switching the B_0 field electronically to any desired value in a short time frame (ms), while maintaining the high field stability and homogeneity required for NMR. A Nuclear Magnetic Relaxation Dispersion (NMRD) profile, which is a plot of the r_1 values as a function of the Larmor frequency or magnetic field on a logarithmic scale can be attained from such measurements.[36, 202] All field cycling relaxometry experiments were preformed on a Spinmaster FFC-2000 Fast Field-Cycling NMR Relaxometer (Stelar; Mede, Italy) in collaboration with Dr Dermot Brougham in the School of Chemical Sciences, Dublin City University (DCU). The NMRD profiles for **Gd.58.Na**, **Gd.69.Na**, **Gd.80.Na** and **Gd.81.Na** measured in H_2O at pH 7.4 (20 mM HEPES, 135 mM KCl) at 25 °C are shown below in Figure 4.14.

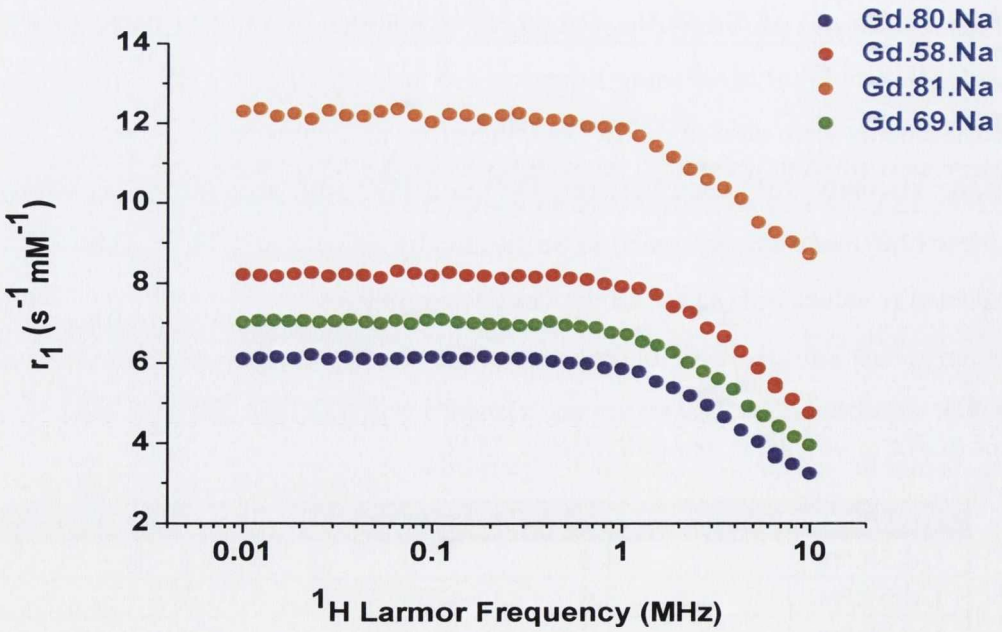

Figure 4.14: *The ^1H NMRD profiles for **Gd.58.Na** (3.5 mM), **Gd.69.Na** (2.1 mM), **Gd.80.Na** (2.2 mM) and **Gd.81.Na** (2.06 mM) at pH 7.4 (20 mM HEPES, 135 mM KCl) and 25 °C.*

All complexes displayed the characteristic NMRD profile which is typically observed for low-molecular weight Gd(III) complexes with either one or two inner sphere water molecules.[35, 36, 39] Unlike that seen with the high field measurements, **Gd.81.Na** showed much higher relaxivity values (*ca.* 50%) then the $q = 1$ complexes at all magnetic fields measured. Another interesting feature from these measurements was that a reduction in the r_1 values were observed when the pendant arms around the macrocyclic cyclen framework were replaced with the iminodiacetate chelating functionalities, where for example **Gd.80.Na**, which has four of these pendant moieties, displayed the lowest relaxivities of all the complexes studied. One possible suggestion for such a response could be related to the increase in negative charge and steric bulk associated with these iminodiacetate groups, which could limit the access of the bulk solvent water molecules to the Gd(III) centre.

To verify the fast molecular rotation of such small Gd(III) chelates in solution, the paramagnetic longitudinal relaxation times (T_{1p}) of all complexes were measured at 30 MHz, 45 MHz and 60 MHz using a re-conditioned Bruker WP80 electromagnet, with the r_1 values obtained summarised in Table 4.4. With no increase in r_1 displayed for any of the Gd(III) chelates and therefore the absence of the characteristic "hump" in the NMRD profile, which is often observed for complexes which display slow rotation, confirmed that **Gd.58.Na**, **Gd.69.Na**, **Gd.80.Na** and **Gd.81.Na** undergo rapid molecular reorientation.

Table 4.4: *Relaxivity values (r_1, $s^{-1}mM^{-1}$) in H_2O (20 mM HEPES, 135 mM KCl) of **Gd.58.Na**, **Gd.69.Na**, **Gd.80.Na** and **Gd.81.Na** at 30 MHz, 45 MHz and 60 MHz at 25 °C.*

Complex	*r_1 at 30 MHz ($s^{-1}mM^{-1}$)*	*r_1 at 45 MHz ($s^{-1}mM^{-1}$)*	*r_1 at 60 MHz ($s^{-1}mM^{-1}$)*
Gd.58.Na	**4.21**	**4.17**	**4.09**
Gd.69.Na	**3.60**	**3.54**	**3.50**
Gd.80.Na	**3.01**	**3.02**	**3.00**
Gd.81.Na	**8.48**	**8.46**	**8.45**

With no unusual features being observed in the NMRD profiles of these complexes and with similar trends to other previously reported Gd(III) complexes with amido oxygen donor atom groups being displayed, no fitting of the NMRD data was carried out.[69, 205] The next stage was to investigate the effect on the relaxivity of these Gd(III) chelates as a function of pH. The following section will therefore detail these pH studies, with any dependence in r_1 within the physiological pH window highlighted.

4.10 pH effect on r_1 for Gd.58.Na, Gd.69.Na, Gd.80.Na and Gd.81.Na

In order to investigate any possible changes in T_{1p} and subsequently r_1 for all the Gd(III) chelates as a function of pH, pH titrations were carried out in H_2O using 0.1 M NEt_4ClO_4

(TEAP) in order to maintain a constant ionic strength. The acid and base used for these titrations were $HClO_4$ and NEt_4OH, respectively. The concentration of each Gd(III) complex investigated was determined using the bulk susceptibility shift technique previously described. The pH of the samples were adjusted at first to *ca.* pH 12 using NEt_4OH, and, after each T_1 measurement at 10 MHz, the sample pH was lowered by the addition of small quantities of $HClO_4$. On completion of each titration, the Gd(III) complex concentration was again measured to ensure that it was not altered by the additions made. The pH relaxivity profiles at 10 MHz for the $q = 1$ tetraamide complexes **Gd.58.Na**, **Gd.69.Na** and **Gd.80.Na** are shown below in Figure 4.15.

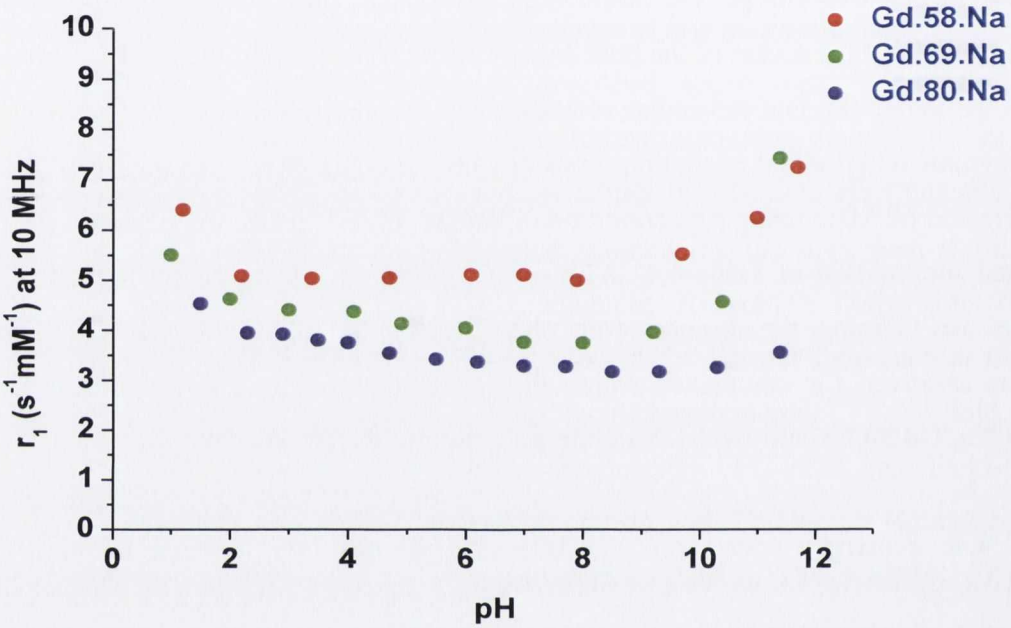

Figure 4.15: *The relaxivity pH profiles of **Gd.58.Na** (3.3 mM), **Gd.69.Na** (2.4 mM) and **Gd.80.Na** (2.4 mM) recorded at 10 MHz and 25 °C.*

The profiles of **Gd.58.Na** and **Gd.69.Na** are typical of what has previously been observed for tetraamide derivates of DOTA, which are essentially flat between pH 2 – 9 with an increase in relaxivity being observed at very basic and acidic regions of the pH scale.[62, 205, 206] The enhanced relaxivity at high pH has been ascribed to an increase in the rate of prototropic exchange between the protons of the bound water molecule and the coordinating amide. Verification of this can be seen by evaluation of the pH profile of **Gd.80.Na**, which displayed no significant relaxivity enhancement below pH 9, with the absence of any N-H amide group suggested as a probable cause for this response. For all three complexes below pH 2, an increase in the r_1 values were observed, suggesting successful acid catalysed prototropic exchange. The work of Parker and co-workers has demonstrated that the counter ions (CF_3SO_3) for tetraamide based complexes are closely associated with the Gd(III) metal centre, occupying space above the co-ordinated water molecule. However, they have also

shown that this strong ion pair interaction becomes progressively weaker as the pH is lowered, with complete break up occurring below pH 2. This has been suggested to provide a more efficient pathway for water proton exchange from the inner co-ordination sphere to the bulk and thus helps explain relaxivity enhancement in acidic media.[62, 205] The possibility of acid catalysed dissociation of the Gd(III) metal for **Gd.58.Na**, **Gd.69.Na** and **Gd.80.Na** was eliminated by the fact that a decrease in the r_1 values for all complexes were observed as the pH was increased to pH 2 again.

As shown in Figure 4.16, a very different pH relaxivity profile was observed for the *q* = 2 complex **Gd.81.Na**, where no modulation in r_1 resulted between pH 5.5 – 7.5, however, a large increase and decrease was displayed below pH 5.5 and above pH 7.5, respectively.

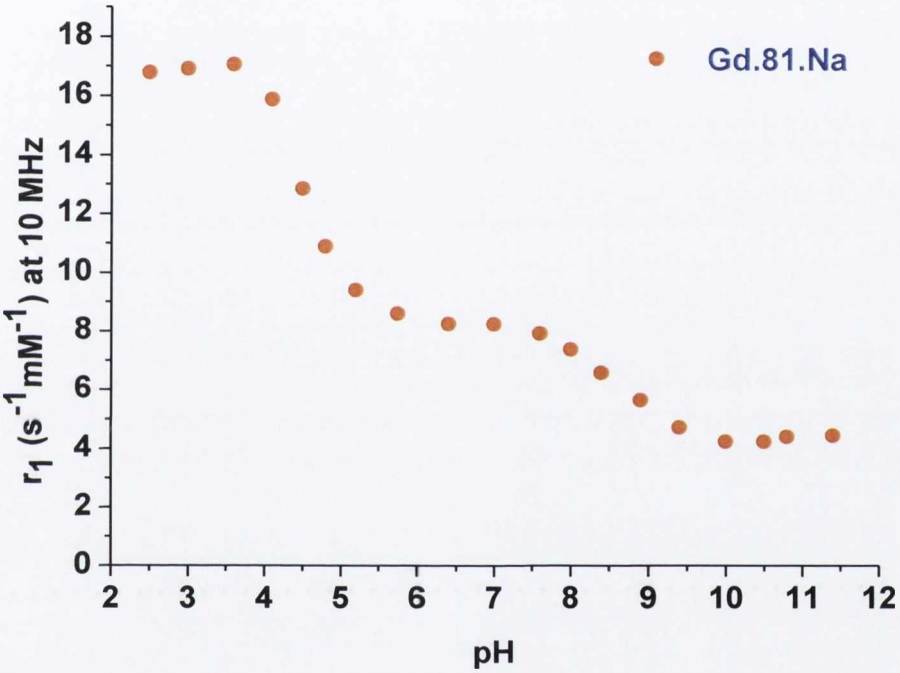

Figure 4.16: *The relaxivity pH profile of **Gd.81.Na** (1.5 mM) recorded at 10 MHz and 25 °C.*

At pH 3, the r_1 value recorded for **Gd.81.Na** was 16.9 $s^{-1}mM^{-1}$, which is 51% higher than the 8.6 $s^{-1}mM^{-1}$ value measured at pH 5.5. This pH response is identical to that measured for a heptadentate DO3A-like complex previously reported by Terreno *et al.*[207] It has been suggested for such heptadentate based complexes, that acid-catalysed demetallation of the Gd(III) metal is the principle cause for the large increase in relaxivity at low pH. In a more alkaline environment the r_1 value for **Gd.81.Na** was reduced by 49%, with a relaxivity of 4.3 $s^{-1}mM^{-1}$ being measured at pH 10.5. Based on reported literature for heptadentate based complexes, formation of ternary adducts with anionic species like carbonate (dissolved CO_2) and hydroxide anions within this pH range, which can result in displacement of the metal bound water molecule(s), has a dramatic effect on relaxivity of the Gd(III) chelate.[208] Confirmation of this was gained by measuring the lifetimes of the Eu(III) analogue **Eu.81.Na**

in both H_2O and D_2O at pH 12. With values of $\tau_{O\text{-}H} = 0.47 \pm 0.01$ ms and $\tau_{O\text{-}D} = 1.47 \pm 0.01$ ms being recorded for **Eu.81.Na** and using Equation 1.2, a *q* value of *ca.* 1.4 ± 0.25 was calculated, suggesting possible displacement of a metal bound water molecule with a hydroxide anion. The decrease observed in r_1 at high pH values may also help explain the much lower than expected relaxivity values measured for **Gd.81.Na** at high fields (400 MHz and 600 MHz) using the inversion recovery NMR method (Section 4.8). These measurements were carried out in D_2O, which as result of its more basic pH value of 8.6 may have resulted in T_{1p} and therefore r_1 values which are much lower than what would be obtained at pH 7.4. From the pH profile shown in Figure 4.16, a 35% reduction in r_1 is measured at pH 8.6 in comparison to that recorded at pH 7.4. This did not occur for the **Gd.58.Na**, **Gd.69.Na** and **Gd.80.Na**, as these complexes displayed pH independence at pH 8.6.

Overall all the Gd(III) complexes investigated displayed pH independence within the important physiological pH range, with any modulations in the r_1 values measured at 10 MHz, occurring in more acidic and basic regions of the pH scale. As these complexes are to be used for selective detection of damaged bone structure, where high exposure of Ca^{2+} ions occur, any effect in relaxivity as a function of Ca^{2+} ion concentration needed to be investigated. The following section will therefore detail any effect on the paramagnetic longitudinal relaxation times (T_{1p}) and therefore r_1 of these Gd(III) chelates in the presence of this metal ion.

4.10.1 Effect on r_1 for Gd.58.Na, Gd.69.Na, Gd.80.Na and Gd.81.Na in the presence of Ca^{2+} ions

In order to investigate any effect on the r_1 values of **Gd.58.Na**, **Gd.69.Na**, **Gd.80.Na** and **Gd.81.Na** upon the addition of Ca^{2+} ions to the solution, a series of titrations were carried out where various aliquots of $Ca(CH_3COO)_2$ were added to a known concentration of each of the Gd(III) complexes, with a T_1 measurement at 10 MHz being recorded after a 3 min mixing period. As previously discussed in Chapter 2 (Section 2.10 and 2.18), the luminescent analogues of **Gd.58.Na** and **Gd.69.Na** displayed no significant modulation in their phosphorescence properties as a function of low Ca^{2+} concentration. However, it was unknown what effect Ca^{2+} ions may have on the relaxivity values of these complexes. The relaxivity profiles of all the Gd(III) complexes as a function of Ca^{2+} equivalents at 10 MHz are shown below in Figure 4.17. It is evident from these measurements that up to a concentration of *ca.* 0.1 M Ca^{2+}, no significant effect on r_1 for **Gd.58.Na**, **Gd.69.Na** and **Gd.80.Na** occurred. However, a 50% decrease in r_1 for **Gd.81.Na** was observed upon addition of 30 equivalents Ca^{2+}, with an r_1 value of 4.4 $s^{-1}mM^{-1}$ being recorded. This

relaxivity value is similar to those obtained for **Gd.81.Na** when the pH of the solution was increased above pH 7.5 (Figure 4.16), which as previously discussed was due to interference with the metal bound water molecules. It is therefore possible that the acetate counter ion may be displaying a H_2O molecule from the inner coordination sphere and resulting in the observed decrease in relaxivity. To investigate this, the Ca^{2+} ion titration for **Gd.81.Na** was repeated using $CaCl_2$, which as expected showed no modulation in the T_{1p} and therefore r_1 of **Gd.81.Na** (Figure A2.5).

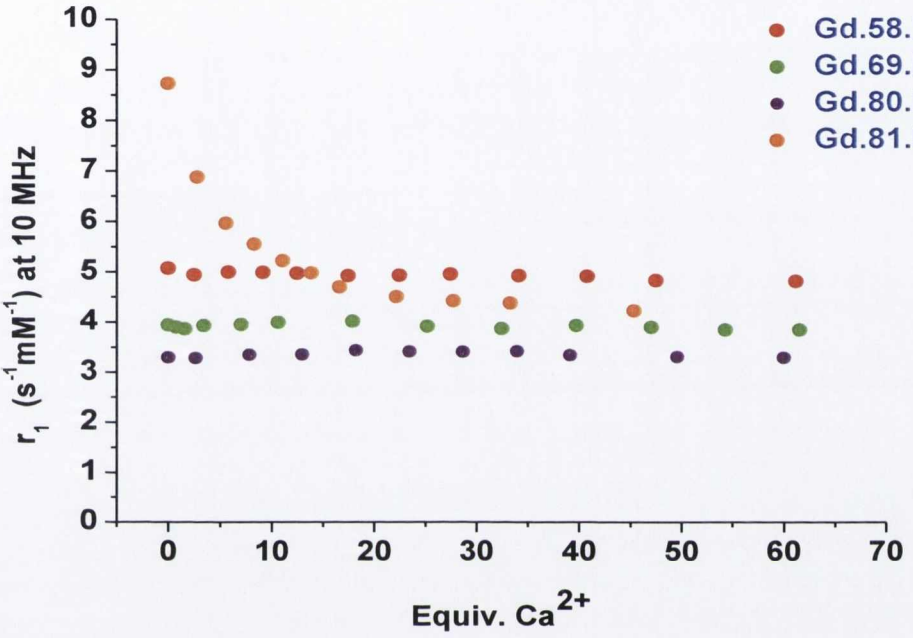

Figure 4.17: *Changes in relaxivity of **Gd.58.Na** (3.2 mM), **Gd.69.Na** (3.0 mM), **Gd.80.Na** (2.0 mM) and **Gd.81.Na** (2.0 mM) in the presence of $Ca(CH_3COO)_2$ (0 – 0.1/0.2 M) at pH 7.4 (20mM HEPES, 135 mM KCl) at 10 MHz and 25 °C.*

With the response of these Gd(III) complexes as a function of Ca^{2+} ion concentration determined, the next stage was to investigate any effect on their relaxivities in the presence of various biologically relevant metal ions and anions. The following section will therefore highlight the results obtained from these studies.

4.11 The influence of various biologically relevant metals and anions on r_1 for Gd.58.Na, Gd.69.Na, Gd.80.Na and Gd.81.Na

In order to investigate any relaxivity changes for these Gd(III) chelates upon addition of various metal ions and anions, a batch solution (0.1 M HEPES, pH 7.4) of each complex of known concentration was prepared. The metal ions and anions which were studied were $ZnCl_2$, $MgCl_2$, $CdCl_2$ and NaCl, hydrogen carbonate (HCO_3^-), fluoride (F^-), lactate, sulphate (SO_3^{2-}), citrate and pyrophosphate (sodium salts). With the exception of NaCl, where a 100 mM addition was used, a 10 mM addition of all the other ions to the Gd(III) solutions was

carried out. After a 4 h mixing period, T_1 measurements at 10 MHz for all the solutions were recorded and compared to those measured for the Gd(III) complexes prior to ion addition. With the concentrations of the solutions known and the T_1 values measured, the relaxivities for the Gd(III) complexes in the presence of all these ions were determined. As shown by the bar chart in Figure 4.18, for the tetraamide based complex **Gd.58.Na**, no significant changes in r_1 were observed, even for the metal ions Cd^{2+} and Zn^{2+}, which are known to show significant chelation with the iminodiacetate binding motif.

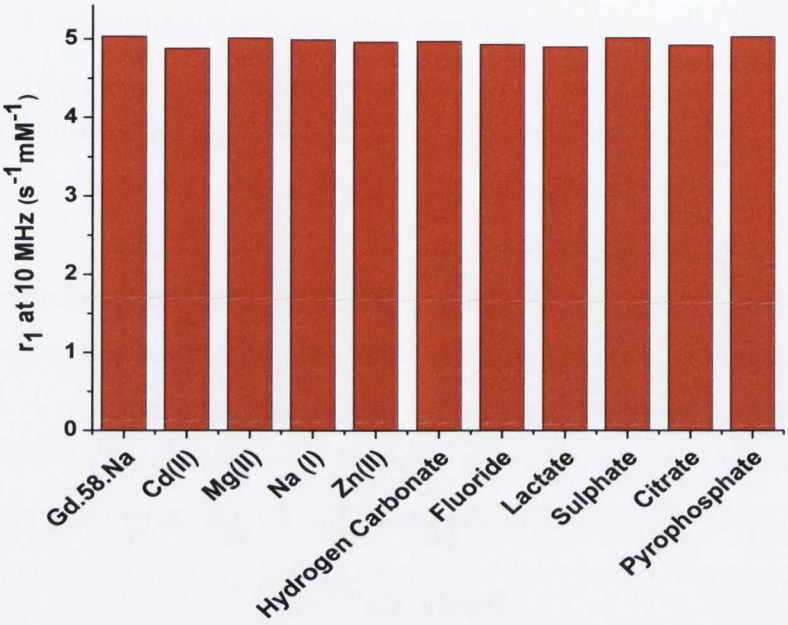

Figure 4.18: *Changes in r_1 at 10 MHz for **Gd.58.Na** (2.8 mM) in the presence of various biologically relevant metal ions and anions (Total error on r_1 calculation ca. 2.23%).*

Although **Gd.69.Na** and **Gd.80.Na** also displayed no significant relaxivity changes with the majority of ions investigated, upon the addition of Zn^{2+} and Cd^{2+} ions to these complexes, an increase in r_1 was displayed (Figure 4.19). For the case of Zn^{2+}, a relaxivity enhancement of *ca.* 12.5% and 14.2% was observed for **Gd.69.Na** and **Gd.80.Na**, respectively, with the slightly lower enhancements of 7.8% and 9.6% being measured for Cd^{2+}. This suggests that upon interaction of these ions at the iminodiacetate moieties of these complexes, the relaxation rate of the surrounding water molecules is enhanced slightly. A possible reason for this response could be due to the fact that upon binding of the metal ions, the negative charges of the iminodiacetate groups would be neutralised, allowing easier access of the bulk solvent molecules to the Gd(III) metal ion. This may also help explain why **Gd.58.Na** showed no relaxivity enhancements with these ions, as its iminodiacetate binding unit is located away from the Gd(III) centre.

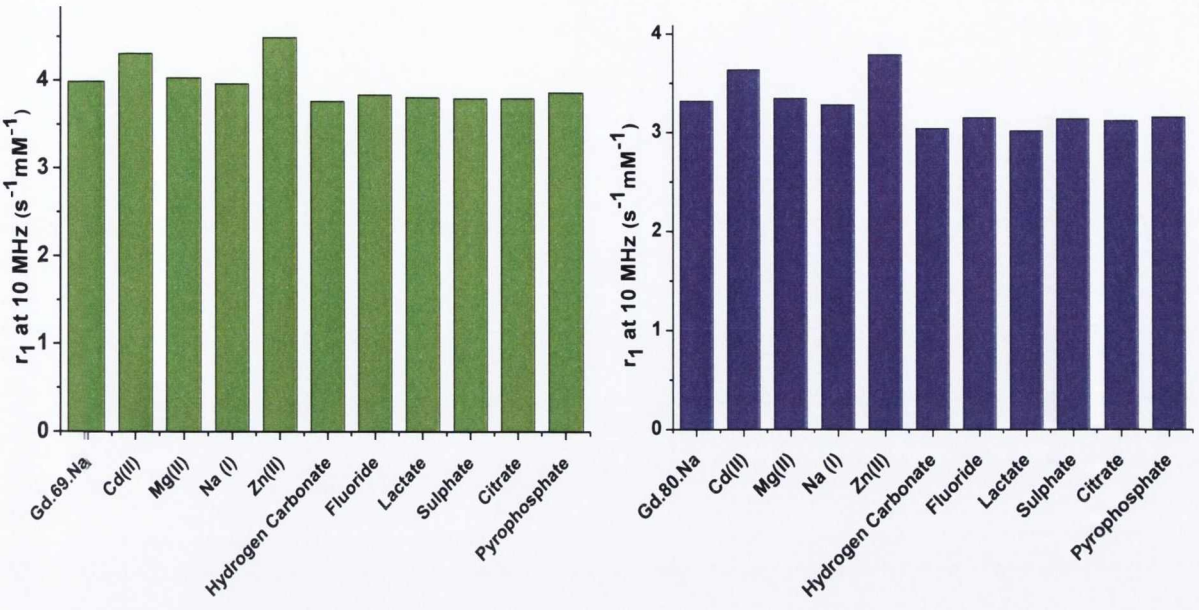

Figure 4.19: *Changes in r_1 at 10 MHz for a) **Gd.69.Na** (2 mM) and b) **Gd.80.Na** (2.3 mM) in the presence of various biologically relevant metal ions and anions (Total error on r_1 calculation ca. 2.23%)*

As expected a similar modulation in the relaxivity of **Gd.81.Na** was observed upon the addition of $ZnCl_2$ and $CdCl_2$, with enhancements of *ca.* 11.6% and 6.0%, respectively being measured. However, the most significant response was observed for the anion solutions, where a large reduction in r_1 occurred in the presence of hydrogen carbonate, and lactate (Figure 4.20). A 33% and 62% reduction in the relaxivity of **Gd.81.Na** was measured for these ions, respectively. With the pH of the solution maintained at 7.4 by the 0.1 M HEPES buffer, the principle cause therefore for this decrease is possibly displacement or deprotonation of the metal bound water molecules from the Gd(III) centre.[209] This reduction in q value would explain the slightly poorer relaxation of the surrounding water molecules and therefore the lower r_1 value obtained. This interference with the metal bound water molecules was verified by the increase in the luminescence observed upon addition of these ions to **Eu.81.Na**, the Eu(III) analogue of **Gd.81.Na** (Figure A2.6). A reduction in the luminescence quenching from the O-H oscillators upon H_2O displacement or deprotonation explains the observed emission increase. Further confirmation was achieved by measuring the lifetimes of **Eu.81.Na** in the presence of excess amounts of these ions. For the case of HCO_3^-, with a $\tau_{OH} = 0.47 \pm 0.01$ ms and $\tau_{OD} = 1.46 \pm 0.01$ ms recorded, a q value of 1.4 ± 0.5 was determined, suggesting deprotonation of the metal bound H_2O molecule. However, for the lactate anion, the lifetime values obtained were $\tau_{OH} = 0.82 \pm 0.01$ ms and $\tau_{OD} = 1.67 \pm 0.01$ ms, resulting in a q of 0.4 ± 0.25 being calculated.

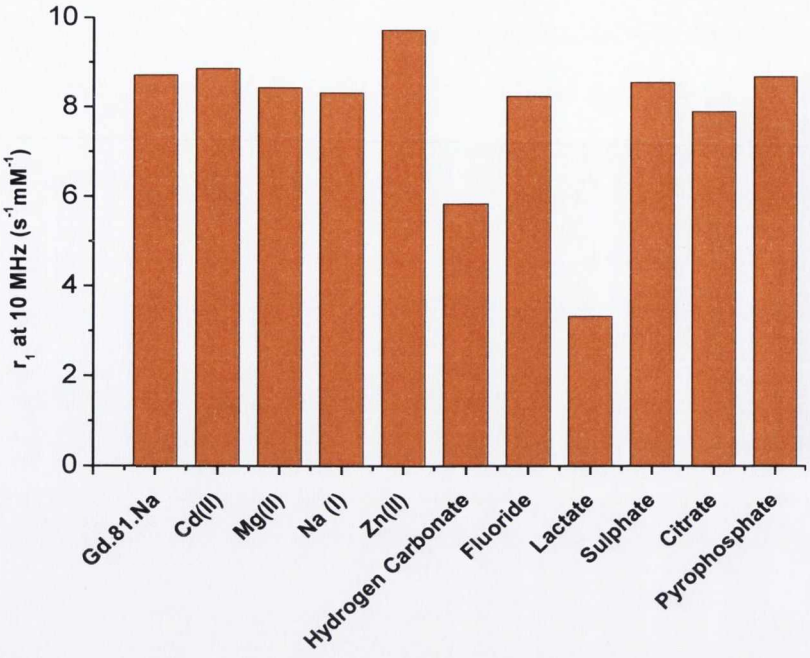

Figure 4.20: *Changes in r_1 at 10 MHz for Gd.81.Na (2.8 mM) in the presence of various biologically relevant metal ions and anions (Total error on r_1 calculation ca. 2.23%).*

With a general understanding of the effect on the relaxivities of these Gd(III) complexes as a function of pH, Ca^{2+} ion concentration and in the presence of various biologically relevant metal ions gained from all the above measurements, the next stage was to investigate their potential to be used as contrast agents for damaged bone structure. It was anticipated that preferential binding at areas of high Ca^{2+} ion exposure would provide a significant contrast from the remaining healthy bone matrix. The following section will therefore highlight some preliminary MR imaging of damaged bovine bone material using a 7T animal MRI scanner and the above Gd(III) complexes as the contrast agents.

4.12 MRI of damaged bovine bone structure using a 7T animal scanner

4.13.1 Detection of microscratches on external bone surfaces

A similar sample preparation method to that described in Chapter 3 (Section 3.2) was used, where longitudinal sections of cortical bone from the mid-diaphysis were cut into beam shaped specimens (*ca.* 20 mm x 7 mm x 7 mm) using a low speed diamond saw. To remove any rough edges formed during the cutting process, all bone surfaces were polished with sandpaper (P1200). As shown by the illustration in Figure 4.21, using a surgical scalpel, scratches of *ca.* 20 mm in length were induced on the under surface of the bone sample as well as on both sides. The sample was then immersed in a vial containing a 4 mM buffered solution of the Gd(III) contrast agent (20 mM HEPES, 135 mM KCl) and stored under vacuum for 24 h. After this staining period, the sample was removed from the vial, washed thoroughly with deionised water and glued, as shown in Figure 4.21 into a 40 mL

polystyrene sample tube. This tube was filled to the maximum with water and the lid secured while still immersed to try and eliminate any potential air bubbles.

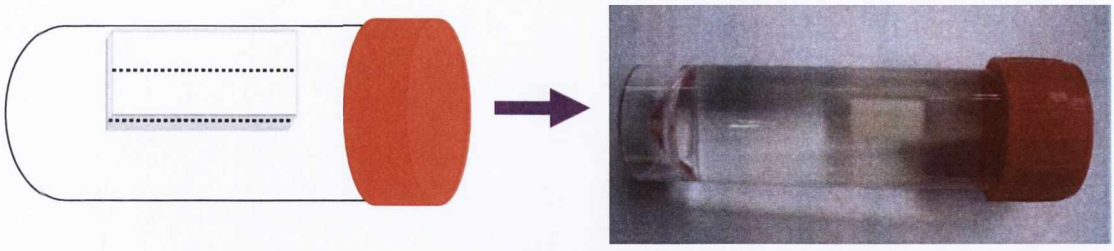

Figure 4.21: *a) Illustration and b) photograph of sample preparation method used for MRI experiments.*

With the luminescent analogues of **Gd.69.Na** allowing for successful visualisation of the microdamaged region as a direct result of preferential localisation within the scratched area, the initial MRI studies were carried out using a 4 mM concentration of this Gd(III) complex. The MRI imaging of all the samples was carried out by Dr Christian Kerskens in the Institute of Neuroscience TCD using a 7T MRI animal scanner. As shown by the T_1-weighted MR images in Figure 4.22, it is clear that a large contrast of the entire bone surface can be observed as a result of the presence of **Gd.69.Na**. The resulting positive T_1 contrast is due to more rapid relaxation of the ^1H nuclei of the H_2O molecules which are in close proximity to the bone surface. However, no distinction or more efficient contrast of the areas of damaged bone structure (location of scratches highlighted by white arrows) could be observed. It is also evident from these images that a large contrast of the internal structure of the bone sample is also occurring, which is possibly as a result of **Gd.69.Na** remaining within the bone's vascular network.

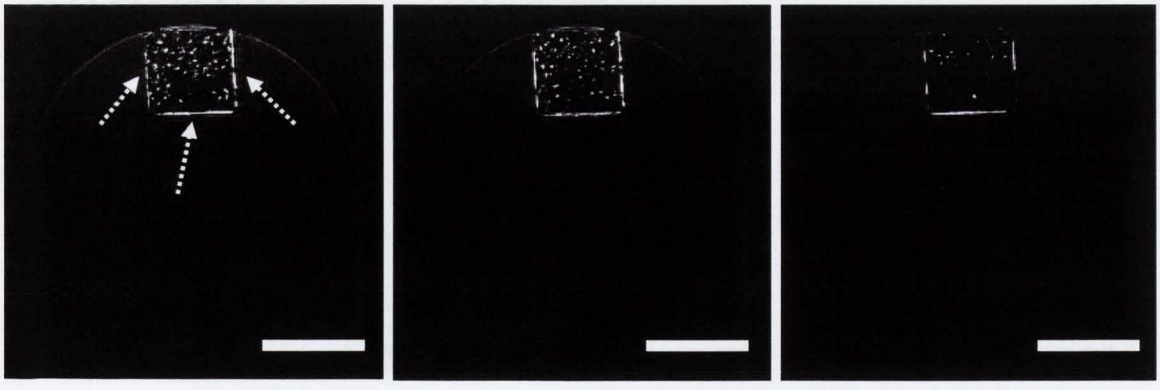

Figure 4.22: *T_1-weighted MRI slices of scratched bovine bone sample immersed in a 4 mM aqueous solution (20 mM HEPES, 135 mM KCl) of **Gd.69.Na** for 24 h under vacuum using a 7T animal scanner. (White arrows indicate location of scratches) Scale bar = 5 mm. Resolution = 0.1 mm/px.*

To ensure that the observed contrast was directly related to the presence of the Gd(III) chelating agent, a MR image of a bone sample which had no contact with the contrast agent

was taken. Along with this sample, a bone specimen which was immersed in 4 mM **Gd.69.Na** and a sample which was immersed in 4 mM **Gd.81.Na** were also placed in the same sample tube. One modification which was made to the staining procedure was that after removal of the bone specimens from the Gd(III) solutions, the samples were placed in water under vacuum for 5 min, the water was then replaced and this washing technique repeated five times. The samples were also subjected to sonification. It was anticipated that this more intense cleaning protocol would allow for removal of any unbound contrast agent within the vascular canals of the bone structure. As shown by the control bone sample in Figure 4.23a, very little contrast in comparison to those immersed in **Gd.69.Na** and **Gd.81.Na** of the outer bone surfaces was observed. Another interesting observation was that a large reduction in the contrast of the internal bone structure occurred, suggesting much less trapped contrast agent within the vascular canals as a result of the more extensive washing procedure. Although **Gd.81.Na** displayed higher r_1 values than **Gd.69.Na** due to the presence of its two metal bound water molecules, the contrast obtained for the bovine bone specimens using both Gd(III) complexes was similar.

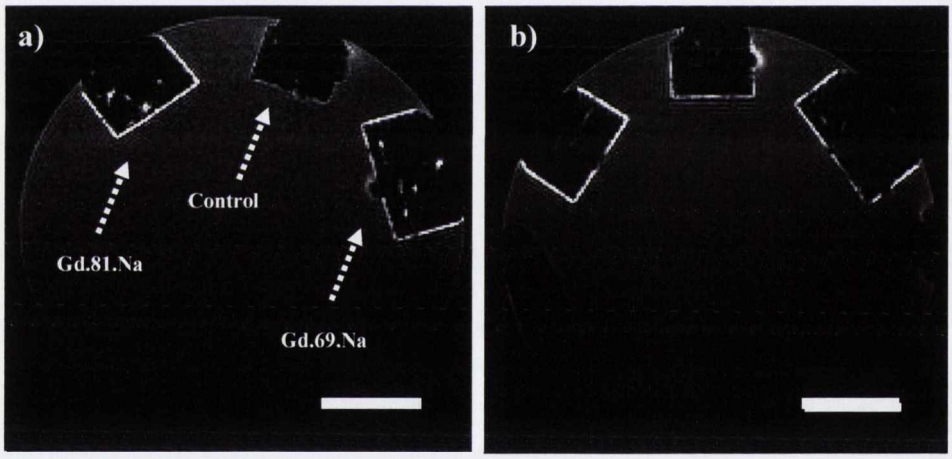

Figure 4.23: *a) T_1-weighted MR image of control bovine bone sample as well as samples which were immersed in a 4 mM aqueous solution (20 mM HEPES, 135 mM KCl) of either* ***Gd.69.Na*** *or* ***Gd.81.Na*** *for 24 h under vacuum using a 7T animal scanner. b) T_1-weighted MR image of same samples a week later. Scale Bar = 5 mm. Resolution = 0.1 mm/px*

One major challenge with the sample preparation method used was that although precautions to reduce the number of air bubbles were taken, it is still clear from the images shown in Figure 4.23a that the surfaces of the bone samples still had a large number of bubbles attached. In fact for the sample which was immersed in **Gd.69.Na**, air bubbles located in the region of the scratched area were seen in nearly every MR image slice. Another interesting observation was that when the sample tube was imaged a week later, the control bone specimen now displayed a strong contrast of its surface with the signal intensity within the vascular canals of the other bone samples further reduced (Figure 4.23b). This suggests

that over time the unchelated Gd(III) contrast agents within the bone structure were removed and preferentially targeted the bone surface of the control sample. This reduction in internal contrast was verified by measuring the intensities through an identical slice of the bone sample immersed in **Gd.69.Na** for each measurement and comparing the intensities recorded using Image J 1.43. As shown in Figure 4.24, it is clear that for the MR images which were taken a week later, a large reduction in the internal contrast intensity was observed, with values comparable to the background water

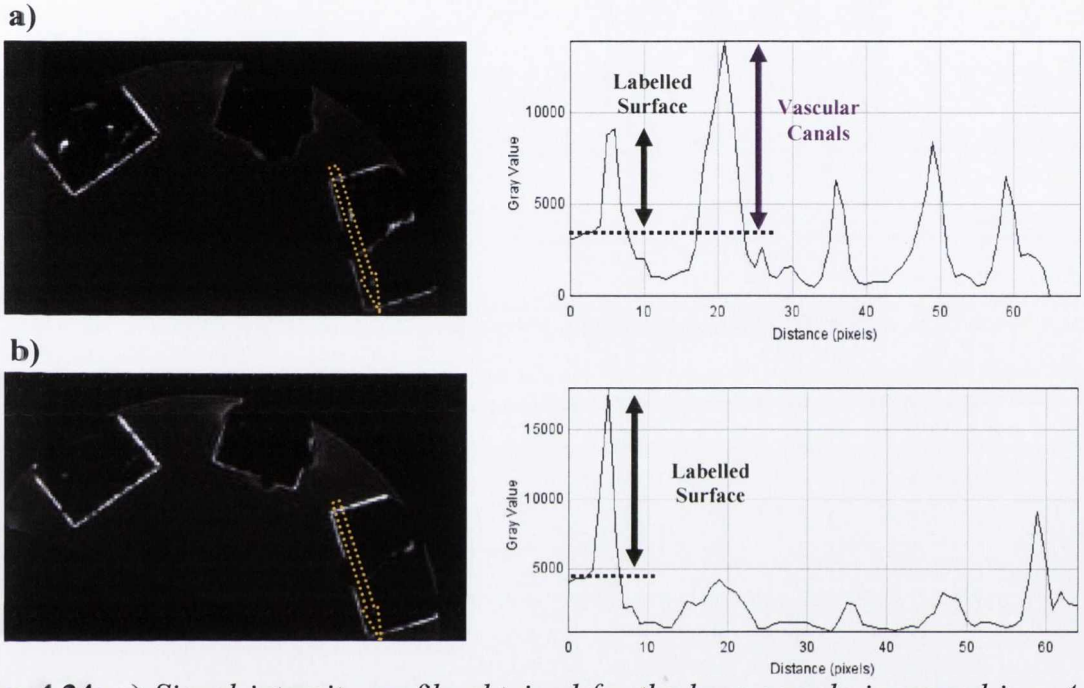

Figure 4.24: a) *Signal intensity profile obtained for the bone sample immersed in a 4 mM aqueous solution (20 mM HEPES, 135 mM KCl) of* **Gd.69.Na** *for 24 h under vacuum. b) Signal intensity profile recorded at same region for the MR image which was taken a week later. Scale bar = 5 mm. Resolution = 0.1 mm/px.*

Although no contrast enhancement of the scratched regions which were induced on the external surfaces of the bone specimens was observed, it was decided to still investigate the effect of the contrasting abilities of **Gd.69.Na** on the reduction of the staining time. It has been previously discussed in Chapter 3 for **Eu.69.Na** and **Tb.69.Na** that upon lowering the immersion time to 4 h, a significant reduction in the emission intensity was observed. Therefore, it was anticipated that the MR contrast of the outer bone surfaces would show a similar response with a reduction in the staining time used. It was also decided to investigate any modulation in the contrast displayed when the samples were stored at atmospheric pressure instead of the usual vacuum staining conditions. Another slight modification was made to the sample preparation protocol, where instead of using a large sample polystyrene tube, the bone specimens were placed in small individual plastic eppendorfs. Several eppendorfs could then be tied together using parafilm and imaged simultaneously without the

possibility of the previously discussed problem of the contrast agent leaching out from one sample and staining another. Initially it appeared, as shown by the MR image in Figure 4.25, that the 24 h staining period resulted in a more significant contrast of the other bone surfaces than that observed using the 4 h immersion time.

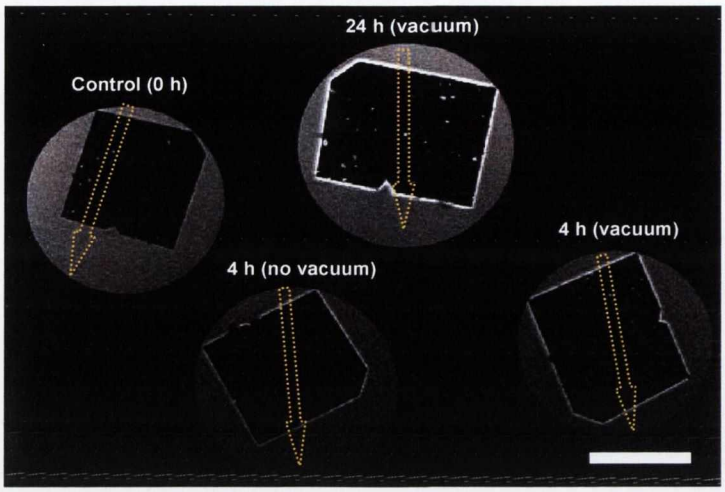

Figure 4.25: *T_1-weighted MR image of bone samples immersed in a 4 mM aqueous solution (20 mM HEPES, 135 mM KCl) of* **Gd.69.Na** *for 0 h, 4 h (no vacuum), 4 h (vacuum) and 24 h (vacuum) using a 7T animal scanner. Scale bar = 5 mm. (Yellow arrows indicate were intensity profiles were measured). Resolution = 0.5 mm/px.*

However, when the signal intensities were measured using Image J 1.43, a similar signal enhancement of the outer surfaces was obtained using both time frames (Figure 4.26). It was also clear that the presence or absence of vacuum in the staining protocol played no significant role in the contrast abilities of **Gd.69.Na**. As expected the control sample displayed no signal intensity enhancement of the bone surfaces.

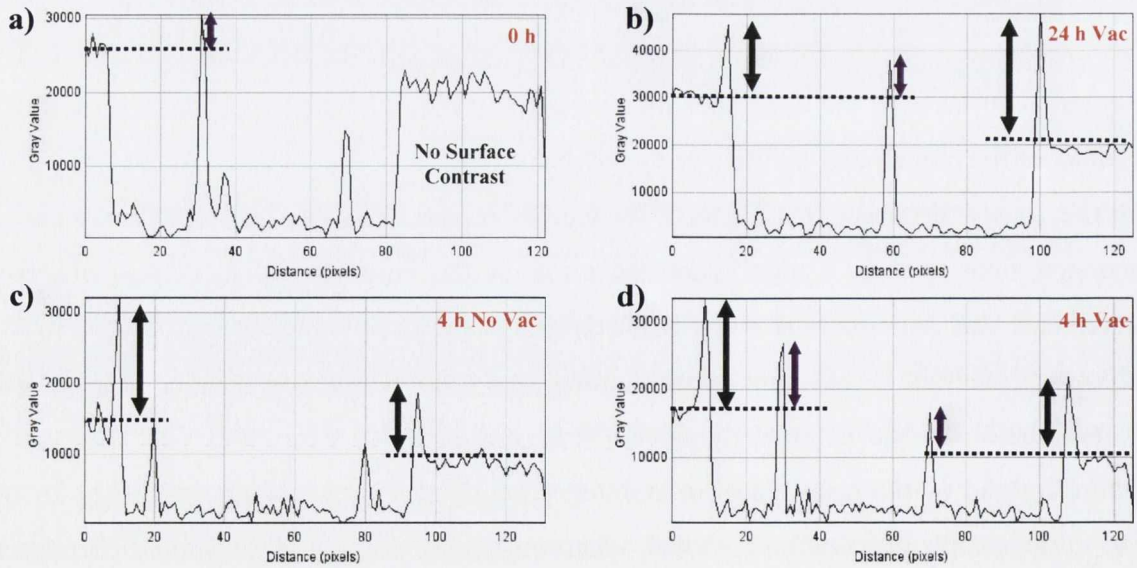

Figure 4.26: *Signal intensity profiles of bone samples which were immersed in a 4 mM aqueous solution (20 mM HEPES, 135 mM KCl) of* **Gd.69.Na** *for a) 0 h, b) 24 h (vacuum), c) 4 h (no vacuum) d) 4 h (vacuum).*

These results suggest that after a 4 h immersion period, no further contrast enhancement of the outer bone surfaces can be gained using these contrast agents. A possible reason for this could be due to the fact that their design incorporates the iminodiacetate binding unit, which has previously been shown to only display strong chelation at sites of high Ca^{2+} ion exposure. As the hydroxyapatite structure of these smooth surfaces remains undamaged and therefore has few Ca^{2+} sites exposed, the contrast which is observed at the surfaces could be as a result of the complexes lodging within the bone structure, with very little Ca^{2+} interactions occurring. This would explain why no significant contrast enhancement was observed between the 4 h and 24 h immersion times. A similar response was previously seen in Chapter 3 for **Eu.69** and **Tb.69**, the Eu(III) and Tb(III) ester analogues of **Gd.69.Na**. These complexes had their iminodiacetate groups protected as their diethyl ester forms and therefore as a result of weak interaction with the Ca^{2+} ions displayed little emission enhancement of the scratched regions when the immersion time was increased above 4 h.

Although the MR images showed a contrast of the outer surfaces of the bone samples using the Gd(III) complexes, no selective detection of the microscratches on the external surfaces could be gained. With the previous problem of trapped air bubbles on the surface of the bone samples, it is difficult to determine whether these extremely small scratches contain water. It is possible that due to the surface tension between the water molecules and the bone surface that a small air gap could exist. If this was the case, then even if the scratched areas had a higher concentration of the Gd(III) contrast agent, due to the absence of any nearby water molecules, the enhanced contrast would not be observed. It was therefore decided to investigate the ability of these types of Gd(III) agents to selectively detect internal microcracks, which lack any exposure to air during the preparation procedures and should therefore contain sufficient water. The following section will detail the results obtained from these studies, using **Gd.69.Na** as the contrast agent

4.13.2 Detection of internal microcracks using Gd.69.Na as a contrast agent

With little success achieved in the selective detection of damaged bone structure using the surface scratching technique, it was decided to investigate the ability of these complexes to penetrate the bone matrix and selectively chelate at sites of internal bone damage. A similar fatigue stressing protocol to that described in Chapter 3 (Section 3.10) was employed to induce internal microdamage in the waisted sections of cylindrical bone samples. After sample compression, the bone specimens were placed in a 4 mM aqueous solution (20 mM HEPES, 135 mM KCl, pH 7.4) of **Gd.69.Na** for 24 h under vacuum. MR imaging of the

waisted sections, where internal microcracking is most likely to have occurred, was carried out using the 7T animal scanner. As shown by the image in Figure 4.27, the expected contrast enhancement of the entire outer bone surface was observed,. Furthermore, any large cracks which were produced internally as a result of the fatiguing protocol also displayed a significant signal enhancement. This made distinction of these large macrocracks from the remaining undamaged bone matrix more efficient. Intensity profiles were obtained for both bone samples, where as shown in Figure 4.28, a clear signal intensity enhancement of the damaged bone regions could be observed. Preliminary data from μCT analysis of these samples indicates that these larger macrocracks are *ca.* 30 – 50 μm wide and 3 – 8 mm long. This offers the possibility of using such Gd(III) based agents for *in vivo* detection of so called stress fractures, which commonly have sizes ranging within these values, and are currently not possible to detect by conventional x-ray examination.

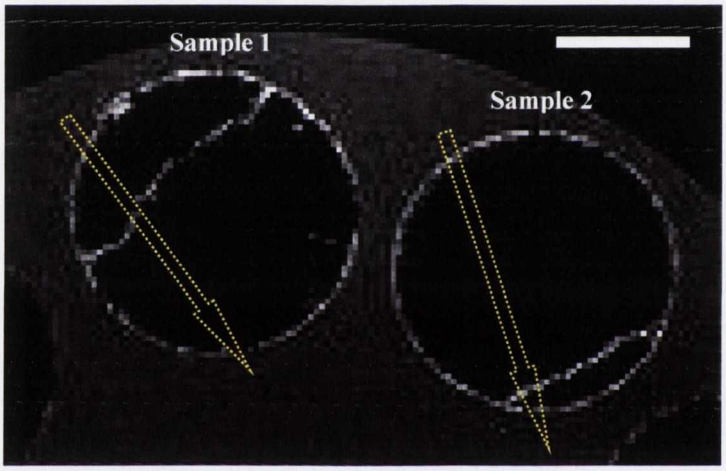

Figure 4.27: *T_1-weighted MR image of fatigued bone samples immersed in a 4 mM aqueous solution (20 mM HEPES, 135 mM KCl) of* ***Gd.69.Na*** *for 24 h (vacuum) using a 7T animal scanner. Scale bar = 2.5 mm. Resolution = 0.1 mm/px. (Yellow arrows indicate were intensity profiles were measured)*

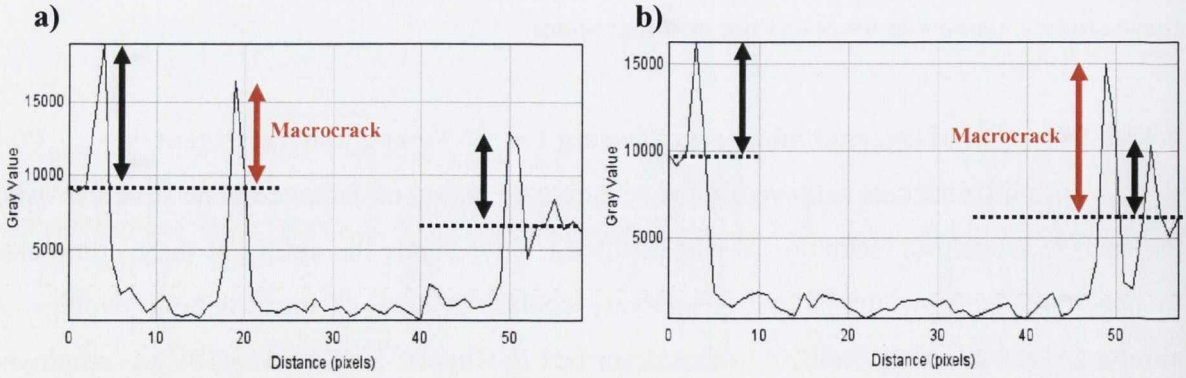

Figure 4.28: *Signal intensity profile of a) fatigued bone sample 1 and b) fatigued bone sample 2 which were immersed in a 4 mM aqueous solution (20 mM HEPES, 135 mM KCl) of* ***Gd.69.Na*** *for 24 h under vacuum.*

Although, these studies allowed clear distinction of the large macrocracks which were produced internally using **Gd.69.Na** as the MRI contrast agent, due to the low resolution of MR images obtained, identification of any smaller microdamage regions was not possible. Smaller areas of signal enhancement were observed for the fatigued bone samples, however, it was difficult to determine if these areas were region of microdamage accumulation or just the vascular canals of the bone structure. Further studies are currently being carried out to obtain higher resolution images, with the aim that in addition to successful detection of the large macrocracks, identification of smaller microcracks using **Gd.69.Na** can also be gained.

4.13 Conclusion

This chapter focused on the development of Gd(III) based contrast agents for selective detection of damaged bone structure using the non-invasive imaging technique MRI. The ligand structures of these Gd(III) complexes allowed for the incorporation of the iminodiacetate chelating units, which as previously discussed in Chapter 3, through interaction with exposed Ca^{2+} ions, should allow for preferential localisations within areas of damaged bone matrix. With great success being observed for the luminescent Ln complexes of ligands **58** and **69**, the Gd(III) analogues of these ligands (**Gd.58**, **Gd.69**) were formed. The syntheses of two other structurally similar ligands **80** and **81**, and their corresponding Gd(III) complexes **Gd.80** and **Gd.81** were also discussed. With the iminodiacetate chelating units of all these complexes protected as their diethyl ester forms, base hydrolysis was required to give the more targeting microdamage Gd(III) contrast agents **Gd.58.Na**, **Gd.69.Na**, **Gd.80.Na** and **Gd.81.Na**.

The initial studies involved measurement of the paramagnetic spin lattice relaxation times (T_{1p}) for all the Gd(III) chelates at several magnetic fields (B_0). The high field measurements at 400 MHz and 600 MHz were carried out using an inversion recovery NMR sequence. In order to calculate the relaxivities (r_1) for all the Gd(III) complexes using these T_{1p} values, accurate determination of their concentrations, using the bulk magnetic susceptibility shift technique, was required. Overall, the general trend of a decrease in relaxivity at the higher 600 MHz field was observed for all complexes, however, for the $q = 2$ complex **Gd.81.Na**, much lower relaxivity values than expected were obtained. The r_1 values of 3.9 $s^{-1}mM^{-1}$ and 3.1 $s^{-1}mM^{-1}$ at 400 MHz and 600 MHz, respectively are in a similar range to those observed for the $q = 1$ complexes. Low field (0.01 MHz – 10 MHz) T_1 measurements were carried using the fast field cycling NMR method, with the relaxivity NMRD profiles characteristic for such low molecular weight Gd(III) chelates. For these measurements **Gd.81.Na** displayed much higher (*ca.* 50%) relaxivities values then all the

other $q = 1$ complexes. Confirmation of the rapid molecular rotation for these complexes was gained by the absence of any "hump like" structure when the relaxivities were measured at several magnetic fields between 20 MHz and 100 MHz.

The effect of pH on the relaxivities of all the contrast agents at 10 MHz was investigated, with the tetraamide based complexes **Gd.58.Na** and **Gd.69.Na** displaying the expected pH profiles, essentially flat between the pH range 2 – 9 with an increase in relaxivity at the very acidic and basic regions of the pH scale. The enhanced relaxivity at high pH suggests an increase in the rate of prototropic exchange between the protons of the bound water molecule and the coordinating amide. This helps explain the much less pronounced increase for **Gd.80.Na**, which has no amide protons within its ligand structure. A relaxivity increase at low pH was observed for all three complexes with acid catalysed prototypic exchanged suggested as a possible cause. The $q = 2$ complex **Gd.81.Na** displayed a similar response to other heptadentate based chelates, with a large increase and decrease in r_1 being observed below pH 4.5 and above pH 7.5, respectively. At high pH, displacement of a metal bound water molecule can cause the observed decrease in r_1, with demetallation of the Gd(III) metal at low pH resulting in the observed increase. The 35% decrease in r_1 at pH 8.6 in comparison to pH 7.4 may help explain the much lower than expected r_1 values obtained for **Gd.81.Na** at 400 MHz and 600 MHz, as these high field measurements were carried out in D_2O, which has a pH of *ca.* 8.6.

Gd.58.Na, **Gd.69.Na** and **Gd.80.Na** displayed no modulation in their relaxivities at 10 MHz upon the addition of $Ca(CH_3COO)_2$. However, as a result of displacement of a metal bound water molecule in **Gd.81.Na** by the acetate counter ion, a 50% decrease in r_1 was observed. Verification of this was gained when no change in r_1 resulted when a $CaCl_2$ titration was preformed. Several metal and anion studies showed that the most significant response observed for **Gd.58.Na**, **Gd.69.Na** and **Gd.80.Na** was upon the addition of $ZnCl_2$ and $CdCl_2$. Binding of these metals to iminodiacetate units caused a subsequent increase in r_1 at 10 MHz. **Gd.81.Na** showed a similar response to these metal ions but displayed a more significant relaxivity change in the presence of anions such as lactate and HCO_3^-. Displacement of the metal bound water molecules was stated as a cause for the observed reduction in r_1.

MR imaging of damaged bone structure using the above Gd(III) complexes as potential contrast agents was carried out using a 7T animal MRI scanner. Initially a similar scratching method to that described in Chapter 3 was used. Although a significant contrast of the entire bone surface was observed due to more efficient relaxation of the proton nuclei of the nearby water molecules by the Gd(III) agent, distinction of the scratched regions from the

healthy bone surface was not possible. The contrast enhancement of the outer surface showed little modulation when the immersion time was reduced from 24 h to 4 h, suggesting little chelation of the Gd(III) agents to the surface after a 4 h staining period. To overcome any potential surface tension problem between the water molecules and the solid bone surface and the potential for *in vivo* application, the ability of **Gd.69.Na** to selectively label internal microdamage was investigated. A similar fatigue stressing protocol of cylindrical bone specimens was carried out to induce internal microcracking within the waisted regions of these samples. The relatively low resolution of the MR images obtained did not allow for clear identification of small microcracks, however, a significant contrast enhancement of the large macrocracks was observed. This renders the possibility of these MRI contrast agents to be used for clinical applications in the detection of structural bone damage.

Chapter 5

Lanthanide Luminescent Thiol Sensor

5.1 Introduction

Characterised by the presence of sulfhydryl residues, biological thiols (biothiols) play a crucial role in various physiological processes such as reversible redox reactions and in carrying out important cellular functions such as detoxification and metabolism.[210-213] Also with a strong link to a number of well known diseases such as liver damage, cancer, osteoporosis, cardiovascular disease and AIDS, it is clear why selective detection of intracellular thiols has become an active area of research in recent years.[214-217] Cysteine (Cys), homocysteine (Hcy) and glutathione (GSH), Figure 5.1, have all become principle targets for such biothiol studies. Low levels of Cys have been connected to many health issues such as hematopoiesis reduction, retarded growth, liver damage, hair depigmentation and skin lesion development.[216] Whereas, Hcy is a common risk factor for disorders such as Alzheimer's disease,[218] osteoporosis,[217] thrombosis and cardiovascular disease.[214] The most abundant intracellular non-proteinogenic thiol, GSH, which will be discussed in more detail in the following section, plays a pivotal role in maintaining the reducing environment within cells and therefore acts as a key indicator of oxidative stress and overall cell health.[219-221] With all this in mind, it is evident that the detection and discrimination of these thiol containing molecules in biological samples is of great importance.

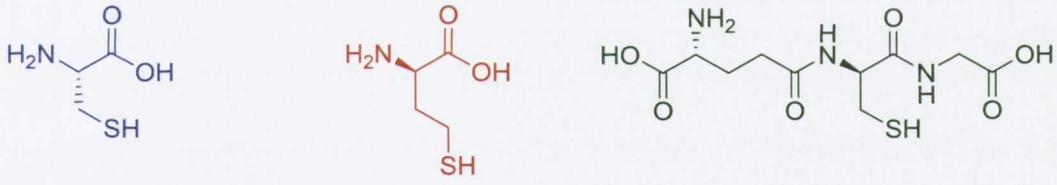

Cys **Hcy** **GSH**

Figure 5.1: *Structure of cysteine (Cys), homocysteine (Hcy) and glutathione (GSH).*

5.2 Glutathione and its role in physiopathology

As previously mentioned, glutathione (γ-L-glutamyl-L-cysteineglycine; GSH) is the most predominant low-molecular-mass, non protein tripeptide thiol produced in all organs, especially the liver and found in nearly all mammalian tissues.[219] Existing essentially in its reduced sulfhydryl form, GSH can be rapidly oxidized to its dimeric disulfide GSSG form in response to oxidative stress within a cell. The major cause of such cellular stress is due to the formation of various reactive oxygen species (ROS) which are produced during normal aerobic metabolism or as a result of some inflammatory or immunomediated based disease. These ROS molecules, consisting of free radicals (superoxide ($O_2^{\cdot-}$) and hydroxyl radicals ($OH^{\cdot}$)) and non-radical species (hydrogen peroxide (H_2O_2)) possess high chemical reactivity due to the presence of one or more unpaired electron(s). This in turn makes them susceptible

to attack major cellular components and cause sufficient damage to surrounding tissues.[213, 222] It was therefore necessary for cells and tissues to develop a sophisticated antioxidant defence mechanism, involving the use of GSH, which provides some form of protection by converting these potentially dangerous oxidising agents into a series of harmless derivates.[223] This cellular defence strategy has a significant effect on the GSH/GSSG ratio and as a result any significant shift in concentrations of reduced (GSH) to oxidised (GSSG) form is a key indicator of excessive oxidative stress occurring within a cell. For a healthy individual, it is well known that the oxidised GSSG form rarely exceeds 10% of the total GSH concentration within a cell, with a mean value of 68 ± 26 mmol/L being measured for GSSG and a value of 486 ± 85 mmol/L for the reduced sulfhydryl form.[223] However, if for some reason a cell is exposed to high levels of ROS or any other type of free radical species, excessive depletion of the reduced GSH concentration can increase the cells vulnerability to future attacks, resulting in the development of various diseases. Therefore, in order for a cell to rapidly recover, the concentration levels of reduced GSH must be returned to a healthy balance, which involves the nicotinamide adenine dinucleotide phosphate (NADPH) dependent reduction of GSSG using the cellular enzyme glutathione reductase. The mechanism of this enzymatic reduction process of GSSG will be discussed in more detail at a later stage within this chapter.

A recent report by Shaw *et al.*[221] effectively highlights the role that GSH plays in maintaining cellular functions and the consequences of its sudden depletion on an individual's overall health. Investigating the link between motor neurone disease (MND) and GSH depletion, the report concentrates on the percentage of people that have MND in the Nelson area of New Zealand. Between 2002 and 2005, in Nelson alone, 1.4/100,000 population/year were diagnosed with the disease, which quite surprisingly is of the same order as the worlds overall cases of MND (2/100,000 population/year). Another interesting observation was that all diagnoses made were for individuals that had previously worked at the Nelson port. One suggestion, which has not been proven as of yet, was that high exposure of the free radical generator methyl bromide (CH_3Br), which was used to fumigate wood and fruit for export, caused subsequent irreversible methylation, as shown in Figure 5.2, of GSH within the cells. This would leave the cells unprotected from future attacks from CH_3Br or any other reactive species, leading to overall cell and tissue damage. This report suggests the first statistical evidence that an imbalance in free radical activity could be a possible risk factor for MND development.

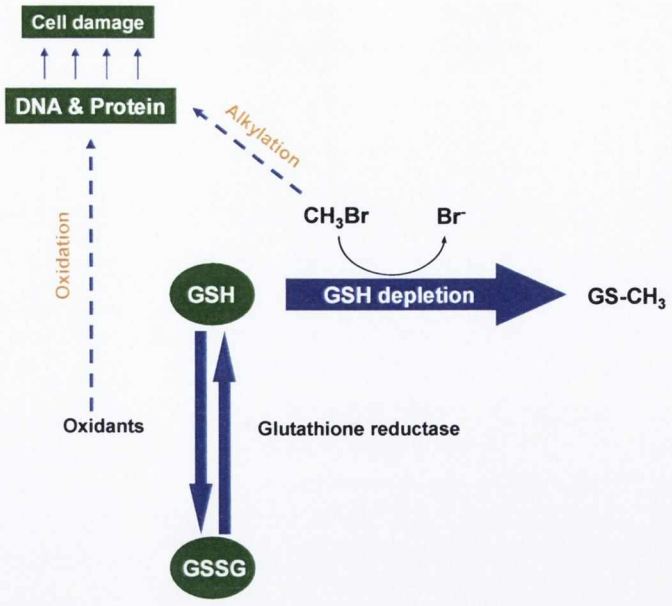

Figure 5.2: *Schematic representation showing the GSH and GSSG interconversion process and the detrimental effect that exposure of high levels of the free radical generator CH_3Br has on this redox process.*[221]

5.3 Methods for thiol detection

With the potential for efficient diagnosis of a variety of well known diseases and the ability to gain a greater understanding of any intracellular oxidative stress which may be occurring, it is no surprise that a large variety of different methods have been developed for the selective detection of these sulfhydryl based molecules. Techniques such as high performance liquid chromatography (HPLC),[224-226] capillary electrophoresis[227-229] and immunoassays[213, 220] have in the past earned a great deal of attention, however, in more recent years, due to the higher selectivity and sensitivity obtained with spectrofluorimetric methods, a greater interest in the development of fluorescent and colorimetric sensors has occurred. In the design of these probes, various mechanisms of detection have been exploited including Michael addition,[230-238] cyclisation reaction with aldehydes,[239-241] cleavage reactions by thiols[242-249] and many others.[210, 250, 251] Therefore, the following sections will focus on various thiol probes which have been developed to date, highlighting the variety of different detection methods which have been used.

5.3.1 Fluorescent and colorimetric probes for thiol detection

Zhu *et al.*[243] developed the naphthalimide based colorimetric fluorescent probe **84** (λ_{em} = 485 nm), which as shown in Scheme 5.1, uses a cleavage reaction mechanism for successful GSH detection. The authors selected 4-aminonaphthalimide as their fluorophore framework due to its efficient ICT structure and its attractive photophysical properties, such as large Stokes' shift, long emission wavelength and its insensitivity to pH. Studies were

carried out in an EtOH/H_2O (1:9, v/v) solution mixture at pH 7.4 and showed that upon addition of the sulfhydryl based molecule GSH to **84**, subsequent cleavage of the disulfide carbamate protecting group was observed. Such deprotection of the 4-aminonaphthalimide **85**, resulted in a restoration of its strong green fluorescence at λ_{em} = 533 nm and an 85 nm red shift of its maximum absorption band.

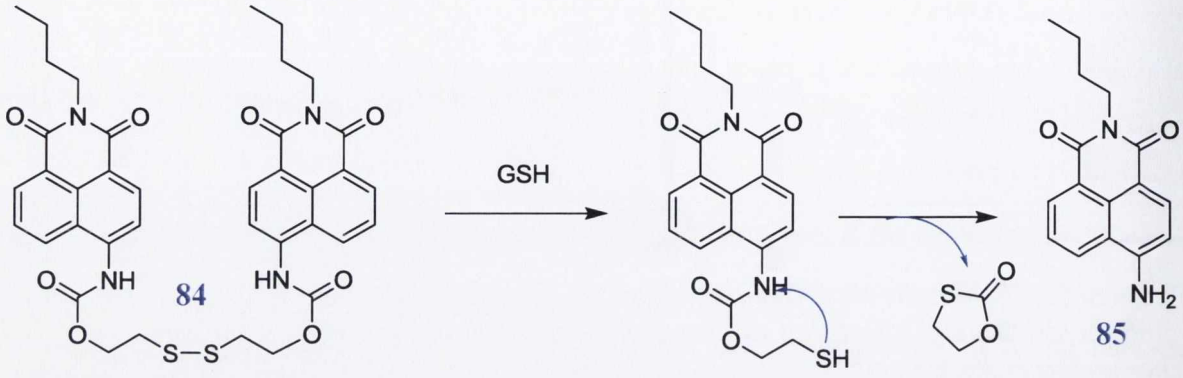

Scheme 5.1: *Cleavage of the disulfide based carbamate protecting group of probe **84** upon addition of GSH.*[243]

The potential of **84** to detect GSH quantitatively using a ratiometric fluorescence method was also demonstrated due to a significant change in the intensity ratio between the 533 nm and 485 nm emission bands. As expected, probe **84** displayed a strong fluorescence response for other low molecular weight thiols (LMWTs), such as Cys and 1,4-dithiothreitol (DTT), however, in the presence of various other natural amino acids lacking the thiol functionality, no significant response was observed. The authors finally demonstrated the ability of **84** to penetrate the membrane of HeLa cells and show a strong emission response upon detection of biological thiols.

The thiol sensors **86** and **87** which were developed by Wang *et al.*[249] and Jiang *et al.*,[248] respectively, used a very different cleavage mechanism whereby the addition of a thiol based molecule resulted in the subsequent removal of a dinitrobenzenesulfonyl (DNS) group from both probes through a well known thiol mediated nucleophilic aromatic substitution (S_NAr) process. In the case of probe **86**, incorporation of the electron withdrawing DNS group to a merocyanine chromophore resulted in a significant change in the chromophore's ICT character, completely "switching off" the probes fluorescence. However, upon the addition of Cys, Hcy and GSH to a CH_3OH/H_2O (3:7, v/v) solution mixture of **86**, significant changes were observed in both the UV-vis and fluorescence properties of the probe. A red shift of *ca.* 150 nm was observed in the absorption spectrum resulting in a visible colour change of the solution from faint yellow to a bright orange, demonstrating "naked eye" detection of thiols using **86**. The thiol mediated cleavage of the DNS group also resulted in a

significant "turn on" effect of the fluorescence emission, allowing a detection limit of 2.4 $x10^{-8}$ mol/L to be calculated.

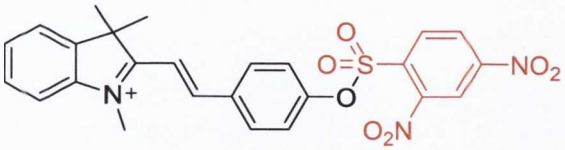

86

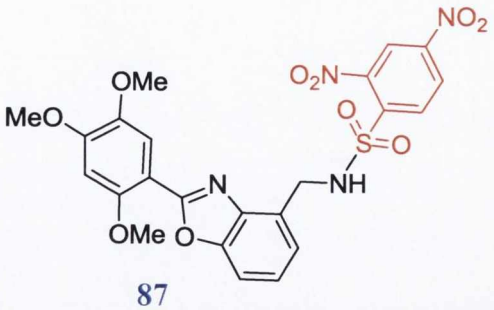

87

Jiang *et al.*[248] designed the benzoxazole based probe **87**, with the plan of using the same thiol detection technique as previously described for compound **86**. However, their study concentrated more on the selective detection of a variety of thiophenols in the presence of simpler aliphatic based thiols. Taking advantage of the difference in their pK_a values (thiophenols ($pK_a = 6.5$) and aliphatic thiols ($pK_a = 8.5$)), it was observed that the thiophenols underwent the S_NAr process much quicker then the aliphatic thiols at physiological pH due to fact that their thiolate anion was the dominant species at this pH value. The slightly higher pK_a for the aliphatic thiols ensured that their dominant species was the less reactive neutral form and therefore cleavage of the DNS group occurred at a much slower rate. This study also highlighted that not only does the DNS group allow efficient reduction of the chromophore's fluorescence (due to the PET quenching process of the nitro groups) but also is required for the thiolate mediated S_NAr mechanism to occur more efficiently. This was verified by the synthesis of an analogue of **87**, where the DNS moiety was replaced by a *p*-methylbenzenesulfonyl (Ts) group. Due to the absence of the nitro groups and therefore the PET process, the molecule displayed strong fluorescence with no modulation observed upon the addition of a thiophenol.

It is clear from the above examples that upon thiol mediated cleavage, the thiol group does not directly attach itself to the molecule and therefore any changes in the probes photophysical properties was due to the removal of certain functional groups from their initial structures. However, a number of examples exist where the observed changes in the probe's UV-vis and emission properties is as a direct result of attachment of the sulfhydryl based molecules to the probe's original framework. This detection mechanism can be demonstrated by compounds **88** and **89**, which were previously reported by Zhang *et al.*[250] and Chen *et al.*,[251] respectively. In the case of **88**, upon the addition of Cys and Hcy to a CH_3OH/H_2O (7:3, v/v) solution mixture, a 70-fold enhancement in the fluorescence intensity was observed (Scheme 5.2). UV-vis absorption studies showed a decrease in the λ_{max} centred at 430 nm and the appearance of a new band at 580 nm. This ensured "naked eye" detection, with a solution colour change from yellow-green to red-orange. The authors suggested that

the selectivity of **88** for Cys and Hcy over other larger thiols such as GSH was possibly due to steric hindrance at the reaction site.

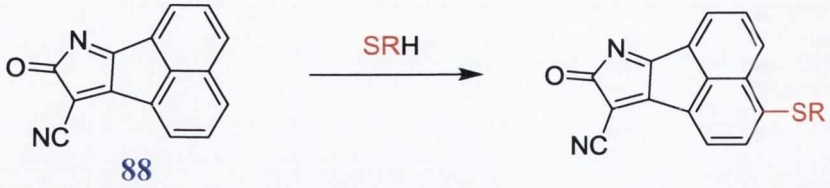

88

Scheme 5.2: *Reaction of probe **88** with a sulfhydryl based molecule.*[250]

In the case of probe **89**, the mechanism used to initiate a response involved a 1,4 addition of the thiol functionality to an α,β unsaturated ketone followed by the spiro ring opening of the fluorescein chromophore (Scheme 5.3). UV-vis absorption and fluorescence studies demonstrated the ability of **89** to selectively detect Cys, Hcy and GSH over other natural amino acids, giving detection limits of 50 nM, 100 nM, and 53 nM, respectively. The ability of **89** to monitor biothiols in living cells and organisms was shown using murine P19 embryonic carcinoma cells and a three day old zebrafish. Upon incubation with a 10 μM solution of **89**, strong fluorescence was observed from both. To verify that thiol detection was the principle cause for this observed emission enhancement, experiments were carried out were the cells and zebrafish were pre-treated with the thiol trapping agent *N*-methylmaleimide. As expected, compared to the initial tests, a reduction in the emission intensity was observed, indicating the specific detection of intracellular thiols by **89**.

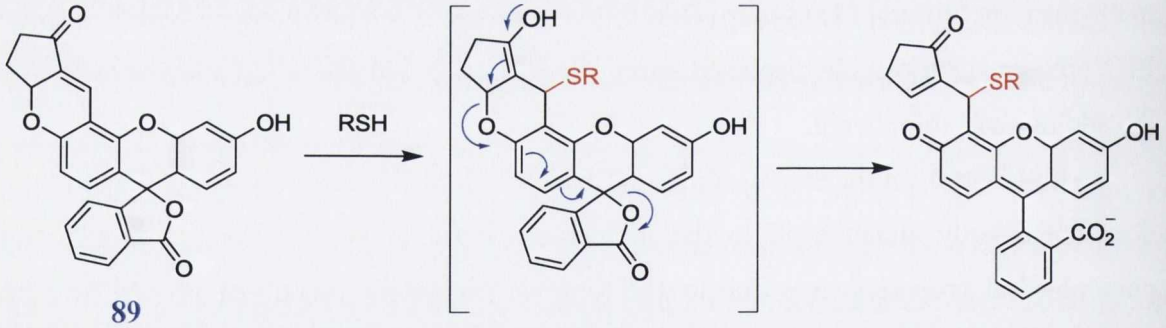

89

Scheme 5.3: *A plausible mechanism of response for **89** in the presence of a thiol.*[251]

Although only used as a control during the cellular studies of **89**, *N*-methylmaleimide has in recent years been incorporated into a variety of chromophoric systems resulting in the development of a large variety of fluorescent probes which show selective detection of sulfhydryl based molecules. As this chapter focuses exclusively on the detection of thiols using this functionality, the following section will give a brief literature review of previously reported thiol probes which have utilised a 1,4-Michael addition to the maleimide moiety as their principle detection mechanism.

5.3.2 Thiol probes which incorporate the maleimide functionality

N-(4'-(7-diethylamino-4-methylcoumarin-3-yl)phenylmaleimide (CPM, **90**), developed by Sippel *et al.*[235, 252] in 1981 was the first example of a thiol probe which employed a 1,4-Michael addition of 2-mercaptoethanol, **91**, to a maleimide moiety as its principle detection mechanism (Scheme 5.4). Studies showed the ability of **90** to regain its bright blue fluorescence upon condensation with the thiol based molecule **91**.

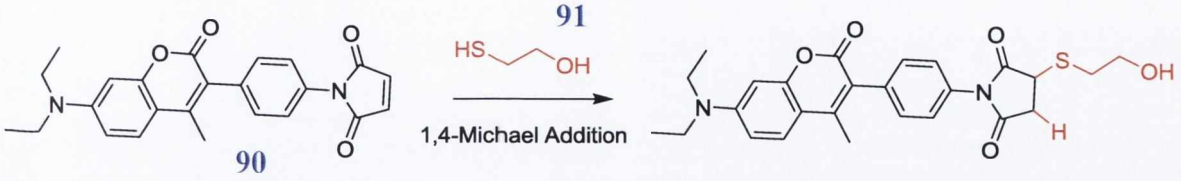

90

Scheme 5.4: *1,4-Michael addition of* ***91*** *to the maleimide functionality of the thiol probe* ***90****.*[235]

Inspired by Sippel's earlier work, Langmuir and co-workers developed a series of naphthopyrane based thiol probes, **92-96** which showed very poor fluorescence due to the presence of the low lying n-π* transition associated with the maleimide unit. However, saturation of the alkene bond of this ring moiety upon the addition of GSH, *N*-acetyl-L-cysteine and **91** resulted in observable Stokes' shift and a significant enhancement in the fluorescence quantum yields of all these probes. The authors also stated that cellular studies were carried out to confirm the ability of **94** and **95** to selectively detect GSH using Chinese hamster V79 cells.

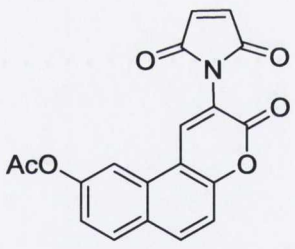

92

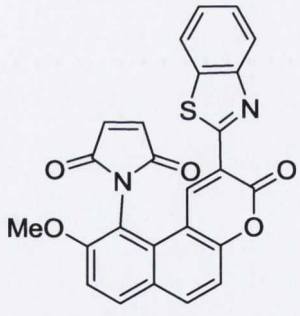

93

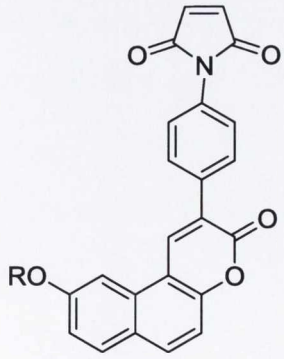

94: R = Ac
95: R = Me

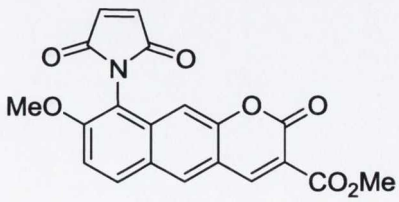

96

Corrie *et al.*[233] extended on this work by developing a series of fluorophore probes, **97-99**, where, unlike the examples shown above, the maleimide functionality was completely separated from the chromophore moiety by an alkyl chain of varying lengths. Initial studies showed that upon addition of the thiol based molecule 2-sufanylethanesulfonate to a predominantly (>90%) ethanolic aqueous solution of each probe, significant fluorescence enhancement were observed for all, with compound **97** displaying a 31-fold emission increase. It was also shown that increasing the distance between the maleimide functionality and the chromophore had a significant effect on the probes response with a large reduction in the emission enhancement being observed. For example, the emission increase observed for probe **98** was reduced by more then 50% when an extra sigma bond was added to the alkyl chain.

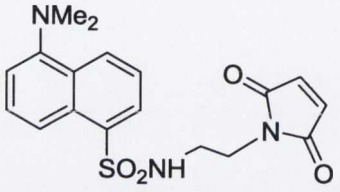

97

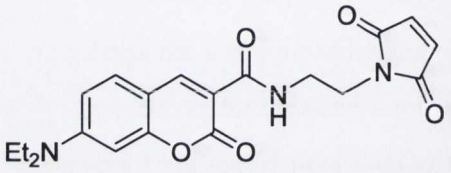

98

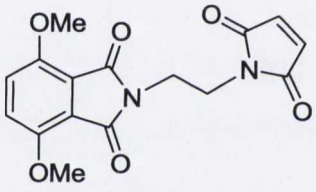

99

The design of several PET based fluorescence probes incorporating a pyrene **100**, phenanthrene **101** and 1,8-naphthalimide **102** chromophore unit was carried out by de Silva *et al.*[230] Short aliphatic hydrocarbon spacers were incorporated between the maleimide functionality and the fluorophore moieties so as to allow for the fast and efficient electron transfer from the excited state of the fluorophore to the electron deficient alkene of the maleimide moiety. The succinimide derivatives which were formed upon reaction of **91**, 1-butanethiol and Cys with the alkene group of each of these probes possessed a much higher reduction potential and as a result of PET quenching, a large enhancement in the fluorescence quantum yields was observed.

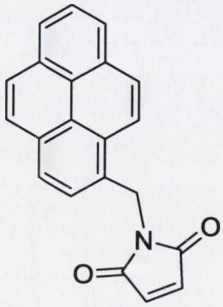

100

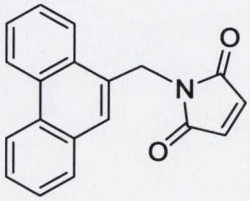

101

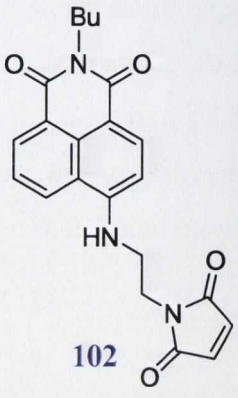

102

As previously discussed, an essential requirement in order for the PET process to occur is that the spacer used between the chromophoric unit and the electron deficient alkene of the maleimide moiety is short. This was verified more recently by Matsumoto *et al.*,[234] through the design of a series of boron-dipyrromethene (BODIPY) based fluorescent thiol probes. These *ortho-* **103**, *meta-* **104** and *para-* **105** substituted maleimide derivates of BODIPY successfully showed that as the distance between the electron donor (BODIPY) and the electron acceptor (maleimide) units was reduced, the more strongly the fluorescence was quenched. Therefore, as expected the PET process proved most efficient for **103**, with the emission almost completely "switched off". However, the addition of *N*-acetylcysteine (NAC) to the maleimide double bond resulted in an almost 350-fold enhancement of its fluorescence intensity. The ability of **104** and **105** to show an observable response in the presence of NAC was not carried out as the probes were already significantly fluorescent even in the absence of any thiol.

BODIPY

103: R =

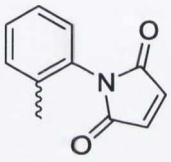

104: R =

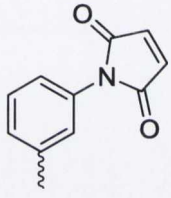

105: R =

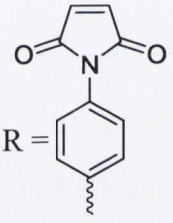

Girouard *et al.*[238] were the first to develop a series of thiol probes **106-109**, which allowed for the incorporation of two maleimide groups into the fluorophore core. Initial studies carried out in a H_2O/DMSO (9:1, v/v) solution mixture showed that upon addition of two equivalents of ethanethiol to each of the dimaleimide fluorogens a large enhancement in their fluorescence intensities was observed, with probe **107** displaying an overall emission enhancement of *ca.* 700%. However, as expected when the dithiol 4,4'-bis(mercaptomethyl) benzophenone (BMMB) was used, the emission intensity reached a maximum after addition of only one equivalent. This demonstrated the ability of BMMB to react with both maleimide functionalities, forming a single dithiol adduct in solution. The significant advantage of these dimaleimide fluorophores is their potential use in protein labelling. The group's initial *in vitro* tests involved the use of the small monomeric protein Cys35Ala, which consists of only one Cys residue within its structure. The reaction of 45.8 μM **108** with 45.8 μM Cys35Ala (1:1, 1 h, 70 °C) resulted in the formation of a monothiolated addition product were only one of the maleimide units reacted with the Cys residue. However, no increase in the probes emission response was observed. The authors suggested that a significant enhancement in the probes fluorescence would only be observed if a thiol reaction occurred at both maleimide

units. This was verified by using a recombinant α-helical protein which was designed to bear two Cys residues in positions complimentary to the maleimide groups of these probes. Using similar reaction conditions as above, formation of a dithiol protein adduct with each of the probes displayed a significant fluorescence response, highlighting their potential ability in specific protein labelling.

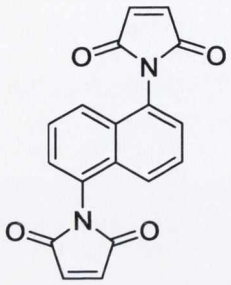

106

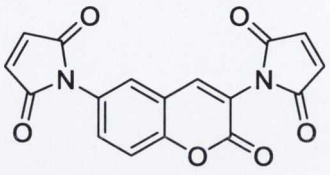

107

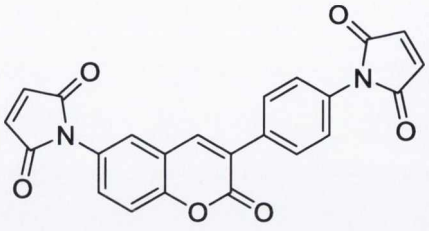

108

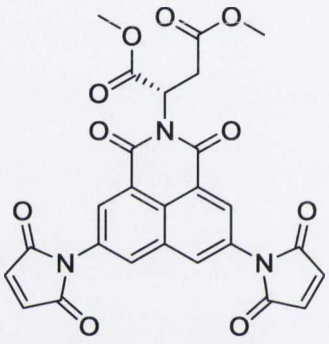

109

5.4 Project objective

From the fluorescent thiol probes described above, it is clear that utilisation of the 1,4-Michael addition to a maleimide functionality has proven an extremely successful mechanism for detection of various sulfhydryl based molecules. It has been shown that saturation of the alkene bond *via* the thiol moiety not only occurs at an extremely rapid rate but also results in significant modulation of the photophysical properties of a variety of different fluorophoric based systems. However, as of yet incorporation of this thiol specific maleimide unit into a Ln based probe has not been reported. Such systems could benefit from the unique photophysical properties these "rare earth elements" have to offer such as their long lived excited states, allowing them to overcome the autofluorescence associated with biological material.[34, 253] Therefore, this chapter describes the design, synthesis and photophysical evaluation of a novel Tb(III) thiol probe **Tb.110**, which incorporates the maleimide ring into its overall structure. It was anticipated that 1,4-Michael addition of a thiol molecule to the maleimide unit, as shown in Scheme 5.5, would bear significant consequences on the energy transfer process from the phenyl antenna to the Tb(III) centre,

effecting the luminescence response of **Tb.110**. The following section begins by detailing the synthesis and characterisation of ligand **110**.

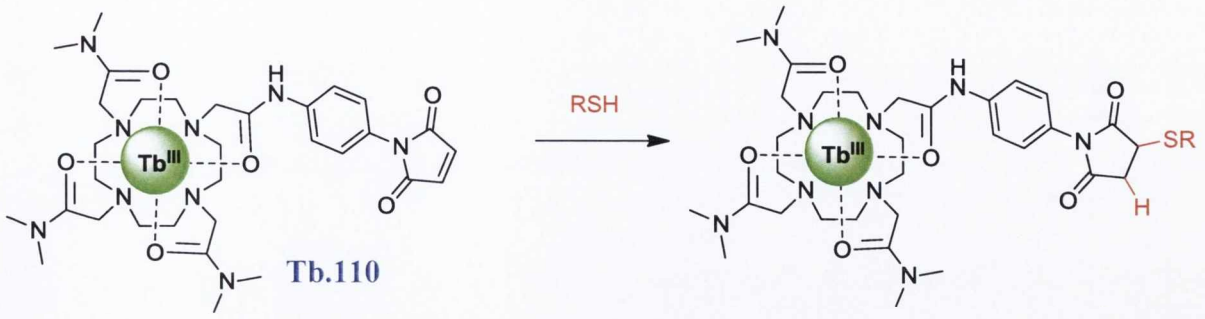

Scheme 5.5: *1,4-Michael addition of a sulfhydryl based molecule to the maleimide ring of Tb.110.*

5.5 Synthesis and characterisation of ligand 110

Being utilised as both an antenna for successful sensitisation of the Ln metal centre and as a site for incorporation of the thiol specific maleimide moiety, the first step in the synthesis of ligand **110** involved the modification of 4-nitro-phenylamine, **111**, with a short α-chloroamide connector, thus providing a link for direct attachment to the macrocylic cyclen framework, Scheme 5.6. This step involved the slow addition of excess chloroacetyl chloride, **65**, along with Et_3N, to a CH_2Cl_2 solution of **111**, at -10 °C (acetone/ice bath). The resulting brown solution was stirred at room temp. for a period of 48 h. Upon reaction completion (monitored by TLC), unreacted **65** along with the NEt_3 salt were removed by extraction with H_2O, 0.1 M HCl and brine, followed by re-crystallisation of the crude mixture from EtOH to give **112**, in 39% yield. The spectral data, including ^1H NMR, ^{13}C NMR, HRMS and IR obtained for this product agreed with previously published characterisation, with the most useful indication of product formation being the appearance of a broad NH resonance at 8.53 ppm in the ^1H NMR spectrum (400 MHz, DMSO), suggesting successful alkylation at the amine site of **111**.[21] Similar to that described for the synthesis of ligand **58** in Chapter 2, the next step in the synthesis of **110** involved monoalkylation of **66** with **112**. The reaction conditions for this step involved refluxing overnight four equivalents of **66** with one equivalent of **112** in freshly distilled $CHCl_3$, in the presence of Et_3N (Scheme 5.6). Isolation of **113** in 69% yield was achieved after successful removal of any unreacted **66** by extraction using a 1 M NaOH solution.

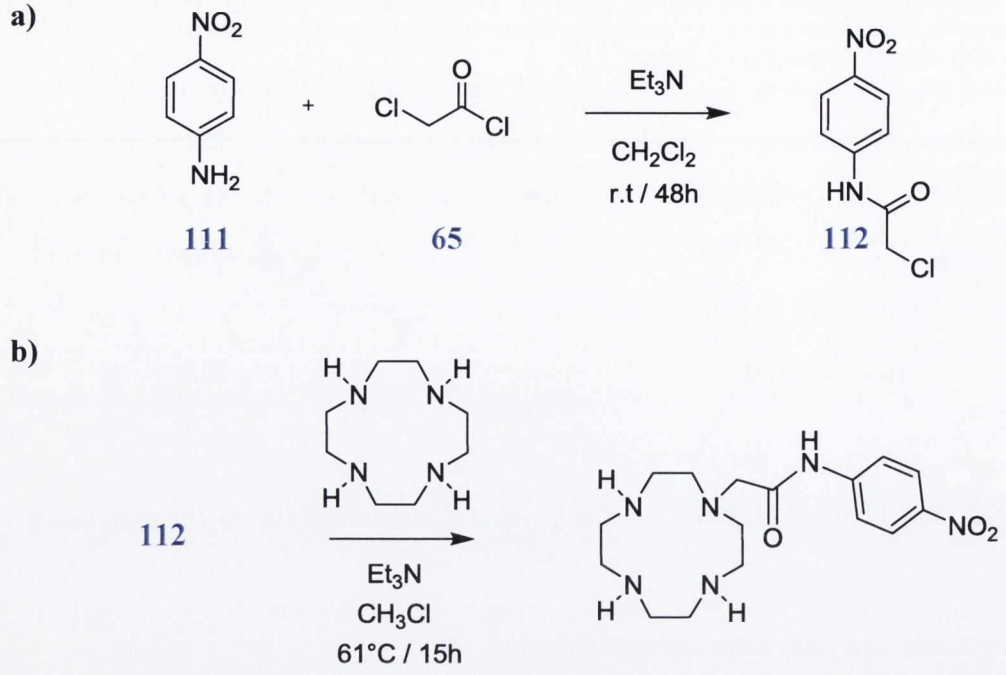

Scheme 5.6: *a) Synthetic pathway of the α-chloroamide 112, followed by b) its selective mono-alkylation onto the cyclen framework to give 113.*

The ^{1}H NMR spectrum of **113**, Figure 5.3, clearly shows the success of this monoalkylation procedure, with the three remaining NH protons of **113** resonating as a broad singlet at 2.21 ppm. The CH_2 resonances of the cyclen framework were observed as a series of overlapping signals between the spectral range 2.77-2.88 ppm, with a total integration value of sixteen. ^{13}C NMR also confirmed successful product formation, with HRMS displaying a *m/z* peak at 373.1962, corresponding to a [**113**+Na]$^{+}$ species in solution.

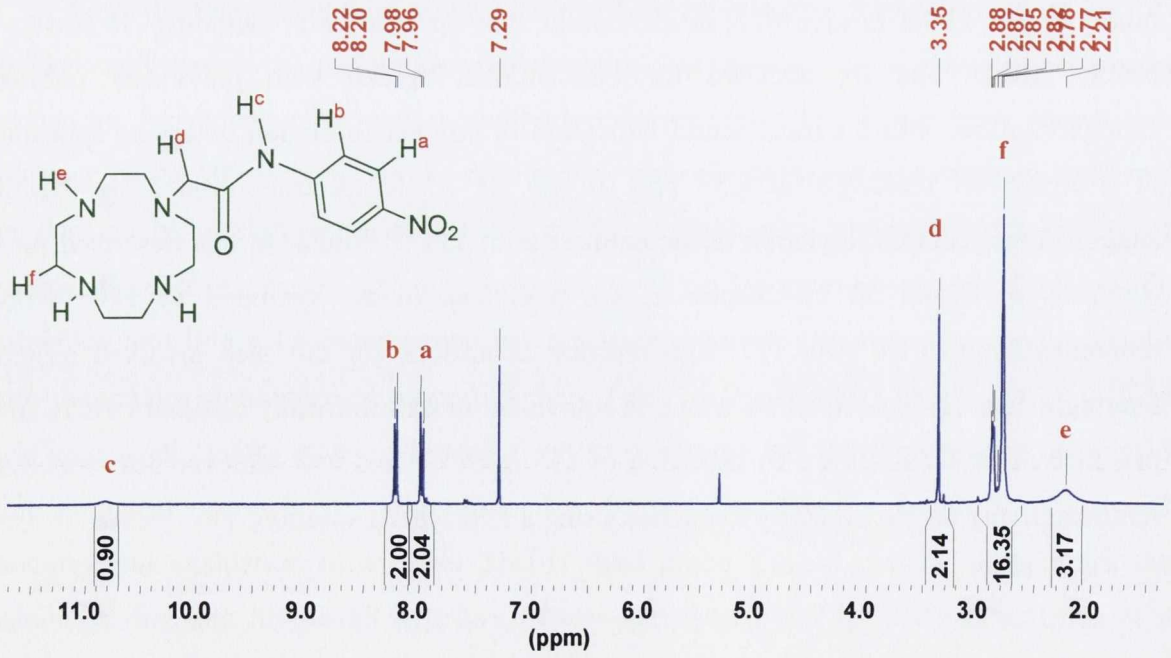

Figure 5.3: *The ^{1}H NMR spectrum (400 MHz, $CDCl_3$) of the monoalkylated species 113.*

Alkylation of the remaining amine sites of the cyclen framework involved refluxing **113** with three and a half equivalents of the α-chloroamine pendant arm 2-chloro-*N,N*-dimethyl-acetamide, **68**, in freshly distilled CH_3CN, in the presence of K_2CO_3 and KI (Scheme 5.7). After refluxing for five days under an inert atmosphere the resulting dark orange oil was purified by alumina column chromatography (elution gradient 100 to 80:20 CH_2Cl_2:CH_3OH), to give the desired product 1,4,7-tris(dimethylcarbamoylmethyl)-10-[(4-nitro-phenylcarbamoyl)-methyl]-1,4,7,10-tetraaza-cyclododec-1-yl}-acetamide, **114**, as a bright orange crystalline solid in 92% yield. In order to allow for incorporation of the maleimide ring into the phenyl chromophore, reduction of the nitro group of **114** to its corresponding amine using excess $N_2H_4.H_2O$ in the presence of 10% Pd/C was undertaken. Initially the reaction was carried out in refluxing EtOH, however, even after a period of 48 h, ^{1}H NMR analysis of the crude reaction mixture seemed to suggest that the reaction had only gone to 50% completion. Therefore, it was decided to try and decrease this reaction time by subjecting the reaction mixture to microwave radiation. After irradiating the sample for 2 h at 80 °C, complete reduction of the nitro group was observed by ^{1}H NMR. Purification of the resulting pale yellow solid was achieved by alumina column chromatography using a gradient elution of 100 to 80:20 CH_2Cl_2:CH_3OH. The desired product, 1,4,7-tris(dimethylcarbamoylmethyl)-10-[(4-amino-phenylcarbamoyl)-methyl]-1,4,7,10-tetraaza-cyclododec-1-yl}-acetamide, **115**, was isolated as a pale yellow solid in 66% yield.

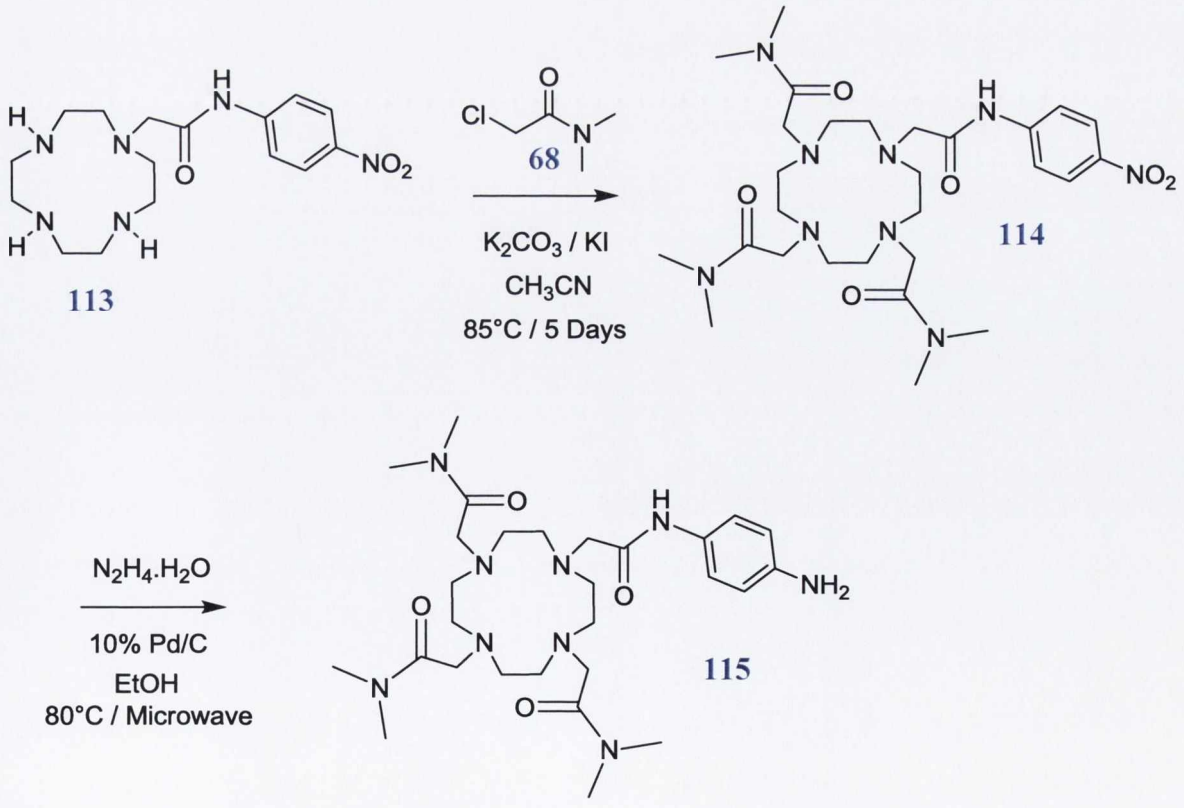

Scheme 5.7: *Synthetic pathway of ligand 115.*

The ^{1}H NMR spectrum (400 MHz, $CDCl_3$) of **115**, displayed in Figure 5.4 shows the expected aromatic signals of the phenyl chromophore, each of which appear as a doublet at 7.57 ppm and 6.56 ppm, respectively. On comparison with the ^{1}H NMR spectrum of the monalkylated species **113** (Figure 5.3), it is clear that successful reduction of the nitro group can be easily monitored by a significant shift in the signals for these aromatic protons. As seen previously in Chapter 2 for the structurally similar ligand **58**, the cyclen CH_2 (16H) protons along with the CH_2 (8H) and CH_3 (18H) protons of the acetamide arms appear as a multiplet of broad overlapping peaks which resonate between the spectral range 2.48-3.72 ppm with a total integration of forty two. ^{13}C NMR along with IR spectroscopy were also used to help verify the formation of **115**, with ESMS displaying a peak at m/z = 576.40, corresponding to a $[\mathbf{115} + H]^+$ species in solution.

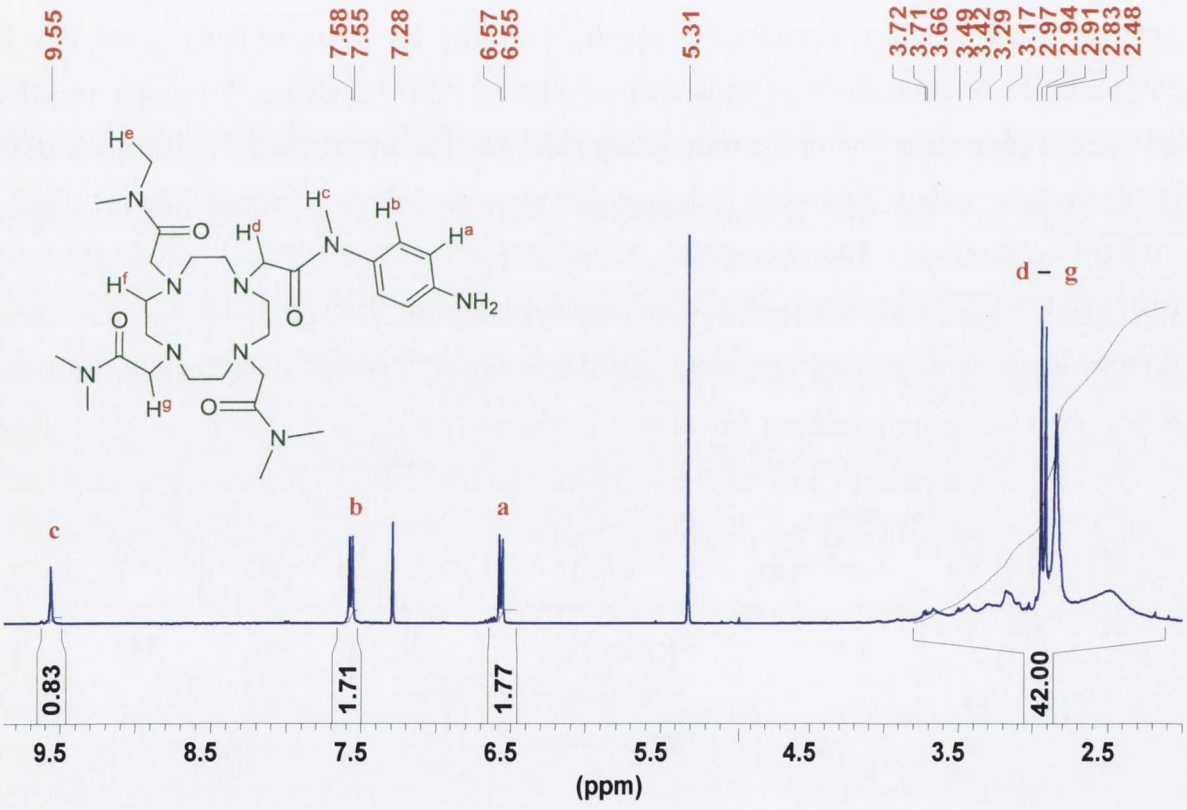

Figure 5.4: *The ^{1}H NMR spectrum (400 MHz, $CDCl_3$) of ligand **115**.*

Incorporation of the maleimide ring into **115** was carried out using a modified version of a procedure previously reported by Cava *et al.*[254] The initial step, as shown in Scheme 5.8, involved refluxing **115** with excess maleic anhydride, **116**, in freshly distilled CH_3CN for 24 h. The reaction was monitored by ESMS, with the appearance of a peak at m/z = 696.38 ($[\mathbf{117}+Na]^+$) signifying successful formation of the acid amide derivate **117**. Upon reaction completion, the solvent was reduced to 80 % of its volume and any excess **116** remaining was removed by precipitation from dry diethyl ether. ^{1}H NMR analysis in $CDCl_3$ of the

resulting crude reaction mixture confirmed the formation of **117** due to the appearance of a new NH resonance at 11.35 ppm (Figure A3.1). Also as a result of the electron withdrawing effect from the newly formed acid amide group, the aromatic doublet which appeared at 6.56 ppm in the ^{1}H NMR spectrum for ligand **115** experienced a significant downfield shift in its resonance to 7.54 ppm. The two protons of the alkene group appeared as two distinct signals at 6.40 ppm and 6.32 ppm.

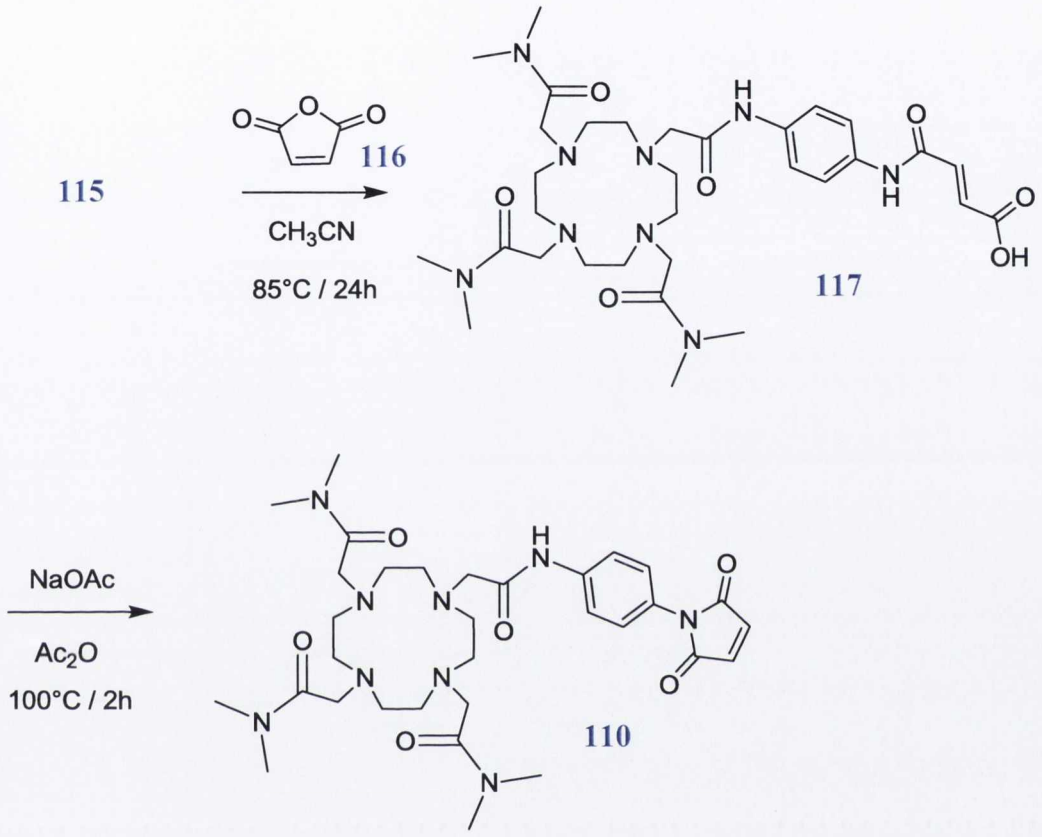

Scheme 5.8: *Schematic representation of the incorporation of the maleimide ring into **115** giving the final ligand **110**.*

The final step in the synthesis of ligand **110** involved treating the crude reaction mixture of **117** with 2.1 equivalents of NaOAc in acetic acid at 100 °C for 2 h (Scheme 5.8). Upon completion, the reaction was cooled to room temp. and poured over a large volume of ice. The resulting aqueous solution was extracted with CH_2Cl_2, dried over $MgSO_4$, filtered and the solvent removed under reduced pressure to yield the final ligand **110** in 27% yield. No further purification methods were required using this work up procedure. A possible reason for attaining such a low yield in this final step is the fact that **110** is partially water soluble, making the final extraction into CH_2Cl_2 quite difficult. An attempt to increase the overall yield involved removal of the acetic acid directly by distillation. The excess NaOAc was then removed by dissolving the resulting orange residue in CH_2Cl_2, followed by filtration. However, unlike that obtained using the initial work up procedure, ^{1}H NMR

analysis showed that the reaction mixture was not pure. Purification by alumina column chromatography proved to no avail and on analysis of the ^{1}H NMR spectrum of the column fractions it appeared that the maleimide ring was reopening, possibly as a result of the basic nature associated with the alumina column.

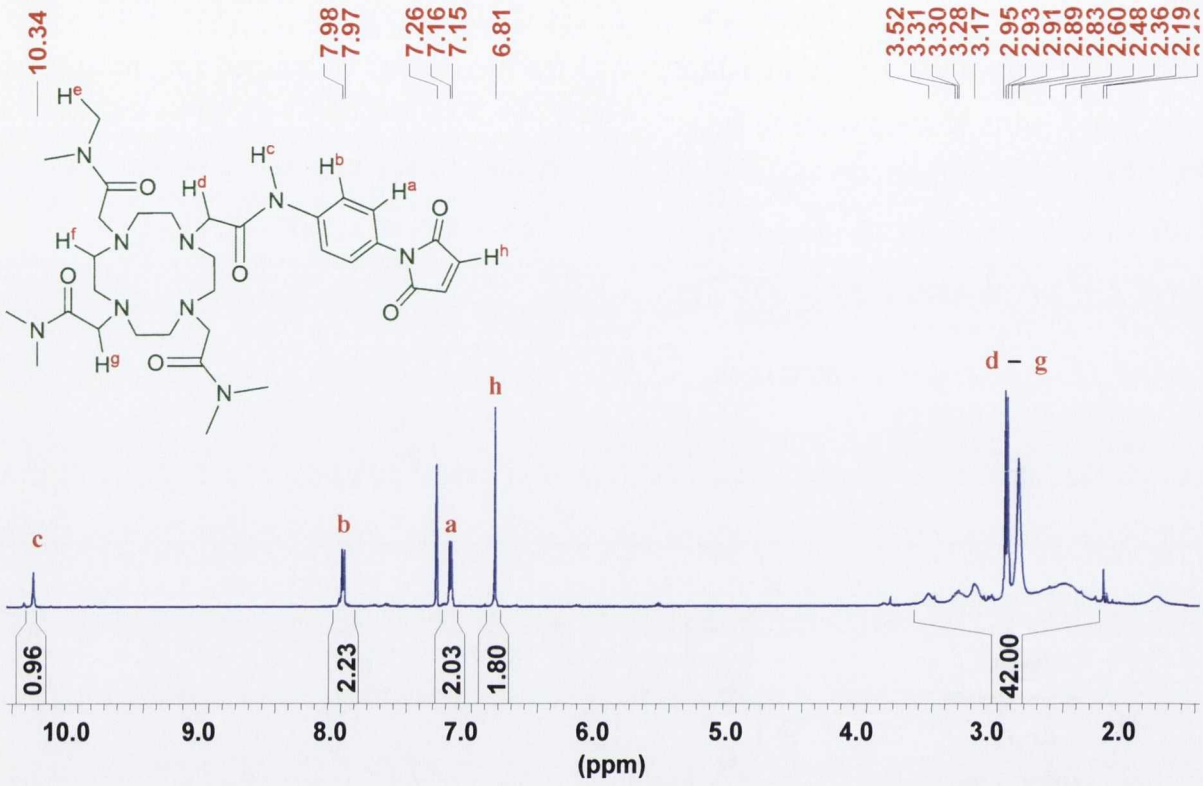

Figure 5.5: *The ^{1}H NMR spectrum (600 MHz, $CDCl_3$) of ligand **110**, verifying successful maleimide ring formation.*

The successful closure of the maleimide functionality and thus subsequent formation of the final ligand **110** was easily verified using ^{1}H and ^{13}C NMR spectroscopy. As shown above in Figure 5.5, the alkene CH protons no longer appear as two distinct signals but as one single resonance at 6.81 ppm with a total integration value of two. This symmetry gain upon ring closure was also observed using ^{13}C NMR, where one of the CH signals which was originally observed for the acid amide derivative **117** disappeared in the ^{13}C NMR spectrum of **110**. Another clear indication of successful maleimide ring formation, using the reaction conditions described above, was the disappearance of the NH resonance at 11.35 ppm, previously observed in the ^{1}H NMR spectrum of **117**. ESMS analysis was also used to confirm the presence of **110**, with a peak at m/z = 656.39 ppm, corresponding to the $[\mathbf{110}+H]^{+}$ species in solution. Overall, the formation of the cyclen based maleimide ligand **110** was carried out in a total of six synthetic steps, with all intermediates characterised using conventional methods such as ^{1}H NMR, ^{13}C NMR, HRMS and IR spectroscopy. Full

characterisation for ligand **110** and all precursor compounds can be found in the experimental section of Chapter 7.

5.6 Synthesis, characterisation and photophysical evaluation of the Tb(III) complex of ligand 110

As previously shown in Chapter 2 and 4, after synthetic completion of **110**, the next step involved successful complexation of this new maleimide based ligand with an appropriate Ln metal ion. As ligand **58**, which also had a phenyl chromophore incorporated into its overall structure, displayed poor energy transfer to its Eu(III) analogue, **Eu.58**, it was decided to only form the Tb(III) complex of **110**. This involved, as shown in Scheme 5.9, refluxing overnight **110** with an equivalent amount of Tb(III) triflate ($Tb(CF_3SO_3)_3$) in freshly distilled CH_3CN, under an inert atmosphere. Precipitation of the resulting orange residue into a large volume of swirling dry diethyl ether gave **Tb.110** as a dark orange solid in 93% yield.

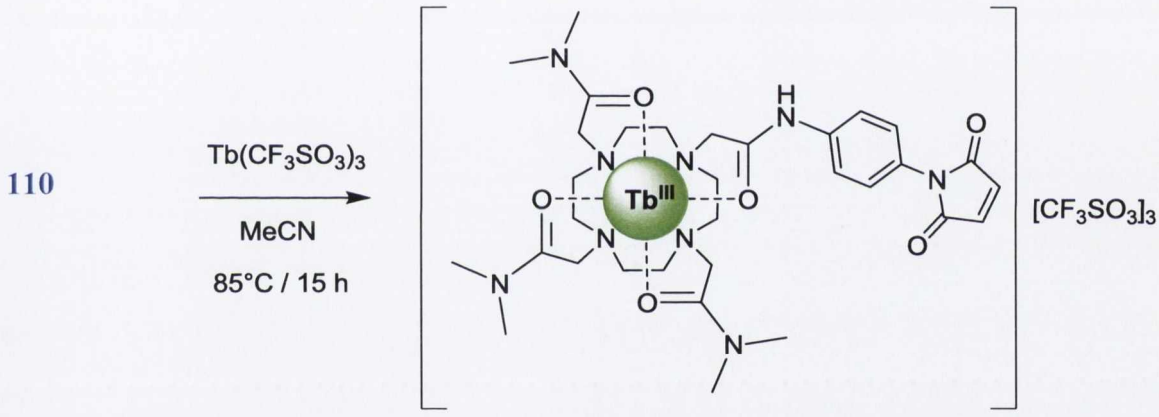

Scheme 5.9: *Synthesis of Tb.110 by complexation of $Tb(CF_3SO_3)_3$ with equivalent amounts of ligand 110.*

Similar to what was observed for all other cyclen based Ln complexes described within this thesis, the ^1H NMR spectrum (400 MHz, D_2O) of **Tb.110** showed the characteristic broadening and shifting of signals, verifying the successful complexation of the Tb(III) ion within the macrocyclic cyclen cavity of **110**. Such interaction, as shown in Figure 5.6, resulted in all the proton resonances, including the equatorial and axial protons of the cyclen ring, being shifted over a total spectral range of *ca.* 180 ppm. The remainder of the ^1H NMR spectrum of **Tb.110** is shown in Appendix 3 (Figure A3.2).

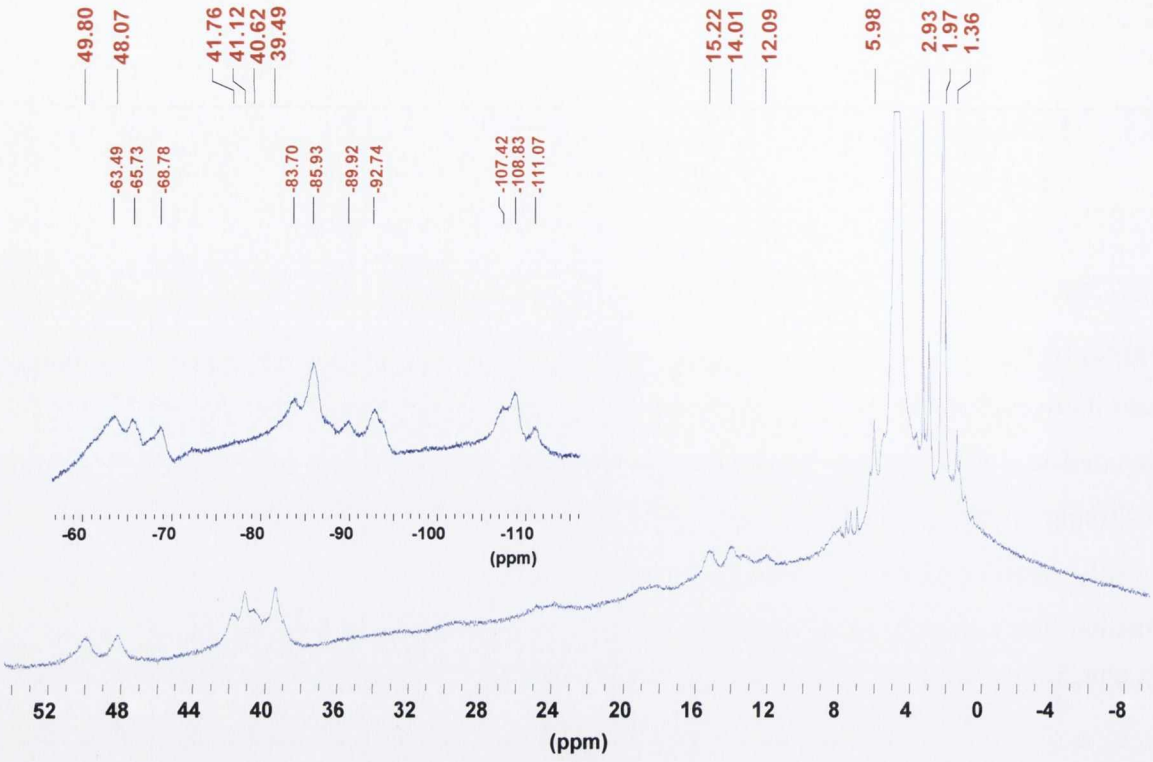

Figure 5.6: *The ^{1}H NMR spectrum (400 MHz, D_2O) of complex* ***Tb.110****.*

Further proof that complexation of the Tb(III) ion had occurred solely within the macrocyclic cavity was gained using IR spectroscopy, where the carbonyl bands of the acetamide pendant arms experienced a shift in their stretching frequencies from 1639 cm^{-1} to 1619 cm^{-1} upon binding to the Ln centre. As expected, no significant shift in the carbonyl bands of the maleimide functionality were observed, confirming that these moieties play no role in the encapsulation of the Tb(III) ion. The last method of characterisation used for **Tb.110** was HRMS, where a peak at *m/z* =1112.21, corresponding to a $[^{159}$**Tb.110**$+2(CF_3SO_3)]^+$ species in solution, was found using MALDI-TOF analysis. The expected isotopic distribution pattern associated with Tb(III) complexes was also observed (Figure A3.3).

The design of **Tb.110** anticipated indirect excitation of the Tb(III) centre *via* the covalently attached phenyl antenna, enabling sensitisation of the Tb(III) $^5D_4$ excited state, which upon relaxation to the ^7F_J (J = 6, 5, 4, 3) ground states gives rise to the characteristic line-like Tb(III) emission bands. Indeed, as shown in Figure 5.7, upon excitation of **Tb.110** at 252 nm (λ_{max} of phenyl antenna), metal centred emission at 490, 545, 586, and 622 nm were observed in an aqueous buffered pH 7.4 (20 mM HEPES, 135 mM KCl) solution.

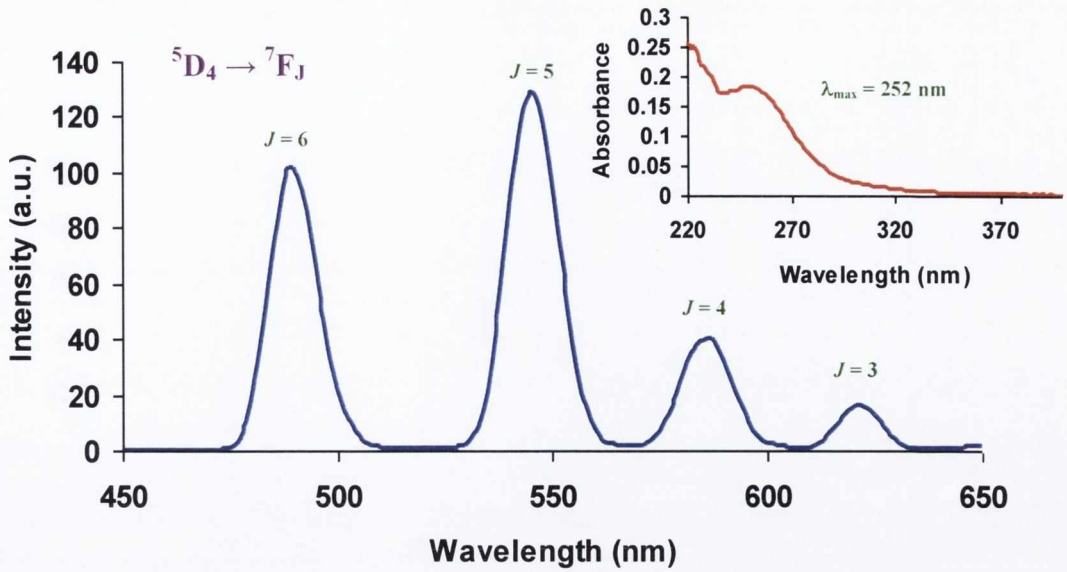

Figure 5.7: *Lanthanide luminescence spectra of* ***Tb.110*** *(10 μM) recorded in an aqueous buffered pH 7.4 (20 mM HEPES, 135 mM KCl) solution using excitation wavelength of 252 nm. Inset: UV-vis absorption spectrum of* ***Tb.110*** *(10μM) with a* λ_{max} *at 252 nm.*

As described in previous chapters, the Ln ions posses a high coordination number, which usually consists of nine for the Tb(III) ion.[34, 41] Therefore, with ligand **110** bearing potentially eight coordination sites for Ln complexation, four from the macrocyclic nitrogens and four from the oxygens of the carboxylic amides, it was expected that in aqueous solution, the ninth and final site would be occupied by a single H_2O molecule. This assumption was verified by recording the excited state lifetimes of **Tb.110** in both H_2O and D_2O by indirect excitation of Tb(III) at 252 nm with values of 1.30 ± 0.01 and 1.99 ± 0.01 ms being measured, respectively. Using Equation 3 (Chapter 1, Section 1.3.2), a hydration state (q) of 1.0 ± 0.25 was calculated.

Having established that excitation of the maleimide functionalised phenyl chromophore of **Tb.110** resulted in sufficient energy transfer to the $^5D_4$ excited state of the Tb(III) ion and that the high coordination requirements associated with such Ln ions was fulfilled (eight ligand donor atoms and one chelating H_2O molecule), the next step was to investigate the response of **Tb.110** in the presence of various sulfhydryl based molecules such as the biothiols Cys and Hcy, with a stronger emphasis being placed on GSH detection. It was anticipated, based on the examples discussed above, that successful 1,4-Michael addition of a thiol based molecule to the maleimide functionality of **Tb.110** would cause significant modulations in the ground state properties of the phenyl chromophore and subsequently effect the sensitisation process from the antenna to the Tb(III) excited state of **Tb.110**. Therefore, the following sections will discuss the results obtained for a series of UV-vis and phosphorescence titrations which were carried out for **Tb.110**.

5.7 UV-vis absorption and luminescence studies of Tb.110

5.7.1 General experimental details

All photophysical measurements were carried out using an aqueous buffered pH 7.4 (20 mM HEPES, 135 mM KCl) solution at 25 °C. To enable initial solubility for preparation of the concentrated 1 mM stock solution of **Tb.110**, 1 % CH_3OH was required. 30 μL of this 1 mM stock solution was then added to 2970 μL of the aqueous pH 7.4 HEPES solution, to give an overall titration concentration of 10 μM for **Tb.110**. A 1 mM aqueous solution of each of the thiols (Cys, NAC, Hcy and GSH) was prepared, with various aliquots of this solution added to the cuvette during the titration measurements. After each thiol addition, a 2 min stirring period was required before a UV-vis or luminescence measurement was recorded. Due to the potential sensitivity of the maleimide ring to hydrolysis over a long period of time, new stock solutions of **Tb.110** were made up before each batch of titrations.

5.7.2 Ground state investigation of Tb.110 in the presence of biothiols

As previously shown in Figure 5.7, the UV-vis absorption spectrum of **Tb.110**, in an aqueous pH 7.4 buffered solution, appears as one broad π–π* absorption band centred at 252 nm. Upon the addition of various aliquots of a 1 mM GSH solution, the absorption spectrum displayed a slight increase in the absorbance as a well as a 4 nm bathochromic shift.

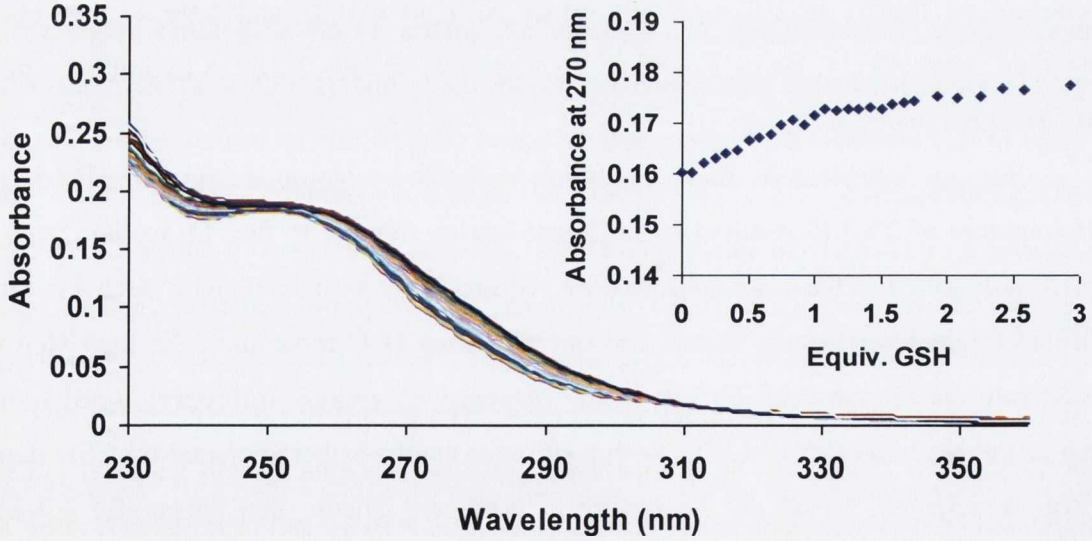

Figure 5.8: *Overall absorption spectrum of Tb.110 (10 μM) as a function of GSH concentration at pH 7.4 aqueous solution (20 mM HEPES, 135 mM KCl). Inset: The changes in the absorbance at 270 nm as a function of GSH equivalents added.*

The titration profile of the absorbance changes at 270 nm versus the number of equivalents of GSH added, shown as an inset in Figure 5.8, suggests that although the changes are relatively small, the most significant UV-vis response is observed upon the

addition of 0 → 1 equivalent of the thiol (*ca.* 10% increase) before becoming much smaller (< 3%) at higher equivalents of GSH. This confirms, as expected, that the 1,4-Michael addition of GSH to the maleimide moiety of the Tb(III) complex forms a 1:1 **Tb.110-GSH** adduct in solution. Upon titration of other biothiols such as Cys and Hcy, a similar effect was observed, with an initial increase in the absorbance spectra, followed by a much lower response after 1 equivalent addition of the thiol based molecule to **Tb.110**. With such small overall changes being observed for the ground state properties of **Tb.110**, no further UV-vis measurements with these biothiols were required. However, the effect of such molecules on the luminescence response of **Tb.110** and therefore its potential for selective biothiol detection needed to be investigated.

5.7.3 Tb(III) luminescence investigations of Tb.110 in the presence of biothiols

As was the case for the UV-vis absorption measurements described above, investigations of the Tb(III) luminescence response of **Tb.110** (using time gated techniques), in the presence of various biothiols were carried out in aqueous pH 7.4 buffered solutions (20 mM HEPES, 135 mM KCl). The initial study involved determination of an appropriate mixing time, ensuring that the 1,4-Michael addition reaction, which was occurring in solution, had time to equilibrate before the luminescence measurements were recorded. Kinetics studies showed that after a 2 min mixing period, the response from the Tb(III) probe was stable, confirming that this short time frame between each thiol addition and measurement was sufficient.

The first biothiol to be investigated was GSH. As shown in Figure 5.9, the addition of GSH to a 10 μM aqueous solution of **Tb.110** resulted in a large enhancement in the probe's Tb(III) emission intensity. Similar to that observed in the UV-vis absorption measurements, at one equivalent of GSH, the emission response from **Tb.110** reached its maximum before gradually decreasing upon further thiol additions. By plotting the intensity of the $J = 5$ emission band as a function of GSH equivalents, it is clear that an overall intensity enhancement of *ca.* 525% was observed due to the formation of the 1:1 **Tb.110-GSH** adduct in solution (Figure 5.9, Inset). A similar response was observed upon plotting all other ΔJ transitions ($J = 6, 4, 3$) as a function of GSH equivalents (Figure A3.4). This significant increase suggests that upon saturation of the alkene bond of the maleimide ring, an enhancement in the energy transfer process to the $^5D_4$ excited state of the Tb(III) ion occurs.

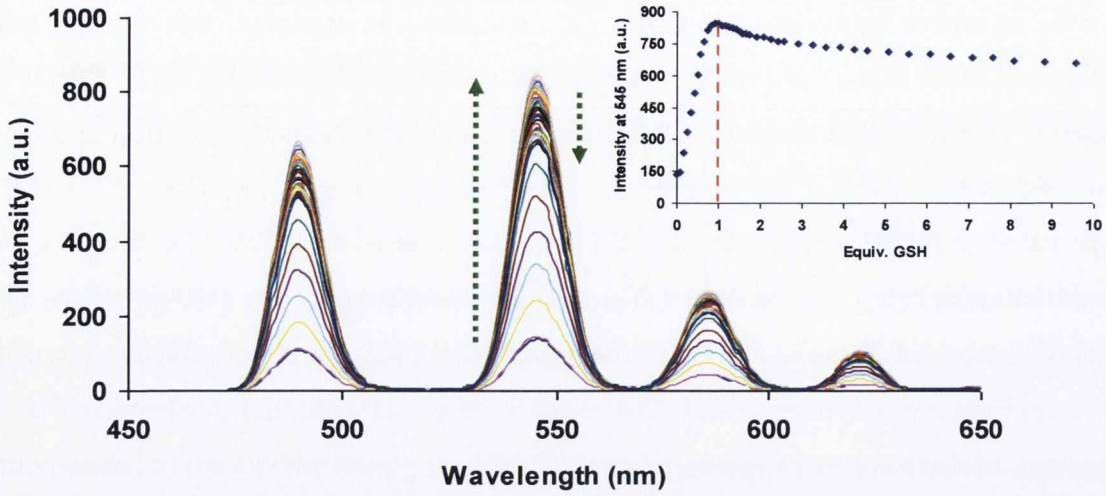

Figure 5.9: *Changes in the Tb(III) emission of Tb.110 (10 μM) in the presence of GSH at pH = 7.4 (20 mM HEPES, 135 mM KCl). Inset: Plot of intensity at 545 nm with equivalents of GSH added.*

To ensure that the observed spectral response for **Tb.110** was as a direct result of the 1,4-Michael addition to the maleimide framework and not just simple displacement of the coordinated H_2O molecule by the nucleophilic thiol moiety of GSH, a series of lifetime measurements were undertaken. This involved recording the excited state lifetimes of the Tb(III) complex in the presence of one equivalent of the GSH molecule both in D_2O and H_2O. As shown in Table 5.1, a slight increase in the excited state lifetimes was observed ($\tau_{O\text{-}H}$ = 1.42 ± 0.01 ms and $\tau_{O\text{-}D}$ = 2.19 ± 0.01 ms), however, when Equation 1.3 was employed to calculate the hydration state of the **Tb.110-GSH** adduct, a value of 0.9 ± 0.25 was obtained. Even in high excess of GSH (10 equivalents), the *q* value calculated never decreased, confirming that in the presence of GSH, the Tb(III) complex still has one H_2O molecule in its coordination environment.

Table 5.1: *Summary of the lifetimes and q values obtained for complex Tb.110 and Tb.110-GSH.*

Compound	$\tau_{O\text{-}H}$ *(± 0.01 ms)*	$\tau_{O\text{-}D}$ *(± 0.01 ms)*	*q (±0.25)*
Tb.110	**1.31**	**1.99**	**1.0**
Tb.110-GSH	**1.42**	**2.19**	**0.9**

Attempts to analyse the titration solutions by mass spectroscopy, using MALDI-TOF and ESMS analysis, was undertaken. However, as a result of the low concentrations used for these measurements, it was not possible to locate a *m/z* peak for the **Tb.110-GSH** adduct. Therefore, a small scale reaction involving **Tb.110** and one equivalent of GSH in H_2O at room temp. for 2 h was carried out (Scheme 5.10). ESMS was employed to analyse the crude

reaction mixture, which showed the presence of a peak at m/z = 1119.38, which corresponds to the [(^{159}**Tb.110-GSH**)-2H]$^{+}$ species in solution. The expected isotopic distribution pattern associated with the ^{159}Tb(III) complexes was also observed for this species (Figure A3.5).

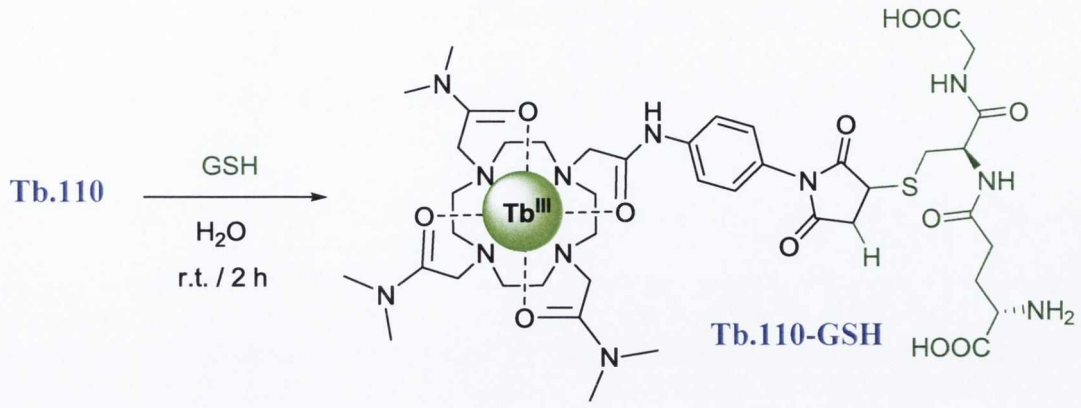

Scheme 5.10: *Reaction scheme of* ***Tb.110*** *and GSH with the subsequent formation of the* ***Tb.110-GSH*** *adduct in solution.*

Using the same titration conditions as previously described for GSH, **Tb.110** displayed a similar Tb(III) emission enhancement upon the addition of Hcy to the solution (Figure 5.10). Again by plotting the intensity of the J = 5 emission band (λ = 545 nm) as a function of Hcy equivalents, it became clear that **Tb.110** experienced an increase in its emission intensity of *ca.* 500%, with the formation of a 1:1 **Tb.110-Hcy** adduct in solution (Inset, Figure 5.10).

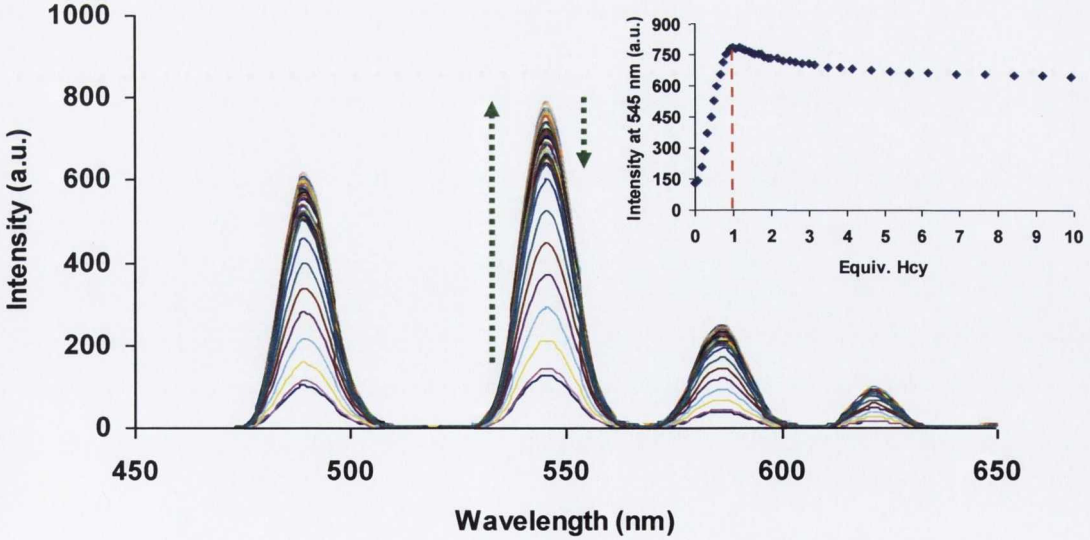

Figure 5.10: *Changes in the Tb(III) emission of* ***Tb.110*** *(10 μM) in the presence of Hcy at pH = 7.4 (20 mM HEPES, 135 mM KCl). Inset: Plot of intensity at 545 nm with equivalents of Hcy added.*

However, when a similar titration was carried out with Cys, although a maximum intensity was reached after addition of one equivalent of the thiol molecule, the intensity

enhancement observed was significantly lower, being *ca.* 230%. Another surprising feature which can be seen by plotting the intensity at 545 nm as a function of Cys equivalents is that upon addition of higher equivalents of Cys to the solution, the Tb(III) emission of **Tb.110** experienced a much larger decrease in intensity of *ca.* 50% (Figure 5.11, Inset).

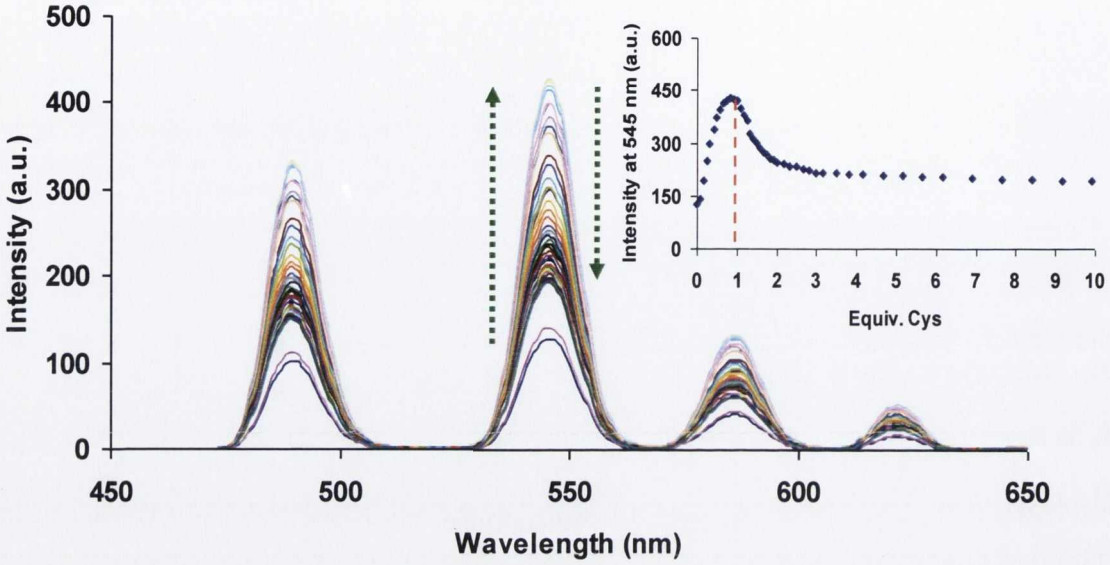

Figure 5.11: *Changes in the Tb(III) emission of* ***Tb.110*** *(10 μM) in the presence of Cys at pH = 7.4 (20 mM HEPES, 135 mM KCl). Inset: Plot of intensity at 545 nm with equivalents of Cys added.*

Confirmation of 1,4-Michael addition of the Cys molecule to the maleimide moiety of **Tb.110** was gained using ESMS analysis, where the presence of a peak at *m/z* = 1083.27, corresponding to a $[(^{159}$**Tb.110-Cys**$)\text{-}2H]^+$ species, verified formation of a 1:1 **Tb.110-Cys** adduct in solution (Figure A3.6).

The only structural variation between Cys and Hcy is the extra CH_2 group located between the thiol functionality and the amine and carboxylic residues in Hcy. Therefore, to investigate the potential interference of the position of this NH_2 group with the 1,4-Michael addition, a titration with the amine protected analogue of Cys, *N*-acetylcysteine (NAC), was carried out. As shown in Figure 5.12, a much larger enhancement was observed in the emission intensity of **Tb.110** upon the addition of NAC, with a total increase of *ca.* 480%. Also from the plot of emission intensity as a function of NAC equivalents, no significant decrease was observed in the Tb(III) intensity at higher concentrations of NAC (Inset, Figure 5.13). These studies seem to suggest that the NH_2 residue in Cys is causing some form of interference at the reaction site, resulting in a much lower intensity enhancement followed by a decrease in the emission profile at higher thiol concentrations. The changes observed for the $\Delta J = 6$, $\Delta J = 4$ and $\Delta J = 3$ transitions of **Tb.110** in the presence of Hcy, Cys and NAC are shown in Figure A3.7.

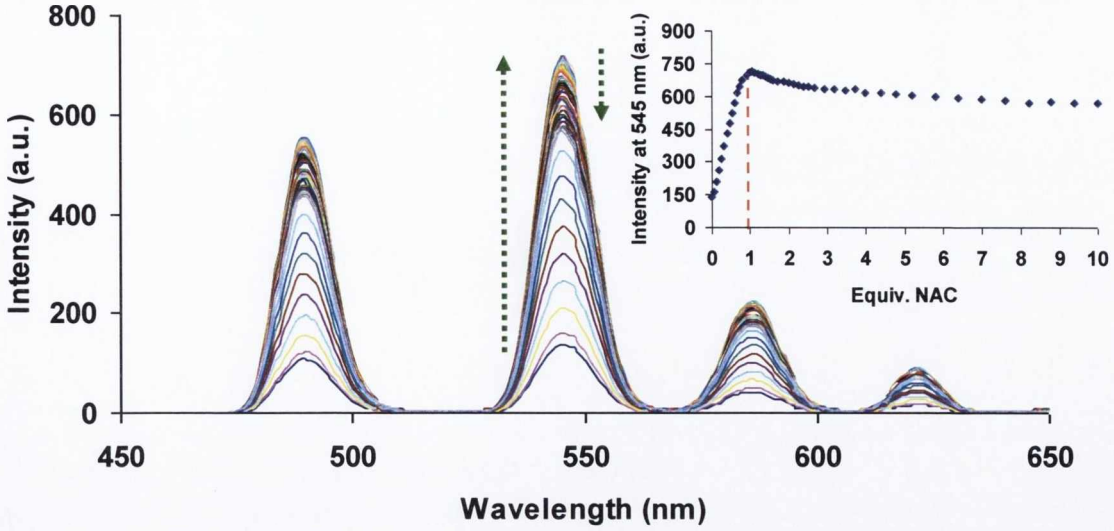

Figure 5.12: *Changes in the Tb(III) emission of* ***Tb.110*** *(10 μM) in the presence of NAC at pH = 7.4 (20 mM HEPES, 135 mM KCl). Inset: Plot of intensity at 545 nm with equivalents of NAC added.*

In summary, the above luminescence titrations confirmed the ability of the sulfhydryl residue of GSH, Hcy and Cys to undergo a 1,4-Michael addition at the alkene bond of the maleimide functionality of **Tb.110**. This detection mechanism was accompanied by a large enhancement in the emission intensity of the Tb(III) ion, where the largest changes were seen up to the addition of one equivalent of the thiol molecule. For both GSH and Hcy, a slight intensity decrease of *ca.* 20% was observed upon further thiol additions to the solution, whereas Cys showed a much larger response, with an *ca.* 50% decrease in its emission intensity being observed. Investigation using NAC, the amine protected analogue of Cys, showed a similar response to what was previously seen for Hcy and GSH suggesting that the position of the amine in relation to the thiol residue bears some significant effect on the reaction mechanism. Taking the 10% error associated with the spectrofluorimeters used, a detection limit of *ca.* 1 μM for Cys, Hcy and GSH was determined.

With pH often playing a pivotal role in the ability of the thiol molecule to undergo 1,4 addition to the maleimide ring, it was essential to investigate the effect of pH on the overall detection response of **Tb.110**. The following section will therefore discuss the results obtained from these studies.

5.7.4 Luminescence response of Tb.110 to GSH as a function of pH

The addition of thiols to the double bond of the maleimide unit typically proceed as a result of nucleophilic attack of their thiolate anions, without the requirement for general base assistance.[238] Therefore, at pH values below the thiols pK_a, the dominant species in solution is the less reactive SH neutral form. With this in mind, it was anticipated that in very acidic

media, the 1,4 reaction mechanism of the sulfhydryl residue of GSH at the alkene double bond of the maleimide unit would be less efficient, possibly resulting in a much poorer emission response from **Tb.110**. However, although in a basic environment, where the GSH molecule exists essentially as its more reactive thiolate anion, potential hydrolysis of the maleimide ring at such pH values must also be considered.[233] Such base-mediated ring opening of the maleimide unit will in turn have a significant effect on the overall response of **Tb.110**.

The effect of pH on the luminescence response of **Tb.110** in the absence of any thiol species was first investigated. This involved the preparation of various individual 10 μM HEPES buffered solutions of **Tb.110**, with pH values ranging over the entire pH scale. As shown below in Figure 5.13, between the pH range 2-7, very little modulation was observed in the luminescence properties of the Tb(III) complex, however, a decrease in the emission intensity of *ca.* 65% was observed at more alkaline pH. With the secondary amide of **Tb.110** bearing a pK_a value within this pH range, it is possible that deprotonation of this site could be responsible for the observed emission decrease. However, the probability that this emission decrease could also be a direct result of base-mediated ring opening of the maleimide functionality must not be ruled out. One conclusion which can be made from this initial study is that within acidic media, the luminescence response of **Tb.110** remains stable, suggesting that there are no protonation or deprotonation processes occurring within this pH range and that the maleimide unit remains closed.

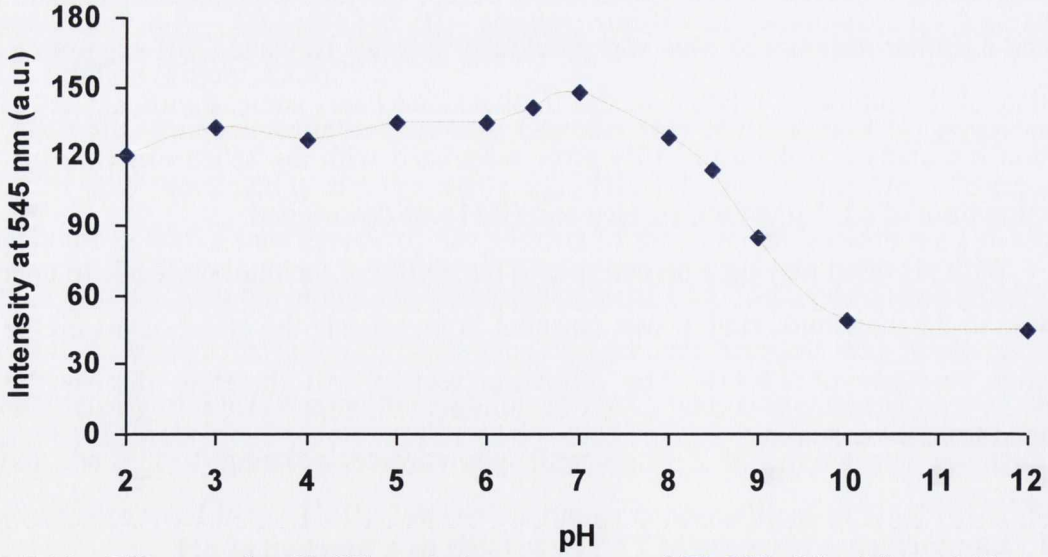

Figure 5.13: *Effect on the Tb(III) emission response of* ***Tb.110*** *(10 μM) at 545 nm as a function of pH. Note: Individual aqueous buffered solutions (25 mM HEPES, 135 mM KCl) with various pH values were prepared.*

The next investigation involved monitoring any change in the response of the Tb(III) complex in the presence of one equivalent of GSH. As described in the previous section,

introduction of GSH to a 10 μM solution of **Tb.110**, at pH 7.4, resulted in a 525% enhancement in its emission intensity, however, any modulation of this response with respect to pH environment needed to be studied. One equivalent of GSH was added to each of the solutions which were used in the previous titration and after a mixing period of 3 min, a luminescence spectrum was recorded (Figure A3.8).

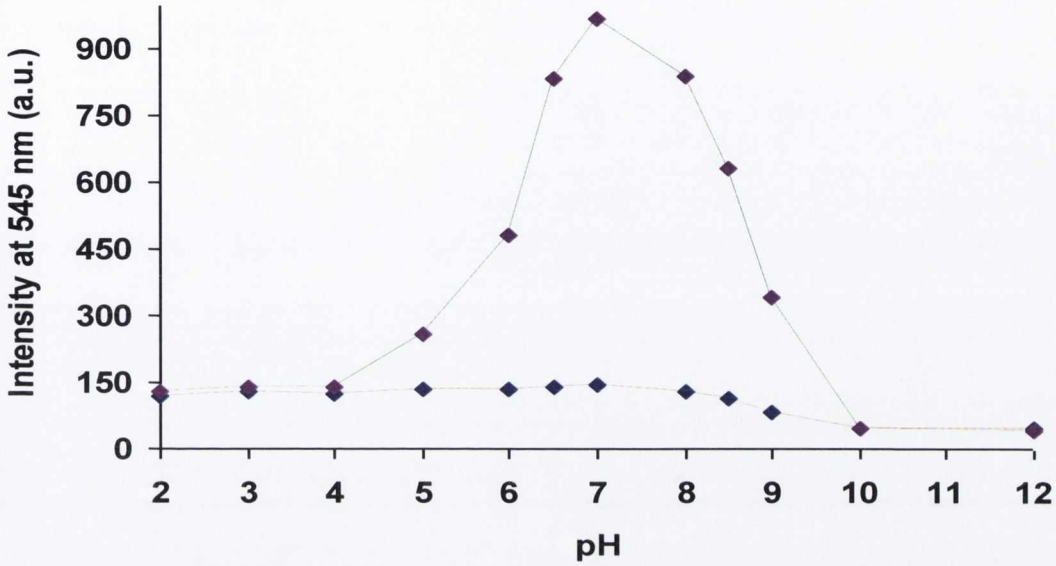

Figure 5.14: *Luminescence response of Tb.110 (10 μM) at 545 nm in the presence of one equivalent of GSH, at various pH values (-----). Luminescence response of Tb.110 (10 μM) at 545 nm in the absence of GSH, at various pH values (-----). Note: Individual aqueous buffered solutions (25 mM HEPES, 135 mM KCl) with various pH values were prepared.*

As shown by the plot of emission intensity at 545 nm as a function of pH in Figure 5.14, a significant change was observed for the emission response of **Tb.110**. One interesting observation was that as the solution was shifted to a more basic environment the emission intensity of the Tb(III) probe diminished dramatically. This seems to support the previous suggestions that these maleimide ring systems undergo rapid ring opening in very extreme basic environments, explaining the observed decrease in emission intensity and why beyond a pH value of 9, **Tb.110** showed no enhancement in the presence of GSH. Further verification for potential ring opening was gained by basifying a 10 μM pH 7.4 solution of **Tb.110** to pH 12, followed by acidification back to its original physiological pH value. Addition of one equivalent GSH to this solution no longer showed any emission enhancement suggesting that basification had caused the maleimide framework to open. It can also be seen from Figure 5.14 that as the pH of the solution was lowered to a more acidic environment, a similar decrease in the luminescence response of **Tb.110** was observed. This supports the fact that as the pH is decreased below the pK_a of GSH, the less reactive neutral SH form of the thiol is the dominant species in solution. This would explain the significant intensity decrease of **Tb.110**, due to its much poorer ability to undergo 1,4-Michael addition

to the maleimide unit. To ensure that this dramatic decrease in emission response was not due to ring opening, a similar study was carried out as before, where a 10 μM solution of **Tb.110** at pH 7.4 was acidified to pH 2, followed by basification back to neutral. However, unlike that previously shown, upon addition of GSH to this solution, the large intensity enhancement was still observed, confirming that the decrease in emission intensity was not due to ring opening but as a result of a decrease in the reaction rate at the maleimide site.

With significant modulations being observed both in acidic and basic pH environments, one important observation from this study is that at physiological pH, the ability of **Tb.110** to detect GSH in solution is extremely efficient. In fact, as shown above in Figure 5.14, at a pH value of 7, the addition of GSH to the maleimide unit of **Tb.110** resulted in a maximum intensity enhancement being observed. This ensures that if this system was to be introduced into a physiological media such as blood, the detection of biothiols would be extremely efficient, with a large emission enhancement accompanying this detection process. The next stage was to investigate its selectivity for biothiols over other non-thiol based amino acids. Therefore, the following section will discuss a screening method which was employed to determine the selectivity of this Tb(III) based probe for sulfhydryl based molecules only.

5.7.5 Selectivity of Tb.110 for biothiols over other non-thiol based amino acids

In order for the selective detection of sulfhydryl based molecules in solution, it is essential that **Tb.110** shows minimal response to other non-thiol based amino acids. Although lacking the nucleophilic SH moiety, it was possible that in large excess of these amino acids, the slightly less nucleophilic amine group could undergo 1,4 addition to the maleimide framework. If this were to occur, then **Tb.110** would have shown a similar emission enhancement which was observed previously, making selective detection of Cys, GSH and Hcy difficult. The screening method involved addition of *ca.* 40 equivalents of each amino acid to a separate 10 μM aqueous pH 7.4 solution of **Tb.110**. Any changes in the luminescence response of the Tb(III) probe were monitored by recording a phosphorescence spectrum 10 min after the initial addition was made. As shown in Figure 5.15, on screening a wide variety of amino acids, any changes in the emission intensity of **Tb.110** were negligible, verifying that even after a 10 min period in solution, no addition to the maleimide functionality and thus modulation in the photophysical properties of **Tb.110** had occurred. The ability of **Tb.110** to retain its detection response for biothiols in the presence of these amino acids was also monitored. As displayed by the red bars in Figure 5.15, upon the addition of excess GSH (20 μM) to each solution, large emission enhancements, representative of successful 1,4 addition to the maleimide functionality, were observed.

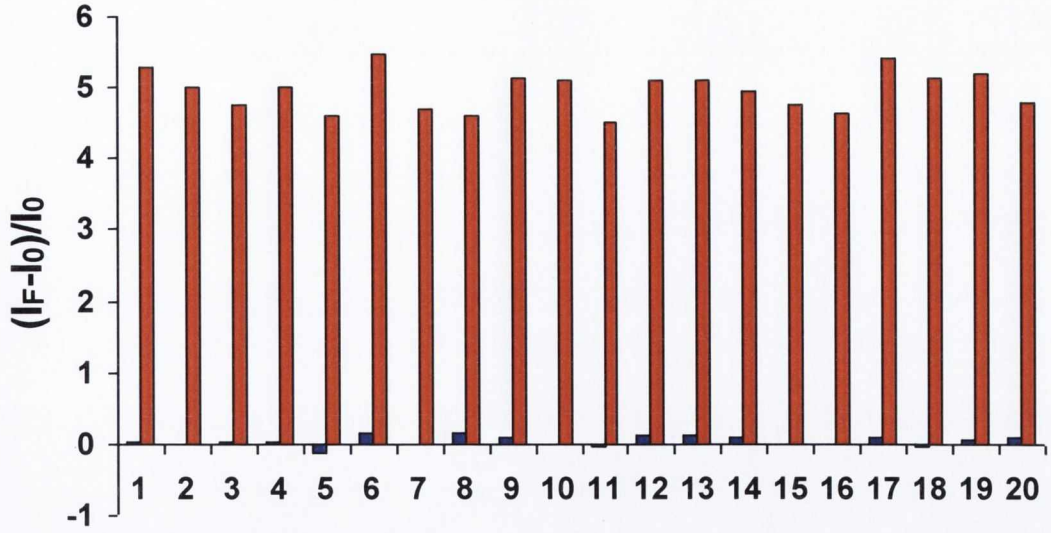

Figure 5.15: *Luminescence response of* ***Tb.110*** *(10μM) in the presence of various physiologically important amino acids (20μM) in H_2O (20mM HEPES, 135 mM KCl, pH 7.4) Bars represent the final emission intensity (I_F) subtracting the initial intensity (I_0) over I_0 at λ_{em} = 545 nm. Blue bars represent the addition of the amino acids: (1) Ala, (2) Asp, (3) His, (4) Arg, (5) Phe, (6) Ser, (7) Val, (8) Ile, (9) GSSG, (10) GSH, (11) Pro, (12) Thr, (13) Tyr, (14) Gly, (15) Leu, (16) Lys, (17) Met, (18) Glu, (19) Sar, (20) Asn. Red bars represent the subsequent addition of GSH (20μM) to the solution of these amino acids.*

One amino acid, not represented in Figure 5.15, which resulted in significant modulation of **Tb.110** emission properties and therefore required a more detailed study, was tryptophan (Trp). Upon the addition of 40 equivalents of this amino acid, the Tb(III) emission intensity was decreased by *ca.* 76%. However, subsequent addition of GSH to the solution resulted in the expected 530% enhancement in the Tb(III) emission intensity, verifying that the modulation in the Tb(III) emission of **Tb.110**, in the presence of Trp, was not due to any binding or reaction event with the maleimide moiety (Figure 5.16).

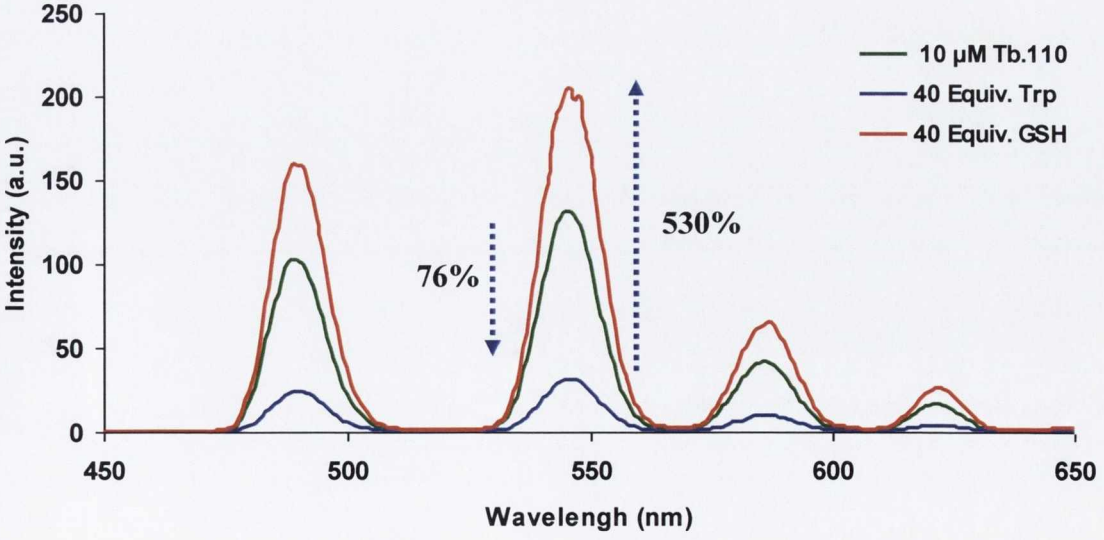

Figure 5.16: *Changes in the Tb(III) emission of* ***Tb.110*** *(10 μM) in the presence of 40 equivalents Trp and upon addition of 40 equivalents GSH at pH = 7.4 (20 mM HEPES, 135mM KCl).*

On analysis of the UV-vis absorption spectra of both **Tb.110** and Trp, it became evident that a possible reason for this initial emission decrease was due to the large spectral overlap which occurred between the π-π* absorption bands of both the Tb(III) complex and the amino acid (Figure 5.17). Therefore, upon excitation at 252 nm, subsequent excitation of Trp was also occurring, this competition resulted in a severe reduction in the population of the $^5D_4$ excited state of the Tb(III) ion and thus lower emission intensity from **Tb.110**.

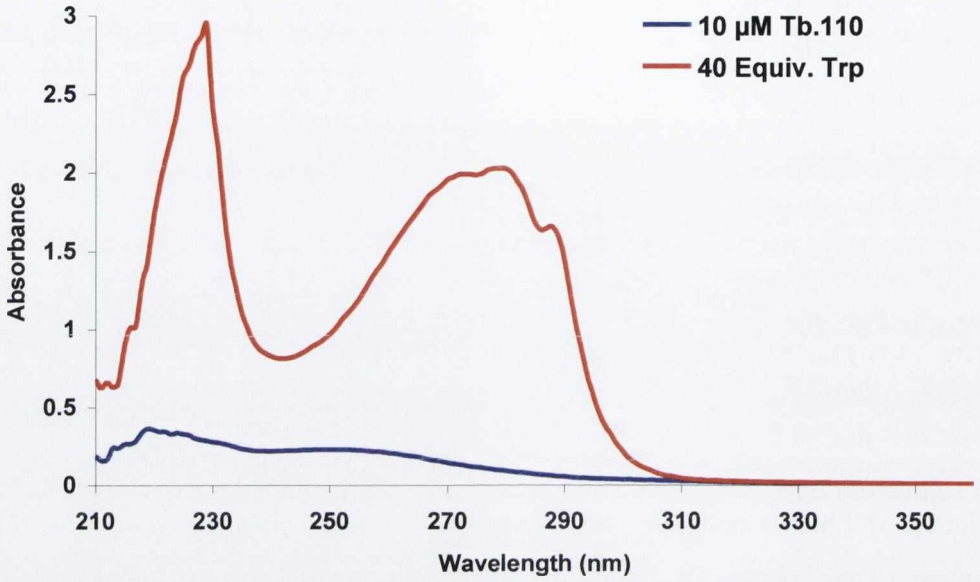

Figure 5.17: *Changes in the UV-vis absorption spectrum of Tb.110 (10 μM) upon the addition of 40 equivalents of Trp at pH = 7.4 (20 mM HEPES, 135 mM KCl).*

Overall, these screening studies helped confirm that **Tb.110** displayed high selectivity for sulfhydryl based molecules over various other naturally occurring non-thiol based amino acids. Although a significant decrease in the emission intensity was observed for Trp due to its spectral overlap with the Tb(III) complex, the detection mechanism was not affected, with a large intensity enhancement upon 1,4 addition still being observed. One significant result of these selectivity studies, which has not been discussed, was the ability of **Tb.110** to display a selective response to GSH over the oxidized GSSG form. As shown in Figure 5.15, in the presence of a high excess of GSSG (40 equiv), **Tb.110** displayed no modulation in its photophysical properties, suggesting its potential to be used as an assay in monitoring the conversion of GSSG to its reduced GSH form in solution. Also, as a shift in the concentration of reduced to oxidized GSH is often used as a clear indicator of a cells overall health and any oxidative damage which may be occurring, the possibility of **Tb.110** to behave as a biomarker for overall health status needed to be investigated. The following sections will therefore discuss a series of enzymatic titrations, where **Tb.110** was used to monitor the conversion of GSSG to GSH using the NADPH dependant enzyme, glutathione reductase.

5.8 Enzymatic conversion of GSSG to GSH using Tb.110 as the luminescent probe

5.8.1 Glutathione reductase mechanism

Glutathione reductase (GR) is a homodimeric flavoenzyme which plays an indirect but crucial role in the prevention of oxidative damage in the cell by helping to maintain appropriate levels of intracellular GSH.[220, 221] Involved in the conversion of oxidised GSSG to its reduced GSH form, GR requires the co-enzyme NADPH along with an active flavin adenine dinucleotide (FAD) site in order for efficient enzymatic activity to occur (Figure 5.18).[255] Previous X-ray diffraction analysis has confirmed that GR is composed of two identical subunits, each with a molecular weight of 50,000 daltons and that the binding sites of NADPH and GSSG are located on opposite sides of one of these units.[256-258] In close proximity to the GSSG binding site is the active FAD group of the enzyme and also a redox active disulfide composed of two Cys residues (Cys_{58}-Cys_{63}). Upon binding to the enzyme site, GSSG positions itself so its sulphur atom is extremely close to the sulphur of one of the Cys residues (Cys_{58}), facilitating more efficient reduction.

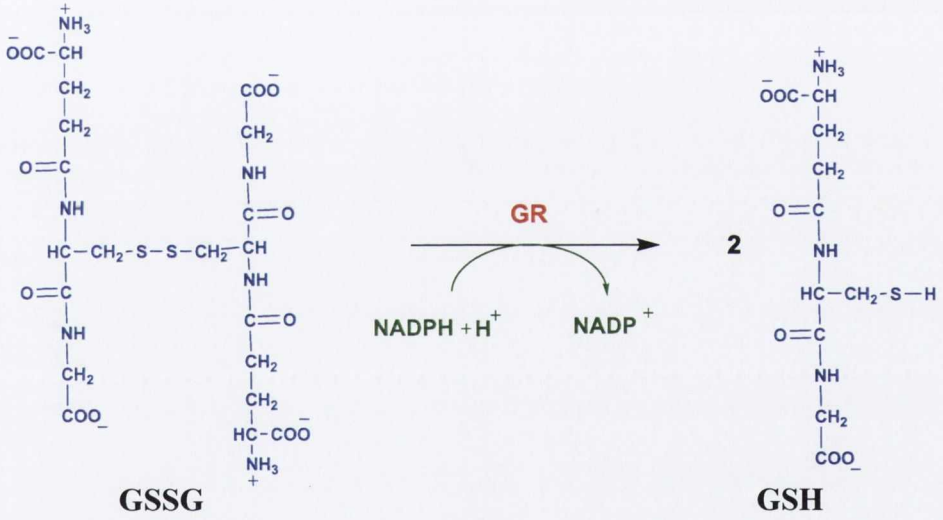

Figure 5.18: *Reduction of GSSG by glutathione reductase (GR) and NADPH.*[259]

Initially it was suggested that the mechanism involved "hydride transfer" directly from the NADPH to the redox active disulfide and therefore to the GSSG molecule. However, due to the location of the FAD moiety and its ability to behave as a molecular wall, it was quickly determined that this process could not occur. On further investigation and with confirmation by spectroscopic analysis, it was determined that the electron transfer sequence in this enzymatic process actually involves a flow of reduction equivalents from NADPH to the FAD unit, then to the redox active disulfide and finally to the bound GSSG molecule.[260]

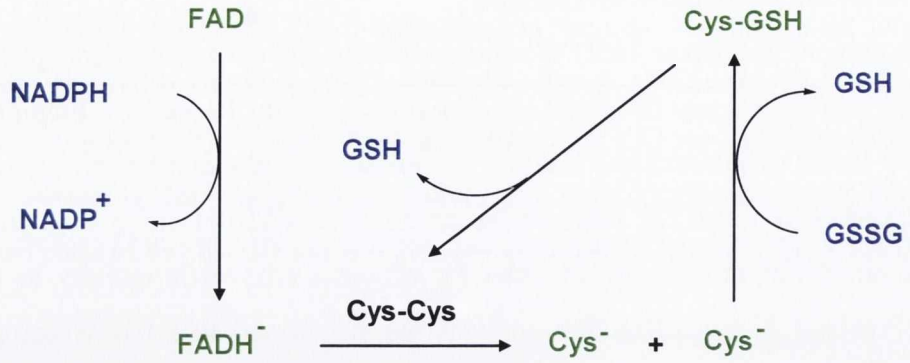

Figure 5.19: *Illustration of the enzymatic GSSG reduction process.*[260]

Therefore, the proposed catalytic mechanism for GR, as shown in Figure 5.19, involves the initial reduction of FAD by binding of NADPH to the enzyme, resulting in the formation of the transient $FADH^-$ anion. This results in subsequent cleavage of the redox active disulfide Cys-Cys residue, releasing the extremely nucleophilic Cys thiolate anions. Direct attack of the disulfide bond of GSSG by one of these Cys residues results in the formation of one molecule of GSH and a mixed Cys-GSH species. Subsequent attack of this mixed adduct by the remaining Cys anion regenerates the disulfide Cys-Cys bond of the enzyme, releasing another GSH molecule during the process. Overall, during this enzymatic process, GSSG is converted to two molecules of its reduced GSH form.

5.8.2 Luminescence response of Tb.110 during the enzymatic conversion of GSSG to GSH

The GR enzyme which was required to investigate the response of **Tb.110** to the conversion of GSSG to GSH was obtained from Sigma and Aldrich Ireland as an aqueous buffered (25 mM TRIS-HCl, 1 mM EDTA) pH 7.4 solution. This 74 μM stock was diluted by a factor of ten by adding 5 μL of the enzyme to 45 μL of a 0.1 M TRIS, 0.135 mM KCl solution. A 1 mM solution of the co-enzyme NADPH was also prepared prior to the titration studies. To completely mimic physiological conditions it was necessary to carry out all enzymatic titrations at 37 °C, using a 0.1 M TRIS, 135 mM KCl solution as the buffered pH 7.4 environment.

With previously reported literature confirming that high concentrations of NADPH can have inhibitory effects on the enzymatic mechanism of GR and due to the presence of its π-π* absorbance band at 260 nm the initial study involved optimising the NADPH concentration.[261] These investigations ensured that any potential inhibitory response would be eliminated and also minimise the effect its spectral overlap may have with the π-π* absorbance band of **Tb.110**. Initially, the effect of this spectral overlap upon the addition of

NADPH alone (3.3 μM, 6.6 μM and 10 μM) to a 10 μM solution of **Tb.110** was determined, where a decrease in emission intensity of *ca.* 7% was observed for the lowest 3.3 μM concentration (Figure A3.9). This suggests that although the NADPH has an absorbance band at 260 nm, when low concentrations of this co-enzyme are used the modulation of **Tb.110** emission response is small. The next step involved initiation of the enzymatic process by introduction of the disulfide GSSG molecule and the GR enzyme to the titration solution. An excess of GSSG (5 equivalents) was used with an extremely low concentration of 4.93 nM required for GR. This kinetic study involved recording the luminescence changes of **Tb.110** every two min until the enzymatic process ceased *i.e.* no further response from **Tb.110** was observed (Figure A3.10).

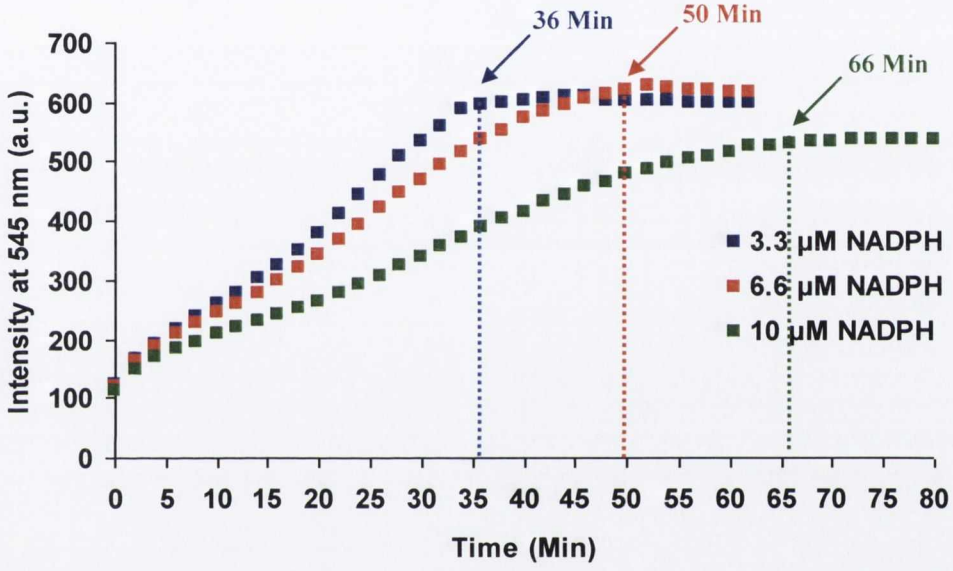

Figure 5.20: *Luminescence response of **Tb.110** (10 μM) at 545 nm as a result of the enzymatic conversion of GSSG to its reduced GSH form using the enzyme GR (4.93 nM) and various concentrations of NADPH. All enzymatic titrations were carried out in aqueous pH 7.4 buffered solutions (0.1 M TRIS, 135 mM KCl) at 37 °C.*

Shown above in Figure 5.20 is the Tb(III) emission response of **Tb.110** at 545 nm as a result of the enzymatic conversion of the oxidised GSSG species to its reduced GSH form. As expected, upon exposure of the sulfhydryl residue, subsequent 1,4 addition to the maleimide functionality resulted in a significant enhancement in the emission intensity of **Tb.110**. It was also observed that as the concentration of the co-enzyme NADPH was increased, the reduction of GSSG occurred at a much slower rate, confirming NADPH's inhibitory response with increased concentration. For example, when 3.3 μM NADPH was used, the time scale required for the redox process to cease and thus a plateau to form was 36 min compared to 66 min in the presence of 10 μM NADPH. One observation made from this investigation was that the intensity enhancement observed was *ca.* 400%, a value slightly lower then that which was observed for the GSH titrations previously discussed (525%). As a

large excess of GSSG was used, this slight decrease in response cannot be attributed to insufficient GSH production in solution. This was verified by the fact that when excess GSH was added at the end of this kinetic study, no further increase in the emission intensity was observed. Also to eliminate the possibility that changing the buffer from HEPES to TRIS may have resulted in a lower response for **Tb.110**, the modulation upon the addition of one equivalent GSH to a 10 μM TRIS solution of the Tb(III) probe was investigated. As previously seen for the HEPES studies, an enhancement greater then 500% was observed. This seems to suggest that this slightly lower Tb(III) response is directly related to introduction of the GR enzyme and the NADPH co-enzyme to the solution.

With a sufficient enzymatic response being observed using 3.3 μM NADPH, the next investigation was to study the effect of increasing the concentration of GR on the GSSG to GSH conversion rate (Figure A3.11). As shown in Figure 5.21, doubling the concentration of GR to 9.86 nM resulted in a reduction in the time scale for the redox process by 50%, with a plateau of the emission intensity of **Tb.110** being observed after a period of 18 min. A further reduction to 10 min was observed when the concentration of GR was increased to 19.72 nM. This verifies the expected linear relationship between enzyme concentration and the time scale for the enzymatic process to occur. It also confirms the fast response of **Tb.110** in monitoring the conversion of GSSG to the reduced GSH species.

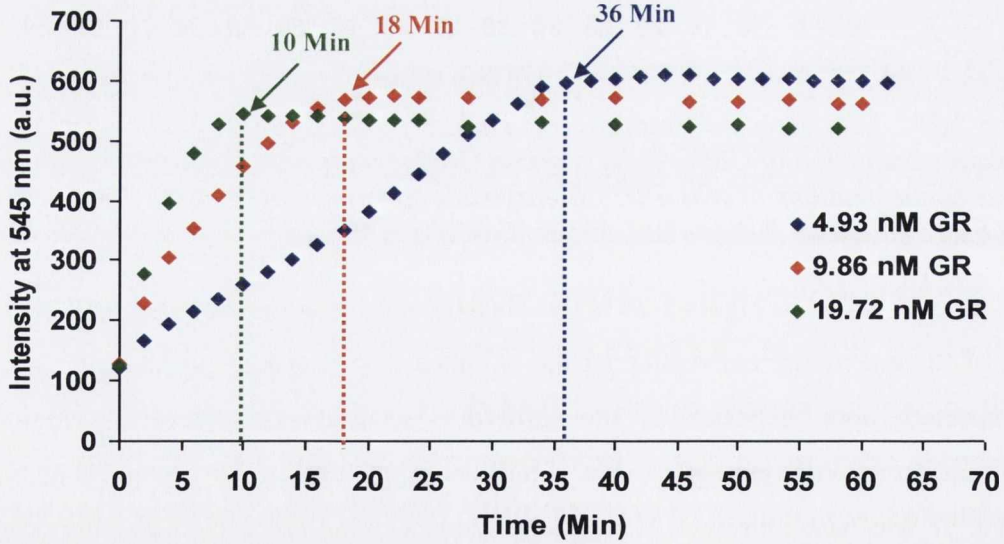

Figure 5.21: *Luminescence response of **Tb.110** (10 μM) as a result of the enzymatic conversion of GSSG to its reduced GSH form using NADPH (3.3 μM) and various concentrations of the enzyme GR. All enzymatic titrations were carried out in aqueous pH 7.4 buffered solutions (0.1 M TRIS, 135 mM KCl) at 37 °C.*

One technique commonly used to monitor this GSSG to GSH redox process and which forms the basic principle behind commercially available GR assays, is the difference in the absorbance bands of NADPH and its oxidized $NADP^+$ form. As previously discussed,

the initiation step in this enzymatic process involves formation of the transient $FADH^-$ anion by oxidation of NADPH to $NADP^+$. This oxidation stage is accompanied by a decrease in the absorption band of NADPH at 340 nm, thus providing a simplified spectroscopic method to monitor the overall GSSG reduction process. Therefore, to ensure that the response which was occurring for **Tb.110** was as a result of GSH formation, a UV-vis absorption titration was carried out, where 3.3 μM NADPH and 19.72 nM GR were used. As shown in Figure 5.22, the usual minimal changes were observed for the absorption band at 252 nm for **Tb.110** (Figure 5.8), however, successful $NADP^+$ production was clearly confirmed by the decrease in the absorption band at 340 nm. By plotting the absorbance changes at 340 nm as a function of time, an approximately 10 min time scale was required for the process to occur, supporting the results obtained previously from the luminescence measurements using such enzymatic conditions.

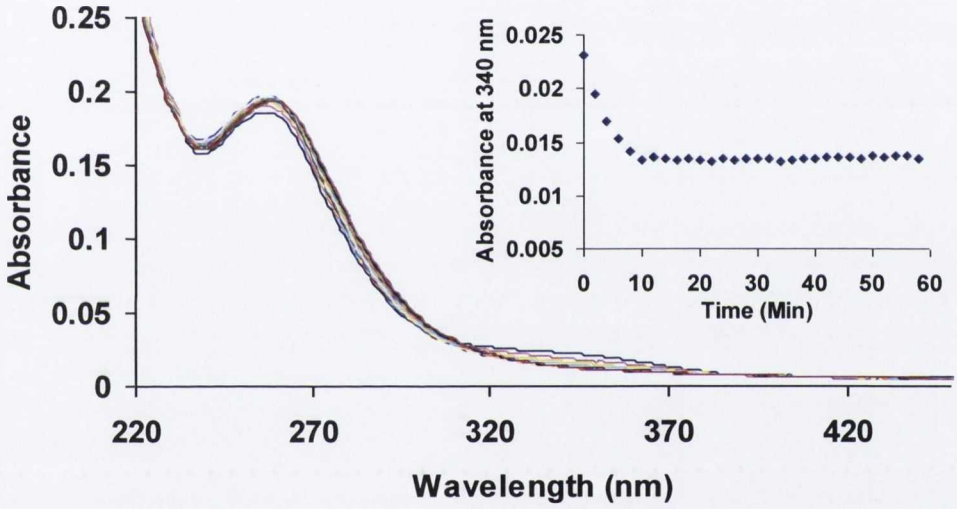

Figure 5.22: *Overall absorbance response of **Tb.110** (10 μM) as a result of the enzymatic conversion of GSSG to its reduced GSH form using NADPH (3.3 μM) and the enzyme GR (19.72 nM). Inset: Plot of absorbance at 340 nm as a function of time.*

Overall, both the luminescence and UV-vis absorption studies for **Tb.110** demonstrated the efficiency of this cyclen based Tb(III) probe in monitoring the enzymatic conversion of GSSG to its reduced GSH form. Subsequent addition of the thiol residue to the maleimide framework resulted in a modulation of the energy transfer process from the phenyl antenna and thus a large enhancement in emission intensity for **Tb.110** was observed. Studies also confirmed that at high NADPH concentrations, an inhibitory effect on this enzymatic process occurred and that a linear response between GR concentration and time scale for the redox conversion existed. With a greater understanding of the reaction conditions required, the next stage was to monitor any changes to the response of **Tb.110** in the presence of high excess of a variety of naturally occurring amino acids. It is essential to understand what

modulations may occur if this Tb(III) probe was utilised in a physiological media. Therefore, the results and any conclusions which could be made from these set of titrations will be discussed in the following section.

5.8.3 Luminescence response of Tb.110 during the enzymatic conversion of GSSG to GSH in the presence of naturally occurring amino acids

In order to determine any modulation in the emission response of **Tb.110** in the presence of other physiologically important species, an aqueous pH 7.4 solution (0.1 M TRIS, 135 mM KCl), containing 40 equivalents of all the amino acids previously used for the selectivity screening studies (Section 5.7.5), were prepared. The concentration of the co-enzyme NADPH was kept constant at 3.3 μM, while the concentrations for the GR enzyme used were 4.93 nM and 9.86 nM. The initial luminescence spectrum recorded for the 10 μM **Tb.110** solution before any of the enzymatic components were added was significantly lower in the presence of all these amino acids, with an intensity decrease of *ca.* 30 % for the $\Delta J = 2$ emission band at 545 nm.

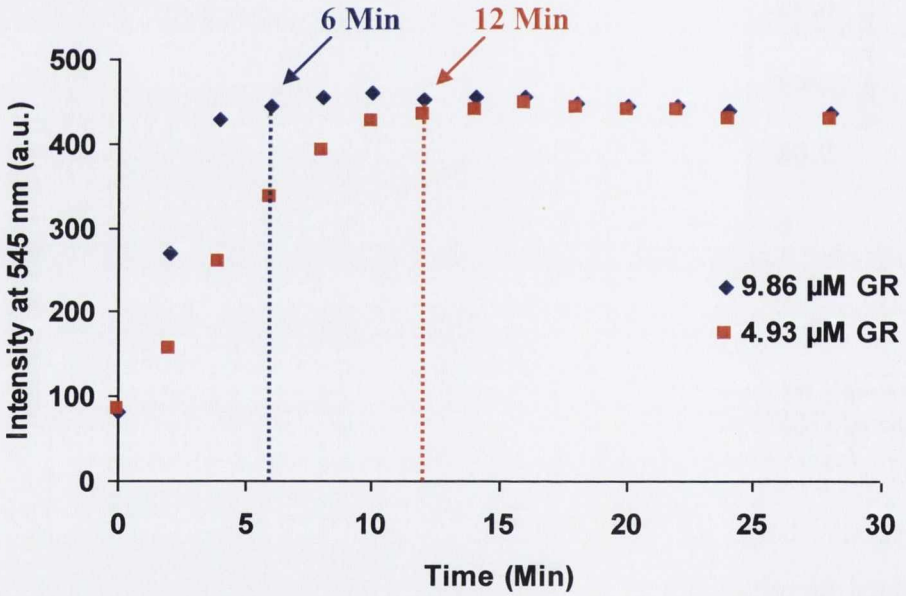

Figure 5.23: *Luminescence response of Tb.110 (10 μM) at 545 nm as a result of the enzymatic conversion of GSSG to its reduced GSH form using the enzyme glutathione reductase (4.93 nM and 9.86 nM) and NADPH (3.3 μM) in the presence of 40 equiv of Ala, Asp, His, Arg, Phe, Ser, Val, Ile, Pro, Thr, Tyr, Gly, Leu, Lys, Met, Glu, Sar and Asn at 37 °C.*

Upon the addition of NADPH, GSSG and the GR enzyme the expected enhancement in the emission intensity from **Tb.110** occurred, however, as shown in Figure 5.23, the rate at which this enzymatic process occurred increased significantly by a factor of three. For example, when a GR concentration of 4.93 nM was used, the time taken for a plateau to be reached was only 12 min, compared to the 36 min which was recorded in the absence of the

amino acids. Although, the initial decrease in **Tb.110** emission intensity was observed when in the presence of all these amino acids, the enhancement displayed upon GSH formation was *ca.* 400%, a similar value to that which was seen in the absence of these species. Therefore, although the rate of the enzymatic reduction of GSSG in solution displayed a significant enhancement, the overall response of **Tb.110** was not affected by the presence of these physiologically important species. It was decided to leave Trp out of this amino acid study as overlap of its π-π* absorption band with that of **Tb.110** would complicate the study and also the intensity of the initial Tb(III) emission spectrum would be extremely low. It was also necessary to exclude Hcy and Cys from this amino acid mixture, as previous studies have shown **Tb.110** to show similar modulation of its photophysical properties in the presence of these sulfhydryl based molecules (Section 5.7.3). However, of all the thiol containing components of blood, the GSH content makes up 90% of its entire composition with previous literature stating that due to this extremely high concentration of GSH, all other potential thiol molecules can be disregarded.[214, 262] This suggests that if **Tb.110** was to be used in blood sample analysis, any emission enhancement which was observed could possibly be directly related to the GSH composition within the sample, ignoring any effect that may be as a result of other biothiols such as Hcy and Cys.

Overall, all these enzymatic studies have shown the ability of **Tb.110** to be used in monitoring the conversion of GSSG to GSH in solution using the NADPH dependent GR enzyme process. However, to gain a real understanding of intracellular oxidative stress, it was necessary to investigate the potential of **Tb.110** to determine the ratio of reduced to oxidised glutathione within a sample. Therefore the following section will apply the knowledge gained from these GR enzymatic studies to develop a method of determining the ratio of GSSG to GSH within a sample mixture.

5.8.4 Determination of the GSSG:GSH ratio in a sample using Tb.110

It is well known that within a healthy cell, the oxidized GSSG form rarely exceeds 10% of total cell glutathione concentration and that any major modulation from this GSSG:GSH ratio is a clear indicator of oxidative stress within a cellular environment.[222] With this in mind, it was essential to study the ability of **Tb.110** to monitor any significant changes in this ideal GSSG:GSH ratio. As shown in Table 5.2, different concentrations of GSSG and GSH, with an overall combined concentration of 10 μM were added to a 10 μM solution of the Tb(III) probe.

Table 5.2: *Various concentrations of GSSG and GSH added to a 10 μM solution of Tb.110 to give various overall GSSG:GSH percentage ratios.*

Investigation	*[Tb.110] μM*	*[GSSG] μM*	*[GSH] μM*	*GSSG:GSH (%)*
1	10	1.0	9.0	10%:90%
2	10	9.0	1.0	90%:10%

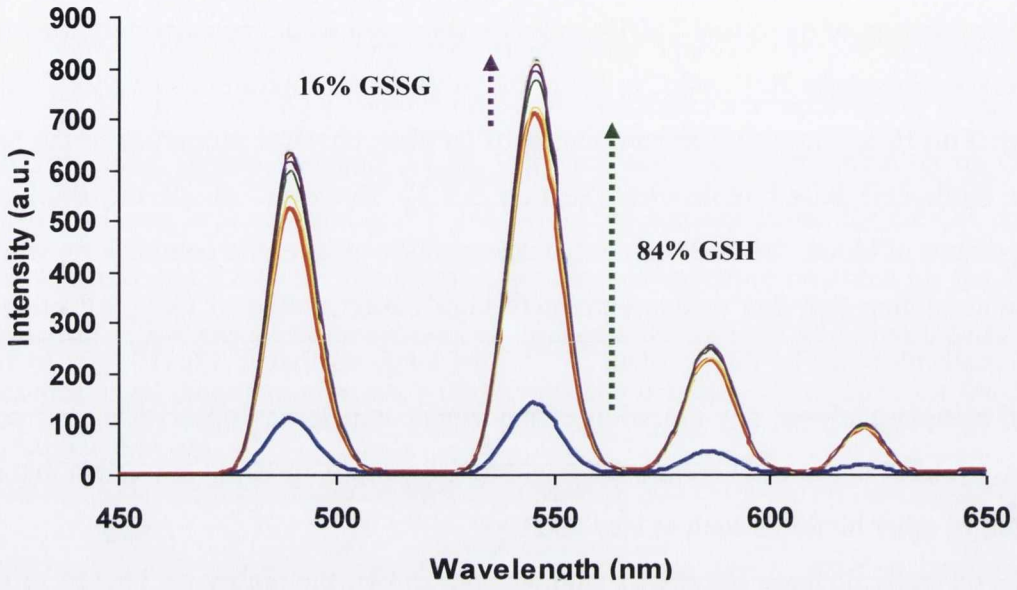

Figure 5.24: *Overall luminescence response of Tb.110 (10 μM) in a 10%:90% (GSSG:GSH) solution mixture. The initial GSH response was recorded followed by addition of 3.3 μM NADPH and 4.93 nM glutathione reductase to allow for the enzymatic conversion of the GSSG in solution to its reduced GSH form. All enzymatic titrations were carried out in aqueous pH 7.4 buffered solutions (0.1 M TRIS, 135 mM KCl) at 37 °C.*

After a 5 min mixing time, ensuring that all the GSH which was present in solution had completely reacted with the maleimide framework of **Tb.110**, a luminescence spectrum was recorded. As previous luminescent measurements have shown that **Tb.110** shows little modulation of its photophysical properties in the presence of the oxidised GSSG form, any initial enhancement which was observed could be directly related to the GSH species. The next step involved introduction of 3.3 μM NADPH and 4.93 nM GR to the solution to allow for reduction of the GSSG composition. Luminescence spectra were recorded until no further Tb(III) emission enhancements were observed. By comparing the emission intensity modulation before and after introduction of the enzyme, a rough estimation of the GSSG:GSH ratio of the solution could be determined

As shown in Figure 5.24, on analysis of the 10%:90% GSSG:GSH solution, **Tb.110** showed an initial large emission enhancement due to subsequent saturation of the maleimide alkene bond, however, as expected upon introduction of NADPH and GR, a much lower

response from **Tb.110** was observed. On comparison of the modulation in its emission intensity, a ratio of 16%:84% GSSG:GSH was determined. In the case of the 90%:10% GSSG:GSH sample, an opposite response was displayed where due to the much lower concentration of free GSH in solution, the initial intensity enhancement was significantly lower then that previously seen in Figure 5.24. However, upon initiation of the GR enzymatic process and conversion of the GSSG to its reduced GSH form, a much larger increase was observed in the Tb(III) emission intensity. Again, on comparison of the intensity enhancements displayed, a ratio of 93%:7% GSSG:GSH was determined from these changes (Figure 5.25).

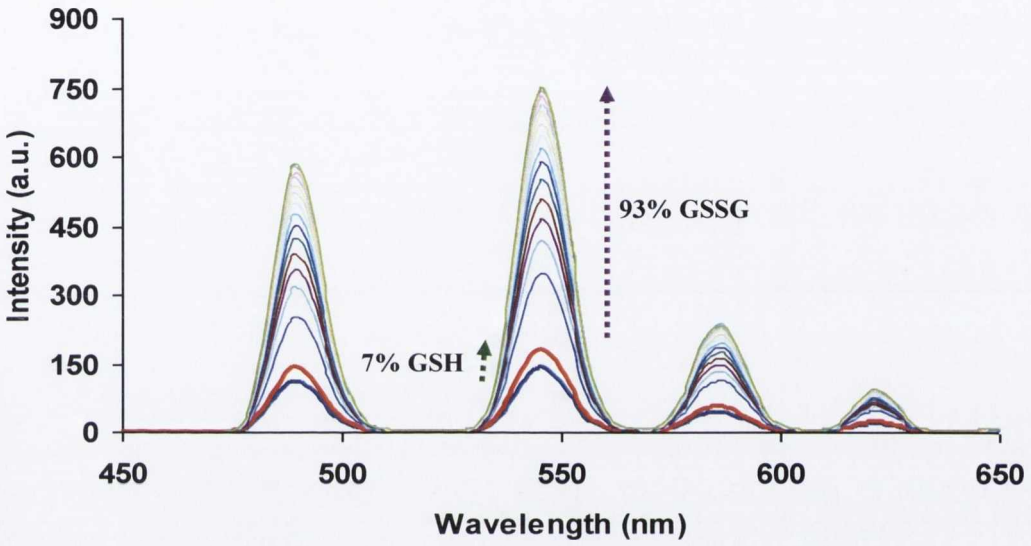

Figure 5.25: *Overall luminescence response of* ***Tb.110*** *(10 μM) in a 90%:10% (GSSG:GSH) solution mixture. The initial GSH response was recorded followed by addition of 3.3 μM NADPH and 4.93 nM glutathione reductase to allow for the enzymatic conversion of the GSSG in solution to its reduced GSH form. All enzymatic titrations were carried out in aqueous pH 7.4 buffered solutions (0.1 M TRIS, 135 mM KCl) at 37 °C.*

In reality, reduction of the GSSG species in solution will result in the formation of two molecules of GSH, suggesting that if a 10%:90% (GSSG:GSH) solution is analyzed and the intensity modulations before and after introduction of the enzyme are compared, it is likely that this comparison will overestimate the GSSG concentration and give a ratio of *ca.* 20%:80%. It is therefore necessary to take this formation of two molecules of GSH from GSSG into consideration when the intensity enhancements are being compared. This was not required for the measurements described above as the concentration of the Tb(III) probe was not in excess in comparison to the total GSH concentration formed. Overall, after the enzymatic reduction, the concentration of GSH in solution was greater then 10 μM therefore, after saturation of the emission intensity was observed, it is possible that half the GSH which was formed from the GSSG reduction mechanism had still not reacted with the probe. To

prove this was the case, analysis of the 10%:90% GSSG:GSH mixture was repeated, where this time a high excess of **Tb.110** (40 μM) was used, in comparison to the overall GSH concentration. As expected, on comparison of the intensity enhancements, a ratio estimate of 24%:76% was obtained, however, taking the formation of two GSH molecules from GSSG into account, the real ratio estimation of 12%:88% was determined (Figure A3.12).

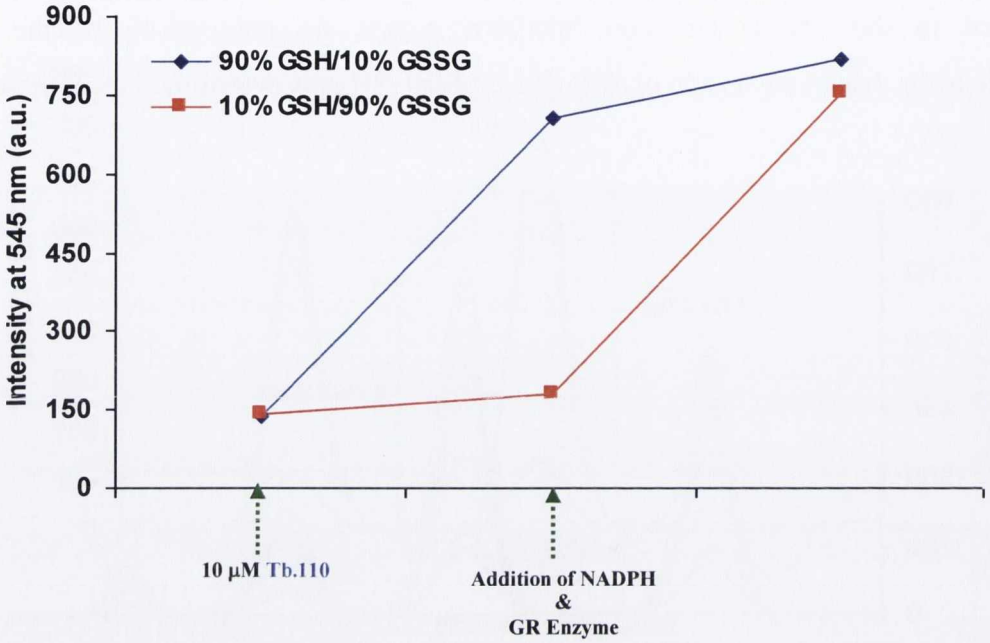

Figure 5.26: *Luminescence response of* ***Tb.110*** *(10 μM) at 545 nm in 10%:90% and 90%:10% (GSSG:GSH) solution mixtures. The initial GSH response was recorded followed by addition of 3.3 μM NADPH and 4.93 nM GR to allow for the enzymatic conversion of the GSSG in solution to its reduced GSH form. All enzymatic titrations were carried out in aqueous pH 7.4 buffered solutions (0.1 M TRIS, 135 mM KCl) at 37 °C.*

These studies successfully highlighted, as summarised by the graph in Figure 5.26, the ability of **Tb.110** to display very different responses when the concentration of GSH in comparison to GSSG is dramatically reduced, making this novel Ln based probe a potential candidate in monitoring intracellular oxidative stress.

5.9 Conclusion

This chapter has focused on a very different application of the Ln complexes, detailing the synthesis, characterisation and photophysical studies of a novel cyclen based Tb(III) complex, **Tb.110**, which allowed for the incorporation of the thiol specific maleimide functionality.

The detection mechanism of this Tb(III) probe involved successful 1,4-Michael addition of the sulfhydryl residues of GSH, Cys and Hcy to the electron deficient alkene bond of the maleimide ring resulting in a large modulation of its photophysical properties. Initially UV-vis absorption studies showed that upon saturation of the alkene bond (addition

of 1 equivalent), a slight increase of *ca.* 10 % was observed for the π-π* absorption band at 252 nm. More significant modulation was observed for the Tb(III) $^5D_4$ excited state upon introduction of GSH, Hcy and Cys with an intensity enhancement for the $J = 5$ emission band of 525%, 500% and 230%, respectively. Luminescence studies with the amine protected analogue of Cys, NAC, seemed to suggest that the reduction in the initial intensity enhancement observed for Cys was possibly due to its amine functionality. Lifetime measurements along with mass spectroscopy analysis were employed to ensure that the increase in the emission of **Tb.110** was not related to displacement of the coordinated H_2O molecule and as a direct result of 1,4 addition of thiol group.

Selectivity studies confirmed that all other non-thiol based amino acids displayed negligible modulation in the Tb(III) luminescence, confirming the detection mechanism at the maleimide site was discriminative for sulfhydryl based molecules only. The aromatic based amino acid Trp showed an initial 76% reduction in emission intensity due to overlap of its π-π* absorption band with that of **Tb.110**. However, upon introduction of GSH, the Tb(III) probe showed the expected > 500% increase confirming that the initial decrease was not due to any binding or recognition event at the maleimide framework. pH investigations showed that the maximum intensity response for **Tb.110** for GSH was at physiological pH, with a dramatic reduction in emission intensity being observed in both extremely acidic and basic environments (bell shaped profile). Formation of the less reactive neutral SH form of GSH at low pH and based mediated ring opening of the maleimide moiety were stated as possible reasons for this large reduction in the response of **Tb.110**.

The most important observation made in this chapter was the ability of **Tb.110** to distinguish GSH from its disulfide GSSG form. In the presence of high excess GSSG, no significant modulation in the luminescence properties of the Tb(III) probe was observed. This resulted in the utilisation of **Tb.110** in monitoring the reduction of GSSG to GSH using the NADPH dependant glutathione reductase enzymatic process. A series of titrations were carried out, confirming the inhibitory response of NADPH at high concentration and the linear response that existed between GSSG to GSH conversion rate and concentration of enzyme present. The last investigation carried out was the potential of **Tb.110** to show varied emission responses when the ratio of GSSG and GSH within a sample mixture is dramatically changed from the ideal physiologically healthy ratio of 10%:90%.

Overall this chapter described the first example of a Ln based thiol probe which showed selectivity for sulfhydryl based molecules over non thiol based amino acids. Its ability to discriminate between the reduced GSH and oxidised GSSG form of glutathione

highlights its potential to be used as an indicator of oxidative stress within the cell and therefore gain a greater understanding of overall health status.

Future work would involve intracellular studies, investigating the ability of **Tb.110** to display a large intensity enhancement in the presence of biothiols, concentrating on its response to GSH in particular. It's potential to determine the GSSG to GSH ratio within MND tissue and compare it to normal healthy tissue would also be of great interest, confirming the abilty of **Tb.110** to monitor oxidative stress. It would also be of interest to expand the range of Ln based probes and incorporate other antennae which display absorption bands at longer wavelengths. This would eliminate the interference which may occur with the aromatic based amino acid Trp and any problem which may occur using such a low excitation wavelength. Another possible avenue for these Ln based thiol systems would be to combine the knowledge gained from this chapter with previous work carried out within the Gunnlaugsson group on mixed Ru^{II}-Ln based systems, to develop the first example of a NIR based Ln thiol probe with a structure similar to complex **118** shown below.

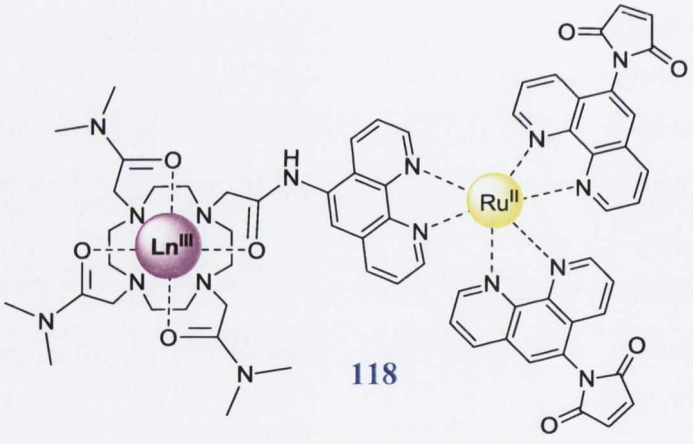

118

Chapter 6

Cyclen Based Lanthanide Luminescent Copper(II) and Mercury(II) Sensor

6.1 Introduction

As discussed in Chapter 1, the unique photophysical properties that the Ln metal ions have to offer make them attractive candidates for applications in *in vivo* sensing and biological imaging.[34, 37, 253] Careful design of suitable ligands, for example, those based on the cyclen framework, which allow for the formation of thermodynamically stable and kinetically inert complexes and incorporate a suitable antenna which allows for successful sensitisation of the Ln excited state and a receptor unit which upon binding to a metal ion can induce a photophysical change in the Ln emission properties has resulted in the development of a large variety of Ln based chemosensors for selective metal ion detection.[79, 83, 88, 101]

The design of sensors which have the ability to detect both Cu^{2+} and Hg^{2+} ions in aqueous solution at extremely low concentrations would be advantageous in areas such as environmental and biomedical monitoring. Cu^{2+} plays a vital role in the human body with many enzymes including, ceruloplasm, superoxide dismutase, tyrosinase and phenylalanine hydroxylase having a major Cu^{2+} composition.[263, 264] While trace amounts are essential, a large introduction of Cu^{2+} into the human body can disrupt and damage many biological processes resulting in potential liver failure.[265] There are also several genetic disorders which affect Cu^{2+} utilisation, the most serious of which are associated with Menkes syndrome and Wilson disease.[266] Common amongst infants under the age of three, Menkes syndrome involves a disruption in Cu^{2+} transport throughout the body, which as a result of poor absorption through the gut can lead to severe Cu^{2+} deficiency causing both mental and physical deterioration.[263] Wilson disease is another type of transport disorder which results in accumulation of Cu^{2+} in the liver and brain of affected individuals. Hg^{2+} is also extremely toxic and once exposed to the human body can travel and accumulate in the blood-brain barrier resulting in severe neurological disorders.[267, 268] Taking into account the human health hazards associated with both Cu^{2+} and Hg^{2+} and the rise in their environmental exposure, the design and development of novel sensors which show a strong and selective response at low concentrations for these ions is a vital area of research.

This chapter will therefore discuss the ability of **Tb.58.Na** in sensing Cu^{2+} and Hg^{2+} ions in aqueous solution. Through incorporation of a phenyl iminodiacetate receptor unit, it was anticipated that binding of these metal ions could cause a significant effect on the energy transfer process to the Tb(III) centre by disrupting the redox potential of the phenyl antenna. Quenching of the singlet excited state of the chromophore moiety as a result of this binding event could hinder successful population of the Tb(III) excited state and therefore cause a significant quenching of its luminescence emission. As the synthesis and pH response of **Tb.58.Na** were previously discussed in Chapter 2, the following section will begin with the

effect on its ground state, singlet excited state and Tb(III) excited state properties upon the addition of Cu^{2+} ions.

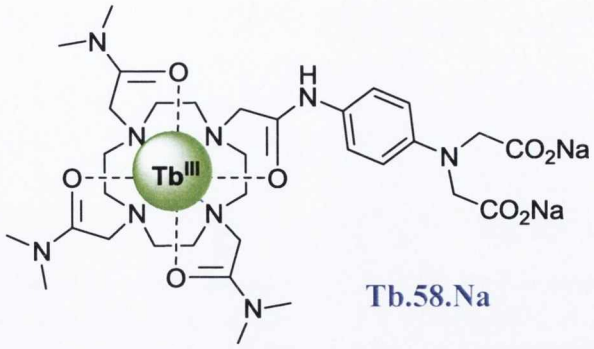

Tb.58.Na

6.2 Titration response of Tb.58.Na in the presence of Cu^{2+} ions

As previously discussed, binding of Cu^{2+} ions within the iminodiacetate receptor unit of **Tb.58.Na** could perturb its photophysical properties resulting in significant changes in its UV-vis absorption, fluorescence and above all phosphorescence spectra. In order to investigate these possible spectral changes, a Cu^{2+} spectroscopic ion titration was first carried out in an aqueous pH 7.4 buffered (20 mM HEPES, 135 mM KCl) solution. Various aliquots of a 1 x 10^{-2} M solution of $Cu(ClO_4)_2$ were added, with the spectra recorded after a 2 min mixing period.

6.2.1 UV-vis absorption response of a HEPES buffered solution of Tb.58.Na upon the addition of Cu^{2+} ions

Firstly, the effect on the ground state properties of **Tb.58.Na** in the presence of Cu^{2+} ions was investigated. As shown in Figure 6.1, upon the addition of $Cu(ClO_4)_2$ to a 10 μM aqueous solution (20 mM HEPES, 135 mM KCl) of **Tb.58.Na**, a large enhancement in the UV-vis absorption spectrum along with a 25 nm hypsochromic shift of the λ_{max} at 285 nm to 260 nm, was observed. On plotting the absorption at 285 nm as a function of Cu^{2+} equivalents, an almost linear response was observed, with no formation of a plateau at higher Cu^{2+} concentrations. This suggests that the observed response may not be as a direct result of Cu^{2+} binding within the iminodiacetate receptor unit of **Tb.58.Na** but due to some other form of Cu^{2+} complexation occurring in solution.

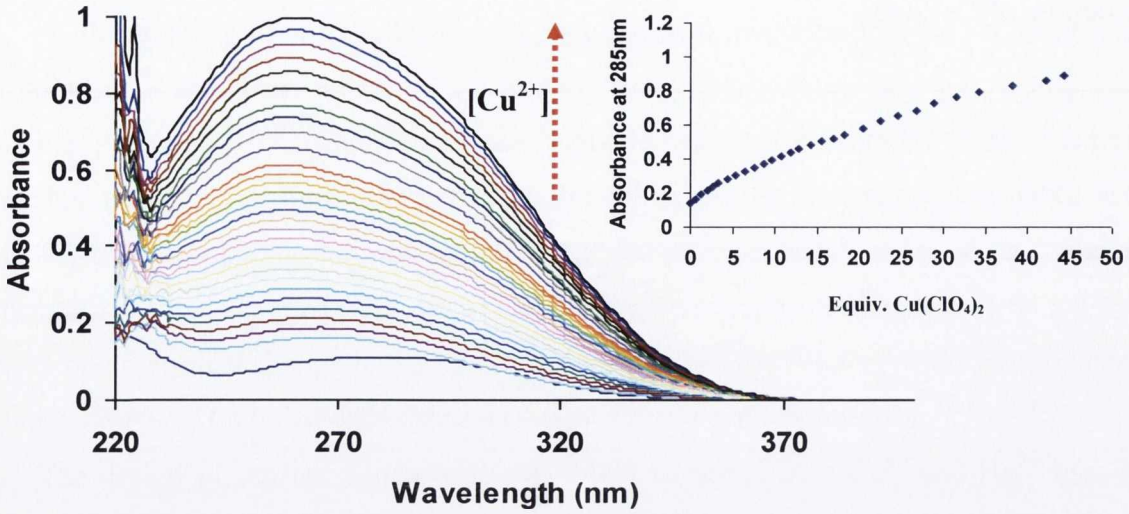

Figure 6.1: *The overall changes in the UV-vis absorption spectrum of* **Tb.58.Na** *(10 μM) in the presence of $Cu(ClO_4)_2$ at pH 7.4 (20 mM HEPES, 135 mM KCl). Inset: Plot of absorbance at 285 nm with equivalents of $Cu(ClO_4)_2$ added.*

To investigate the possibility that the HEPES buffer may be interacting with the Cu^{2+} ions in solution, $Cu(ClO_4)_2$ was added to a 20 mM HEPES solution and a UV-vis absorption spectrum was recorded in the absence of **Tb.58.Na**. As shown in Figure 6.2, the formation of an absorbance band with a λ_{max} at 260 nm occurred, suggesting complexation of the Cu^{2+} ions with the HEPES buffer. This verifies that the above UV-vis absorption enhancements of **Tb.58.Na** were not as a direct result of Cu^{2+} binding within the iminodiacetate moiety.

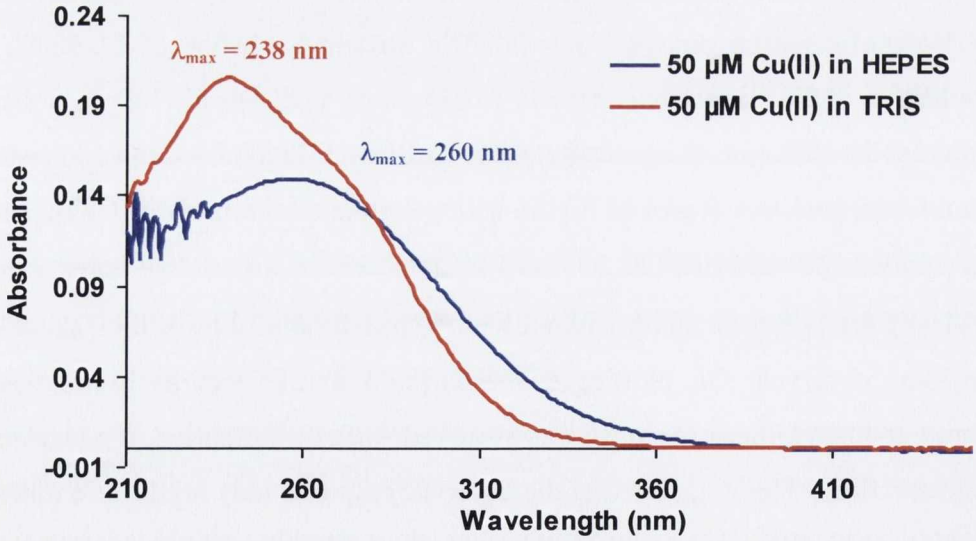

Figure 6.2: *The UV-vis absorption spectrum of 50 μM $Cu(ClO_4)_2$ in 125 mM HEPES (—) and 125 mM TRIS (—).*

A similar response was observed when the TRIS buffer was investigated, with the appearance of a large absorption band with a λ_{max} at 238 nm (Figure 6.2). This Cu^{2+} interaction with both HEPES and TRIS verified that in order to determine an accurate

response of **Tb.58.Na** towards this metal ion, the titrations would have to be carried out in the absence of any buffer.

6.2.2 UV-vis absorption, fluorescence and phosphorescence response of an aqueous solution of Tb.58.Na upon the addition of Cu^{2+} ions

In the absence of HEPES, the UV-vis absorption response of **Tb.58.Na** upon the addition of $Cu(ClO_4)_2$ differed greatly. As shown in Figure 6.3, the changes observed in the spectra clearly indicates an interaction between the Cu^{2+} ions in solution and the iminodiacetate moiety of **Tb.58.Na**, where the absorption band centred at 285 nm was blue shifted to 260 nm with the formation of an isosbestic point at *ca.* 266 nm. The titration profile of the absorbance changes at 285 nm versus the number of equivalents of Cu^{2+} added, shown as an inset in Figure 6.3, suggests the most significant interaction occurs between 0→1 equiv. of Cu^{2+} (0→10 μM), with the formation of a plateau at higher Cu^{2+} concentrations. Due to the absence of buffer, it was necessary to monitor the pH throughout the titration to ensure that any modulations observed were not as a result of significant changes in the solutions pH. Overall, the pH was found not to change by more than 0.2 pH units during this titration.

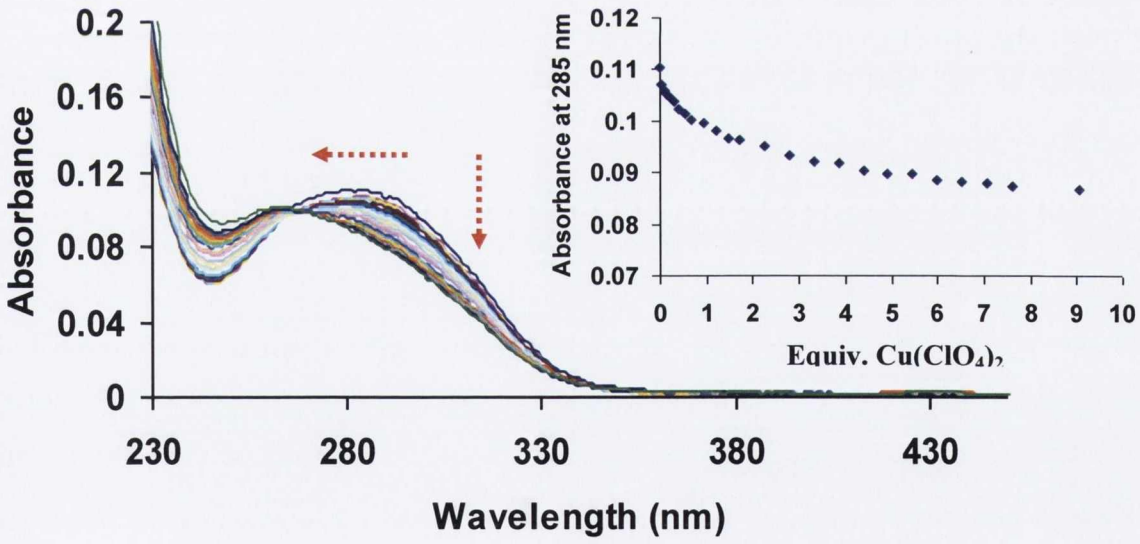

Figure 6.3: *The overall changes in the UV-vis absorption spectrum of* ***Tb.58.Na*** *(10 μM) upon titration with $Cu(ClO_4)_2$ in non-buffered H_2O solution. Inset: Plot of absorbance at 285 nm with equivalents of $Cu(ClO_4)_2$ (0 → 90 μM added).*

A similar response was observed on analysis of the singlet excited state properties of **Tb.58.Na**, where as shown in Figure 6.4, in the absence of Cu^{2+} a broad emission band was observed, centred at 358 nm with a slight shoulder at *ca.* 290 nm. However, upon binding to Cu^{2+}, a 67% decrease in the fluorescence properties of the Tb(III) complex was displayed

with an 18 nm hypsochromic shift of the λ_{max} to 340 nm. By plotting the emission intensity at 358 nm as a function of Cu^{2+} equivalents, the formation of a plateau after the addition of *ca.* 2 equivalents of $Cu(ClO_4)_2$ was observed, with the most significant emission reduction occurring between 0→1 equiv. of Cu^{2+} (Figure 6.3, Inset). These results verify those previously discussed for the ground state properties and suggest that binding of the Cu^{2+} ion at the iminodiacetate receptor unit causes a significant quenching effect of the singlet excited state of the phenyl antenna.

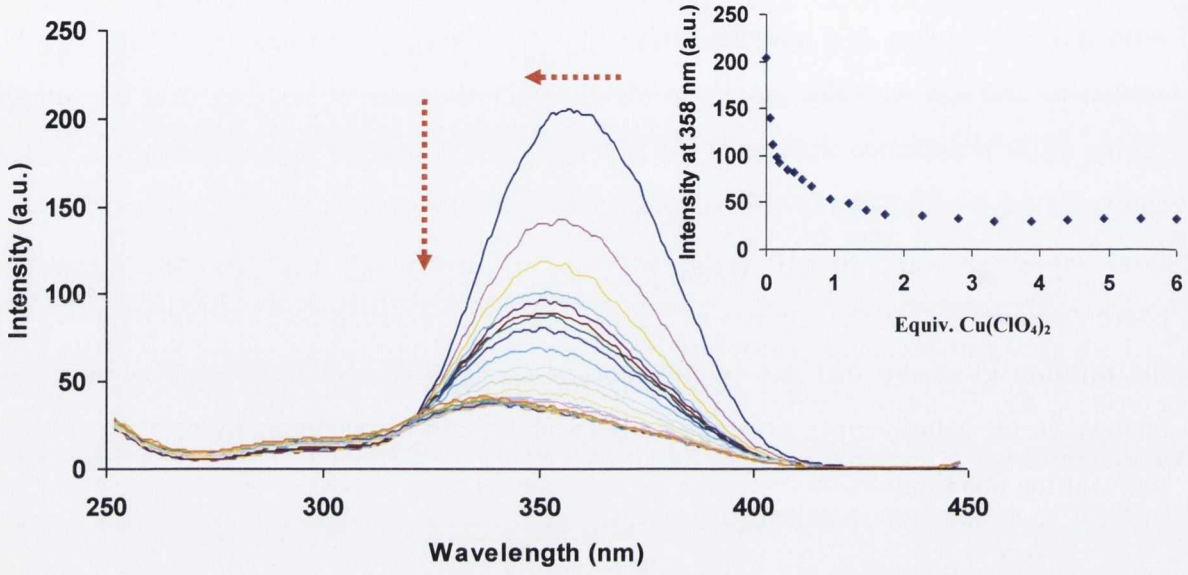

Figure 6.4: *The overall changes in the fluorescence emission spectrum of* **Tb.58.Na** *(10 μM) upon titration with $Cu(ClO_4)_2$ in non-buffered H_2O solution. Inset: Plot of emission intensity at 358 nm with equivalents of $Cu(ClO_4)_2$ (0 → 60 μM) added.*

Having investigated the interaction of Cu^{2+} with the iminodiacetate receptor of **Tb.58.Na** by observing the changes in the ground and excited states properties of the phenyl chromophore, the effect of this interaction on the Tb(III) emission was next monitored. It was expected that strong Cu^{2+} binding to the receptor unit may in turn alter the energy transfer process and therefore have a quenching effect on the Tb(III) luminescence. As anticipated, the Tb(III) luminescence response of **Tb.58.Na,** as shown in Figure 6.5, showed a gradual decrease (*ca.* 65%) in its emission intensity as a function of Cu^{2+} concentration, with the formation of a plateau after the addition of *ca.* 2 equivalents. With the free Cu^{2+} concentrations in serum being in the range of 12.5 – 21 μM,[269] it is clear from the titration profile of emission intensity at 545 nm versus Cu^{2+} equivalents (Figure 6.5 Inset), that **Tb.58.Na** can detect Cu^{2+} within this concentration window. For the case of other previously reported Ln luminescent sensors, for example the phenanthroline based Eu(III) complex (**17**) developed by Gunnlaugsson and co-workers, binding of Cu^{2+} at the receptor moiety resulted in a complete quenching of the Eu(III) luminescence.[88] Such a response was not observed for

Tb.58.Na, which is possibly as a result of the Tb(III) metal ion bearing an absorption band at *ca.* 285 nm, therefore, although the indirect excitation pathway *via* the phenyl antenna is hindered upon Cu^{2+} addition, direct excitation of the Tb(III) ion is still possible.

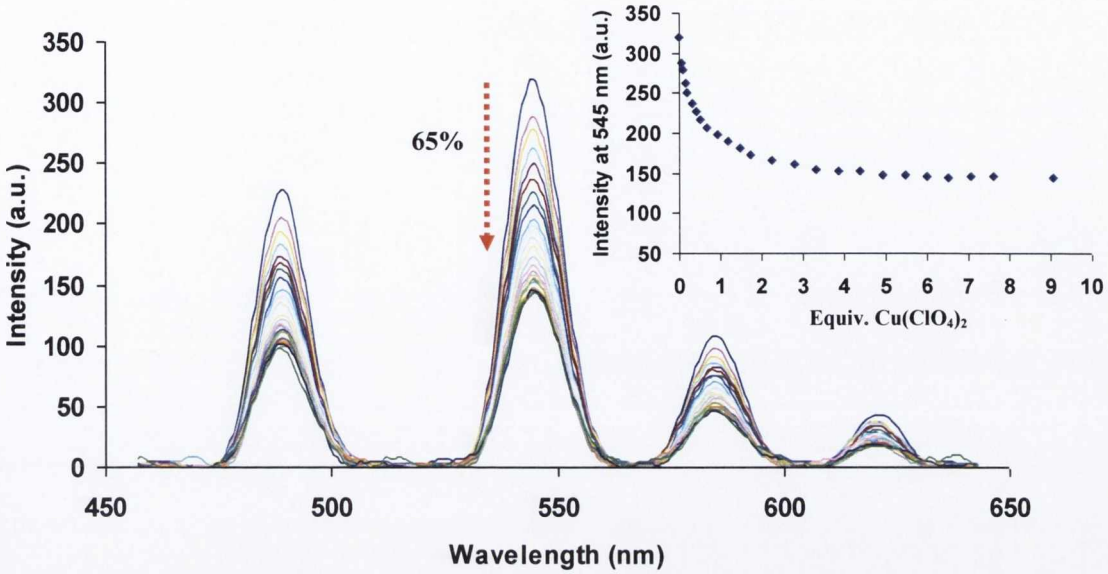

Figure 6.5: *The overall changes in the Tb(III) luminescence spectra of* ***Tb.58.Na*** *(10 μM) upon titration with $Cu(ClO_4)_2$ in non-buffered H_2O solution. Inset: Plot of emission intensity at 545 nm with equivalents of $Cu(ClO_4)_2$ (0 → 90 μM) added.*

To verify that the observed reduction in luminescence was not due to displacement of the Tb(III) metal from the cyclen cavity *via* the Cu^{2+} ions, lifetime measurements of **Tb.58.Na** in the presence of excess (4 equivalents) $Cu(ClO_4)_2$ were recorded in both H_2O and D_2O (λ_{ex} = 285 nm). With a τ_{OH} = 1.18 ms ± 0.01 ms and τ_{OD} = 1.82 ± 0.01 ms being measured, a q value of 1.2 ± 0.25 was calculated, confirming the presence of one metal bound water molecule. Given the fact that the Tb(III) emission can be considered as pH independent within the large pH window 5.5–11.5, as demonstrated in Chapter 2 (Section 2.9), the observed response of the Tb(III) luminescence cannot be related to any shift in pH which may occur as the titrations were carried out in absence of buffer.

In summary, the above measurements demonstrated that upon binding of Cu^{2+} ions at the iminodiacetate receptor unit of **Tb.58.Na**, a significant modulation in the complexes photophysical properties occurred. Quenching of the singlet excited state properties of **Tb.58.Na** in the presence of $Cu(ClO_4)_2$ resulted in a subsequent 65% quenching effect on the complexes Tb(III) luminescence emission. All studies verified that the most significant changes occurred between 0→1 equivalents of Cu^{2+}, with a plateau being reached at higher Cu^{2+} concentrations. With its ability to detect Cu^{2+} ions determined, it was necessary to investigate its luminescence response towards other metal ions. The following section will therefore begin by investigating the effect on the Tb(III) excited state properties of **Tb.58.Na** in the presence of Hg^{2+} ions.

6.3 Phosphorescence response of an aqueous solution of Tb.58.Na upon the addition of Hg^{2+} ions

In order to investigate the ability of **Tb.58.Na** to show a similar response to Hg^{2+} ions in solution, the above phosphorescence titration was repeated using $Hg(ClO_4)_2$. With Hg^{2+} also displaying strong complexation with both HEPES and TRIS and therefore the formation of a large absorption band in the same spectral region as the π-π^* band for **Tb.58.Na**, it was again necessary to complete these titrations in the absence of buffer. As shown by the phosphorescence spectra in Figure 6.6, upon the addition of various aliquots of a 2×10^{-4} M aqueous solution of $Hg(ClO_4)_2$, a similar quenching effect to that previously observed for the Cu^{2+} titration was displayed. By plotting the intensity modulation of the $J = 5$ (545 nm) emission band as a function of Hg^{2+} equivalents added, it became clear that unlike that seen for the Cu^{2+} titration, a plateau was not reached until much higher Hg^{2+} concentrations (Figure 6.6, Inset). After addition of 10 equivalents of $Hg(ClO_4)_2$, an almost 40% reduction in the luminescence response was observed. The slightly lower emission quenching and the higher concentration of Hg^{2+} required in order to reach a plateau, then that seen for the Cu^{2+} titration, suggests slightly stronger interaction of the iminodiacetate receptor unit of **Tb.58.Na** with Cu^{2+} ions. This was verified by fitting the phosphorescence data for both metal ions using a modified Stern Volmer equation, with a binding constant of logK = 5.3 (±0.2, $R^2 = 0.98$) being determined for Cu^{2+} and a logK = 4.5 (±0.2, $R^2 = 0.98$) for Hg^{2+}.[270]

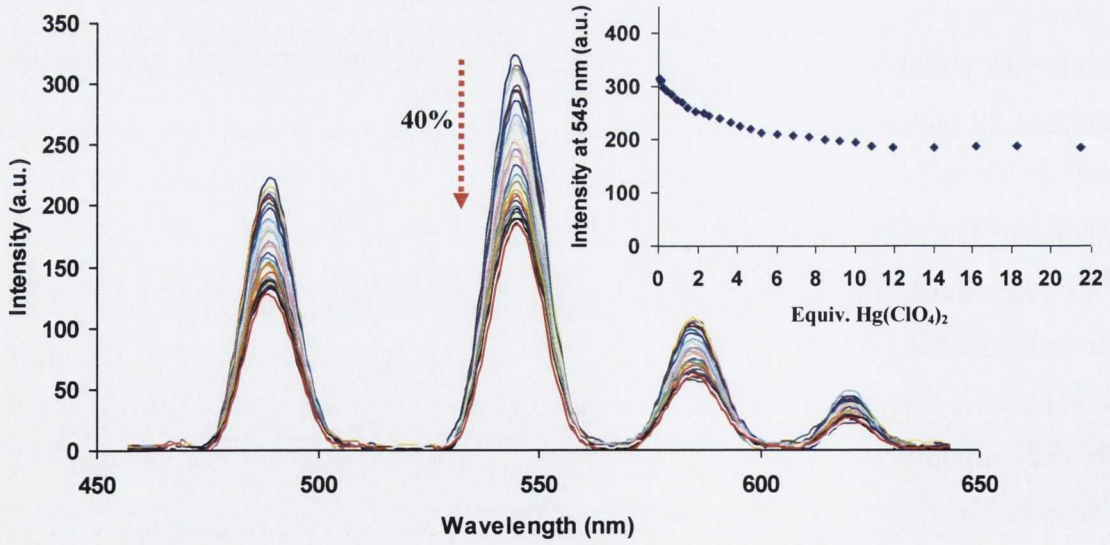

Figure 6.6: *The overall changes in the Tb(III) luminescence spectra of* ***Tb.58.Na*** *(10 μM) upon titration with $Hg(ClO_4)_2$ in non-buffered H_2O solution. Inset: Plot of emission intensity at 545 nm with equivalents of $Hg(ClO_4)_2$ added.*

Similar lifetimes studies were carried out for **Tb.58.Na** in the presence of excess $Hg(ClO_4)_2$, with a τ_{OH} = 1.302 ± 0.01 ms and a τ_{OD} = 1.890 ± 0.01 ms being measured,

resulting in a q value of *ca.* 1 being calculated. This verifies, as was the case for Cu^{2+}, that the observed decrease in luminescence was not as a result of displacement of the Tb(III) metal ion from the cyclen cavity. With the luminescence response of **Tb.58.Na** towards both Hg^{2+} and Cu^{2+} ions determined, the following section will review those results previously discussed in Chapter 2 (Section 2.10), which involved the response of **Tb.58.Na** towards the group II metal ions Ca^{2+} and Mg^{2+} and the transition metals Cd^{2+} and Zn^{2+}.

6.4 Phosphorescence response of an aqueous solution of Tb.58.Na upon the addition of Ca^{2+}, Mg^{2+}, Cd^{2+} and Zn^{2+}

As discussed previously in Chapter 2, upon the addition of the $CaCl_2$, $MgCl_2$, $CdCl_2$ and $ZnCl_2$ to an aqueous solution of **Tb.58.Na**, no significant modulation in the luminescence properties were observed. For the case of the group II metal ions Ca^{2+} and Mg^{2+}, up to a concentration of *ca.* 8 mM, no change in the ground, singlet excited or Tb(III) excited state properties were displayed (Figure 2.14 and Figure A1.7). However, in the presence of high concentrations (> 0.1 mM) of both Zn^{2+} and Cd^{2+} ions, although the ground state and singlet excited state properties confirmed chelation of these ions within the iminodiacetate binding moiety, no effect on the Tb(III) luminescence was observed (Figure 2.15 and Figure 2.16). This suggests that the chelation of these metal ions has little impact on the energy transfer process from the phenyl antenna to the Tb(III) metal centre. Figure 6.7 summaries the luminescence response of **Tb.58.Na** in the presence of Ca^{2+}, Mg^{2+}, Cd^{2+} and Zn^{2+} ions by plotting the intensities of the $J = 5$ emission bands as a function of pM^{2+} [$= -\log M^{2+}$]. To allow for a comparison with the response previously observed for Cu^{2+} and Hg^{2+} ions, the luminescence changes in the presence of these metal species are also plotted. This graph clearly demonstrates that in the presence of Ca^{2+}, Mg^{2+}, Cd^{2+} and Zn^{2+} ions, no significant modulation in the Tb(III) response of **Tb.58.Na** was observed. It also verifies that slightly stronger binding was seen for Cu^{2+} over Hg^{2+}, as **Tb.58.Na** shows much larger changes in its emission properties at lower concentrations of Cu^{2+}.

To further demonstrate **Tb.58.Na** selectivity for Cu^{2+} and Hg^{2+} over these group II and transition metal ions, a 10 μM solution of the Tb(III) complex was prepared in the presence of 10 mM $CaCl_2$, $MgCl_2$, $CdCl_2$ and $ZnCl_2$, along with 100 mM NaCl. After a 5 min mixing period, a luminescence spectrum of this solution was recorded. Upon addition of 50 μM $Cu(ClO_4)_2$, followed by a 3 min mixing time, another phosphorescence spectrum was measured. As shown in Figure 6.8, even in the presence of a large excess of all these potentially competing metal ions, **Tb.58.Na** displayed a similar 65% emission reduction in the presence of the $Cu(ClO_4)_2$, suggesting little interference with the binding event due to the

presence of these metal species. A similar response was observed for Hg^{2+}, where the 40% quenching effect of Tb(III) emission was observed upon the addition of 100 μM $Hg(ClO_4)_2$.

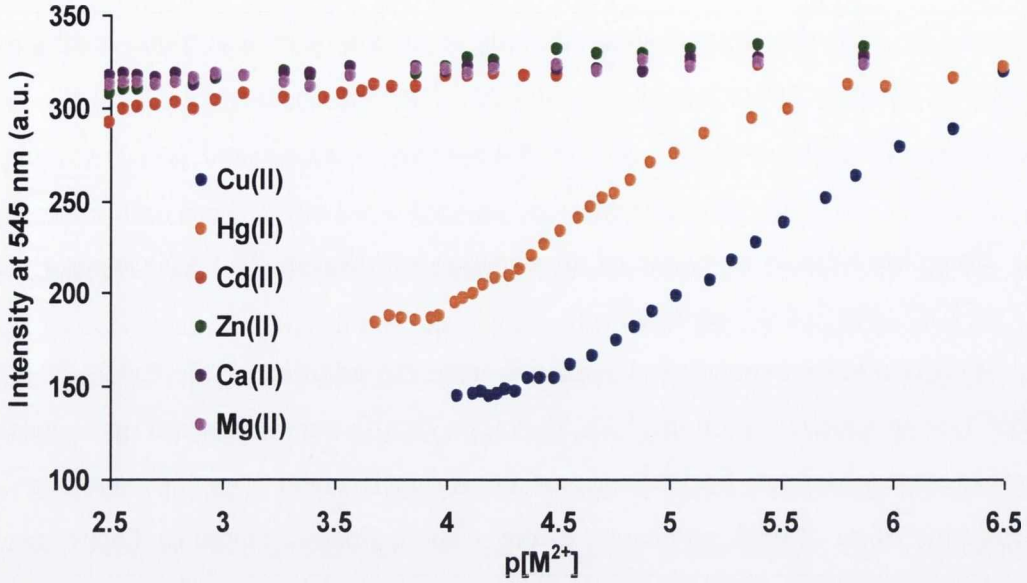

Figure 6.7: *Plot of the changes in the Tb(III) luminescence of* ***Tb.58.Na*** *(10 μM) at 545 nm upon titration with $M(ClO_4)_2$ or MCl_2 (expressed as pM = -log[M^{2+}]).*

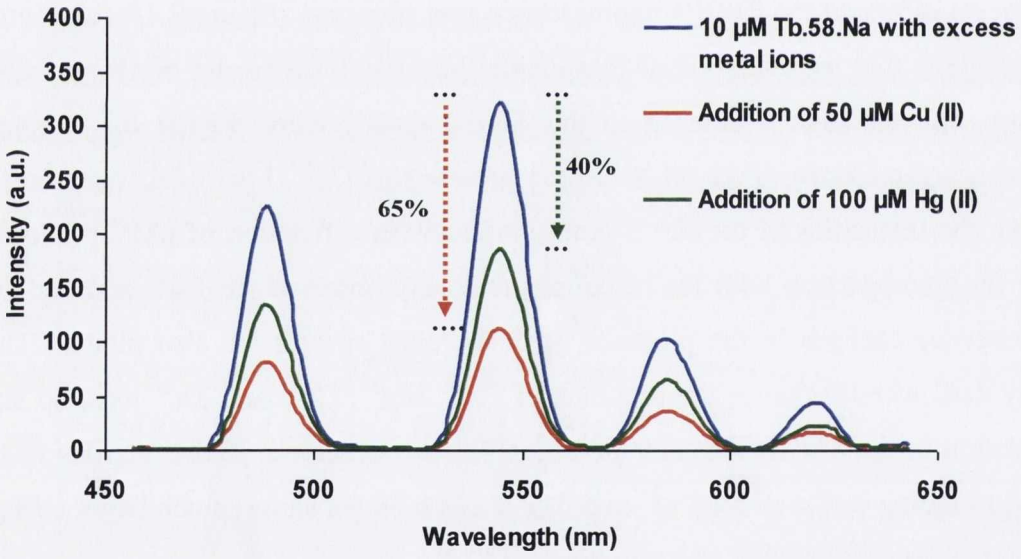

Figure 6.8: *The Tb(III) luminescence response of a 10 μM aqueous solution of* ***Tb.58.Na*** *upon the addition of either 50 μM $Cu(ClO_4)_2$ or 100 μM $Hg(ClO_4)_2$ in the presence of 10 mM $CaCl_2$, $MgCl_2$, $CdCl_2$ and $ZnCl_2$ and 100 mM NaCl.*

Overall these studies helped highlight the selectivity of **Tb.58.Na** for Cu^{2+} and Hg^{2+} over the group II metal ions Ca^{2+} and Mg^{2+} and the transition metal ions Zn^{2+} and Cd^{2+}. However, it was also necessary to investigate any potential binding of other transition metals such as Ni^{2+}, Co^{2+} and Fe^{2+} at the iminodiacetate receptor unit. The following section will therefore detail the luminescence response of **Tb.58.Na** in the presence of these metal species.

6.5 Phosphorescence response of an aqueous solution of Tb.58.Na upon the addition of the transition metal ions Ni^{2+}, Co^{2+} and Fe^{2+}

The first paramagnetic transition metal ion to be investigated was Ni^{2+}, with a similar phosphorescence titration to that previously discussed for Cu^{2+} and Hg^{2+} ions carried out. As shown by the Tb(III) luminescence spectrum in Figure 6.9, a much poorer response in the presence of Ni^{2+} was observed. After addition of 50 equivalents of $Ni(ClO_4)_2$, an 18% decrease in the Tb(III) emission intensity of **Tb.58.Na** resulted, suggesting much weaker interaction with the iminodiacetate functionality. Unlike Cu^{2+} and Hg^{2+} where a 60% and 40% reduction in emission intensity respectively, was observed upon the addition of 10 equivalents of the metal ions, a much lower 11% reduction was observed for Ni^{2+}.

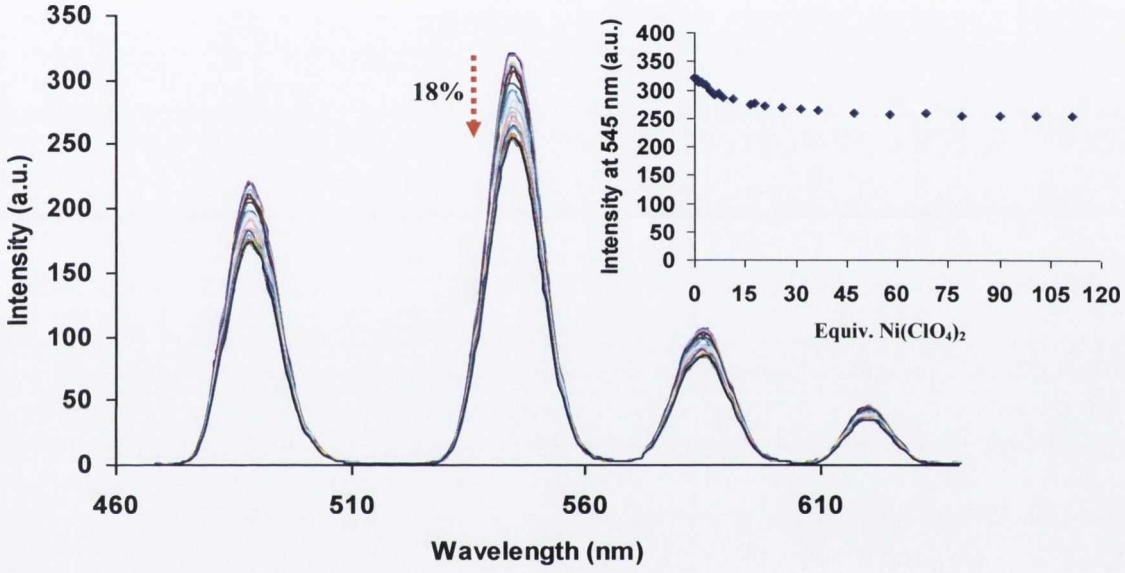

Figure 6.9: *The overall changes in the Tb(III) luminescence spectra of Tb.58.Na (10 μM) upon titration with $Ni(ClO_4)_2$ in non-buffered H_2O solution. Inset: Plot of emission intensity at 545 nm with equivalents of $Ni(ClO_4)_2$ added.*

For the case of Co^{2+}, upon the addition of $Co(ClO_4)_2$ to an aqueous solution of **Tb.58.Na**, a slight reduction in the Tb(III) emission intensity was also observed (Figure 6.10). After addition of 10 equivalents of Co^{2+}, a 22% decrease in the luminescence response resulted, which is still much lower than that observed for the Hg^{2+} and Cu^{2+} ions. As shown by the plot of emission intensity at 545 nm *vs.* equivalents of $Co(ClO_4)_2$ added, unlike that seen for all previously discussed transition metals, no plateau was formed at higher Co^{2+} concentrations. A possible cause for this response is the fact that $Co(ClO_4)_2$ has a d-d transition in its UV-vis absorption spectrum between 430 nm and 570 nm, which is in a similar spectral region in which Tb(III) emission of **Tb.58.Na** occurs. Therefore as a result of this spectral overlap, formation of a plateau at higher concentrations could not occur.

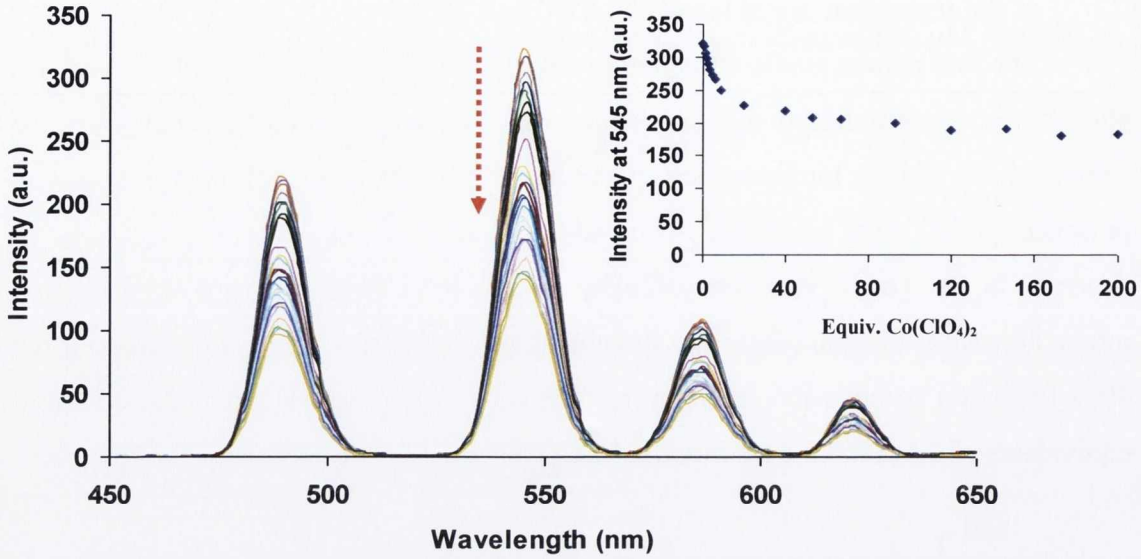

Figure 6.10: *The overall changes in the Tb(III) luminescence spectra of* ***Tb.58.Na*** *(10 μM) upon titration with $Co(ClO_4)_2$ in non-buffered H_2O solution. Inset: Plot of emission intensity at 545 nm with equivalents of $Co(ClO_4)_2$ added.*

A similar spectral problem was observed upon the investigation of the potential binding of Fe^{2+} ions with the iminodiacetate unit of **Tb.58.Na**. As shown by the Tb(III) luminescence spectrum in Figure 6.11, a gradual decrease in the emission intensity of the Tb(III) complex was observed upon addition of various aliquots of an aqueous solution of $Fe(ClO_4)_2$, with no formation of a plateau being displayed at higher Fe^{2+} concentrations.

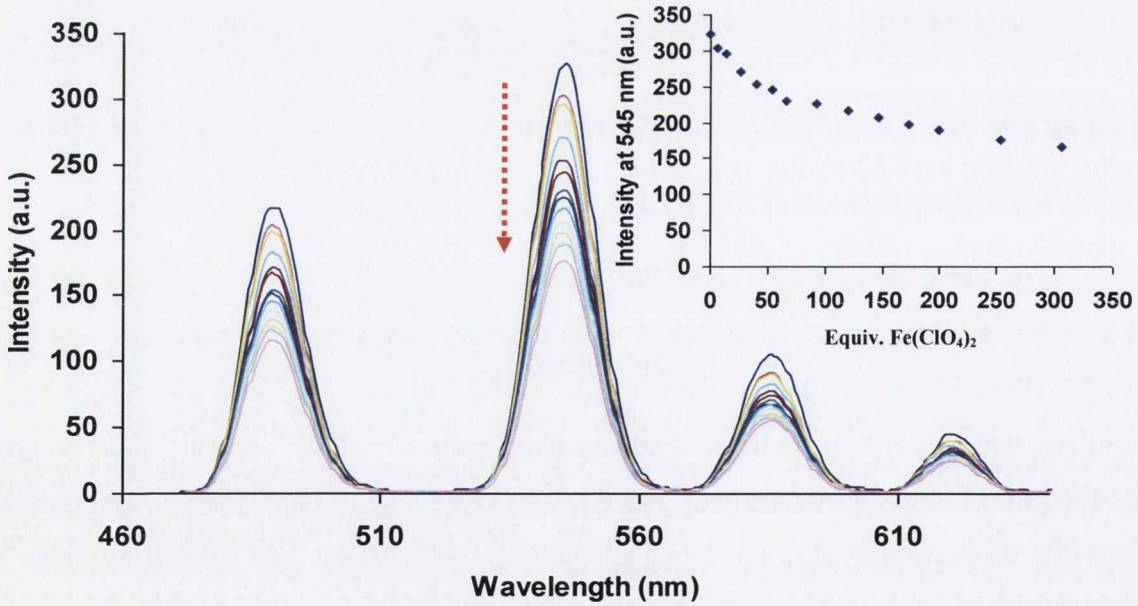

Figure 6.11: *The overall changes in the Tb(III) luminescence spectra of* ***Tb.58.Na*** *(10 μM) upon titration with $Fe(ClO_4)_2$ in non-buffered H_2O solution. Inset: Plot of emission intensity at 545 nm with equivalents of $Fe(ClO_4)_2$ added.*

After addition of 10 equivalents of Fe^{2+}, the decrease in emission intensity was measured as *ca.* 6%, which is the lowest response of all the paramagnetic transition metal

ions studied. When the UV-vis absorption spectrum of $Fe(ClO_4)_2$ was measured, the presence of a broad absorption band in the same spectral region as the π-π* absorption band of **Tb.58.Na** was observed. This spectral overlap helps explain the significant decrease in Tb(III) emission at higher Fe^{2+} concentrations and the absence of a plateau for this titration.

By plotting the emission intensity at 545 nm for the various paramagnetic transition metal ions studied as a function of $p[M^{2+}]$, a direct comparison of the luminescence response of **Tb.58.Na** to each metal ion was possible. As shown in Figure 6.12, this plot clearly verifies that **Tb.59.Na** displays the most significant changes in its luminescence properties in the presence of Cu^{2+} ions. Another interesting observation is that although Co^{2+}, Fe^{2+} and Ni^{2+} ions also cause a reduction in the Tb(III) emission, whether as a result of binding within the iminodiacetate receptor unit or due to some spectral issue, this emission decrease occurs at higher concentrations than that seen for the Cu^{2+} ions. In fact, within the concentration range in which **Tb.58.Na** displays its strongest response to Cu^{2+}, very little modulation in the Tb(III) luminescence properties were observed in the presence of Co^{2+}, Fe^{2+} and Ni^{2+} ions. The only transition metal ion which displayed strong interaction with the iminodiacetate of **Tb.58.Na** at a similar concentration to Cu^{2+} was Hg^{2+}.

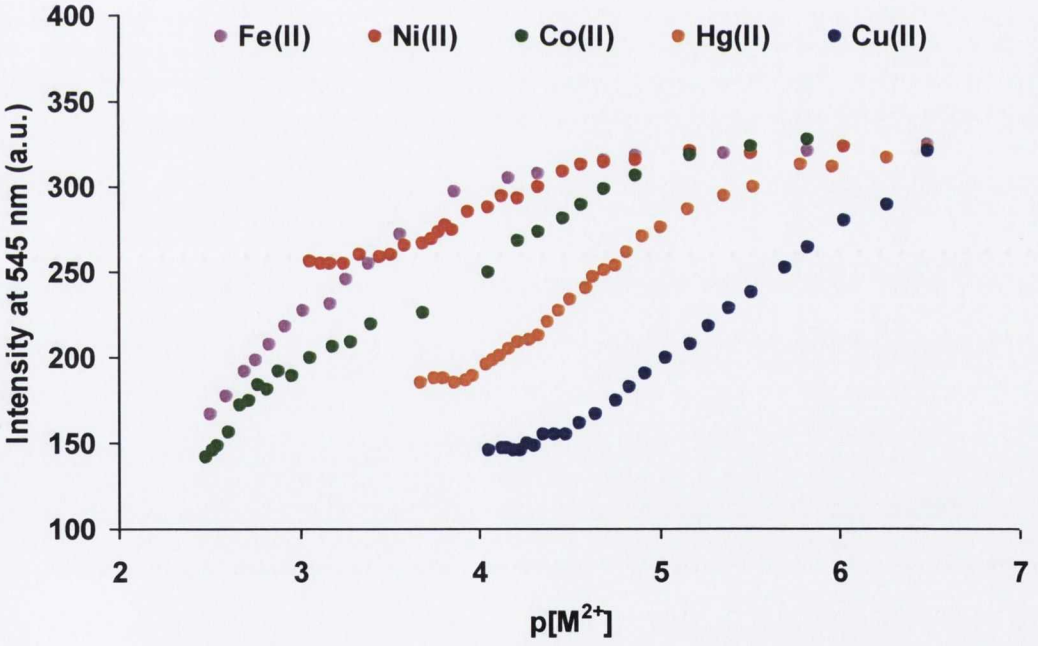

Figure 6.12: *Plot of the changes in the Tb(III) luminescence of* ***Tb.58.Na*** *(10 μM) at 545 nm upon titration with $M(ClO_4)_2$ (expressed as $pM = -log[M^{2+}]$, $M^{2+} = Fe^{2+}$, Ni^{2+}, Co^{2+}, Hg^{2+}, Cu^{2+}).*

These studies helped highlight the preferential binding of Cu^{2+} and Hg^{2+} ions within the iminodiacetate receptor unit of **Tb.58.Na** over other paramagnetic transition metals ions. Although Co^{2+}, Ni^{2+} and Fe^{2+} also displayed a quenching effect on the Tb(III) luminescence

emission of **Tb.58.Na**, this response occurred at slightly higher concentrations then that seen for the Hg^{2+} and Cu^{2+} ions.

6.6 Conclusion

Overall this chapter investigated the potential sensing ability of **Tb.58.Na** for Cu^{2+} and Hg^{2+} ions over other biologically relevant metal species. By incorporation of a phenyl iminodiacetate moiety within the ligand framework of the Tb(III) complex, it was anticipated that binding within this receptor unit may alter the redox potential of the phenyl antenna and therefore cause a subsequent quenching effect of the Tb(III) luminescence emission.

The ground state and singlet excited state properties of **Tb.58.Na** were significantly altered upon the addition of Cu^{2+}, with the Tb(III) luminescence being quenched by *ca.* 65% in the presence of 10 equivalents of $Cu(ClO_4)_2$. The most significant reduction in emission intensity was observed between 0→1 equivalents of Cu^{2+}, with the formation of a plateau at higher concentrations. A similar quenching effect was observed for Hg^{2+}, with a 40% decrease in emission being displayed in the presence of 10 equivalents of $Hg(ClO_4)_2$.

High selectivity of **Tb.58.Na** for Cu^{2+} and Hg^{2+} over the group II metal ions Ca^{2+} and Mg^{2+} and the transition metal ions Cd^{2+} and Zn^{2+} was also observed, where no modulation in the Tb(III) luminescence properties in the presence of these metal species resulted. However, for Co^{2+}, Ni^{2+} and Fe^{2+}, a similar quenching effect of the Tb(III) emission occurred. Upon the addition of $Ni(ClO_4)_2$, **Tb.58.Na** displayed a much poorer response then that seen for Cu^{2+} and Hg^{2+}, with an overall 18% decrease in emission intensity. In the presence of 10 equivalents of Fe^{2+} and Co^{2+}, a 6% and 22% reduction in the Tb(III) luminescence response occurred, respectively. However as a result of certain spectral issues for these metal ions, the formation of a plateau at higher concentrations was not possible. Although Co^{2+}, Ni^{2+} and Fe^{2+} also displayed a quenching effect of the Tb(III) emission properties of **Tb.58.Na**, this response occurred at slightly higher concentrations then that observed for Hg^{2+} and Cu^{2+}, suggesting preferential binding of these ions with the iminodiacetate receptor unit.

Chapter 7

Experimental

7.1 Materials and methods

All chemicals were obtained from Sigma-Aldrich, Strem Chemicals, Fluka and Chematech and, unless otherwise specified, were used without further purification. Deuterated solvents used for NMR analysis were purchased from Apollo Scientific. Dry solvents were prepared using standard procedures, according to Vogel, with distillation prior to each use.[271] Chromatographic columns were run manually using silica gel 60 (230-40 mesh ASTM) or aluminium oxide (activated, neutral, Brockman I STD grade, 150 mesh, or activated basic, Brockman I STD grade, 150 mesh). Chromatographic columns were also run on a Teldyne Isco Combiflash Companion Automatic machine using pre-packed silica or alumina columns. Thin-layer chromatography (TLC) analysis was carried out using Merck Kieselgel 60 F_{254} silica plates and Polygram Alox N/UV_{254} aluminium oxide plates and viewed by UV light or developed using an iodine chamber. Melting points were determined using an Electrothermal IA9000 digital melting point apparatus. Infrared spectra were recorded on a Perkin Elmer Spectrum One FT-IR spectrometer equipped with a universal ATR sampling accessory. NMR spectra were carried out using a Bruker Spectrospin DPX-400 instrument operating at 400.13 MHz for ^{1}H NMR and 100.6 MHz for ^{13}C NMR. NMR spectra were also recorded using a Bruker AV-600 instrument operating at 600.1 MHz for ^{1}H NMR and 150.9 MHz for ^{13}C NMR. Chemical shifts are expressed in parts per million (ppm or δ) relative to the residue non-deuterated solvent peak, followed by the splitting pattern, number of protons, coupling constant (if applicable) and assignment of proton. Tetramethylsilane (TMS) was used as the internal reference standard. Multiplicities are abbreviated as follows: singlet (s), doublet (d), triplet (t), quartet (q), multiplet (m) and broad (b). All NMR spectra and titrations were carried out at 293 K, unless otherwise specified.

Electrospray mass spectra were recorded on a Mass Lynx NT V 3.4 on a Waters 600 controller connected to a 996 photodiode array detector with HPLC-grade methanol as carrier solvents. Accurate molecular weights were determined by a peak-matching method, using leucine enkephaline (H-Tyr-Gly-Gly-Phe-Leu-OH) as the standard reference (*m/z* = 556.2771); all accurate mass were reported within ± 5 ppm of the expected mass. Elemental analysis was carried out at the microanalysis laboratory, School of Chemistry and Chemical Biology, University College Dublin.

7.2 UV-vis absorption and luminescence spectroscopy

UV-visible and luminescence spectra were recorded by means of a Varian CARY 50 and a Varian Cary Eclipse spectrophotometer, respectively. The solvents used were of HPLC grade. The concentrations of the ligands and the complexes investigated were the same for both the UV-visible and luminescence titrations. The parameters used for the UV-vis absorption, fluorescence and lanthanide luminescence measurements in Chapter 2 and Chapter 5 are displayed below in Tables 7.1 – 7.13.

Table 7.1: *UV-vis absorption settings for titrations with Tb.58 and Tb.58.Na in Chapter 2.*

Scan: 200-800 nm
Ex. Slit: 1 nm
Em. Slit: 1 nm
Scan Rate: 600 nm min^{-1}

Table 7.2: *Fluorescence settings for titrations with Tb.58 and Tb.58.Na in Chapter 2.*

Mode: Fluorescence	**Excitation:** 225 nm
Start: 250 nm	**Scan Control:** Medium
Stop: 450 nm	**Excitation Slit Width:** 20 nm
Emission Filter: 250-395 nm	**Emission Slit Width:** 10 nm
PMT Voltage: 650 V	

Table 7.3: *Luminescence settings for titrations with Tb.58 and Tb.58.Na in Chapter 2.*

Mode: Phosphorescence	**Excitation:** 283/285 nm
Total Decay: 0.02 s	**Scan:** 450-650 nm
Flash: 1	**Delay:** 0.1 ms
Gate: 5 ms	**PMT Voltage:** High (900 V)
Excitation Slit Width: 20 nm	**Emission Slit Width:** 10 nm

Table 7.4: *Luminescence settings for lifetime studies of Tb.58 and Tb.58.Na in Chapter 2.*

Indirect Excitation: 283/285 nm	**Total Decay:** 30 ms
Emission: Tb^{III} – 545 nm	**Delay:** 0.2 ms
No Cycles: 100	**PMT Voltage:** High
Flash: 1	**Emission Slit Width:** 10 nm
Gate: 0.1 ms	
Excitation Slit Width: 20 nm	

Table 7.5: *UV-vis absorption settings for titrations with Tb.69, Tb.69.Na, Eu.69 and Eu.69.Na in Chapter 2.*

Scan: 200-800 nm
Ex. Slit: 1 nm
Em. Slit: 1 nm
Scan Rate: 600 nm min^{-1}

Table 7.6: *Fluorescence settings for titrations with Tb.69, Tb.69.Na, Eu.69 and Eu.69.Na in Chapter 2.*

Mode: Fluorescence	**Excitation:** 225 nm
Start: 250 nm	**Scan control:** Medium
Stop: 450 nm	**Excitation Slit Width:** 20 nm
Emission Filter: 250-395 nm	**Emission Slit Width:** 20 nm
PMT Voltage: 650 V	

Table 7.7: *Luminescence settings for titrations with Eu.69 and Eu.69.Na in Chapter 2.*

Mode: Phosphorescence	**Excitation:** 282 nm
Total Decay: 0.02 s	**Scan:** 550-750 nm
Flash: 1	**Delay:** 0.1 ms
Gate: 2 ms	**PMT Voltage:** High (800 V)
Excitation Slit Width: 20 nm	**Emission Slit Width:** 2.5 nm
Cycle: 100	**Average Time:** 0.03 s
Data Interval: 0.5 nm	

Table 7.8: *Luminescence settings for lifetime studies of* ***Eu.69*** *and* ***Eu.69.Na*** *in Chapter 2.*

Indirect Excitation: 282 nm	**Total Decay:** 20 ms
Emission: Eu^{III} – 615 nm	**Delay:** 0.2 ms
No Cycles: 100	**PMT Voltage:** High
Flash: 1	**Emission Slit Width:** 5 nm
Gate: 0.1 ms	
Excitation Slit Width: 10 nm	

Table 7.9: *Luminescence settings for titrations with* ***Tb.69*** *and* ***Tb.69.Na*** *in Chapter 2.*

Mode: Phosphorescence	**Excitation:** 282 nm
Total Decay: 0.02 s	**Scan:** 450-650 nm
Flash: 1	**Delay:** 0.1 ms
Gate: 2 ms	**PMT Voltage:** High (980 V)
Excitation Slit Width: 20 nm	**Emission Slit Width:** 10 nm
Cycle: 100	**Average Time:** 0.03 s
Data Interval: 0.5 nm	

Table 7.10: *Luminescence settings for lifetime studies of* ***Tb.69*** *and* ***Tb.69.Na*** *in Chapter 2.*

Indirect Excitation: 282 nm	**Total Decay:** 20 ms
Emission: Tb^{III} – 545 nm	**Delay:** 0.2 ms
No Cycles: 100	**PMT Voltage:** High
Flash: 1	**Emission Slit Width:** 5 nm
Gate: 0.1 ms	
Excitation Slit Width: 10 nm	

Table 7.11: *UV-vis absorption settings for titrations with* ***Tb.110*** *in Chapter 5.*

Scan: 200-800 nm
Ex. Slit: 1 nm
Em. Slit: 1 nm
Scan Rate: 600 nm min^{-t}

Table 7.12: *Luminescence settings for titrations with Tb.110 in Chapter 5.*

Mode: Phosphorescence	**Excitation:** 252 nm
Total Decay: 0.02 s	**Scan:** 450-650 nm
Flash: 1	**Delay:** 0.1 ms
Gate: 2 ms	**PMT Voltage:** Medium (580 V)
Excitation Slit Width: 20 nm	**Emission Slit Width:** 10 nm
Cycle: 100	**Average Time:** 0.1 s
Data Interval: 1 nm	

Table 7.13: *Luminescence settings for lifetime studies of Tb.110 in Chapter 5.*

Indirect excitation: 252 nm	**Total Decay:** 20 ms
Emission: Tb^{III} – 545 nm	**Delay:** 0.2 ms
No Cycles: 100	**PMT Voltage:** High
Flash: 1	**Emission slit width:** 10 nm
Gate: 0.1 ms	
Excitation slit width: 20 nm	

7.2.1 Sectioning, polishing, *in vitro* scratching and staining of the bovine tibiae specimens

The protocol used to induce *in vitro* microscratches on the outer surface of the bone samples was based on previously established scratching methods (illustrated in Figure 7.1).[129, 133, 138, 163, 272] Fresh bovine tibiae were obtained from a meat wholesaler (KEPAK Ltd, Clonee, Co. Dublin) from animals slaughtered 2-3 days previous. The soft tissue was removed and the bones were stored in water at -20 °C until required. Longitudinal sections of cortical bone from the mid-diaphysis were cut into beam shaped specimens (15 mm x 5 mm x 250 μm) using a low speed diamond saw. To completely mimic the smooth bone surface found *in vivo* and remove any rough edges potentially formed during the cutting process, the bone specimens were finely polished using grades of sand paper up to P1200 grit (15 μm). All machining and preparation procedures were carried out under aqueous conditions to ensure that the bone samples did not dry out at any stage. A 5 mm line was scratched using a surgical scalpel on the surface of each beam and the specimens were immersed in a vial containing a 1 mM buffered solution of the Ln contrast agent (20 mM HEPES, 135 mM KCl, pH 7.4) for 20 h under vacuum. After this time the specimens were removed from the

aqueous solution and a second 5 mm scratch was made. The samples were re-immersed in the solution for a remaining 4 h. After final removal from the contrast agent, a third 5 mm scratch was made. The bone samples were washed thoroughly with deionised water to remove any excess unbound contrast agent from the surface and then adhered to a glass slide using DPX. In total, each bone sample studied contained three 5 mm scratches, one which was exposed to agent for 24 h, one for 4 h and the last scratch having no exposure to the contrast agent (control).

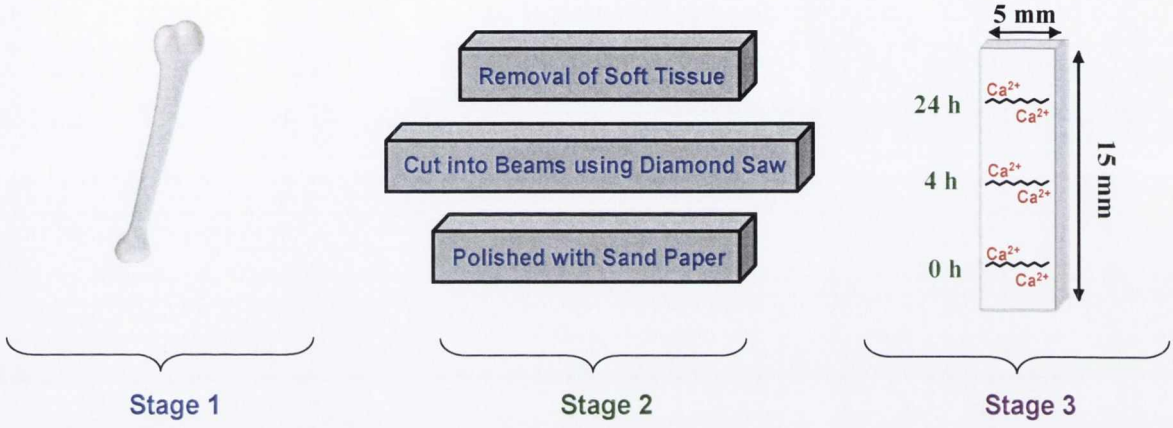

Figure 7.1: *Illustration of the sectioning, polishing and in vitro scratching protocol of the bovine tibia specimens.*

7.3 Epifluorescence and confocal microscopy analysis

The epifluorescence microscopy analysis on the scratched bone samples was carried out in collaboration with Mr. Peter Mauer, a PhD student in Prof. Clive Lee's research group in the Royal College of Surgeons in Ireland (RCSI). The microscope used was a Nikon Eclipse E800 with the images viewed using a CCD colour video camera and analysed using the imaging software Image J 1.43. The emission and excitation properties of the Nikon fluorescence cubes used were described in Chapter 3 (Section 3.2).

Laser scanning confocal microscopy analysis of the bone specimens was carried out in collaboration with Dr. Colin McCoy in Queens University, Belfast using a Leica TCS SP2 confocal laser scanning microscope. After focusing, the sample surface was excited using the 458 nm line from an Ar/ArKr laser and luminescence data collected over the range 463 – 650 nm for **Tb.58**, **Tb.58.Na**, **Tb.69** and **Tb.69.Na** and between 550 – 800 nm for **Eu.69** and **Eu.69.Na**. Luminescence emission micrographs displayed the photomultiplier intensities across the full wavelength range with a look-up table assigning colour to overall intensities ranging from black (zero intensity) to either bright red or green (highest intensity).

7.4 Fast field-cycling NMR relaxometry

The frequency dependence of the ^1H relaxation for the samples was recorded over the frequency range 0.01 – 10 MHz using a Spinmaster FFC-2000 Fast-field cycling NMR relaxometer (Stelar SRL, Mede, Italy) in collabaration with Dr. Dermot Brougham in Dublin City University. The system operated at a measurement frequency of 9.25 MHz for ^1H, with a 90° pulse of 7 μs. T_1 measurements were performed as a function of external field, B_0, with standard pulse sequences incorporating B_0 field excursions. The temperature of the samples was maintained at 25 °C and controlled within ±1 °C through the use of a thermostatted airflow system. All of the ^1H magnetisation recovery curves were mono-exponential within experimental error and the random errors in fitting T_1 were always less than 1%. For higher frequencies (> 20 MHz) a re-conditioned Bruker WP80 electromagnet was used, with the Stelar console. At higher frequency the 90° pulse was typically 5.5 μs.

7.5 MR imaging of bovine bone specimens

The MR imaging of the bovine bone samples was carried out by Dr. Christian Kerskens and Dr. Rustam Rakhmatullin in the Institute of Neuroscience, Trinity College Dublin using a 7T Bruker biospec animal scanner. The general parameters used to obtain the T_1 weighted images are shown below in Table 7.14.

Table 7.14: *General parameters used for MR imaging using the 7T animal scanner.*

Sequence: "MDEFT"	**Averages:** 80
Field of View: *ca.* 2.8 cm	**Inversion Time:** 1100 ms
Matrix Size: 256/512	**Scan Time:** *ca.* 20 h
Resolution: 0.1/0.05 mm/px	**Coil:** Surface Coil
Echo Time: 5 ms	
Repetition Time: 2500 ms	

7.6 General Synthetic Procedures

Procedure 1: Selective monoalkylation of cyclen framework[169]

Selective monoalkylation of the cyclen framework involved refluxing 1 equivalent of the alkylating pendant arm with 4 equivalents of cyclen in the presence of 1.2 equivalents of Et_3N in freshly distilled $CHCl_3$ for 15 h. After reaction completion, the excess cyclen and

Et_3N salt were removed by extraction with 1 M NaOH (2 x 25 mL) and H_2O (2 x 25 mL). The resulting organic layer was dried over $MgSO_4$, filtered and the solvent removed under reduced pressure. The resulting oily residue was dried under vacuum, before being stored in a desiccator till required.

Procedure 2: Synthesis of Ln complexes using $Ln(CF_3SO_3)_3$

Ln complexes were prepared by heating the ligand at reflux, under an inert atmosphere, in the presence of 1 equivalent of the appropriate Ln triflate salt in freshly distilled CH_3CN (25 mL) for 15 h. Following reduction of the solvent to *ca.* 1 mL, the complexes were isolated by precipitation from swirling dry diethyl ether. For some complexes, in order to obtain a fine solid, sonification of the resulting viscous oil in CH_2Cl_2 or CH_3Cl was required. Due to the paramagnetic nature of the Ln complexes, ^1H NMR spectra consisted of broad signals and therefore full characterisation could not be carried out, *i.e.* integration of the signals was not possible. The same properties prevented ^{13}C spectra from being obtained.

Procedure 3: Base hydrolysis of the diethyl iminodiacetate functionalities

Base hydrolysis of the diethyl iminodiacetate groups was carried out by refluxing the Ln complex in a mixed MeOH/H_2O (1:9, v/v) solution in the presence of NaOH for *ca.* 5 h. After reaction completion, the solvent was removed under reduced pressure and the resulting residue re-dissolved in cold MeOH. The fine precipitate which resulted was removed by filtration through a micro syringe. 90% of the solvent was then removed, followed by precipitation of the desired product from an ethanol solution. The product was re-dissolved in MeOH and precipitated from a large volume of dry diethyl ether. For some complexes, in order to obtain a solid, sonification in CH_2Cl_2, CH_3Cl or diethyl ether was required.

7.7 Experimental details for Chapter 2

***N,N*-[Bis(ethoxycarbonylmethyl)-amino]-benzene (62)**[161]

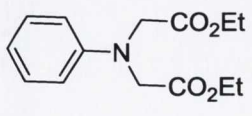

Aniline (1.50 g, 16.11 mmol) was dissolved in 100 mL of CH_3CN along with Na_2HPO_4 (6.86 g, 48.33 mmol) and KI (8 g, 48.33). After stirring the mixture for 10 min, ethyl bromoacetate (5.92 g, 35.44 mmol) was added *via* syringe. The mixture was refluxed at 85 °C for 24 h. The inorganic salts were filtered off and the solvent evaporated to dryness. The residue was dissolved in $CHCl_3$ and washed with 0.1 M HCl (2 x 20 mL), $NaHCO_3$ (2 x 20 mL) and brine (2 x 20 mL). The

resulting organic layer was dried over $MgSO_4$ and the solvent removed under vacuum. The resulting brown residue was dissolved in CH_2Cl_2 and purified by silica column chromatography using an elution gradient 100 to 70:30 Hex:EtOAc. The desired product was collected as a pale yellow oil (2.40 g, 56% yield). HRMS (*m/z*, ES^+): Calculated for $C_{14}H_{19}NO_4Na$ *m/z* = 288.1212 $[M+Na]^+$. Found *m/z* = 288.1223; ^1H NMR (400 MHz, $CDCl_3$, δ_H): 7.24 (t, 2H, *J* = 7.5 Hz, Ar-H), 6.81 (t, 1H, *J* = 7.5 Hz, Ar-H), 6.64 (d, 2H, *J* = 7.5 Hz, Ar-H), 4.24 (q, 4H, *J* = 7 Hz, $N(CH_2CO_2C\underline{H}_2CH_3)_2$), 4.16 (s, 4H, $N(C\underline{H}_2CO_2CH_2CH_3)_2$), 1.31 (t, 6H *J* = 7 Hz, $N(CH_2CO_2CH_2C\underline{H}_3)_2$); ^{13}C NMR (100 MHz, $CDCl_3$, δ_c): 170.54 (qt), 147.42 (qt), 128.81 (CH), 117.83 (CH), 112.05 (CH), 67.73 (CH_2), 53.06, (CH_2), 13.78 (CH_3); IR υ_{max} (cm^{-1}): 2983, 1730, 1601, 1578, 1507, 1446, 1421, 1371, 1342, 1264, 1176, 1096, 1023, 991, 969, 912, 856, 748, 731, 690.

4-Nitro-1-[*N,N*-bis(ethoxycarbonylmethyl)-amino]-benzene (63)[161]

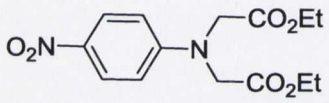

62 (2.00 g, 7.57 mmol) in 40 mL of acetic acid was treated, while stirring at 0 °C, with 1 mL of HNO_3 (70%). After 15 min, the reaction mixture was poured over ice to give a dark green precipitate. Upon recrystallisation from EtOH, the product was obtained as green needles (1.86 g, 93% yield). M.P: 164-165 °C; HRMS (*m/z*, ES^+): Calculated for $C_{14}H_{18}N_2O_6Na$ *m/z* = 333.1063 $[M+Na]^+$. Found *m/z* = 333.1057; ^1H NMR (400 MHz, $CDCl_3$, δ_H): 8.16 (d, 2H, *J* = 9.5 Hz, Ar-H), 6.61 (d, 2H, *J* = 9.5 Hz, Ar-H), 4.27 (q, 4H, *J* = 7 Hz, $N(CH_2CO_2C\underline{H}_2CH_3)_2$), 4.24 (s, 4H, $N(C\underline{H}_2CO_2CH_2CH_3)_2$), 1.33 (t, 6H, *J* = 7 Hz, $N(CH_2CO_2CH_2C\underline{H}_3)_2$); ^{13}C NMR (100 MHz, $CDCl_3$, δ_c): 169.89 (qt), 153.04 (qt), 139.40 (qt), 125.95 (CH), 111.54 (CH), 61.87 (CH_2), 54.78 (CH_2), 14.98 (CH_3); IR υ_{max} (cm^{-1}): 2975, 1743, 1591 1516, 1484, 1456, 1419, 1393, 1371, 1344, 1304, 1273, 1205, 1182, 1115, 1024, 975, 961, 870, 827, 756, 735, 697.

4-Amino-1-[*N,N*-bis(ethoxycarbonylmethyl)-amino]-benzene (64)[161]

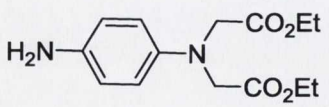

63 (0.70 g, 2.26 mmol) was dissolved in 25 mL of DMF. Pd-C (0.07 g, 10% w/w) was added slowly to the solution. The mixture was hydrogenated at 1.5 atm for 5 h. After the reaction was complete (disappearance of starting material in TLC), the mixture was filtered through celite and the solvent removed under vacuum to yield 64 as a dark brown oil (0.57 g, 90% yield). HRMS (*m/z*, ES^+): Calculated for $C_{14}H_{21}N_2O_4$ *m/z* = 281.1501 $[M+H]^+$. Found *m/z* = 281.1491; ^1H NMR (400 MHz, $CDCl_3$, δ_H): 6.62 (d, 2H, *J* = 9 Hz, Ar-H), 6.54 (d, 2H, *J* = 9 Hz, Ar-H), 4.20 (q, 4H, *J* = 7 Hz, $N(CH_2CO_2C\underline{H}_2CH_3)_2$), 4.08 (s, 4H, $N(C\underline{H}_2CO_2CH_2CH_3)_2$),

3.09 (bs, 2H, NH$_2$), 1.27 (t, 6H, J = 7 Hz, N(CH$_2$CO$_2$CH$_2$CH$_3$)$_2$); ^{13}C NMR (100 MHz, CDCl$_3$, δ_c): 171.33 (qt), 141.29 (qt), 138.05 (qt), 116.60 (CH), 115.01 (CH), 60.91 (CH$_2$), 54.16 (CH$_2$), 14.23 (CH$_3$); IR υ_{max} (cm^{-1}): 3422 2983, 1740, 1655, 1616, 1510, 1393, 1197, 1015, 845, 785, 730.

4-(β-Chloroethanamido)-1-[*N,N*-bis(ethoxycarbonylmethyl)-amino]-benzene (59)

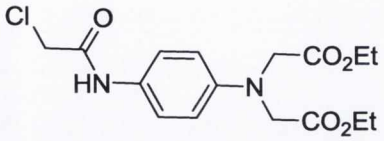

64 (0.57 g, 2.04 mmol) along with Et$_3$N (0.34 mL, 2.45 mmol) was dissolved in 50 mL of CH$_2$Cl$_2$ in a 250 mL RBF. The brown solution was stirred at -15 °C using an acetone/ice bath for 5 min. Chloroacetyl chloride (0.23 g, 2.04 mmol) was added along with 30 mL of CH$_2$Cl$_2$ to the solution using a pressure equalised dropping funnel. The resulting mixture was stirred at room temp. overnight. After reaction completion, the mixture was washed with H$_2$O (2 x 20 mL), 0.1 M HCl (2 x 20 mL) and brine (2 x 20 mL). The organic layer was dried over MgSO$_4$, filtered and the solvent removed under reduced pressure to yield **59** as a dark brown oil (0.63 g, 86% yield). HRMS (*m/z*, ES$^+$): Calculated for C$_{16}$H$_{21}$N$_2$O$_5$ClNa *m/z* = 379.1037 [M+Na]$^+$. Found *m/z* = 379.1025; ^{1}H NMR (400 MHz, CDCl$_3$, δ_H): 8.24 (s, 1H, N-H), 7.36 (d, 2H, J = 9 Hz, Ar-H), 6.58 (d, 2H, J = 9 Hz, Ar-H), 4.20 (q, 4H, J = 7 Hz, N(CH$_2$CO$_2$CH$_2$CH$_3$)$_2$), 4.14 (s, 4H, N(CH$_2$CO$_2$CH$_2$CH$_3$)$_2$), 4.11 (s, 2H, NHCOCH$_2$Cl), 1.27 (t, 6H, J = 7 Hz, N(CH$_2$CO$_2$CH$_2$CH$_3$)$_2$); ^{13}C NMR (100 MHz, CDCl$_3$, δ_c): 170.79 (qt), 163.70 (qt), 145,66 (qt), 127.74 (qt), 122.07 (CH), 112.94 (CH), 61.25 (CH$_2$), 53.68 (CH$_2$), 42.85 (CH$_2$), 14.24 (CH$_3$); IR υ_{max} (cm^{-1}): 3263, 2984, 1736, 1663, 1595, 1514, 1405, 1371, 1341, 1184, 1095, 1019, 966, 923, 830, 816, 789, 728.

1-{4-[*N,N*-bis(ethoxycarbonylmethyl)-amino]phenylcarbamoyl-methyl}-1,4,7,10-tetraazacyclododecane (67)[169]

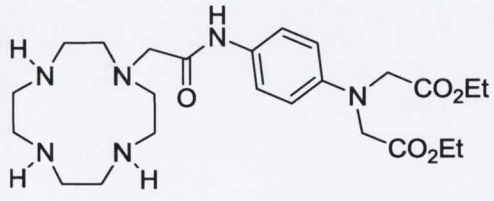

67 was synthesised according to **Procedure 1**, using the alkylating pendant group **59** (0.625 g, 1.83 mmol). The product was isolated as a brown oil (0.76 g, 84% yield). HRMS (*m/z*, ES$^+$): Calculated for C$_{24}$H$_{41}$N$_6$O$_5$ *m/z* = 493.3138 [M+H]$^+$. Found *m/z* = 493.3140; ^{1}H NMR (400 MHz, CDCl$_3$, δ_H): 9.92 (s, 1H, N-H), 7.54 (d, 2H, J = 9 Hz, Ar-H), 6.56 (d, 2H, J = 9 Hz, Ar-H), 4.18 (q, 4H, J = 7 Hz, N(CH$_2$CO$_2$CH$_2$CH$_3$)$_2$), 4.09 (s, 4H, N(CH$_2$CO$_2$CH$_2$CH$_3$)$_2$), 3.21 (s, 2H, 1-NCH$_2$CONH), 2.78 (bs, 4H, cyclen-CH$_2$), 2.70 (bs, 12H, cyclen-CH$_2$), 2.0 (bs, 3H, Cyclen-NH), 1.25 (t, 6H, J = 7 Hz, N(CH$_2$CO$_2$CH$_2$CH$_3$)$_2$); ^{13}C NMR (100 MHz, CDCl$_3$, δ_c):

170.48 (qt), 168.92 (qt), 144.07 (qt), 129.44 (qt), 120.44 (CH), 112.55 (CH), 60.67 (CH_2), 59.27 (CH_2), 53.27 (CH_2), 53.12 (CH_2), 46.73 (CH_2), 46.44 (CH_2), 45.55 (CH_2), 13.77 (CH_3); IR υ_{max} (cm^{-1}): 2918, 1849, 1741, 1664, 1472, 1461, 1324, 1272, 1220, 1104, 974, 900, 818, 774, 730, 719.

1,4,7-Tris(dimethylcarbamoylmethyl)-10-{4-[*N,N*-bis(ethoxycarbonylmethyl)-amino]phenylcarbamoyl-methyl-1,4,7,10-tetraaza-cyclododec-1-yl}-acetamide (58)

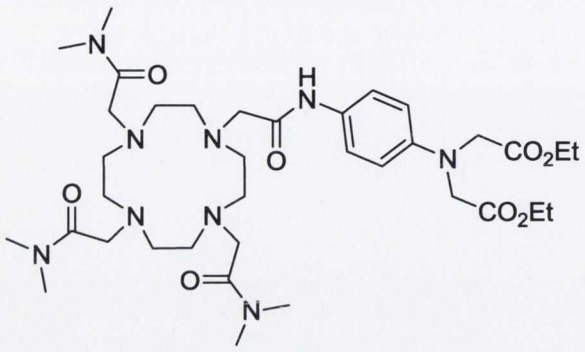

67 (0.53 g, 1.07 mmol) along with 40 mL of CH_3CN was placed in a 100 mL RBF. KI (0.59 g, 3.53 mmol) and K_2CO_3 (0.49 g, 3.53 mmol) were added to the solution, which was then placed in an ice/acetone bath and allowed to cool. A solution of 2 chloro-*N,N*-dimethyl-acetamide (0.43 g, 3.53 mmol) was added quickly and the solution was stirred for 15 min. The solution was then stirred at 85 °C under argon for 5 days. Once the reaction was complete (monitored by mass spec), the solvent was removed under reduced pressure. The brown residue was dissolved in CH_2Cl_2 and purified by silica column chromatography using a gradient elution 100 to 90:10 CH_2Cl_2:CH_3OH. The desired product was obtained as an orange viscous oil (0.50 g, 63% yield). HRMS (*m/z*, ES^+): Calculated for $C_{36}H_{61}N_9O_8Na$ *m/z* = 770.4541 $[M+Na]^+$. Found *m/z* = 770.4549; ^1H NMR (400 MHz, $CDCl_3$, δ_H): 9.53 (s, 1H, N-H), 7.64 (d, 2H, *J* = 9 Hz, Ar-H), 6.47 (d, 2H, *J* = 9 Hz, Ar-H), 4.18 (q, 4H, *J* = 7 Hz, $N(CH_2CO_2CH_2CH_3)_2$), 4.07 (s, 4H, $N(CH_2CO_2CH_2CH_3)_2$), 3.44-2.00 (bm, 42H, cyclen-CH_2 + 4,7,10-$NCH_2CON(CH_3)_2$ + 1-NCH_2CONH), 1.26 (t, 6H, *J* = 7 Hz, $N(CH_2CO_2CH_2CH_3)_2$); ^{13}C NMR (100 MHz, $CDCl_3$, δ_C): 170.47 (qt), 169.08 (qt), 143.71 (qt), 130.05 (qt), 120.68 (CH), 112.01 (CH), 60.92 (CH_2), 60.62 (CH_2), 58.25 (CH_2), 54.54 (CH_2), 54.41 (CH_2), 53.32 (CH_2), 53.03 (CH_2), 50.13 (CH_2), 35.96 (CH_3), 35.21 (CH_3), 35.12 (CH_3), 13.80 (CH_3); IR υ_{max} (cm^{-1}): 2818, 1740, 1646, 1518, 1450, 1400, 1370, 1346, 1297, 1262, 1179, 1102, 1062, 1005, 974, 902, 818, 772, 730.

Diethyl 2,2-(2-chloroacetylamino)diacetate (73)

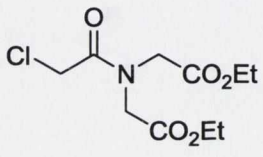

Diethyl iminodiacetate (1.00 g, 5.29 mmol) was dissolved along with Et_3N (0.85 g, 8.38 mmol) in CH_2Cl_2 (50 mL). The resulting clear solution was stirred in an acetone/ice bath for 5 min. Chloroacetyl chloride (1.18 g, 10.48 mmol) was added slowly along with 30 mL of CH_2Cl_2 to the solution using a pressure equalised dropping funnel. The resulting mixture was

stirred at room temp. overnight. After reaction completion, the pale yellow mixture was washed with H_2O (2 x 20 mL), 0.1 M HCl (2 x 20 mL) and brine (2 x 20 mL). The organic layer was dried over $MgSO_4$, filtered and the solvent removed under reduced pressure to yield **73** as a pale orange oil (1.05 g, 75%). HRMS (*m/z*, ES^+): Calculated for $C_{10}H_{16}NO_5NaCl$ *m/z* = 288.0615 $[M+Na]^+$. Found *m/z* = 288.0609; ^1H NMR (400 MHz, $CDCl_3$, δ_H): 4.23 (q, 2H, *J* = 7 Hz, $NCH_2CO_2C\underline{H}_2CH_3$), 4.18 (q, 2H, *J* = 7 Hz, $NCH_2CO_2C\underline{H}_2CH_3$), 4.11 (bs, 4H, $N(C\underline{H}_2CO_2CH_2CH_3)_2$), 4.12 (s, 2H, $COC\underline{H}_2Cl$) 1.29 (t, 3H, *J* = 7 Hz, $NCH_2CO_2CH_2C\underline{H}_3$), 1.27 (t, 3H, *J* = 7 Hz, $NCH_2CO_2CH_2C\underline{H}_3$); ^{13}C NMR (100 MHz, $CDCl_3$, δ_c): 168.66 (qt), 168.45 (qt), 167.36 (qt), 62.01 (CH_2), 61.53 (CH_2), 50.39 (CH_2), 48.55 (CH_2), 40.68 (CH_2), 14.09 (CH_3), 14.08 (CH_3); IR υ_{max} (cm^{-1}): 2986, 1767, 1663, 1464, 1407, 1374, 1352, 1301, 1260, 1115, 1022, 965, 867, 797, 735, 672.

2-Chloro-*N*-(naphthalene-1-yl) acetamide (70)[176]

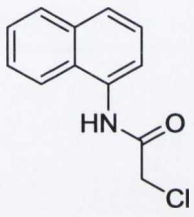

1-Aminonaphthalene (1.0 g, 6.98 mmol) was dissolved along with Et_3N (0.85 g 8.38 mmol) in CH_2Cl_2 (50 mL). The resulting pink solution was stirred in an acetone/ice bath for 5 min. Chloroacetyl chloride (1.18 g, 10.48 mmol) was added slowly along with 30 mL of CH_2Cl_2 to the solution using a pressure equalised dropping funnel. The resulting mixture was stirred at room temp. overnight. After completion of the reaction, the mixture was washed with H_2O (2 x 20 mL), 0.1 M HCl (2 x 20 mL) and brine (2 x 20 mL). The organic layer was dried over $MgSO_4$, filtered and the solvent removed under reduced pressure to yield **70** as a yellow oil (1.32 g, 86% yield). HRMS (*m/z*, ES^+): Calculated for $C_{12}H_{11}NOCl$ *m/z* = 220.0529 $[M+H]^+$. Found *m/z* = 220.0539; ^1H NMR (400 MHz, $CDCl_3$, δ_H): 8.78 (bs, 1H, N-$\underline{H}$), 7.98 (d, 1H, *J* = 7.5 Hz, Ar-$\underline{H}$), 7.88 (m, 2H, Ar-$\underline{H}$), 7.75 (d, 1H, *J* = 8, Ar-$\underline{H}$), 7.58-4.48 (m, 3H, Ar-$\underline{H}$), 4.35 (s, 2H, $COC\underline{H}_2Cl$); ^{13}C NMR (100 MHz, $CDCl_3$, δ_c): 164.41 (qt), 134.11 (qt), 131.10 (qt), 128.91 (CH), 126.96 (qt), 126.74 (CH), 126.52 (CH), 126.26 (CH), 125.70 (CH), 120.64 (CH), 120.24 (CH), 43.36 (CH_2); IR υ_{max} (cm^{-1}): 3268, 2958, 1664, 1550, 1505, 1394, 1348, 1267, 1247, 1169, 1017, 961, 919, 886, 855, 813, 741, 717, 684.

1-{*N*-(Naphthalene-1-yl-acetamide)}-1,4,7,10-tetraazacyclododecane (72)[169]

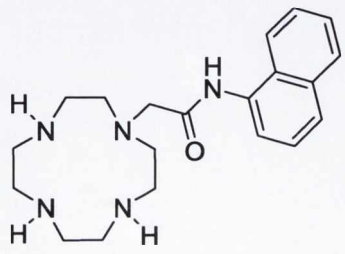

72 was synthesised according to **Procedure 1**, using the alkylating pendant group **70** (0.50 g, 2.28 mmol). The product was isolated as an orange viscous oil (0.73 g, 90% yield). HRMS (*m/z*, ES^+): Calculated for $C_{20}H_{30}N_5O$ *m/z* = 356.2450 $[M+H]^+$.

Found *m/z* = 356.2468; ^{1}H NMR (400 MHz, $CDCl_3$, δ_H): 10.12 (bs, 1H, N-H), 8.15 (d, 1H, *J* = 7.5 Hz, Ar-H), 7.97 (d, 1H, *J* = 7.5 Hz, Ar-H), 7.72 (d, 1H, *J* = 7.5 Hz, Ar-H), 7.55 (d, 1H, *J* = 8 Hz, Ar-H), 7.40-7.34 (m, 3H, Ar-H), 3.30 (s, 2H, 1-CH_2CONH), 2.59 (bs, 12H, cyclen-CH_2), 2.49 (bs, 4H, cyclen-CH_2), 2.19 (bs, 3H, Cyclen-NH); ^{13}C NMR (100 MHz, $CDCl_3$, δ_c): 170.08 (qt), 133.70 (qt), 132.36 (qt), 128.06 (CH), 126.53 (qt), 125.46 (CH), 125.42 (CH), 125.38 (CH), 124.83 (CH), 121.30 (CH), 119.47 (CH), 60.11 (CH_2), 53.34 (CH_2), 47.03 (CH_2), 46.78 (CH_2), 45.67 (CH_2); IR υ_{max} (cm^{-1}): 3279, 2826, 1671, 1597, 1528, 1497, 1450, 1344, 1272, 1252, 1113, 1063, 907, 795, 773, 724, 643.

1,4,7-Tris-(N,N-bis(ethoxycarbonylmethyl)-10-[N-(Naphthalene-1-yl-acetamide)]-1,4,7,10 tetraazacyclododecane (69)

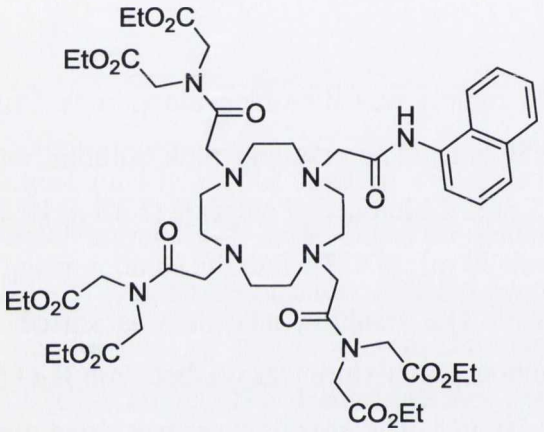

72 (0.44 g, 1.23 mmol) was dissolved along with Et_3N (0.39 g, 4.06 mmol) in 40 mL of freshly distilled CH_3CN. After stirring the solution at 0 °C for 10 min, 73 (1.08 g, 4.06 mmol) was added dropwise to the solution over 30 min *via* syringe. The resulting solution was refluxed for 7 days under argon. After completion of the reaction (monitored by mass spec), the solvent was removed under reduced pressure and the resulting orange oil was re-dissolved in CH_2Cl_2 (30 mL). Removal of the excess Et_3N was achieved by washing the CH_2Cl_2 solution with water (2 x 15 mL). Further purification was achieved by alumina column chromatography using a gradient elution 100 to 80:20 CH_2Cl_2:CH_3OH. The desired product was obtained as a yellow viscous oil (0.69 g, 54% yield). HRMS (*m/z*, ES^+): Calculated for $C_{50}H_{75}N_8O_{16}$ *m/z* = 1043.5301 $[M+H]^+$. Found *m/z* = 1043.5297; ^{1}H NMR (400 MHz, $CDCl_3$, δ_H): 10.39 (s, 1H, N-H), 8.34 (d, 1H, *J* = 8 Hz, Ar-H), 7.74 (m, 2H, Ar-H), 7.59 (d, 1H, *J* = 8 Hz, Ar-H), 7.38-7.36 (m, 3H, Ar-H), 4.31-3.72 (m, 26H, 1-NCH_2CO + 4,7,10-NCH_2CON(CH_2CO$_2$CH_2CH_3)$_2$), 3.37-2.10 (bm, 22H, cyclen-CH_2 + 4,7,10-NCH_2CO), 1.26-1.07 (m, 18H, 4,7,10-NCH_2CON(CH_2CO$_2$CH_2CH_3)$_2$); ^{13}C NMR (100 MHz, $CDCl_3$, δ_c): 171.48 (qt), 171.12 (qt), 168.65 (qt), 168.60 (qt), 168.29 (qt), 168.04 (qt), 133.55 (qt), 133.26 (qt), 127.95 (qt), 127.24 (CH), 125.24 (CH), 125.12 (CH), 125.04 (CH), 124.67 (CH), 123.47 (CH), 121.52 (CH), 61.33 (CH_2), 61.29 (CH_2), 60.58 (CH_2), 56.72 (CH_2), 54.08 (CH_2), 53.97 (CH_2), 53.91 (CH_2), 53.85 (CH_2), 48.86 (CH_2), 48.52 (CH_2), 47.61 (CH_2), 47.12 (CH_2), 13.69 (CH_3), 13.65 (CH_3), 13.54 (CH_3); IR υ_{max} (cm^{-1}): 2978, 2819, 1736, 1660, 1544, 1466, 1403, 1373, 1302, 1253, 1187, 1106, 1023, 971, 904, 866, 778, 736.

Complex Tb.58

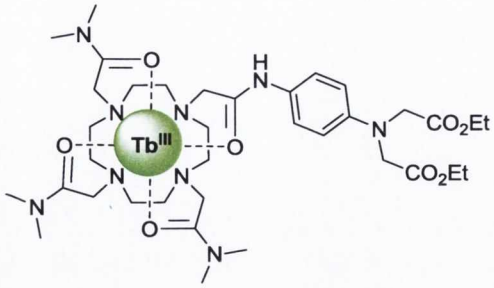

Complex **Tb.58** was synthesised according to **Procedure 2** using ligand **58** (0.150 g, 0.20 mmol) and $Tb(CF_3SO_3)_3$ (0.121 g, 0.20 mmol). The desired product was isolated as a pale orange solid (0.248 g, 92% yield). M.P: decomposed above 200 °C; HRMS (*m/z*, ES^+): Calculated for $C_{38}H_{61}F_6N_9O_{14}S_2{}^{159}Tb$ *m/z* = 1204.2902 $[M+2(CF_3SO_3)]^+$. Found *m/z* =1204.2860; ^1H NMR (400 MHz, CD_3OD, δ_H): 109.06, 105.08, 73.39, 71.41, 51.22, 49.66, 46.08, 42.61, 34.23, 28.65, 23.39, 19.14, 49.85, 17.69, 13.67, 10.65, 10.54, 4.93, 3.34, 2.16, 1.37, 1.34, 0.93, -0.08, -1.53, -2.54, -50.88, -60.82, -70.42, -75.39, -80.14, -84.56, -90.85, -95.60, -96.92, -101.34, -103.55, -106.09, -110.83, -114.70; Calculated for $C_{39}H_{61}F_9N_9O_{17}S_3Tb.3CHCl_3$: C, 29.46; H, 3.77; N, 7.36. Found C, 29.19; H, 3.85; N, 7.47; IR υ_{max} (cm^{-1}): 3458, 2941, 1735, 1618, 1560, 1520, 1459, 1411, 1246, 1224, 1158, 1081, 1028, 958, 910, 823, 759, 635.

Complex Tb.58.Na

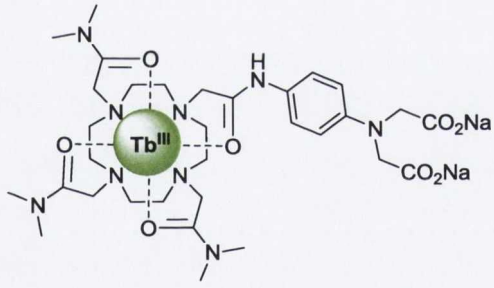

Complex **Tb.58.Na** was synthesised according to **Procedure 3** using complex **Tb.58** (0.100 g, 0.07 mmol) and NaOH (0.007 g, 0.17 mmol). The desired product was obtained as a pale yellow solid (0.080 g, 81% yield). M.P: decomposed above 250 °C; HRMS (*m/z*, ES^+): Calculated for $C_{34}H_{53}N_9O_{14}S_2F_6{}^{159}Tb$ *m/z* = 1148.2311 $[M+2(CF_3SO_3)-2Na+2H]^+$. Found *m/z* = 1148.2356; ^1H NMR (400 MHz, D_2O, δ_H): 84.92, 79.51, 69.02, 67.04, 61.52, 58.42, 54.56, 53.79, 52.79, 49.04, 44.07, 44.38, 22.96, 21.53, 20.53, 16.67, 15.77, 14.20, 11.41, 10.37, 8.35, 7.84, 7.19, 6.72, 6.59, 6.43, 6.34, 3.52, 1.30, 1.17, -0.06, -82.05, -85.69, -88.45, -97.73, -101.59, -103.47; Calculated for $C_{35}H_{51}F_9N_9O_{17}S_3Tb.H_2O.CHCl_3$: C, 29.23; H, 3.68; N, 8.52. Found C, 29.28; H, 3.78; N, 8.10; IR υ_{max} (cm^{-1}): 2972, 1603, 1438, 1251, 1229, 1168, 1088, 1035, 945, 906, 878, 864, 765, 687, 638.

Complex Eu.58

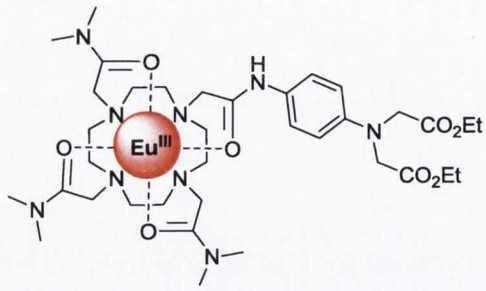

Complex **Eu.58** was synthesised according to **Procedure 2** using ligand **58** (0.088 g, 0.12 mmol) and $Eu(CF_3SO_3)_3$ (0.071 g, 0.12 mmol). The desired product was isolated as a pale orange solid (0.095 g, 80% yield). M.P: decomposed above 240 °C; HRMS (*m/z*, ES^+): Calculated for $C_{38}H_{61}N_9O_{14}F_6S_2{}^{151}Eu$ *m/z* = 1198.2915 $[M+2(CF_3SO_3)]^+$. Found *m/z* = 1198.2896; ^1H NMR (400 MHz, CD_3OD, δ_H): 32.00, 10.98, 8.11, 6.94, 6.62, 6.18, 5.51, 4.71, 4.01, 3.52, 3.15, 2.23, 2.18, 1.12, 0.89, 0.12, -3.55, -7.82, -12.93, -15.73; IR υ_{max} (cm^{-1}): 3476, 2920, 1737, 1615, 1560, 1519, 1459, 1410, 1330, 1250, 1224, 1155, 1080, 102, 957, 909, 821, 802, 757, 636.

Complex Eu.69

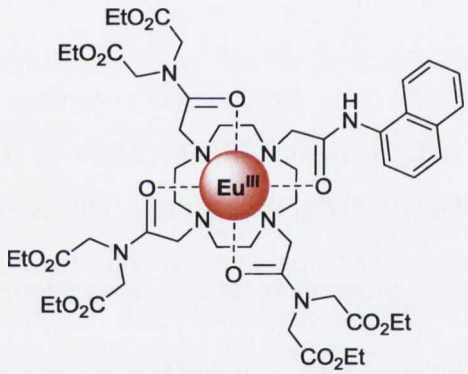

Complex **Eu.69** was synthesised according to **Procedure 2** using ligand **69** (0.050 g, 0.05 mmol) and $Eu(CF_3SO_3)_3$ (0.030 g, 0.05 mmol). The desired product was isolated as an orange solid (0.060 g, 69% yield). M.P: decomposed above 260 °C; HRMS (*m/z*, ES^+): Calculated for $C_{52}H_{74}F_6N_8O_{22}S_2{}^{151}Eu$ *m/z* = 1493.3474 $[M+2(CF_3SO_3)]^+$. Found *m/z* = 1493.3433; ^1H NMR (400 MHz, $CDCl_3$, δ_H): 29.56, 29.06, 28.27, 10.81, 10.51, 10.31, 9.94, 8.07, 6.81, 6.56, 6.38, 6.11, 4.76, 3.93, 3.80, 3.69, 3.60, 3.49, 3.10, 0.81, -0.52, -1.27, -2.94, -5.32, -5.75, -6.96, -10.44, -12.13; Calculated for $C_{53}H_{74}F_9N_8O_{25}S_3Eu.H_2O.2CHCl_3$: C, 34.78; H, 4.14; N, 5.90. Found: C, 34.91; H, 4.06; N, 6.00; IR υ_{max} (cm^{-1}): 2989, 1739, 1603, 1508, 1479, 1398, 1377, 1348, 1218, 1157, 1075, 1027, 971, 910, 874, 837, 784, 759, 670, 572.

Complex Eu.69.Na

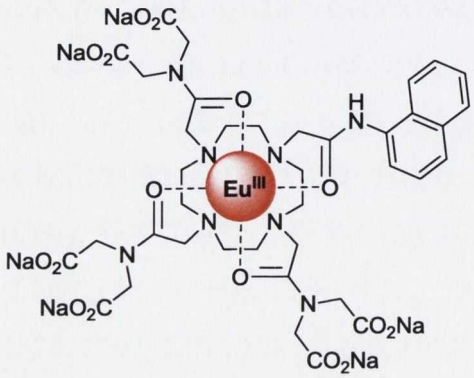

Complex **Eu.69.Na** was synthesised according to **Procedure 3** using complex **Eu.69** (0.100 g, 0.06 mmol) and NaOH (0.017 g, 0.43 mmol). The desired product was obtained as pale yellow solid (0.088 g, 90% yield). M.P: decomposed above 280 °C; HRMS (*m/z*, ES^+): Calculated for $C_{38}H_{47}N_8O_{16}Na^{151}Eu$ *m/z* =

1047.2225 $[M\text{-}5Na+3H]^+$. Found *m/z* = 1047.2191; ^1H NMR (400 MHz, CD_3OD, δ_H): 36.99, 35.52, 31.07, 28.38, 7.77, 7.55, 7.16, 6.62, 6.34, 6.20, 5.77, 5.41, 4.31, 3.95, 3.62, 349, 2.81, 2.33, 1.99, 1.45, 1.30, 1.19, 0.88, 0.72, 0.47, 0.18, -0.23, -0.48, -0.85, -2.21, -2.48, -3.12, -3.42, -3.79, -4.20, -5.69, -6.59, -7.08, -8.45, -10.21, -10.64, -10.96, -11.48, -12.44, -14.10, -15.01, -15.71, -16.42, -16.96, -18.00, -20.56, -21.42; Calculated for $C_{41}H_{44}F_9N_8O_{25}S_3EuNa_6.4H_2O.4CHCl_3$: C, 25.07; H, 2.62; N, 5.20. Found: C, 25.12; H, 2.89; N, 5.16; IR υ_{max} (cm^{-1}): 3389, 1595, 1503, 1395, 1253, 1229, 1169, 1084, 1033, 975, 911, 853, 809, 784, 762.

Complex Tb.69

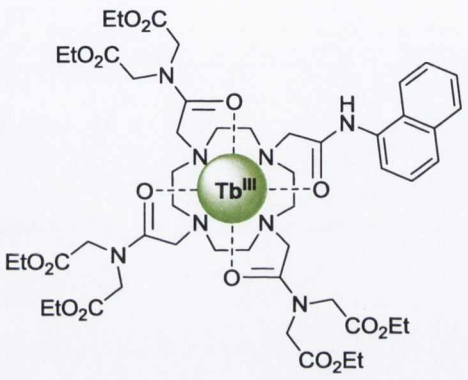

Complex **Tb.69** was synthesised according to **Procedure 2** using ligand **69** (0.160 g, 0.16 mmol) and $Tb(CF_3SO_3)_3$ (0.095 g, 0.16 mmol). The desired product was isolated as an orange solid (0.180 g, 70% yield). M.P: decomposed above 260 °C; HRMS (*m/z*, MALDI): Calculated for $C_{52}H_{74}F_6N_8O_{22}S_2{}^{159}Tb$ *m/z* = 1499.3517 $[M+2(CF_3SO_3)]^+$. Found *m/z* = 1499.3560; ^1H NMR (400 MHz, $CDCl_3$, δ_H): 55.25, 48.32, 47.64, 46.98, 43.06, 37.36, 31.89, 30.99, 24.84, 20.91, 19.36, 18.02, 17.70, 16.08, 15.84, 14.54, 12.64, 10.24, 8.57, 4.38, 3.61, 3.50, 3.15, 2.84, 2.16, 1.42, 1.32, 1.20, 0.91, 0.40, 0.12, -0.86, -3.87; IR υ_{max} (cm^{-1}): 2989, 1736, 1603, 1568, 1508, 1468, 1398, 1377, 1348, 1244, 1216, 1156, 1076, 1027, 998, 972, 911, 875, 837, 784, 757, 670, 573.

Complex Tb.69.Na

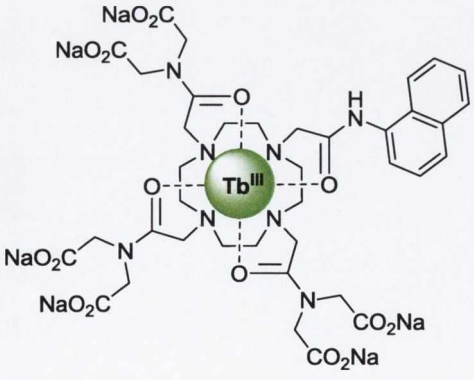

Complex **Tb.69.Na** was synthesised according to **Procedure 3** using complex **Tb.69** (0.100 g, 0.06 mmol) and NaOH (0.017 g, 0.43 mmol). The desired product was obtained as a pale yellow solid (0.075 g, 76% yield). M.P: decomposed above 280 °C; HRMS (*m/z*, MALDI): Calculated for $C_{38}H_{48}N_8O_{16}{}^{159}Tb$ *m/z* = 1031.2441 $[M\text{-}6Na+4H]^+$. Found *m/z* = 1031.2394; ^1H NMR (400 MHz, CD_3OD, δ_H): 61.24, 57.22, 54.39, 49.29, 30.33, 24.26, 18.99, 7.73, 7.47, 4.32, 4.00, 3.84, 3.68, 3.47, 3.25, 3.06, 2.84, 1.81, 1.19, -0.77, -1.18, -81.78, -88.93, -92.06; Calculated for $C_{41}H_{44}F_9N_8O_{25}S_3Tb.Na_6.2H_2O.CHCl_3$: C, 28.53; H, 2.79; N, 6.34. Found C, 28.15; H, 2.67;

N, 5.94; IR υ_{max} (cm^{-1}): 3399, 1596, 1503, 1393, 1252, 1169, 1083, 1031, 999, 975, 910, 853, 782, 762.

7.8 Experimental details for Chapter 4

1,4,7,10-Tetra-(N,N-bis(ethoxycarbonylmethyl)-1,4,7,10 tetraazacyclododecane (80)

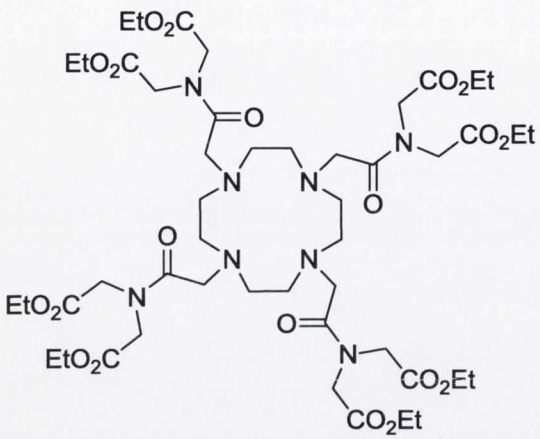

Cyclen (0.40 g, 2.32 mmol), K_2CO_3 (1.35 g, 9.74 mmol) and KI (0.17 g, 1.00 mmol) were placed in a 100 mL RBF along with 40 mL of freshly distilled CH_3CN. The resulting mixture was left stir at room temp. for 1 h, under an inert atmosphere. 73 (2.60 g, 9.74 mmol) dissolved in 10 mL of CH_3CN was added slowly and the solution was stirred at 85 °C, under argon, for 9 days. After reaction completion (monitored by TLC), the inorganic salts were filtered off and the solvent evaporated to dryness. The resulting residue was re-dissolved in CH_2Cl_2, and purified by alumina column chromatography using an elution gradient 100 to 95:5 CH_2Cl_2:CH_3OH. The desired product was obtained as a pale orange viscous oil (1.00 g, 40 % yield). HRMS (*m/z*, MALDI): Calculated for $C_{48}H_{80}N_8O_{20}Na$ *m/z* = 1111.5387 $[M+Na]^+$. Found *m/z* = 1111.5332; ^1H NMR (400 MHz, $CDCl_3$, δ_H): 4.24-4.05 (m, 32H, 1,4,7,10-$CH_2CON(C\underline{H}_2CO_2C\underline{H}_2CH_3)_2$), 3.65-2.10 (bm, 24H, cyclen-$C\underline{H}_2$ + 1,4,7,10-$NC\underline{H}_2CON$), 1.31-1.23 (m, 24H, $N(CH_2CO_2CH_2C\underline{H}_3)_2$); ^{13}C NMR (100 MHz, $CDCl_3$, δ_c): 171.88 (qt), 169.17 (qt), 168.68 (qt), 61.87 (CH_2), 61.07 (CH_2), 54.58 (CH_2) 49.20 (CH_2), 47.81 (CH_2), 14.19 (CH_3), 4.14 (CH_3); IR υ_{max} (cm^{-1}): 2981, 2828, 1735, 1659, 1467, 1409, 1373, 1352, 1301, 1280, 1170, 1106, 1021, 999, 971, 905, 868, 836, 804, 780, 736, 662.

1-butyl-1,4,7,10-tetraazacyclododecane (83)[169]

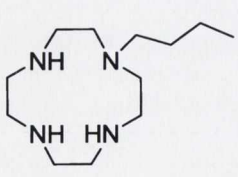

83 was synthesised according to **Procedure 1**, using 1-bromobutane (0.50 g, 3.65 mmol). The product was isolated as clear oil (0.66 g, 79% yield). HRMS (*m/z*, ES^+): Calculated for $C_{12}H_{29}N_4$ *m/z* = 229.2392 $[M+H]^+$. Found *m/z* = 229.2393; ^1H NMR (400 MHz, $CDCl_3$, δ_H): 3.0-2.5 (m, 16H, cyclen-$C\underline{H}_2$), 2.42 (m, 2H, 1-$NC\underline{H}_2CH_2CH_2CH_3$), 1.4-1.3 (m, 4H, 1-$NCH_2C\underline{H}_2C\underline{H}_2CH_3$), 0.92 (m, 3H, 1-$NCH_2CH_2CH_2C\underline{H}_3$); ^{13}C NMR (100 MHz, $CDCl_3$, δ_c): 53.86 (CH_2), 51.27 (CH_2), 46.73 (CH_2), 45.77 (CH_2), 44.85 (CH_2), 29.24 (CH_2), 20.27 (CH_2),

13.74 (CH_3); IR υ_{max} (cm^{-1}): 2928, 2871, 2802, 1460, 1352, 1274, 1201, 1115, 1084, 1038, 933, 751, 731.

1,4,7-Tris-(N,N-bis(ethoxycarbonylmethyl)-10-[butyl]-1,4,7,10 tetraazacyclododecane (81)

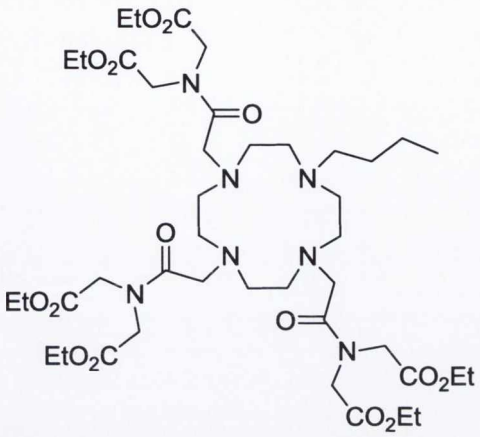

83 (0.52 g, 2.29 mmol) was dissolved along with K_2CO_3 (1.08 g, 7.79 mmol) and KI (1.29 g, 7.79 mmol) in 40 mL of freshly distilled CH_3CN. After stirring the solution at 0 °C for 10 min, **73** (1.95 g, 7.34 mmol) dissolved in 10 mL of CH_3CN was added dropwise to the solution over 30 min *via* syringe. The resulting solution was stirred at 85 °C for 4 days under argon. After reaction completion (monitored by mass spec), the solution was cooled to room temp., the inorganic salts filtered off and the solvent removed under reduced pressure. The resulting dark orange residue was re-dissolved in CH_2Cl_2 and purified by alumina column chromatography using an elution gradient 100 to 80:20 CH_2Cl_2:CH_3OH. The desired product was obtained as a pale yellow viscous oil (0.26 g, 29% yield). HRMS (*m/z*, ES^+): Calculated for $C_{42}H_{74}N_7O_{15}$ *m/z* = 916.5243 $[M+H]^+$. Found *m/z* = 916.5231; ^1H NMR (400 MHz, $CDCl_3$, δ_H): 4.3-4.0 (m, 24H, 4,7,10-$NCH_2CON(C\underline{H}_2CO_2C\underline{H}_2CH_3)_2$), 3.4-2.1 (bm, 24H, cyclen-$C\underline{H}_2$ + 4,7,10-$NC\underline{H}_2CON(CH_2CO_2CH_2CH_3)_2$ + 1-$NC\underline{H}_2CH_2CH_2CH_3$), 1.4-1.1 (m, 22H, 1,4,7-$NCH_2CON(CH_2CO_2CH_2C\underline{H}_3)_2$ + 1-$NCH_2C\underline{H}_2C\underline{H}_2CH_3$), 0.83 (m, 3H, 1-$NCH_2CH_2CH_2C\underline{H}_3$); ^{13}C NMR (150 MHz, $CDCl_3$, δ_c): 172.42 (qt), 171.94 (qt), 168.91 (qt), 168.79 (qt), 168.50 (qt), 61.89 (CH_2), 61.84 (CH_2), 61.15 (CH_2), 61.06 (CH_2), 54.95 (CH_2), 54.65 (CH_2), 53.90 (CH_2), 50.10 (CH_2), 49.74 (CH_2), 49.46 (CH_2), 48.59 (CH_2), 48.43 (CH_2), 48.11 (CH_2), 27.81 (CH_2), 20.62 (CH_2), 14.08 (CH_3), 14.05 (CH_3), 14.03 (CH_3), 13.80 (CH_3); IR υ_{max} (cm^{-1}): 2979, 2827, 1738, 1656, 1469, 1403, 1373, 1272, 1188, 1098, 1024, 972, 779,731.

Complex Eu.80

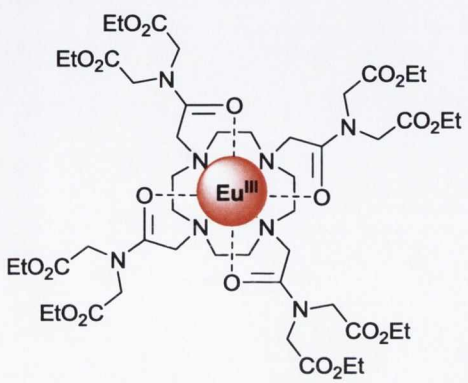

Complex **Eu.80** was synthesised according to **Procedure 2** using ligand **80** (0.063 g, 0.058 mmol) and $Eu(CF_3SO_3)_3$ (0.035 g, 0.058 mmol). A fine orange solid was obtained (0.083 g 84% yield). M.P: decomposed above 260 °C; HRMS (*m/z*, MALDI):

Calculated for $C_{50}H_{80}F_6N_8O_{26}S_2{}^{151}Eu$ *m/z* = 1539.3742 $[M+2(CF_3SO_3)]^+$. Found *m/z* = 1539.3702; ^1H NMR (400 MHz, CD_3OD, δ_H): 27.55, 6.17, 5.51, 4.92, 4.33, 4.2, 4.03, 3.74, 3.33, 3.00, 2.87, 2.33, 2.24, 1.53, 1.42, 1.31, 1.12, 0.65, -1.85, -5.46, -8.44, -10.07, -13.84; Calculated for $C_{51}H_{80}F_9N_8O_{29}S_3Eu.H_2O.2CHCl_3$: C, 32.73; H, 4.35; N, 5.76. Found C, 32.95; H, 4.14; N, 6.08; IR υ_{max} (cm^{-1}): 2981, 1738, 1603, 1504, 1473, 1377, 1249, 1213, 1156, 1084, 1028, 972, 910, 874, 837, 757, 670.

Complex Eu.80.Na

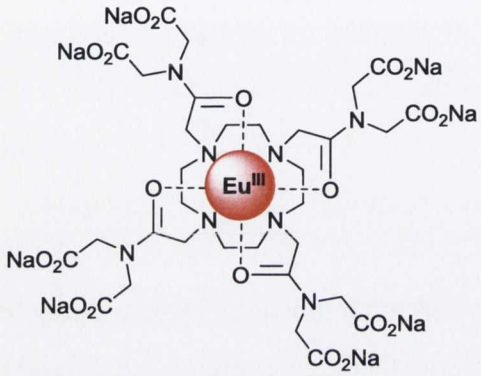

Complex **Eu.80.Na** was synthesised according to **Procedure 3** using complex **Eu.80** (0.058 g, 0.03 mmol) and NaOH (0.012 g, 0.30 mmol). The desired product was obtained as a pale yellow solid. (0.045 g, 81% yield). M.P: decomposed above 280 °C; HRMS (*m/z*, MALDI): Calculated for $C_{32}H_{46}N_8O_{20}{}^{151}Eu$ *m/z* = 1015.2045 $[M-8Na+6H]^+$. Found *m/z* = 1015.2091; ^1H NMR (400 MHz, CD_3OD, δ_H): 35.46, 33.71, 32.90, 32.02, 31.29, 30.80, 29.66, 28.61, 8.32, 7.93, 7.20, 4.14, 3.98, 3.69, 3.35, 2.88, 2.73, 2.64, 2.24, 1.83, 1.12, 0.92, 0.50, 0.12, -0.50, -0.86, -1.37, -3.44, -4.31, -5.36, -6.14, -6.47, -7.36, -8.10, -9.38, -10.02, -10.76, -12.37, -13.59, -14.45, -14.86, -15.95, -16.39, -17.31; Calculated for $C_{35}H_{40}F_9N_8O_{29}S_3Eu.3H_2O.2CHCl_3$: C, 22.99; H, 2.50; N, 5.79. Found C, 22.87; H, 2.31; N, 5.34; IR υ_{max} (cm^{-1}): 3402, 1595, 1394, 1254, 1167, 1032, 1084, 999, 977, 910, 852, 762, 676.

Complex Gd.80

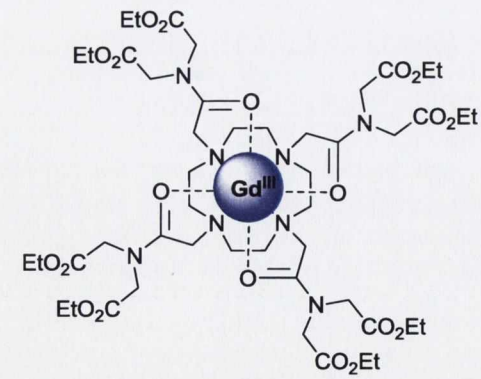

Complex **Gd.80** was synthesised according to **Procedure 2** using ligand **80** (0.092 g, 0.08 mmol) and $Gd(CF_3SO_3)_3$ (0.051 g, 0.08 mmol). The desired product was obtained as a fine orange solid. (0.137 g, 96% yield). M.P: decomposed above 260 °C; HRMS (*m/z*, MALDI): Calculated for $C_{50}H_{80}F_6N_8O_{26}S_2Gd$ *m/z* = 1544.3779 $[M+2(CF_3SO_3)]^+$. Found *m/z* = 1544.3822; Calculated for $C_{35}H_{80}F_9N_8O_{29}S_3{}^{157}Gd.2H_2O.2CHCl_3$: C, 32.34; H, 4.40; N, 5.69. Found C, 32.04; H, 4.09; N, 5.85; IR υ_{max} (cm^{-1}): 2988, 1737, 1603, 1507, 1468, 1417, 1377, 1377, 1352, 1250, 1212, 1155, 1074, 1050, 998, 974, 911, 875, 837, 814, 757, 670.

Complex Gd.80.Na

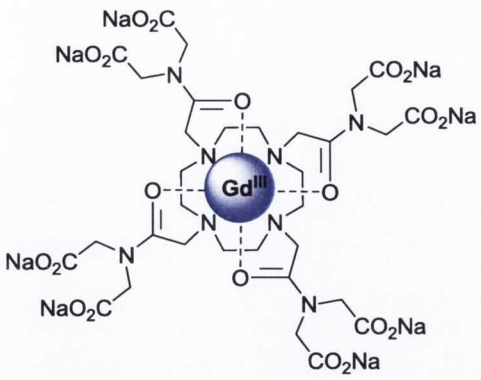

Complex **Gd.80.Na** was synthesised according to **Procedure 3** using complex **Gd.80** (0.100 g, 0.06 mmol) and NaOH (0.021 g, 0.53 mmol). The desired product was obtained as a fine pale yellow crystalline solid. (0.070 g, 84% yield). M.P: decomposed above 280 °C; HRMS (*m/z*, MALDI): Calculated for $C_{32}H_{46}N_8O_{20}Gd$ *m/z* = 1020.2078 $[M\text{-}8Na+6H]^+$. Found *m/z* = 1020.2095; Calculated for $C_{35}H_{40}F_9N_8O_{29}S_3{}^{157}Gd.2H_2O.3CHCl_3$: C, 22.37; H, 2.32; N, 5.49. Found C, 21.97; H, 2.31; N, 5.16; IR υ_{max} (cm^{-1}): 2987, 1590, 1397, 1254, 1229, 1168, 1034, 1168, 1087, 1034, 1000, 978, 910, 854, 763, 718, 676.

Complex Gd.69

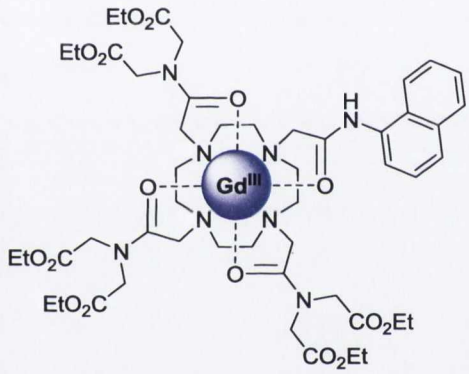

Complex **Gd.69** was synthesised according to **Procedure 2** using ligand **69** (0.044 g, 0.04 mmol) and $Gd(CF_3SO_3)_3$ (0.026 g, 0.04 mmol). The desired product was obtained as a dark orange solid. (0.062 g, 88% yield). M.P: decomposed above 290 °C; HRMS (*m/z*, MALDI): Calculated for $C_{52}H_{74}F_6N_8O_{22}S_2Gd$ *m/z* = 1498.3514 $[M+2(CF_3SO_3)]^+$. Found *m/z* = 1498.3483; Calculated for $C_{53}H_{74}F_9N_8O_{25}S_3{}^{157}Gd.H_2O$: C, 38.22; H, 4.59; N, 6.73. Found C, 37.76; H, 4.10; N, 6.56; IR υ_{max} (cm^{-1}): 2988, 1737, 1603, 1508, 1467, 1398, 1376, 1348, 1244, 1215, 1155, 1076, 1027, 971, 910, 874, 837, 783, 756, 670.

Complex Gd.69.Na

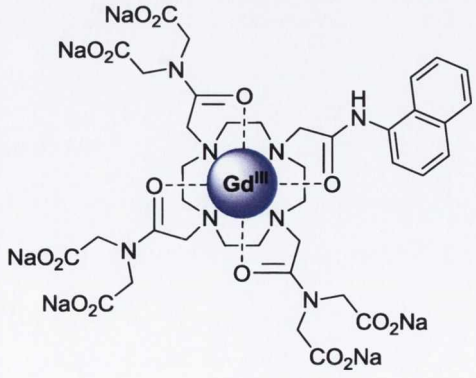

Complex **Gd.69.Na** was synthesised according to **Procedure 3** using complex **Gd.69** (0.058 g, 0.04 mmol) and NaOH (0.010 g, 0.25 mmol) The desired product was obtained as a pale orange solid. (0.042 g, 74% yield). M.P: decomposed above 290 °C; HRMS (*m/z*, MALDI): Calculated for $C_{38}H_{48}N_8O_{16}{}^{157}Gd$ *m/z* = 1030.2439 $[M\text{-}6Na+4H]^+$. Found *m/z* = 1030.2428; Calculated for $C_{41}H_{44}F_9N_8O_{25}S_3Gd.Na_6.H_2O.CH_3Cl$: C, 28.85; H, 2.71; N, 6.41. Found C, 28.83; H, 2.69;

N, 6.18; IR υ_{max} (cm^{-1}): 2987, 1598, 1396, 1252, 1228, 1165, 1084, 1033, 975, 910, 855, 783, 762, 723, 676.

Complex Gd.81

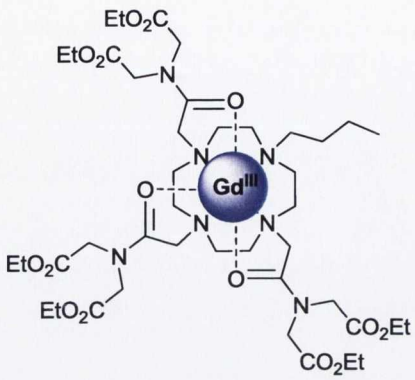

Complex **Gd.81** was synthesised according to **Procedure 2** using ligand **81** (0.166 g, 0.18 mmol) and $Gd(CF_3SO_3)_3$ (0.109 g, 0.18 mmol). The desired product was obtained as a fine orange solid. (0.260 g, 94% yield). M.P: decomposed above 250 °C; HRMS (*m/z*, MALDI): Calculated for $C_{44}H_{73}N_7O_{21}F_6S_2{}^{157}Gd$ *m/z* = 1371.3453 $[M+2(CF_3SO_3)]^+$. Found *m/z* = 1371.3442; Calculated for $C_{46}H_{76}F_9N_7O_{24}S_3Gd.H_2O.2CHCl_3$: C, 32.12; H, 4.50; N, 5.47. Found C, 32.16; H, 4.13; N, 5.60; IR υ_{max} (cm^{-1}): 3463, 2964, 1739, 1603, 1507, 1469, 1376, 1255, 1211, 1159, 1073, 975, 911, 875, 816, 757, 670.

Complex Gd.81.Na

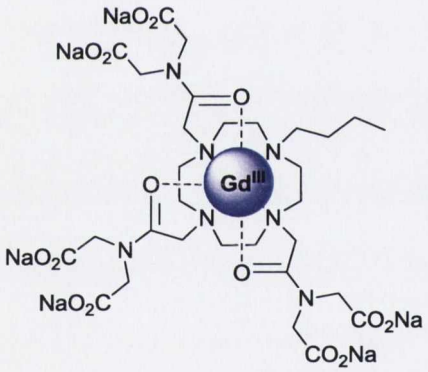

Complex **Gd.81.Na** was synthesised according to **Procedure 3** using complex **Gd.81** (0.226 g, 0.15 mmol) and NaOH (0.037 g, 0.92 mmol) The desired product was obtained as a pale orange solid. (0.140 g, 63% yield). M.P: decomposed above 260 °C; HRMS (*m/z*, MALDI): Calculated for $C_{30}H_{47}N_7O_{15}{}^{157}Gd$ *m/z* = 903.2379 $[M-6Na+4H]^+$. Found *m/z* = 903.2382; Calculated for $C_{33}H_{43}F_9N_7O_{24}S_3GdNa_6.2H_2O.2CHCl_3$: C, 23.90; H, 2.81; N, 5.57. Found C, 23.84; H, 2.76; N, 5.41; IR υ_{max} (cm^{-1}): 3450, 2954, 1591, 1399, 1253, 1167, 1035, 909, 855, 718, 676.

Complex Eu.81

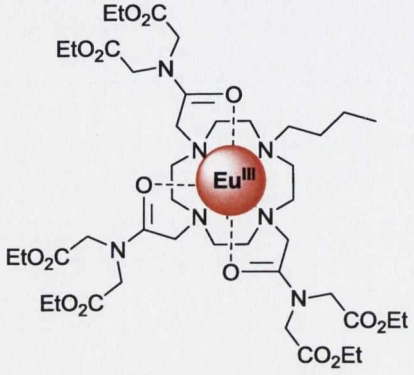

Complex **Eu.81** was synthesised according to **Procedure 2** using ligand **81** (0.049 g, 0.05 mmol) and $Eu(CF_3SO_3)_3$ (0.032 g, 0.05 mmol). The desired product was obtained as a pale orange solid. (0.060 g, 79% yield). M.P: decomposed above 260 °C; HRMS (*m/z*, MALDI): Calculated for $C_{44}H_{73}N_7O_{21}F_6S_2{}^{151}Eu$ *m/z* = 1366.3418 $[M+2(CF_3SO_3)]^+$. Found *m/z* = 1366.3468; ^1H NMR (400

MHz, CD_3OD, δ_H): 20.92, 19.70, 18.39, 4.92, 4.28, 3.61, 3.33, 3.00, 2.79, 2.23, 1.42, 1.31, 1.19, 0.99, 0.15, -0.86, -5.81, -6.59, -8.42, -9.64, -10.33, -11.03, -11.99, -12.77, -14.60, -19.30; IR υ_{max} (cm^{-1}): 2981, 1738, 1603, 1504, 1473, 1377, 1250, 1213, 1085, 972, 910, 874, 837, 757, 670.

Complex Eu.81.Na

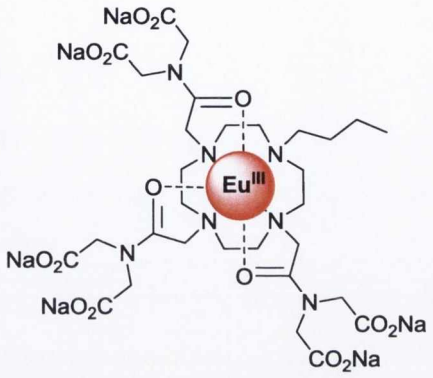

Complex **Eu.81.Na** was synthesised according to **Procedure 3** using complex **Eu.81** (0.033 g, 0.02 mmol) and NaOH (0.006 g, 0.14 mmol). The desired product was obtained as a pale yellow solid (0.029 g, 89% yield). M.P: decomposed above 260 °C; HRMS (*m/z*, MALDI): Calculated for $C_{30}H_{47}N_7O_{15}{}^{151}Eu$ *m/z* = 898.2346 $[M-6Na+4H]^+$. Found *m/z* = 898.2313; ^1H NMR (400 MHz, D_2O, δ_H): 17.14, 11.62, 5.52, 5.12, 5.07, 5.02, 4.92, 4.87, 4.82, 4.77, 4.72, 4.14, 3.99, 3.68, 3.49, 3.33, 3.19, 3.15, 3.02, 2.89, 2.65, 2.46, 2.70, 1.87, 1.32, 1.21, 0.99, 0.12, -3.03, -4.35, -9.32, -10.01, -12.09, -18.02, -22.01; IR υ_{max} (cm^{-1}): 2830, 1591, 1407, 1257, 1230, 1168, 1100, 1064, 1037, 888, 907.

Complex Gd.58

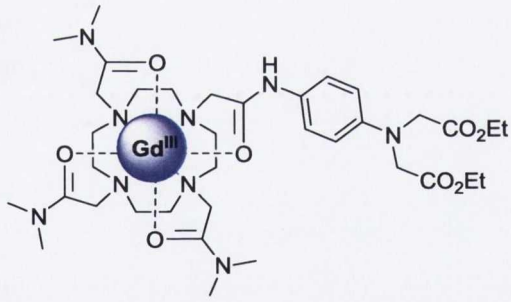

Complex **Gd.58** was synthesised according to **Procedure 2** using ligand **58** (0.075 g, 0.10 mmol) and $Gd(CF_3SO_3)_3$ (0.060 g, 0.10 mmol). The desired product was obtained as a pale yellow solid. (0.125 g, 93% yield). M.P: decomposed above 280 °C; HRMS (*m/z*, MALDI) Calculated for $C_{38}H_{61}F_6N_9O_{14}S_2{}^{157}Gd$ *m/z* = 1203.2930 $[M+2(CF_3SO_3)]^+$. Found *m/z* = 1203.2941; IR υ_{max} (cm^{-1}): 2988, 1737, 1616, 1520, 1459, 1247, 1156, 1080, 1050, 958, 910, 823.

Complex Gd.58.Na

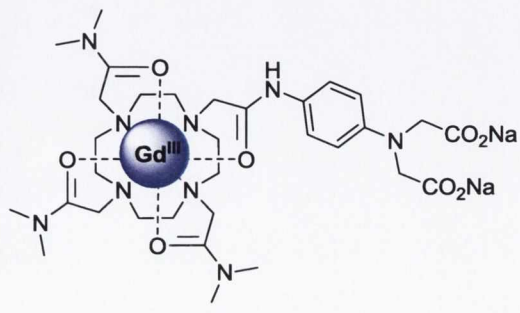

Complex **Gd.58.Na** was synthesised according to Procedure **3** using complex **Gd.58** (0.100 g, 0.07 mmol) and NaOH (0.006 g, 0.16 mmol). The desired product was obtained as pale brown solid. (0.080 g, 81% yield). M.P: decomposed above 280

°C; HRMS (*m/z*, MALDI) Calculated for $C_{32}H_{51}F_9N_9O_8{}^{157}Gd$ *m/z* = 847.3109 $[M-2Na]^+$. Found *m/z* = 847.3138; IR υ_{max} (cm^{-1}): 2986, 1603, 1516, 1458, 1235, 1227, 1160, 1082, 1030, 958, 910, 823, 761, 704.

7.9 Experimental details for Chapter 5

2-Chloro-*N*-(4-nitro-phenyl)-acetamide (112)[21]

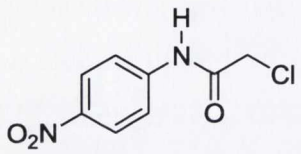

A solution of 4-nitro-phenylamine (0.90 g, 6.51 mmol) and Et_3N (1.98 g, 19.53 mmol) in freshly distilled CH_2Cl_2 (50 mL) was cooled below 0 °C in an acetone/ice bath. A solution of chloroacetyl chloride (0.75 g, 6.51 mmol) in CH_2Cl_2 (20 mL) was added dropwise over a 30 min period. After complete addition, the reaction mixture was allowed to reach room temp. and stirred under argon for 48 h. The resulting brown solution was washed with 0.1 M HCl (4 x 50 mL) and H_2O (2 x 25 mL). The organic layer was dried over $MgSO_4$, filtered and the solvent removed under reduced pressure to yield a brown solid. Recrystallisation from EtOH yielded brown crystals (0.54 g, 39% yield). M.P: 184-185 °C; HRMS (*m/z*, ES^-): Calculated for $C_8H_6N_2O_3Cl$ *m/z* = 213.0067 $[M-H]^-$. Found *m/z* = 213.0063; ^1H NMR (400 MHz, d_6-$(CD_3)_2CO$, δ_H): 8.53 (bs, 1H, N-H), 8.28 (d, 2H, *J* = 9 Hz, Ar-H), 7.80 (d, 2H, *J* = 9 Hz, Ar-H), 4.27 (s, 1H, CH_2); ^{13}C NMR (100 MHz, d_6-$(CD_3)_2CO$, δ_c): 165. 61 (qt), 144.59 (qt), 142.59 (qt), 125.09 (CH), 119.08 (CH), 43.60 (CH_2); IR υ_{max} (cm^{-1}): 3228, 3163, 3105, 2941, 1685, 1622, 1597, 1567, 1503, 1405, 1334, 1255, 1198, 1172, 1112, 968, 923, 871, 850, 772, 748, 718.

1-{4-(nitro-phenylcarbamoyl-methyl)}-1,4,7,10-tetraazacyclododecane (113)[169]

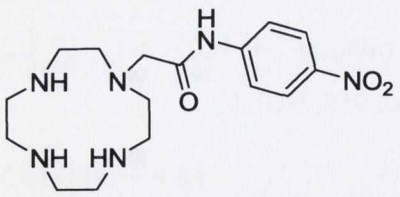

113 was synthesised according to **Procedure 1**, using the alkylating pendant group 112 (0.30 g, 1.40 mmol). The product was isolated as an orange viscous oil (0.34 g, 69% yield). HRMS (*m/z*, ES^+): Calculated for $C_{16}H_{26}N_6O_3Na$ *m/z* = 373.1964 $[M+Na]^+$. Found *m/z* = 373.1962; ^1H NMR (400 MHz, $CDCl_3$, δ_H): 10.80 (bs, 1H, N-H) 8.21 (d, 2H, *J* = 8 Hz, Ar-H), 7.97 (d, 2H, *J* = 8 Hz, Ar-H), 3.35 (s, 1H, 1-CH_2CONH), 2.87 (bs, 4H, cyclen-CH_2), 2.77 (bs, 12H, cyclen-CH_2), 2.21 (bs, 3H, N-H); ^{13}C NMR (100 MHz, $CDCl_3$, δ_c): 170.73 (qt), 143.92 (qt), 142.69 (qt), 124.55 (CH), 118.54 (CH), 59.10 (CH_2), 53.39 (CH_2), 46.92 (CH_2), 46.85 (CH_2), 45.38 (CH_2); IR υ_{max} (cm^{-1}): 3183, 2892, 2830, 1691, 1597, 1532, 1504, 1452, 1408, 1329, 1300, 1257, 1215, 1172, 1109, 1074, 941, 869, 851, 799, 750, 707.

1,4,7-Tris(dimethylcarbamoylmethyl)-10-[(4-nitro-phenylcarbamoyl)-methyl]-1,4,7,10-tetraaza-cyclododec-1-yl}-acetamide (114)[21]

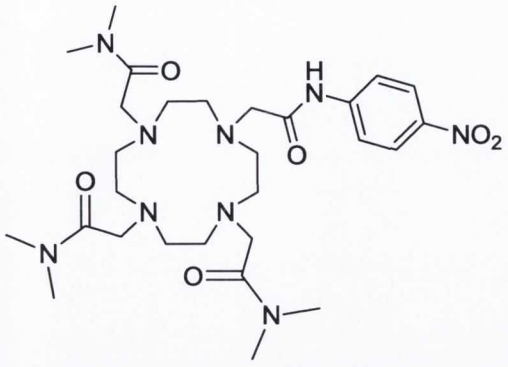

113 (0.21 g 0.61 mmol) along with 40 mL of CH_3CN was placed in a 100 mL RBF. KI (0.36 g 2.14 mmol) and K_2CO_3 (0.30 g 2.14 mmol) were added to the solution, which was then placed in an ice/acetone bath and allowed to cool. A solution of 2 chloro-*N*,*N*-dimethyl-acetamide (0.23 g 1.88 mmol) was added quickly and the solution was stirred at room temp. for 15 min. The reaction mixture was left stir at 85 °C under argon for 5 days. The resulting orange solution was filtered through celite and the solvent removed under reduced pressure. The orange residue was dissolved in CH_2Cl_2 and purified by alumina column chromatography using a gradient elution 100 to 80:20 CH_2Cl_2:CH_3OH. The desired product, after drying under vacuum, was obtained as an orange crystalline solid (0.34 g, 92% yield). M.P: 89-91 °C; HRMS (*m/z*, ES^+): Calculated for $C_{28}H_{47}N_9O_6Na$ *m/z* = 628.3547 $[M+Na]^+$. Found *m/z* = 628.3521; ^1H NMR (400 MHz, $CDCl_3$, δ_H): 10.56 (bs, 1H, N-H), 8.22 (d, 2H, *J* = 9 Hz, Ar-H), 8.14 (d, 2H, *J* = 9 Hz, Ar-H), 4.0 - 1.8 (bm, 42H, cyclen-CH_2 + 4,7,10-$CH_2CON(CH_3)_2$ + 1-CH_2CONH); ^{13}C NMR (100 MHz, $CDCl_3$, δ_c): 171.36 (qt), 169.81 (qt), 169.73 (qt), 144.60 (qt), 142.33 (qt), 123.94 (CH), 119.08 (CH), 58.11 (CH_2), 55.22 (CH_2), 55.06 (CH_2), 53.13 (CH_2), 51.77 (CH_2), 36.08 (CH_3), 36.04 (CH_3), 35.23 (CH_3), 35.15 (CH_3); IR υ_{max} (cm^{-1}): 3430, 2813, 1695, 1639, 1594, 1551, 1504, 1449, 1401, 1329, 1300, 1257, 1173, 1099, 1063, 1006, 918, 856, 826, 771, 753, 724.

1,4,7-Tris(dimethylcarbamoylmethyl)-10-[(4-amino-phenylcarbamoyl)-methyl]-1,4,7,10-tetraaza-cyclododec-1-yl}-acetamide (115)

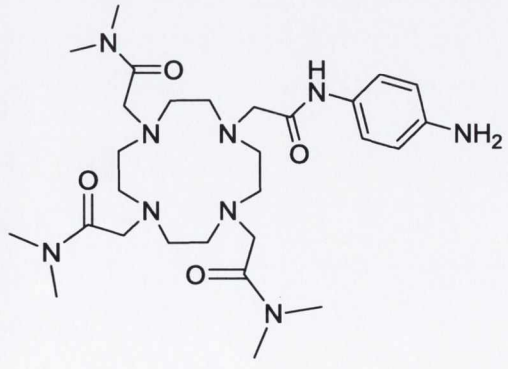

To a stirring solution of **114** (0.33 g, 0.55 mmol) and 10% Pd/C catalyst in EtOH (5 mL), a solution of hydrazine monohydrate (0.22 g, 4.40 mmol) was added dropwise. The resulting reaction mixture was microwave irradiated at 80 °C for 2 h. Upon reaction completion, the mixture was filtered through celite and the solvent removed under vacuum to yield the product as a brown oil. The brown residue was purified by alumina column chromatography using a gradient elution 100 to 80:20 CH_2Cl_2:CH_3OH, resulting in the desired product being obtained as an orange viscous oil (0.21 g, 66% yield). HRMS (*m/z*,

ES$^+$): Calculated for $C_{28}H_{50}N_9O_4$ *m/z* = 576.3986 $[M+H]^+$. Found *m/z* = 576.3965; ^{1}H NMR (400 MHz, $CDCl_3$, δ_H): 9.55 (bs, 1H, N-H), 7.57 (d, 2H, *J* = 8 Hz, Ar-H), 6.56 (d, 2H, *J* = 8 Hz, Ar-H), 3.7-2.4 (bm, 42H, cyclen-CH_2 + 4,7,10-$CH_2CON(CH_3)_2$ + 1-CH_2CONH); ^{13}C NMR (100 MHz, $CDCl_3$, δ_c): 170.57 (qt), 170.40 (qt), 169.16 (qt), 142.47 (qt), 129.71 (qt), 120.69 (CH), 114.49 (CH), 57.99 (CH_2), 54.60 (CH_2), 54.40 (CH_2), 52.42 (CH_2), 50.43 (CH_2), 35.97 (CH_3), 35.81 (CH_3), 35.27 (CH_3), 35.16 (CH_3); IR υ_{max} (cm^{-1}): 3236, 2820, 1637, 1514, 1451, 1401, 1345,1296, 1261, 1158, 1101, 1062, 1005, 951, 902, 828, 725.

2,2',2''-(10-(2-(4-(2,5-dioxo-2,5-dihydro-1H-pyrrol-1-yl)phenylamino)-2-oxoethyl)-1,4,7,10-tetraazacyclododecane-1,4,7-triyl)tris(N,N-dimethylacetamide) (110)

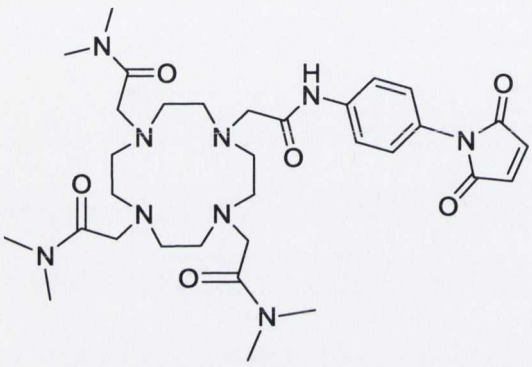

Maleic anhydride (0.012 g, 0.12 mmol) was added and stirred in 10 mL of freshly distilled CH_3CN. Once all the maleic anhydride had dissolved, **115** (0.067 g, 0.12 mmol) was added slowly along with 5 mL of CH_3CN to the solution using a pressure equalised dropping funnel. The resulting yellow solution was left reflux at 85 °C for 24 h. Upon reaction completion, the solvent was reduced to 80% of its volume and any excess maleic anhydride removed by precipitation out of dry diethyl ether (50 mL) to give an orange viscous oil. The crude product (0.060 g, 0.09 mmol) was re-dissolved in 5 mL acetic anhydride and NaOAc (0.016 g, 0.19 mmol) was added. The reaction mixture was left stir at 100 °C for 2 h, which upon cooling to room temp., was poured over a large volume of ice to yield a pale orange oil. The resulting aqueous solution was extracted with CH_2Cl_2 (2 x 20 mL). The combined organic layers were dried over $MgSO_4$, filtered and the solvent removed under reduced pressure to yield **110**, as an orange oil (0.021 g, 27%). HRMS (*m/z*, ES$^+$): Calculated for $C_{32}H_{50}N_9O_6$ *m/z* = 656.3884 $[M+H]^+$. Found *m/z* = 656.3891; ^{1}H NMR (600 MHz, $CDCl_3$, δ_H): 10.34 (s, 1H, N-H), 7.97 (d, 2H, *J* = 8.6 Hz, Ar-H), 7.15 (d, 2H, *J* = 8.6 Hz, Ar-H), 6.81 (s, 2H, CH), 3.5 – 2.2 (bm, 42H, cyclen-CH_2 + 4,7,10-$CH_2CON(CH_3)_2$ + 1-CH_2CONH); ^{13}C NMR (150 MHz, $CDCl_3$, δ_c): 170.90 (qt), 170.72 (qt), 169.60 (qt), 138.87 (qt), 134.16 (CH), 126.23 (CH), 126.13 (qt), 120.27 (CH), 57.93 (CH_2), 54.55 (CH_2), 52.46 (CH_2), 52.43 (CH_2), 50.60 (CH_2), 36.28 (CH_3), 36.11 (CH_3), 35.70 (CH_3), 35.54 (CH_3); IR υ_{max} (cm^{-1}): 3010, 2818, 1713, 1639, 1514, 1456, 1397, 1346, 1315, 1256, 1148, 1102, 1005, 951, 901, 827, 800, 689.

Complex Tb.110

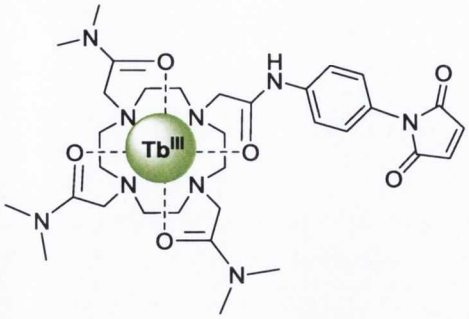

Complex **Tb.110** was synthesised according to **Procedure 2** using ligand **110** (0.018 g, 0.03 mmol) and $Tb(CF_3SO_3)_3$ (0.017 g, 0.03 mmol). The desired product was obtained as an orange solid (0.033 g, 93% yield). M.P: decomposed above 270 °C; HRMS (*m/z*, MALDI): Calculated for $C_{34}H_{49}N_9O_{12}F_6S_2{}^{159}Tb$ *m/z* = 1112.2100 $[M+2(CF_3SO_3)]^+$. Found *m/z* = 1112.2052; ^1H NMR (400 MHz, $CDCl_3$, δ_H): 71.92, 71.37, 70.43, 49.80, 48.07, 41.75, 41.12, 40.62, 39.49, 15.22, 14.01, 12.09, 7.89, 7.56, 7.32, 6.93, 5.98, 2.93, 2.13, 1.97, 1.36, -63.49, -65.73, -68.78,-83.70, -85.93, -89.92, -92.74, -107.42, -108.83, -111.07; IR υ_{max} (cm^{-1}): 3453, 1715, 1619, 1564, 1515, 1460, 1403, 1245, 1225, 1156, 1080, 1028, 957, 910, 824, 690.

Chapter 8

References

References

1. Steed, J. W.; Atwood, J. L., *Supramolecular Chemistry*. Wiley; Chichester: 2000.
2. Dodzuick, H., *Introduction to Supramolecular Chemistry*. Springer: 2002.
3. Freeman, R.; Li, Y.; Tel-Vered, R.; Sharon, E.; Elbaz, J.; Willner, I. *Analyst* **2009**, *134*, 653.
4. Petitjean, A.; Puntoriero, F.; Campagna, S.; Juris, A.; Lehn, J. M. *Eur. J. Inorg. Chem.* **2006**, 3878.
5. Balzani, V.; Bergamini, G.; Marchioni, F.; Ceroni, P. *Coord. Chem. Rev.* **2006**, *250*, 1254.
6. Pease, A. R.; Jeppesen, J. O.; Stoddart, J. F.; Luo, Y.; Collier, C. P.; Heath, J. R. *Acc. Chem. Res.* **2001**, *34*, 433.
7. Ariga, K.; Ji, Q.; Hill, J. P.; Kawazoe, N.; Chen, G. *Expert Opin. Ther.* **2009**, *9*, 307.
8. Pedersen, C. J. *J. Am. Chem. Soc.* **1967**, *89*, 7017.
9. Kyba, E. P.; Helgeson, R. C.; Madan, K.; Gokel, G. W.; Tarnowski, T. L.; Moore, S. S.; Cram, D. J. *J. Am. Chem. Soc.* **1977**, *99*, 2564.
10. Lehn, J. M. *Science* **1985**, *227*, 849.
11. Lehn, J. M. *Angew. Chem. Int. Ed.* **1988**, *27*, 89.
12. Lo, P. K.; Wong, M. S. *Sensors* **2008**, *8*, 5313.
13. Sutherland, I. O. *Pure Appl. Chem.* **1990**, *62*, 499.
14. Lehn, J. M.; Roth, C. O. *Helv. Chim. Acta.* **1991**, *74*, 572.
15. Gunnlaugsson, T.; Leonard, J. P. *Chem. Commun.* **2005**, 3114.
16. Gunnlaugsson, T.; Leonard, J. P. *Dalton Trans.* **2005**, 3204.
17. Gunnlaugsson, T.; Harte, A. J. *Org. Biomol. Chem.* **2006**, *4*, 1572.
18. Gunnlaugsson, T.; Leonard, J. P.; Senechal, K.; Harte, A. J. *J. Am. Chem. Soc.* **2003**, *125*, 12062.
19. Stomeo, F.; Lincheneau, C.; Leonard, J. P.; O'Brien, J. E.; Peacock, R. D.; McCoy, C. P.; Gunnlaugsson, T. *J. Am. Chem. Soc.* **2009**, *131*, 9636.
20. Czarnik, A. W., *Fluorescent Chemosensors of Ion and Molecular Recognition*. ACS: Washington DC, 1993.
21. dos Santos, C. M. G.; Gunnlaugsson, T. *Dalton Trans.* **2009**, 4712.
22. Duke, R. M.; Veale, E. B.; Pfeffer, F. M.; Kruger, P. E.; Gunnlaugsson, T. *Chem. Soc. Rev.* **2010**, *39*, 3936.
23. Caltagirone, C.; Gale, P. A. *Chem. Soc. Rev.* **2009**, *38*, 520.
24. Lavigne, J. J.; Anslyn, E. V. *Angew. Chem. Int. Ed.* **2001**, *40*, 3118.
25. Rurack, K.; Resch-Genger, U. *Chem. Soc. Rev.* **2002**, *31*, 116.
26. Smith, R. V.; Nessen, M. A. *J. Pharm. Sci.* **1971**, *60*, 907.
27. Bell, W. T.; Hext, N. M. *Chem. Soc. Rev.* **2004**, *33*, 589.
28. deSilva, A. P.; Gunaratne, H. Q. N.; Gunnlaugsson, T.; Huxley, A. J. M.; McCoy, C. P.; Rademacher, J. T.; Rice, T. E. *Chem. Rev.* **1997**, *97*, 1515.
29. Mancin, F.; Rampazzo, E.; Tecilla, P.; Tonellato, U. *Chem. Eur. J.* **2006**, *12*, 1844.
30. Callen, J. F.; De Silva, A. P.; Magri, D. C. *Tetrahedron* **2005**, *61*, 8551.
31. Valeur, B.; Leary, L. *Coord. Chem. Rev.* **2000**, *205*, 3.
32. Parkesh, R.; Veale, E. B.; Gunnlaugsson, T., *Fluorescent detection principles and strategies*. Wang, B.; Anslyn, E. V., Eds. John Wiley and Sons: 2010.
33. Tsukanav, A. V.; Dubonosov, A. D.; Bren, V. A.; Minkin, V. I. *Chem. Heterocyc. Compd.* **2008**, *44*.
34. Leonard, J. P.; Nolan, C. B.; Stomeo, F.; Gunnlaugsson, T., *Photochemistry and photophysics of coordination compounds: Lanthanides*. 2007, 281, 1.
35. Caravan, P. *Chem. Soc. Rev.* **2006**, *35*, 512.
36. Merbach, A. E.; Toth, E., *The Chemsitry of Contrast Agents in Medical Magnetic Resonance Imaging*. John Wiley & Sons Ltd: 2001.

37. Bunzli, J. C. G.; Piguet, C. *Chem. Soc. Rev.* **2005**, *34*, 1048.
38. Flockhart, B. D. *Crit. Rev. Anal. Chem.* **1976**, *6*, 69.
39. Caravan, P.; Ellison, J. J.; McMurry, T. J.; Lauffer, R. B. *Chem. Rev.* **1999**, *99*, 2293.
40. http://www.biotek.com/assets/tech_resources/125/synhtfig7.gif (October 2010)
41. Parker, D. *Coordin. Chem. Rev.* **2000**, *205*, 109.
42. Parker, D.; Beeby, A.; Williams, J. A. G. *J. Chem. Soc., Perkin Trans. 2* **1996**, 1565.
43. Wolbers, M. P.; Veggel, F. C.; Snellink-Ruel, B. H. *J. Chem Soc., Perkin Trans. 2* **1998**, 2141.
44. Pope, S. J. A.; Coe, B. J.; Faulkner, S.; Bichenkoa, E. V.; Yu, X.; Douglas, K. T. *J. Am. Chem. Soc.* **2004**, *126*, 9490.
45. Senechal-David, K.; Pope, S. J. A.; Quinn, S.; Faulkner, S.; Gunnlaugsson, T. *Inorg. Chem.* **2006**, *45*, 10040.
46. Nonat, A. M.; Quinn, S. J.; Gunnlaugsson, T. *Inorg. Chem.* **2009**, *48*, 4646.
47. Nonat, A. M.; Allain, C.; Faulkner, S.; Gunnlaugsson, T. *Inorg. Chem.* **2010**, *49*, 8449.
48. Dexter, D. L. *J. Chem. Phys.* **1953**, *21*, 836.
49. Föster, T. *Ann. Phys.* **1984**, *2*, 55.
50. Binnemans, K. *Chem. Rev.* **2009**, *109*, 4283.
51. Horrocks, W. D.; Sudnick, J. D. S. *J. Am. Chem. Soc.* **1979**, *101*, 334.
52. Horrocks, W. D.; Sudnick, J. D. S. *Acc. Chem. Res.* **1981**, *14*, 384.
53. Bunzli, J. C. G. *Chem. Rev.* **2010**, *110*, 2729.
54. Beeby, A.; Clarkson, I. M.; Dickins, R. S.; Faulkner, S.; Parker, D.; Royle, L.; Sousa, A. D.; Williams, J. A. G.; Woods, M. J. *J. Chem. Soc., Perkin Trans. 2* **1999**, 493.
55. Supkowski, R. M.; Horrocks, W. D. *Inorg. Chim. Acta* **2002**, *340*, 44.
56. Bunzli, J. C. G. *Acc. Chem. Res.* **2006**, *39*, 53.
57. Gunnlaugsson, T.; Stomeo, F. *Org. Biomol. Chem.* **2007**, *5*, 1999.
58. Spirlet, M. R.; Rebizant, J.; Desreux, J. F.; Loncin, M. F. *Inorg. Chem.* **1984**, *23*, 359.
59. Franklin, S. J. *Curr. Opin. Chem. Biol.* **2001**, *5*, 201.
60. Kataky, R.; Matthes, K. E.; Nicholson, P. E.; Parker, D. *J. Chem Soc., Perkin Trans. 2* **1990**, 1425.
61. Kataky, R.; Parker, D.; Teasdale, A.; Hutchinson, J. P. *J. Chem Soc., Perkin Trans. 2* **1992**, 1347.
62. Aime, S.; Barge, A.; Botta, M.; Parker, D.; De Sousa, A. S. *J. Am. Chem. Soc.* **1997**, *119*, 4767.
63. Pal, R.; Parker, D. *Org. Biomol. Chem.* **2008**, *6*, 1020.
64. Woods, M.; Sherry, A. D. *Inorg. Chem.* **2003**, *42*, 4401.
65. Parker, D.; Senanayake, P. K.; Williams, J. A. G. *J. Chem Soc., Perkin Trans. 2* **1998**, 2129.
66. Lowe, M. P.; Parker, D.; Reany, O.; Aime, S.; Botta, M.; Castellano, G.; Gianolio, E.; Pagliarin, R. *J. Am. Chem. Soc.* **2001**, *123*, 7601.
67. McCoy, C. P.; Stomeo, F.; Plush, S. E.; Gunnlaugsson, T. *Chem. Mater.* **2006**, *18*, 4336.
68. Gunnlaugsson, T. *Tetrahedron Lett.* **2001**, *42*, 8901.
69. Kálmán, F. K.; Woods, M.; Caravan, P.; Jurek, P.; Spiller, M.; Tircsó, G.; Kiràly, R.; Brücher, E.; Sherry, A. D. *Inorg. Chem.* **2007**, *46*, 5260.
70. Hovland, R.; Glogard, C.; Aasen, A. J.; Klaveness, J. *J. Chem Soc., Perkin Trans. 2* **2001**, 929.
71. Zhang, S.; Wu, K.; Sherry, A. D. *Angew. Chem. Int. Ed.* **1999**, *38*, 3192.
72. Raghunand, N.; Howison, C.; Sherry, A. D.; Zhang, S.; Gillies, R. J. *Magn. Reson. Med.* **2003**, *49*, 249.
73. Garcia-Martin, M. L.; Martinez, G. V.; Raghunand, N.; Sherry, A. D.; Zhang, S.; Gillies, R. J. *Magn. Reson. Med.* **2006**, *55*, 309.

74. Leon-Rodriguez, L. M.; Lubag, A. J. M.; Malloy, C. R.; Martinez, G. V.; Gillies, R. J.; Sherry, A. D. *Acc. Chem. Res.* **2009**, *42*, 948.
75. Thibon, A.; Pierre, V. C. *Anal. Bioanal. Chem.* **2009**, *394*, 107.
76. Kikuchi, K.; Komatsu, K.; Nagano, T. *Curr. Opin. Chem. Biol.* **2004**, *8*, 182.
77. Pope, S. J. A.; Laye, R. H. *Dalton Trans.* **2006**, 3108.
78. Esqueda, A. C.; López, J. A.; Andreu-de-Riquer, G.; Alvarado-Monzón, J. C.; Ratnakar, J.; Lubag, A. J. M.; Sherry, A. D.; De León-Rodriguez, L. M. *J. Am. Chem. Soc.* **2009**, *131*, 11387.
79. Reany, O.; Gunnlaugsson, T.; Parker, D. *J. Chem. Soc., Perkin Trans. 2* **2000**, 1819.
80. Reany, O.; Gunnlaugsson, T.; Parker, D. *Chem. Commun.* **2000**, 473.
81. Major, J. L.; Bolteau, R. M.; Meade, T. J. *Inorg. Chem.* **2008**, *47*, 10788.
82. Andrews, M.; Jones, J. E.; Harding, L. P.; Pope, S. J. A. *Chem. Commun.* **2011**, *47*, 206.
83. Gunnlaugsson, T.; Leonard, J. P. *Chem. Commun.* **2003**, 2424.
84. Li, C.; Law, G. L.; Wong, W. T. *Org. Lett.* **2004**, *6*, 4841.
85. Li, C.; Wong, W. T. *Chem. Commun.* **2002**.
86. Thibon, A.; Pierre, V. C. *J. Am. Chem. Soc.* **2009**, *131*, 434.
87. De Wall, S. L.; Barbour, L. J.; Gokel, G. W. *J. Am. Chem. Soc.* **1999**, *121*, 8405.
88. Gunnlaugsson, T.; Leonard, J. P.; Senechal, K.; Harte, A. J. *Chem. Commun.* **2004**, 782.
89. Nonat, A. M.; Harte, A. J.; Senechal-David, K.; Leonard, J. P.; Gunnlaugsson, T. *Dalton Trans.* **2009**, 4703.
90. Que, E. L.; Chang, C. J. *J. Am. Chem. Soc.* **2006**, *128*, 15942.
91. Li, W. H.; Fraser, S. E.; Meade, T. J. *J. Am. Chem. Soc.* **1999**, *121*, 1413.
92. Dhingra, K.; Maier, M. E.; Beyerlein, M.; Angelovski, G.; Logothetis, N. K. *Chem. Commun.* **2008**, 3444.
93. Dhingra, K.; Fousková, P.; Angelovski, G.; Maier, M. E.; Logothetis, N. K.; Tóth, É. *J. Biol. Inorg. Chem.* **2008**, *13*, 35.
94. Mishra, A.; Logothetis, N. K.; Parker, D. *Chem. Eur. J.* **2011**, *17*, 1529.
95. Abdel Hamid, K.; Tyramianski, M. *J. Neurosci.* **1997**, *17*, 3538.
96. Que, E. L.; Gianolio, E.; Baker, S. L.; Aime, S.; Chang, C. J. *Dalton Trans.* **2010**, *39*, 469.
97. Viguier, R.; Hulme, A. N. *J. Am. Chem. Soc.* **2006**, *128*, 11370.
98. Dickins, R. S.; Gunnlaugsson, T.; Parker, D.; Peacock, R. D. *Chem. Commun.* **1998**, 1643.
99. Dickins, R. S.; Aime, S.; Batsanov, A. S.; Beeby, A.; Botta, M.; Bruce, J. I.; Howard, J. A. K.; Love, C. S.; Parker, D.; Peacock, R. D.; Puschmann, H. *J. Am. Chem. Soc.* **2002**, *124*, 12697.
100. Gunnlaugsson, T.; Harte, A. J.; Leonard, J. P.; Nieuwenhuyzen, M. *Supramol. Chem.* **2003**, *15*, 505.
101. Pope, S. J. A.; Burton-Pye, B. P.; Berridge, R.; Khan, T.; Skabara, P. J.; Faulkner, S. *Dalton Trans.* **2006**, 2907.
102. Massue, J.; Quinn, S. J.; Gunnlaugsson, T. *J. Am. Chem. Soc.* **2008**, *130*, 6900.
103. Yu, J.; Parker, D.; Pal, R.; Poole, R. A.; Cann, M. J. *J. Am. Chem. Soc.* **2006**, *128*, 2294.
104. Poole, R. A.; Bobba, G.; Cann, M. J.; Frias, J. C.; Parker, D.; Peacock, R. D. *Org. Biomol. Chem.* **2005**, *3*, 1013.
105. Law, G.-L.; Pal, R.; Palsson, L. O.; Parker, D.; Wong, K.-L. *Chem. Commun.* **2009**, 7321.
106. Manning, H. C.; Goebel, T.; Thompson, R. C.; Price, R. R.; Lee, H.; Bornhop, D. J. *Bioconjugate Chem.* **2004**, *15*, 1488.
107. Messmer, K.; Reynolds, G. P. *Neurosci. Lett* **1998**, *53*, 241.

108. Vowinckel, E.; Reutens, D.; Becher, B.; Verge, G.; Evans, A.; Owens, T.; Antel, J. P. *J. Neurosci. Res.* **1997**, *50*, 345.
109. Bornhop, D. J.; Griffin, J. M. M.; Goebel, T. S.; Sudduth, M. R.; Bell, B.; Motamedi, M. *Appl. Spectrosc.* **2003**, *57*.
110. Ye, F.; Ke, T.; K., J. E.; Wang, X.; Y., S.; Johnson, M.; Lu, Z. R. *Mol. Pharmaceut.* **2006**, *3*, 507.
111. Jee, W. S. S., *A Textbook of Histology*. Urban Schwarzenberg: Baltimore, 1988.
112. Jee, W. S. S., *Orthopaedics, Principles of Basic and Clinical Science*. Boca Raton: Florida, 1999.
113. Clarke, B. *Clin. J. Am. Soc. Nephrol.* **2008**, *3*, 131.
114. http://www.bcb.uwc.ac.za/Sci_Ed/grade10/mammal/bone.htm. (January 2011)
115. Deng, H. W.; Liu, Y. Z., *Current Topics in Bone Biology*. World Scientific Publishing Co. Pte. Ltd.: Singapore, 2005.
116. Marieb, E. N.; Hoehn, K., *Human Anatomy and Physiology*. Pearson Benjamin Cummings: San Francisco, 2007.
117. http://www.daviddarling.info/encyclopedia/B/bone.html. (Jaunuary 2011)
118. Baron, R., *Primer on the Metabolic Bone Disease and Disorder or Mineral Metabolism* 4th ed.; Lippincott/Williams & Wilkins: Philadelphia, 1999.
119. Gehron-Robey, P.; Boskey, A. L., *Osteoporosis*. Academic Press: San Diego, 1996.
120. Rhinelander, F. W., *The Biochemistry and Physiology of Bone*. Academic Press: New York, 1972.
121. Khosla, S.; Kleerekoper, M., *Primer on the Metabolic Bone diseases and Disorders of Mineral Metabolism*. 4th ed.; Lippincott/Williams & Wilkons: Philadelphia, 1999.
122. Jee, W. S. S. *Bone* **1997**, *21*, 297.
123. Bonewald, L. *J. Musculoskeletal. Neuronal. Interact.* **2006**, *6*, 331.
124. Frost, H. M. *Anat. Rec.* **1990**, *226*, 403.
125. Burr, D. B.; Martin, R. B.; Schaffler, M. B.; Radin, E. L. *J. Biomech.* **1985**, *18*, 189.
126. Barnes, G. L.; Kostenuik, P. L.; Gerstenfield, L. C.; Einhorn, T. A. *J. Bone Miner. Res.* **1999**, *14*, 1805.
127. http://www.lilly.com/pdf/bone_remodeling_process_1003.pdf. (January 2011)
128. Hill, P. A. *J. Orthod.* **1998**, *25*, 101.
129. Parkesh, R.; Mohsin, S.; Lee, T. C.; Gunnlaugsson, T. *Chem. Mater.* **2007**, *19*, 1656.
130. Lee, T. C.; Mohsin, S.; Taylor, D.; Parkesh, R.; Gunnlaugsson, T.; O'Brien, F. J.; Giehl, M.; Gowin, W. *J. Anat.* **2003**, *203*, 161.
131. Lee, T. C.; O'Brien, F. J.; Gunnlaugsson, T.; Parkesh, R.; Taylor, D. *Technol. Health Care* **2006**, *14*, 359.
132. Lee, T. C.; Taylor, D. *J. Biomech.* **1998**, *31*, 1177.
133. O'Brien, F. J.; Taylor, D.; Dickins, G. R.; Lee, T. C. *J. Anat.* **2000**, *197*, 413.
134. Frost, H. M. *Henry Ford Hos. Bull.* **1960**, *8*, 35.
135. Bentolila, V.; Boyce, T. M.; Fyhrie, D. P.; Drumb, R.; Skerry, T. M.; Schaffler, M. B. *Bone* **1998**, *23*, 275.
136. Mori, S.; Burr, D. B. *Bone* **1993**, *14*, 103.
137. Lee, T. C.; Staines, A.; Taylor, D. *J. Anat.* **2002**, *201*, 437.
138. O'Brien, F. J.; Hardiman, D. A.; Hazenberg, J. G.; Mercy, M. V.; Mohsin, S.; Taylor, D.; Lee, T. C. *Eur. J. Morphol.* **2005**, *42*, 71.
139. Schaffler, M. B.; Choi, K.; Milgrom, C. *Bone* **1995**, *17*, 521.
140. Lee, T. C.; O'Brien, F. J.; Taylor, D. *Int. J. Fatigue* **2000**, *22*, 847.
141. Burr, D. B.; Forwood, M. R.; Fyhrie, D. P.; Martin, R. B.; Schaffler, M. B. *J. Bone Miner. Res.* **1997**, *12*, 6.
142. McLeod, K.; McCann, S. E.; Horvath, P. J.; Wende, J. W. *J. Nutr.* **1968**, *137*, 1968.
143. http://cheap-online-pharmacyad.eu/order_osteoporosis_en-us.html. (October 2011)
144. http://www.medicinenet.com/osteoporosis/article.htm. (October 2011)

145. Burr, D. B.; Stafford, T. *Clin. Orthop. Relat. R.* **1990**, 305.
146. Lee, T. C.; Myers, E. R.; Hayes, W. C. *J. Anat.* **1998**, *193*, 179.
147. Lee, T. C.; Arthur, T. L.; Gibson, L. J.; Hayes, W. C. *J. Orthop. Res.* **2000**, *18*, 322.
148. O'Brien, F. J.; Taylor, D.; Lee, T. C. *J. Biomech.* **2002**, *35*, 523.
149. Tsien, R. Y. *Annu. Rev. Neurosci.* **1989**, *12*, 227.
150. Ramaswami, M.; Krishnan, K. S.; Kelly, R. B. *Neuron.* **1994**, *13*, 363.
151. Canepari, M.; Mammano, F. *J. Neurosci. Meth.* **1991**, *180*, 209.
152. Parkesh, R.; Lee, T. C.; Gunnlaugsson, T. *Tetrahedron Lett.* **2009**, *50*, 4114.
153. Stover, S. M.; Marti, R. B.; Pool, R. R.; Taylor, K. T.; Harrington, T. M. *Proc. Orthop. Res. Soc.* **1993**, *18*, 541.
154. Leng, H.; Wang, X.; Ross, R. D.; Niebur, G. L.; Roeder, R. K. *J. Mech. Behav. Biomed.* **2008**, *1*, 68.
155. Ni, Q.; Nicolella, D. P. *Meas. Sci. Technol.* **2005**, *16*, 659.
156. Thurner, P. J.; Erickson, B.; Schriock, Z. J. *J. Mater. Res.* **2006**, *21*, 1093.
157. Silva, M. J.; Uthgenannt, B. A.; Rutlin, J. R.; Wohl, G. R.; Lewis, J. S.; Welch, M. J. *Bone* **2006**, *39*, 229.
158. Li, J.; Miller, M. A.; Hutchins, G. D.; Burr, D. B. *Bone* **2005**, *37*, 819.
159. Tang, S. Y.; Vashishth, D. *Bone* **2007**, *40*, 1259.
160. Wang, X.; Masse, D. B.; Leng, H.; Hess, K. P.; Ross, R. D.; Roeder, R. K. *J. Biomechanics* **2007**, *40*, 3397.
161. Parkesh, R.; Gowin, W.; Lee, T. C.; Gunnlaugsson, T. *Org. Biomol. Chem.* **2006**, *4*, 3611.
162. Zhang, Z.; Ross, R. D.; Roeder, R. K. *Nanoscale* **2010**, *2*, 582.
163. O'Brien, F. J. *Microcracks and the Fatigue Behaviour of Compact Bone, Ph.D. Thesis, Royal College of Surgeons in Ireland.* **2000**.
164. Parkesh, R.; Lee, T. C.; Gunnlaugsson, T.; Gowin, W. *J. Biomech.* **2006**, *39*, 1552.
165. Parkesh, R.; Lee, T. C.; Gunnlaugsson, T. *Org. Biomol. Chem.* **2007**, *5*, 310.
166. Chapurlat, R. D.; Delmas, P. D. *Osteoporos. Int.* **2009**, *20*, 1299.
167. Bulman, R. A., *Metal Ions in Biological Systems*. Marcel Dekker Inc.: New York, 2003, 40, 683.
168. Turro, C.; Fu, K.-L.; Bradley, P. M., *Metal Ions in Biological Systems*. Sigel, A.; Sigel, H., Eds. Marcel Dekker Inc.: New York, 2003, 40, 323.
169. Massue, J.; Plush, S. E.; Bonnet, C. S.; Moore, D. A.; Gunnlaugsson, T. *Tetrahedron Lett.* **2007**, *48*, 8052.
170. Akitt, J. W. *NMR and chemistry : an introduction to modern NMR spectroscopy; 4th ed.; Stanley Thornes,* **2000**.
171. Yan, B.; Zhang, H.; Wang, S.; Ni, J. *Monatsh. Chem.* **1998**, *129*, 567.
172. Sabbatini, N.; Guardigli, M. *Chem. Rev.* **1993**, *123*, 201.
173. Bissel, R. A.; de Silva, A. P.; Gunaratne, H. Q. N.; Lynch, P. L. M.; McCoy, C. P.; Maguire, G. E. M.; Sandanayake, K. R. A. S. *Top. Curr. Chem.* **1993**, 223.
174. Gunnlaugsson, T.; Mac Donaill, D. A.; Parker, D. *J. Am. Chem. Soc.* **2001**, *123*, 12866.
175. Murov, S. L.; Carmichael, I.; Hug, G. L., *Handbook of Photochemistry*. Marcel Dekker Inc.: New York, 1993.
176. Plush, S. E.; Clear, N. A.; Leonard, J. P.; Fanning, A.-M.; Gunnlaugsson, T. *Dalton Trans.* **2010**, *39*, 3644.
177. Burr, D. B.; Stafford, T. *J. Biomech. Eng.* **1999**, *121*, 616.
178. Burr, D. B.; Hooser, M. *Bone* **1995**, *17*, 431.
179. Fazzalari, N. L.; Forwood, M. R.; Manthey, B. A.; Smith, K.; Kolesik, P. *Bone* **1998**, *23*, 373.
180. Zioupos, P. *J. Micros.* **2001**, *201*, 270.
181. http://www.cetus-online.com.br/epi-fluo.htm. (June 2009)

182. Coling, D.; Kachar, B., *Current Protocols in Neuroscience*. John Wiley and Sons: New York, 1997.
183. Gadian, D. G., *NMR and its applications to living systems*. 2 ed.; Oxford University Press: USA, 1996.
184. Geraldes, C. F. G. C.; Laurent, S. *Contrast Media Mol. I.* **2009**, *4*, 1.
185. Bloch, F. *Nature* **1952**, *170*, 911.
186. Ewen, H. I.; Purcell, E. *Nature* **1951**, *168*, 356.
187. Damadian, R. V. *Science* **1971**, *171*, 1151.
188. Hore, P. J., *Nuclear Magnetic Resonance*. Oxford University Press Inc.: New York, 1995.
189. http://www.e-radiography.net/mrict/Basic_MR.pdf. (February 2010)
190. Bakhmutov, V. I., *Practical NMR Relaxation for Chemists*. John Wiley & Sons Ltd: Chichester, 2005.
191. Kaupp, M.; Buhl, M.; Malkin, V. G., *Calculation of NMR and EPR Parameters: Theory and Applications*. Wiley-VCH: 2004.
192. Aime, S.; Crich, S. G.; Gianolio, E.; Giovenzana, G. B.; Tei, L.; Terreno, E. *Coord. Chem. Rev.* **2006**, *250*, 1562.
193. Bottrill, M.; Kwok, L.; Long, N. J. *Chem. Soc. Rev.* **2006**, *35*, 557.
194. Lauffer, R. B. *Chem. Rev.* **1987**, *87*, 901.
195. Bligh, S. W. A.; Harding, C. T.; McEwen, A. B.; Adler, P. J.; Kelly, J. D.; Marriott, J. A. *Polyhedron* **1994**, *13*, 1937.
196. Alves, F. C.; Donato, P.; Sheery, A. D.; Zaheer, A.; Zhang, S.; Lubag, A. J. M.; Merritt, M. E.; Lenkinski, R. E.; Frangioni, J. V.; Neves, M.; Prata, M. I. M.; Santos, A. C.; de Lima, J. J. P.; Geraldes, C. F. G. C. *Invest. Radiol.* **2003**, *38*, 750.
197. Kubicek, V.; Rudovsky, J.; Kotek, J.; Hermann, P.; Elst, L. V.; Muller, R. N.; Kolar, Z. I.; Wolterbeek, H. T.; Peters, J. A.; Lukes, I. *J. Am. Chem. Soc.* **2005**, *127*, 16477.
198. Vitha, T.; Kubicek, V.; Hermann, P.; Elst, L. V.; Muller, R. N.; Kolar, Z. I.; Wolterbeek, H. T.; Breeman, W. A. P.; Lukes, I.; Peters, J. A. *J. Med. Chem.* **2008**, *51*, 677.
199. Vitha, T.; Kubicek, V.; Hermann, P.; Kolar, Z. I.; Wolterbeek, H. T.; Peters, J. A.; Lukes, I. *Langmuir* **2008**, *24*, 1952.
200. Vitha, T.; Kubicek, V.; Kotek, J.; Hermann, P.; Elst, L. V.; Muller, R. N.; Lukes, I.; Peters, J. A. *Dalton Trans.* **2009**, 3204.
201. Gittens, S. A.; Bansal, G.; Zernicke, R. F.; Uludag, H. *Adv. Drug Deliv. Rev.* **2005**, *57*, 1011.
202. Jacobsen, N. E., *NMR Spectrocopy Explained*. John Wiley & Sons Inc.: New Jersey, 2007.
203. Corsi, D. M.; Platas-Iglesia, C.; Bekkum van, H.; Peters, J. A. *Magn. Reson. Chem.* **2001**, *39*, 723.
204. Nonat, A.; Fries, P. H.; Pécaut, J.; Mazzanti, M. *Chem. Eur. J.* **2007**, *13*, 8489.
205. Aime, S.; Barge, A.; Bruce, J. I.; Botta, M.; Howard, J. A. K.; Moloney, J. M.; Parker, D.; de Sousa, A. S.; Woods, M. *J. Am. Chem. Soc.* **1999**, *121*, 5762.
206. Woods, M.; Zhang, S.; Ebron, V. H.; Sherry, A. D. *Chem. Eur. J.* **2003**, *9*, 4634.
207. Terreno, E.; Boniforte, P.; Botta, M.; Fedeli, F.; Milone, L.; Mortillaro, A.; Aime, S. *Eur. J. Inorg. Chem.* **2003**, 3530.
208. Aime, S.; Barge, A.; Botta, M.; Howard, J. A. K.; Kataky, R.; Lowe, M. P.; Moloney, J. M.; Parker, D.; De Sousa, A. S. *Chem. Commun.* **1999**, 1047.
209. Terreno, E.; Botta, M.; Boniforte, P.; Bracco, C.; Milone, L.; Mondino, B.; Uggeri, F.; Aime, S. *Chem. Eur. J.* **2005**, *11*, 5531.
210. Chen, X.; Zhou, Y.; Peng, X.; Yoon, J. *Chem. Soc. Rev.* **2010**, *39*, 2120.
211. Hama, I.; Nakagomi, S.; Konishi, H.; Kiyama, H. *Brain Res. 1306*, 1.
212. Zhang, Y.; Li, Y.; Yan, X.-P. *Anal. Chem.* **2009**, *81*, 5001.

213. Rayman, I.; Kode, A.; Biswas, S. K. *Nat. Protoc.* **2006**, *1*, 3159.
214. Refsum, H.; Ueland, P. M.; Nygard, O.; Vollset, S. E. *Annu. Rev. Med.* **1998**, *49*, 31.
215. Perricone, C.; De Carolis, C.; Perricone, R. *Autoimmun. Rev.* **2009**, *8*.
216. Shahrokhian, S. *Anal. Chem.* **2001**, *73*, 5972.
217. van Meurs, J. B. J.; Dhonukshe-Ruttens, R. A. M.; Pluijm, S. M. F.; van der Klift, M.; de Jonge, R.; Lindemans, J.; de Groot, L. C. P. G. M.; Hoffman, A.; Witteman, J. C. M.; van Leeuwen, J. P. T. M.; Breteler, M. B.; Lips, P.; Pols, H. A. P.; Uitterlinden, A. G. *N. Engl. J. Med.* **2004**, *350*, 2033.
218. Seshadri, S.; Beiser, A.; Selhub, J.; Jacques, P. F.; Rosenberg, I. H.; D'Agostino, R. B.; Wilson, P. W. F.; Wolf, P. A. *N. Engl. J. Med.* **2002**, *346*, 476.
219. Huang, G. G.; Han, X. X.; Hossain, M. K.; Ozaki, Y. *Anal. Chem.* **2009**, *81*, 5881.
220. Timur, S.; Odaci, D.; Dincer, A.; Zihnioglu, F.; Telefoncu, A. *Talanta* **2008**, *74*, 1492.
221. Shaw, I. *Hum. Exp. Toxicol.* **2010**, *29*, 241.
222. Chi, L.; Ke, Y.; Luo, C.; Gozal, D.; Liu, R. *Neuroscience* **2007**, *144*, 991.
223. Perricone, C.; De Carolis, C.; Perricone, R. *Autoimmun. Rev.* **2009**, *8*, 697.
224. Chawatko, G.; Bald, E. *Talanta* **2000**, *52*, 509.
225. Amarnath, K.; Armarnath, V.; Amarnath, K.; Valentine, H. L.; Valentine, W. M. *Talanta* **2003**, *60*, 1229.
226. Tcherkas, Y. V.; Denisenko, A. D. *J. Chromatogr. A* **2001**, *913*, 309.
227. Bhattacharyay, D.; Dutta, K.; Banerjee, S.; Turner, A. P. F.; Sarkar, P. *Electroanal.* **2008**, *20*, 1947.
228. Chen, G.; Zang, L.; Wang, J. *Talanta* **2004**, *64*, 1229.
229. Inoue, T.; Kirchhoff, J. R. *Anal. Chem.* **2002**, *74*, 1349.
230. De Silva, A. P.; Gunaratne, H. Q. N.; Gunnlaugsson, T. *Tetrahedron Lett.* **1998**, 5077.
231. Wang, Z.; Zhang, D.-Q.; Zhu, D.-B. *Chinese J. Chem.* **2006**, *24*, 1122.
232. Liu, Y.; Yu, Y.; Lam, J. W. Y.; Hong, Y.; Faisal, M.; Yuan, W. Z.; Tang, B. Z. *Chem. Eur. J.* **2010**, *16*, 8433.
233. Corrie, J. E. T. *J. Chem Soc., Perkin Trans. 1* **1994**, 2975.
234. Matsumoto, T.; Urano, Y.; Shoda, T.; Kojima, H.; Nagano, T. *Org. Lett.* **2007**, *9*, 3375.
235. Sippel, T. O. *J. Histochem. Cytochem.* **1981**, *29*, 314.
236. Song, H. Y.; Ngai, M. H.; Song, Z. Y.; MacAry, P. A.; Hobley, J.; Lear, M. J. *Org. Biomol. Chem.* **2009**, *7*, 3400.
237. Mare, S.; Penugonda, S.; Ercal, N. *Biomed. Chromatogr.* **2005**, 80.
238. Girouard, S.; Houle, M. H.; Grandbois, A.; Keillor, J. W.; Michnick, S. W. *J. Am. Chem. Soc.* **2005**, *127*, 559.
239. Rusin, O.; St. Luce, N. N.; Agbaria, R. A.; Escobedo, J. O.; Jiang, S.; Warner, I. M.; Strongin, R. M. *J. Am. Chem. Soc.* **2004**, *126*, 438.
240. Wang, W.; Rusin, O.; Xu, X.; Kim, K.; Escobedo, J. O.; Fakayode, S. O.; Fletcher, A.; Lowry, M.; Schowalter, C. M.; Lawerence, C. M.; Fronczek, F. R.; Warner, I. M.; Strongin, R. M. *J. Am. Chem. Soc.* **2005**, *127*, 15949.
241. Tanaka, F.; Mase, N.; Barbas, C. F. *Chem. Commun.* **2004**, 1762.
242. Shang, L.; Yin, J.; Li, J.; Jin, L.; Dong, S. *Biosens. Bioelectron.* **2009**, *25*, 269.
243. Zhu, B.; Zhang, X.; Li, Y.; Wang, P.; Zhang, H.; Zhuang, X. *Chem. Commun.* **2010**, *46*, 5710.
244. Liu, J.; Bao, C.; Zhong, X.; Zhao, C.; Zhu, L. *Chem. Commun. 46*, 2971.
245. Kim, D. H.; Han, M. S. *Bioorg. Med. Chem. Lett.* **2003**, *13*, 2543.
246. Bouffard, J.; Kim, Y.; Swager, T. M.; Weissleder, R.; Hilderbrand, S. A. *Org. Lett.* **2007**, *10*, 37.
247. Huang, S.-T.; Ting, K.-N.; Wang, K.-L. *Anal. Chim. Acta* **2008**, *620*, 120.

248. Jiang, W.; Cao, Y.; Liu, Y.; Wang, W. *Chem. Commun.* **2010**, *46*, 1944.
249. Wang, S.-P.; Deng, W.-J.; Sun, D.; Yan, M.; Zheng, H.; Xu, J.-G. *Org. Biomol. Chem.* **2009**, *7*, 4017.
250. Zhang, M.; Yu, M.; Li, F.; Zhu, M.; Li, M.; Gao, Y.; Li, L.; Liu, Z.; Zhang, J.; Zhang, D.; Yi, T.; Huang, C. *J. Am. Chem. Soc.* **2007**, *129*, 10322.
251. Chen, X.; Ko, S.-K.; Kim, M. J.; Shin, I.; Yoon, J. *Chem. Commun.* **2010**, *46*, 2751.
252. Sippel, T. O. *J. Histochem. Cytochem.* **1981**, *29*, 1377.
253. Parker, D.; Dickins, R. S.; Puschmann, H.; Cossland, C.; Howard, J. A. K. *Chem. Rev.* **2002**, *102*, 1977.
254. Cava, M. P.; Deana, A. A.; Muth, K. *Org. Synth.* **1961**, *41*, 93.
255. Yawata, Y.; Tanaka, K. R. *Blood* **1974**, *43*, 99.
256. Krohne-Enrich, G.; Schirmer, R. H.; Untucht-Grau, R. *Eur. J. Biochem.* **1971**, *80*, 65.
257. Schulz, G. E.; Zappe, H.; Worthington, D. J.; Rosemeyer, M. A. *FEBS Lett.* **1975**, *54*, 86.
258. Paiz, E. F.; Schulz, G. E. *J. Biol. Chem.* **1983**, *258*, 1752.
259. http://www.trevigen.com/protocols/pdf/7510-100-K.pdf. (September 2010)
260. Page, M. I.; Williams, A., *Enzyme Mechanisms*. RSC: London, 1887.
261. Staal, G. E. J.; Veeger, C. *Biochim. Biophys. Acta* **1969**, *185*, 49.
262. Wang, L.; Wang, L.; Xia, T.; Bian, G.; Dong, L.; Tang, Z.; Wang, F. *Spectrochim. Acta A.* **2005**, *61*, 2533.
263. Sarkar, B. *Chem. Rev.* **1999**, *99*, 2535.
264. Lindar, M. C.; Hazegh-Azam, M. *Am. J. Clin. Nutr.* **1996**, *63*, 8215.
265. Nolan, E. M.; J., L. S. *Chem. Rev.* **2008**, *108*, 3443.
266. Sarkar, B., Handbook on Metals in Clinical and Analytical Chemistry. Inc., M. D., Ed. M. Dekker: New York, 1994.
267. Barja, B. C.; Armendia, P. F. *Photoch. Photobio. Sci.* **2008**, *7*, 1391.
268. Liu, Y.; Yu, M.; Chen, Y.; Zhang, N. *Bioorgan. Med. Chem.* **2009**, *17*, 3887.
269. Pesak, J.; J., O. *J. Acta Univ. Palacki. Olomuc., Fac. Med.* **2000**, *143*, 71.
270. Lakowicz, J. R., *Principles of Fluorescence Spectroscopy* 3rd ed.; Springer Science: New York, 2000.
271. Vogel, A. I.; Tatchell, A. R.; Furnis, B. S.; Hannaford, A. J.; Smith, P. W. G., *Vogel's Textbook of Practical Organic Chemistry*. 5th ed.; Prentice Hall: New York, 1996.
272. J., O. B. F.; Taylor, D.; Mohsin, S.; Mercy, M. V.; Hazenberg, J. G.; Hardiman, D. A.; Lee, T. C. *Eur. J. Morphol.* **2005**, *42*, 71.

Appendix

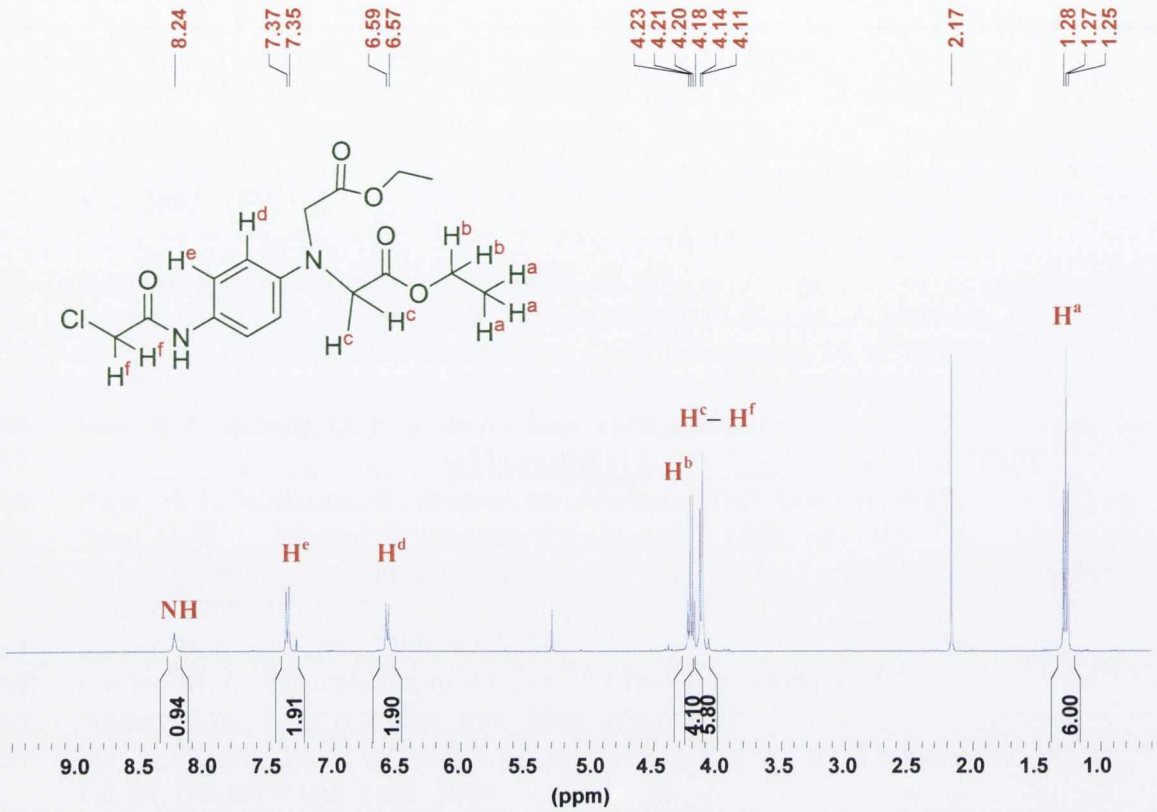

Figure A1.1: *The ^{1}H NMR spectrum (400 MHz, $CDCl_3$) of* ***59****.*

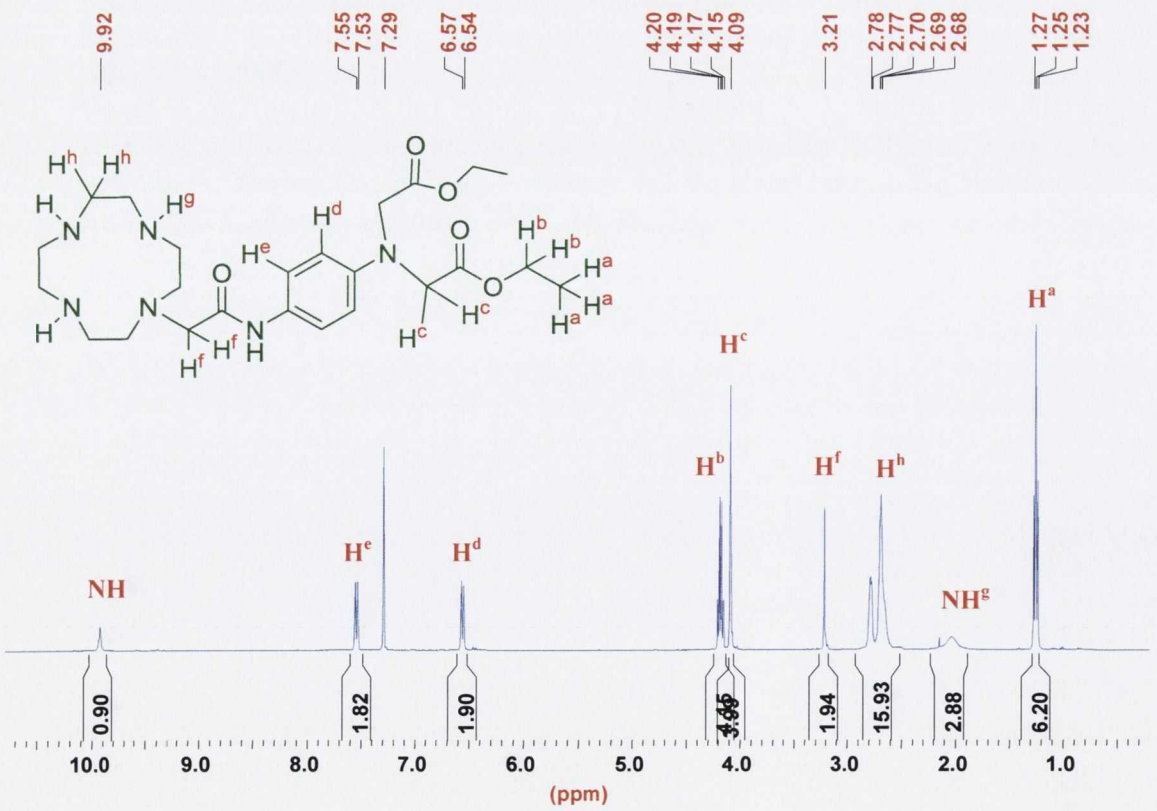

Figure A1.2: *The ^{1}H NMR spectrum (400 MHz, $CDCl_3$) of* ***67****.*

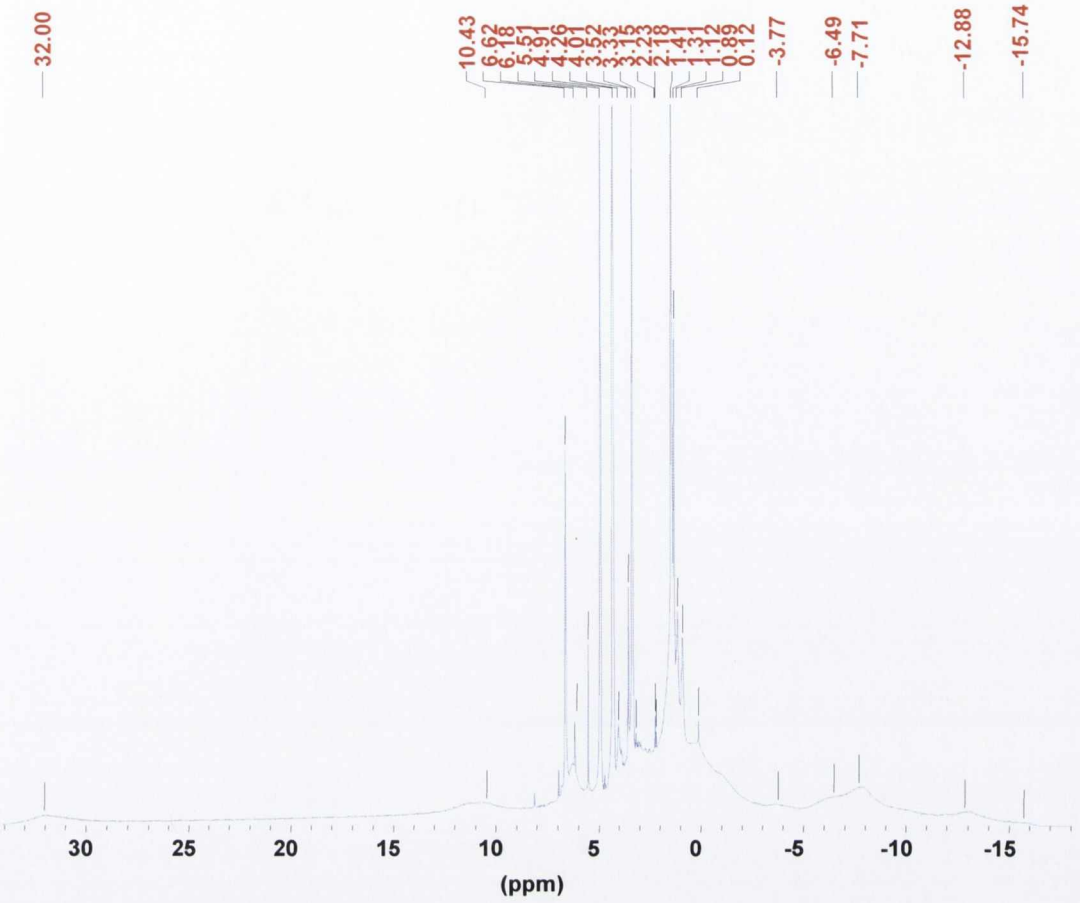

Figure A1.3a: *The ^{1}H NMR spectrum (400 MHz, CD_3OD) of complex* ***Eu.58****.*

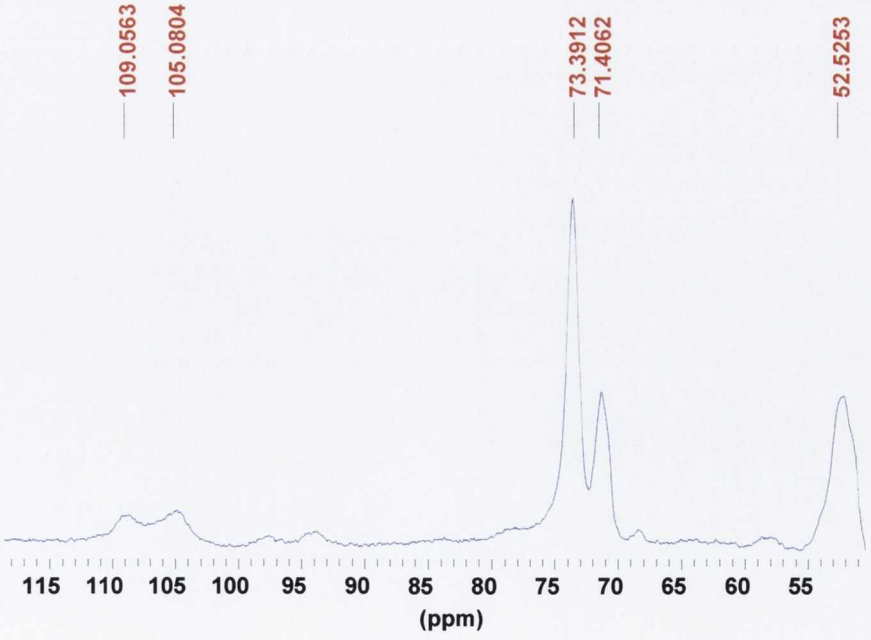

Figure A1.3b: *The remainder of the ^{1}H NMR spectrum (400 MHz, CD_3OD) of complex* ***Tb.58*** *not shown in Chapter 2.*

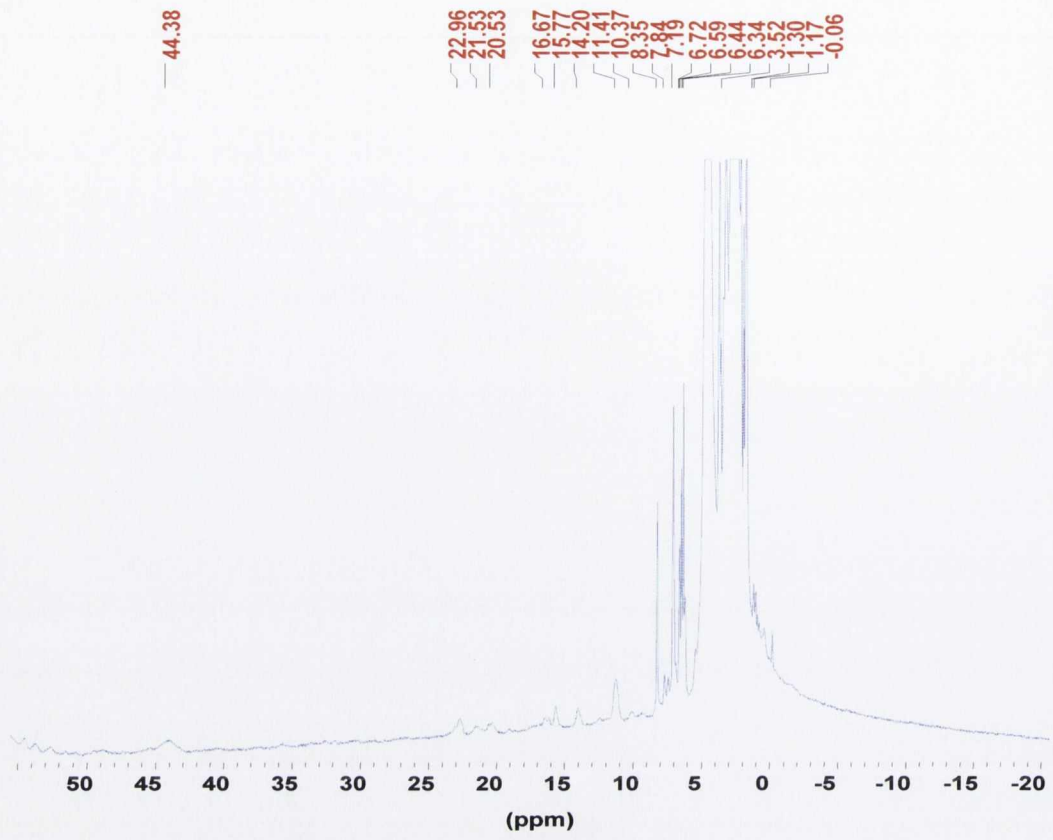

Figure A1.4a: *The ^{1}H NMR spectrum (400 MHz, D_2O) of complex* ***Tb.58.Na****.*

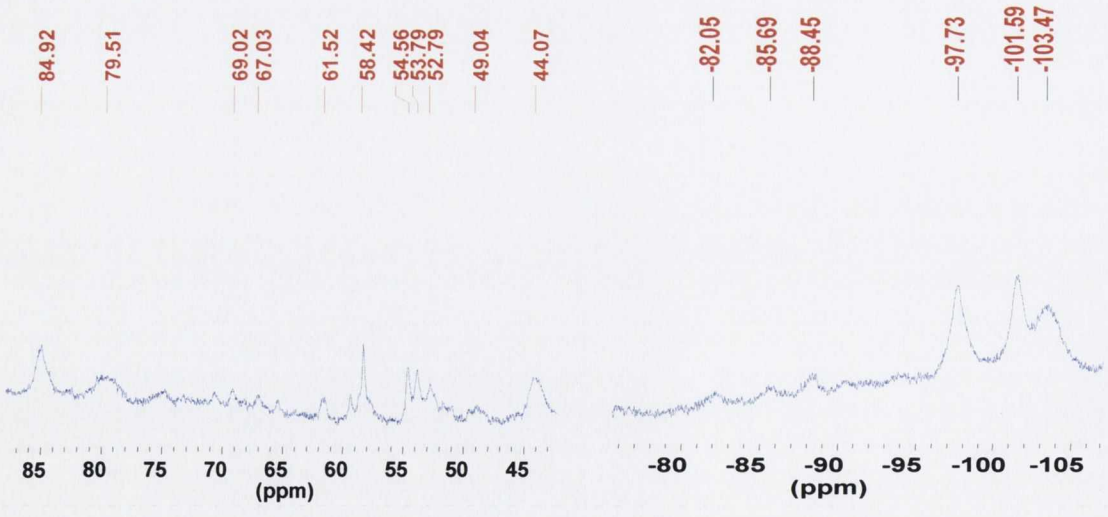

Figure A1.4b: *The ^{1}H NMR spectrum (400 MHz, D_2O) of complex* ***Tb.58.Na****.*

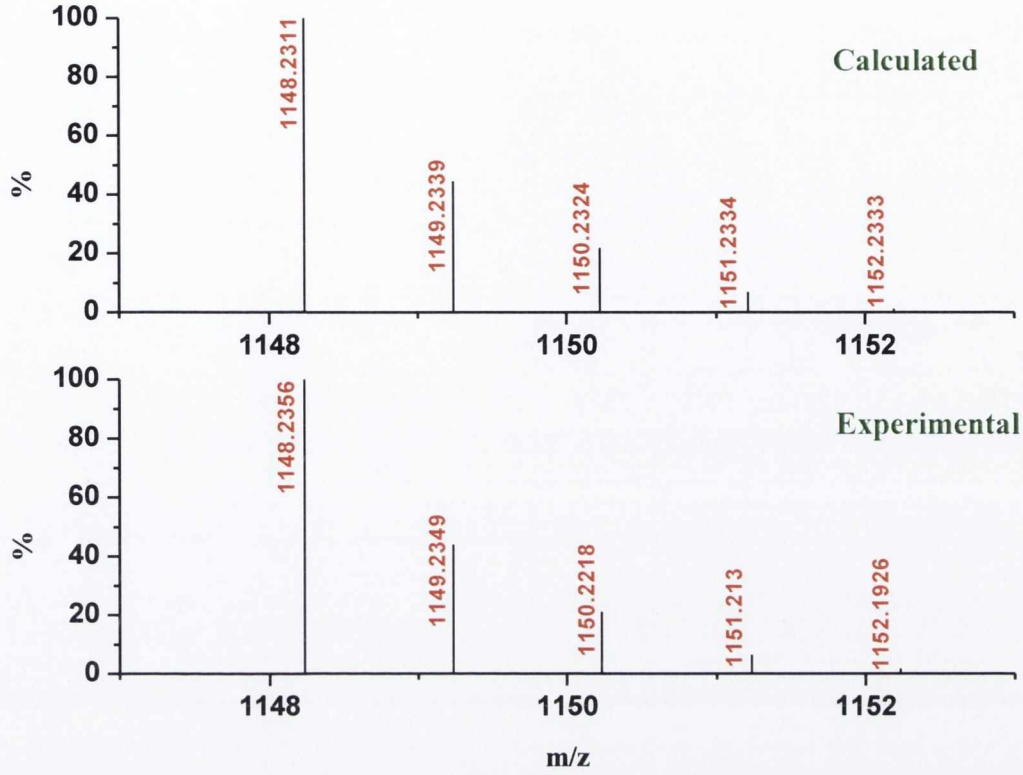

Figure A1.5: *The ESMS of* ***Tb.58.Na*** *displaying the expected* ^{159}*Tb(III) isotopic distribution patterns for the* $[M+2(CF_3SO_3)-2Na+2H]^+$ *species.*

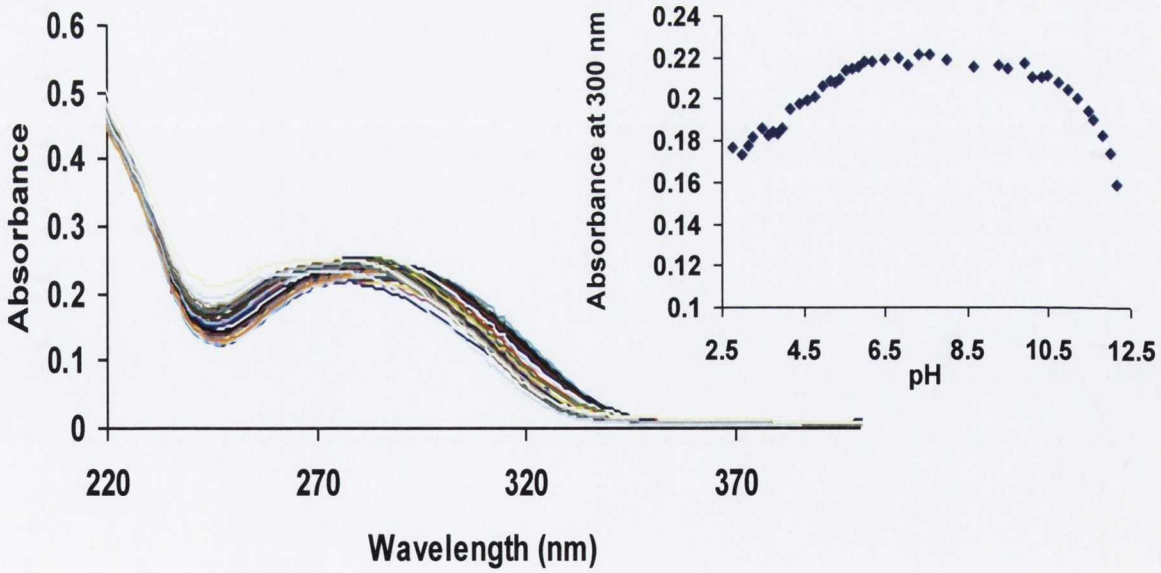

Figure A1.6a: *The UV-vis absorption spectra of* ***Tb.58.Na*** *as a function of pH in* H_2O *[I = 0.1M* NEt_4ClO_4 *(TEAP)].Inset: Changes in the UV-vis absorption of* ***Tb.58.Na*** *at 300 nm.*

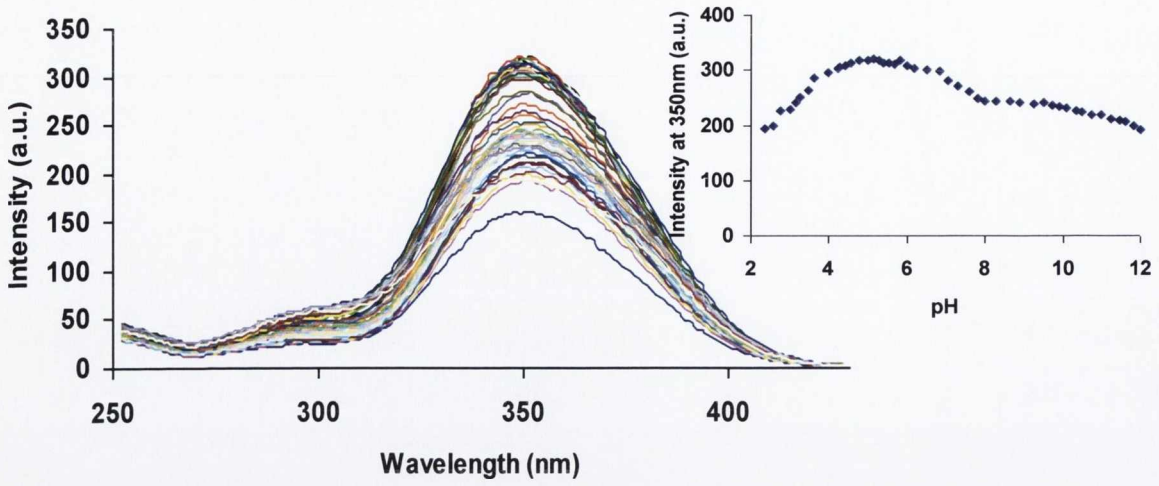

Figure A1.6b: *The fluorescence spectra of* ***Tb.58.Na*** *as a function of pH in H_2O [I = 0.1M NEt_4ClO_4 (TEAP)]. Inset: Changes at 350 nm as a function of pH.*

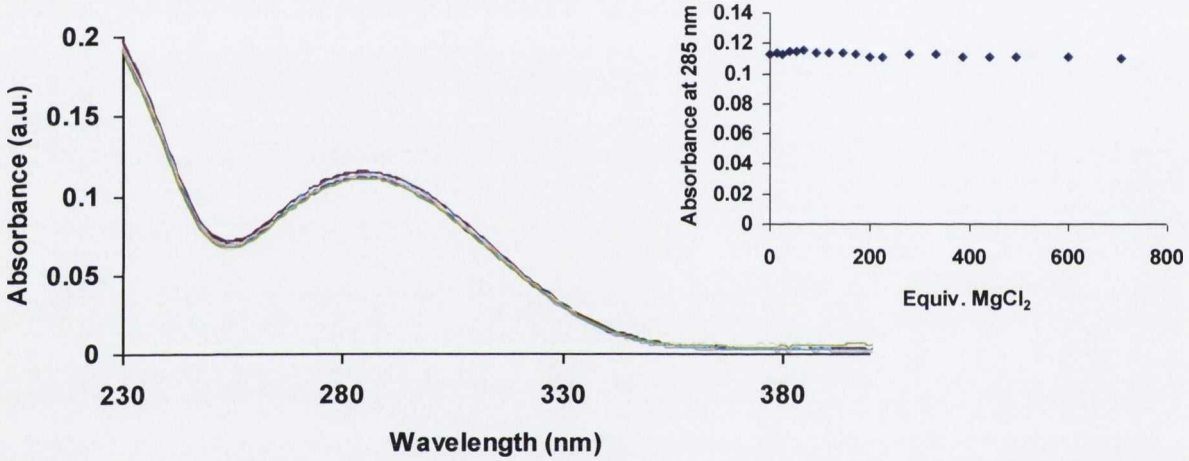

Figure A1.7a: *Changes in the UV-vis absorption spectra of* ***Tb.58.Na*** *(10 μM) in the presence of $MgCl_2$ (0 – 7.5 mM) at pH = 7.4 (20 mM HEPES, 135 mM KCl). Inset: Plot of the absorbance at 285 nm with equivalents of $MgCl_2$ added.*

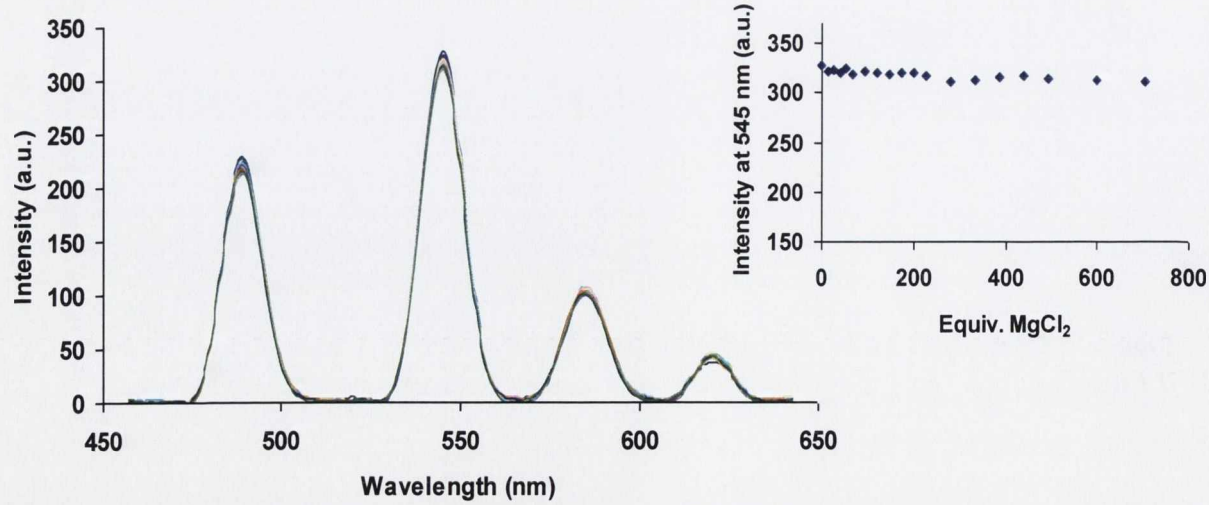

Figure A1.7b: *The Tb(III) luminescence response of* ***Tb.58.Na*** *(10 μM) upon the addition of $MgCl_2$ (0 – 7.5 mM) at pH = 7.4 (20 mM HEPES, 135 mM KCl). Inset: Plot of the emission intensity at 545 nm with equivalents of $MgCl_2$ added.*

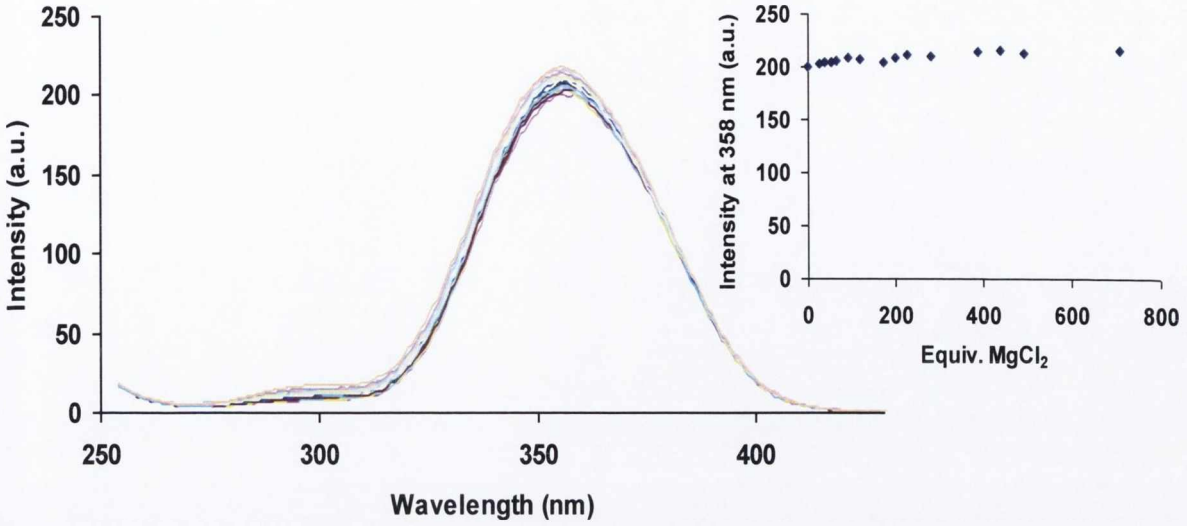

Figure A1.7c: *The fluorescence response of* ***Tb.58.Na*** *(10 μM) upon the addition of $MgCl_2$ (0 – 7.5 mM) at pH = 7.4 (20 mM HEPES, 135 mM KCl). Inset: Plot of the emission intensity at 358 nm with equivalents of $MgCl_2$ added.*

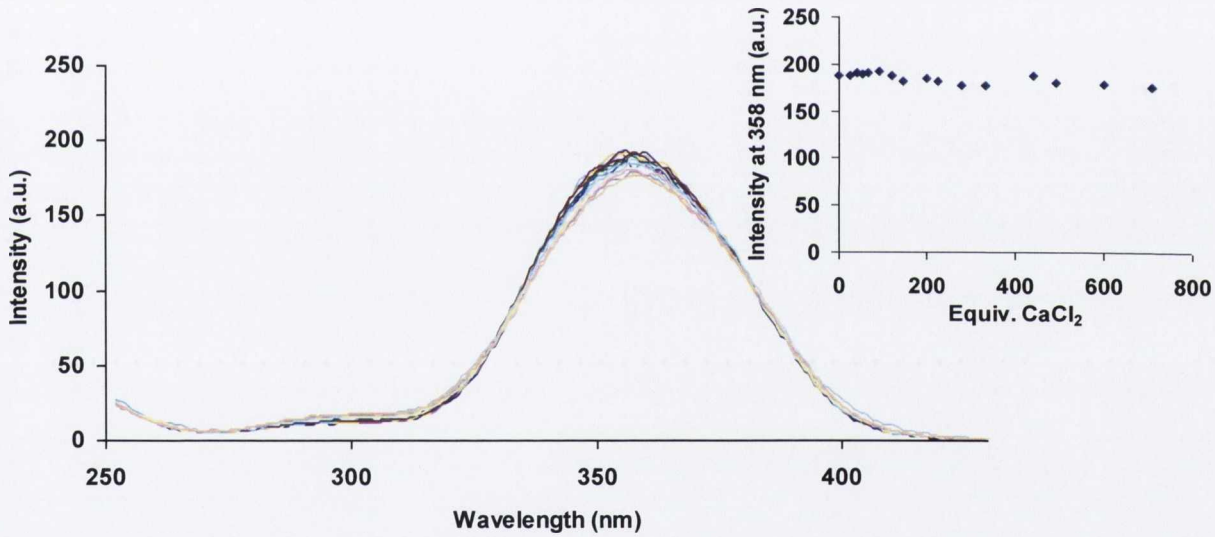

Figure A1.7d: *The fluorescence response of* ***Tb.58.Na*** *(10 μM) upon the addition of $CaCl_2$ (0 – 7.5 mM) at pH = 7.4 (20 mM HEPES,* 135 mM KCl*). Inset: Plot of the emission intensity at 358 nm with equivalents of $CaCl_2$ added.*

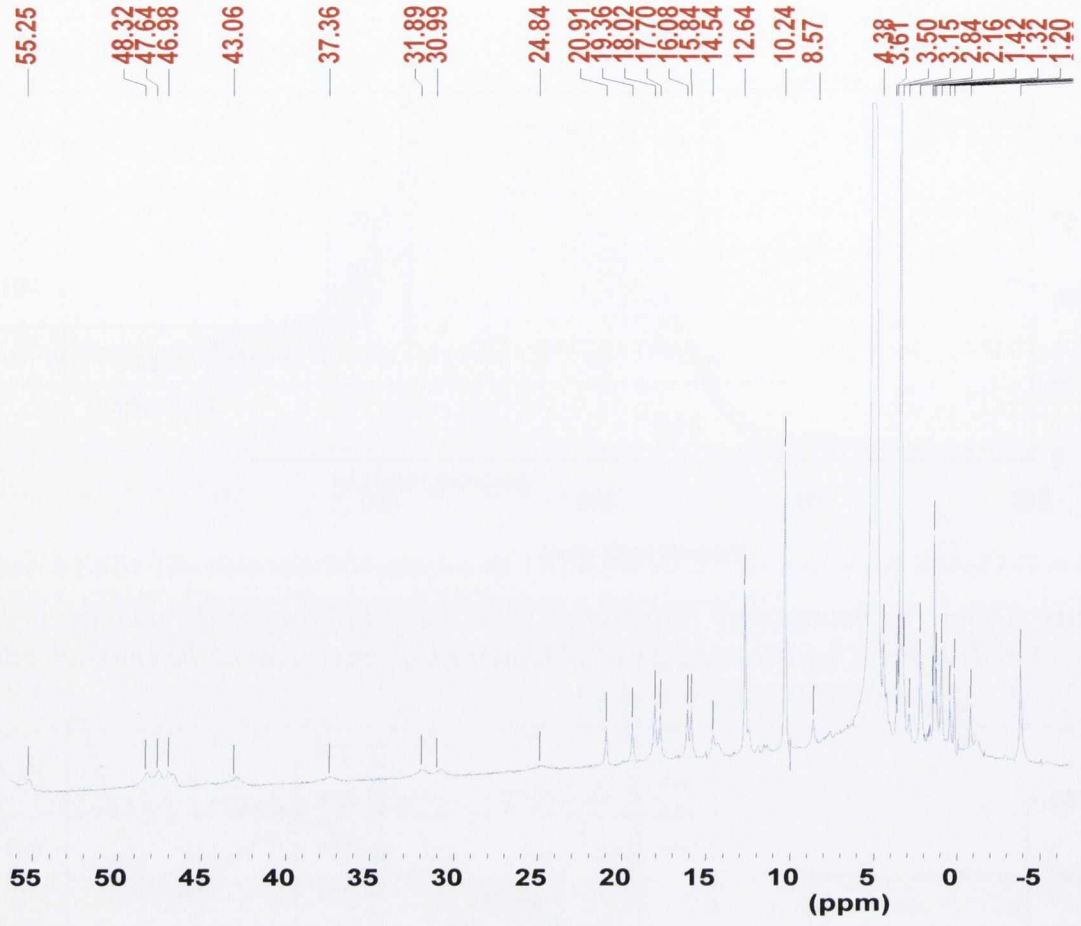

Figure A1.8a: *The ^{1}H NMR spectrum (400 MHz, $CDCl_3$) of* **Tb.69**.

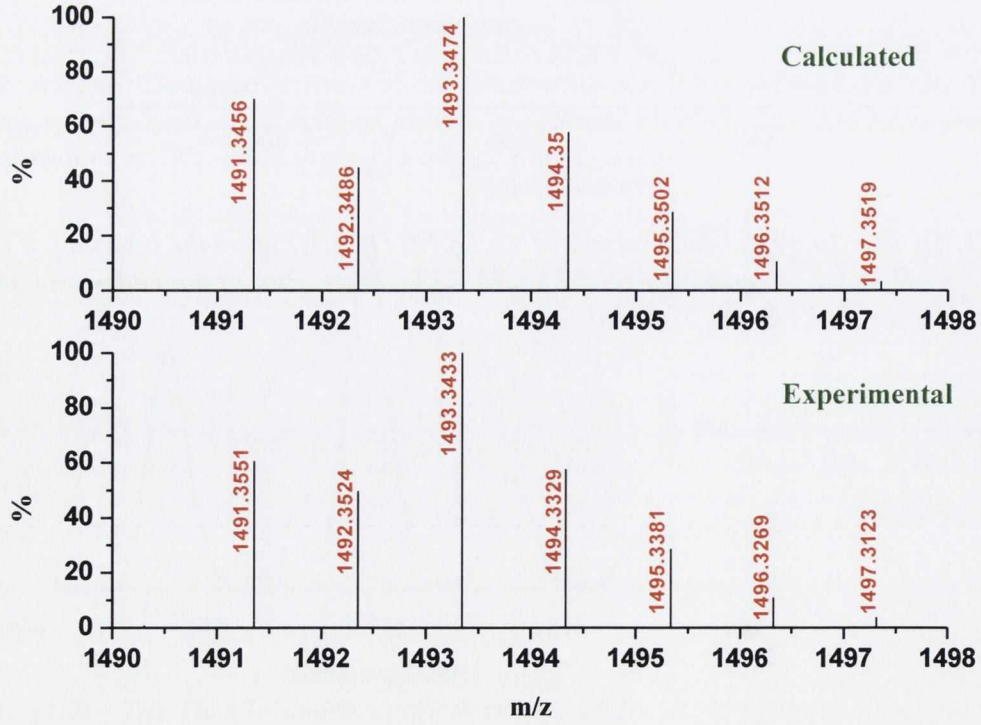

Figure A1.8b: *The ESMS of* **Eu.69** *displaying the expected $^{151}Eu(III)$ isotopic distribution pattern for the* [**Eu.69**+2(CF_3SO_3)]$^{+}$ *species.*

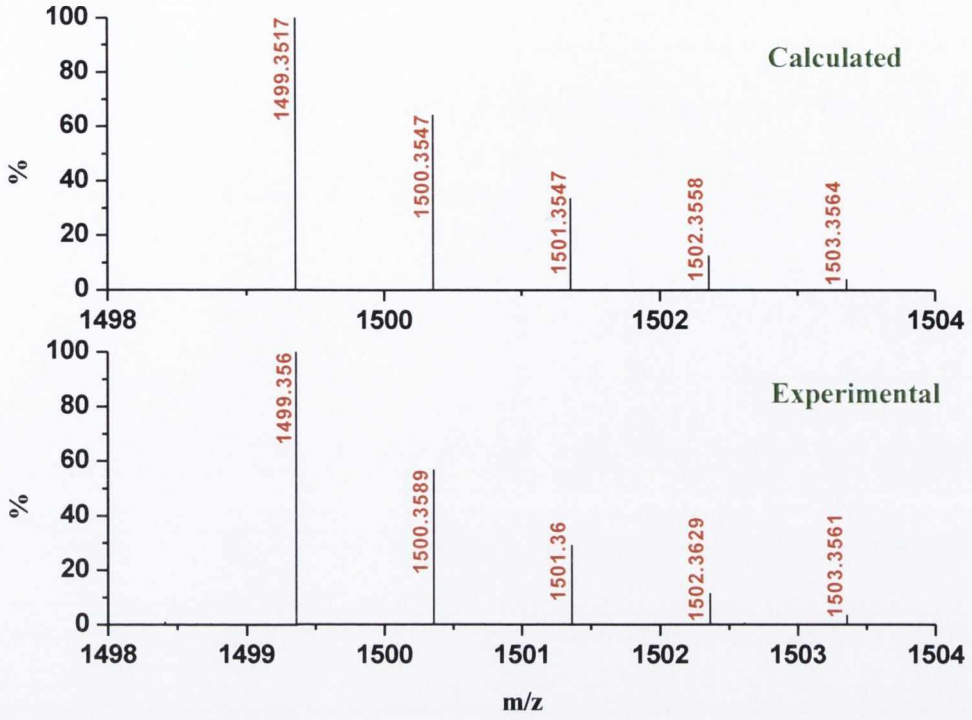

Figure A1.8c: *MALDI-TOF analysis of* **Tb.69** *displaying the expected* $^{159}Tb(III)$ *isotopic distribution pattern for the* [**Tb.69**+2(CF_3SO_3)]$^+$ *species.*

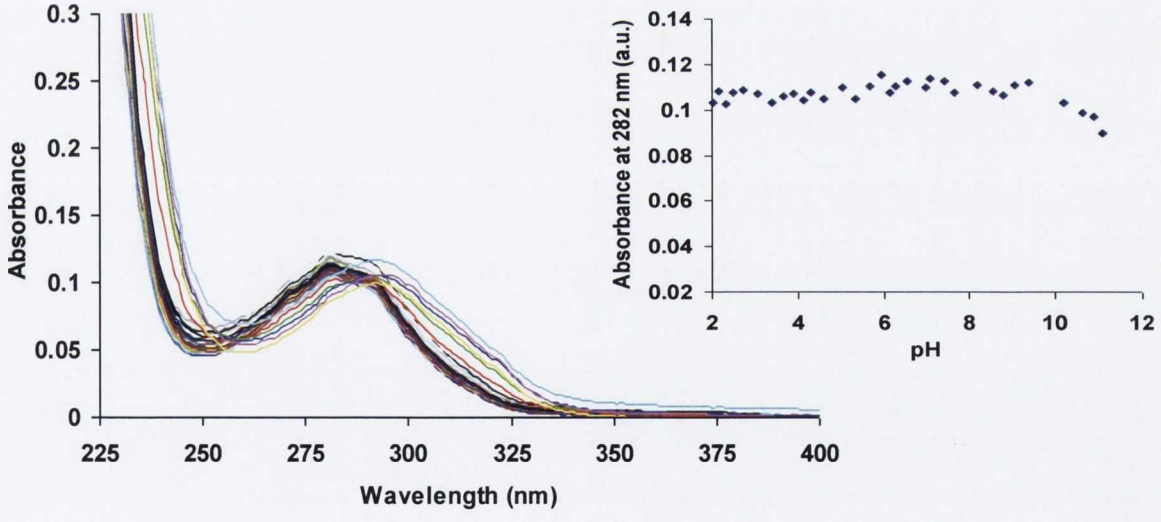

Figure A1.9a: *The UV-vis absorption spectra of* **Eu.69** *as a function of pH in a mixed MeOH:*H_2O *(1:99 v/v) solution [I = 0.1M* NEt_4ClO_4 *(TEAP)]. Inset: Changes in the UV-vis absorption of* **Eu.69** *at 282 nm.*

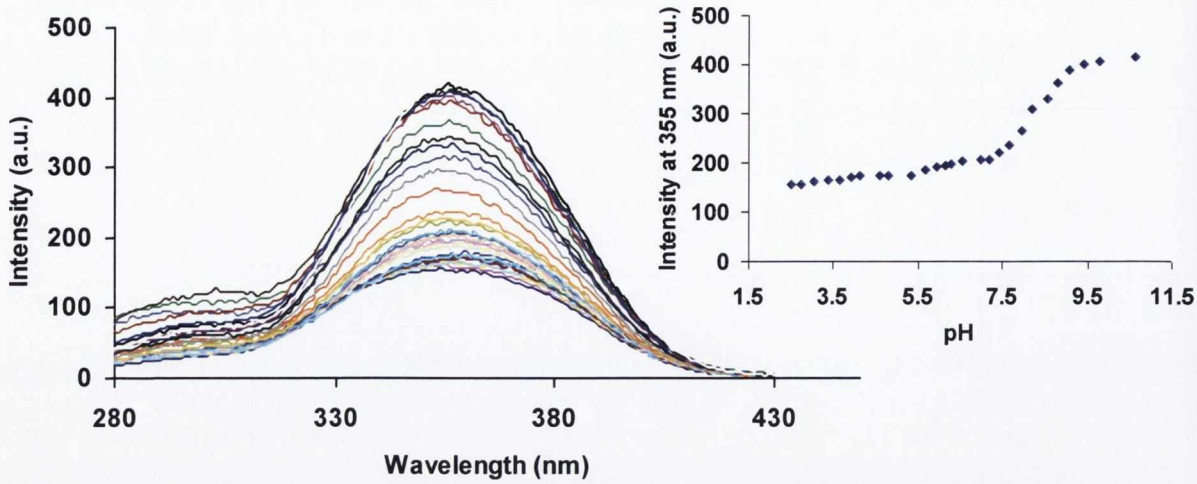

Figure A1.9b: *The fluorescence emission spectra of* ***Eu.69*** *as a function of pH in a mixed MeOH:H_2O (1:99 v/v) solution [I = 0.1M NEt_4ClO_4 (TEAP)]. Inset: Changes in the fluorescence spectra of* ***Eu.69*** *at 355 nm.*

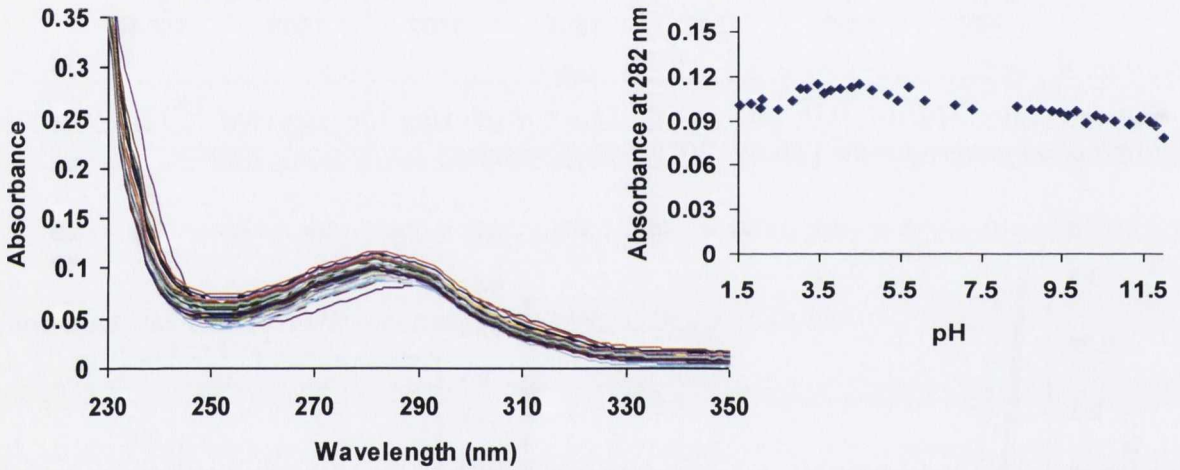

Figure A1.9c: *The UV-vis absorption spectra of* ***Tb.69*** *as a function of pH in a mixed MeOH:H_2O (1:99 v/v) solution [I = 0.1M NEt_4ClO_4 (TEAP)]. Inset: Changes in the UV-vis absorption of* ***Tb.69*** *at 282 nm.*

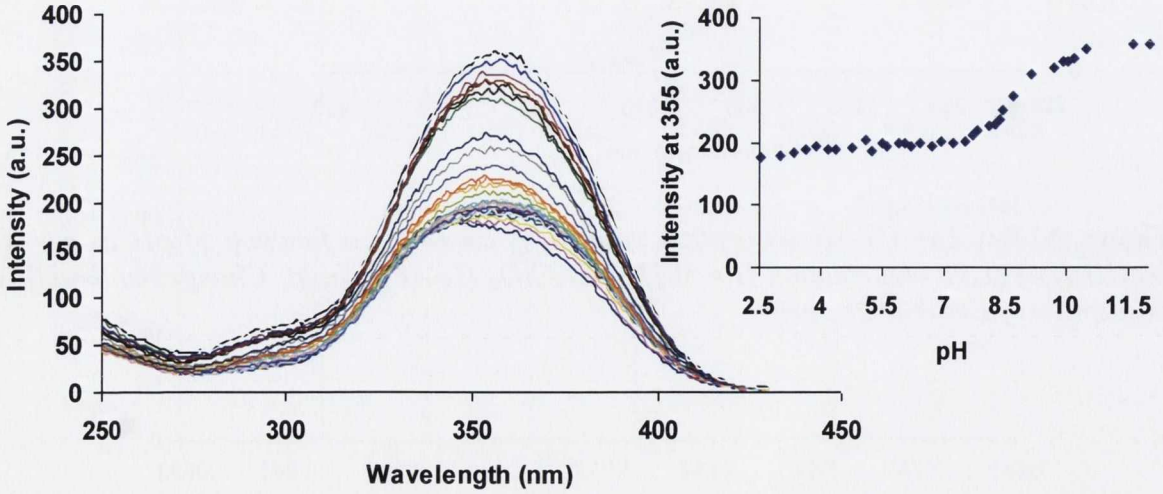

Figure A1.9d: *The fluorescence spectra of* ***Tb.69*** *as a function of pH in a mixed MeOH:H_2O (1:99 v/v) solution [I = 0.1M NEt_4ClO_4 (TEAP)]. Inset: Changes in the fluorescence spectra of* ***Tb.69*** *at 355 nm.*

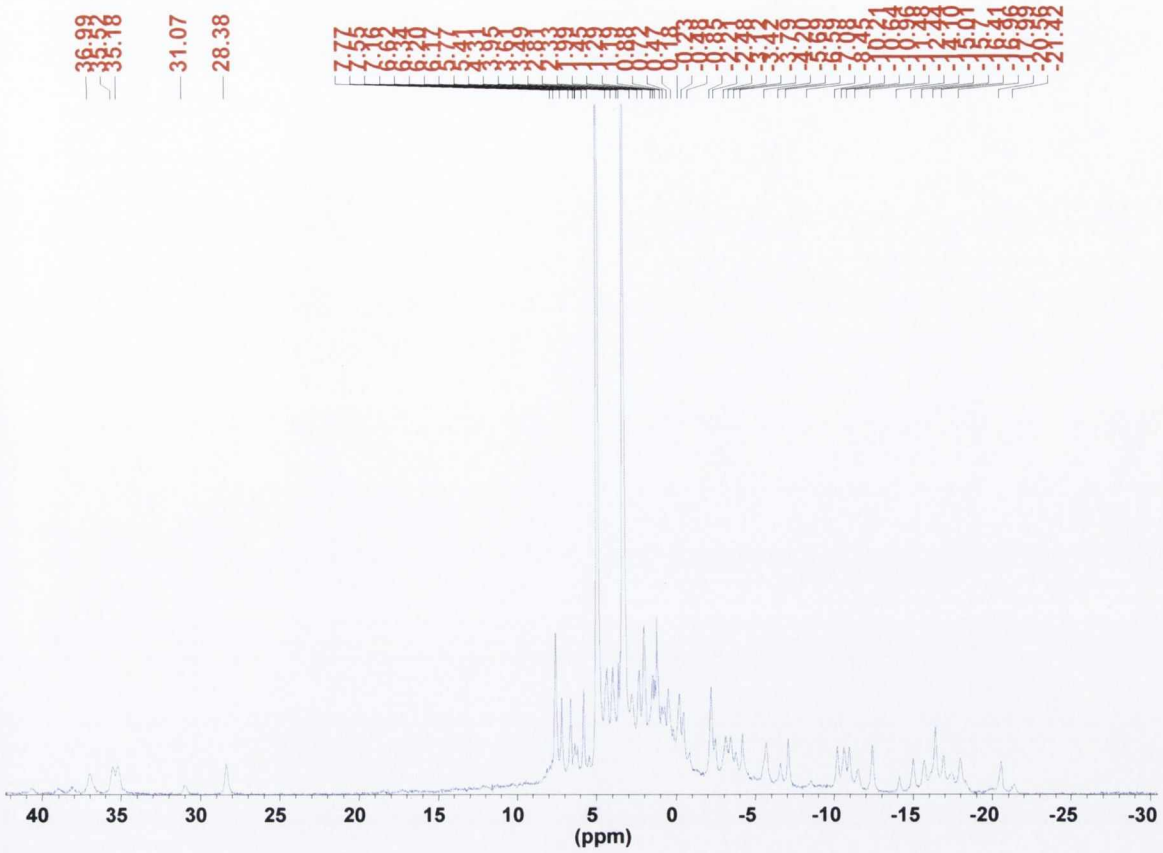

Figure A1.10a: *The ^{1}H NMR spectrum (400 MHz, CD_3OD) of* ***Eu.69.Na****.*

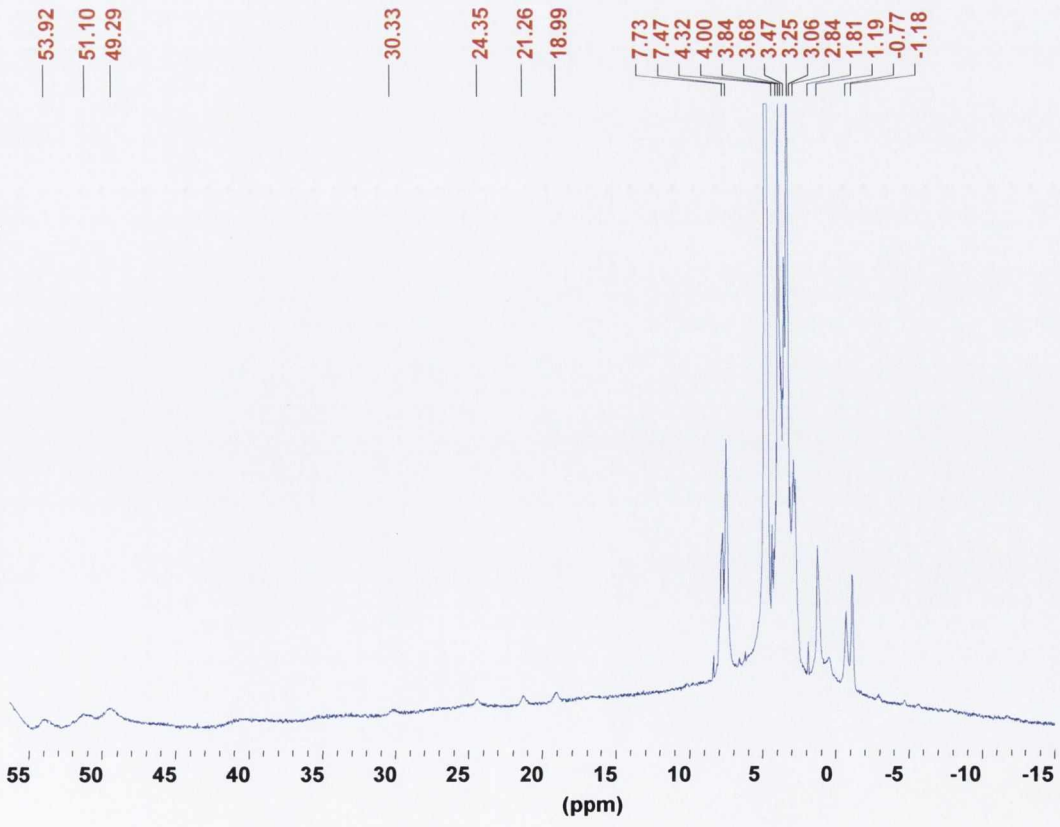

Figure A1.10b: *The ^{1}H NMR spectrum (400 MHz, CD_3OD) of* ***Tb.69.Na****.*

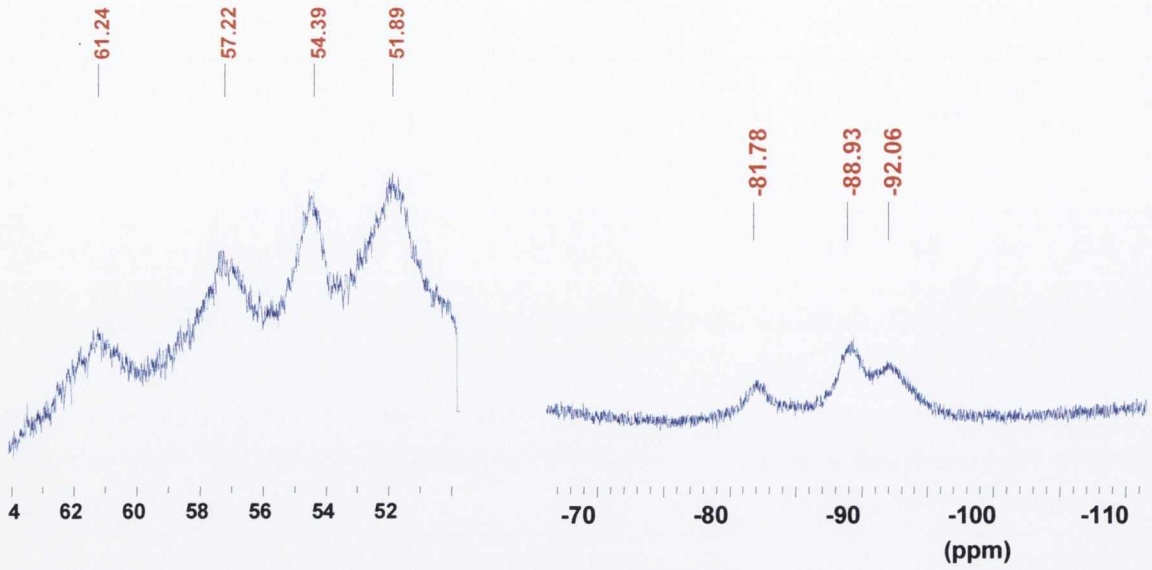

Figure A1.10c: *The ^{1}H NMR spectrum (400 MHz, CD_3OD) of* ***Tb.69.Na****.*

Figure A1.11a: *The ESMS of* ***Eu.69.Na*** *displaying the expected $^{151}Eu(III)$ isotopic distribution pattern for the* [**Eu.69.Na**-5Na+3H]$^{+}$ *species.*

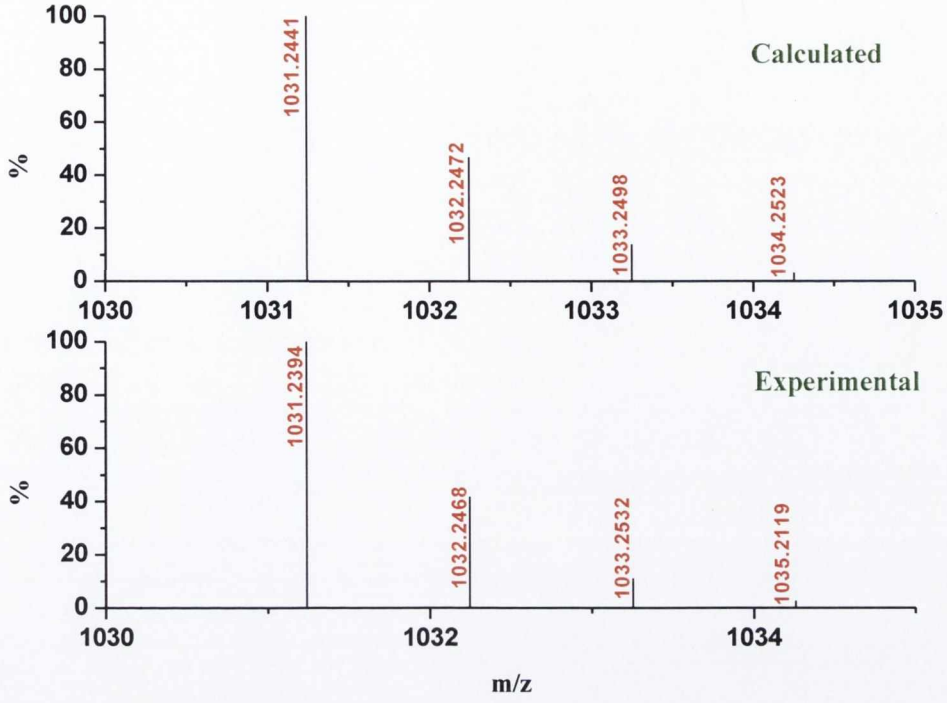

Figure A1.11b: *MALDI-TOF analysis of* ***Tb.69.Na*** *displaying the expected* $^{159}Tb(III)$ *isotopic distribution pattern for the* [**Tb.69.Na**-6Na+4H]$^{+}$ *species.*

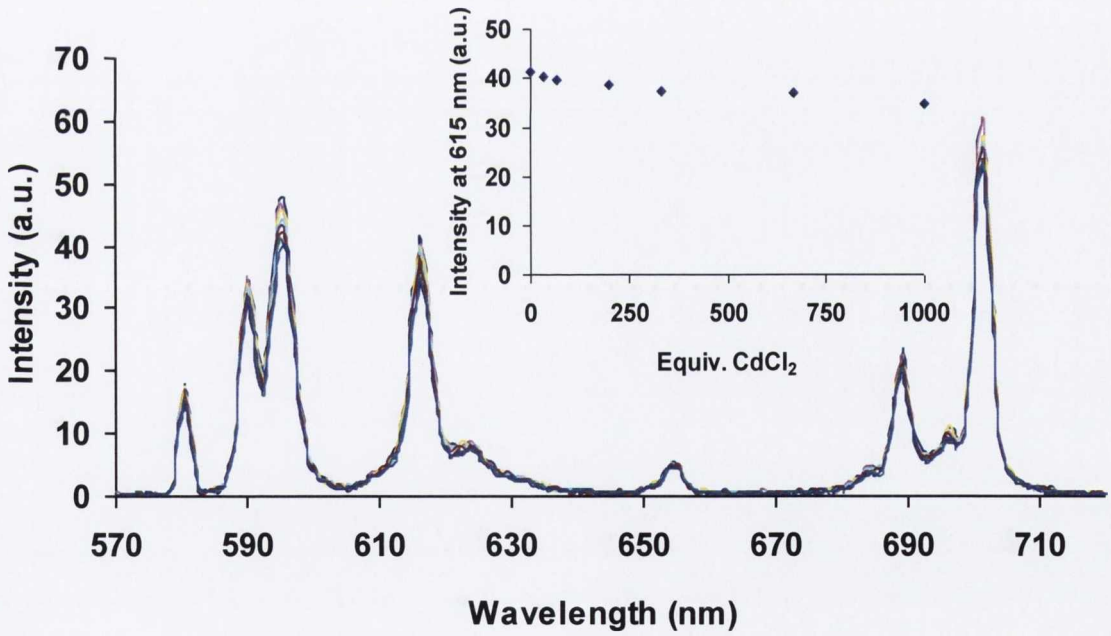

Figure A1.12a: *The Eu(III) luminescence response of* ***Eu.69.Na*** *(10 μM) upon the addition of* $CdCl_2$ *at pH = 7.4 (20 mM HEPES,* 135 mM KCl*). Inset: Plot of the emission intensity at 615 nm with equivalents of* $CdCl_2$ *added.*

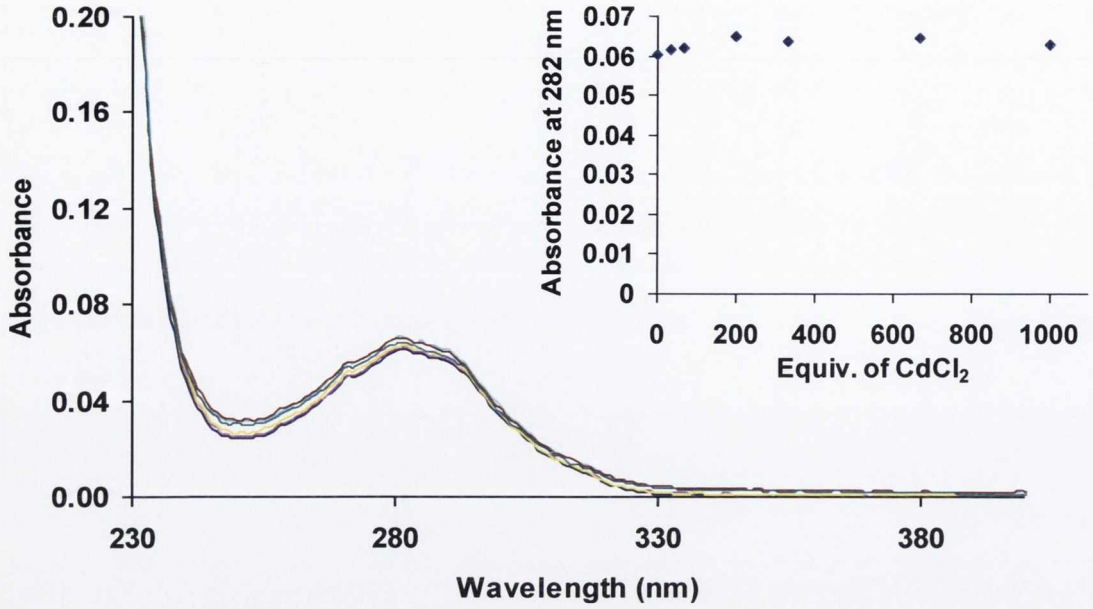

Figure A1.12b: *Changes in the UV-vis absorption spectra of* ***Eu.69.Na*** *in the presence of* $CdCl_2$ *at pH = 7.4 (20 mM HEPES, 135 mM KCl). Inset: Plot of absorbance at 282 nm vs. equivalents of* $CdCl_2$.

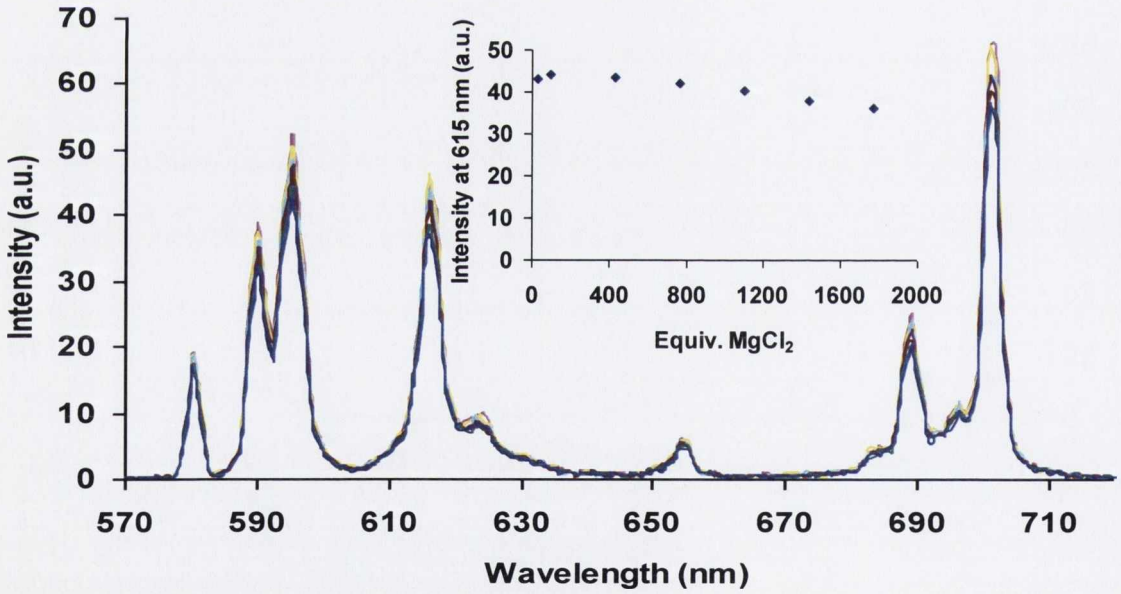

Figure A1.12c: *The Eu(III) luminescence response of* ***Eu.69.Na*** *(10 μM) upon the addition of* $MgCl_2$ *at pH = 7.4 (20 mM HEPES,* 135 mM KCl*). Inset: Plot of the emission intensity at 615 nm with equivalents of* $MgCl_2$ *added.*

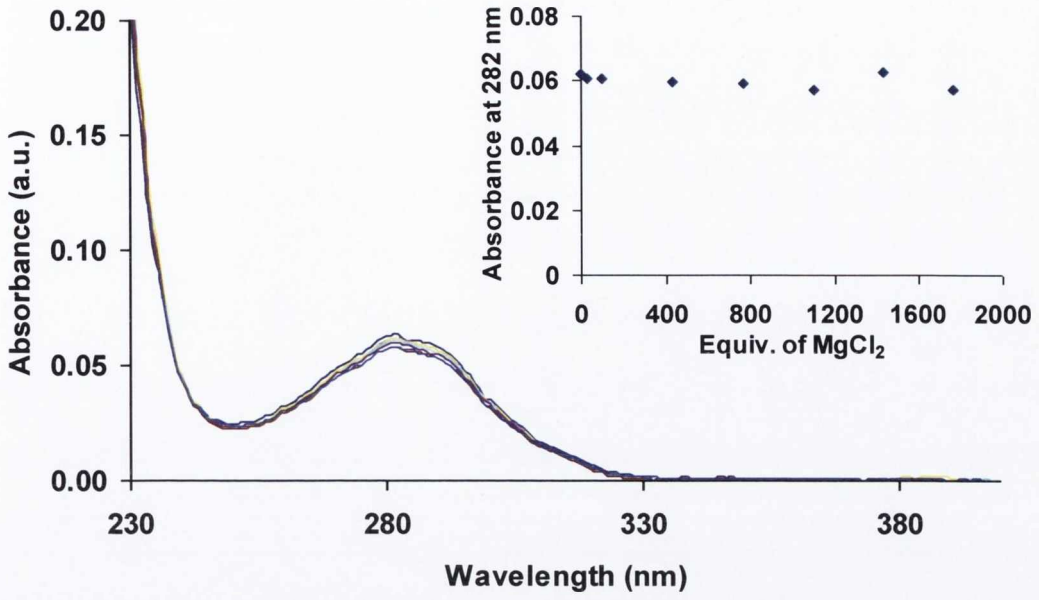

Figure A1.12d: *Changes in the UV-vis absorption spectra of* ***Eu.69.Na*** *in the presence of* $MgCl_2$ *at pH = 7.4 (20 mM HEPES, 135 mM KCl). Inset: Plot of absorbance at 282 nm vs. equivalents of* $MgCl_2$.

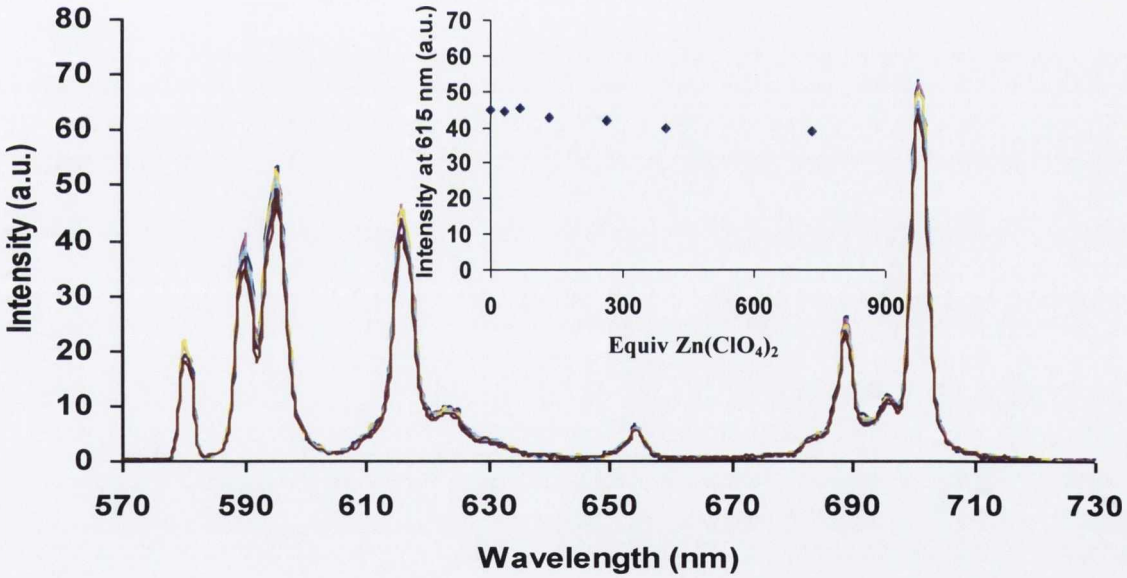

Figure A1.12e: *The Eu(III) luminescence response of* ***Eu.69.Na*** *(10 μM) upon the addition of* $Zn(ClO_4)_2$ *at pH = 7.4 (20 mM HEPES,* 135 mM KCl*). Inset: Plot of the emission intensity at 615 nm with equivalents of* $Zn(ClO_4)_2$ *added.*

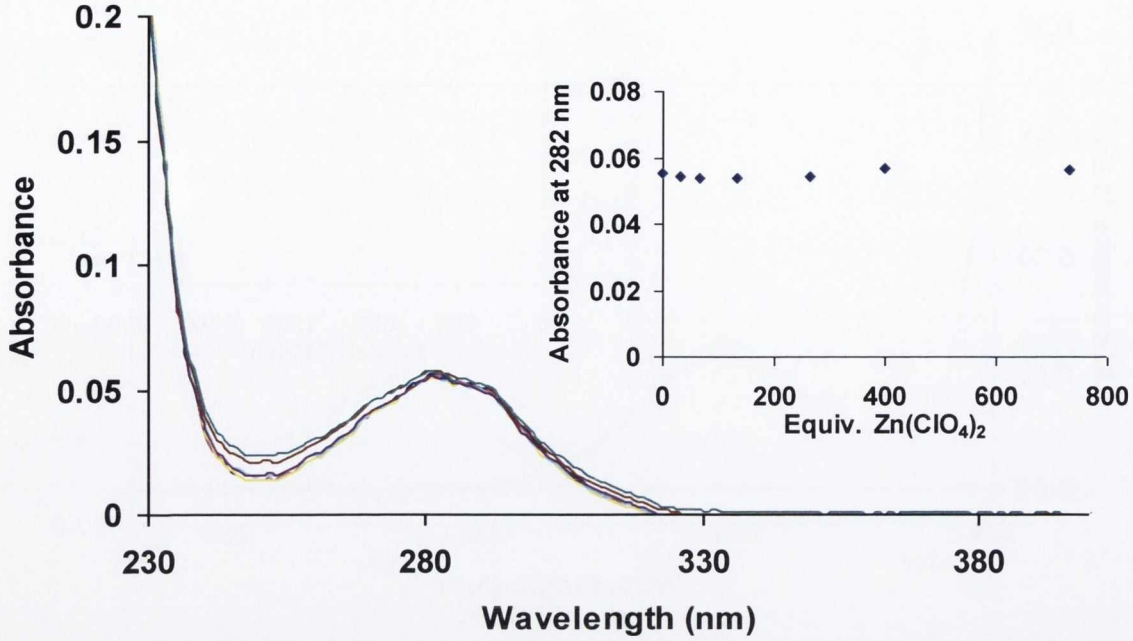

Figure A1.12f: *Changes in the UV-vis absorption spectra of* ***Eu.69.Na*** *in the presence of* $Zn(ClO_4)_2$ *at pH = 7.4 (20 mM HEPES, 135 mM KCl). Inset: Plot of absorbance at 282 nm vs. equivalents of* $Zn(ClO_4)_2$.

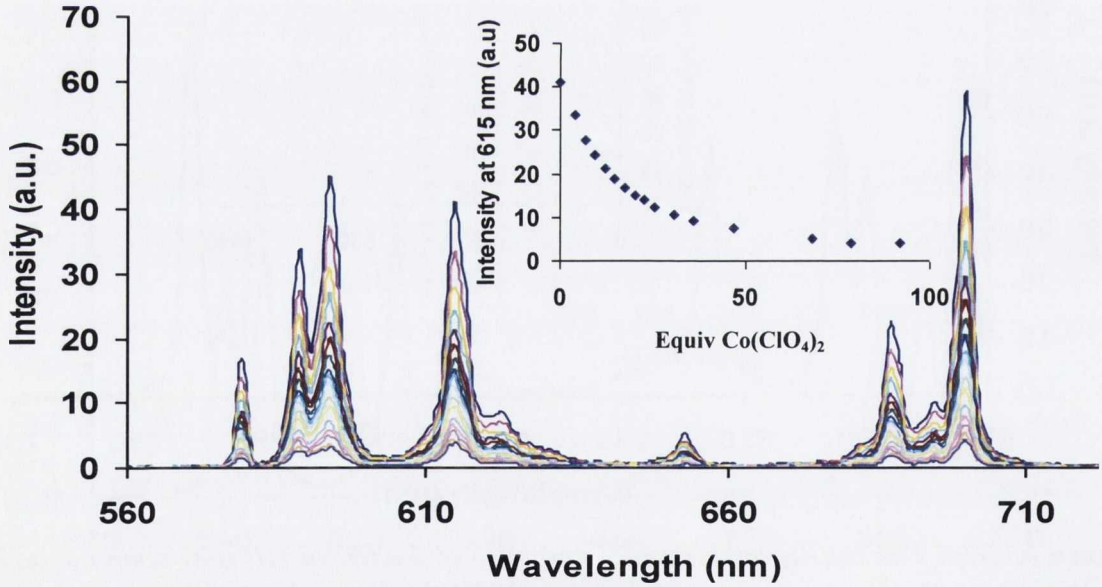

Figure A1.12g: *The Eu(III) luminescence response of* ***Eu.69.Na*** *(10 μM) upon the addition of* $Co(ClO_4)_2$ *at pH = 7.4 (20 mM HEPES, 135 mM KCl). Inset: Plot of the emission intensity at 615 nm with equivalents of* $Co(ClO_4)_2$ *added.*

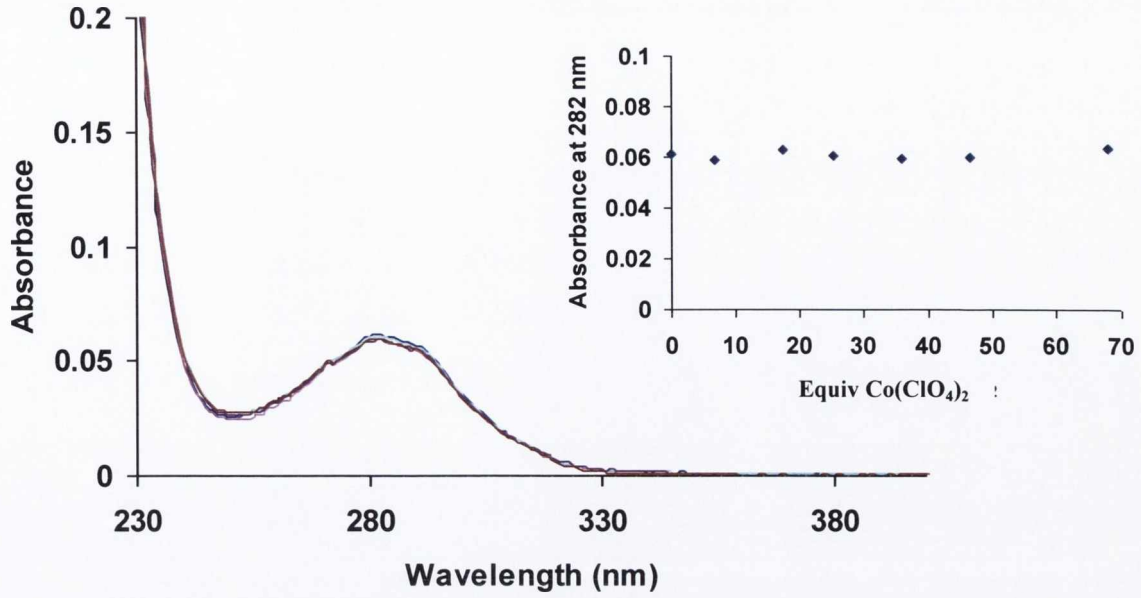

Figure A1.12h: *Changes in the UV-vis absorption spectra of* ***Eu.69.Na*** *in the presence of* $Co(ClO_4)_2$ *at pH = 7.4 (20 mM HEPES, 135 mM KCl). Inset: Plot of absorbance at 282 nm vs. equivalents of* $Co(ClO_4)_2$.

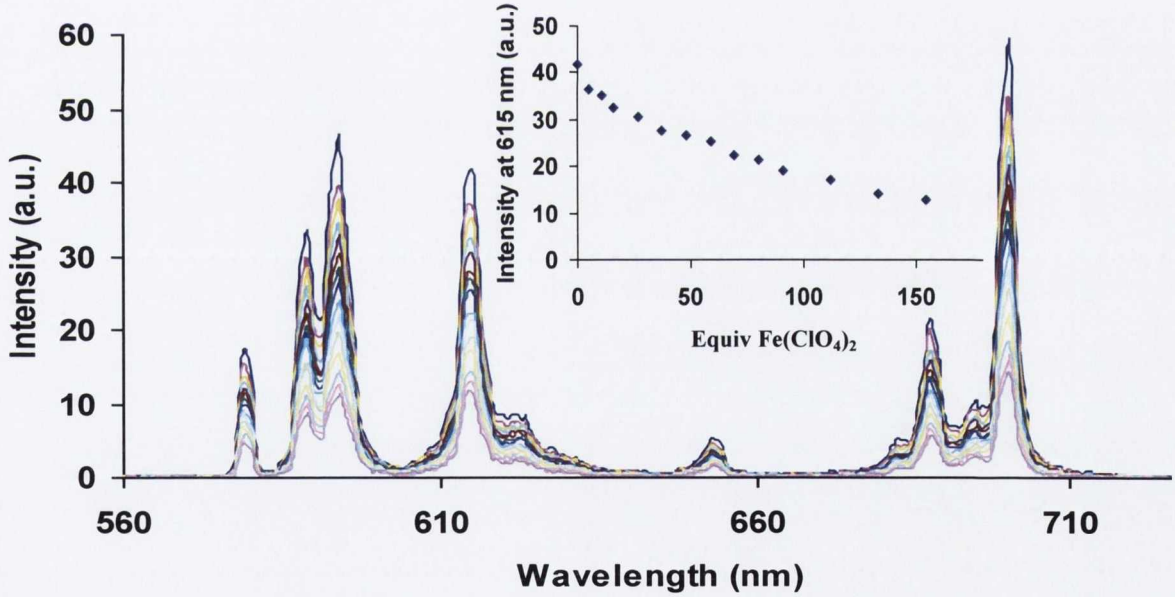

Figure A1.12i: *The Eu(III) luminescence response of* ***Eu.69.Na*** *(10 μM) upon the addition of* $Fe(ClO_4)_2$ *at pH = 7.4 (20 mM HEPES, 135 mM KCl). Inset: Plot of the emission intensity at 615 nm with equivalents of* $Fe(ClO_4)_2$ *added.*

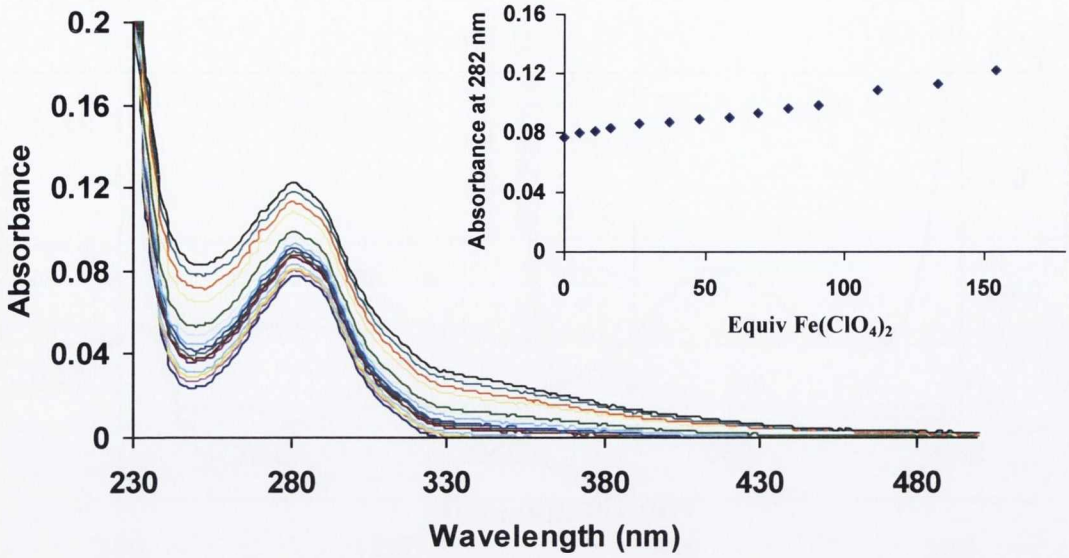

Figure A1.12j: *Changes in the UV-vis absorption spectra of* ***Eu.69.Na*** *in the presence of* $Fe(ClO_4)_2$ *at pH = 7.4 (20 mM HEPES, 135 mM KCl). Inset: Plot of absorbance at 282 nm vs. equivalents of* $Fe(ClO_4)_2$.

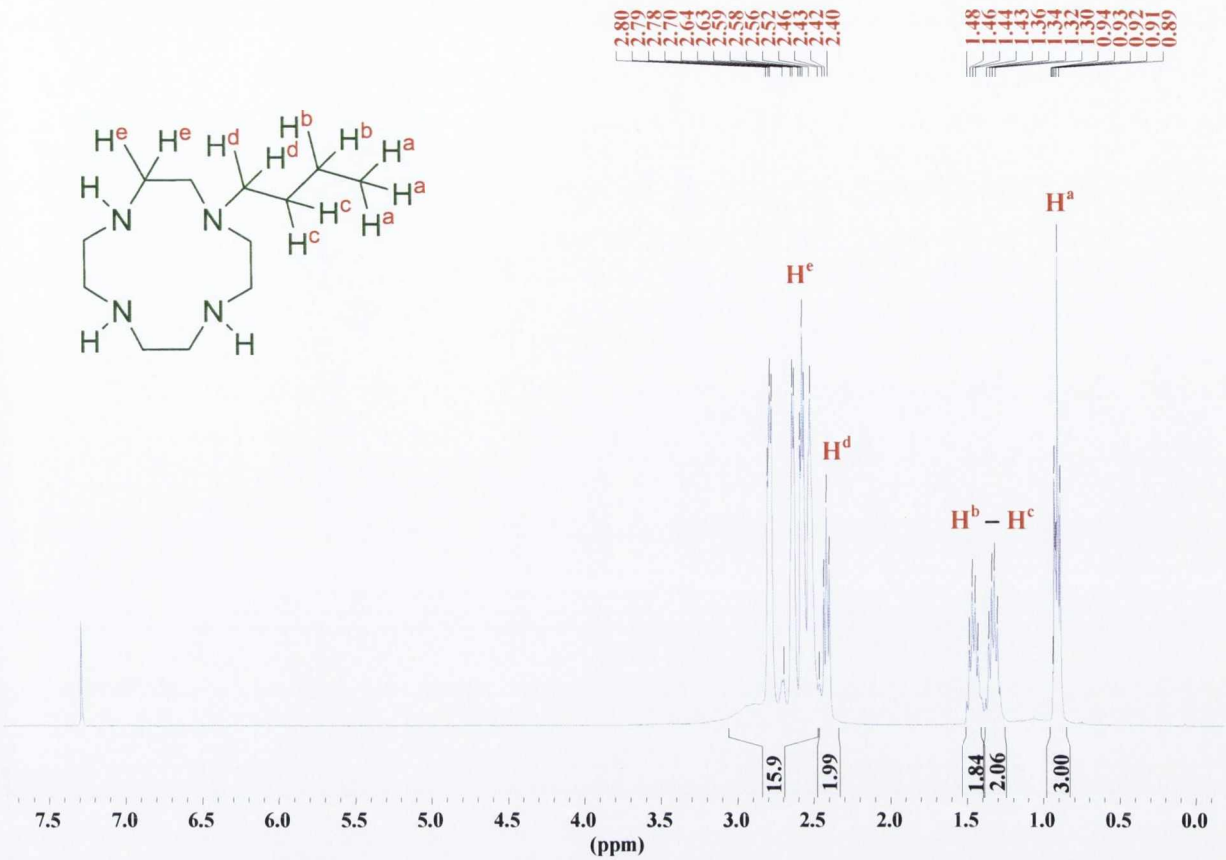

Figure A2.1: *The ^{1}H NMR spectrum ($CDCl_3$, 400 MHz) of ligand* ***83****.*

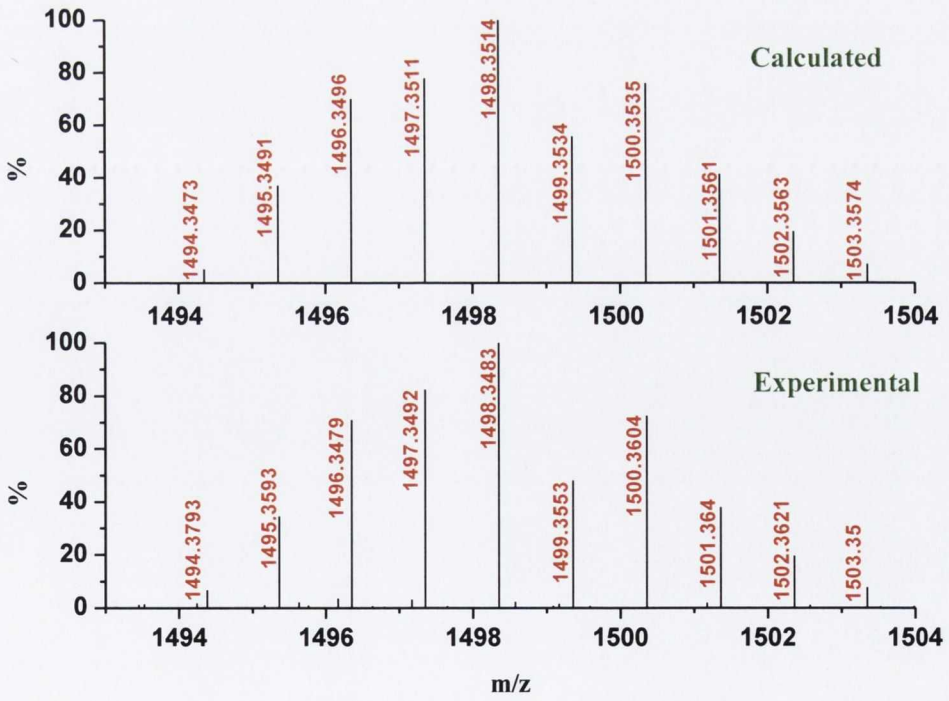

Figure A2.2a: *HRMS using MALDI-TOF analysis of* ***Gd.69*** *displaying the expected $^{157}Gd(III)$ isotopic distribution pattern for the $[M+2(CF_3SO_3)]^+$ species.*

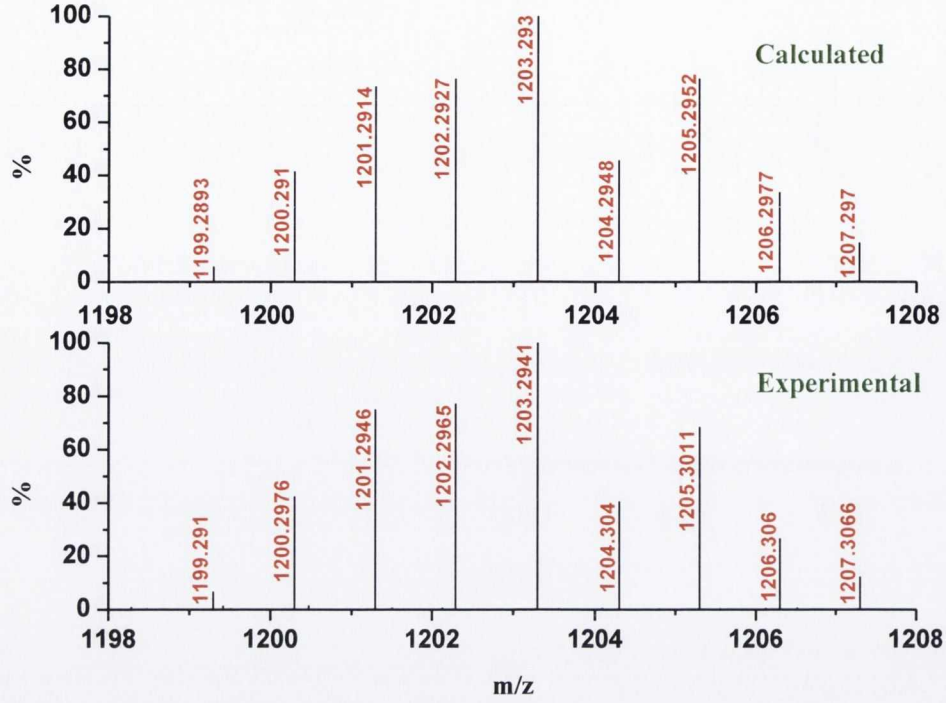

Figure A2.2b: *HRMS using MALDI-TOF analysis of* ***Gd.58*** *displaying the expected* $^{157}Gd(III)$ *isotopic distribution pattern for the* $[M+2(CF_3SO_3)]^+$ *species.*

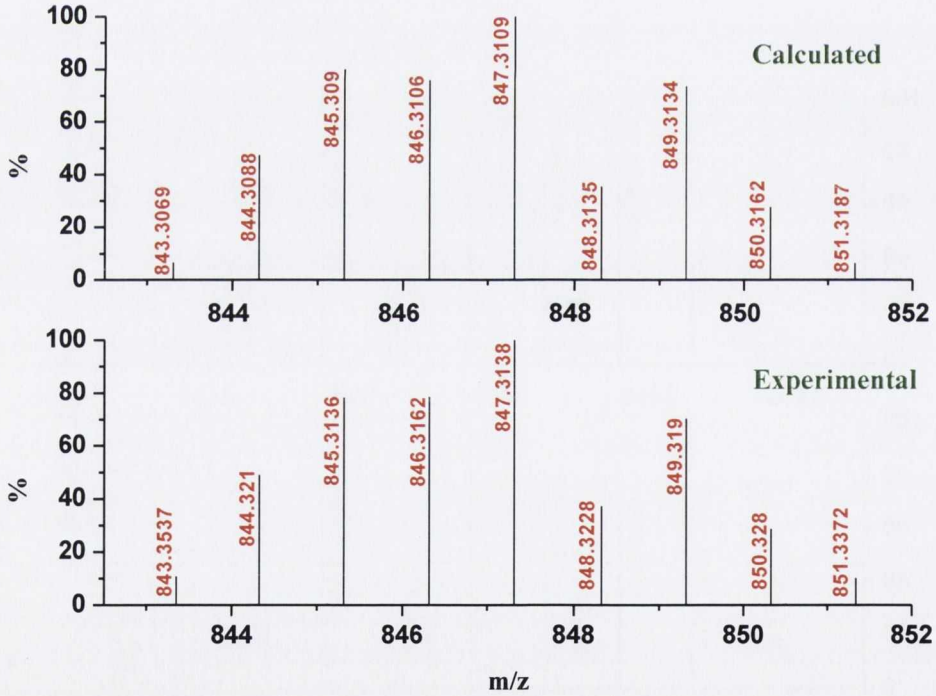

Figure A2.3a: *HRMS using MALDI-TOF analysis of* ***Gd.58.Na*** *displaying the expected* $^{157}Gd(III)$ *isotopic distribution pattern for the* $[M-2Na]^+$ *species.*

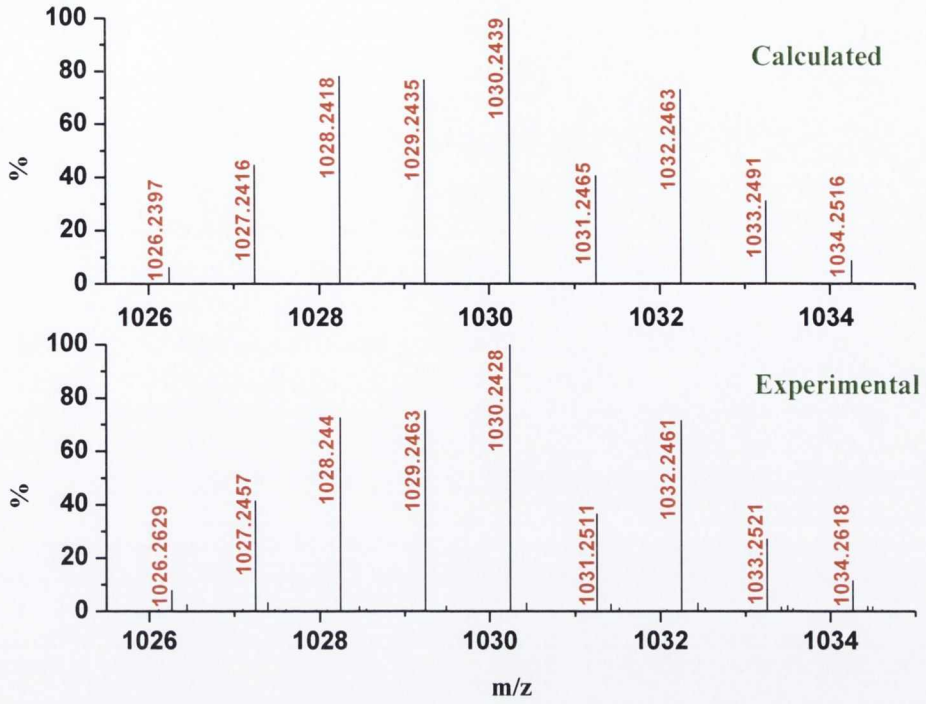

Figure A2.3b: *HRMS using MALDI-TOF analysis of* ***Gd.69.Na*** *displaying the expected* $^{157}Gd(III)$ *isotopic distribution pattern for the* $[M\text{-}6Na+4H]^+$ *species.*

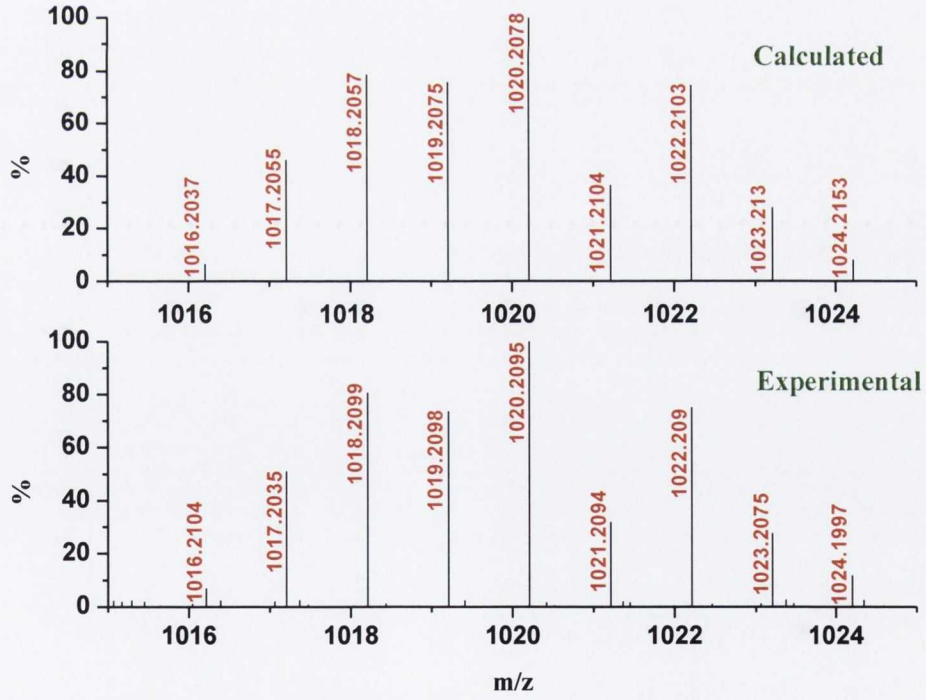

Figure A2.3c: *HRMS using MALDI-TOF analysis of* ***Gd.80.Na*** *displaying the expected* $^{157}Gd(III)$ *isotopic distribution pattern for the* $[M\text{-}8Na+6H]^+$ *species.*

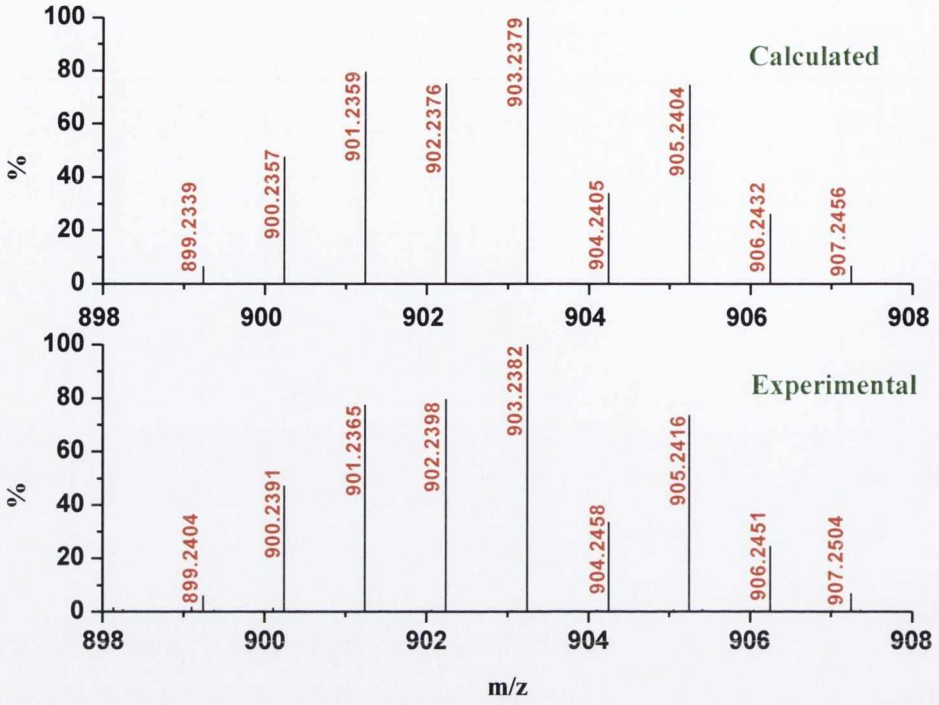

Figure A2.3d: *HRMS using MALDI TOF analysis of* ***Gd.81.Na*** *displaying the expected* $^{157}Gd(III)$ *isotopic distribution pattern for the* $[M\text{-}6Na+4H]^+$ *species.*

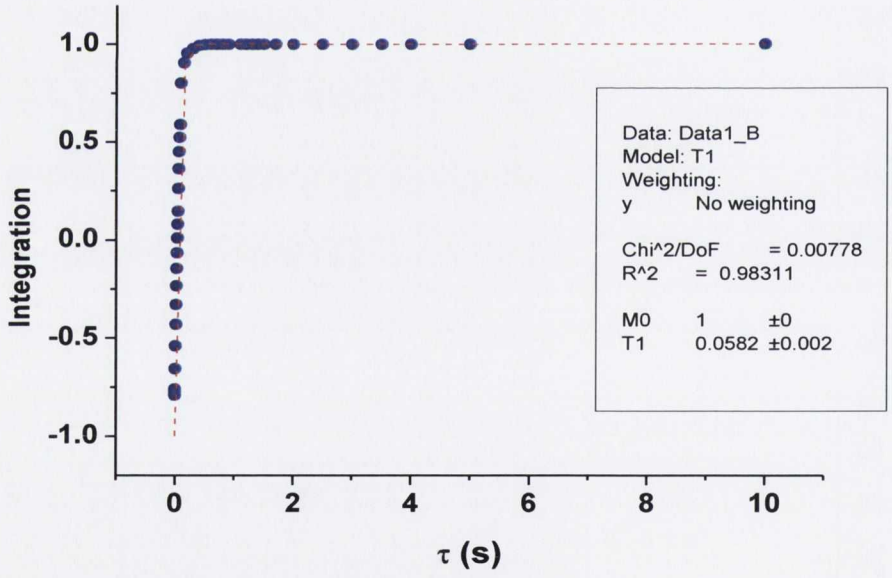

Figure A2.4a: *Plot of integration of the* H_2O *resonances as a function of delay time* τ *using the inversion-recovery NMR sequence in an external magnetic field of 400 MHz at 25°C in the presence of 3.2 mM* ***Gd.58.Na*** *in* D_2O.

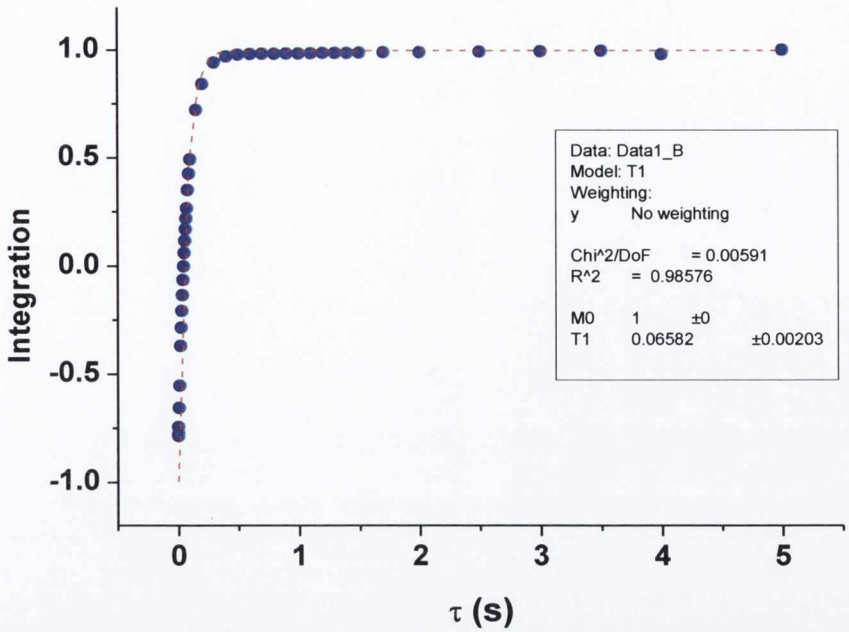

Figure A2.4b: *Plot of integration of the H_2O resonances as a function of delay time τ using the inversion-recovery NMR sequence in an external magnetic field of 600 MHz at 25°C in the presence of 3.2 mM* ***Gd.58.Na*** *in D_2O.*

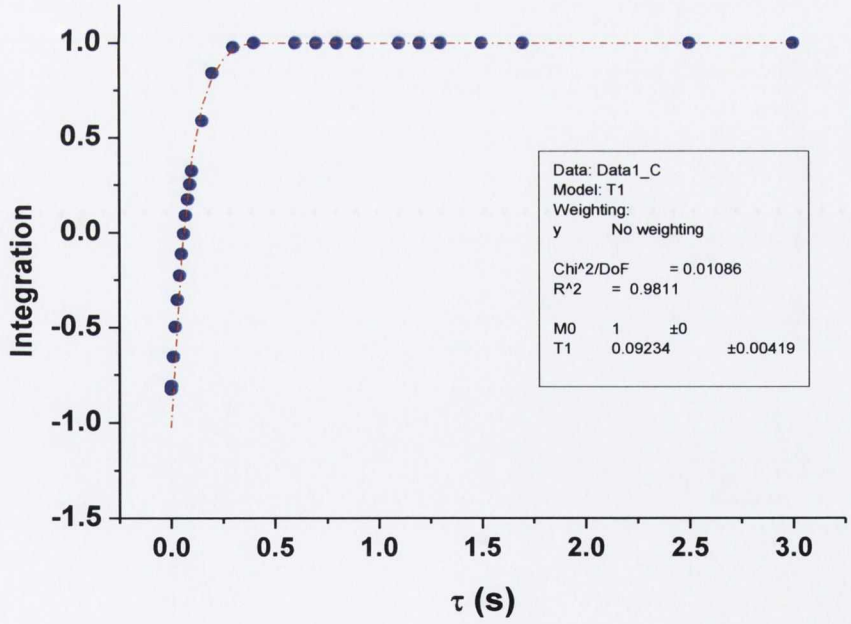

Figure A2.4c: *Plot of integration of the H_2O resonances as a function of delay time τ using the inversion-recovery NMR sequence in an external magnetic field of 600 MHz at 25°C in the presence of 2.6 mM* ***Gd.69.Na*** *in D_2O.*

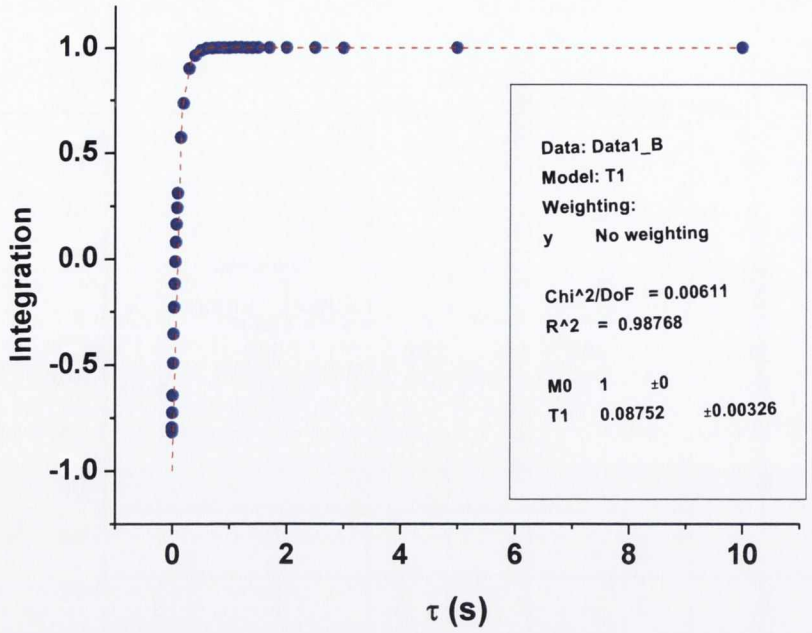

Figure A2.4d: *Plot of integration of the H_2O resonances as a function of delay time τ using the inversion-recovery NMR sequence in an external magnetic field of 400 MHz at 25°C in the presence of 2.8 mM* ***Gd.80.Na*** *in D_2O.*

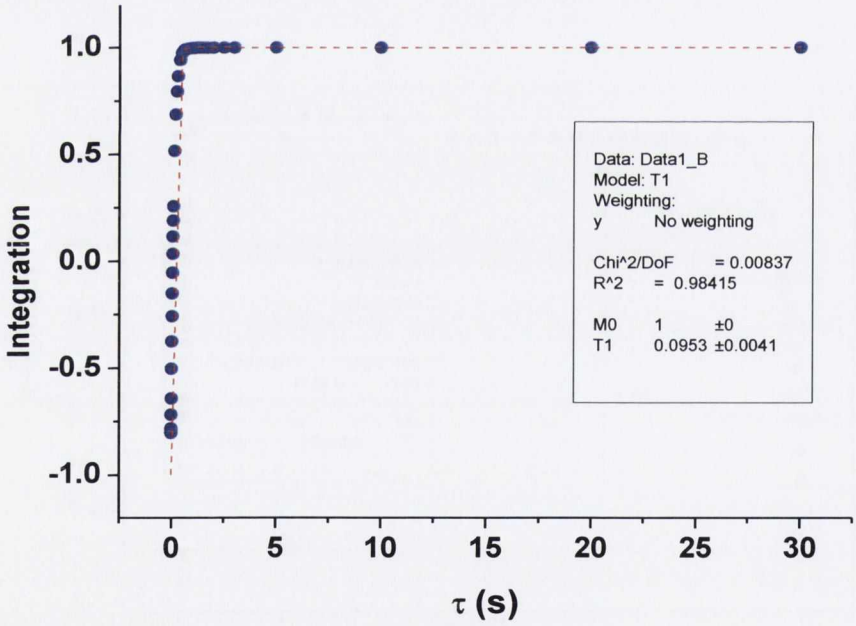

Figure A2.4e: *Plot of integration of the H_2O resonances as a function of delay time τ using the inversion-recovery NMR sequence in an external magnetic field of 600 MHz at 25°C in the presence of 2.8 mM* ***Gd.80.Na*** *in D_2O.*

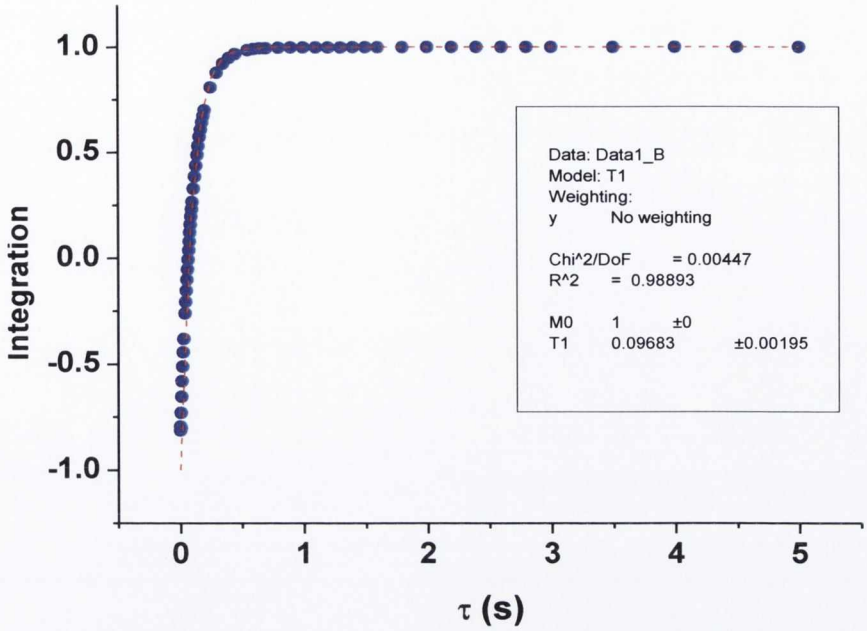

Figure A2.4f: *Plot of integration of the H_2O resonances as a function of delay time τ using the inversion-recovery NMR sequence in an external magnetic field of 400 MHz at 25°C in the presence of 2.1 mM* ***Gd.81.Na*** *in D_2O.*

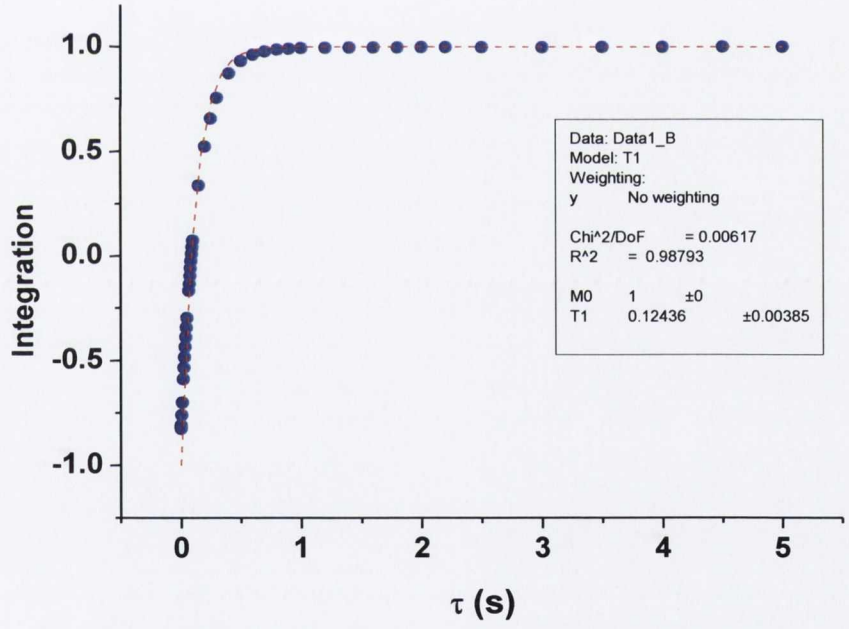

Figure A2.4g: *Plot of integration of the H_2O resonances as a function of delay time τ using the inversion-recovery NMR sequence in an external magnetic field of 600 MHz at 25°C in the presence of 2.1 mM* ***Gd.81.Na*** *in D_2O.*

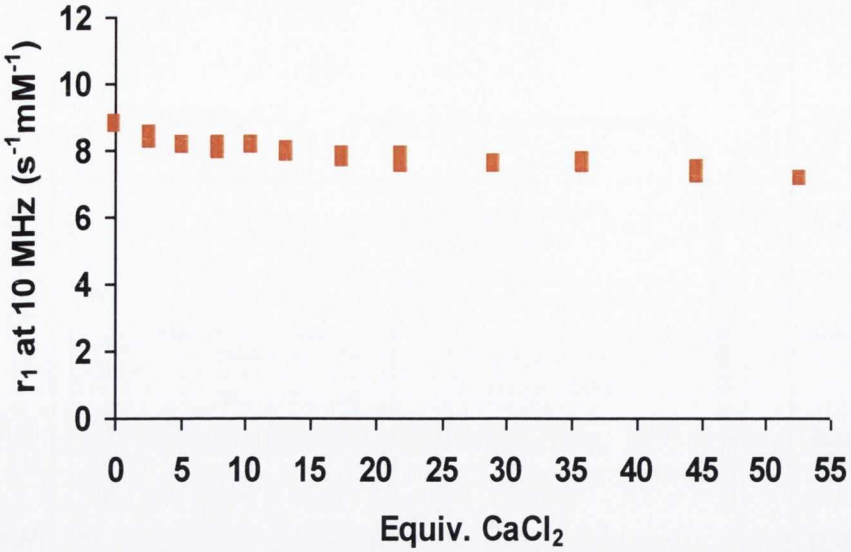

Figure A2.5: *Changes in relaxivity at 10 MHz of Gd.81.Na (2.7 mM) in the presence of $CaCl_2$ (0 – 0.1M) at pH 7.4 (20mM HEPES, 135 mM KCl) at 10 MHz and 25 °C.*

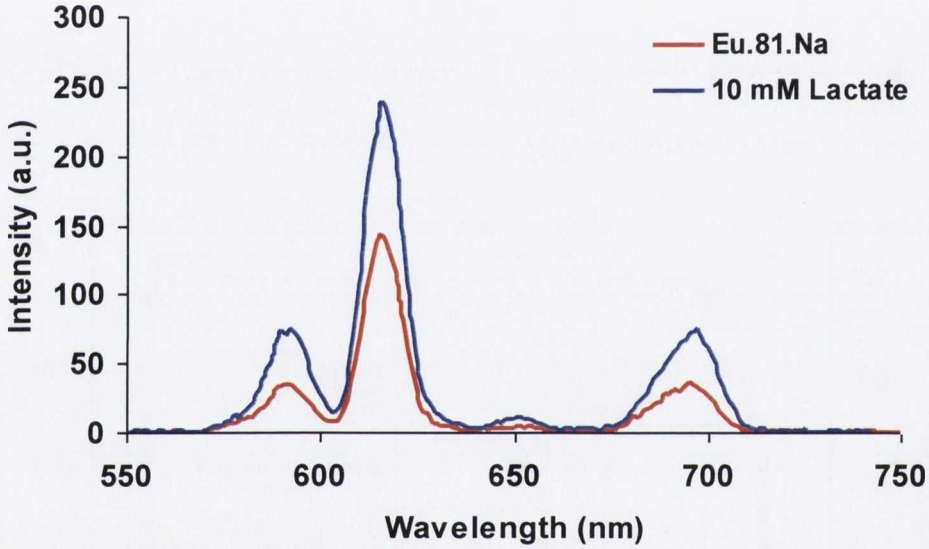

Figure A2.6a: *Changes in the Eu(III) emission response of Eu.81.Na (10 μM) upon the addition of 10 mM lactate.*

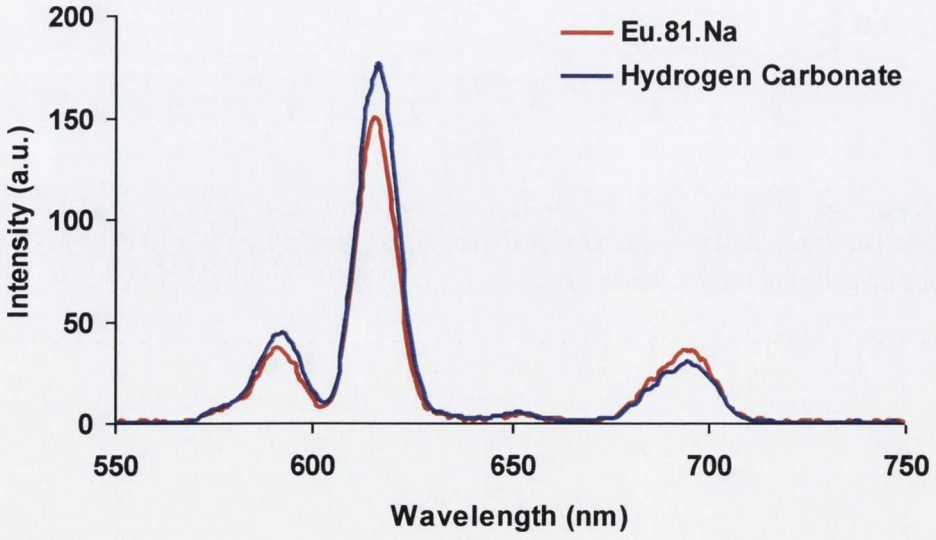

Figure A2.6b: *Changes in the Eu(III) emission response of Eu.81.Na (10 μM) upon the addition of 10 mM hydrogen carbonate.*

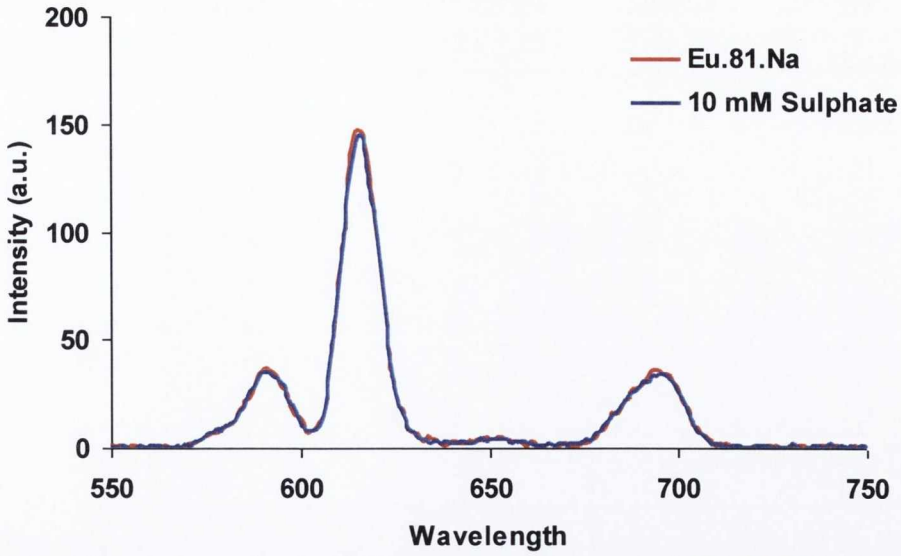

Figure A2.6c: *Changes in the Eu(III) emission response of Eu.81.Na (10 μM) upon the addition of 10 mM sulphate.*

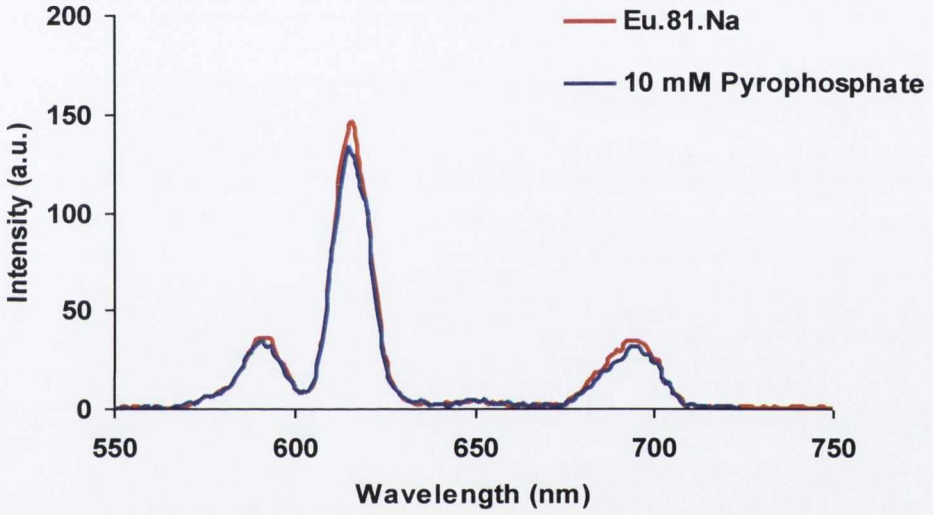

Figure A2.6d: *Changes in the Eu(III) emission response of Eu.81.Na (10 μM) upon the addition of 10 mM pyrophosphate.*

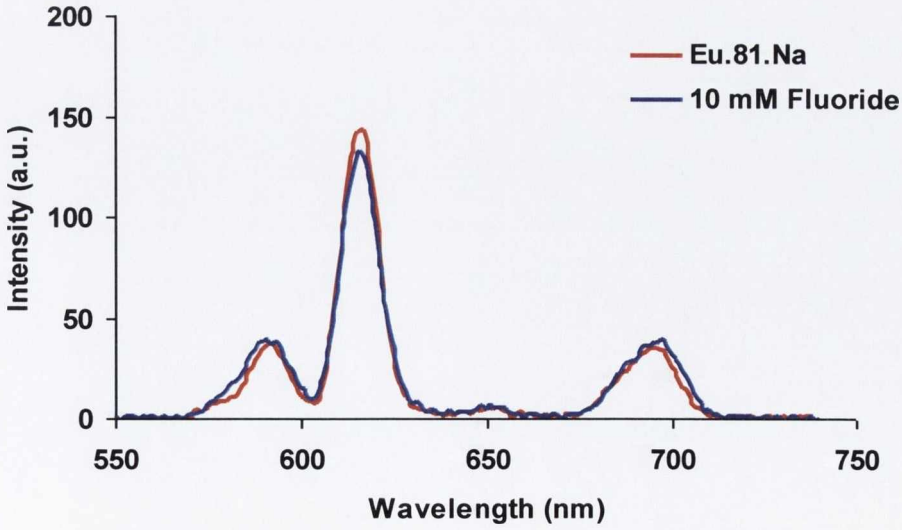

Figure A2.6e: *Changes in the Eu(III) emission response of Eu.81.Na (10 μM) upon the addition of 10 mM fluoride.*

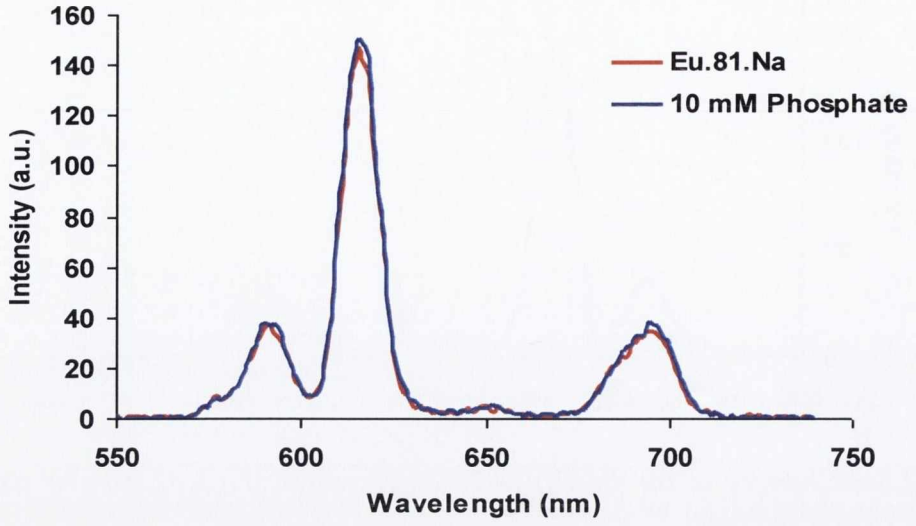

Figure A2.6f: *Changes in the Eu(III) emission response of Eu.81.Na (10 μM) upon the addition of 10 mM phosphate.*

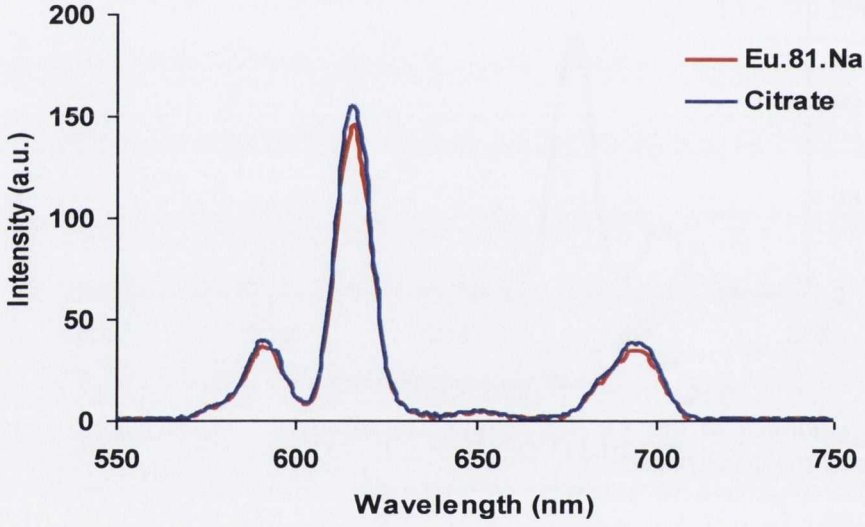

Figure A2.6g: *Changes in the Eu(III) emission response of Eu.81.Na (10 μM) upon the addition of 10 mM citrate.*

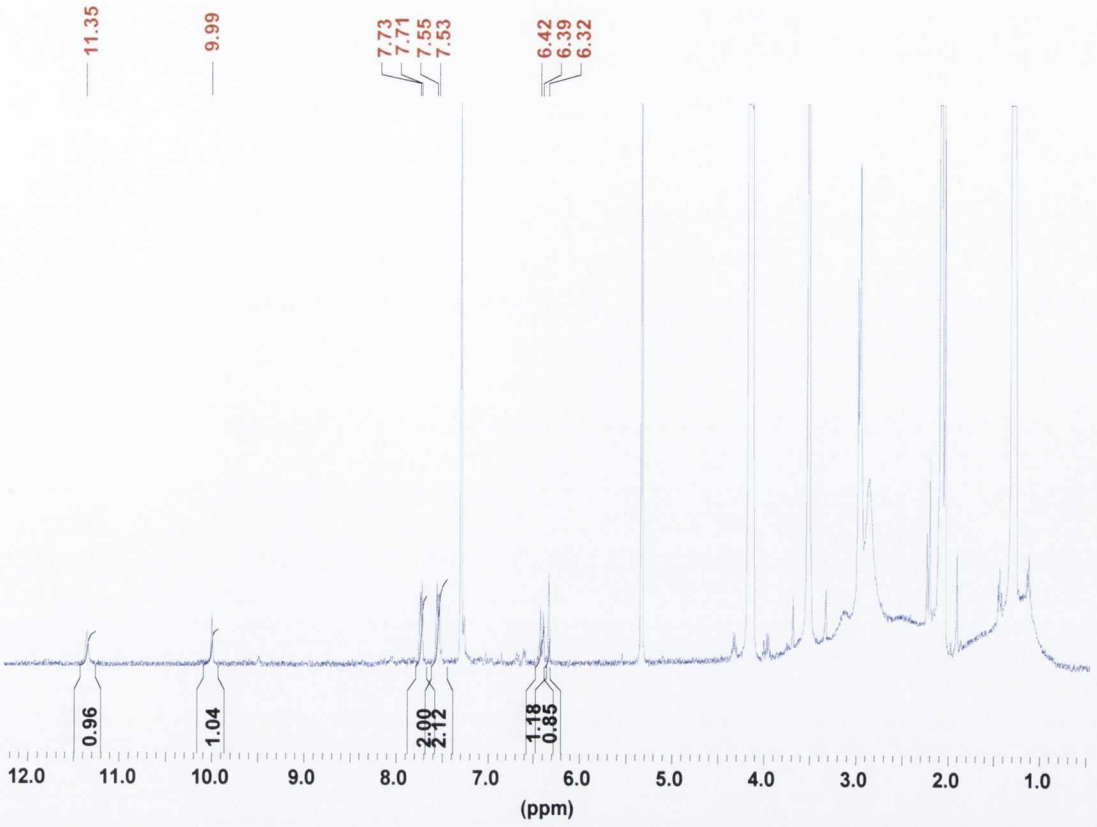

Figure A3.1: *The ^{1}H NMR spectrum (400 MHz, $CDCl_3$) of the crude acid amide derivative 117.*

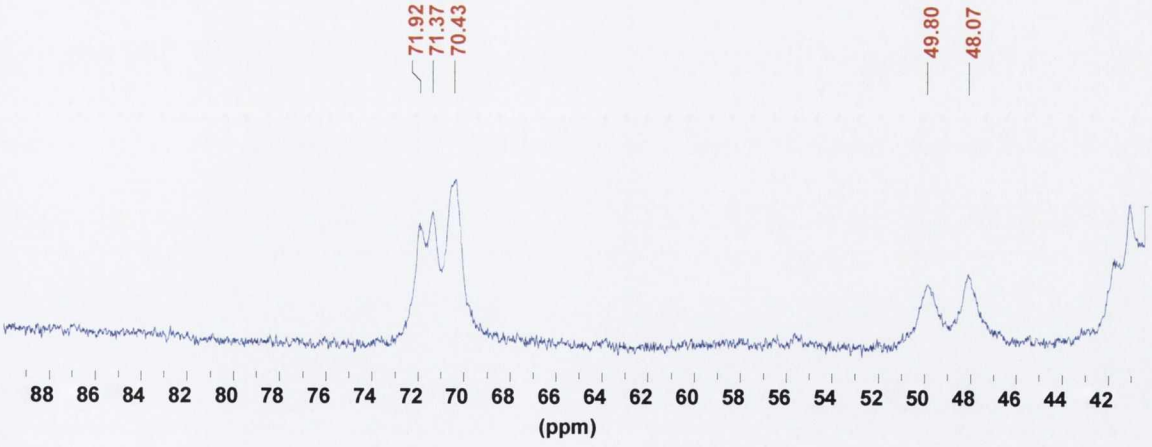

Figure A3.2: *Remainder of the ^{1}H NMR spectrum (400MHz, D_2O) of complex Tb.110.*

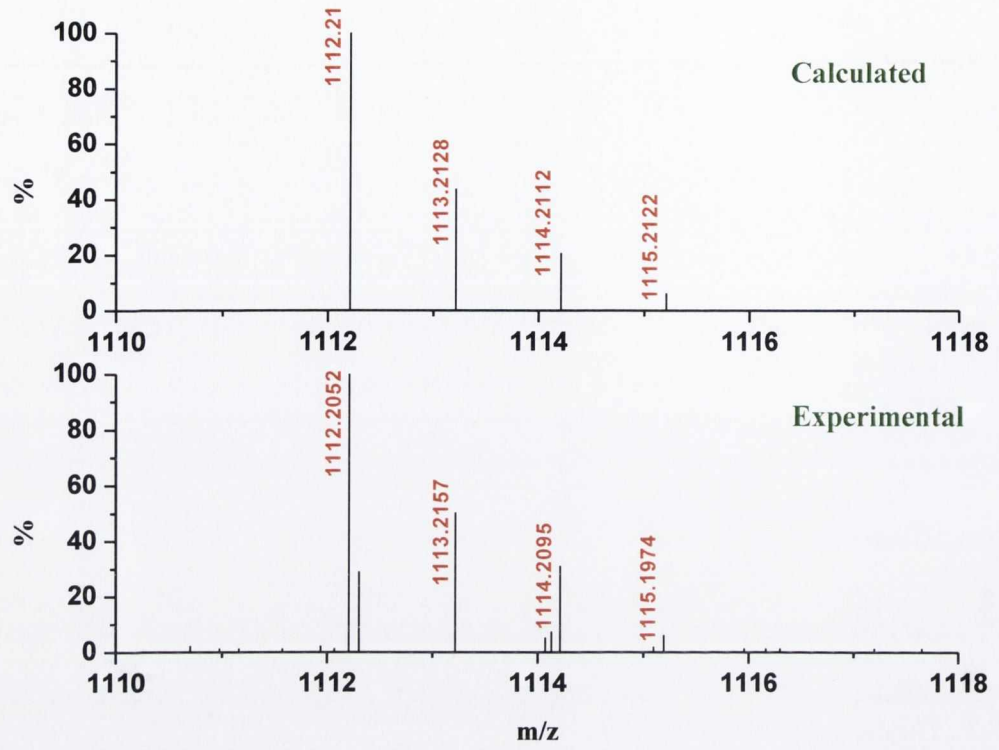

Figure A3.3: *HRMS using MALDI-TOF analysis of* ***Tb.110*** *displaying the expected* Tb^{III} *isotopic distribution pattern for the* $[\mathbf{Tb.110}+2(CF_3SO_3)]^+$ *species.*

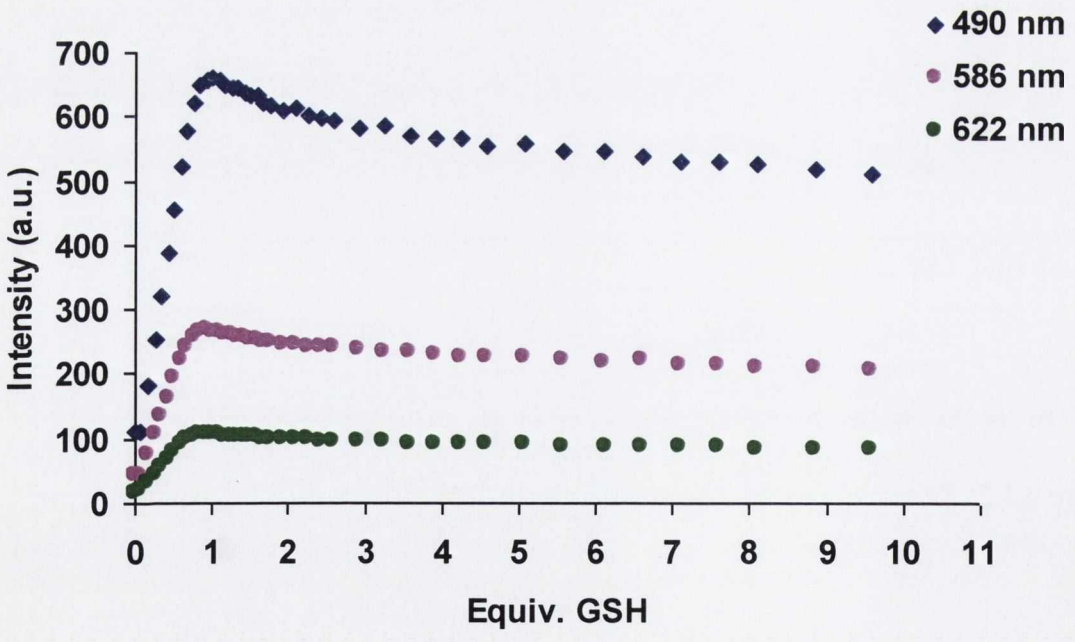

Figure A3.4: *Changes in the Tb(III) emission of* ***Tb.110*** *(10 μM) at 490 nm (J = 6), 586 nm (J = 4) and 622 nm (J = 3) as a function of GSH equivalents at pH = 7.4 (20 mM HEPES, 135 mM KCl).*

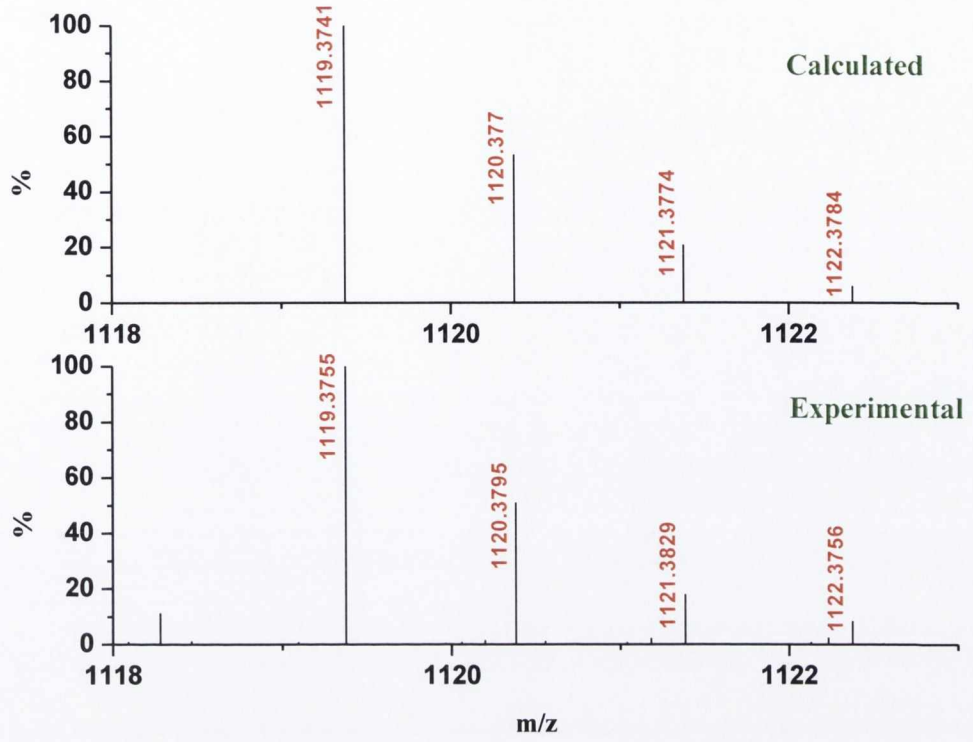

Figure A3.5: *ESMS of Tb.110-GSH displaying the expected $^{159}Tb^{III}$ isotopic distribution patterns for the [Tb.110-GSH-2H)]$^{+}$ species.*

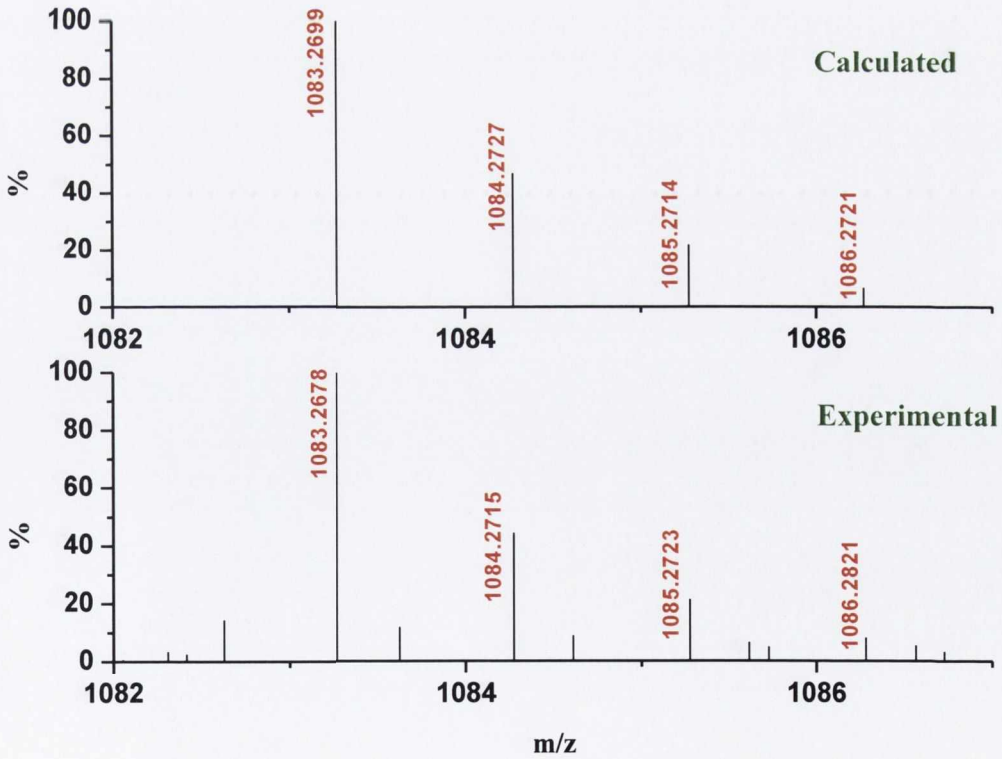

Figure A3.6: *ESMS of Tb.110-Cys displaying the expected $^{159}Tb^{III}$ isotopic distribution patterns for the [Tb.110-Cys-2H)]$^{+}$ species.*

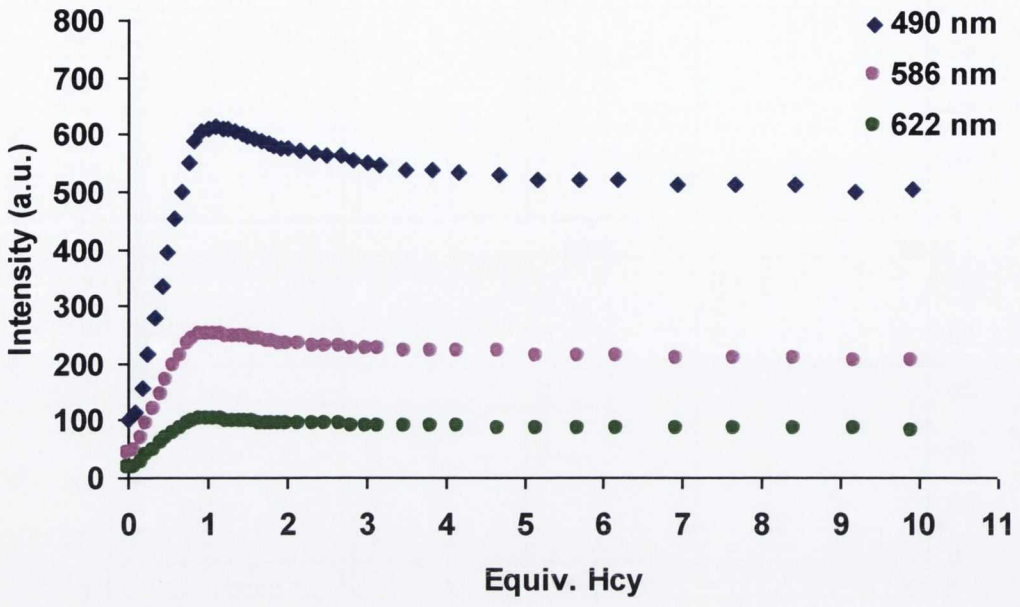

Figure A3.7a: *Changes in the Tb(III) emission of Tb.110 (10 μM) at 490 nm (J = 6), 586 nm (J = 4) and 622 nm (J = 3) as a function of Hcy equivalents at pH = 7.4 (20 mM HEPES, 135 mM KCl).*

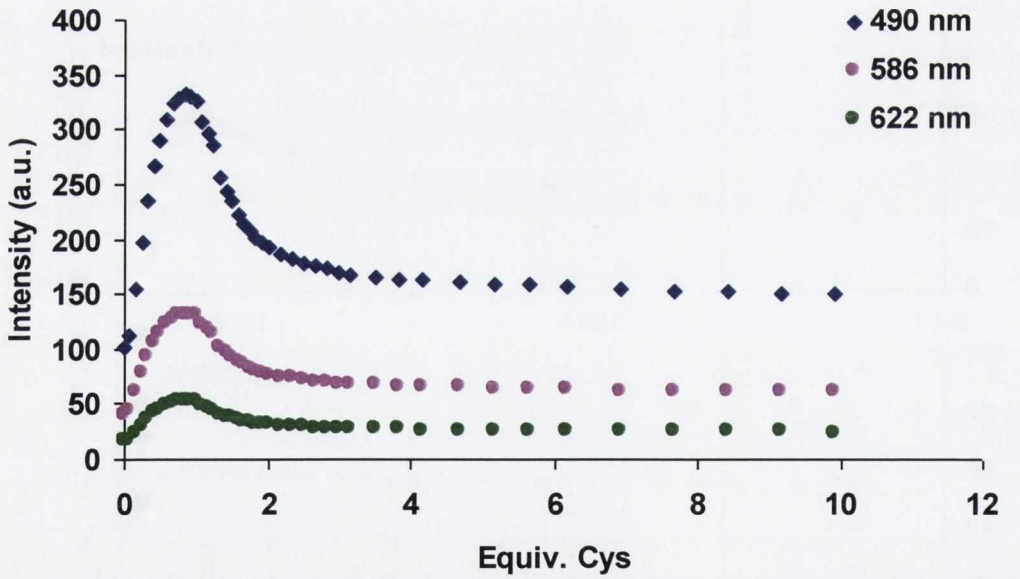

Figure A3.7b: *Changes in the Tb(III) emission of Tb.110 (10 μM) at 490 nm (J = 6), 586 nm (J = 4) and 622 nm (J = 3) as a function of Cys equivalents at pH = 7.4 (20 mM HEPES, 135 mM KCl).*

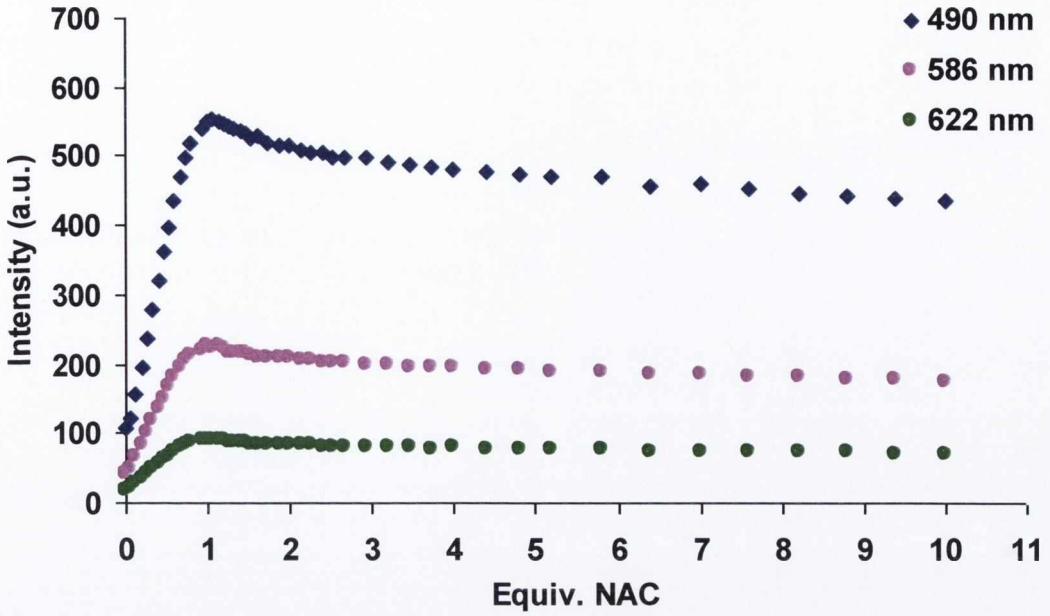

Figure A3.7c: *Changes in the Tb(III) emission of* ***Tb.110*** *(10 μM) at 490 nm (J = 6), 586 nm (J = 4) and 622 nm (J = 3) as a function of NAC equivalents at pH = 7.4 (20 mM HEPES, 135 mM KCl).*

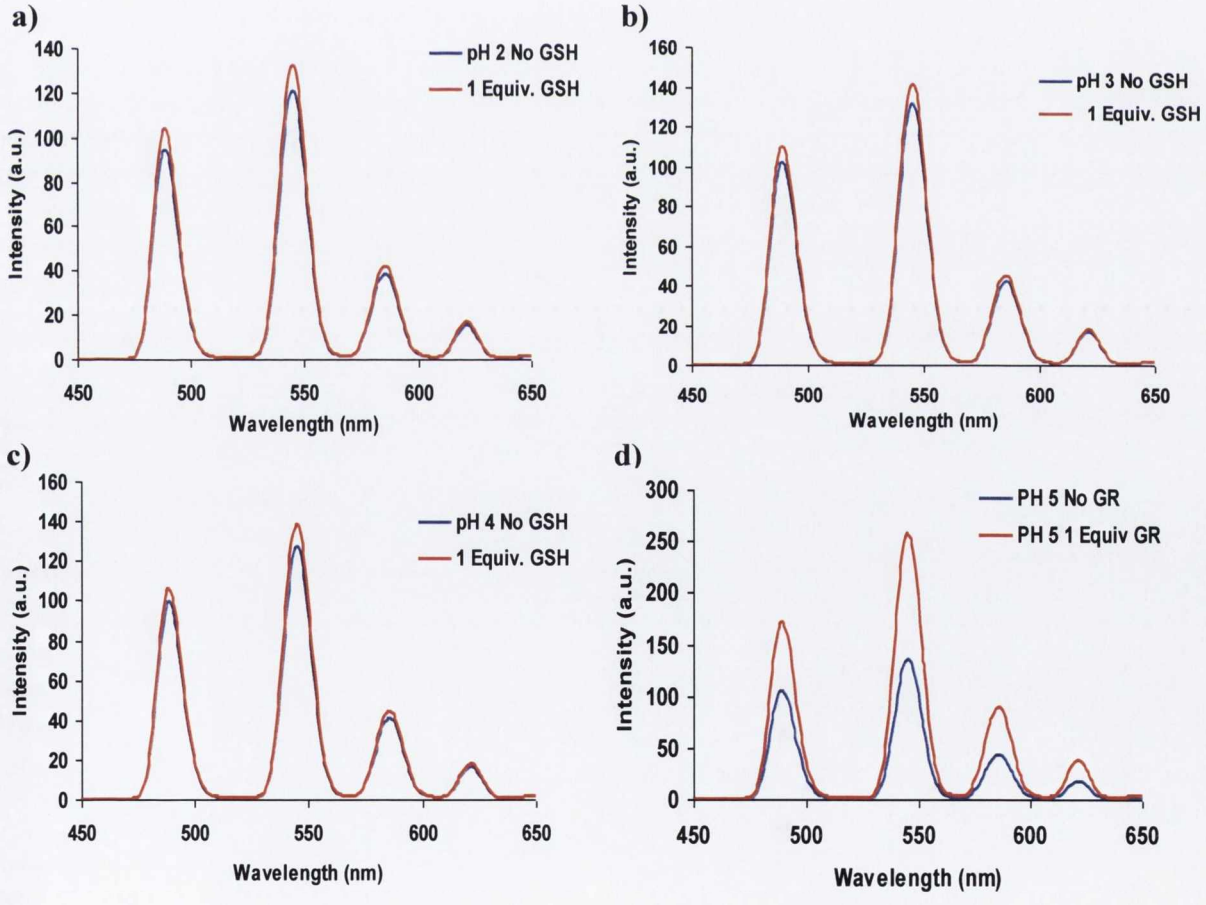

Figure A3.8a: *Changes in the Tb(III) emission of* ***Tb.110*** *(10 μM) at 545 nm at a) pH 2, b) pH 3, c) pH 4 and d) pH 5 upon the addition of 1 equivalent of GSH.*

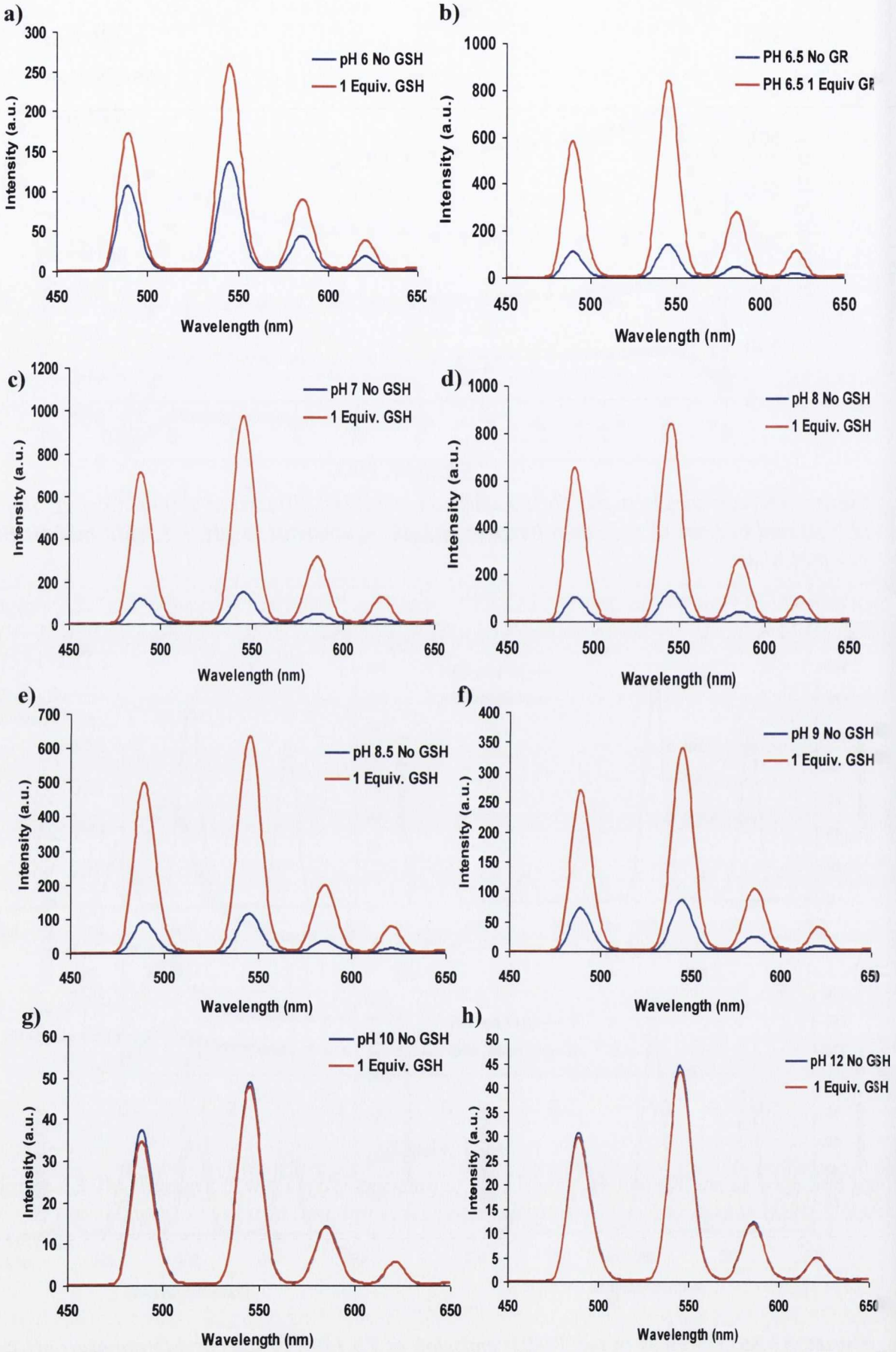

Figure A3.8b: *Changes in the Tb(III) emission of* ***Tb.110*** *(10 μM) at 545 nm at a) pH 6, b) pH 6.5, c) pH 7, d) pH 8, e) pH 8.5, f) pH 9, g) pH 10 and h) pH 12 upon the addition of 1 equivalent of GSH.*

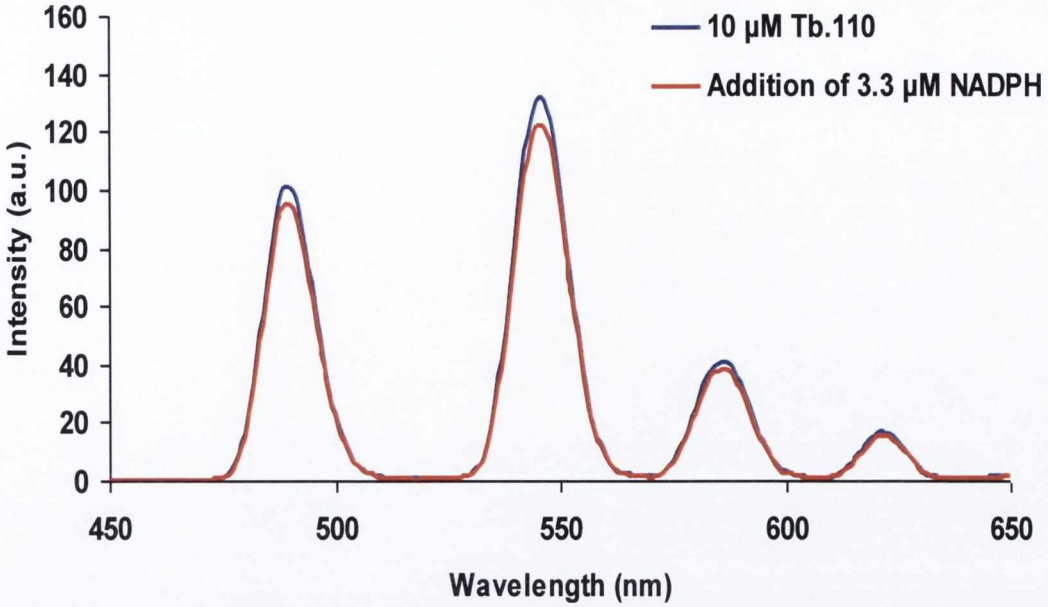

Figure A3.9: *The Tb(III) luminescence response of* ***Tb.110*** *(10 µM) recorded in an aqueous buffer pH 7.4 (20 mM HEPES, 135 mM KCl) in the presence of 3.3 µM NADPH.*

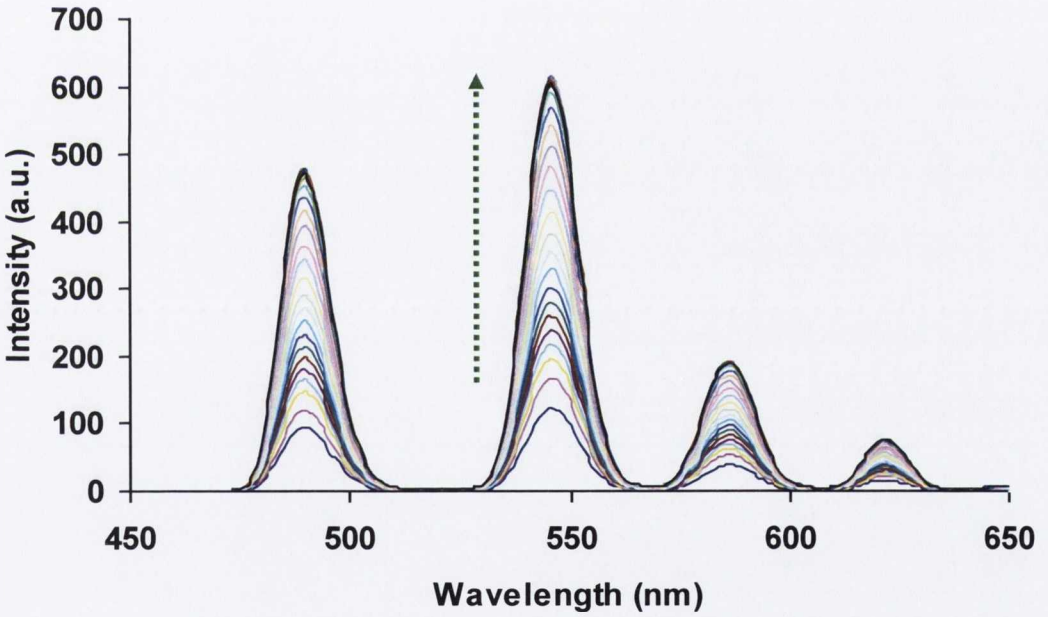

Figure A3.10a: Overall *luminescence response of* ***Tb.110*** *(10 µM) as a result of the enzymatic conversion of GSSG to its reduced GSH form using the enzyme GR (4.93 nM) and NADPH (3.3 µM). All enzymatic titrations were carried out in aqueous pH 7.4 buffered solutions (0.1 M TRIS, 135 mM KCl) at 37 °C.*

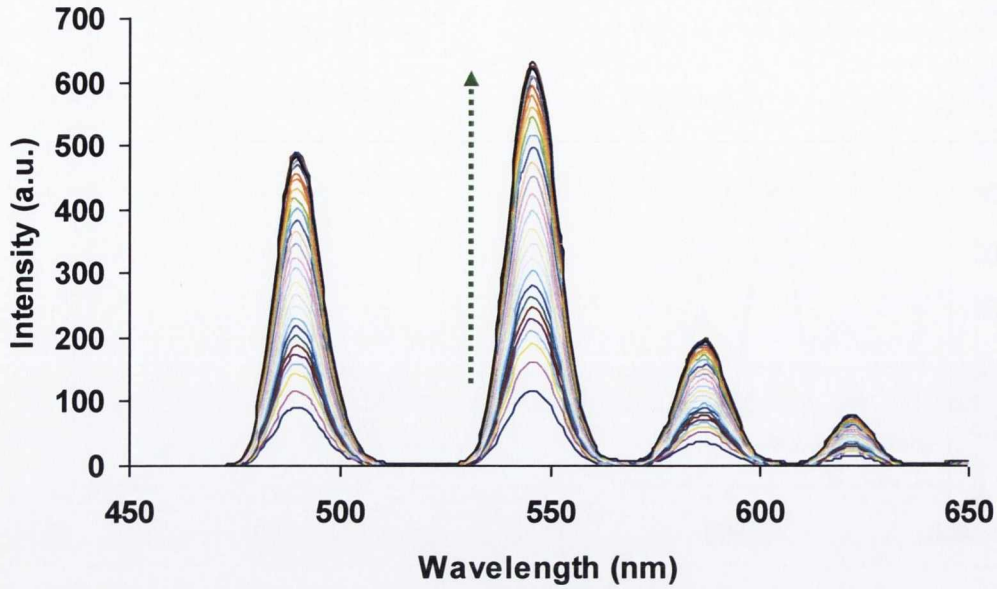

Figure A3.10b: Overall *luminescence response of* ***Tb.110*** *(10 μM) as a result of the enzymatic conversion of GSSG to its reduced GSH form using the enzyme GR (4.93 nM) and NADPH (6.6 μM). All enzymatic titrations were carried out in aqueous pH 7.4 buffered solutions (0.1 M TRIS, 135 mM KCl) at 37 °C.*

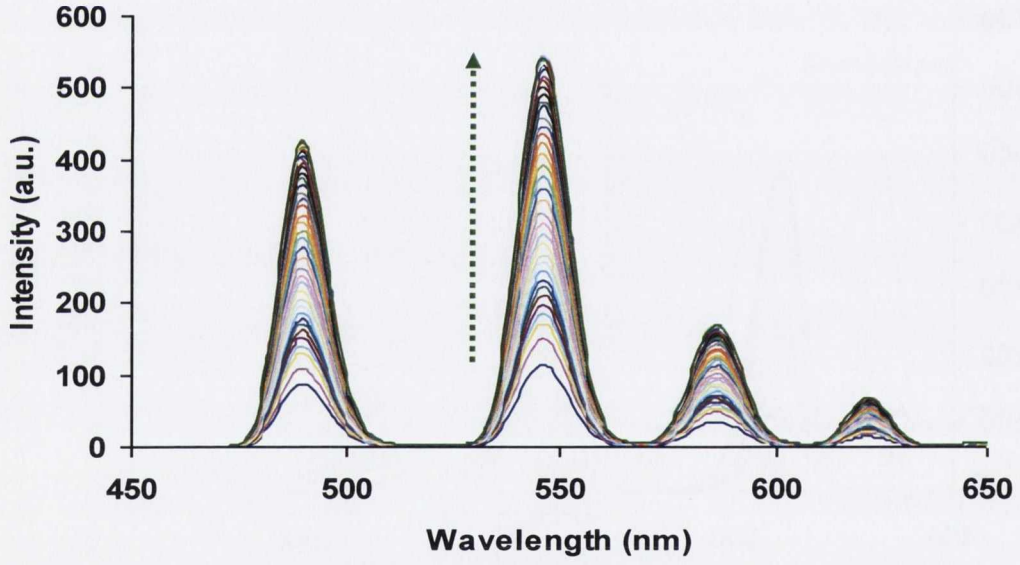

Figure A3.10c: Overall *luminescence response of* ***Tb.110*** *(10 μM) as a result of the enzymatic conversion of GSSG to its reduced GSH form using the enzyme GR (4.93 nM) and NADPH (10 μM). All enzymatic titrations were carried out in aqueous pH 7.4 buffered solutions (0.1 M TRIS, 135 mM KCl) at 37 °C.*

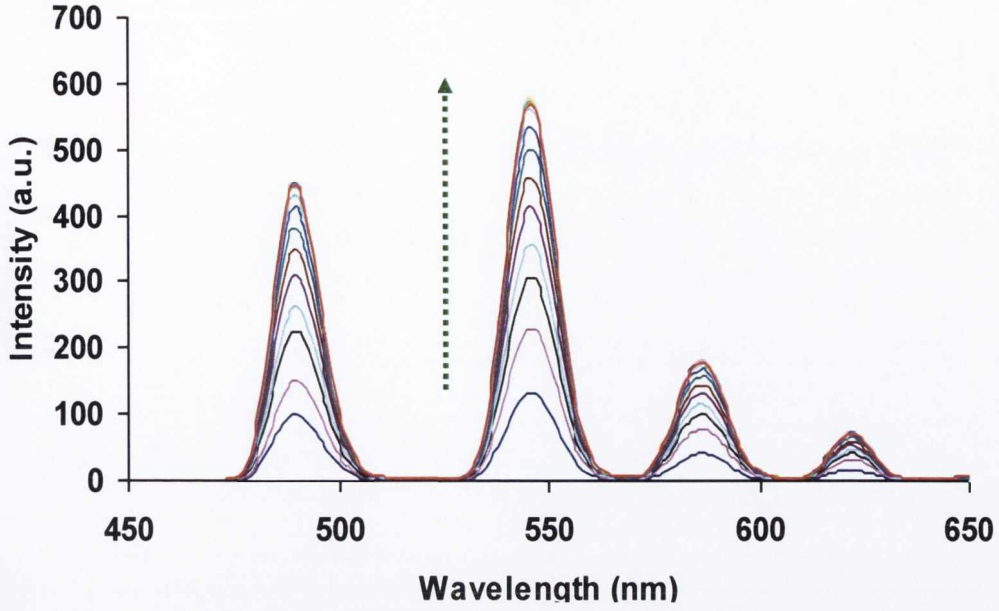

Figure A3.11a: *Luminescence response of* ***Tb.110*** *(10 μM) as a result of the enzymatic conversion of GSSG to its reduced GSH form using NADPH (3.3 μM) and GR (9.86 nM). All enzymatic titrations were carried out in aqueous pH 7.4 buffered solutions (0.1 M TRIS, 135 mM KCl) at 37 °C.*

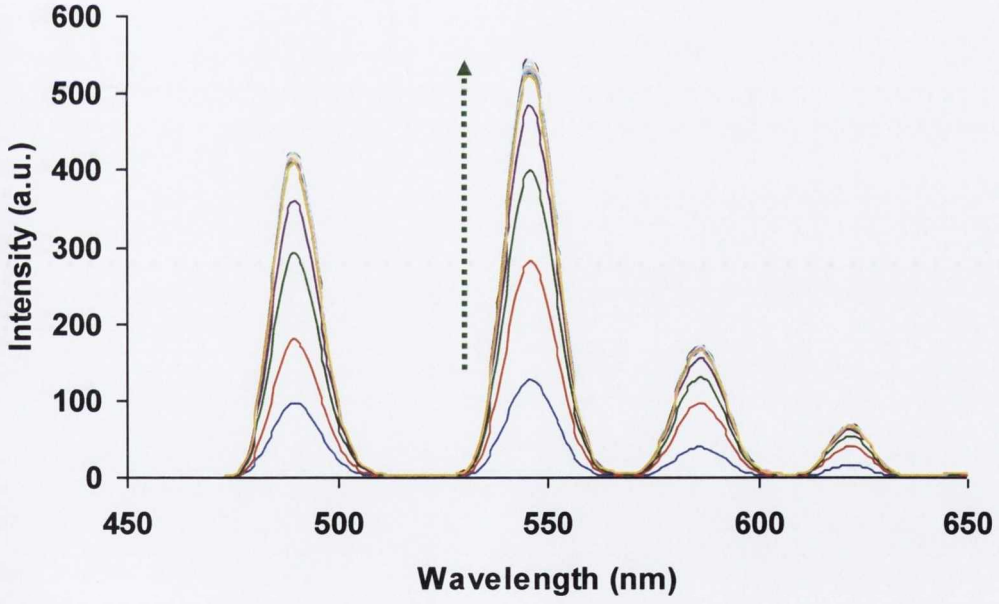

Figure A3.11b: *Luminescence response of* ***Tb.110*** *(10 μM) as a result of the enzymatic conversion of GSSG to its reduced GSH form using NADPH (3.3 μM) and GR (19.72 nM). All enzymatic titrations were carried out in aqueous pH 7.4 buffered solutions (0.1 M TRIS, 135 mM KCl) at 37 °C.*

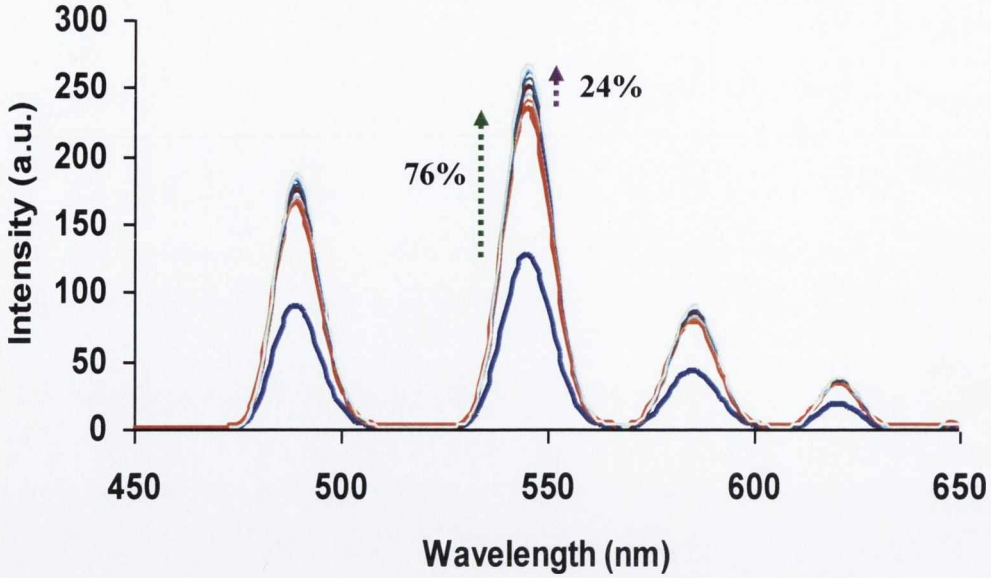

Figure A3.12: *Overall luminescence response of Tb.110 (40 μM) in a 10%:90% (GSSG:GSH) solution mixture. The initial GSH response was recorded followed by addition of 3.3 μM NADPH and 4.93 nM glutathione reductase to allow for the enzymatic conversion of the GSSG in solution to its reduced GSH form. All enzymatic titrations were carried out in aqueous pH 7.4 buffered solutions (0.1 M TRIS, 135 mM KCl) at 37 °C. PMT = 400V.*

Publications